Astrophysics and Space Science Proceedings 36

Dimitris Stamatellos
Simon Goodwin
Derek Ward-Thompson *Editors*

The Labyrinth of Star Formation

Springer

Astrophysics and Space Science Proceedings
Volume 36

For further volumes:
http://www.springer.com/series/7395

Dimitris Stamatellos • Simon Goodwin
Derek Ward-Thompson
Editors

The Labyrinth of Star Formation

Conference Dedicated to Prof. Anthony Whitworth

Springer

Editors
Dimitris Stamatellos
Jeremiah Horrocks Institute
for Mathematics, Physics and Astronomy
University of Central Lancashire, UK

Simon Goodwin
Department of Physics and Astronomy
University of Sheffield
Sheffield, UK

Derek Ward-Thompson
Jeremiah Horrocks Institute
for Mathematics, Physics and Astronomy
University of Central Lancashire
Preston, UK

ISSN 1570-6591
ISBN 978-3-319-03040-1
DOI 10.1007/978-3-319-03041-8
ISSN 1570-6605 (electronic)
ISBN 978-3-319-03041-8 (eBook)
Springer Cham Heidelberg New York Dordrecht London

Library of Congress Control Number: 2014934573

Printed on acid-free paper

Springer is part of Springer Science+Business Media (www.springer.com)

This book is dedicated to Ant from all his friends. We wish him all the best in his future quests in Astrophysics and in life.

Preface

The idea for organising a conference to celebrate Ant's contributions to star formation has been floating around for a few years. We considered various locations and we finally chose Crete inspired by Ant's declared love for the place. The meeting took place near Chania at the Orthodox Academy of Crete, a conference centre next to a seventeenth-century monastery. It was attended by around 120 participants from all over the world, many of which have interacted with Ant in the past.

The conference theme was chosen to reflect Ant's interests in star formation and computational astrophysics. We covered many topics: low-mass star formation, young circumstellar discs, computational methods, triggered star formation, the stellar initial mass function, high-mass star formation, and stellar clusters. Each chapter starts with a review contribution that is followed by papers focusing on recent theoretical and observational work.

We would like to thank the members of the SOC (Philippe André, Matthew Bate, Ian Bonnell, Cathie Clarke, Patrick Hennebelle, Shu-ichiro Inutsuka, Ralf Klessen, Pavel Kroupa, Mark Krumholz, Mark McCaughrean, Jan Palous, Hans Zinnecker) and LOC (Annabel Cartwright Thomas Bisbas, David Hubber, Spyros Kitsionas, Steffi Walch, Richard Wünsch) for their enthusiasm to contribute to the meeting.

We also thank Spyros Kitsionas for his help with the conference proceedings, David Nutter for the conference photo, Samantha Emmot and the Cardiff University Conference Centre, and Richard Frewin for his support with the conference webpage. Finally, we would like to thank Emmanuela Larentzakis and the staff at the Orthodox Academy of Crete for their help in organising a wonderful conference.

It was amazing to hear and discuss new ideas, and argue over older ideas in a relaxing environment overlooking the Aegean sea. We hope that new theories and observations using new facilities will soon draw a more complete picture of star formation.

Crete, Greece
June 2012

Dimitris Stamatellos
Simon Goodwin
Derek Ward-Thompson

Contents

Contributors

David M. Acreman Department of Physics and Astronomy, University of Exeter, Exeter, UK

Nancy Ageorges Max-Planck-Institut für extraterrestrische Physik, Garching, Germany

J.M. Alcalá INAF-Capodimonte, Napoli, Italy

L. Allen National Optical Astronomy Observatory, Tucson, AZ, USA

Catarina Alves de Oliveira European Space Astronomy Centre (ESA), Villanueva de la Cañada, Madrid, Spain

Philippe André Laboratoire d'Astrophysique (AIM) de Paris-Saclay, CEA/DSM-CNRS-Université Paris Diderot, IRFU/Service d'Astrophysique, CEA Saclay, Orme des Merisiers, Gif-sur-Yvette, France

Doris Arzoumanian Laboratoire d'Astrophysique (AIM) de Paris-Saclay, CEA/DSM-CNRS-Université Paris Diderot, IRFU/Service d'Astrophysique, CEA Saclay, Orme des Merisiers, Gif-sur-Yvette, France

IAS, CNRS (UMR 8617), Université Paris-Sud; Orsay, France

A. Bacmann Universite Joseph Fourier/CNRS, Institut de Planetologie et d'Astrophysique de Grenoble (IPAG) UMR, Grenoble, France

Adrian J. Baddeley School of Mathematics and Statistics, University of Western Australia, Crawley, Australia

J. Bally Center for Astrophysics and Space Astronomy, University of Colorado, Boulder, CO, USA

Robi Banerjee Hamburger Sternwarte, Hamburg, Germany

David Barrado y Navacués Centro de Astrobiologa (INTA-CSIC), Villanueva de la Cañada, Spain

Shantanu Basu Department of Physics and Astronomy, The University of Western Ontario, London, Canada

Matthew R. Bate School of Physics and Astronomy, University of Exeter, Exeter, UK

Cara Battersby Harvard-Smithsonian Center for Astrophysics, Cambridge, MA, USA

Giacomo Beccari European Southern Observatory, Garching bei München, Germany

Space Science Department, ESA, Noordwijk, The Netherlands

Space Telescope Science Institute, Baltimore, MD, USA

INAF-CT, Osservatorio Astrofisico di Catania, Catania, Italy

Supernova Ltd, Virgin Gorda, British Virgin Islands

A. Belloche Max-Planck Institut für Radiodastronomie, Bonn, Germany

Milena Benedettini INAF-IAPS, Roma, Italy

Henrik Beuther Max-Planck-Institut für Astronomie, Heidelberg, Germany

Arjan Bik Max-Planck-Institut für Astronomie, Heidelberg, Germany

Thomas G. Bisbas Department of Physics and Astronomy, University College London, London, UK

P. Boley Max-Planck-Institut für Astronomie, Heidelberg, Germany

Ian Bonnell School of Physics and Astronomy, University of St Andrews, North Haugh, Scotland, UK

Sylvain Bontemps University of Bordeaux/CNRS, LAB, Floirac, France

Steve Boudreault Instituto de Astrofísica de Canarias (IAC), La Laguna, Tenerife, Spain

Departamento de Astrofísica, Universidad de La Laguna (ULL), E-38205 La Laguna, Tenerife, Spain

Tyler L. Bourke SAO-Harvard-Smithsonian Center for Astrophysics, Cambridge, MA, USA

Jerôme Bouvier UJF-Grenoble 1/CNRS-INSU, IPAG UMR5274, Grenoble, France

Herve Bouy CAB-LAEFF, Villanueva de la Cañada, Madrid, Spain

Wolfgang Brandner Max-Planck-Institut für Astronomie, Heidelberg, Germany

Eli Bressert European Southern Observatory, Garching bei München, Germany

Crystal L. Brogan National Radio Astronomy Observatory, Charlottesville, VA, USA

Leonardo Bronfman Universidad de Chile, Santiago, Chile

Patrick S. Broos Department of Astronomy & Astrophysics, Pennsylvania State University, University Park, PA, USA

Andreas Burkert Universitäts-Sternwarte München, Ludwig-Maximilians-Universität, München, Germany

Heather A. Busk Department of Astronomy & Astrophysics, Pennsylvania State University, University Park, PA, USA

S. Cabrit Observatoire de Paris, LERMA, Paris, France

Annabel Cartwright Cardiff School of Physics and Astronomy, Cardiff University, Cardiff, UK

CALYPSO Collaboration

A.H. Cerqueira Laboratório de Astrofísica Teórica e Observacional, DCET-UESC, Rodovia Ilhéus-Itabuna, Bahia, Brazil

Seung-Hoon Cha Department of Physics and Astronomy, Texas A&M University-Commerce, Commerce, TX, USA

Chandra Cygnus OB2 Team

Tao-Chung Ching National Tsing Hua University, Hsinchu, Taiwan

Antonio Chrysostomou Joint Astronomy Centre, Hilo, HI, USA

School of Physics, Astronomy and Mathematics, University of Hertfordshire, Hatfield, Hertfordshire, UK

Ed Churchwell Department of Astronomy, University of Wisconsin-Madison, Madison, WI, USA

Andrea Ciardi Laboratoire de Radioastronomie, LERMA, Observatoire de Paris, École Normale Supérieure, Université Pierre et Marie Curie (UMR 8112 CNRS), Paris Cedex, France

Cathie J. Clarke Institute of Astronomy, Cambridge, UK

C. Codella INAF-Osservatorio Astrofisico di Arcetri, Firenze, Italy

Benoît Commerçon Ecole normale supérieure, Paris, France

Yanett Contreras Universidad de Chile, Santiago, Chile

Max-Planck-Institut für Radioastronomie, Bonn, Germany

Michiel Cottaar Institute for Astronomy, ETH Zurich, Zurich, Switzerland

E. Covino INAF-Capodimonte, Napoli, Italy

Timea Csengeri Max-Planck-Institut für Radioastronomie, Bonn, Germany

Claudia J. Cyganowski NSF Astronomy and Astrophysics Postdoctoral Fellow, Harvard-Smithsonian Center for Astrophysics, Cambridge, MA, USA

James E. Dale Excellence Cluster 'Universe', Garching, Germany

N.R. Deacon Max-Planck-Institute für Astronomie, Heidelberg, Germany

Lise Deharveng Laboratoire d'Astrophysique de Marseille, Marseille, France

Guido De Marchi Space Science Department, ESA, Noordwijk, The Netherlands

Sami Dib Blackett Laboratory, Imperial College London, London, UK

Clare L. Dobbs University of Exeter, Exeter, UK

Andrew E. Dolphin Raytheon Company, Tucson, AZ, USA

Horacio Dottori Instituto de Física, Universidade Federal do Rio Grande do Sul, Porto Alegre, Brazil

Jeremy J. Drake SAO-Harvard-Smithsonian Center for Astrophysics, Cambridge, MA, USA

Janet E. Drew CAR/STRI, University of Hertfordshire, Hatfield, UK

Ana Duarte-Cabral University of Bordeaux/CNRS, LAB, UMR 5804, Floirac, France

School of Physics, University of Exeter, Exeter, UK

Gaspard Duchêne Astronomy Department, University of California, Berkeley, CA, USA

Barbara Ercolano Excellence Cluster 'Universe', Garching, Germany

A. Esquivel Instituto de Ciencias Nucleares, Universidad Nacional Autónoma de México, México

Diego Falceta-Gonçalves Escola de Artes, Ciências e Humanidades, Universidade de São Paulo, São Paulo, Brazil

Eric D. Feigelson Department of Astronomy & Astrophysics, Pennsylvania State University, University Park, PA, USA

Beatriz Fernandes Universidade de São Paulo, IAG, São Paulo, Brazil

Katharina Fierlinger Max-Planck-Institut für extraterrestrische Physik, Garching, Germany

Francesco Fontani INAF-Arcetri, L.go E. Fermi 5, Firenze, Italy

J. Forbrich SAO-Harvard-Smithsonian Center for Astrophysics, Cambridge, MA, USA

F. Fraternali Department of Physics and Astronomy, University of Bologna, Bologna, Italy

Yuri I. Fujii Nagoya University, Furo-cho, Chikusa-ku, Nagoya, Aichi, Japan

Gary A. Fuller Jodrell Bank Centre for Astrophysics, School of Physics and Astronomy, University of Manchester, Manchester, UK

Ray S. Furuya Subaru Telescope, National Astronomical Observatory of Japan, Hilo, HI, USA

Current address: Center for General Education, University of Tokushima, Minami Jousanjima, Tokushima, Japan

Marc Gagné Department of Geology & Astronomy, West Chester University, West Chester, PA, USA

D. Garcia-Alvarez Instituto de Astrofísica de Canarias, La Laguna, Tenerife, Spain

A. Gatto Max-Planck-Institut für Astrophysik, Garching, Germany

Mario Gennaro Max-Planck-Institut für Astronomie, Heidelberg, Germany

Thomas Gerner Max-Planck-Institut für Astronomie, Heidelberg, Germany

Konstantin V. Getman Department of Astronomy & Astrophysics, Pennsylvania State University, University Park, PA, USA

Adam Ginsburg Center for Astrophysics and Space Astronomy, University of Colorado, Boulder, CO, USA

Philipp Girichidis Max-Planck-Institut für Astrophysik, Garching, Germany

Simon C.O. Glover Zentrum für Astronomie der Universität Heidelberg, Institut für Theoretische Astrophysik, Heidelberg, Germany

Simon Goodwin Department of Physics and Astronomy, University of Sheffield, Sheffield, UK

Dimitrios A. Gouliermis Zentrum für Astronomie der Universität Heidelberg, Institut für Theoretische Astrophysik, Heidelberg, Germany

Jane Gregorio-Hetem Universidade de São Paulo, IAG, São Paulo, Brazil

Matthias Gritschneder Astronomy and Astrophysics Department, University of California, Santa Cruz, CA, USA

Preben Grosbøl European Southern Observatory, Garching, Germany

Mario Giuseppe Guarcello Harvard-Smithsonian Center for Astrophysics, Cambridge, MA, USA

F. Gueth IRAM, Saint Martin d'Heres, France

H.M. Günther SAO-Harvard-Smithsonian Center for Astrophysics, Cambridge, MA, USA

Rolf Güsten Max-Planck-Institut für Radioastronomie, Bonn, Germany

R.A. Gutermuth Department of Astronomy, University of Massachusetts, Amherst, MA, USA

Harvard-Smithsonian Center for Astrophysics, Cambridge, MA, USA

N.C. Hambly Scottish Universities Physics Alliance (SUPA), Institute for Astronomy, School of Physics & Astronomy, University of Edinburgh, Royal Observatory, Blackford Hill, Edinburgh, UK

Tim J. Harries Department of Physics and Astronomy, University of Exeter, Exeter, UK

L. Hartman University of Michigan, Ann Arbor, MI, USA

Thomas J. Haworth Department of Physics and Astronomy, University of Exeter, Exeter, UK

Fabian Heitsch Department of Physics & Astronomy, University of North Carolina Chapel Hill, NC, USA

Patrick Hennebelle Laboratoire AIM, Paris-Saclay, CEA/IRFU/SAp – CNRS – Université Paris Diderot, Gif-sur-Yvette, France

Martin Hennemann Laboratoire d'Astrophysique (AIM) de Paris-Saclay, CEA/DSM-CNRS/INSU-Université Paris Diderot, IRFU/Service d'Astrophysique, CEA Saclay, Gif-sur-Yvette, France

Thomas Henning Max-Planck-Institut für Astronomie, Heidelberg, Germany

Herschel Gould Belt Survey Consortium http://www.herschel.fr/cea/gouldbelt/en/index.php

Herschel Gould Belt Team http://gouldbelt-herschel.cea.fr

Tracey Hill Laboratoire d'Astrophysique (AIM) de Paris-Saclay, CEA/DSM-CNRS-Université Paris Diderot, IRFU/Service d'Astrophysique, CEA Saclay, Orme des Merisiers, Gif-sur-Yvette, France

HOBYS Consortium http://www.herschel.fr/cea/hobys/en/

Katy Holman Cardiff School of Physics and Astronomy, Cardiff University, Cardiff, UK

J.L. Hora Harvard-Smithsonian Center for Astrophysics, Cambridge, MA, USA

David Anthony Hubber Technical University Munich, Excellence Cluster Universe, Garching, Germany

Department of Physics, University Observatory Munich, Ludwig-Maximilians-University Munich, Munich, Germany

Núria Huélamo CAB-LAEFF, Villanueva de la Cañada, Madrid, Spain

Todd R. Hunter National Radio Astronomy Observatory, Charlottesville, VA, USA

Tsuyoshi Inoue Aoyama Gakuin University, Fuchinobe, Sagamihara-city, Kanagawa, Japan

Shu-ichiro Inutsuka Department of Physics, Graduate School of Science, Nagoya University, Furo-cho, Chikusa-ku, Nagoya, Japan

JCMT Gould Belt Survey Consortium http://www.jach.hawaii.edu/JCMT/surveys/gb/

Katharine G. Johnston Max-Planck-Institut für Astronomie, Heidelberg, Germany

Marc Joos Laboratoire de Radioastronomie, LERMA, Observatoire de Paris, École Normale Supérieure, Université Pierre et Marie Curie (UMR 8112 CNRS), Paris Cedex, France

V. Kashyap Harvard-Smithsonian Center for Astrophysics, Cambridge, MA, USA

Akimasa Kataoka National Astronomical Observatory of Japan, Mitaka, Tokyo, Japan

Department of Astronomical Science, Graduate University for Advanced Studies, Mitaka, Tokyo, Japan

E. Keto Center for Astrophysics, Cambridge, MA, USA

Robert R. King School of Physics, University of Exeter, Exeter, UK

Jason Kirk Jeremiah Horrocks Institute, University of Central Lancashire, Preston, Lancashire, UK

Yoshimi Kitamura Institute of Space and Astronautical Science, Japan Aerospace Exploration Agency, Sagamihara, Kanagawa, Japan

Hubert Klahr Max-Planck-Institut für Astronomie, Heidelberg, Germany

Ralf S. Klessen Zentrum für Astronomie der Universität Heidelberg, Institut für Theoretische Astrophysik, Heidelberg, Germany

Christine Koepferl Universitäts-Sternwarte München, München, Germany

Vera Könyves Laboratoire d'Astrophysique (AIM) de Paris-Saclay, CEA/DSM-CNRS-Université Paris Diderot, IRFU/Service d'Astrophysique, CEA Saclay, Orme des Merisiers, Gif-sur-Yvette, France

Institut d'Astrophysique Spatiale, UMR8617, CNRS/Université Paris-Sud 11, Orsay, France

Pavel Kroupa Argelander-Institute for Astronomy, University of Bonn, Bonn, Germany

J.M. Diederik Kruijssen Max-Planck-Institut für Astrophysik, Garching, Germany

Natalia Kudryavtseva Max-Planck-Institut für Astronomie, Heidelberg, Germany

Michael A. Kuhn Department of Astronomy & Astrophysics, Pennsylvania State University, University Park, PA, USA

Rolf Kuiper Jet Propulsion Laboratory, California Institute of Technology, Pasadena, CA, USA

Shih-Ping Lai National Tsing Hua University, Hsinchu, Taiwan

Douglas N.C. Lin Astronomy and Astrophysics Department, University of California, Santa Cruz, CA, USA

Hendrik Linz Max-Planck-Institut für Astronomie, Heidelberg, Germany

Nicolas Lodieu Instituto de Astrofísica de Canarias (IAC), La Laguna, Tenerife, Spain

Departamento de Astrofísica, Universidad de La Laguna (ULL), La Laguna, Tenerife, Spain

Oliver Lomax Cardiff School of Physics and Astronomy, Cardiff University, Cardiff, UK

Steven N. Longmore European Southern Observatory, Garching bei München, Germany

Veronica Lora Astronomisches Rechen-Institut, Heidelberg, Germany

Fabien Louvet Laboratoire d'Astrophysique (AIM) de Paris-Saclay, CEA/DSM-CNRS-Université Paris Diderot, IRFU/Service d'Astrophysique, CEA Saclay, Orme des Merisiers, Gif-sur-Yvette, France

Kevin L. Luhman Department of Astronomy & Astrophysics, Pennsylvania State University, University Park, PA, USA

H. Lux School of Physics and Astronomy, University of Nottingham, University Park, Nottingham, United Kingdom

Masahiro N. Machida Department of Earth and Planetary Sciences, Kyushu University, Fukuoka, Japan

Carlo Felice Manara ESO-Garching, Garching bei München, Germany

S. Maret Universite Joseph Fourier/CNRS, Institut de Planetologie et d'Astrophysique de Grenoble (IPAG) UMR 5274, Grenoble, France

F. Marinacci Heidelberg Institute for Theoretical Studies, Heidelberg, Germany

Thomas Maschberger Institut de Planétologie et d'Astrophysique de Grenoble, Grenoble Cédex 9, France

Anaëlle J. Maury Harvard-Smithsonian Center for Astrophysics, Cambridge, MA, USA

Andrew D. McLeod Astrophysics Group, School of Physics, University of Exeter, Exeter, UK

S.T. Megeath Ritter Observatory, Department of Physics and Astronomy, University of Toledo, Toledo, OH, USA

Alexander Men'shchikov Laboratoire d'Astrophysique (AIM) de Paris-Saclay, CEA/DSM-CNRS-Université Paris Diderot, IRFU/Service d'Astrophysique, CEA Saclay, Orme des Merisiers, Gif-sur-Yvette, France

Karl M. Menten Max-Planck-Institut für Radioastronomie, Bonn, Germany

Michael R. Meyer Institute for Astronomy, ETH Zurich, Zurich, Switzerland

G. Micela INAF – Osservatorio Astronomico di Palermo, Palermo, Italy

Faviola Z. Molina Zentrum für Astronomie der Universität Heidelberg, Institut für Theoretische Astrophysik, Heidelberg, Germany

Member of the International Max Planck Research School for Astronomy and Cosmic Physics at the University of Heidelberg (IMPRS-HD), Heidelberg Graduate School of Fundamental Physics (HGSFP), Heidelberg, Germany

Esteban F.E. Morales Max-Planck-Institute for Astronomy, Heidelberg, Germany

Max-Planck-Institut für Radioastronomie, Bonn, Germany

Estelle Moraux UJF-Grenoble 1/CNRS-INSU, IPAG UMR5274, Grenoble, France

Frédérique Motte Laboratoire d'Astrophysique (AIM) de Paris-Saclay, CEA/DSM-CNRS/INSU-Université Paris Diderot, IRFU/Service d'Astrophysique, CEA Saclay, Gif-sur-Yvette, France

Paola Mucciarelli Universitäts-Sternwarte München, Ludwig-Maximilians-Universität, München, Germany

P. Myers SAO-Harvard Center for Astrophysics, Cambridge, MA, USA

MYStIX Collaboration http://astro.psu.edu/mystix

A. Natta INAF-Arcetri, Firenze, Italy

Tim Naylor School of Physics, University of Exeter, Exeter, UK

Judith Ngoumou Universitäts-Sternwarte München, Ludwig-Maximilians-Universität, München, Germany

Quang Nguyen-Luong Canadian Institute for Theoretical Astrophysics, Toronto, Canada

Evangelia Ntormousi Universitäts-Sternwarte München, Ludwig-Maximilians-Universität, München, Germany

David Nutter School of Physics and Astronomy, Cardiff University, Cardiff, UK

M. Sally Oey Astronomy Department, University of Michigan, Ann Arbor, MI, USA

Stella S.R. Offner Yale University, New Haven, CT, USA

Satoshi Okuzumi Department of Earth and Planetary Sciences, Tokyo Institute of Technology, Meguro-ku, Tokyo, Japan

J.M. Oliveira School of Physical & Geographical Sciences, Lennard-Jones Laboratories, Keele University, Staffordshire, UK

Volker Ossenkopf I. Physikalisches Institut der Universität zu Köln, Köln, Germany

James E. Owen Canadian Institute for Theoretical Astrophysics, Toronto, Canada

Roberta Paladini NASA Herschel Science Center, California Institute of Technology, Pasadena, CA, USA

Pedro Palmeirim Laboratoire d'Astrophysique (AIM) de Paris-Saclay, CEA/DSM-CNRS-Université Paris Diderot, IRFU/Service d'Astrophysique, CEA Saclay, Orme des Merisiers, Gif-sur-Yvette, France

Jan Palouš Astronomical Institute, Academy of Sciences of the Czech Republic, Prague 4, Czech Republic

Nino Panagia Space Telescope Science Institute, Baltimore, MD, USA

INAF-CT, Osservatorio Astrofisico di Catania, Catania, Italy

Supernova Ltd, Virgin Gorda, British Virgin Islands

Richard J. Parker Institute for Astronomy, ETH Zürich, Zürich, Switzerland

Anna Pasquali Astronomisches Rechen Institut, Zentrum für Astronomie der Universität Heidelberg, Heidelberg, Germany

Stephanie Pekruhl Universitäts-Sternwarte München, Ludwig-Maximilians-Universität, München, Germany

Tzu-Cheng Peng Max-Planck-Institut für Radioastronomie (MPIfR), Bonn, Germany

Université de Bordeaux, Observatoire Aquitain des Sciences de l'Univers, Floirac Cedex, France

Nicolas Peretto Laboratoire d'Astrophysique (AIM) de Paris-Saclay, CEA/DSM-CNRS-Université Paris Diderot, IRFU/Service d'Astrophysique, CEA Saclay, Orme des Merisiers, Gif-sur-Yvette, France

School of Physics & Astronomy, Cardiff University, The Parade, Cardiff, UK

Ignazio Pillitteri SAO-Harvard Center for Astrophysics, Cambridge, MA, USA

J.L. Pipher University of Rochester, Rochester, NY, USA

Danae Polychroni Faculty of Physics, Department of Astronomy, Astrophysics and Mechanics, University of Athens, Panepistimiopolis, Athens, Greece

Matthew S. Povich Department of Astronomy & Astrophysics, Pennsylvania State University, University Park, PA, USA

Thomas Preibisch Universitäts-Sternwarte München, Ludwig-Maximilians-Universität, München, Germany

Daniel J. Price Monash Centre for Astrophysics (MoCA), School of Mathematical Sciences, Monash University, Clayton, Victoria, Australia

Ralph E. Pudritz Department of Physics and Astronomy, McMaster University, Hamilton, ON, Canada

Ciara Quinn Cardiff University, Cardiff, UK

A.C. Raga Instituto de Ciencias Nucleares, Universidad Nacional Autónoma de México, México

S. Randich INAF-Arcetri, Firenze, Italy

J. Read University of Surrey, Guildford, Surrey, United Kingdom

L. Rebull CALTECH, Pasadena, CA, USA

Maddalena Reggiani Institute for Astronomy, ETH Zurich, Zurich, Switzerland

Ken Rice Institute for Astronomy, The University of Edinburgh, The Royal Observatory, Blackford Hill, Edinburgh, UK

E. Rigliaco University of Arizona, Tucson, AZ, USA

Thomas P. Robitaille Max Planck Institut für Astronomie, Heidelberg, Germany

Boyke Rochau Max-Planck-Institut für Astronomie, Heidelberg, Germany

Javier A. Rodón European Souther Observatory, Santiago, Chile

Martino Romaniello European Southern Observatory, Garching, Germany

Kazi L.J. Rygl INAF-IAPS, Rome, Italy

Elena Sabbi Space Telescope Science Institute, Baltimore, MD, USA

Kazuya Saigo NAOJ Chile Observatory, National Astronomical Observatory of Japan, Mitaka, Tokyo, Japan

Anna M.M. Scaife Physics & Astronomy, University of Southampton, Highfield, Southampton, UK

Eugenio Schisano INAF-IAPS, Roma, Italy

Stefan Schmeja Zentrum für Astronomie der Universität Heidelberg, Astronomisches Rechen-Institut, Heidelberg, Germany

Nicola Schneider Laboratoire d'Astrophysique (AIM) de Paris-Saclay, CEA/DSM-CNRS/INSU-Université Paris Diderot, IRFU/Service d'Astrophysique, CEA Saclay, Orme des Merisiers, Gif-sur-Yvette, France

Laboratoire d'Astrophysique de Bordeaux, Floirac cedex, France

Frédéric Schuller Max-Planck-Institut für Radioastronomie, Bonn, Germany

European Southern Observatory, Santiago, Chile

S. Sciortino INAF – Osservatorio Astronomico di Palermo, Palermo, Italy

Walter Seifert Landessternwarte Königstuhl, Zentrum für Astronomie Heidelberg, Heidelberg, Germany

Daniel Seifried Hamburger Sternwarte, University of Hamburg, Hamburg, Germany

Dmitry Semenov Max-Planck-Institut für Astronomie, Heidelberg, Germany

R. Shetty Zentrum für Astronomie der Universität Heidelberg, Institut für Theoretische Astrophysik, Heidelberg, Germany

Hiroko Shinnaga Subaru Telescope, National Astronomical Observatory of Japan, Hilo, HI, USA

Rowan J. Smith ZAH/ITA, University of Heidelberg, Heidelberg, Germany

SOXS Collaboration

Loredana Spezzi European Southern Observatory, Garching bei München, Germany

B. Spitzbart SAO-Harvard-Smithsonian Center for Astrophysics, Cambridge, MA, USA

Dimitris Stamatellos Jeremiah Horrocks Institute for Mathematics, Physics and Astronomy, University of Central Lancashire, UK

J. Stauffer CALTECH, Pasadena, CA, USA

B. Stelzer INAF-Palermo, Palermo, Italy

Andrea Stolte Argelander Institut für Astronomie, Bonn, Germany

L. Testi ESO-Garching, Garching bei München, Germany

Jesús A. Toalá Instituto de Astrofísica de Andalucía, CSIC, Granada, Spain

Kengo Tomida Department of Astrophysical Sciences, Princeton University, Princeton, NJ, USA

Kohji Tomisaka National Astronomical Observatory of Japan, Mitaka, Tokyo, Japan

Department of Astronomical Science, Graduate University for Advanced Studies, Mitaka, Tokyo, Japan

Leisa K. Townsley Department of Astronomy & Astrophysics, Pennsylvania State University, University Park, PA, USA

Terrence S. Tricco Monash Centre for Astrophysics (MoCA), School of Mathematical Sciences, Monash University, Clayton, Victoria, Australia

Yusuke Tsukamoto Nagoya University, Nagoya, Japan

James S. Urquhart Max-Planck-Institut für Radioastronomie, Bonn, Germany

R. van Boekel Max-Planck-Institut für Astronomie, Heidelberg, Germany

M.J. Vasconcelos Laboratório de Astrofísica Teórica e Observacional, DCET-UESC, Rodovia Ilhéus-Itabuna, Bahia, Brazil

Tatiana Vasyunina University of Virginia, Charlottesville, VA, USA

Enrique Vázquez-Semadeni Centro de Radioastronomía y Astrofísica, Universidad Nacional Autónoma de México, Morelia, Michoacán, México

Eduard Vorobyov Department of Astrophysics, The University of Vienna, Vienna, Austria

Research Institute of Physics, Southern Federal University, Rostov-on-Don, Russia

Stefanie K. Walch Max-Planck-Institut für Astrophysics, Garching bei München, Germany

Malcolm Walmsley Osservatorio Astrofisico di Arcetri, Firenze, Italy

F. Walter SAO-Harvard Center for Astrophysics, Cambridge, MA, USA

Yuan Wang Purple Mountain Observatory, Chinese Academy of Sciences, Nanjing, People's Republic of China

Derek Ward-Thompson Jeremiah Horrocks Institute for Mathematics, Physics and Astronomy, University of Central Lancashire, Preston, UK

Barbara A. Whitney Department of Astronomy, University of Wisconsin-Madison, Madison, WI, USA

Anthony Peter Whitworth Cardiff School of Physics and Astronomy, Cardiff University, Cardiff, UK

Marion Wienen Max-Planck-Institut für Radioastronomie, Bonn, Germany

Elaine Winston Research and Scientific Support Division, European Space Agency, Noordwijk, The Netherlands

S.J. Wolk SAO-Harvard Center for Astrophysics, Cambridge, MA, USA

K. Wood School of Physics & Astronomy, University of St Andrews, St Andrews, UK

Nicholas J. Wright SAO-Harvard-Smithsonian Center for Astrophysics, Cambridge, MA, USA

Richard Wünsch Astronomical Institute of the Academy of Sciences, Praha 4, Czech Republic

Friedrich Wyrowski Max-Planck-Institut für Radioastronomie, Bonn, Germany

Manuel Zamora-Avilés Centro de Radioastronomía y Astrofísica, Universidad Nacional Autónoma de México, Morelia, Michoacán, México

Luis A. Zapata Centro de Radioastronomía y Astrofísica, UNAM, Morelia, Michoacán, México

Annie Zavagno Laboratoire d'Astrophysique de Marseille, Marseille, France

Qizhou Zhang Harvard-Smithsonian Center for Astrophysics, Cambridge, MA, USA

Part I
Review of Prof. Whitworth's Work

The Life and Times of Anthony Peter Whitworth

Derek Ward-Thompson

Abstract In this very brief introductory chapter I pay tribute to Anthony and give a little of his background, family and upbringing. I briefly outline his education and schooling. I describe a few of his research results. Anthony was an early champion of Smoothed Particle Hydrodynamic (SPH) calculations, particularly in the UK. His interactions with the Cambridge group, and subsequent spawning of many theoretical groups in this area, are part of his lasting legacy in the field of theoretical star formation.

1 Education and Early Years

Anthony Peter Whitworth was born on the 20th March 1946. His father was an anthropologist of some repute, who had worked with Richard Leakie amongst others. He was at Durham University for a number of years, and this was the city where the young Anthony spent much of his childhood. He reports that his childhood was very happy, and he grew up in a loving family (Figs. 1–2).

Anthony first attended the Dragon School in Oxford. However, when his father took up his position in Durham, Anthony moved to the Durham Chorister School, although he reports that he never sang in the choir. Whilst there, he met the young Tony Blair, who was a few years his junior. Apparently Blair did not sing in the choir. Another famous pupil at the school at this time was Rowan Atkinson. He didn't sing in the choir either (Fig. 3).

He went on from there to Sedbergh, where he flourished both academically and in sport, representing the school at cross-country running (Figs. 4–6). His early ability at mathematics was not lost on his teachers, and he was advised to sit for the Oxford

D. Ward-Thompson (✉)
Director, Jeremiah Horrocks Institute for Mathematics, Physics and Astronomy, University of Central Lancashire, Preston, UK
e-mail: DWard-Thompson@uclan.ac.uk

D. Stamatellos et al. (eds.), *The Labyrinth of Star Formation*, Astrophysics and Space Science Proceedings 36, DOI 10.1007/978-3-319-03041-8_1,

Fig. 1 An early family holiday circa 1950. The sky-line of Florence is clearly visible in the background

Fig. 2 Ant with his mother

Fig. 3 Ant attended the Dragon School in Oxford and the Chorister School in Durham, before going to public school at Sedbergh. In this photograph from the Chorister School the *two ringed faces* are Tony Blair and Rowan Atkinson, his contemporaries

Fig. 4 From an early age the young Anthony showed that he was a chap to be taken seriously

Fig. 5 The Sedbergh school running team. Ant is in typical pose at the front

Fig. 6 Anthony has maintained his interest in running throughout his life. Here he is in a marathon race in Cardiff in 1985

entrance examination. He went up to Oriel College, Oxford in 1965, achieving first class honours. By all accounts he enjoyed his time at Oxford, although he has been known to note ruefully that, amongst his contemporaries, those who have made the most money in their lives since leaving Oxford were not necessarily those who did best in their studies.

Anthony pursued a PhD in theoretical astrophysics at Manchester University from 1968 until 1972 under the tutelage of the late Professor Franz Kahn.

2 Research

Anthony held a post-doctoral position at Leiden from 1972 until 1974. His first published paper dates from this period. It was on the topic of UV radiation fields in dark clouds, and its extinction by dust grains [5] (Fig. 7).

In 1974 Anthony joined Cardiff University, first as a fixed-term lecturer, but eventually rising to the position of Personal Chair in Theoretical Astrophysics. He saw the University pass through many turbulent times, including many mergers and re-organisations. In fact, he started in the Department of Mathematics, and is now in the School of Physics and Astronomy, which is itself part of the College of Natural Sciences (Figs. 8–9).

UV RADIATION FIELDS IN DARK CLOUDS*

A. P. WHITWORTH**
Sterrewacht, Leiden, The Netherlands

(Received 14 October, 1974)

Abstract. How dark is it inside a dark cloud? If – as is currently believed – interstellar extinction at UV wavelengths is mainly due to scattering with a strongly forward throwing phase-function, the interior of a dark cloud may be much better illuminated at UV wavelengths than its measured extinction would suggest. We consider the penetration of radiation into a dark cloud against scattering and absorption by grains; and we define a new group property for interstellar grains, the exclusion optical depth τ_d. τ_d is a measure of the ability of the grains to exclude radiation from the interior of an externally illuminated cloud. Radiation – as measured by the radiation energy density – penetrates the cloud approximately as if against pure absorption only, with effective optical depth τ_d. Thus τ_d is a conceptually and numerically useful quantity when estimating the role of UV radiation in the thermal and chemical balance within a dark cloud. Computations are made of the radiation fields in (1200, 4500) Å, at the centres of dark clouds with measured visual extinctions. It is found that even in very dark clouds, the radiation energy density in (1200, 1800) Å may be significant, due to the high grain albedo at these short wavelengths.

Fig. 7 Ant's first paper [5]

Nature Vol. 257 September 11 1975

Interstellar dustmen's convention

from Ant. Whitworth

A workshop on Interstellar Grains was organised by University College Cardiff at Gregynog Hall on July 11–13.

DUST gets into everything, or so they always say, and certainly it seems the cosmos is no exception. In astrophysics, dust grains (sub-micron sized particles constituted of compounds of Si, C, N, O, Fe, Mg) are continually invoked, and invested with new capabilities, to explain puzzling observations. Yet the recent increase in constraints on dust models has not resulted in a more definite picture of dust grains, but rather in the introduction of more free parameters (such as multi-component models and localised variations). Nevertheless, a pattern emerges, and with it the realisation that grains have many very fundamental roles in the cosmos.

At the recent workshop H. C. van de Hulst (Sterrewacht, Leiden) stressed that the interstellar medium is a very hostile environment for grains; and J. M. Greenberg (Sterrewacht, Leiden) cule into elongated grains of polyoxymethylene (POM). There remains outstanding the problem of producing sufficient formaldehyde, but there is already good evidence in support of the general thesis. D. A. Mendis (University of California, La Jolla) reported on the physical parameters for the grains producing 10 and 18 μm features in comets, and indicating an evaporation temperature ~500 K: this rules out silicates, but is very compatible with many polymers, including POM. B. Thomas and co-workers (University of Wales Institute of Science and Technology, Cardiff) have measured strong absorption bands around 10 and 18 μm in thin films of POM.

M. J. Barlow (Sussex University) proposed a resolution of the problem of supplying sufficient refractory grains to the interstellar medium: refractory grains condense in almost every stellar mass loss situation, and are probably only destroyed by direct involvement in star formation after a mean lifetime $\gtrsim 10^9$ yr. D. P. Gilra (University College, Cardiff) deduced the existence of a temperature minimum in the atmospheres of late N-type carbon stars where SiC_2 grains are condensing. C. D. Andriesse (Sterrewacht, Roden) presented infrared observations of η Car as evidence of dust suddenly condensing in the mass outflow at a radius ~0.03 pc. H. Okuda (Kyoto University)

Fig. 8 Ant has always enjoyed a good conference [6]

Anthony built a number of strong research teams over the years. Rather like a football manager he spotted young talent and nurtured it. He was an ardent supporter of Smoothed Particle Hydrodynamic (SPH) calculations from their very earliest days. In fact, he was one of the first in the UK to spot the potential of SPH. As each research team moved on he built another. The first team that became internationally famous involved Simon Chapman, Jake Turner and Helen Pongracic. This was the team that published their first SPH code results in Nature [3] (Fig. 10).

This proved highly influential. Amongst others, the Cambridge group of Jim Pringle and Cathie Clarke took note of this seminal work, and thereafter established a core SPH activity in Cambridge. Between them, Cambridge and Cardiff have

Fig. 9 The IAU General Assembly in Brighton in 1970. Ant can be seen towards the centre of the picture

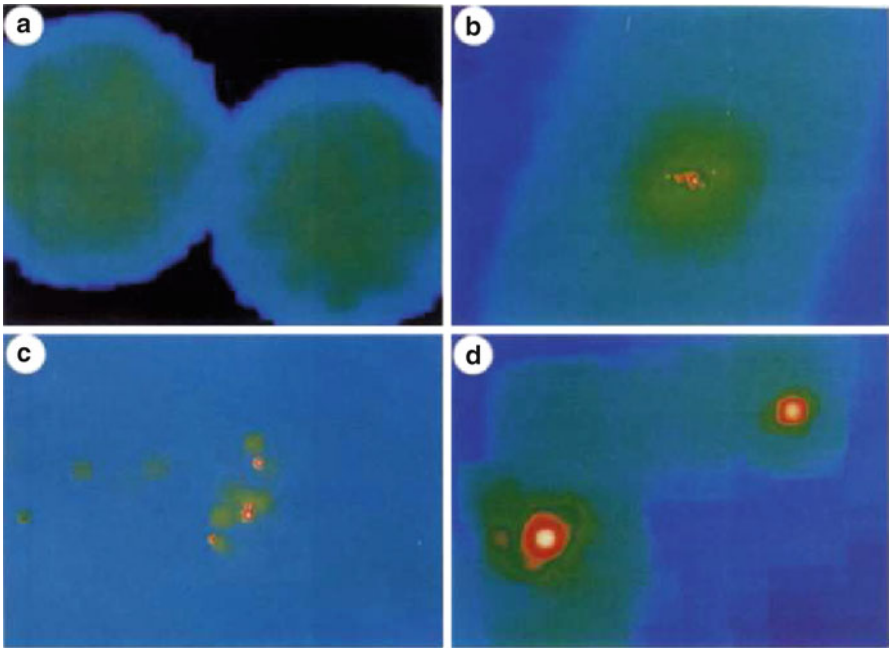

Fig. 10 The famous SPH Nature paper [3]

Self-similar condensation of spherically symmetric self-gravitating isothermal gas clouds

Ant Whitworth *Department of Applied Mathematics and Astronomy, University College, PO Box 78, Cardiff CF1 1XL*

Danny Summers *Department of Mathematics and Statistics, Memorial University of Newfoundland, St John's, Newfoundland A1C 5S7, Canada*

Accepted 1984 December 7. Received 1984 November 22; in original form 1984 June 29

Summary. We show that similarity solutions for the condensation of spherically symmetric self-gravitating isothermal gas clouds are much more abundant than was hitherto believed; we have discovered that each of the discrete solutions found by previous authors must be replaced by a bounded two-parameter continuum of such solutions. Moreover, the two parameters (z_0, w_0) admit a clear and useful physical interpretation. z_0 characterizes the asymptotic form (see equation 3.6) of a solution as $t \to -\infty$ (i.e. at very early times), and reflects how intrinsically unstable against contraction the cloud interior is from the outset. w_0 characterizes the asymptotic form (equation 3.7) of a solution as $t \to +\infty$ (i.e. at very late times) and reflects how important external pressure is in driving compression. The evolution of the flow is as follows.

If the cloud interior is initially close to hydrostatic equilibrium, sound waves propagate inwards tending to establish hydrostatic equilibrium, and there are regions where the gas flows outwards for a time; in these cases, it is only the arrival of a compression wave driven into the cloud by external pressure which converts the cloud to overall contraction. If the cloud interior is initially far from hydrostatic equilibrium, it starts overall contraction immediately; the arrival of a compression wave simply amplifies an already established contraction flow. The compression wave propagates sonically through the gas, leaving behind a uniform velocity field in the outer parts of the cloud, and eventually impinging on the centre. At this stage a central point mass forms and subsequently grows by accretion, whilst a rarefaction wave propagates outwards through the infalling gas, leaving behind a freefall velocity field in the inner parts of the cloud.

Fig. 11 This is Ant's most highly cited paper [10]

subsequently spawned many other theoretical star formation groups, both in the UK and abroad. Anthony's role in bringing SPH to star formation cannot be over-stated, especially in the UK.

Anthony's most cited paper was published in 1985 with Danny Summers, on the topic of similarity solutions for self-gravitating isothermal spheres [10] (Fig. 11). However, he was not a fan of the 'singular isothermal sphere' (SIS) model of star formation. In fact, he pointed out on many occasions that the SIS was only one of an infinite number of similarity solutions.

Anthony has contributed to almost every aspect of his field, from high mass star formation [8] and HII regions [1, 2, 7], to brown dwarfs and planets [9]. Amongst his many achievements are explanations of binary star parameters and a natural explanation of the brown dwarf desert [4].

3 Summary

Anthony's contribution to our field is immense. One short introduction cannot even begin to scratch the surface of this subject. However, the remainder of this volume attempts to address some of the many fields to which Anthony has contributed during his long and illustrious career (Fig. 12).

Fig. 12 Ant has remained a dedicated husband and father throughout, being first and foremost a family man

Acknowledgements I would like to thank Hilary for providing most of the pictures in this paper. However, mostly, I would like to thank Anthony for his guidance and friendship throughout my career.

References

1. Bhattal, A. S., Francis, N., Watkins, S. J., & Whitworth, A. P. 1998, *MNRAS*, 297, 435
2. Bisbas, T. G., Wünsch, R., Whitworth, A. P., Hubber, D. A., & Walch, S. 2011, *ApJ*, 736, 142
3. Chapman, S., Pongracic, H., Disney, M., et al. 1992, *NATURE*, 359, 207
4. Stamatellos, D., & Whitworth, A. P. 2009, *MNRAS*, 392, 413
5. Whitworth, A. P. 1975, *Ap&SS*, 34, 155
6. Whitworth, A. 1975, *NATURE*, 257, 91
7. Whitworth, A. 1979, *MNRAS*, 186, 59
8. Whitworth, A. P., Bhattal, A. S., Chapman, S. J., Disney, M. J., & Turner, J. A. 1994, *MNRAS*, 268, 291
9. Whitworth, A. P., & Stamatellos, D. 2006, *A&A*, 458, 817
10. Whitworth, A., & Summers, D. 1985, *MNRAS*, 214, 1

Working with Ant Whitworth

Simon Goodwin

Abstract A short tribute about working with Ant Whitworth.

This conference was held as a tribute to Ant Whitworth and his work in all sorts of areas associated with star formation. Many people at the conference have known Ant for many years, and some will have met him for the first time at the meeting. But quite a few of the people at the conference have had the pleasure of working directly with Ant as a PhD student, postdoc, or a fellow of some description.

Here I present a personal view of what I have learnt from Ant about how to do astronomy, although I am sure (and hope) that much of it is not unique to Ant.

The first, and most obvious, lesson is to try as hard as possible to be correct in what you do. If you lay-out your starting point and assumptions then hopefully everything that follows in your work is correct given that starting-point. The point of laying-out your assumptions clearly is that in theory they are almost certainly wrong. Wrong in that they will not exactly match reality and will ignore various physics you know to be important. One thing that can be guaranteed with absolute certainty is that no star formation simulation has ever had the right initial conditions, or included all of the important physics. But we can still make progress, and we can still gain huge insights into reality, as long as we remember this.

The second important lesson is to be extremely careful when writing-up your research. I learnt from Ant to read every word, in every sentence, in every paragraph carefully. Does it say what I mean it to say? Does it inform the reader? Is it grammatically correct in the most painstakingly anal way possible? Write, read,

S. Goodwin (✉)
Department of Physics and Astronomy, University of Sheffield, Hicks Building, Hounsfield Road, Sheffield S3 7RH, UK
e-mail: s.goodwin@sheffield.ac.uk

D. Stamatellos et al. (eds.), *The Labyrinth of Star Formation*, Astrophysics and Space Science Proceedings 36, DOI 10.1007/978-3-319-03041-8_2,

re-write, then re-read, then re-write again. Then get comments from Ant and re-write from scratch. At first a horribly painful process, but one that gets ingrained (just ask my students).

It is also important not to get too attached to your own ideas and theories. They are almost certainly wrong (or at best, not completely right). If you are lucky you are the one to show that you are wrong, but probably it will be somebody else... and be ready to change your mind when observations finally destroy your wonderful theory.

The final, and by far the most important, thing I learnt from Ant was to have fun. Doing astronomy should be enjoyable. It shouldn't involve heated arguments, but friendly exchanges of views. The point is to enjoy trying to get at some of the deep mysteries of the Universe, and make lots of good friends along the way. And if you're lucky, to get to go to lots of fantastic conferences like this.

On behalf of everybody who has been a student, postdoc, or whatever with Ant I would like to thank him for making the whole process so enjoyable and enriching, both scientifically and personally. The large number of us who wanted to come to this conference and thank Ant in person speaks volumes for his influence on us. And long may it continue.

Part II
Low-Mass Star Formation

The Formation of Low-Mass Stars and Brown Dwarfs

Dimitris Stamatellos

Abstract It is estimated that ∼60 % of all stars (including brown dwarfs) have masses below 0.2 $M_\odot$. Currently, there is no consensus on how these objects form. I will briefly review the four main theories for the formation of low-mass objects: turbulent fragmentation, ejection of protostellar embryos, disc fragmentation, and photo-erosion of prestellar cores. I will focus on the disc fragmentation theory and discuss how it addresses critical observational constraints, i.e. the low-mass initial mass function, the brown dwarf desert, and the binary statistics of low-mass stars and brown dwarfs. I will examine whether observations may be used to distinguish between different formation mechanisms, and give a few examples of systems that strongly favour a specific formation scenario. Finally, I will argue that it is likely that all mechanisms may play a role in low-mass star and brown dwarf formation.

1 Introduction

Star formation is a process that produces objects with a wide range of masses: from a few Jupiter masses up to a few hundred solar masses. The initial mass function (IMF), i.e. the distribution of stellar masses at birth, is relatively well constrained down to ∼20–30 M_J, but it is uncertain at lower masses due to the difficulty in observing low-mass objects. The IMF can be approximated either by power laws [33] or by a log-normal distribution [13, 14]. Most stars in the Galaxy have low-mass; more than ∼60 % of all stars (including brown dwarfs) have masses below 0.2 $M_\odot$ (e.g. using the Kroupa IMF; [33]).

D. Stamatellos (✉)
Jeremiah Horrocks Institute for Mathematics, Physics and Astronomy, University of Central Lancashire, UK
e-mail: dstamatellos@uclan.ac.uk

D. Stamatellos et al. (eds.), *The Labyrinth of Star Formation*, Astrophysics and Space Science Proceedings 36, DOI 10.1007/978-3-319-03041-8_3,

The low-mass end of the IMF is populated by three types of objects: low-mass hydrogen-burning stars, brown dwarfs, and planets. The distinction between these types of objects is done solely on their masses: stars can sustain H-burning ($m > 80\,\mathrm{M_J}$), brown dwarfs cannot sustain H-burning but they can burn deuterium ($13\,\mathrm{M_J} < m < 80\,\mathrm{M_J}$), and planets ($m < 13\,\mathrm{M_J}$) cannot sustain deuterium burning. However, it is possible that all these type of objects may form similarly, i.e. by gravitational fragmentation of gas. Indeed there is no theoretical reason for fragmentation to stop functioning at the H-burning or the D-burning limit. The theoretical minimum mass for gas fragmentation is the opacity limit at $\sim$1–5 $\mathrm{M_J}$ (e.g. [59]).

Brown dwarf and low-mass star formation requires high densities. The critical mass that a lump of gas needs to have in order to collapse is

$$M_{\mathrm{JEANS}} = \frac{4\pi^{5/2}}{24} \frac{c_s^3}{(G^3\rho)^{1/2}} \tag{1}$$

where c_s is the sound speed, and ρ is the density of the lump. Thus, assuming that this lump will form a brown dwarf then $M_{\mathrm{JEANS}} < 80\,\mathrm{M_J}$, from which we obtain that $\rho > 10^{-16}\,\mathrm{g\,cm^{-3}}$, and $R \sim 500\,\mathrm{AU}$. Brown dwarf formation theories attempt to either explain how these high densities are attained (e.g. in converging turbulent flows or discs) or they circumvent this requirement by forming brown dwarfs as failed stars (e.g. by ejection or photo-evaporation).

2 Turbulent Fragmentation of Molecular Clouds

In the turbulent fragmentation model the high densities that are required for the formation of low-mass stars and brown dwarfs are achieved in converging turbulent flows [24, 25, 43].

The theory reproduces the IMF and predicts that it depends on various parameters, such as the global Mach number and the thermodynamics of gas. However, the dependance is rather small for Galactic environments and only at very low-masses, for which current observations are incomplete (e.g. see review by Bastian et al. [4]). Nevertheless, the theory can in principle be tested by observations in extreme environments and with more sensitive observations of the low-mass end of the IMF.

Turbulent fragmentation has difficulty in explaining the formation of low-mass binaries. Random pairing of stars with masses drawn randomly from the IMF does not seem to reproduce the properties of low-mass binaries [44]. Furthermore, the theory predicts the existence of gravitationally bound brown dwarf-mass cores, which have not been observed in the large numbers that are expected. However, there are examples of such cores, e.g. the pre-brown dwarf core Oph B-11 [2].

3 Ejection of Protostellar Embryos

In this theory the collapse of a prestellar core results in the formation of a few ($\gtrsim$3) objects. Inevitably, as these objects dynamically interact with each other, the lowest mass object(s) will be ejected from the system. The mass growth of the ejected objects stops as soon as they leave their parent core; therefore if these ejection(s) happens early on, then the mass of an ejected object would be low, even in the brown dwarf-mass regime [8,21,45].

Initially it was thought that these ejections mean that the velocity dispersion of brown dwarfs seen in clusters should be higher than the velocity dispersion of stars; however, later it was shown that both populations have similar velocity dispersions (e.g. [9]) as low-mass stars are also frequently ejected in these type of dynamical interactions. It was also argued that ejections should be rather disruptive for discs around brown dwarfs, but simulations (e.g. [7]) show that brown dwarf discs may survive ejections.

4 Disc Fragmentation

Discs form during cloud collapse due to the initial rotation and/or turbulence of prestellar cores and conservation of angular momentum. They can grow in mass as they are being fed with material from the infalling prestellar core and can become gravitationally unstable and fragment to form low-mass stars and brown dwarfs (e.g. [3,50]).

Numerical simulations have shown that most of the objects form by disc fragmentation are brown dwarfs, but low-mass stars are also likely to form [48,50]. Planetary-mass objects may also form [10] but they tend to be ejected from the system becoming free-floating planets, and thus contributing to a possibly large population of such objects [54]. The IMF of the objects formed by disc fragmentation is consistent with the low-mass end of the stellar IMF. The brown dwarfs that form by this mechanism have discs with masses up to a few tens of M_J and sizes up to a few tens of AU. The model predicts that brown dwarfs that stay as companions to Sun-like stars are more likely to have discs than brown dwarfs in the field, as discs are likely to be disrupted during ejections [50].

The disc fragmentation model uniquely among other formation mechanisms can explain the brown dwarf desert. This terms refers to the lack of brown dwarfs as close companions to Sun-like stars [23,38,46]; on the contrary low-mass hydrogen-burning stars and planets are frequently observed as close companions to Sun-like stars. In the disc fragmentation model all objects that form in the disc start off with a mass of a few M_J and they grow in mass as they accrete material from the disc [51]. The objects that form first and migrate inwards gain enough mass to become stars, whereas the ones that stay in the outer disc region increase in mass but not as much, becoming brown dwarfs. If one of the brown dwarfs from the outer disc region drifts

inwards, then it is quickly ejected again into the outer disc region due to dynamical interactions with the higher-mass objects of the inner region. Therefore, the region close to the central star is populated by low-mass hydrogen-burning stars, and it is almost devoid of brown dwarfs [50]. Moreover, the inner disc region is populated by planets that form by core accretion at a later stage (after $\sim$1 Myr). Most of the brown dwarfs are either ejected from the system becoming field brown dwarfs, or stay bound to the central star at relatively wide orbits ($\sim$200–10^4 AU); such wide-orbit brown dwarfs companions to Sun-like stars have been observed [18, 19, 60].

The predictions of the disc fragmentation model regarding the properties of low-mass binaries are broadly consistent with observations. Close and wide brown dwarf-brown dwarf and brown dwarf-low-mass star binaries are common. Binaries form either by capture when two objects are still in the disc of the host star, or by pairing up of individual objects as they are ejected from the disc [50]. The low-mass binary fraction predicted by the model is $\sim$0.16, similar to the binary fraction in young star forming regions (e.g. in Chamaeleon 0.15–0.20; [1]). Most of the binaries have components with similar masses ($q > 0.7$) in accordance with observations ([12], note though that this may be due to observational biases, see [28]). Another interesting observational fact that the model reproduces is that brown dwarfs to Sun-like stars are more likely to be in binaries than brown dwarfs in the field [11, 20].

Can the conditions for disc fragmentation (i.e. disc size, disc mass) be realised in nature? Discs that are large enough so that their outer regions can cool fast enough (i.e. discs with radii >70 AU) and have enough mass to be gravitationally unstable at such radii can indeed fragment. Stamatellos et al. [49] show that even a 0.25 $M_\odot$-mass disc with radius of 100 AU around a 0.7 $M_\odot$-star fragments. Dynamical interactions in a cluster may also trigger fragmentation of discs with even lower masses [56]. Observations of a small sample of young protostars did not reveal any massive early stage discs [41]. However, Stamatellos et al. [49] argue that finding early stage fragmenting discs is unlikely due to the short duration of the process (a few 10^3 year). Therefore a large number of young protostars needs to be observed.

An issue that has been explored recently is whether radiative feedback from the central protostar heats and stabilises the disc suppressing brown dwarf and low-mass star formation [5, 7, 42]. Most of the radiation than young protostars emit is due to accretion of material onto their surfaces. Offner et al. [42] and Bate [5,7] have assumed that the accretion of material onto protostars is continuous. However, there is growing evidence that accretion of material may be episodic. FU Ori-type stars are objects whose luminosity increases for a few orders of magnitude for a few hundred years. During these events the accretion rates may be up to $10^{-4}\,M_\odot\,\mathrm{year}^{-1}$. Additional evidence for episodic accretion comes from the luminosity problem: if one assumes a continuous accretion rate then the expected protostar luminosities are much larger than the observed ones (e.g. [16]). Stamatellos et al. [52, 53] have included the effects of episodic accretion in hydrodynamic simulations of star formation and have found that episodic accretion limits the effect of radiative feedback from the central protostar and allows disc fragmentation. In their model the luminosities of young protostars are high only during the episodic accretion events (for a few hundred years), but relatively low in-between episodic outbursts (for a

few thousand years); there is ample time between successive accretion outbursts during which the disc is relatively cool and therefore gravitational instabilities can grow and the disc can fragment.

The presence of magnetic fields is expected to act against the formation of centrifugally supported discs because angular momentum is removed by magnetic effects (e.g. magnetic braking, outflows). However, it is uncertain whether magnetic fields can totally suppress the formation of self-gravitating discs. Hennebelle and Fromang [26] find that in the ideal MHD approximation the formation of a disc is suppressed if the magnetic field is strong enough and parallel to the rotation axis of the collapsing star-forming core. This is supported by ideal MHD simulations that include the effects of radiative transfer [15]. The situation changes in resistive MHD calculations. Machida et al. [36] and Vorobyov [57] find that disc formation is possible (see also [17, 32, 34]). More recently Seifried et al. [47] and Joos et al. [29] find that turbulence can offset the effect of magnetic breaking and allow the formation of discs with sizes up to 100 AU.

5 Photo-Erosion of Prestellar Cores

In this model a prestellar core with mass of a few $M_\odot$ is overrun by an HII region and it is photo-eroded [27, 58]. Therefore, only a fraction of the initial mass of the pre-stellar core forms a low-mass star or a brown dwarf. The typical mass of an object produced by this mechanism is

$$\sim 0.01 M_\odot \left(\frac{c_s}{0.3\,\mathrm{km\,s^{-1}}}\right)^6 \left(\frac{\dot{\mathcal{N}}_{\mathrm{LyC}}}{10^{50}\,\mathrm{s^{-1}}}\right)^{-1/3} \left(\frac{n_0}{10^3\,\mathrm{cm^{-3}}}\right)^{-1/3}, \qquad (2)$$

where c_s is the sound speed of the neutral gas of the core, $\dot{\mathcal{N}}_{\mathrm{LyC}}$ is the rate of ionising photons emitted by nearby stars, and n_0 is the density of the HII region. This mechanism produces brown dwarfs and low-mass stars for a wide range of initial conditions, but it is inefficient, i.e. a rather massive pre-stellar core is needed for forming a brown dwarf. It can work only in the vicinity of OB stars (e.g. in Trapezium-like clusters); therefore, it cannot be the dominant mechanism for the formation of low-mass stars and brown dwarfs.

6 Observational Tests to Distinguish Between Different Formation Mechanisms?

IMF. The turbulent fragmentation model reproduces the core mass function and the IMF, assuming a star formation efficiency [25]. Disc fragmentation also reproduces the low-mass end of the IMF [50]. The simulations of Bate [7] that combine different formation mechanisms (turbulent fragmentation, ejection, disc fragmentation) also reproduce the IMF. Therefore, it appears that the IMF cannot be used to distinguish

between different formation scenarios. However, Thies and Kroupa [55] argue that when unresolved binaries are taken into account, the IMF is discontinuous around the H-burning limit, which suggests that brown dwarfs may form differently than Sun-like stars.

Discs. All formation models produce brown dwarfs and low-mass stars with discs. Brown dwarfs that form in collapsing pre-brown dwarf cores will almost always form with discs [37]. Brown dwarfs that form in fragmenting discs of Sun-like stars are also likely to form with their own discs, but these discs may be partially or totally disrupted during the liberation/ejection process, resulting in a lower fraction of brown dwarfs with discs [50]. In the ejection scenario it is even more likely for discs to be disrupted during ejection but many still survive [7]. Therefore, although different formation mechanisms may result in different disc fractions around brown dwarfs, observations of discs (and associated phenomena, i.e. accretion, outflows) around brown dwarfs do not favour any given formation theory.

The brown dwarf desert. The disc fragmentation theory reproduces the lack of brown dwarf companions to Sun-like stars (in contrast to low-mass star companions and planetary companions; see Sect. 4, [50]). It has also been argued that angular momentum conservation of prestellar cores favours the formation of wide companions [30] in the turbulent fragmentation scenario.

Low-mass binaries. The distribution of the projected separations of low-mass binaries peaks at $\sim$3 AU; close (sub-AU) and wide binaries ($>$20 AU) are also common (see http:www.vlmbinaries.org). Low-mass binaries tend to have components with similar masses, but this may be due to observational biases [28]. These trends are broadly reproduced by the disc fragmentation model [50]. The simulations of Bate [6, 7] that combine different formation mechanisms (turbulent fragmentation, ejection, disc fragmentation) also reproduce the binary properties. This suggests that dynamical interactions may play a dominant role in forming binaries and shaping their properties, and that the effect of the formation mechanism is secondary. However, it seems unlikely that brown dwarf-brown dwarf binaries that are companions to Sun-like star form by dynamical interactions in a cluster [31].

7 Examples of Different Mechanisms at Play

The recently observed isolated core Oph B-11 provides an example of turbulent fragmentation working in the brown dwarf-mass regime. This is an isolated core, with mass is $\sim$15–20 M_J and size $<$460 AU, that is gravitationally bound [2]. This core will probably collapse to form a single brown dwarf. Another example of brown dwarf formation by turbulent fragmentation is the young wide brown dwarf binary FU Tau A,B [35]. The components of the binary have masses $\sim$5 and $\sim$15 M_J. This pair is located in the Barnard 215 dark cloud and there is no higher-mass star nearby, in the disc of which the pair could have formed and then ejected.

The HL Tau system provides a possible example of disc fragmentation. The system consists of a star with mass $\sim 0.3\,M_{\odot}$ that has a disc with mass $\sim 0.2\,M_{\odot}$ and radius of >100 AU. 1.3 cm VLA observations have revealed the presence of a condensation with mass $\sim 14\,M_{J}$ at distance of ~ 65 AU from the central star [22]. Simulations have shown that disc fragmentation may be responsible for forming this object [22]. The planetary system of HR8799 [39, 40] also provides a possible example of disc fragmentation. This is 4-planet system with four giant planets (each one with mass $\sim 10\,M_{J}$) on wide orbits (15–70 AU) around a 1.5-$M_{\odot}$ A-type star. These planets are unlikely to have formed by core accretion as they are relatively massive and orbit at large distances from the central star.

8 Conclusions

All formation mechanisms are probably feasible in nature and are likely to produce brown dwarfs and low-mass stars, even working in conjunction with each other. This is evident in the hydrodynamic simulations of cluster formation (e.g. [6, 7]). In simulations with no radiative transfer $\sim 75\,\%$ of brown dwarfs form by disc fragmentation, and 25 % in dense filaments caused by turbulence (with ejections happening in both cases; [6]). In simulations with radiative transfer $\sim 20\,\%$ of brown dwarfs form by disc fragmentation, and $\sim 80\,\%$ in dense filaments [7]. However, these simulations do not include the effects of episodic accretion that promote disc fragmentation [53]. Thus, the actual fraction of brown dwarfs formed in discs could be between the previously mentioned limits (i.e. 20–75 %). Therefore, it is important for star formation theories to determine the fraction of low-mass stars and brown dwarfs that form with different mechanisms and in what extent these fractions are affected by the environment and the physical processes involved in star formation.

References

1. Ahmic, M., Jayawardhana, R., Brandeker, A., et al. 2007, *ApJ*, 671, 2074
2. André, P., Ward-Thompson, D., & Greaves, J. 2012, Science, 337, 69
3. Attwood, R., Goodwin, S., Stamatellos, D., & Whitworth, A. 2009, *A&A*, 495, 201
4. Bastian, N., Covey, K. R., & Meyer, M. R. 2010, *ARA&A*, 48, 339
5. Bate, M. R. 2009a, *MNRAS*, 392, 1363
6. Bate, M. R. 2009b, *MNRAS*, 392, 590
7. Bate, M. R. 2012, *MNRAS*, 419, 3115
8. Bate, M. R., Bonnell, I. A., & Bromm, V. 2002, *MNRAS*, 332, L65
9. Bate, M. R., Bonnell, I. A., & Bromm, V. 2003, *MNRAS*, 339, 577
10. Boley, A. C. 2009, *ApJ*, 695, L53
11. Burgasser, A. J., Kirkpatrick, J. D., & Lowrance, P. J. 2005, *AJ*, 129, 2849
12. Burgasser, A., Reid, I., Siegler, N., et al. 2007, Protostars and Planets V, 427
13. Chabrier, G. 2003, *PASP*, 115, 763

14. Chabrier, G. 2005, The Initial Mass Function 50 years later. Edited by E. Corbelli and F. Palle, 327, 41
15. Commerçon, B., Hennebelle, P., Audit, E., Chabrier, G., & Teyssier, R. 2010, *A&A*, 510, L3
16. Dunham M. M., Evans, II N. J., Terebey S., Dullemond C. P., Young C. H., 2010, *ApJ*, 710, 470
17. Dapp, W. B., Basu, S., & Kunz, M. W. 2012, *A&A*, 541, A35
18. Dhital, S., Burgasser, A. J., Looper, D. L., & Stassun, K. G. 2011, *AJ*, 141, 7
19. Faherty, J. K., Burgasser, A. J., Cruz, K. L., et al. 2009, *AJ*, 137, 1
20. Faherty, J. K., Burgasser, A. J., West, A. A., et al. 2010, *AJ*, 139, 176
21. Goodwin, S., Whitworth, A., & Ward-Thompson, D. 2004, *A&A*, 414, 633
22. Greaves, J. S., Richards, A. M. S., Rice, W. K. M., & Muxlow, T. W. B. 2008, *MNRAS*: Letters, 391, L74
23. Grether, D. & Lineweaver, C. H. 2006, *ApJ*, 640, 1051
24. Hennebelle, P. & Chabrier, G. 2008, *ApJ*, 684, 395
25. Hennebelle, P. & Chabrier, G. 2009, *ApJ*, 702, 1428
26. Hennebelle, P. & Fromang, S. 2008, *A&A*, 477, 9
27. Hester, J. J., Scowen, P. A., Sankrit, R., et al. 1996, *AJ*, 111, 2349
28. Janson, M., Hormuth, F., Bergfors, C., et al. 2012, *ApJ*, 754, 44
29. Joos, M., Hennebelle, P., & Ciardi, A. 2012, *A&A*, 543, 128
30. Jumper, P. H. & Fisher, R. T. 2012, ArXiv e-prints
31. Kaplan, M., Stamatellos, D., & Whitworth, A. P. 2012, *Ap&SS*, 341, 395
32. Krasnopolsky, R., Li, Z.-Y., & Shang, H. 2010, *ApJ*, 716, 1541
33. Kroupa, P. 2001, *MNRAS*, 322, 231
34. Li, Z.-Y., Krasnopolsky, R., & Shang, H. 2011, *ApJ*, 738, 180
35. Luhman, K. L., Mamajek, E. E., Allen, P. R., Muench, A. A., & Finkbeiner, D. P. 2009, *ApJ*, 691, 1265
36. Machida, M. N., Inutsuka, S., & Matsumoto, T. 2011, *ApJ*, 729, 42
37. Machida, M. N., Shu-ichiro Inutsuka, & Matsumoto, T. 2009, *ApJ*, 699, L157
38. Marcy, G. W. & Butler, R. P. 2000, *PASP*, 112, 137
39. Marois, C., Macintosh, B., Barman, T., et al. 2008, Science, 322, 1348
40. Marois, C., Zuckerman, B., Konopacky, Q. M., Macintosh, B., & Barman, T. 2010, Nature, 468, 1080
41. Maury, A. J., André, P., Hennebelle, P., et al. 2010, *A&A*, 512, 40
42. Offner, S., Klein, R., McKee, C., & Krumholz, M. 2009, *ApJ*, 703, 131
43. Padoan, P. & Nordlund, *A&A*. 2004, *ApJ*, 617, 559
44. Reggiani, M. M. & Meyer, M. R. 2011, *ApJ*, 738, 60
45. Reipurth, B. & Clarke, C. 2001, *AJ*, 122, 432
46. Sahlmann, J., Ségransan, D., Queloz, D., et al. 2011, *A&A*, 525, 95
47. Seifried, D., Banerjee, R., Pudritz, R. E., & Klessen, R. S. 2012, *MNRAS*: Letters, 423, L40
48. Stamatellos, D., Hubber, D. A., & Whitworth, A. P. 2007, *MNRAS*, 382, L30
49. Stamatellos, D., Maury, A., Whitworth, A., & André, P. 2011a, *MNRAS*, 413, 1787
50. Stamatellos, D. & Whitworth, A. P. 2009a, *MNRAS*, 392, 413
51. Stamatellos, D. & Whitworth, A. P. 2009b, *MNRAS*, 400, 1563
52. Stamatellos, D., Whitworth, A. P., & Hubber, D. A. 2011b, *ApJ*, 730, 32
53. Stamatellos, D., Whitworth, A. P., & Hubber, D. A. 2012, *MNRAS*, 427, 1182
54. Sumi, T., Kamiya, K., Bennett, D. P., et al. 2011, Nature, 473, 349
55. Thies, I. & Kroupa, P. 2007, *ApJ*, 671, 767
56. Thies, I., Kroupa, P., Goodwin, S. P., Stamatellos, D., & Whitworth, A. P. 2010, *ApJ*, 717, 577
57. Vorobyov, E. I. 2011, *ApJ*, 729, 146
58. Whitworth, A. P. & Zinnecker, H. 2004, *A&A*, 427, 299
59. Whitworth, A. P. & Stamatellos, D. 2006, *A&A*, **458**, 817
60. Zhang, Z. H., Pinfield, D. J., Day-Jones, A. C., et al. 2010, *MNRAS*, 404, 1817

From the Companion Mass Ratio Distribution to the Planetary Mass Function: Using Multiple Systems to Constrain Models of Star and Planet Formation

Maddalena Reggiani and Michael R. Meyer

Abstract We present new results regarding the companion mass ratio distribution (CMRD) of stars, and sub-stellar objects. Considering the new survey of multiples for solar type field stars (Raghavan et al. ApJS 190:1, 2010) and M dwarfs (Janson et al. ApJ 754(1):26, 2012), we test the universality of the CMRD derived in Reggiani and Meyer (ApJ 738:60, 2011). Whereas we do not find significant differences in the CMRD for M dwarfs compared to previous results, the solar type CMRD appears to inconsistent with the previously derived CMRD from Reggiani and Meyer (ApJ 738:60, 2011). Despite the fact that this survey spans a wider range of angular separations than the previously studied samples, there is no evidence for variations in the CMRD as a function of orbital separation. Assuming that we can extrapolate both the stellar CMRD into the BD regime and the radial velocity planetary Companion Mass Function (Cumming et al. PASP 120:531, 2008) to larger separations, we can run MC simulations to test in which mass range we expect the planet population to become more important than BDs as companions to stars. This tool can be useful to predict the outcome of future surveys for very low mass companions or to analyze already existing datasets.

1 Why Do We Really Care About Multiple Systems?

As a large fraction of stars form in multiple systems, both in the field [5, 11] and in star forming regions [10], to understand star formation in general we need to investigate how binary and higher order multiple star formation proceeds [4]. Moreover, different theories of binary formation predict different binary properties. Therefore, the study of these properties may help us in understanding which are the

M. Reggiani (✉) • M.R. Meyer
Institute for Astronomy, ETH Zurich, Zurich, Switzerland
e-mail: reggiani@phys.ethz.ch,mmeyer@phys.ethz.ch

D. Stamatellos et al. (eds.), *The Labyrinth of Star Formation*, Astrophysics and Space Science Proceedings 36, DOI 10.1007/978-3-319-03041-8_4,

main mechanisms for the formation of multiple stars. Among those properties, we think that the mass ratio, conventionally defined as $q = M_2/M_1$ in a binary system of stars with masses M_1 and M_2 ($M_1 > M_2$), is a key parameter. Analogous to the initial mass function (IMF) for single objects, one can study the companion mass ratio distribution (hereafter CMRD) as the distribution of q for a chosen primary mass. Different binary formation models predict different mass ratio distributions and dependencies of the CMRD on the primary mass. For example, in tidal capture one expects that for each primary star the mass of the secondary is chosen randomly from the single star mass function and the CMRD would reflect the IMF [6]. In the case of fragmentation scenarios subsequent continued accretion onto both objects from a common reservoir tends to equalize the masses, moving the q distribution towards unity [1]. Even though tidal capture is unlikely to be the most relevant binary formation mechanism, capture may still occur during the dissolution phase of star clusters, causing differences in the shape of the CMRD as a function of orbital separation [8, 9].

At the same time, the mass ratio distribution extends well into the brown dwarf (BD) and planetary mass regime when studying substellar companions. In these mass regimes, other mechanisms have been proposed for the formation of companions (e.g. core fragmentation, disk fragmentation or core accretion) and each one of them is able to produce objects of different masses.

Therefore, if we really want to understand stars, BDs and planets as companions to stars and determine the most likely mechanisms for forming companions in every mass bin, we need to have a detailed knowledge of the CMRD both in the stellar regime and across the substellar boundary.

2 Universality of the Companion Mass Ratio Distribution

The CMRD appears to be mostly universal over a wide range of q values and primary masses [7, 12]. In particular, over the separation range 1–2,400 AU and mass range 0.25–6.5 $M_\odot$, the CMRD seems to follow a single slope power law $dN/dq \propto q^\beta$ and there is no evidence for variation of the CMRD with orbital separation [12]. Instead of a χ^2 fit of the binned distribution, as done in [12], a more robust analysis is achieved through a maximum likelihood estimation method, since it does not depend on the choice of the bin size [3]. This method gives a new best fit power law $dN/dq \propto q^\beta$, with $\beta = -0.18 \pm 0.33$, based on the sample and analysis described in [12].

In this context, it is also worth analyzing two recent studies of the CMRD for solar type [11] and M dwarf primaries [5] in the field. In the first one [11], roughly 200 solar type primary binaries are considered to determine the CMRD over a large range of separations (10^{-1}–10^5 AU) and mass ratios (0.02–1). The CMRD appears to be more peaked towards unity than observed previously. We used the KS test to compare this CMRD with Montecarlo simulations of the updated fit of the CMRD presented in [12], over the same range of q values. The statistical test gives

a probability of $\sim 10^{-2}$ of the two distributions being consistent with each other. We tested, then, the possibility of a variation of the CMRD with angular separation, but we could not find any evidence for that. Motivated by these results, we used again a maximum likelihood method to fit the distribution and found a power-law $dN/dq \propto q^{\beta}$, with $\beta = 0.16 \pm 0.13$. While these slopes β are formally consistent with each other (within the errors), the change in sign is notable.

In the second study [5], the most complete sample of M dwarf primary binaries to date has been presented. It consists of 85 systems with separations between 3 and 227 AU and mass ratios between 0.1 and 1. The CMRD appears to be flat. We tested this distribution against the Monte Carlo simulations of the new fit of the stellar CMRD, but in this case the KS test does not allow us to reject the hypothesis that the newer data was drawn from the same parent sample.

At the moment, therefore, the universality of the CMRD is still matter of debate. The most recent updates on the Universality of the CMRD can be found in Reggiani and Meyer [13]. Larger samples in the future will allow us to test even more subtle variations of the CMRD with separation, perhaps testing theories of capture in dissolving clusters.

3 Companion Mass Ratio Distribution and Planet Mass Function

In the substellar regime, both planets and BDs contribute to the companion mass function (hereafter CMF). From radial velocity surveys, we know that the planetary CMF follows a power law of the form $dN/dm \propto m^{\alpha}$, with $\alpha = -1.31$, for masses between 1 and 13 M_J and orbital radius between 0.3 and 2.5 AU [2].

Assuming that we can extrapolate both the stellar CMRD [12] into the BD regime and the radial velocity planetary CMF [2] to larger separations, we can predict in which mass range we expect the planet population to become more important than BDs as companions to stars. If we assume that we can also scale the planetary CMF with stellar mass, we can describe the distribution of BDs and planets with an equation of the form:

$$dN = C_{0,1}\, q^{\alpha_{0,1}}\, a^{\beta_{0,1}} dq\, da \tag{1}$$

where C is a constant, q is the mass ratio, a is the semi-major axis and the subscripts 0 and 1 indicate BDs and planets, respectively. In the case we suppose that the maximum mass for BDs is set by the hydrogen burning limit (80 M_J), the BD minimum mass by the opacity limit for fragmentation ($\sim$5 M_J) and the maximum mass for planets is limited by the maximum mass available in the disk (e.g. a tenth of the mass of the host star), the substellar CMF would appear close to what presented in Fig. 1.

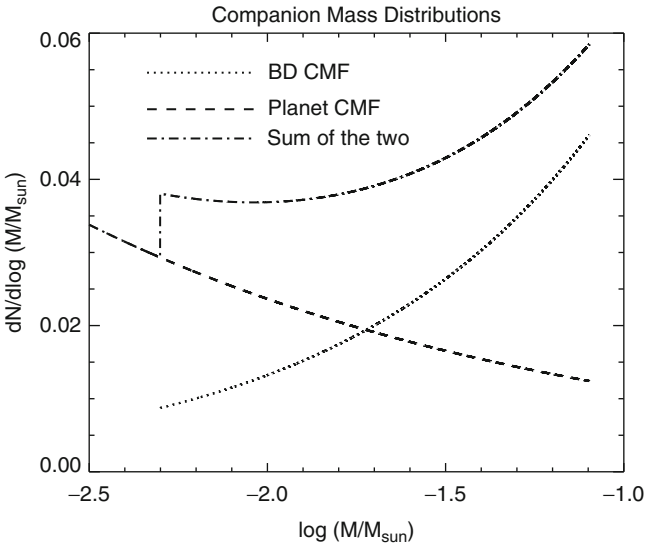

Fig. 1 Planet and BD companion mass functions as described in the text

Current and future observations will help us testing the peculiar features of this distribution. For instance, the preliminary results from an ESO Large Program, utilizing NACO on the VLT as a precursor to SPHERE (Jean-Luc Beuzit, PI) and aimed at providing a homogeneous statistically significant study of the occurrence of giant planets and BDs in wide (5–500 AU) orbit around young nearby stars, are consistent with this simple model.

4 Conclusions

Concerning the stellar CMRD, the new results from [11], showing a CMRD more peaked to 1:1, support fragmentation models. From the analysis of recent binarity studies from the field [5, 11] we do not have evidence yet for a CMRD dependence on separation, as it would be expected by cluster dissolution models. We certainly need larger samples to look for subtle variations of the CMRD with separation.

Assuming that we can extrapolate the stellar CMRD [12] into the BD regime and the radial velocity planetary CMF [2] to larger separations, we have created a simple model for the substellar companion mass function. Current results from direct imaging surveys are consistent with this picture.

In the coming future we would like to study the CMRD in other star forming regions (e.g. ONC) and test its dependence on separation for wide systems. Upcoming instruments will also allow us to test our CMF model and to study the detail shape of the CMRD in the sub-stellar regime.

References

1. Bate, M. R. 2000, *MNRAS*, 314, 33
2. Cumming, A., Butler, R. P., Marcy, G. W., et al. 2008, *PASP*, 120, 531
3. Feigelson, E. D. & Babu, G. J. 2011, Modern Statistical Methods for Astronomy with Applications, Cambridge Univ. Press
4. Goodwin, S. P., Kroupa, P., Goodman, A., & Burkert, A. 2007, Protostars and Planets V, 133
5. Janson, M., Hormuth, F., Bergfors, C., et al. 2012, *ApJ*, 754, 44
6. McDonald, J. M., & Clarke, C. J. 1993, *MNRAS*, 262, 800
7. Metchev, S. A., & Hillenbrand, L. A. 2009, *ApJS*, 181, 62
8. Moeckel, N., & Bate, M. R. 2010, *MNRAS*, 404, 721
9. Moeckel, N., & Clarke, C. J. 2011, *MNRAS*, 415, 1179
10. Patience, J., Ghez, A. M., Reid, I. N., & Matthews, K. 2002, *AJ*, 123, 1570
11. Raghavan, D., McAlister, H. A., Henry, T. J., et al. 2010, *ApJS*, 190, 1
12. Reggiani, M. M., & Meyer, M. R. 2011, *ApJ*, 738, 60
13. Reggiani, M., & Meyer, M. R. 2013, *A&A*, 553, 3

Radio Emission from YSOs: Tackling the (Reverse) Luminosity Problem

Anna M.M. Scaife

Abstract The 'classic luminosity problem' has been known for some time, where the minimum accretion luminosities produced by the standard spherical collapse model are up to several orders of magnitude larger than those observed for embedded protostars. The solution to this problem has been proposed as non-steady or episodic accretion rate onto such objects, and recent radiative transfer simulations have demonstrated that a combination of these effects can indeed reproduce the observed luminosity distribution. However, this work has also predicted a 'reverse luminosity problem', whereby an overabundance of objects is expected at very low luminosities relative to those observed. Although this effect is currently ascribed to observational completeness issues, further accurate comparison will not be possible without directed observational studies. Unfortunately, such low luminosity sources are difficult to identify in the infra-red as they are typically heavily embedded in thick dust cores, and the molecular emission from their outflows is frequently so weak that it is not easily or consistently detected. Radio emission from these objects provides a reliable alternative method for detection, as the dense dust cores are optically thin to the longer wavelength emission. Here I present results from a number of recent radio surveys specifically targeted at low and very low luminosity objects and discuss the new physical insights into star formation processes which can be drawn from these data.

1 The Luminosity Problem

Spitzer measurements of the luminosity distribution of low-mass protostars [5, 7] have aggravated the 'luminosity problem' first noted by [8]. These data show an increasing number of protostars with internal luminosities as low as $L_{\rm int} \simeq 0.1\,{\rm L}_{\odot}$,

A.M.M. Scaife (✉)
Physics & Astronomy, University of Southampton, Highfield, Southampton SO17 1BJ, UK
e-mail: a.scaife@soton.ac.uk

D. Stamatellos et al. (eds.), *The Labyrinth of Star Formation*, Astrophysics and Space Science Proceedings 36, DOI 10.1007/978-3-319-03041-8_5,

below which point a decline begins. For young embedded protostars, simple star formation models (e.g. [14]) predict that a low mass source on the stellar/brown dwarf boundary ($M \simeq 0.08\,\mathrm{M}_{\odot}$) should have an internal luminosity $L_{\mathrm{int}} \simeq 1.6\,\mathrm{L}_{\odot}$ from accretion alone [7]. The qualitative alternative of non-steady accretion is often invoked to explain this observed discrepancy, but it is most difficult to rectify in very low luminosity objects (VeLLOs) with extreme luminosities $L_{\mathrm{int}} \leq 0.1\,\mathrm{L}_{\odot}$. The physical state of such objects is unclear, whether they are young Class 0 protostars in the early stages of accretion, or are more evolved but in a low accretion state [5, 7].

Recent predictions of the luminosity distribution expected from non-steady accretion scenarios (e.g. [6]) have instead predicted an over-abundance of low luminosity objects: the so-called 'reverse luminosity problem'. These results emphasize the point that understanding the true accretion mechanism depends on observationally constraining the shape of the luminosity distribution at low luminosities. The existing sample of VeLLO sources, although expanded by *Spitzer*, is in no way complete. VeLLOs are difficult to confirm as protostars in the infra-red due to their low luminosity and embedded nature. It is also the case that VeLLOs are often found in cores which are not only assumed to be starless, but which were also not believed to be approaching collapse [3]. Nevertheless, identifying a complete sample of these low luminosity embedded protostars is vital for understanding low mass star formation.

2 Radio Emission from YSOs

Longer wavelength radio emission from young YSOs is capable of escaping from the high column density dust envelopes which surround deeply embedded young protostars, making such objects detectable in the radio band even when opacity effects conceal them at infared frequencies. In general, the radio emission from low-mass YSOs has been observed to possess a rising spectrum, indicating that it occurs as a consequence of free–free radiation from partially optically thick ionized plasma, with spectral indices in the range $-0.1 \leq \alpha \leq 2$, see Fig. 1. The physics behind the ionization around high-mass stars is reasonably well understood as arising from photoionization due to the strong UV flux from such objects. However, the ionizing flux from low-mass stars is not high enough to produce such emission and a number of mechanisms have been proposed to produce the ionization responsible for free–free emission in the immediate vicinity of low-mass young stellar objects. The most widely accepted of these is that the molecular outflows from young, low-mass protostars and the neutral winds thought to initiate them can generate free–free emission through shock ionization as they impact on the surrounding envelope [4, 9], which will produce a free–free flux density proportional to the outflow force, F_{out}, which is equivalent to the rate of outflow momentum and is often calculated as $F_{\mathrm{out}} = P/\tau_{\mathrm{dyn}}$.

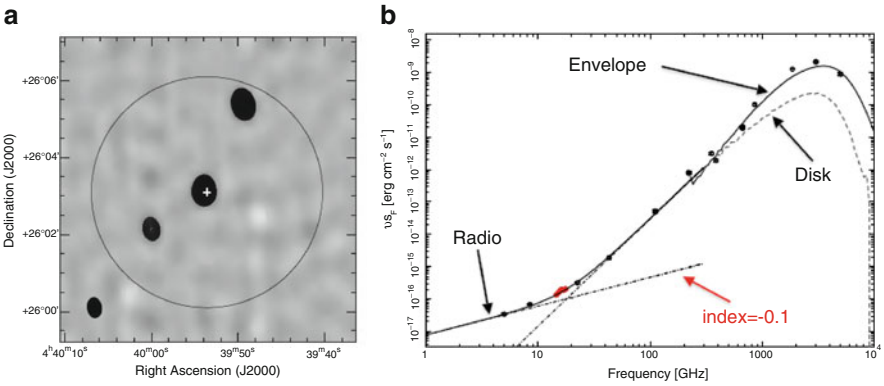

Fig. 1 L1527. (**a**) Radio map from the AMI-LA; (**b**) radio to sub-mm spectrum [11]

3 Characteristic Correlations

A strong correlation between radio and bolometric luminosity has been known for some time in the case of low-mass YSOs [1] and recent surveys have shown that this correlation appears to hold towards lower luminosities [11], see Fig. 2a.

Where measured, the outflow force of many protostellar jets has been found to be energetically viable to explain the observed cm-wave radio emission in terms of shock ionization [1]. However, as increasingly sensitive molecular observations reveal weaker and weaker outflows the measured momentum flux is also found to be insufficient to explain the total radio emission in a rising number of objects (objects below the solid line in Fig. 2b; [12,13]) and it is likely that a combination of multiple mechanisms is in fact responsible for the observed radio emission.

In many cases those known protostellar objects which are not detected in the radio have bolometric luminosities which make them discrepant with the observed $L_{\rm bol} - L_{\rm rad}$ correlation shown in Fig. 2a. Noticeably, however, this population does not appear correspondingly unusual when considered in terms of their envelope mass. A possible reason for this is the high ratio of bolometric luminosity to envelope mass, r, measured for these objects.

4 Discussion and Conclusions

The relationship of $L_{\rm bol}$ and $M_{\rm env}$ is often used to describe the evolution of embedded YSOs. Those objects which are discrepant with the $L_{\rm rad} - L_{\rm bol}$ trend, but not the $L_{\rm rad} - M_{\rm env}$, have values of r which place them in a similar range of evolutionary state. Under the simple evolutionary scenario of Bontemps et al. [2] they appear to be objects which have evolved from a relatively large initial mass

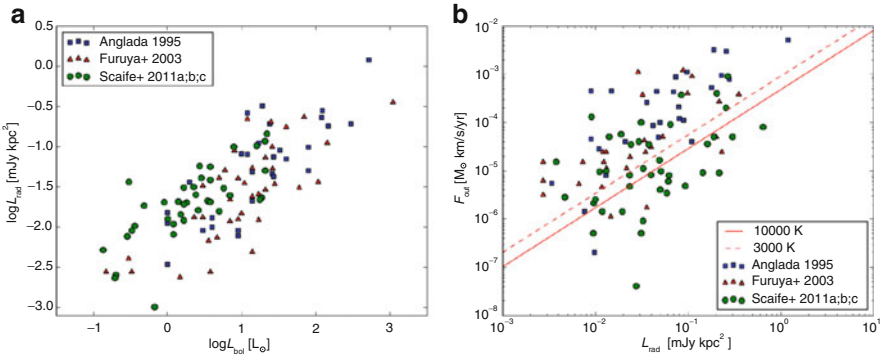

Fig. 2 (**a**) $L_{\rm bol} - L_{\rm rad}$ distribution; (**b**) $L_{\rm rad} - F_{\rm out}$ distribution (Figures from Scaife [10])

reservoir and are approaching their characteristic timescale, where ≈50 % of their initial mass will have been accreted. This detection pattern indicates that radio surveys for low-mass YSOs will be biased towards very young objects, early in their accretion history. This is highly complementary to infra-red surveys which are biased against such objects due to their heavily embedded nature.

Acknowledgements I thank the staff of the Lord's Bridge Observatory for their invaluable assistance in the commissioning and operation of the Arcminute Microkelvin Imager. The AMI-LA is supported by Cambridge University and the STFC.

References

1. Anglada G., 1995, RMxAC, 1, 67
2. Bontemps et al., 1996, A&A, 311, 858
3. Bourke T. L., et al. 2006, ApJ, 649L, 37B
4. Curiel S., Canto J., Rodriguez L. F., 1987, RMxAA, 14, 595
5. Dunham M. M., Crapsi A., Evans N. J., II, Bourke T. L., Huard T. L., Myers P. C., Kauffmann J., 2008, ApJS, 179, 249
6. Dunham M. M. & Vorobyov E. I., 2012, ApJ, 747, 52
7. Evans N. J., et al., 2009, ApJS, 181, 321
8. Kenyon S. J., et al., 1990, AJ, 99, 869K
9. Rodríguez L. F. & Reipurth B., 1996, RMxAA, 32, 27
10. Scaife, 2012, AstRv, 7d, 26S
11. AMI Consortium: Scaife et al., 2012, MNRAS, 420, 1019
12. AMI Consortium: Scaife et al., 2011b, MNRAS, 415, 893
13. AMI Consortium: Scaife et al., 2011a, MNRAS, 410, 2662
14. Shu F. H., 1977, ApJ, 214, 488S

Radiation Magnetohydrodynamic Simulations of Protostellar Core Formation

Kengo Tomida

Abstract We perform 3D nested-grid radiation magnetohydrodynamic (RMHD) simulations of the formation of proto-stellar cores from molecular cloud cores with and without the Ohmic dissipation of magnetic fields. In the ideal RMHD models, the evolution of the protostellar core is very similar to that in the spherically symmetric non-rotating model due to the efficient angular momentum transport. However, if the resistivity presents, the angular momentum transport is considerably suppressed due to the loss of magnetic flux, and rotationally-supported circumstellar disks are rapidly built up in the vicinity of the protostellar cores. Magnetic fields are amplified by rotation and fast outflows are launched from the protostellar cores via magnetic pressure gradient force. To our knowledge, these are the first 3D RMHD simulations resolving the protostellar cores in the world.

1 Introduction

Since Larson [1] first showed the scenario of the protostellar collapse, collapse of molecular cloud cores has been well studied so far. Computational simulations of star formation processes have been improved step by step by introducing new physical processes [2–8]. There has been no multidimensional simulation which directly resolves the protostellar (second) core including both magnetic fields and radiation transfer. Radiation transfer plays a crucial role in the thermal evolution in protostellar collapse and magnetic fields are of critical importance in the angular momentum transport. Moreover, the Ohmic dissipation is supposed to be crucial to resolve the magnetic flux problem and so-called "magnetic braking catastrophe"

K. Tomida (✉)
Department of Astrophysical Sciences, Princeton University, Princeton, NJ 08544, USA
e-mail: tomida@astro.princeton.edu

D. Stamatellos et al. (eds.), *The Labyrinth of Star Formation*, Astrophysics and Space Science Proceedings 36, DOI 10.1007/978-3-319-03041-8_6,

[9]. These physical processes must be properly considered in numerical simulations to construct realistic theoretical models of star formation processes.

Here we present new results of RMHD simulations of protostellar collapse including many ralistic physical processes required to understand star formation processes. The details of this work are presented in [10, 11].

2 Method and Model

We solve radiation magnetohydrodynamics with self-gravity and the Ohmic dissipation on nested-grid hierarchy. Each level of the nestd-grid consists of 64^3 cells and a finer grid is generated to resolve the local Jeans length with 16 cells [12]. We use the HLLD approximate Riemann solver [13] for magnetohydrodynamics. We adopt Flux Limited Diffusion (FLD) approximation [14, 15] for radiation transfer and solve the radiation subsystem implicitly. To solve the Ohmic dissipation, we use the resistivity based on [16] and introduce Super-Times-Stepping (STS) method [17] to accelerate calculation. In order to calculate the second collapse, we implement realistic equation of state including the effects of chemical reactions.

We calculated five models but here we focus on two rotating magnetized models with and without the resistivity. We start from 1Ms unstable Bonnor-Ebert-like sphere with uniform magnetic fields of $20\,\mu$G and rigid-body rotation of $\Omega = 2.4\times10^{-14}\,\mathrm{s}^{-1}$. We stop the calculations when the central temperature reaches about 10^5 K, about 1 year after the formation of the protostellar cores.

3 Results

The models with and without the Ohmic dissipation show qualitatively similar evolutions until the second collapse begins. The resistivity significantly extracts magnetic flux from the first core and suppresses the angular momentum transport but the evolution of the first core is not so different from the spherical case because the magnetic braking is still efficient. Slow loosely-collimated outflows are launched by the magneto-centrifugal force from both the ideal and resistive models and their properties are almost identical.

However, the evolutions after the formation of the protostellar cores are completely different (Fig. 1). The protostellar core in the ideal MHD model evolves essentially in the same way as the spherical model because there remains virtually no angular momentum. In the resistive model, on the other hand, the angular momentum in the protostellar core is far larger than the ideal model, more than two orders of magnitude. The circumstellar disk is quickly built up in the vicinity of the protostellar core just after the formation of the protostellar core. Thus the Ohmic dissipation remedies the magnetic braking catastrophe and enables the circumstellar disk formation.

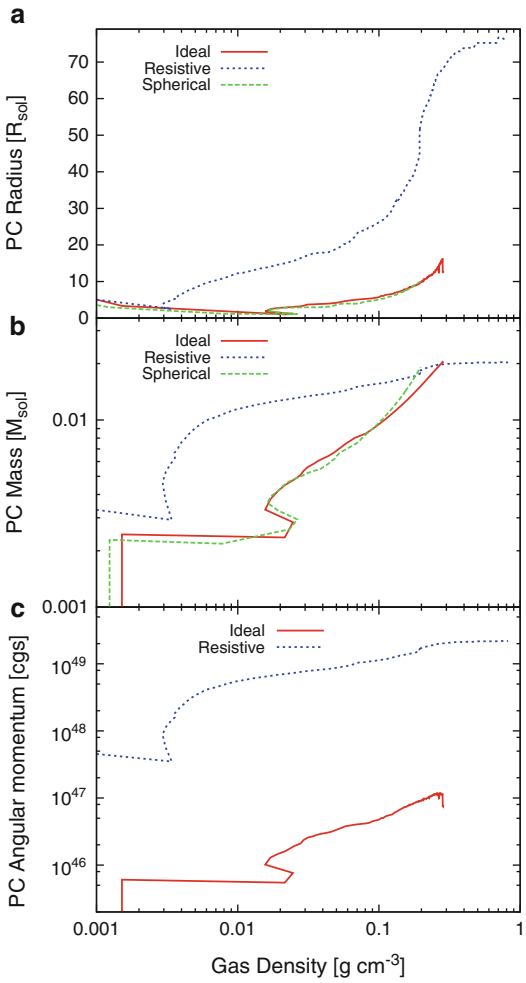

Fig. 1 The evolution of the radii, mass and angular momenta (from top to bottom) of the protostellar cores versus the central gas density. The ideal MHD model (*red solid lines*) shows virtually the same evolution as the spherical model (*green dashed*), while the resistive MHD model (*blue dotted*) evolves differently because of the large angular momentum

In the resistive MHD model, the toroidal magnetic fields are tightly wound up and rapidly amplified in the rotating protostellar core (Fig. 2). Then, the magnetic pressure drives the fast and well collimated outflows from the protostellar core. The outflow velocity reaches about 15 km s^{-1} and is still getting faster as the protostellar core grows. The tightly-wound magnetic fields are perturbed by the kink instability.

4 Discussion

We first successfully revealed the earliest phase of the formation of the protostellar cores with realistic physical processes. The thermal evolution during the protostellar collapse is consistent with the previous spherically symmetric simulations using

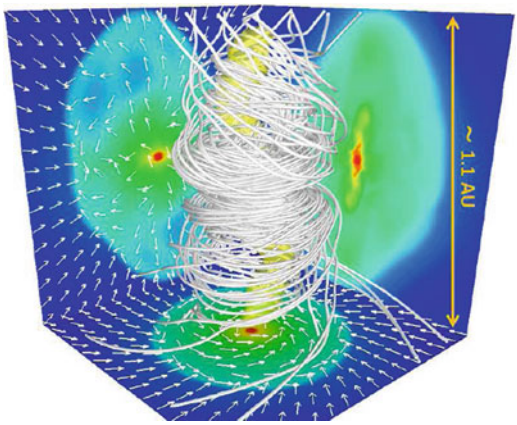

Fig. 2 The 3D view of the protostellar core and the outflow in the resistive model. The *left* and *bottom panels* show the gas density cross sections and the *right panel* is the gas temperature. *White arrows* denote the gas velocity and *white lines* represent the magnetic field lines

full non-gray radiation transfer [18]. We confirmed the results of preceding MHD simulations that the Ohmic dissipation remedies the magnetic braking catastrophe and enables the circumstellar disk formation [19]. We also showed that two different types of outflows are spontaneously launched from the first cores and the protostellar cores due to the interaction between the rotation and the magnetic fields [4, 5].

It is computationally too expensive to continue these direct simulations of the protostellar cores because the timescale within the protostellar core is too short. We need to adopt the sink partcle techinique to reduce the computational load.

Acknowledgements KT is supported by the Research Fellowship from the Japan Society for the Promotion of Science. Numerical computations were partly performed on NEC SX-9 at Center for Computational Astrophysics of National Astronomical Observatory of Japan, at Japan Aerospace Exploration Agency and at Osaka University.

References

1. R.B. Larson, MNRAS **145**, 271 (1969)
2. M.R. Bate, ApJL **508**, L95 (1998).
3. K. Tomisaka, ApJL **502**, L163+ (1998).
4. M.N. Machida, S.i. Inutsuka, T. Matsumoto, ApJL **647**, L151 (2006).
5. M.N. Machida, S.i. Inutsuka, T. Matsumoto, ApJ **676**, 1088 (2008).
6. M.R. Bate, MNRAS **404**, L79 (2010).
7. B. Commerçon, P. Hennebelle, E. Audit, G. Chabrier, R. Teyssier, A&A **510**, L3+ (2010).
8. K. Tomida, K. Tomisaka, T. Matsumoto, K. Ohsuga, M.N. Machida, K. Saigo, ApJL **714**, L58 (2010).
9. Z.Y. Li, R. Krasnopolsky, H. Shang, ApJ **738**, 180 (2011).
10. K. Tomida, K. Tomisaka, T. Matsumoto, Y. Hori, S. Okuzumi, M.N. Machida, K. Saigo, ArXiv e-prints (2012)
11. K. Tomida, Radiation Magnetohydrodynamic Simulations of Star Formation Processes. Ph.D. thesis, The Graduate University for Advanced Studies (2012)

12. J.K. Truelove, R.I. Klein, C.F. McKee, J.H. Holliman, II, L.H. Howell, J.A. Greenough, ApJL **489**, L179 (1997).
13. T. Miyoshi, K. Kusano, Journal of Computational Physics **208**, 315 (2005).
14. C.D. Levermore, G.C. Pomraning, ApJ **248**, 321 (1981).
15. C.D. Levermore, Journal of Quantitative Spectroscopy and Radiative Transfer **31**, 149 (1984).
16. S. Okuzumi, ApJ **698**, 1122 (2009).
17. V. Alexiades, G. Amiez, P. Gremaud, Communications in numerical methods in engineering **12**(1), 31 (1996)
18. H. Masunaga, S.i. Inutsuka, ApJ **531**, 350 (2000).
19. M.N. Machida, T. Matsumoto, MNRAS **413**, 2767 (2011).

Implications of Protostellar Disk Fragmentation

Eduard Vorobyov and Shantanu Basu

Abstract We review several outcomes of disk gravitational fragmentation in the early evolution of solar-mass protostars. In particular, we focus on the ejection of fragments into the intracluster medium, formation of wide-separation brown-dwarf companions to solar-type stars and annealing of amorphous silicates in the depths of massive and hot fragments.

1 Introduction

Gravitational instability and fragmentation of embedded disks in the early evolution of solar-mass protostars is a common occurrence. Numerical hydrodynamics simulations demonstrate that protostellar disks undergo multiple episodes of fragmentation if formed from pre-stellar cores of sufficiently high mass and angular momentum (e.g. [5, 7–9]). Semi-analytic studies seem to confirm this (e.g. [6]).

Although disk fragmentation has long been known as a possible source for binary/multiple stars, brown dwarfs, and even massive giant planets [3, 7, 10], its importance yet to be fully appreciated. In this article, we show how ejection of fragments into the intracluster medium via many-body gravitational interaction can account for the formation of freely-floating brown dwarfs [2]. We also demonstrate that fragments may escape fast inward migration or ejection and settle onto stable wide-separation orbits [10]. Finally, we will show how disk fragmentation can

E. Vorobyov (✉)
Department of Astrophysics, The University of Vienna, 1180 Vienna, Austria

Research Institute of Physics, Southern Federal University, Rostov-on-Don 344092, Russia
e-mail: eduard.vorobiev@univie.ac.at

S. Basu
Department of Physics and Astronomy, The University of Western Ontario, London, Canada

D. Stamatellos et al. (eds.), *The Labyrinth of Star Formation*, Astrophysics and Space Science Proceedings 36, DOI 10.1007/978-3-319-03041-8_7,

account for the presence of crystalline silicates in the Solar System comets [11]. The main concepts of our numerical approach are explained in detail in Vorobyov and Basu [8, 9] and the reader is referred to these papers for the in-depth analysis.

2 Ejection of Fragments via Many-Body Gravitational Interaction

The disk propensity to fragment increases along the sequence of increasing initial core mass and angular momentum. Recent work [2] has shown that there is also a tendency for a fragment to be ejected from a disk due to interaction between multiple fragments and the primary object. This supports a new hybrid paradigm of brown dwarf (BD) formation by disk fragmentation followed by fragment ejection (rather than by ejection of finished BDs). This scenario naturally accounts for the presence of disks around BDs and the observed velocity dispersion and physical location of BDs relative to young stellar objects.

The top panels in Fig. 1 show a sequence of column density images for a prototype model at various times after the formation of a central object. Within

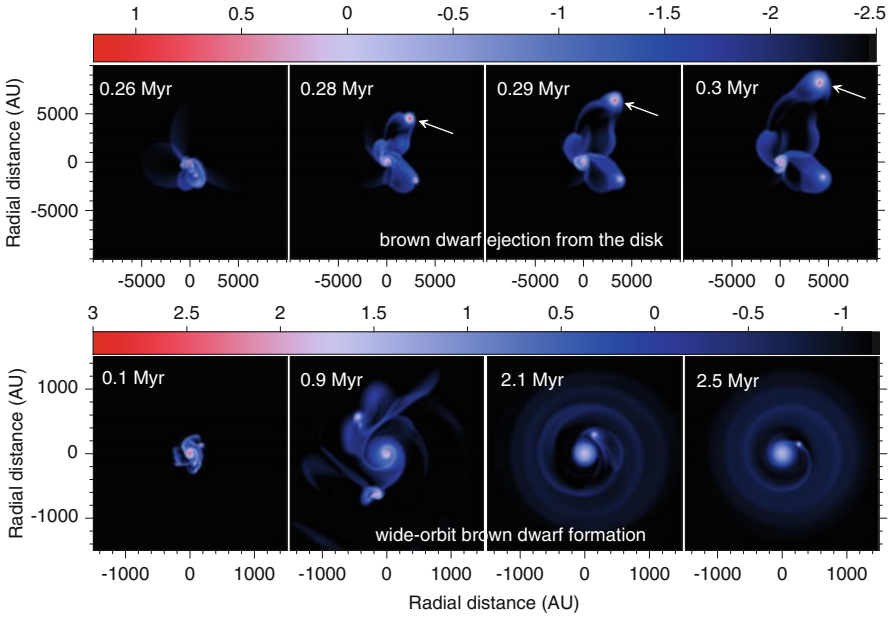

Fig. 1 *Top*. Ejection of a proto-brown-dwarf embryo (shown by the *arrows*) from the protostellar disk (the inner region) due to many-body interaction. Shown is the gas surface density (in g cm^{-2}) in the 20,000 times 20,000 AU box at several consecutive times after the ejection instant. *Bottom*. Formation of a wide-separation brown-dwarf companion

the first 0.25 Myr, multiple fragments are formed in the relatively massive disk, at distances greater than about 50 AU and less than a few hundred AU. They are generally torqued inward through gravitational interaction with trailing spiral arms, others located at large radii may eventually disperse. However, under sometime-favorable conditions, a fragment within a multi-fragment environment can be ejected through many-body interaction. Such an event begins at about 0.26 Myr. The velocity of the ejected fragment is about 0.9 km s^{-1}, which is a factor of 3 greater than the escape velocity. This means that the clump will truly be lost to the system. The total mass of the clump is 0.15 $M_{\odot}$. This value includes not only the compact core but also a diffuse envelope and even fragments of a spiral. We speculate that upon contraction this fragment may form a substellar object. In general, the ejection rate is about one fragment per model.

2.1 Formation of Wide-Orbit Brown-Dwarf Companions

In most cases, fragments either migrate inward to the inner boundary and onto the star or are dispersed in outer regions. One fragment per model is usually ejected into the intracluster medium. There is yet another gateway along which the evolution of fragments may proceed – a "lucky" fragment may escape migration, dispersal or ejection and settle onto a quasi-stable, wide orbit. The bottom panel in Fig. 1 demonstrates this phenomenon. Several fragments condense in the disk as early as 0.1 Myr after disk formation. By $t = 0.9$ Myr, only two most massive fragments survive, others were driven onto the star or dispersed. Finally, one of the two fragments was able to carve out a gap in the disk and settled into a stable orbit at around 400 AU from the central object. The mass of the fragment is about 25 Jovian masses. The necessary prerequisite for this phenomenon is the initial core mass $>1.0\ M_{\odot}$ and the ratio of rotational to gravitational energy >0.5 %.

3 Crystallization of Silicates in the Fragment Interiors

Two mechanisms for dust crystallization have been put forward: (a) evaporation of the original, amorphous dust grains followed by recondensation under conditions of high temperature and density (e.g. [4]) and (b) thermal annealing of the amorphous grains at temperatures 800–1,300 K via viscous heating, shock wave heating or disk surface heating during EX-Lupi-like outbursts (e.g. [1]).

Recently, Vorobyov [11] has suggested another promising gateway for the production of crystalline silicates in protostellar disks – thermal annealing of amorphous dust grains in the hot interiors of massive fragments. Figure 2 presents the gas surface density (left), gas temperature (middle) and, crystalline silicate fraction ξ in the inner 400 AU of a young protostellar disk. There are three distinct fragments present in the disk, but only one (shown by the arrow) is characterized

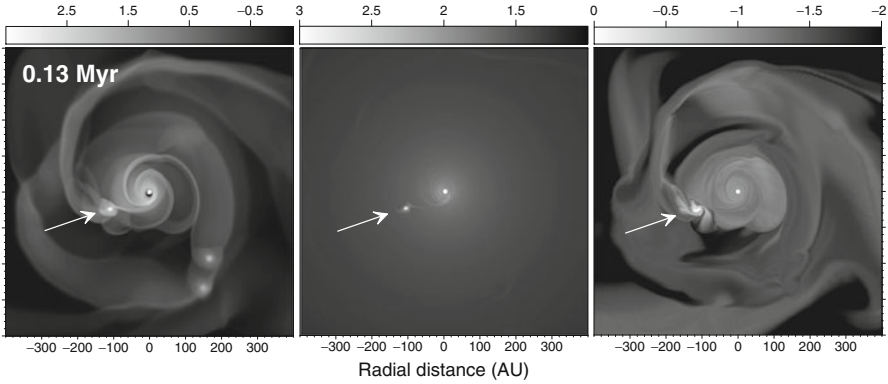

Fig. 2 Gas surface density (*left panel*, g cm^{-2}), gas midplane temperature (*middle panel*, K), and the crystalline silicate fraction (*right panel*) in the protostellar disk at $t = 0.13$ Myr after the formation of the central star (quantities are on a log scale)

by the gas temperature in its interior exceeding 800 K (middle panel). These high temperatures are sufficient to anneal pristine amorphous silicates in the fragment interiors (right panel). The processed dust can be released at (sub-)AU scales if fragments are destroyed on their close approach to the central star, or at 10-AU and even 100-AU scales if they are dispersed by tidal torques exerted by spiral arms. We stress that this mechanism can provide a direct source of crystalline silicates at large distances, thus naturally explaining the relatively large abundance of crystalline silicates in such comets as Wild 2 and Tempel 1.

Acknowledgements This research was partly supported by RFBR grants 10-02-00278 and 11-02-92601. Numerical simulations were done at the Atlantic Computational Excellence Network (ACEnet) and the Shared Hierarchical Academic Research Computing Network (SHARCNET).

References

1. Ábrahám et al. 2009, Nature, 459, 224
2. Basu, S. & Vorobyov, E. 2012, ApJ, 750, 30
3. Boss, A. P. 2012, MNRAS, 419, 1930
4. Grossman L. 1972, Geochim. Cosmochim. Acta, 36, 597
5. Machida, M. N., Inutsuka, S., Matsumoto, T. 2011, ApJ, 729, 42
6. Rice, W. K. M., Mayo, J. H., & Armitage, P. J. 2010, MNRAS, 402, 1740
7. Stamatellos, D., & Whitworth, A. P. 2009, MNRAS, 392, 413
8. Vorobyov, E. I., & Basu, S. 2006, ApJ, 650, 956
9. Vorobyov, E. I., & Basu, S. 2010, ApJ, 719, 1896
10. Vorobyov, E. I., & Basu, S. 2010, ApJL, 714, 133
11. Vorobyov, E. I. 2011, ApJL, 728, 45

An X-Shooter Analysis of Chromospheric Activity of Class III Low Mass Sources

Carlo Felice Manara, L. Testi, J.M. Alcalá, E. Covino, A. Natta, S. Randich, E. Rigliaco, and B. Stelzer

Abstract The knowledge of the photospheric parameters and the level of chromospheric activity in young pre-main sequence stars is one of the main limitations when trying to measure mass accretion rates in Class II YSOs. A detailed characterization of photospheres and chromospheric activities in low-mass, young stars without disks (late K and M type Class III YSOs) is still missing. Using VLT/X-Shooter spectra we have analyzed a sample of Class III in the Spectral Type range between K5 and M9.5. We report on the characterization of the chromospheric emission in the stars in our sample and on the implications that our work has on accurate measurements of mass accretion rates in YSOs.

1 Observations and Sample

During the X-Shooter-INAF GTO survey: "*An X-Shooter survey in galactic Star Formation Regions: low and sub-stellar mass objects*" [1], 19 Spitzer selected (e.g. [4]) Class III objects have been observed in nearby ($d < 500$ pc) star forming regions with low extinction ($A_V < 0.2$ mag). Most of our sources (80 %) have spectral type

C.F. Manara (✉) • L. Testi
ESO-Garching, Karl-Schwarzschild-Str 2, 85748 Garching bei München, Germany
e-mail: cmanara@eso.org

J.M. Alcalá • E. Covino
INAF-Capodimonte, via Moiariello 16, 80131 Napoli, Italy

A. Natta • S. Randich
INAF-Arcetri, Largo E. Fermi 5, 50125 Firenze, Italy

E. Rigliaco
University of Arizona, E. University Blvd, Tucson, AZ 85719, USA

B. Stelzer
INAF-Palermo, Piazza del Parlamento 1, 90134 Palermo, Italy

D. Stamatellos et al. (eds.), *The Labyrinth of Star Formation*, Astrophysics and Space Science Proceedings 36, DOI 10.1007/978-3-319-03041-8_8,

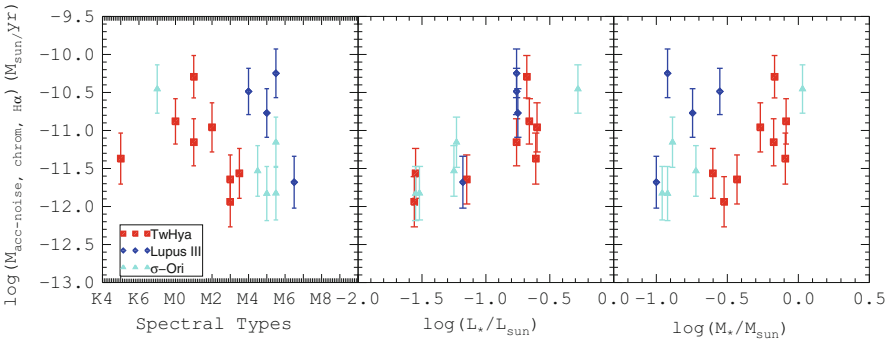

Fig. 1 $\dot{M}_{\rm acc-noise}$ obtained considering the chromospheric emission of our Class III sources as accretion indicator and using the $H\alpha$ line luminosity and the relation by Rigliaco et al. [5] to obtain the $L_{\rm acc-noise}$, that is the accretion luminosity noise that would be obtained if the excess luminosity in this line would have been due to accretion. We plot these values as a function of SpT, L_* and M_* with different colors for the three different regions

between M0 and M6.5. We have also two Brown Dwarfs in our sample, with spectral types M9 and M9.5, and two K-type stars. The sources in our sample are located in 3 regions: 10 sources are in the TW Hydrae, 4 in the Lupus III and 5 in the σ-Orionis region.

2 Analysis

The analysis of the emission lines present in our Class III spectra showed that the Balmer series lines, Ca HK, Ca IRT are always present. Instead, Paschen and Brackett series lines, as well as all the forbidden lines, are never detected.

Using the relationships between the emission line luminosity and the accretion luminosity ($L_{\rm acc}$) derived in the literature (e.g., [2, 5]), we computed the values of the noise in the Mass Accretion Rates estimate ($\dot{M}_{\rm acc-noise}$) due to chromospheric emission, using the chromospheric induced excess as due to accretion. Figure 1 shows that our values of $\dot{M}_{\rm acc-noise}$ are in the range $\log(\dot{M}_{\rm acc-noise}) \sim -10.5$ to $-12\,M_\odot$/year [3], depending on the target luminosity and indicator used (here we show only the $H\alpha$ line emission).

3 Conclusions

In this work we have observed 19 K5-M9.5 Class III YSOs with X-Shooter and derived accurate estimates of the SpT. We detected chromospheric emission from all our sources. We then analyzed the impact of chromospheric emission on

measurements of $\dot{M}_{\rm acc}$ in YSOs, assuming the same level of activity in Class III and Class II of similar SpT, L_* and M_*. The derived chromospheric noise level in $\dot{M}_{\rm acc}$ measurements is of the order of $\log(\dot{M}_{\rm acc-noise}) \sim -10.5$ to $-12\, M_\odot/{\rm year}$, depending on photospherical parameters. We conclude that measurements of $\dot{M}_{\rm acc}$ in Class II YSOs of these orders are unreliable, when based on unresolved line luminosity.

References

1. Alcalá, J. M., Stelzer, B., Covino, E., et al. 2011, Astronomische Nachrichten, 332, 242
2. Herczeg, G. J., & Hillenbrand, L. A. 2008, ApJ, 681, 594
3. Manara, C.F., Testi, L., Rigliaco, E., Alcala, J.M., Natta, A. et al. 2013, A&A, 551, A107
4. Merín, B., Jørgensen, J., Spezzi, L., et al. 2008, ApJS, 177, 551
5. Alcalá, J.M., Natta, A., Manara, C.F., Spezzi, L., Stelzer, B. et al. 2014, A&A, 561, A2

Part III
Young Circumstellar Discs

A Review of Circumstellar Discs

Ken Rice

Abstract It is now accepted that stars form from collapsing molecular cloud cores and that they are typically surrounded – at early times – by circumstellar discs that have lifetimes of a few million years. These discs are thought to go through a number of different phases. During the earliest stages of star formation they are expected to evolve through disc self-gravity and may undergo a number of outbursts. The magnetorotational instabilty is thought to dominate at later times and may occur, initially at least, in the upper, ionised layers of the discs. The final stages evolve through dispersal via a disc wind, driven by photoevaporation. I will review, here, the evolution of these discs and will discuss some observations that support this general picture.

1 Introduction

It is now well established that low-mass stars form through the collapse of cold, dense molecular cloud cores [33, 35]. Conservation of angular momentum requires, however, that most of the mass must first pass through a circumstellar disc before accreting onto the central star. These discs therefore provide the mechanisms for transporting angular momentum outwards, allowing mass to accrete onto the central star.

In this paper I will introduce some of the basic properties of circumstellar discs and then discuss how they evolve. I will consider their evolution at early times, when disc self-gravity [34] is significant, through to the later stage when the

K. Rice (✉)
Institute for Astronomy, The University of Edinburgh, The Royal Observatory, Blackford Hill, Edinburgh EH93HJ, UK
e-mail: wkmr@roe.ac.uk

D. Stamatellos et al. (eds.), *The Labyrinth of Star Formation*, Astrophysics and Space Science Proceedings 36, DOI 10.1007/978-3-319-03041-8_9,

magnetorotational instability (MRI; [4]) is likely to dominate. I will then discuss how these discs are finally dispersed and will also mention some observational results that support this general picture.

2 Basic Properties

Young stellar objects (YSOs) are typically divided into four different classes, Class 0, I, II and III [1, 20] with Class 0 objects being the youngest and Class III being the oldest. In these systems, discs can be observed directly [6, 26] or can be inferred through the existence of an infrared excess [20]. The infrared excess can also be used to estimate disc lifetimes. Haisch et al. [15] have shown that the fraction of YSOs with infrared excesses – and hence discs – in different star forming regions decreases as star forming regions get older, suggesting that typical disc lifetimes are $\sim 5 - 6$ Myr.

The disc mass is also observed to decrease with increasing YSO age. Figure 1 [14] shows the disc mass distributions for Class 0 (red), Class I (blue) and Class II (black) YSOs. The disc mass clearly decreases from Class 0 through to Class II and during the Class 0 phase can be quite massive ($M_{\rm disc} > 0.1$ M$_\odot$). There is also an indication that during the Class 0 phase, discs are very compact [25]. The basic picture is that circumstellar discs have lifetimes of $\sim$5 Myr, start with

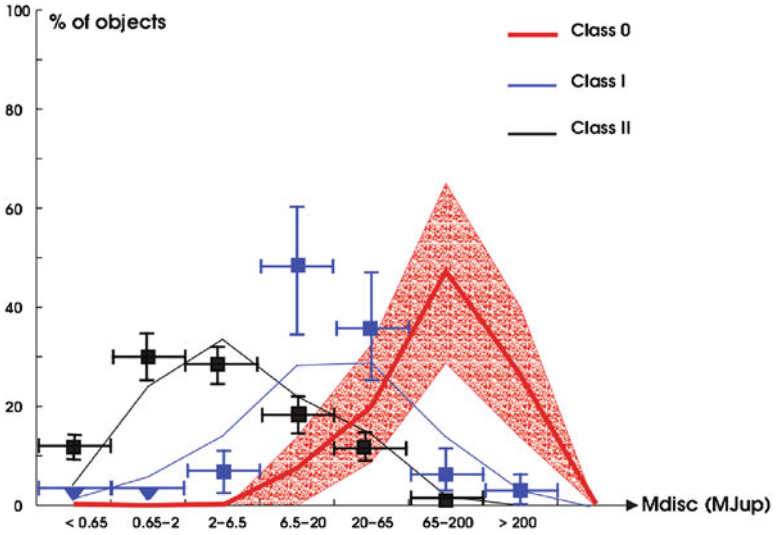

Fig. 1 Disc mass distributions for Class 0, Class I and Class II YSOs [14]. This clearly shows that the typical disc mass decreases with increasing YSO age and shows that, during the Class 0 phase, the disc mass can be quite substantial

relatively large masses (compared to that of the central star) that reduce with time, and typically appear to start with small outer radii ($r_{\rm out} < 30$ AU).

3 Disc Evolution

It is reasonably clear that circumstellar discs are the conduit for transferring angular momentum outwards, allowing mass to accrete onto the central star. Since the material in these discs orbit with Keplerian velocities, producing a radially dependent azimuthal velocity (shear), it is typically assumed that some kind of viscosity acts to transport angular momentum. This viscosity cannot be molecular as this would produce disc lifetimes that far exceeded that observed. Shakura and Sunyaev [31] therefore introduced what is now called the α viscosity and has the form $\nu = \alpha c_s H = \alpha c_s^2/\Omega$, where α represents the viscous efficiency and is typically $\ll 1$, c_s is the disc sound speed, and H is the disc scaleheight. This doesn't tell us anything about what provides the viscosity but does allows us to consider how such discs will evolve under the action of a viscosity of this form. A disc with surface density Σ will evolve in time according to [24, 28]

$$\frac{d\Sigma}{dt} = \frac{3}{r}\frac{\partial}{\partial r}\left[r^{1/2}\frac{\partial}{\partial r}\left(\nu\Sigma r^{1/2}\right)\right]. \tag{1}$$

In a quasi-steady state it can then be shown that this will produce mass accretion at a rate $\dot{M} = 3\pi\nu\Sigma$ and will dissipate energy per unit area at a rate

$$D(r) = \frac{9}{4}\nu\Sigma\Omega^2. \tag{2}$$

In most astrophysical discs it is generally accepted that the viscosity is provided by the magnetorotational instabilty (MRI; [4]). This requires that the disc be partially ionised, threaded by a weak magnetic field and that $d\Omega/dr < 0$, as is the case in Keplerian discs. YSOs, however, form from cold, dense molecular clouds cores and so the discs, at early times, probably do not have even the very small degree of ionization needed to sustain this magnetohydrodynamic (MHD) turbulence [7]. The disc is, however, expected to be quite massive, relative to the mass of the central star, and so disc self-gravity may provide an alternate, and possibly dominant, transport mechanism at these early times [21, 22, 34].

3.1 Disc Self-Gravity

A disc is susceptible to the growth of the gravitational instability if the Toomre Q parameter [34] satisfies $Q = c_s\Omega/\pi G\Sigma \sim 1$, where Ω is the angular frequency. It is

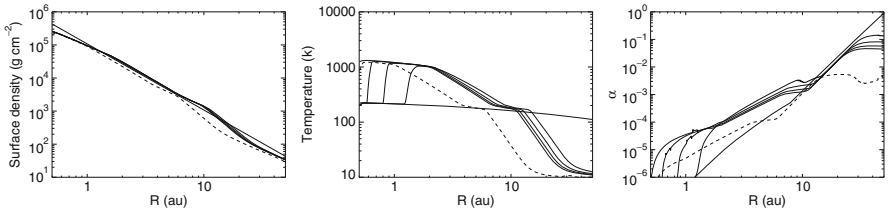

Fig. 2 The structure of quasi-steady, self-gravitating circumstellar discs [30] showing a steep surface density profile with lots of mass in the inner disc (*left-hand panel*), high temperatures in the inner disc (*middle panel*), and a viscous α that is very small in the inner disc and increases with increasing radius (*right-hand panel*)

now known that a self-gravitating disc can settle into a quasi-steady state in which the instability acts to transport angular momentum [5, 13, 23]. If the disc cools with a cooling time $t_{\rm cool}$, then the cooling rate can estimated as

$$\frac{du}{dt} = \frac{u}{t_{\rm cool}} = \frac{c_s^2 \Sigma}{\gamma(\gamma-1)t_{\rm cool}}, \tag{3}$$

where u is the internal energy, and γ is the specific heat ratio. Equation 3 can then be equated with Eq. 2, and using $\nu = \alpha c_s^2/\Omega$, to show that a quasi-steady self-gravitating discs has an effective viscous α given by

$$\alpha_{\rm grav} = \frac{4}{9\gamma(\gamma-1)t_{\rm cool}\Omega}. \tag{4}$$

If the cooling time is determined realistically [8, 30], one can then use Eq. 1 together with Eq. 4 to determine the quasi-steady state of a self-gravitating protostellar disc. Figure 2 [30] shows the quasi-steady nature of such a disc. The surface density is very steep with lots of mass in the inner disc, the temperature is consequently high in the inner disc, and the self-gravitating α is very low ($\alpha < 10^{-4}$). I discuss below some observational properties of YSOs that are consistent with these properties of self-gravitating protostellar discs.

3.1.1 FU Orionis Outburst

An FU Orionis outburst is a rapid and large increase in the luminosity of, what is thought to be, a very young stellar object [16]. The left-hand panel of Fig. 3 shows the lightcurve of V1057 Cyg, with the x-axis in years and the y-axis in magnitudes. This illustrates the rapid increase in luminosity (four or more magnitudes) that takes $\sim$1 year, followed by a slow recovery lasting $\sim$100 years. The rapid rise time suggests that outburst must originate at $r \sim 1$ AU. If occuring in a YSO, the peak luminosity would correspond to an accretion rate of $\dot{M} \sim 10^{-4}\,{\rm M}_\odot\,{\rm yr}^{-1}$.

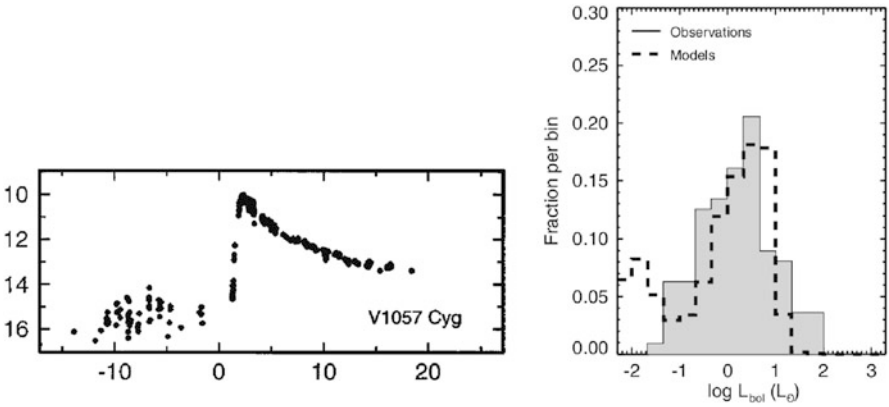

Fig. 3 The *left-hand panel* shows *lightcurve* of the FU Orionis object V1057 Cyg with the x-axis in years and the y-axis in magnitudes. This shows a rapid rise in luminosity (taking ∼1 year) in which the luminosity increases by over four magnitudes and a slow recovery taking many 10s of years. The *right-hand panel* shows histrograms of the observed luminosities of YSOS (*filled*) and those determined from a model (*dashed*)

If the outburst lasts for ∼100 years, this would suggest a total mass accretion of $\sim 0.01\,M_{\odot}$. The quasi-steady self-gravitating disc structures shown in Fig. 2 have sufficient mass in the inner disc and reach temperatures high enough for the onset of MRI. It has therefore been suggested [3] that FU Orionis outburst may be a consequence of an outer self-gravitating disc that feeds an inner disc which goes into outburst when the temperature in the inner disc is high enough for MRI to operate. Simulations [36] suggest that this may indeed be a viable mechanism for generating FU Orionis outbursts.

3.1.2 The Luminosity Problem

The luminosity problem was first noted by S.J. Kenyon et al.[19]. Given that most of the mass added to a typical YSO will occur during a period of $\sim 10^5$ years, we would expect the luminosity to by $\sim 100\,L_{\odot}$. Typical luminosities are, however, $\sim 1\,L_{\odot}$. The solution to this is related to the FU Orionis mechanism discussed above. The outer parts of discs arounds very young YSOs are thought to be self-gravitating. The inner parts can, however, become very hot, allowing MRI to operate, producing an outburst. Once this outburst is over, the inner parts ($r < 1$ AU) are depleted and are refilled by the outer self-gravitating disc. The luminosity of this outer accretion is low ($L \sim 1\,L_{\odot}$) and refilling the inner disc can take ∼10,000 years. The system will therefore typically have a low luminosity ($L \sim 1\,L_{\odot}$) which will increase significantly during the outburst phase, lasting ∼100 years. The filled histrogram in the right-hand panel of Fig. 3 shows the distribution of luminosities for YSOs, illustrating that they typically have luminosities of $\sim 1\,L_{\odot}$. The dashed histogram

is the luminosity distribution for models with an outer self-gravitating disc and an inner disc that "turns-on" episodically [9] and shows that the above scenario can potentially resolve the luminosity problem.

3.2 Later Disc Evolution and Dispersal

The gravitational instability is only effective in transporting angular momentum when disc masses are high [30]. This suggests an alternate transport mechanism must take over when the system is still relatively young. It is thought [12] that this could occur through MRI operating in the upper layers of the disc, which are ionised through cosmic rays. As the disc mass decreases, the fraction of the mass in these MRI active layers will increase and it will eventually become the dominant transport mechanism. The outer regions of the disc may become fully ionised and hence fully MRI active. There may, however, remain a dead zone at intermediate radii (0.1 to a few AU) where there is no turbulent activity and which may play a role in the accumulation of planet building material.

If discs were to evolve solely through viscously-driven angular momentum transport, disc lifetimes would be significantly longer than observed. This suggests that there must be some kind of dispersal mechanism that starts to dominate once the mass accretion rate drops below a few $\times 10^{-8}\,\mathrm{M}_{\odot}\ \mathrm{yr}^{-1}$. The basic idea is that photoevaporation drives a disc wind [18]. In the inner parts of the disc, the escape velocity will be too high for this wind to operate. There will, however, be a radius beyond which the escape velocity is low enough for photoevaporation to drive a disc wind. Once the mass accretion through the disc is low enough, the inner and outer disc will decouple. The inner disc will drain onto the star through viscous evolution, while the outer disc will be dispersed through this disc wind. It was originally thought [2] that this wind would be driven by FUV and EUV photons. Recent work has, however, suggested that x-rays dominate [10,27]. There are indeed observations of systems with near-IR deficit that are consistent with this disc wind dispersal mechanism. There are, however, other processes – such as embedded planets [29] – that can also produce near-IR deficits and so not all such systems are thought to be a consequence of disc dispersal [11].

4 Conclusion

I have reviewed here the evolution of circumstellar accretion discs around young stellar objects. It is thought that these start with masses quite high relative to the mass of the central star and hence evolve, initially, through disc self-gravity. This is very ineffective in the inner disc and so provides a mechanism for driving FU Orionis outbursts and also explains the well-known luminosity problem. At later times, when disc self-gravity is less effective due to the lower disc masses,

the magnetorotational instability (MRI) dominates. These discs cannot, however, evolve solely through viscous-like angular momentum transport and are thought be dispersed via a disc wind driven by photoevaporation. What I have not discussed here is the role of global magnetic field which may play a role in angular momentum transport and may result in compact discs at early times [17]. I have also not discussed the fragmentation of self-gravitating protostellar discs, which may result, typically, in the formation of low-mass stars or brown dwarfs [32].

References

1. P.D. Andre, D. Ward-Thompson, M. Barsony, Astrophys. J., **406**, 122–141 (1993)
2. R.D. Alexander, C.J. Clarke, J.E. Pringle, Mon. Not. Royal Astron. Soc., **369**, 216–228 (2006)
3. P.J. Armitage, M. Livio, J.E. Pringle, Mon. Not. Royal Astron. Soc., **324**, 705–711 (2001)
4. S.A. Balbus, J.F. Hawley, Astrophys. J., **376**, 214–233 (1991)
5. S.A. Balbus, J.C.B. Papaloizou, Astrophys. J., **521**, 650–658 (1999)
6. J. Bally, R.S. Sutherland, D. Devine, D. Johnstone, Astron. J., **116**, 293–321 (1998)
7. O.M. Blaes, S.A. Balbus, Astrophys. J., **421**, 163–177 (1994)
8. C.J. Clarke, Mon. Not. Royal Astron. Soc., **396**, 1066–1074 (2009)
9. M.M. Dunham, E.I. Vorobyov, Astrophys. J., **747**, 52–62 (2012)
10. B. Ercolano, C.J. Clarke, J.J. Drake, Astophys. J., **699**, 1639–1649 (2009)
11. B. Ercolano, C.J. Clarke, Mon. Not. Royal Astron. Soc., **402**, 2735–2743 (2010)
12. C.F. Gammie, Astrophys. J., **457**, 355–362 (1996)
13. C.F. Gammie, Astrophys. J., **553**, 174–183 (2001)
14. J.S. Greaves, W.K.M. Rice, Mon. Not. Royal Astron. Soc., **412**, L88–L92 (2011)
15. K.E. Haisch, E.A. Lada, C.J. Lada, Astrophys. J. Lett., **553**, L153–L156 (2001)
16. L. Hartmann, S.J. Kenyon, Ann. Rev. Astron. Astrophys., **34**, 207–240 (1996)
17. P. Hennebelle, A. Ciardi, Astron. Astrophys., **506**, L29–L32 (2009)
18. D. Hollenbach, D. Johnstone, S. Lizano, F. Shu, Astrophys. J., **428**, 654–669 (1994)
19. S.J. Kenyon, L.W. Hartmann, K.M. Strom, S.E. Strom, Astron. J., **99**, 869–887 (1990)
20. C.J. Lada, in *Star forming regions*, ed. by M. Peimbert & J. Jugaka. IAU symposium, vol 115, p. 1 (1987)
21. G. Laughlin, P. Bodenheimer, Astrophys. J., **436**, 335–354 (1994)
22. D.N.C. Lin, J.E. Pringle, Mon. Not. Royal Astron. Soc., **225**, 607–613 (1987)
23. G. Lodato, W.K.M. Rice, Mon. Not. Royal Astron. Soc., **351**, 630–642 (2004)
24. D. Lynden-Bell, J.E. Pringle, Mon. Not. Royal Astron. Soc., **168**, 603–637 (1974)
25. A.J. Maury, et al., Astron. Astrophys., **512**, A40 (2010)
26. M.J. McCaughrean, C.R. O'dell, Astron. J., **111**, 1977–1986 (1996)
27. J.E. Owen, B. Ercolano, C.J. Clarke, R.D. Alexander, Mon. Not. Royal Astron. Soc., **410**, 1415–1428 (2010)
28. J.E. Pringle, Ann. Rev. Astron. Astrophys., **19**, 136–162 (1981)
29. W.K.M. Rice, K. Wood, P.J. Armitage, B.A. Whitney, J.E. Bjorkman, Mon. Not. Royal Astron. Soc., **342**, 79–85 (2003)
30. W.K.M. Rice, P.J. Armitage, Mon. Not. Royal Astron. Soc., **396**, 2228–2236 (2009)
31. N.I. Shakura, R.A. Sunyaev, Astron. Astrophys., **24**, 337–355 (1973)
32. D. Stamatellos, A.P. Whitworth, Mon. Not. Royal Astron. Soc., **392**, 413–327 (2009)
33. S. Terebey, F.H. Shu, P. Cassen, Astrophys. J., **286**, 529–551 (1984)
34. A. Toomre, Astrophys. J., **139**, 1217–1238 (1964)
35. A.P. Whitworth, D. Summers, Mon. Not. Royal Astron. Soc., **214**, 1–25 (1985)
36. Z. Zhu, L. Hartmann, C.F. Gammie, Astrophys. J., **694**, 1045–1055 (2009)

The Formation and Early Evolution of Protostars and Protoplanetary Disks

Shu-ichiro Inutsuka

Abstract We discuss the formation and early evolution of protostars and protoplanetary disks. Recent advances in theoretical modelling with resistive magnetohydrodynamical codes with various numerical techniques has dramatically improved our understanding on the driving of outflows/jets and the formation of protoplanetary disks. The circumstellar disk is born in a "dead zone," a region that is de-coupled from the magnetic field. The outer radius of the disk increases with the outer boundary of the dead zone during the phase of gas accretion from the envelope of the molecular cloud core. The rapid increase of the disk size occurs after the depletion of the envelope. Circumstellar disks remain massive in their formation phase, and are subject to gravitational instability, even at 10 AU from the central stars.

1 Formation of Protostars

There are two basic problems in the theory of star formation: The angular momentum problem and the magnetic flux problem. The typical angular momentum of a newly-formed protostar is a very small fraction of the observationally inferred angular momentum of a parental molecular cloud core. Likewise the typical magnetic flux of the protostar is also a very small fraction of that of a cloud core. Theory of star formation should explain how to reduce the angular momentum and magnetic flux in the process of the self-gravitational collapse. Three-dimensional non-ideal magnetohydrodynamical simulation with self-gravity is essential in solving the problems. This article briefly explains the efforts to answer these problems that are given by the recent theoretical modeling with resistive

S. Inutsuka (✉)
Department of Physics, Graduate School of Science, Nagoya University, Furo-cho, Chikusa-ku, Nagoya 464-8602, Japan
e-mail: inutsuka@nagoya-u.jp

D. Stamatellos et al. (eds.), *The Labyrinth of Star Formation*, Astrophysics and Space Science Proceedings 36, DOI 10.1007/978-3-319-03041-8_10,

magnetohydrodynamical codes that cover a huge dynamic range from molecular cloud core density ($10^4\,\mathrm{cm}^{-3}$) to stellar density ($10^{22}\,\mathrm{cm}^{-3}$) in a self-consistent manner [4].

Notable findings of non-ideal magnetohydrodynamics simulations are two distinct flows (low- and high-velocity flows) that are driven from different objects with different size scales (the first and second cores) [7]. We can simply expect that the low-velocity flow from the first core corresponds to the molecular outflow, while the high-velocity flow from the protostar corresponds to the optical jet [14, 15]. In simulations with typical initial parameters, the flow appearing around the first core has a wide opening angle and slow speed, while the flow appearing around the protostar has a well-collimated structure and high speed. The flow speed corresponds to the escape speed of each object (the first and the second cores). Note that gas around the protostar has already experienced the magnetic flux loss during the collapsing motion through the magnetically dead zone [6]. Substantially reduced magnetic flux at the center results in the passively wound-up magnetic field lines just after the formation of a protostar. This is followed by driving of a fast bipolar jet along the rotation axis by the resultant strong magnetic pressure due to excessive winding. Strong collimation of the jet is due to the hoop stress of piled-up toroidal field lines ([7], see also [1, 2, 5, 12, 13].)

2 Formation of Protoplanetary Disks

The masking of the central region in the protostellar collapse simulation that requires short time-resolution enables us to observe the formation of a circumstellar disk around the central star and the long-term evolution of the disk as a protoplanetary disk. Since protoplanetary disks are sites of planet formation, this kind of calculations essentially determines the initial condition for planet formation [3, 8–11] .

2.1 Emergence of a Circumstellar Disk in the Deadzone

Figure 1 is a typical “bird’s eye-view” snapshot of the non-ideal MHD simulation that shows the formation of circumstellar disk [3]. Most of angular momenta in gravitationally collapsing objects are removed by the Maxwell stress of the field, which is called magnetic braking [6]. In addition the outflowing gas carries away angular momentum during this phase. The upper right panel of Fig. 1 shows an enlarged view of the region inside the outflow launching regions, where the resistivity is so significant that the magnetic field is de-coupled from the gas. The outflow region envelops the “dead zone” for magnetic field where magnetic braking is not operating [7]. Therefore, “the second-collapsing” gas in the first core maintains angular momentum and reaches the radius of the centrifugal barrier to form a circumstellar disk-like structure. The formation of this disk-like structure

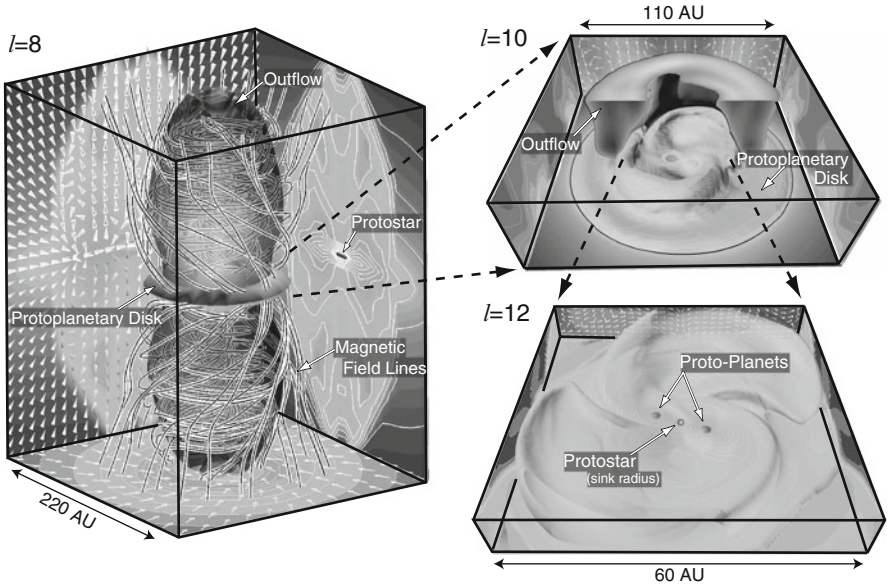

Fig. 1 Bird's eye-view of the result of non-ideal MHD simulation with nested grid technique, covering the evolution of the molecular cloud core to the protostar. The *left panel* shows the structure in the grid, level $l = 8$, where the high-density region ($n = 10^{10}\,\mathrm{cm}^{-3}$; *blue* isodensity surface) and magnetic field lines are plotted. Two cocoon-like structures (*brown*) above and below the flattened core denote the zero-velocity surface inside of which the gas is outflowing from the center. The density contours (*color* and *contour lines*) and velocity vectors (*thin white arrows*) are projected on each wall surface. The *right upper panel* shows the structure in part of the 10th grid, where we can clearly see the central cavity in the outflowing region. The *right lower panel* (12th grid) shows the protoplanetary disk in the formation phase, and two newly-formed planetary-mass objects in the disk

corresponds to the birth of the protoplanetary disk, and happens in the dead zone inside the outflow launching region.

The infalling from the cloud envelope to the central region continues, and the radius of the outflow launching region increases with time, as does the outer boundary of the magnetic dead zone. Likewise, both the mass and the outer radius of the circumstellar disk increase with time. Eventually, the radius of the disk extends beyond the initial radius of the first core and the first core disappears; In other words, *the first core transforms itself into a protoplanetary disk*.

2.2 Completion of Disk Formation

Figure 2 is a schematic diagram of the circumstellar disk formation. The horizontal axis denotes the evolutionary time, while the vertical axis corresponds to the length scale. $t = t_*$ corresponds to the formation of the protostar. $t < t_*$ describes the

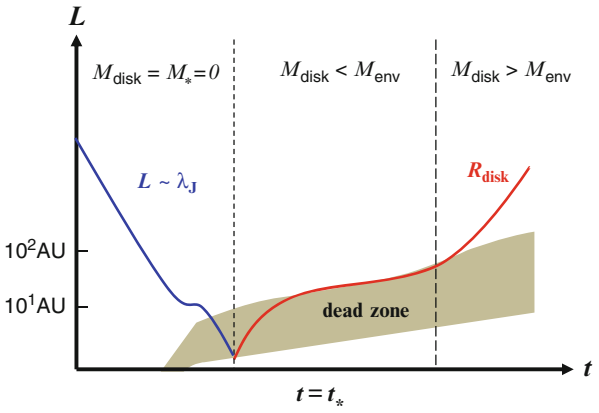

Fig. 2 A schematic diagram of the disk formation [4]. The abscissa denotes the evolutionary time, while the ordinate denotes the length scale. $t = t_*$ corresponds to the formation of the protostar. The *shaded region* denotes the *dead zone* where the magnetic field lines are not effectively coupled to the gas. The disk outer radius rapidly grows with time after the disk mass exceed the envelope mass [10]

gravitational collapse prior to the formation of the protostar. The shaded region corresponds to the magnetically dead zone where the magnetic field lines are not effectively coupled to the gas. We can summarize the formation of disk in the following way [10]: When the mass of the envelope is much larger than the disk mass, the magnetic braking is so effective so that disk formation is possible only in the dead zone. After the disk mass exceed the envelope mass, the magnetic braking become less effective and the outer radius of the disk rapidly grows with time.

The circumstellar disks remain massive in their formation phase, and are subject to gravitational instability, even at 10 AU from the central stars [3]. The further long-term evolutions of massive disks are also described [9, 10]. This may provide improved description for the realistic initial condition and environments for planet formation in gaseous protoplanetary disks.

References

1. B. Commerçon, R. Teyssier, E. Audit, P. Hennebelle, & G. Chabrier A&Ap 510, L3 (2010)
2. B. Commerçon, R. Teyssier, E. Audit, P. Hennebelle, & G. Chabrier A&Ap 529, 35 (2011)
3. S. Inutsuka, M. N. Machida, & T. Matsumoto, ApJ 718, L58 (2010)
4. S. Inutsuka, Progress of Theoretical and Experimental Physics (2012) in press
5. M. N. Machida, S. Inutsuka, & T. Matsumoto, ApJL, 647, L151 (2006)
6. M. N. Machida, S. Inutsuka, & T. Matsumoto, ApJ 670, 1198 (2007)
7. M. N. Machida, S. Inutsuka, & T. Matsumoto, ApJ, 676, 1088 (2008)
8. M. N. Machida, S. Inutsuka, & T. Matsumoto, ApJ 724, 1006 (2010)
9. M. N. Machida, S. Inutsuka, & T. Matsumoto, ApJ 729, 42 (2011)
10. M. N. Machida, S. Inutsuka, & T. Matsumoto, PASJ 63, 555 (2011)
11. M. N. Machida & T. Matsumoto, MNRAS 413, 2767 (2011)
12. K. Tomida et al. ApJ 714, L58 (2010)
13. K. Tomida et al. submitted to ApJ (arXiv:1206.3567)
14. K. Tomisaka, ApJ 502, L163 (1998)
15. K. Tomisaka, ApJ 575, 306 (2002)

The Lifetime of Protoplanetary Discs: Observations and Theory

Barbara Ercolano and Christine Koepferl

Abstract The time-scale over which and modality by which young stellar objects (YSOs) disperse their circumstellar discs dramatically influences the eventual formation and evolution of planetary systems. By means of extensive radiative transfer (RT) modelling, we have developed a new set of diagnostic diagrams in the infrared colour–colour plane (K - [24] vs. K - [8]), to aid with the classification of the evolutionary stage of YSOs from photometric observations. Our diagrams allow the differentiation of sources with un-evolved (primordial) discs from those evolving according to different clearing scenarios (e.g. homologous depletion vs. inside-out dispersal), as well as from sources that have already lost their disc. Classification of over 1,500 sources in 15 nearby star-forming regions reveals that approximately 39 % of the sources lie in the primordial disc region, whereas between 31 and 32 % disperse from the inside-out and up to 22 % of the sources have already lost their disc. Less than 2 % of the objects in our sample lie in the homogeneous draining regime. Time-scales for the transition phase are estimated to be typically a few 10^5 years independent of stellar mass. Therefore, regardless of spectral type, we conclude that currently available infrared photometric surveys point to fast (of order 10 % of the global disc lifetime) inside-out clearing as the preferred mode of disc dispersal.

B. Ercolano (✉)
Excellence Cluster 'Universe', Boltzmannstraße 2, 85748 Garching, Germany
e-mail: ercolano@usm.lmu.de

C. Koepferl
Universitäts-Sternwarte München, Scheinerstraße 1, 81679 München, Germany
e-mail: koepferl@usm.lmu.de

D. Stamatellos et al. (eds.), *The Labyrinth of Star Formation*, Astrophysics and Space Science Proceedings 36, DOI 10.1007/978-3-319-03041-8_11,

1 Introduction

The lifetime and modality for the dispersal of protoplanetary discs around newly formed low mass stars (approximately solar mass or lower) is a key parameter that influences the formation and evolution of eventual planetary systems. The classical picture that emerged from the last decade of photometric observations, mainly carried out with the Spitzer Space telescope is that of disc evolution being described by two different timescales. The first timescale could be defined as a global timescale, i.e. the total time it takes from a star to go from disc-bearing to disc-less, and a dispersal timescale, i.e. the time it takes for a disc to disappear once dispersal has set in. Global timescales, which can be inferred from the study of disc frequencies (e.g. [11]), are of order a few million years (e.g. [12, 16]). Dispersal time-scales, as determined from the study of infrared colours of young stars, appear to be much shorter, indicating that the dispersal mechanism must be fast (e.g. [8, 13, 15]). Such observed two-timescale behaviour has favoured the development of disc dispersal models that involve a rapid disc clearing phase, contrary to the predictions of simple viscous draining, and in agreement with photoevaporation [1,2,4,6,9,10,17–20] or possibly planet formation [3]. The interpretation of infrared colours in relation to the evolutionary state of a disc is, however, far from being trivial. This is particularly true with regards to the classification of transition discs, the latter being intended as objects caught in the act of disc dispersal. The evolution of the dust component in a disc is mirrored by the evolution of colours in the infrared plane. By means of radiative transfer modelling, Ercolano, Clarke, and Hall (2011, henceforth [8]) identified the regions in the K - [8] vs. K - [24] plane where primordial discs, discs with inner-holes (i.e. presumably being dispersed from the inside-out) and discs which lose mass homogeneously at all radii, are expected to be found. Their study, which was limited to M-stars, showed that in the case of the cluster IC348, most discs disperse from the inside-out and undergo the transition on a short time-scale, as predicted by standard photoionisation models. These conclusions are in contrast with the conclusions of [5], who claimed instead a large number of homogeneously depleting discs, for the same cluster. Such discrepancies highlight the need for detailed modelling in the interpretation of IR colours of discs. The study of [8] was restricted to M-stars in only one cluster, which prevented the authors from being able to make a more general statement with regards to disc dispersal. Here we present results from a forthcoming paper [14], which significantly improves on the work of [8] by performing further RT calculation to evaluate evolutionary tracks in the IR colour plane for stars of different spectral types. We then apply our results to the photometric data of 15 nearby star-forming regions, that we collected from the literature, in order to address the question of what is the preferred mode of disc dispersal.

2 Disc Evolution in the Infrared Two Colour Plane

By means of radiative transfer modelling we identify five areas in the K - [8] vs. K - [24] plane corresponding to discs at different evolutionary stages or with different geometries, these are shown in Fig. 1. Namely, primordial optically thick (flared and/or mixed) discs occupy area A, while disc-less objects cluster in area B and area C is for primordial ultra-settled (flat) discs. Discs that are in the act of dispersal belong to area D and E, where the former is for discs that are clearing from the inside-out, and the latter is for discs that are progressively going optically thin homogeneously at all discs radii (as would be expected from viscous evolution alone). Our classification scheme allows us to use currently available infrared photometric surveys from nearby star-forming regions in order to address the question of what is the preferential mode of disc dispersal. We therefore applied our colour–colour diagnostic diagrams to classify 1,529 objects in 15 nearby star-forming regions. As an example, we overplot the data for Taurus (taken from [15]) to the diagnostic diagram in Fig. 1. In summary, 39 % of the objects out of the entire sample lie in the primordial disc region whereas between 31 and 32 % disperse their discs from the inside-out and up to 22 % of the sources have already lost their disc. So, almost a third of the available sources are currently clearing their discs from the inside-out. Less than 2 % of the objects lie in the homogeneous draining region E. We interpret this result as strong evidence against homogeneous disc depletion as the main disc dispersal mode.

3 Dispersal Time-Scales Across Spectral Types

With the sample of YSOs in different star-forming regions becoming larger and larger, it is now possible to estimate the typical time-scales for the disc dispersal phase, even though cluster ages of course always introduce a large uncertainty in the estimates. The disc-evolution time-scale of a star-forming region can be roughly estimated by multiplying the age of the region by the ratio of the number of evolved object to the total number of objects in the region. Typical transition time-scales for the considered star-forming regions are of order 10^5 years. The average time-scale across all spectral types is $6.9 \cdot 10^5$ years and roughly the same as the average cluster time-scale of $6.6 \cdot 10^5$ years. This is partially because there is no significant difference for timescales amongst spectral types. We further illustrate that disc dispersal time-scales appear to be independent of spectral type. We plot in Fig. 2, the time-scale ratio between K and M-stars and show that this ratio is consistent with unity. This suggests that there is no significant dependence of the time-scale on stellar mass, as has already been pointed out by Ercolano et al. [7], who performed a

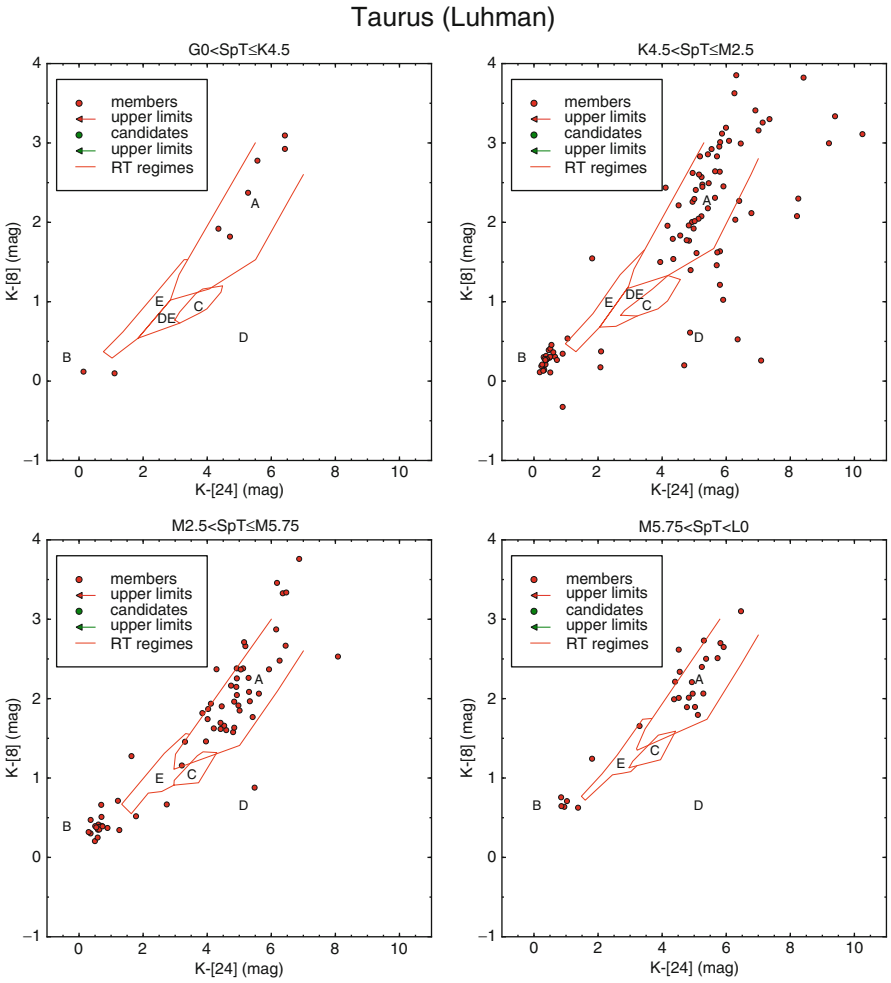

Fig. 1 Disc evolution diagnostic diagram applied to the YSOs in the 1 Myr old cluster Taurus. Twenty sample points lie outside the limits of this plot, but they are still included in the final statistics. (51 % primordial optically thick (*A*), 0 % primordial ultra-settled (*C*), 23 % disc-less (*B*), 14 % inside-out clearing (*D*), < 1 % homogeneous draining (*E*))

spatial analysis of the distribution of K and M-stars with discs in young star-forming regions and found no significant difference in the distributions.

4 Summary

We have calculated the SEDs of protoplanetary discs of different spectral types, geometries, settling and inclination. We then considered the evolution of the infrared colours (K - [8] vs. K - [24]) of the model disks as they disperse according

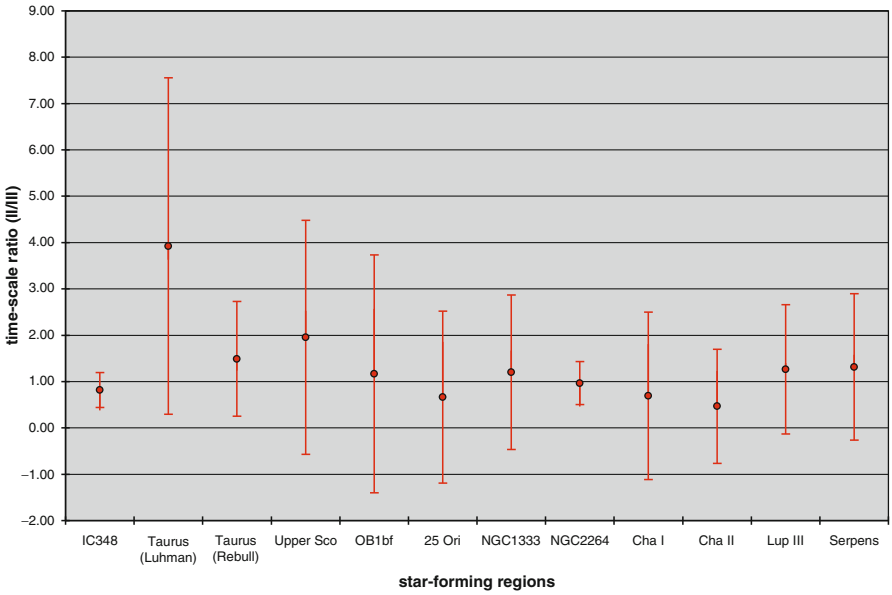

Fig. 2 Time-scale ratio $\tau_{(II)}/\tau_{(III)}$ for K and M stars for the star-forming regions considered in this work with $N_{tot} > 10$. Three star-forming regions are not listed, because they lack evolving objects in one or both spectral type intervals

to different scenarios (homologous depletion, inside-out and outside-in clearing). Based on our models we propose a new diagnostic infrared colour–colour diagram to classify the evolutionary stage of YSOs. We have applied our infrared colour–colour diagnostic diagram to classify YSOs in 15 nearby star-forming regions and study the evolution of their disc populations. We estimate time-scales for transition phase of typically a few 10^5 years independent of stellar mass. We conclude that, regardless of spectral type, current observations point to fast inside-out clearing as the preferred mode of disc dispersal.

References

1. Alexander R. D., Clarke C. J., Pringle J. E., 2006a, *MNRAS*, 369, 216
2. Alexander R. D., Clarke C. J., Pringle J. E., 2006b, *MNRAS*, 369, 229
3. Armitage P. J., Hansen B. M. S., 1999, *NATURE*, 402, 633
4. Clarke C. J., Gendrin A., Sotomayor M., 2001, *MNRAS*, 328, 485
5. Currie T., Kenyon S. J., 2009, *AJ*, 138, 703
6. Ercolano B., 2008, in Star Formation Across the Milky Way Galaxy
7. Ercolano B., Bastian N., Spezzi L., Owen J., 2011a, *MNRAS*, 416, 439
8. Ercolano B., Clarke C. J., Hall A. C., 2011b, *MNRAS*, 410, 671
9. Ercolano B., Drake J. J., Clarke C. J., 2009, *A&A*, 496, 725
10. Gorti U., Dullemond C. P., Hollenbach D., 2009, *ApJ*, 705, 1237

11. Haisch, Jr. K. E., Lada E. A., Lada C. J., 2001, *ApJ*, 553, L153
12. Hernández J. et al., 2007, *ApJ*, 671, 1784
13. Kenyon S. J., Hartmann L., 1995, *ApJS*, 101, 117
14. Koepferl C. M., Ercolano B., Dale J., Teixeira P. S., Ratzka T., Spezzi L., 2012, Disc clearing of young stellar objects: evidence for fast inside-out dispersal, submitted to *MNRAS*
15. Luhman K. L., Allen P. R., Espaillat C., Hartmann L., Calvet N., 2010, *ApJS*, 186, 111
16. Mamajek E. E., 2009, in American Institute of Physics Conference Series, Vol. 1158, American Institute of Physics Conference Series, Usuda T., Tamura M., Ishii M., eds., pp. 3–10
17. Owen J. E., Clarke C. J., Ercolano B., 2012, *MNRAS*, 422, 1880
18. Owen J. E., Ercolano B., Clarke C. J., 2011a, *MNRAS*, 412, 13
19. Owen J. E., Ercolano B., Clarke C. J., 2011b, *MNRAS*, 411, 1104
20. Owen J. E., Ercolano B., Clarke C. J., Alexander R. D., 2010, *MNRAS*, 401, 1415

Protostellar Disk Formation and Angular Momentum Transport During Magnetized Core Collapse

Marc Joos, Patrick Hennebelle, and Andrea Ciardi

Abstract Theoretical studies of collapsing clouds have found that even a relatively weak magnetic field may prevent the formation of disks and their fragmentation. However, most previous studies have been limited to cases where the magnetic field and the rotation axis of the cloud are aligned, and very few studies investigated the combined effects of magnetic field and turbulence.

We perform three-dimensional, adaptive mesh, numerical simulations of magnetically supercritical collapsing dense cores in both non-turbulent and turbulent environment.

At variance with earlier analyses, we show that the transport of angular momentum acts less efficiently in collapsing cores with non-aligned rotation and magnetic field. We also show that the turbulence is responsible for a misalignment between the rotation axis and the magnetic field and can diffuse out the magnetic field of the inner regions efficiently. The magnetic braking is therefore reduced, and massive disks can be built. If the disks are massive enough and the magnetization not too strong, fragmentation can occur. These results are presented in details in [7, 8].

M. Joos (✉) • A. Ciardi
Laboratoire de Radioastronomie, LERMA, Observatoire de Paris, École Normale Supérieure, Université Pierre et Marie Curie (UMR 8112 CNRS), 24 rue Lhomond, 75231 Paris Cedex 05, France
e-mail: marc.joos@lra.ens.fr; andrea.ciardi@obspm.fr

P. Hennebelle
Laboratoire AIM, Paris-Saclay, CEA/IRFU/SAp – CNRS – Université Paris Diderot, 91191 Gif-sur-Yvette Cedex, France
e-mail: patrick.hennebelle@lra.ens.fr

D. Stamatellos et al. (eds.), *The Labyrinth of Star Formation*, Astrophysics and Space Science Proceedings 36, DOI 10.1007/978-3-319-03041-8_12,

1 Introduction

The formation of protostellar disks plays a central role in the context of star and planet formation. Their formation is however still not well understood. Unlike Class I (and more evolved) disks, Class 0 disks formation remains unclear. Recent studies showed no clear evidence for disks or fragmentation for Class 0 protostars [10].

Theoretically, one of the main problems regarding disk formation is the magnetic braking, which transports angular momentum so efficiently that it can prevent massive disk formation, even at relatively low magnetic intensities ($\mu \lesssim 5-10$, μ being the magnetization parameter [6, 11, 12]), largely compatible with the observational measurements [2].

Most previous simulations have been performed in an idealized configuration, where the magnetic field and the rotation axis are initially aligned. As emphasized in [4] (see also [12]), the results of the collapse depend critically on the initial angle α between the magnetic field **B** and the rotation axis (which is the direction of the angular momentum **J**). Moreover, very few studies investigated the role of turbulence in magnetized low-mass cores (see [9], or [5, 13] for high-mass cores).

Following the previous studies of [4] (see also [1]), we investigate in detail the transport of angular momentum, and the effects of magnetic braking in collapsing prestellar cores with aligned and misaligned configurations (α between 0 and 90°), and in non-turbulent and turbulent environments.

2 Collapse in a Non-turbulent Environment

We first perform 3D AMR-MHD simulations of the collapse of a $1\,M_\odot$ core with the RAMSES code [3, 14]. The Jeans length is resolved with at least ten cells. We typically have a maximum spatial resolution of ∼0.5 AU. The initial density profile is that of a Plummer-like sphere. The magnetization parameter is taken between 2 and 17 (strong and low magnetization cases, respectively). The angle between the initial magnetic field and the initial rotation axis α is taken to be between 0 and 90°.

2.1 Transport of Angular Momentum

In the regions of the disk ($n > 10^9\,\mathrm{cm}^{-3}$) and the adiabatic core ($n > 10^{10}\,\mathrm{cm}^{-3}$) the angular momentum increases with α. Therefore, in misaligned rotators, more angular momentum will be available to "build" centrifugally supported disks.

To have a better understanding of the angular momentum transport, we consider the azimuthal component of the conservation of angular momentum in cylindrical coordinates, given by

$$\partial_t \left(\rho r v_\phi\right) + \nabla \cdot r \left[\rho v_\phi \mathbf{v} + \left(P + \frac{B^2}{8\pi} - \frac{g^2}{8\pi G}\right)\mathbf{e_\phi} - \frac{B_\phi}{4\pi}\mathbf{B} + \frac{g_\phi}{4\pi G}\mathbf{g}\right] = 0. \quad (1)$$

The fluxes of angular momentum of interest in this equation are $r\rho v_\phi \mathbf{v}$ for the mass flow, $rB_\phi \mathbf{B}/4\pi$ for the magnetic field. The integrals are taken over the surface S of a cylinder, corresponding approximately to the disk, of radius $R \simeq 300$ AU and height $h \simeq 150$ AU.

More angular momentum is carried away by magnetic braking from the central region of the collapsing core for relatively small α (below 70°) than for larger α (above 70°). As for the transport by the flow, When the angle α increases, the amount of angular momentum carried away decreases and in the perpendicular case, the total angular momentum transported by the flow is about ten times smaller than in the aligned case. The suppression of the outflows with increasing α is responsible for this decrease (see [1]).

2.2 Disk Formation

When enough angular momentum is left in the envelope, a disk can form around the adiabatic core. A simple rotation criterion is insufficient to define a disk because several parts of the envelope are rotating but do not belong to the disk. We define disks by employing a combination of five different criteria: $v_\phi > v_r$ (disks are expected to be Keplerian), $v_\phi > v_z$ (they are expected to be near the hydrostatic equilibrium), $\rho v_\phi^2/2 > P_{\rm th}$ (they are rotationally supported), $n > 10^9\,{\rm cm}^{-3}$ (to obtain more realistic estimate of the shape of the disk) and a connectivity criterion.

Figure 1 shows that the disk mass increases with the angle α. This agrees with our previous discussions, which indicated that the magnetic braking is more efficient in less tilted configurations, thus limiting the effective mass of disks. It is also clear that for increasing magnetic field strength, thus increasing magnetic braking, disks with masses greater than $0.05 M_\odot$ are only found in misaligned configurations. The limiting case corresponds to a magnetization of $\mu = 2$, where the removal of angular momentum by the magnetic field is so efficient that the mass of rotating gas does not exceed $0.05 M_\odot$, even in the perpendicular case.

3 Collapse in a Turbulent Environment

The initial conditions are the same as in the non-turbulent simulations, except for the initial mass of the core, which is 5 $M_\odot$. We also impose a turbulent velocity field with a Kolmogorov spectrum and $E_{\rm turb}/E_{\rm grav}$ between 0 and 0.5.

Two main effects are stressed here: first, the turbulence is responsible for a misalignment between the rotation axis and the magnetic field, which leads to a decrease of the magnetic braking efficiency, as we discussed previously. It is also responsible for an effective magnetic diffusion, which leads to a decrease of the magnetic field strength and therefore of the magnetic braking.

The mass of the disk as a function of time for different turbulence levels, is presented in Fig. 2. It shows a trend to form bigger disks when $E_{\rm turb}$ is higher;

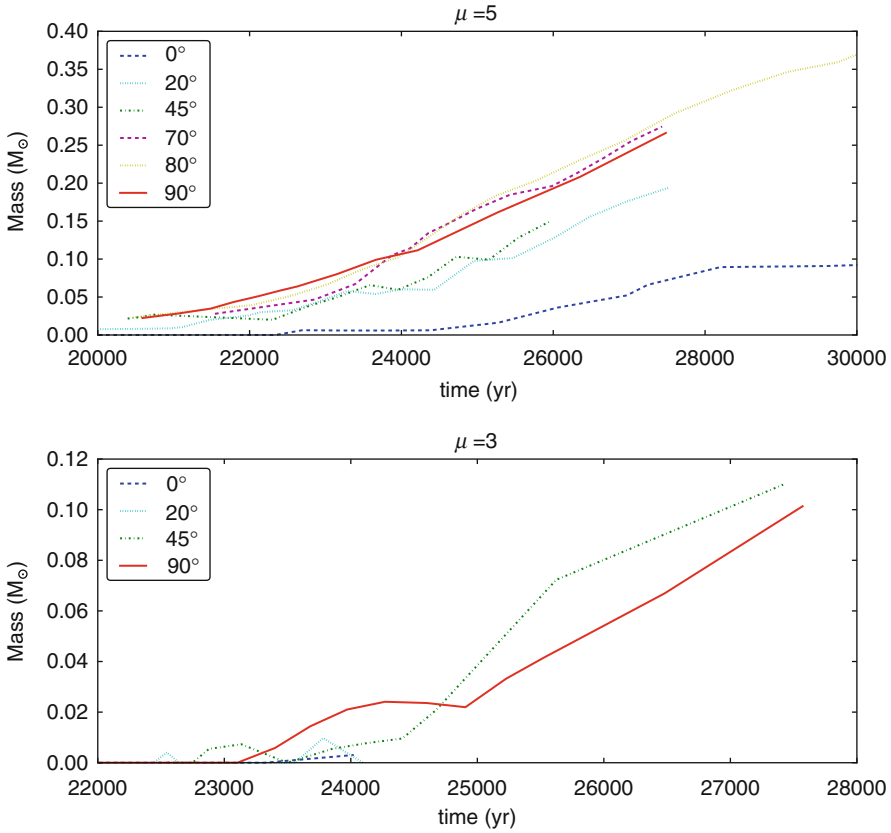

Fig. 1 Mass of the disks as a function of time for $\mu = 5$ and 3

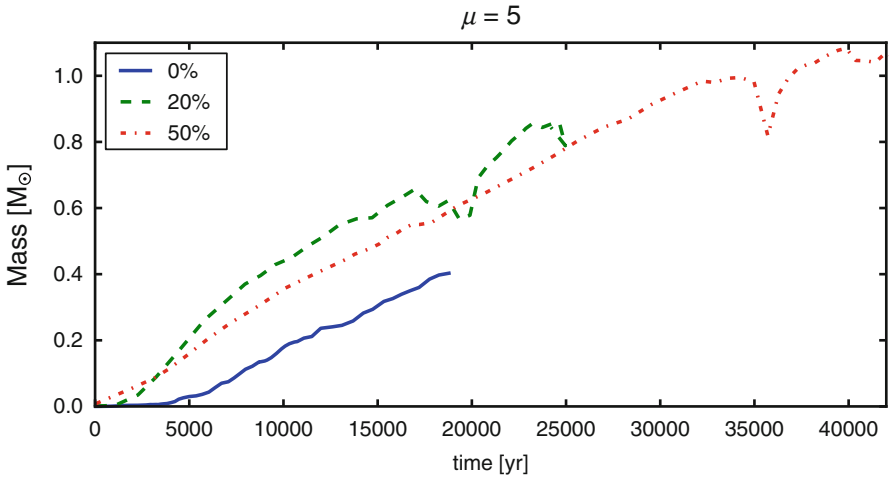

Fig. 2 Mass of the disk evolution for $\mu = 5$, with $E_{\text{turb}}/E_{\text{grav}} = 0$, 0.2 and 0.5

the possible cause is the reduced magnetic braking, as discussed in the previous sections. At the same time, it is still clear that for increasing magnetic field strength, and thus magnetic braking, disks tend to be smaller.

4 Conclusions

Magnetic braking is not a fatality: the early formation of massive disks can take place at moderate magnetic intensities if the rotation axis is tilted or in a turbulent environment, because of misalignment and turbulent diffusion.

References

1. Ciardi, A. & Hennebelle, P. 2010, MNRAS, 409, L39
2. Crutcher, R. M. 1999, ApJ, 520, 706
3. Fromang, S., Hennebelle, P., & Teyssier, R. 2006, A&A, 457, 371
4. Hennebelle, P. & Ciardi, A. 2009, A&A, 506, L29
5. Hennebelle, P., Commerçon, B., Joos, M., & et al. 2011, A&A, 528, A72+
6. Hennebelle, P. & Fromang, S. 2008, A&A, 477, 9
7. Joos, M., Hennebelle, P., & Ciardi, A. 2012, 543, 128
8. Joos, M., Hennebelle, P., Ciardi, A., & Fromang, S. 2013, 554, 17
9. Matsumoto, T. & Hanawa, T. 2011, ApJ, 728, 47
10. Maury, A. J., André, P., Hennebelle, P., & et al. 2010, A&A, 512, A40+
11. Mellon, R. R. & Li, Z. 2008, ApJ, 681, 1356
12. Price, D. J. & Bate, M. R. 2007, Ap&SS, 311, 75
13. Seifried, D., Banerjee, R., Pudritz, R. E., & Klessen, R. S. 2012, MNRAS, L442
14. Teyssier, R. 2002, A&A, 385, 337

Disc Formation in Turbulent Cloud Cores: Circumventing the Magnetic Braking Catastrophe

Daniel Seifried, Robi Banerjee, Ralph E. Pudritz, and Ralf S. Klessen

Abstract We present collapse simulations of strongly magnetised, $100\,M_{\odot}$, turbulent cloud cores. Around the protostars formed during the collapse Keplerian discs with typical sizes of up to 100 AU build up in contrast to previous simulations neglecting turbulence. Analysing the condensations in which the discs form, we show that the magnetic flux loss is not sufficient to explain the build-up of Keplerian discs. The average magnetic field is strongly inclined to the disc which might reduce the magnetic braking efficiency. However, the main reason for the reduced magnetic braking efficiency is the highly disordered magnetic field in the surroundings of the discs. Furthermore, due to the lack of a coherently rotating structure in the turbulent environment of the disc no toroidal magnetic field necessary for angular momentum extraction can build up. Simultaneously the angular momentum inflow remains high due to local shear flows created by the turbulent motions. We suggest that the "magnetic braking catastrophe" is an artefact of the idealised non-turbulent initial conditions and that turbulence provides a natural mechanism to circumvent this problem.

D. Seifried (✉)
Hamburger Sternwarte, University of Hamburg, Gojenbergsweg 112, 21029 Hamburg, Germany
e-mail: dseifried@hs.uni-hamburg.de

R. Banerjee
Hamburger Sternwarte, Gojenbergsweg 112, 21029 Hamburg, Germany

R.E. Pudritz
Department of Physics and Astronomy, McMaster University, Hamilton, ON, L8S 4M1, Canada

R.S. Klessen
Zentrum für Astronomie, Institut für Theoretische Astrophysik, Universität Heidelberg, Albert-Ueberle-Str. 2, 69120 Heidelberg, Germany

D. Stamatellos et al. (eds.), *The Labyrinth of Star Formation*, Astrophysics and Space Science Proceedings 36, DOI 10.1007/978-3-319-03041-8_13,

1 Introduction

In recent years a number of authors have studied the formation of protostellar discs during the collapse of strongly magnetised magnetic cloud cores [1, 4]. In simulations with magnetic field strengths comparable to observations no rotationally supported discs were found. As strong magnetic braking is responsible for the removal of the angular momentum, this problem is also called the "magnetic braking catastrophe". The results of these simulations stand in contrast to observations which show that discs are present in the earliest stage of protostellar evolution. Here we present results from a number of simulations investigating the role of turbulence in reducing the magnetic braking efficiency and allowing for the formation of protostellar discs.

We now shortly describe the basic simulation setup (see [5] for a more detailed description). We simulate the collapse of a $100\,\mathrm{M}_\odot$ molecular cloud core which is 0.25 pc in size, threaded by a magnetic field in the z-direction – the mass-to-flux ratio is $\mu = 2.6$ – and rotating around the z-axis. Additionally, we add a supersonic turbulence field with a power-law exponent of $\mathrm{p} = 5/3$. The turbulent energy is equal to the rotational energy, i.e. $\beta_{turb} = 0.04$, corresponding to a turbulent rms-Mach number of ∼2.5. We performed several simulations with different turbulence seeds to test the dependence of our results on the initial conditions. We find that the results do not depend on the chosen initial turbulence field.

2 Results

After a initial collapse phase of about 15 kyr sink particles form in the simulations around which the protostellar discs develop. We follow each simulation for another 15 kyr to analyse the evolution of the discs. In Fig. 1 we analyse the velocity structure of one of the discs in detail. We calculate the rotation and radial velocity in the frame of reference of the disc and show their radial dependence. As can be seen in the right panel of Fig. 1, the rotation scatters around the Keplerian velocity. The radial velocity, in contrast, scatters around 0 and is almost always smaller than the rotation velocity typical for a Keplerian disc. This result is in strong contrast to the results for identical simulations but without initial turbulence [4].

Why, even in the case of such strongly magnetised cores, are Keplerian discs formed? The suppression of Keplerian disc formation in previous studies without turbulence is due to the very efficient magnetic braking which removes angular momentum from the midplane at a very high rate. Hence, in our runs the magnetic braking efficiency has to be reduced significantly.

In a first step we try to estimate the dynamical importance of the magnetic field for the gas dynamics. For this reason we calculate the mass-to-flux ratio in a sphere with a radius of 500 AU around the centre of each disc. We find that μ is always smaller than 10 which defines the critical value determined in previous simulations

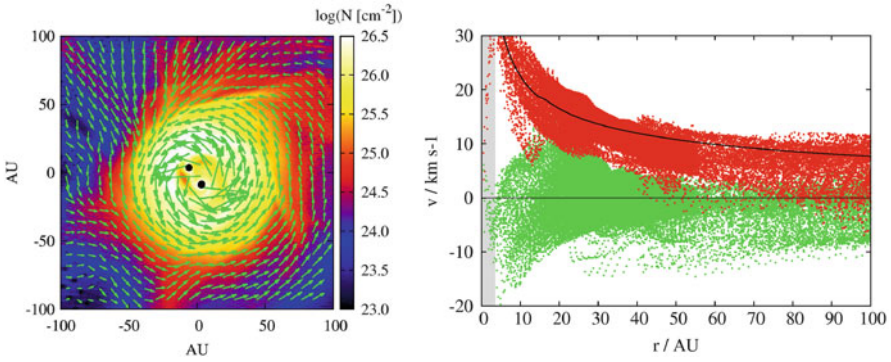

Fig. 1 *Left*: Top-on view of a protostellar disc formed in one of the simulations. The velocity structure (*green arrows*) and the position of the sink particles (*black dots*) are overplotted on the column density. *Right*: Velocity structure of the same disc showing the rotating velocity (*red dots*), the radial velocity (*green dots*) and the Keplerian velocity (*black line*)

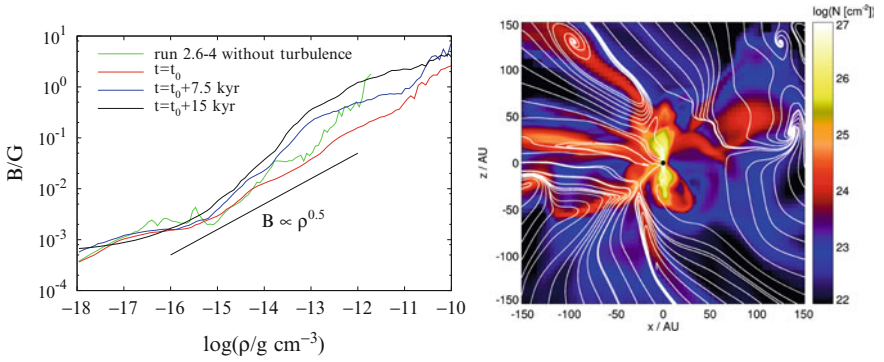

Fig. 2 *Left*: Scaling of the magnetic field for different times in one of the turbulence runs as well as in the corresponding non-turbulent run (*green line*). *Right*: Magnetic field structure for the edge-on view of one of the discs formed in the simulations

below which the formation of Keplerian discs is suppressed. Hence one would expect the magnetic field being strong enough to prevent the formation of Keplerian discs which is clearly not the case as seen in Fig. 1.

In the left panel of Fig. 2 we plot the scaling of the magnetic field with the density. As can be seen, the observed scaling $B \propto \rho^{0.5}$ is very similar to that of the non-turbulent run (green line). Hence, we argue that in our case no significant turbulent reconnection occurs and that magnetic flux loss is not responsible for the formation of Keplerian discs as proposed recently [3].

Considering the magnetic field structure around one of the discs in the right panel of Fig. 2, one can see that the magnetic field is highly disordered. Hence, it is not surprising that the direction of the mean magnetic field $|B|$ significantly differs from

the disc rotation axis which might decrease the magnetic braking efficiency [2]. However, due to the highly disordered structure the approximation of the magnetic field by a mean magnetic field is at least questionable.

However, this highly disordered magnetic field indicates why the magnetic braking efficiency is reduced strongly. Considering the left panel of Fig. 1 it can be seen that in the surroundings of the disc there is a turbulent velocity field with no signs of a coherent rotation structure. Therefore no toroidal magnetic field component can be built up. But as the angular momentum is mainly extracted by toroidal Alfvénic waves, it is not surprising that the magnetic braking efficiency is strongly reduced in the environment of the disc despite a low mass-to-flux ratio. Moreover, the disordered magnetic field structure itself impedes the coupling of the fast rotating gas in the inner parts to slowly rotating gas in the outer parts necessary for the magnetic braking mechanism to work efficiently. Hence, the magnetic braking efficiency is reduced due to the lack of a proper toroidal magnetic field component and the highly disordered magnetic field structure in the disc environment. Despite the lack of a coherent rotation structure, locally the inwards angular momentum transport can remain high due to local shear flows driving large angular momentum fluxes. Indeed when comparing the torques exerted by the gas and the magnetic field it can be seen that the gas torque exceeds the magnetic torque by at least a factor of a few. Hence there is a net angular momentum flux inwards [5] resulting in the observed build-up of a Keplerian disc. In contrast, for the corresponding non-turbulent run the gas torque is almost perfectly balanced by the (negative) magnetic torque.

3 Conclusions

We have observed the formation of rotationally supported discs during the collapse of massive, magnetised and turbulent cloud cores. We attribute this to the turbulent surroundings of the discs which reveal a highly disordered magnetic field and no signs of a coherent rotation structure. In contrast, magnetic flux loss is not able to account for the formation of Keplerian discs as only on the disc scale ($\leq$100 AU) significant flux loss is observed. However, we emphasise that the magnetic braking efficiency has to be reduced already on larger scales ($\geq$500 AU) even before the gas falls onto the disc. This is demonstrated by a corresponding non-turbulent run where the angular momentum is removed largely already outside the disc. Furthermore, non-ideal MHD effects, which have already been shown that they cannot account for the formation of early-type Keplerian discs, are not required as turbulence alone provides a natural and simple mechanism to circumvent the "magnetic braking catastrophe". Hence, our work strongly suggests that the magnetic braking problem as reported in numerous papers is more or less a consequence of the highly idealised initial conditions neglecting turbulent motions.

References

1. Hennebelle, P. & Fromang, S. 2008, A&A, 477, 9
2. Joos, M., Hennebelle, P., & Ciardi, A. 2012, A&A, 543, A128
3. Santos-Lima, R., de Gouveia Dal Pino, E., & Lazarian, A. 2012, ApJ, 747, 21
4. Seifried, D., Banerjee, R., Klessen, R., Duffin, D., & Pudritz, R. E. 2011, MNRAS, 417, 1054
5. Seifried, D., Banerjee, R., Pudritz, R., & Klessen, R. 2012, MNRAS, 423, L40

Magnetohydrodynamics with Time-Dependent Ionization Degree in Protoplanetary Disks with Grain Evolution

Yuri I. Fujii, Satoshi Okuzumi, and Shu-ichiro Inutsuka

Abstract Understanding of the ionization degree is necessary in order to study disk dynamics especially when the magnetorotational instability (MRI) is the main mechanism for disk accretion. In this work, we investigate the effect of vertical mixing by eddies by using a time-dependent method for calculating the ionization degree [1]. Our method enables us to calculate the ionization degree with dust grains as large as 1cm, which tend to be highly charged and can be conveniently plugged into various magnetohydrodynamics codes. We calculate the ionization degree of a protoplanetary disk considering cosmic rays, X-rays, and the decay of radionuclides as ionization sources. We use a simplified model of turbulent mixing, and find that the vertical mixing of ionized gas can decrease the size of a MRI-inactive region.

1 Introduction

The most promising mechanism for explaining gas accretion in protoplanetary disks is the turbulence driven by magnetorotational instability (MRI). To be MRI-active, gas in the disk should be sufficiently ionized. Without small grains, ionized gas at

Y.I. Fujii (✉)
Nagoya University, Furo-cho, Chikusa-ku, Nagoya, Aichi 464-8602, Japan
e-mail: yuri.f@nagoya-u.jp

S. Okuzumi
Department of Earth and Planetary Sciences, Tokyo Institute of Technology, Meguro-ku, Tokyo 152-8551, Japan
e-mail: okuzumi@geo.titech.ac.jp

S. Inutsuka
Department of Physics, Graduate School of Science, Nagoya University, Furo-cho, Chikusa-ku, Nagoya 464-8602, Japan
e-mail: inutsuka@nagoya-u.jp

D. Stamatellos et al. (eds.), *The Labyrinth of Star Formation*, Astrophysics and Space Science Proceedings 36, DOI 10.1007/978-3-319-03041-8_14,

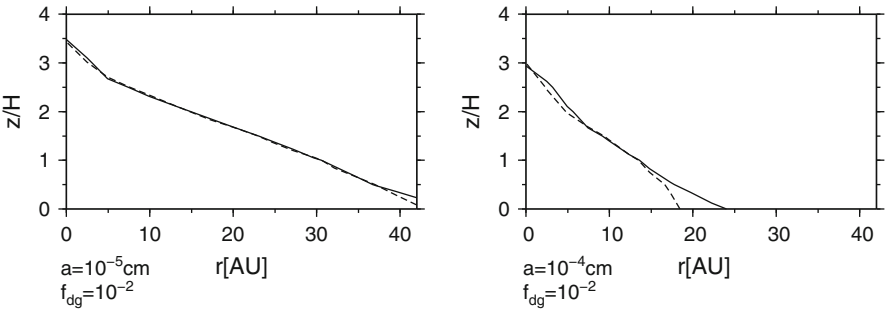

Fig. 1 The boundaries of dead zones with grain size $a = 10^{-5}$ cm (*left panel*) and $a = 10^{-4}$ cm (*right panel*). The *horizontal axis* denotes the radius of protoplanetary disks, and the *vertical axis* is the vertical extent of the disk that is normalized by the scale height of the corresponding radius. *Solid lines* show the case without eddies, and *dashed lines* show the case with eddies. Regions below the lines are dead zones

the surface layer is brought to the inside of the disk by turbulence and decreases the MRI-inactive region, or so called "dead zone" [3]. In this study, we investigate the effect of turbulent mixing with dust grains.

2 Settings and Results

We adopt the MMSN model [2] and choose a dust-to-gas mass ratio $f_{\rm dg} \equiv \rho_{dust}/\rho_{gas} = 10^{-2}$, and a plasma beta $\beta \equiv p_{\rm gas}/p_{\rm mag} = 10^4$. We consider cosmic rays, X-rays, and radionuclide as ionization sources, and model the vertical movement of fluid elements as follows:

$$z = 2H \sin(\Omega t/2) + 2H. \tag{1}$$

Time-evolution of the ionization degree along the eddy is calculated to observe the effect of turbulent mixing. Figure 1 shows the results. With sub-micron grains, there seems almost no difference between the case with an eddy and that without. With a slight increase in the size of the grains, however, we can see a difference between the two. In this case, the timescale of the mixing is smaller than that of chemical reactions. Time scales of chemical reaction depends on grain size (or number density of gains), gas density, ionization rate, and so on [1, 4].

3 Conclusions

We found that the sizes of dead zones may decrease through vertical mixing. This suggests that we may need time-dependent calculation of the ionization degree with MHD simulation. Since the dynamic timescale is small, the effect of turbulent mixing is thought to be more important in circumplanetary disks.

References

1. Fujii, Y. I., Okuzumi, S., & Inutsuka, S., 2011, ApJ, 743, 53
2. Hayashi, C., 1981, Prog. Theor. Phys. Suppl., 70, 35
3. Inutsuka, S., & Sano, T., 2005, ApJ, 628, L155
4. Okuzumi, S., 2009, ApJ, 698, 1122

The Effect of Mass Accretion for Formation and Thermal Evolution of Circumstellar Disks

Yusuke Tsukamoto, Masahiro N. Machida, and Shu-ichiro Inutsuka

1 Introduction

The planet formation process via direct disk fragmentation is a necessary mechanism to explain the diversity of exo-planetary systems. Examples of planetary systems which might form by disk fragmentation are HR8799 and GJ758. The formation of the planets in these systems via core accretion seems to be unlikely.

Disk fragmentation studies have been mostly focused on the thermal energy balance between radiative cooling and heating by gravitational instability for isolated disks [2]. However, they do not take into account the effect of mass accretion. Boley [1] considered mass accretion by adding mass at the boundary mesh. He showed that mass accretion actually pushes the disk toward fragmentation. But his simulations did not take into account the effect of heating by accretion which may stabilize the disk.

In this study, we simulated the evolution of the disk under realistic accretion from envelope with radiative hydrodynamical simulations.

Y. Tsukamoto (✉)
Nagoya University, Nagoya, Japan
e-mail: tsukamoto.yusuke@c.mbox.nagoya-u.ac.jp

M.N. Machida
Department of Earth and Planetary Sciences, Kyushu University, Fukuoka 812-8581, Japan

S. Inutsuka
Department of Physics, Graduate School of Science, Nagoya University, Furo-cho, Chikusa-ku, Nagoya 464-8602, Japan
e-mail: inutsuka@nagoya-u.jp

D. Stamatellos et al. (eds.), *The Labyrinth of Star Formation*, Astrophysics and Space Science Proceedings 36, DOI 10.1007/978-3-319-03041-8_15,

2 Results

In Fig. 1, we show the time evolution of the disk surface density and its temperature. The early phase evolution of first core is very similar to the case of the barotropic approximation. After that, the evolution process changes compared with the barotropic approximation case. When the second collapse occurs, strong spiral patterns have already arisen. The spiral pattern is irregular compared with the barotropic approximation case. As accretion proceeds, the disk is heated up due to accretion from the envelope and spiral shocks rather than cools down by the radiation.

In Fig. 2, we show the radial profile of $t_{cool}\Omega$. The value of $t_{cool}\Omega$ quickly decreases with radius and $t_{cool}\Omega < 5$ at $r > 40$ AU. Thus, fragmentation is

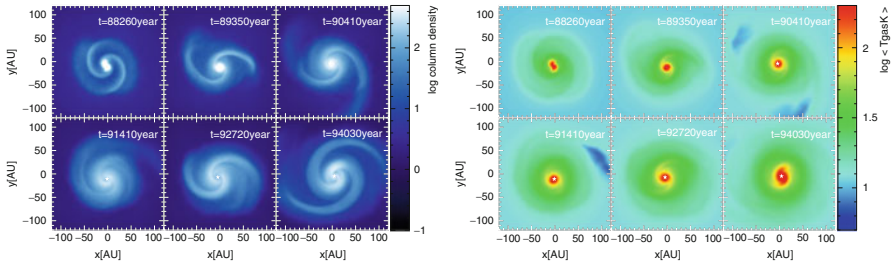

Fig. 1 Time sequence of the logarithm of the face-on surface density and the density weighted gas temperature before and after the protostar formation, for model 1 ($\beta = 1 \times 10^{-2}$). *Top left* and *top middle panels* show the snapshot about 2.2×10^3 and 1.0×10^3 years before the protostar formation. *Top right panel* shows the snapshot just when the protostar forms. *The bottom left*, *middle* and *right* show the snapshots 1.0×10^3, 2.3×10^3 and 3.6×10^3 years after the protostar formation

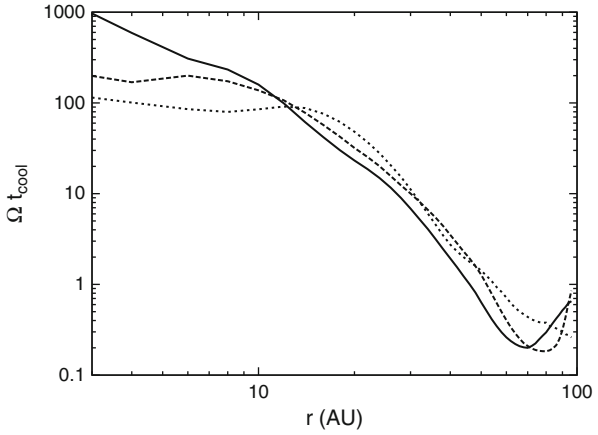

Fig. 2 Radial profile of $t_{cool}\Omega$. *Solid*, *long-dashed* and *short-dashed* correspond the epoch of top right, bottom left and right panel of Fig. 1, respectively

expected in the region $r < 40$ AU according to criterion suggested by Gammie [2]. The disk, however, does not fragment, because heating due to accretion suppresses fragmentation.

References

1. Boley, A. C. 2009, *ApJ*, 695, L53
2. Gammie, C. F. 2001, *ApJ*, 553, 174

Disk Survival in the Extremely Massive Association Cygnus OB2

Mario Giuseppe Guarcello, Jeremy J. Drake, Nicholas J. Wright, Janet E. Drew, D. Garcia-Alvarez, R.A. Gutermuth, J.L. Hora, V. Kashyap, Robert R. King, Tim Naylor, and Chandra Cygnus OB2 Team

Abstract Star formation in massive clusters proceeds under the influence of the intense ionizing flux emitted by OB stars. Among the massive star forming regions in our Galaxy, Cygnus OB2 is the best available target to study these processes given its relative proximity and large content of OB and low-mass stars. We present our preliminary results on the photoevaporation of circumstellar disks in Cyg OB2 induced by the UV radiation emitted by OB stars.

1 Star Formation in Massive Clusters

Star forming regions in our Galaxy vary from those hosting a small number of intermediate to low mass stars to regions with thousands of stars, where low mass Pre-Main Sequence (PMS) stars coexist with massive OB stars. Despite their short lives, OB stars have dramatic effects on the star formation in the surrounding

M.G. Guarcello (✉) • R.A. Gutermuth • J.L. Hora • V. Kashyap
Harvard-Smithsonian Center for Astrophysics, 60 Garden St., 02138 Cambridge, MA, USA
e-mail: mguarcel@head.cfa.harvard.edu

J.J. Drake • N.J. Wright
SAO-Harvard-Smithsonian Center for Astrophysics, 60 Garden St., Cambridge, MA 02138, USA

J.E. Drew
CAR/STRI, University of Hertfordshire, College Lane, Hatfield AL10 9AB, UK

D. Garcia-Alvarez
Instituto de Astrofísica de Canarias, E-38205 La Laguna, Tenerife, Spain

R.R. King • T. Naylor
School of Physics, University of Exeter, Stocker Road, Exeter, UK

Chandra Cygnus OB2 Team

D. Stamatellos et al. (eds.), *The Labyrinth of Star Formation*, Astrophysics and Space Science Proceedings 36, DOI 10.1007/978-3-319-03041-8_16,

cloud, due to their high ionizing fluxes. Since it is likely that most stars form in environments hosting OB stars, including our Sun, it is crucial to understand these effects.

1.1 Externally Induced Disk Photoevaporation

Disk photoevaporation occurs when Far- and Extreme-Ultraviolet (FUV and EUV) radiation is incident on disks, whose gas is heated up to thousands of degrees and evaporates in a pressure driven wind. Since the Hubble Space Telescope observations of the protoplanetary disks (proplyds) in the Orion Nebula Cluster, it is known that UV radiation from OB stars can induce a fast photoevaporation of nearby disks, drastically reducing their lifetimes [1].

2 Cygnus OB2

The massive association Cygnus OB2 in the Cygnus X region is the best target to study star formation in the presence of OB stars, since it is the closest region to the Sun (1,400 pc [2]) that contains thousands of OB stars [3].

Our study aims to identify young stars in Cyg OB2, and to study how the intense ionizing radiation from the massive stars affects the evolution of circumstellar disks. Candidate cluster members have been selected adopting a photometric multiwavelength approach, using data from X-rays to the mid-infrared.

3 Spatial Variation of Disk Fraction in Cygnus OB2

A total of 1,843 disk-bearing cluster members have been identified based on their infrared excesses by combining several selection criteria, including a careful identification of candidate foreground/background contaminants [4].

Candidate disk-less cluster members have been selected based on their intense X-ray emission. The selection includes 3,966 candidate disk-less members.

Figure 1 shows how the disk fraction varies as a function of the incident FUV flux emitted by the OB stars. The decline of the disk fraction toward high values of incident UV flux is evident, decreasing from $\sim$43 to $\sim$19 %. This result is compatible with a scenario where protoplanetary disks near OB stars experience a large ionizing flux and are dissipated faster than those more distant. Obviously, sequential star formation may affect this interpretation, so an accurate determination of stellar ages is necessary to clearly assess this point.

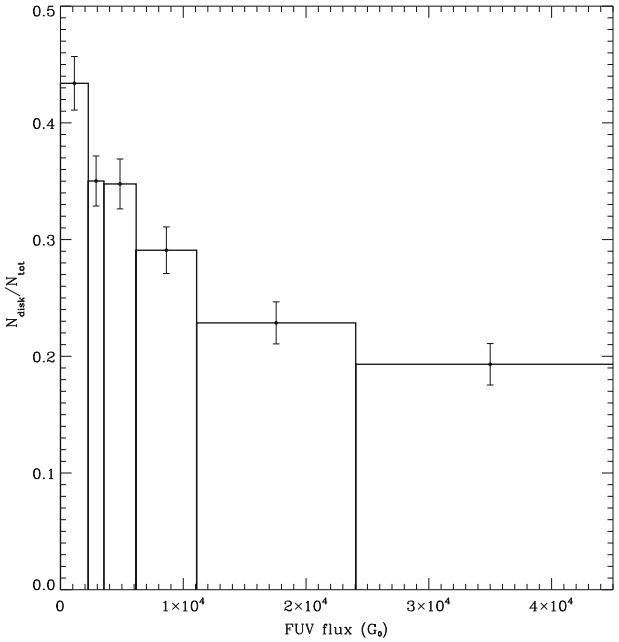

Fig. 1 Variation of the disk fraction as a function of the incident FUV flux emitted by the OB stars, in terms of the Habing flux

It should be noted that the spatial range where disks experience the externally induced photoevaporation in Cyg OB2 is larger than in the Trapezium, NGC 6611 [5], and NGC 2244 [6], a product of the larger OB population in Cyg OB2.

References

1. Störzer, H.; Hollenbach, D., ApJ, 669–684 (1999)
2. Rygl, K. L. J.; Brunthaler, A.; Sanna, A.; et al., A&A, 539, 79, (2012)
3. Wright, N. J.; Drake, J. J.; Drew, J. E.; Vink, J. S., ApJ, 713, 871 (2010)
4. Guarcello, M. G.; Drake, J. J.; Wright, N. J.; et al., ApJ, 773–135 (2013)
5. Guarcello, M. G.; Micela, G.; Peres, G.; et al., A&A, 512, 61 (2010)
6. Balog, Zoltan; Muzerolle, James; Rieke, G. H.; ApJ, 660, 1532, ApJ (2007)

Part IV
Computational Star Formation: Models, Techniques, and Predictions

Review of Computational Star Formation

David Anthony Hubber

Abstract We will review the current state of computational star formation discussing past limitations of both grid and particle methods and their consequences on interpreting star formation models. We will also discuss recent algorithmic advances and the possibilities for future numerical investigations.

1 A Brief History of Computational Star Formation

Computational star formation is the modelling of star formation problems using numerical hydrodynamics schemes coupled with other important physical processes, such as gravity, radiation transport, magnetohydrodynamics, thermal physics, chemistry, and other processes. As well as the large range of physics that we can include in our simulations, the available resolution also defines what class of problem we can realistically investigate. Over the last half-century, starting with the pioneering 1D simulations of [17], many important algorithmic advancements have enabled a larger range of astrophysical problems to be tackled.

There are two main traditional algorithmic paradigms that are used in astrophysical hydrodynamics; grid and particle codes. In recent years, a third paradigm, tessellation codes, have become more abundant and will likely be widely used in future. We describe each method briefly below, and compare the relative advantages and disadvantages in Table 1.

D.A. Hubber (✉)
Technical University Munich, Excellence Cluster Universe, Boltzmannstr. 2,
D-85748 Garching, Germany

Department of Physics, University Observatory Munich, Ludwig-Maximilians-University Munich, Scheinerstr.1, D-81679 Munich, Germany
e-mail: david.hubber@googlemail.com

D. Stamatellos et al. (eds.), *The Labyrinth of Star Formation*, Astrophysics and Space Science Proceedings 36, DOI 10.1007/978-3-319-03041-8_17,

Table 1 Relative advantages and disadvantages of static grid, particle and tessellation codes. Points highlighted with a grey background represent advantageous features of that method

Grid	Particle	Tessellation
Eulerian (cells represent fluid volumes). Not Galilean invariant.	Lagrangian (particles represent discrete fluid masses).	Galilean invariant (but not strictly Lagrangian)
Adaptive grids to increase resolution (complex algorithms)	Adaptive smoothing lengths automatically increase resolution	Tessellation (complex algorithms) adapts to particle distribution.
Error control depends on integration scheme	Errors determined by smoothing and resolution (little control)	No formal error control (because of irregular grid).
Fixed geometry; must select region of interest a priori	No limitation on geometry or size of computational domain	Tessellation optimal for periodic system
Complex algorithms (for AMR); difficult to code	Simple to code. Doesn't crash, but generates noise if 'buggy'	Very difficult to code, even from simple brute-force case
Riemann solvers accurately capture shocks with minimal dissipation	Requires artificial dissipation terms to handle discontinuities	Captures shocks better than particle schemes, but not as well as grid codes
Models hydrodynamical phenomena (e.g. instabilities) very well	Struggles to model complex hydrodynamical phenomena	Models hydrodynamical phenomena well, without advection problems of fixed grid codes

- Grid codes are the earliest and most widespread form of numerical hydrodynamics. The simplest form of grid hydrodynamics use finite-differences to construct gradients of hydrodynamical quantities and to numerically integrate the partial differential equations. An important advancement was the development of 2nd-order finite-volume codes [32] which allowed Riemann solvers to be used to calculate numerical fluxes without the need for artificial viscosity to accurately capture shock discontinuities. The development of adaptive-mesh refinement [AMR 4, 5] allowed high resolution grids to capture small-scale features without the huge computational expense required of uniform grids. A wide-range of codes have been developed and made publicly available for astrophysical purposes, such as ZEUS [29], RAMSES [30], FLASH [8], MG [33], ENZO [23] and ORION (http://flash.uchicago.edu/~rfisher/orion/).
- Particle codes are (usually) Lagrangian codes that represent the fluid with many discrete particles. Smoothed Particle Hydrodynamics [10, 19] was the first mesh-free particle code developed for astrophysics problems. SPH is fully Lagrangian and conservative, but requires artificial viscosity to capture shocks. In combination with a tree [see 14] and block timesteps, SPH is well adapted to following gravitational collapse problems. Many variant algorithms have been developed (e.g. Godunov SPH, RKPM, MLSH), although these are seldom used in astronomy. SPH codes available to the astrophysics community include TREESPH [14], GADGET2 [25], SEREN [15] and SPHNG.
- Tessellation codes use particles as elements that represent the fluid flow and then construct a Voronoi tessellation to determine how neighbouring fluid elements interact with each other. Tessellation codes inherit many of the advantages of both

grid and particle codes, although at the cost of increased algorithmic complexity. In recent years, several tessellation codes have been developed for astrophysical purposes, such as AREPO [26], PHURBAS and TESS.

2 Additional Physics

In addition to the core hydrodynamical algorithms used in numerical star formation, various important physics modules have been developed to allow more 'realistic' simulations of the star formation process.

- Radiation transport: The transport of radiation during star formation heavily influences the thermal properties and hence the hydrodynamics of the gas. However, full radiation transport is an expensive algorithm that cannot be solved in full for time-dependent hydrodynamics with current technology. Therefore, various 'cheap' approximations have been developed such as Flux-limited diffusion [18], Ray-tracing [1], Monte Carlo photon packets [20], Approximate radiative cooling [28]. Various hybrid schemes have been developed recently, often using ray-tracing for point sources, and flux-limited diffusion for the diffuse field.
- Thermal physics and chemistry: The gas in prestellar cores can collapse through up to 20 orders of magnitude in density and 5 orders of magnitude in temperature. This requires a diverse treatment of the gas properties (either by tables or on-the-fly solutions of equations). This is particularly important for Population III star formation where the metallicity is vastly different to now [11].
- MHD: Magnetohydrodynamics codes have been used in grid codes for many decades, particularly in the popular grid code ZEUS [29]. Although used in early implementation, eliminating spurious numerical effects in SPH with MHD proved troublesome. More recent work by Price and collaborators has produced more stable implementations which may allow tenable SPH with MHD simulations in the future (See [24], for a review).

3 Numerical Resolution

In order to resolve gravitational fragmentation, we must resolve the Jeans length at all times [31]. When the opacity limit is reached during spherical collapse, this sets a minimum Jeans mass which prevents further fragmentation.

However, the formation of discs can allow adequate time for the disc to cool and then subsequently fragment via the Toomre instability. Finally, we must be able to resolve the disc scale height. Therefore, additional resolution criteria are needed to resolve fragmentation in discs [22]. These criteria are:

- Resolving the Jeans length

$$\Delta x \leq \frac{\lambda_{\rm JEANS}}{J} \qquad \text{where} \qquad \lambda_{\rm JEANS} = \left(\frac{\pi \, c}{G \, \rho} \right)^{1/2} \quad J \geq 4 \tag{1}$$

- Resolving the Toomre length

$$\Delta x \leq \frac{\lambda_{\rm TOOMRE}}{T} \qquad \text{where} \qquad \lambda_{\rm TOOMRE} = \frac{2 \, c^2}{G \, \sigma} \; T \geq 4 \tag{2}$$

- Resolving the disc height

$$\Delta x \ll H \tag{3}$$

Analogous SPH criteria can be derived either by computing the equivalent mass quantities, or using the smoothing length in place of Δx. Typical values suggest that resolving disc fragmentation requires up to an order or magnitude more resolution (either grid cells or particles) than spherical opacity limited fragmentation.

One recent caveat to this issue was shown by Meru and Bate [21] who demonstrated that disc SPH fragmentation models do not appear to converge with increasing resolution. It's not clear yet if this is a problem with SPH, evidence that the above resolution constraints in discs are more demanding that previously believed, or is simply the true physical consequence of the model.

4 Star Formation Simulations

Star formation simulations can be divided into three main types, which often look at different scales and with different physics options.

- Large-scale molecular cloud simulations: We model (i) Development of structure in the cloud due to turbulence (e.g. [13]), (ii) Large-scale fragmentation of clouds into sub-clumps, (iii) Large-scale disruption and dissolution of clouds due to feedback (e.g. [6]), and (iv) Formation of high-mass star clusters. Resolving opacity limited fragmentation is necessarily not achieved due to (i) lack of resolution, (ii) suppression of fragmentation due to a modified equation of state, or (iii) using sink particles. Therefore, we can only gain insight about the large-scale properties of the cloud, or high-mass stars.
- Fragmentation of prestellar cores: We model the fragmentation down to the opacity-limit of either (i) Individual prestellar cores (e.g. [12]), (ii) Larger-scale simulations of turbulent clumps that can resolve individual stars and binary systems (e.g. [3, 16]).
- Evolution of protostellar discs: Disc simulations typically model (i) Intermediate-high resolution simulations of disc accretion and fragmentation (e.g. [7, 9, 27])

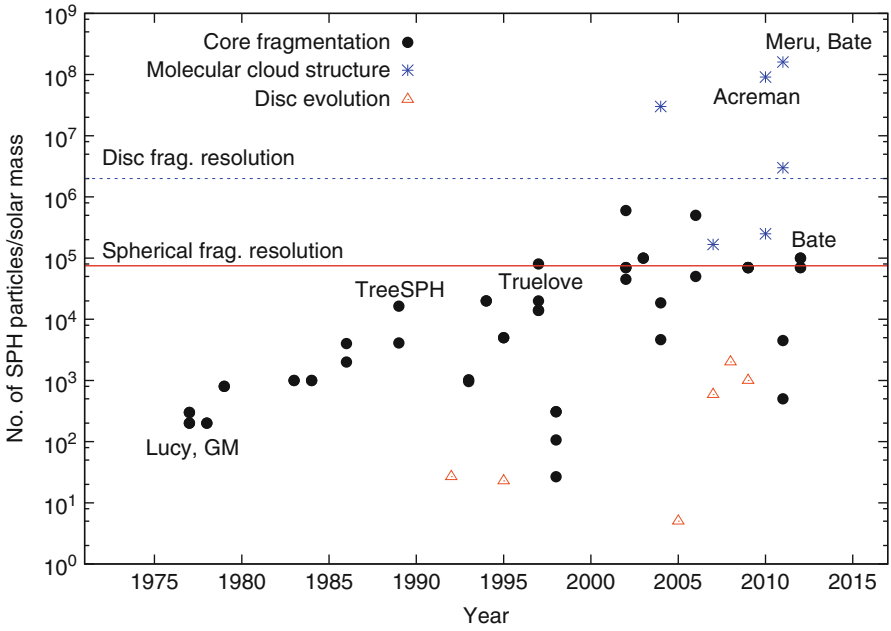

Fig. 1 Comparative resolution of various 3D star formation simulations of core fragmentation (*black spheres*), large-scale molecular cloud evolution (*blue stars*) and disc evolution and fragmentation (*red triangles*). The *horizontal red line* represents the spherical fragmentation resolution limit, and the *dashed-blue line* represents a typical disc fragmentation limit

(ii) High resolution radiative transfer models of the disc structure (e.g. [2]). The first mode usually requires fulfilling all three resolution criteria suggested above. The second requires even higher resolution to resolve the radiation field.

The improvements in computational power and algorithms has altered the scope for simulations over the years. Figure 1 shows how the resolution of star formation SPH simulations has evolved with time. The available computer resources were not adequate enough to resolve spherical opacity limited fragmentation in individual cores until the mid-1990s. Since then, a wide range of resolutions have been used, ranging from extremely under-resolved (large-scale simulations, red triangles) to highly over-resolved (high resolution disc simulations, blue stars). Many intermediate-resolution simulations which model core fragmentation lie around the opacity-limit, but below the disc fragmentation limit. We now have the computing power to either explore even larger star formation scales in the future, or to investigate core fragmentation at even higher resolution than previously considered.

Acknowledgements I would like to thank Prof. Anthony Whitworth for all his guidance during my PhD and subsequently during my academic career.

References

1. Abel T, Wandelt BD (2002). MNRAS 330:L53–L56
2. Acreman DM, Harries TK, Rundle DA (2010). MNRAS 403:1143–1155
3. Bate MR (2009). MNRAS 392:590–616
4. Berger MJ, Colella P (1989). Journal of Computational Physics 82:64–84
5. Berger MJ, Oliger J (1984). Journal of Computational Physics 53:484
6. Dale JE, Ercolano B, Bonnell IA (2012). MNRAS 424:377–392
7. Forgan D, Rice K, Cossins P, Lodato G (2011). MNRAS 410:994–1006
8. Fryxell B, Olson K, Ricker P, Timmes FX, Zingale M, Lamb DQ, MacNeice P, Rosner R, Truran JW, Tufo H (2000). ApJs 131:273–334
9. Gammie CF (2001). ApJ 553:174–183
10. Gingold RA, Monaghan JJ (1977). MNRAS 181:375–389
11. Glover SCO, Jappsen A-K (2007). ApJ 666:1–19
12. Goodwin SP, Whitworth AP, Ward-Thompson D (2004). A&A 414:633–650
13. Heitsch F, Slyz AD, Devriendt JEG, Hartmann LW, Burkert A (2006). ApJ 648:1052–1065
14. Hernquist L, Katz N (1989). ApJs 70:419–446
15. Hubber DA, Batty CP, McLeod A, Whitworth AP (2011). A&A 529:A27+
16. Krumholz MR, Klein RI, McKee CF (2011). ApJ 740:74
17. Larson RB (1969). MNRAS 145:271
18. Levermore CD, Pomraning GC (1981). ApJ 248:321–334
19. Lucy LB (1977). AJ 82:1013–1024
20. Lucy LB (1999). A&A 344:282–288
21. Meru F, Bate MR (2011). MNRAS 411:L1–L5
22. Nelson AF (2006). MNRAS 373:1039–1073
23. O'Shea BW, Bryan G, Bordner J, Norman ML, Abel T, Harkness R, Kritsuk A (2004). http://arxiv.org/abs/astro-ph/0403044
24. Price DJ (2012). Journal of Computational Physics 231:759–794
25. Springel V (2005). MNRAS 364:1105–1134
26. Springel V (2010). MNRAS 401:791–851
27. Stamatellos D, Whitworth AP (2009). MNRAS 392:413–427
28. Stamatellos D, Whitworth AP, Bisbas T, Goodwin S (2007). A&A 475:37–49
29. Stone JM, Norman ML (1992). ApJs 80:753–790
30. Teyssier R (2002). A&A 385:337–364
31. Truelove JK, Klein RI, McKee CF, Holliman JH II, Howell LH, Greenough JA (1997) . ApJL 489:L179
32. van Leer B (1979). Journal of Computational Physics 32:101–136
33. Van Loo S, Falle SAEG, Hartquist TW (2006). MNRAS 370:975–980

Modelling Magnetised Protostellar Jets with SPH

Matthew R. Bate, Daniel J. Price, and Terrence S. Tricco

Abstract We present results from the first smoothed particle hydrodynamics (SPH) simulations to produce stable long-lived magnetised protostellar jets. We briefly discuss the problems that have arisen in modelling magnetic fields within the SPH formalism in the past, and describe our new method for satisfying the magnetic divergence constraint. We then present results from calculations that follow the collapse of molecular cloud cores to the formation of the first hydrostatic core and follow the magnetised jets launched from the vicinity of the core to distances in excess of 2,000 AU.

1 Introduction

Smoothed particle magnetohydrodynamical (SPMHD) simulations have been used to study a wide variety of astrophysical objects over the past 25 years. Phillips [10] and Phillips and Monaghan [11] applied SPMHD to star formation, modelling the collapse of magnetised molecular cloud cores and finding that magnetic fields stopped fragmentation. Hosking and Whitworth [8] introduced ambipolar diffusion, but still found that strong magnetic braking inhibited disc formation and fragmentation [7]. Price and Bate [12] agreed that magnetic fields inhibit disc formation and fragmentation, but found that fragmentation could still occur with weak fields and/or strongly perturbed clouds. Price and Bate [13, 14] studied star cluster formation, finding that strong magnetic fields could reduce the star formation rate by an order

M.R. Bate (✉)
School of Physics and Astronomy, University of Exeter, Stocker Road, Exeter EX4 4QL, UK
e-mail: mbate@astro.ex.ac.uk

D.J. Price • T.S. Tricco
Monash Centre for Astrophysics (MoCA), School of Mathematical Sciences, Monash University, Clayton, VIC 3800, Australia
e-mail: daniel.price@monash.edu; terrence.tricco@monash.edu

D. Stamatellos et al. (eds.), *The Labyrinth of Star Formation*, Astrophysics and Space Science Proceedings 36, DOI 10.1007/978-3-319-03041-8_18,

of magnitude over that obtained from purely hydrodynamical calculations. Recently, Bürzle et al. [2, 3] modelled the collapse of molecular cloud cores and managed to follow the initial stages of jet formation from the first hydrostatic core. In other areas of astrophysics, Dolag et al. [5] and Dolag and Stasyszyn [6] modelled magnetic fields in galaxy clusters, while Price and Rosswog [18] modelled the mergers of magnetised neutron stars.

However, although SPMHD has been used successfully in the past, there have also been a number of numerical difficulties in formulating a robust SPMHD method. Some problems were solved early on [1,9,11,15,16], but the most persistent problem has been avoiding the growth of magnetic divergence (i.e. failing to satisfy $\nabla \cdot \mathbf{B} = 0$). An implementation of SPMHD based on Euler potentials, for which the magnetic divergence is zero by construction, can be used [12–14, 18]. However, this formulation cannot represent all field geometries – for example, helical fields, which makes it impossible to model magnetic jets. In standard SPMHD, while magnetic divergence can be controlled to some extent via artificial resistivity, it often fails at some point, particularly in star formation calculations where the range of densities modelled can be vary large. Price and Monaghan [17] had some success in reformulating the divergence cleaning method of Dedner et al. [4] for use with SPMHD, however, this did not solve the divergence problem in star formation simulations.

2 A New Divergence Cleaning Method

To maintain the magnetic divergence constraint without the restrictions of Euler potentials, we have recently developed a new divergence cleaning method. The full method and the results of a large number of test calculations are presented in [20]. Here we briefly mention the main points. The basic idea [4] is that if $\nabla \cdot \mathbf{B}$ is generated in the numerical solution it is spread as a wave from the source and damped as the wave propagates. This is accomplished by introducing a scalar field ψ which is coupled to the magnetic field $\mathbf{B}$ as

$$\left(\frac{\mathrm{d}\mathbf{B}}{\mathrm{d}t}\right) = -\nabla\psi, \tag{1}$$

and evolves as

$$\frac{\mathrm{d}\psi}{\mathrm{d}t} = -c_\mathrm{h}^2 \nabla \cdot \mathbf{B} - \frac{\psi}{\tau} - \frac{1}{2}\psi \nabla \cdot \mathbf{v}. \tag{2}$$

where c_h is the propagation speed of the divergence wave (typically the maximum allowed by the timestep), and $\tau = h/(c_\mathrm{h}\sigma)$ where σ is a constant that specifies the strength of the damping (typically order unity). With the exception of the last term in Eq. (2), the above equations were previously implemented in SPMHD by Price and Monaghan [17]. However, it turns out that their specific implementation did not

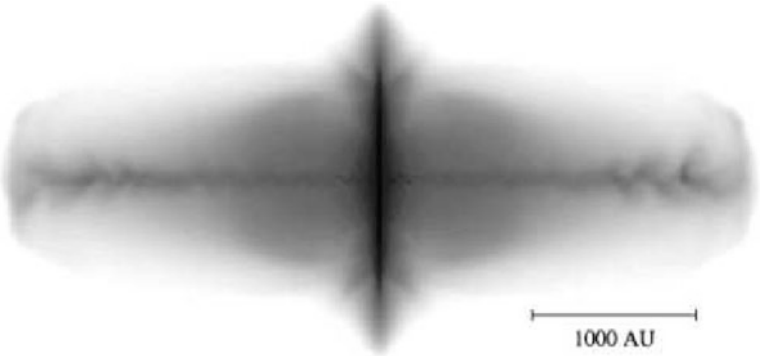

Fig. 1 Column density during the evolution of the collapse of a 1-$M_\odot$ rotating molecular cloud core to form a protostar. The jets (horizontal orientation) and pseudo-disc (vertical) are clearly visible. The initial mass-to-flux ratio was five times the critical value. The jets are followed to a distance in excess of 2,000 AU

conserve total energy in the absence of damping. To ensure that energy is always conserved or dissipated, two modifications to the method of Price and Monaghan [17] must be made. The first is the addition of the last term on the right-hand side of Eq. (2). The second is that the SPH equations for $\nabla\cdot\mathbf{B}$ and $\nabla\psi$ must form a conjugate pair (one using the symmetric SPH operator, the other the difference operator). Price and Monaghan [17] used difference operators for both. In practice, Tricco and Price [20] find that the best results are obtained using

$$(\nabla\cdot\mathbf{B})_a = -\frac{1}{\Omega_a\rho_a}\sum_b m_b(\mathbf{B}_a-\mathbf{B}_b)\cdot\nabla_a W_{ab}(h_a), \tag{3}$$

$$\left(\frac{\mathrm{d}\mathbf{B}}{\mathrm{d}t}\right)_a = -\rho_a\sum_b m_b\left[\frac{\psi_a}{\Omega_a\rho_a^2}\nabla_a W_{ab}(h_a)+\frac{\psi_b}{\Omega_b\rho_b^2}\nabla_a W_{ab}(h_b)\right], \tag{4}$$

where the symbols have their usual SPH meanings. The result is a stable SPMHD method that maintains a negligible magnetic divergence, but does not have the limitations of Euler potentials.

In Price et al. [19], we applied this new SPMHD method to the collapse of rotating magnetised molecular cloud cores and demonstrated that we could obtain stable long-lived jets from calculations that followed the collapse down to the first hydrostatic core. An example is given in Fig. 1. Following the formation of the first hydrostatic core, we inserted a sink particle to allow the calculations to be followed well beyond the core formation, until essentially all of the original molecular cloud core had either been accreted by the sink particle, or been ejected in the jet/outflow. We followed the jets for distances in excess of 2,000 AU and found that they were well collimated (opening angles of $\sim$2–3°) and that up to 40 % of the original molecular cloud core could be ejected in the jet/outflow.

References

1. Børve, S., Omang, M., & Trulsen, J. 2001, *ApJ*, 561, 82
2. Bürzle, F., Clark, P. C., Stasyszyn, F., Dolag, K., & Klessen, R. S. 2011a, *MNRAS*, 417, L61
3. Bürzle, F., Clark, P. C., Stasyszyn, F., et al. 2011b, *MNRAS*, 412, 171
4. Dedner, A., Kemm, F., Kröner, D., et al. 2002, Journal of Computational Physics, 175, 645
5. Dolag, K., Bartelmann, M., & Lesch, H. 1999, *A&A*, 348, 351
6. Dolag, K. & Stasyszyn, F. 2009, *MNRAS*, 398, 1678
7. Hosking, J. G. & Whitworth, A. P. 2004a, *MNRAS*, 347, 1001
8. Hosking, J. G. & Whitworth, A. P. 2004b, *MNRAS*, 347, 994
9. Morris, J. P. 1996, PASA, 13, 97
10. Phillips, G. J. 1986, *MNRAS*, 221, 571
11. Phillips, G. J. & Monaghan, J. J. 1985, *MNRAS*, 216, 883
12. Price, D. J. & Bate, M. R. 2007, *MNRAS*, 377, 77
13. Price, D. J. & Bate, M. R. 2008, *MNRAS*, 385, 1820
14. Price, D. J. & Bate, M. R. 2009, *MNRAS*, 398, 33
15. Price, D. J. & Monaghan, J. J. 2004a, *MNRAS*, 348, 123
16. Price, D. J. & Monaghan, J. J. 2004b, *MNRAS*, 348, 139
17. Price, D. J. & Monaghan, J. J. 2005, *MNRAS*, 364, 384
18. Price, D. J. & Rosswog, S. 2006, Science, 312, 719
19. Price, D. J., Tricco, T. S., & Bate, M. R. 2012, *MNRAS*, 423, L45
20. Tricco, T. S. & Price, D. J. 2012, Journal of Computational Physics, 231, 7214

Impact of Tangled Magnetic Fields on Star Formation

Philipp Girichidis and Robi Banerjee

Abstract We investigate the impact of tangled magnetic fields on the collapse of dense molecular cloud cores, the resulting morphology of the cloud, and the formation of protostars using three-dimensional hydrodynamic simulations. The initial density profile as well as the structure and strength of the magnetic field are varied, and supersonic turbulent motions are applied.

The simulations show that the structure of the magnetic field leads to significantly larger differences in the cloud morphology and the number of stars than the magnetic field strength. Clouds with an initially tangled magnetic field form of the order of twice as many protostars as clouds with a homogeneous magnetic field of the same strength. Variations in the strength of the magnetic field only show a relatively weak impact on the overall evolution of the cloud.

1 Introduction

Magnetic fields are ubiquitous in the interstellar medium with field strengths of the order of 6 μG (e.g., [2,11]). In star-forming regions, in particular in embedded high-mass infrared dark cores, the magnetic field strength reaches values of a few 10^2 μG (e.g., [5]), or even mG (e.g., [3]). Concerning the structure of the field much less is known. Early observations suggested a large-scale field structure [4, 10, 15]. More recent observations, however, find evidence for more small-scale structures of the magnetic field in dense cores [3,7,12].

P. Girichidis (✉)
Max-Planck-Institut für Astrophysik, Karl-Schwarzschild-str. 1, 85741 Garching, Germany
e-mail: philipp@girichidis.com

R. Banerjee
Hamburger Sternwarte, Gojenbergsweg 112, 21029 Hamburg, Germany
e-mail: banerjee@hs.uni-hamburg.de

D. Stamatellos et al. (eds.), *The Labyrinth of Star Formation*, Astrophysics and Space Science Proceedings 36, DOI 10.1007/978-3-319-03041-8_19,

In numerical simulations of star forming regions only large-scale magnetic fields have been investigated. It is unclear to what extend small-scale magnetic fields change the morphology of a collapsing region, the fragmentation behaviour and the accretion process in young protostellar clusters.

We present simulations of dense magnetised cores, investigating the impact of different magnetic field strengths and structures in the presence supersonic turbulence. We use homogeneous fields as well as strongly tangled magnetic fields, finding that the structure of the field has a significantly larger impact on the morphology of the cloud and the formation process of stars than the magnetic field strength.

2 Initial Conditions and Numerical Techniques

We simulate the collapse of $100\,M_\odot$ core with a radius of 0.1 pc, embedded in a computational box of $L_{\rm Box} = 0.26\,{\rm pc}$. The free-fall time for the resulting average density of $1.76 \times 10^{-18}\,{\rm g\,cm^{-3}}$ is $t_{\rm ff} = 50.2\,{\rm kyr}$. The gas has a molecular weight of 2.3 and is assumed to be isothermal throughout the simulation at a temperature of 20 K, yielding a constant sound speed of $c_{\rm s} = 2.68 \times 10^4\,{\rm cm\,s^{-1}}$. The corresponding Jeans length and mass are $\lambda_{\rm J} = 9{,}300\,{\rm AU}$ and $M_{\rm J} = 1.23\,M_\odot$.

The simulations were performed using the adaptive mesh refinement code FLASH with an effective resolution of $4{,}096^3$ cells. This corresponds to a smallest cell size of $\Delta x \approx 13\,{\rm AU}$. The Jeans length has to be resolved with at least four grid cells [14], which gives an upper limit for the density. We chose eight cells and introduce accreting lagrangian sink particles [1, 6, 13], once the density exceeds the threshold density, $\rho = 2.46 \times 10^{-14}\,{\rm g\,cm^{-3}}$. These sink particles are referred to as protostars.

As the density profile has strong influence on the collapse of the cloud and the fragmentation process [8, 9], we use two different initial density configurations, a rescaled Bonnor-Ebert sphere and a power-law profile $\rho \propto r^{-1.5}$.

The turbulence is modelled with a random velocity field created in Fourier space with a power spectrum of the form $P(k) \propto k^{-2}$ and then transformed back to real space. The r.m.s. Mach number of the turbulent motions is $\mathscr{M} \approx 3.5$. The turbulent velocities are only set initially and not driven during the simulation. We apply two different random realisations of the turbulence for each density profile.

For the magnetic field we distinguish between a homogeneous and a tangled magnetic field, created similarly to the turbulent motions but projected to divergence-free modes in Fourier space. The power spectrum of the tangled field takes the form $P(k) \propto k^3$ for $kL_{\rm Box}/2\pi \in 1 \ldots 30$ and $P(k) \propto k^{-1.5}$ for $kL_{\rm Box}/2\pi > 30$. The field strength is set such that $v_{\rm rms}/v_{\rm A} = 0.5, 1, 2$, where $v_{\rm rms}$ is the root-mean-square velocity of the gas and $v_{\rm A} = B/\sqrt{4\pi\langle\rho\rangle}$ is the Alfvén velocity, giving $B_{1,2,3} = 217.3,\ 434.7,\ 869.3\,\mu{\rm G}$.

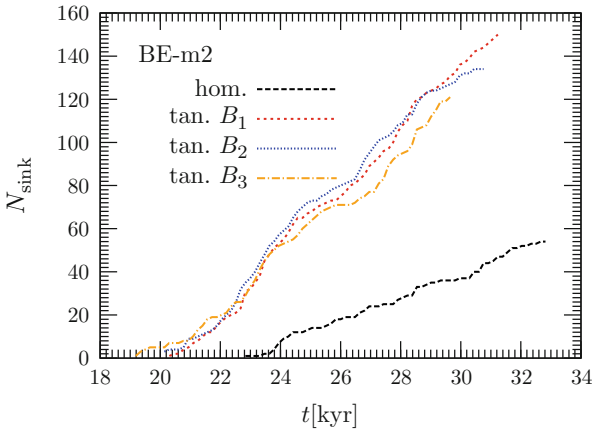

Fig. 1 Number of sink particles as a function of simulation time for the rescaled Bonnor-Ebert density profile and random turbulent realisation 2. The simulations with homogeneous magnetic field form significantly less sink particles than the simulations with tangled fields of different strength. The difference between the tangled fields is not significant

3 Results

We run the simulations until 20 % of the gas are accreted by sink particles. For all runs this takes about the same time of ∼24 kyr for power-law density profile and ∼30 kyr for the rescaled Bonnor-Ebert sphere irrespective of the structure of the magnetic field. Overall the magnetised cores form less protostars than the similar simulations without magnetic fields in [9]. In the simulations with tangled fields, the additional perturbations introduced by the field result in more collapsing regions, which leads to more sink particles in the simulation (see Fig. 1). The strength of the magnetic field does not have a significant impact on the number of sink particles. Similar results hold for the morphology of the cloud. Tangled magnetic fields show a remarkably different morphology at the end of the simulation (see Fig. 2), a different field strength in contrast only leads to small variations.

4 Summary and Conclusion

We investigate the impact of tangled magnetic fields on the collapse process, the morphology of the cloud and the number of protostars. We vary the initial density profile, the random realisation of the turbulence as well as the structure and strength of the magnetic field. All simulations with magnetised cores form less protostars than the corresponding non-magnetic simulations. The runs with tangled

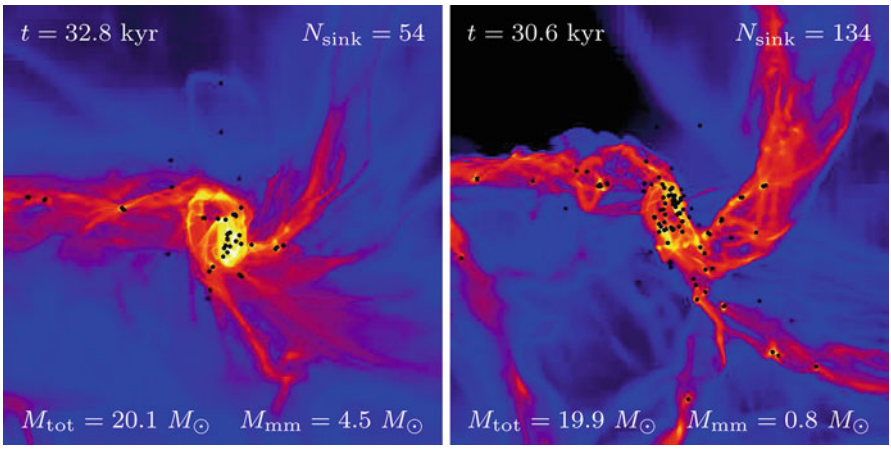

Fig. 2 Column density plot for the simulation with a rescaled Bonnor-Ebert sphere and turbulent random seed 2. The *left plot* corresponds to the initially homogeneous magnetic field, the *right plot* to the tangled field with the same rms field strength B_2

magnetic fields form significantly more protostars, of the order of twice as many as the simulations with homogeneous magnetic fields. Among the simulations with tangled magnetic fields the field strength plays a minor role and leads to a very similar number of protostars. The morphology of the cloud also shows significant differences between the tangled and homogeneous field configuration, but only small differences for tangled magnetic fields of varying strength.

References

1. Bate, M. R., Bonnell, I. A., & Price, N. M. 1995, *MNRAS*, 277, 362
2. Beck, R. 2009, Astrophysics and Space Sciences Transactions, 5, 43
3. Beuther, H., Vlemmings, W. H. T., Rao, R., & van der Tak, F. F. S. 2010, *ApJ*, 724, L113
4. Crutcher, R. M., Nutter, D. J., Ward-Thompson, D., & Kirk, J. M. 2004, *ApJ*, 600, 279
5. Crutcher, R. M., Wandelt, B., Heiles, C., Falgarone, E., & Troland, T. H. 2010, *ApJ*, 725, 466
6. Federrath, C., Banerjee, R., Clark, P. C., & Klessen, R. S. 2010, *ApJ*, 713, 269
7. Girart, J. M., Beltrán, M. T., Zhang, Q., Rao, R., & Estalella, R. 2009, Science, 324, 1408
8. Girichidis, P., Federrath, C., Allison, R., Banerjee, R., & Klessen, R. S. 2012, *MNRAS*, 420, 3264
9. Girichidis, P., Federrath, C., Banerjee, R., & Klessen, R. S. 2011, *MNRAS*, 413, 2741
10. Goodman, A. A., Bastien, P., Menard, F., & Myers, P. C. 1990, *ApJ*, 359, 363
11. Heiles, C., & Troland, T. H. 2005, *ApJ*, 624, 773
12. Kirk, J. M., Ward-Thompson, D., & Crutcher, R. M. 2006, *MNRAS*, 369, 1445
13. Krumholz, M. R., McKee, C. F., & Klein, R. I. 2004, *ApJ*, 611, 399
14. Truelove, J. K., Klein, R. I., McKee, C. F., Holliman, J. H., Howell, L. H., & Greenough, J. A. 1997, *ApJ*, 489, L179
15. Ward-Thompson, D., Kirk, J. M., Crutcher, R. M., Greaves, J. S., Holland, W. S., & André, P. 2000, *ApJ*, 537, L135

Modelling Star Formation in Ophiuchus

Oliver Lomax, Anthony Peter Whitworth, Annabel Cartwright, Dimitris Stamatellos, and Stefanie K. Walch

Abstract We perform simulations of prestellar core collapse with initial conditions inferred from observations of Ophiuchus. The cores in Ophiuchus are mostly isolated, hence we run multiple simulations of individual cores. We statistically model the intrinsic shapes of cores as a population of triaxial ellipsoids with a single free parameter which is fitted to aspect ratio data. We assume a turbulent velocity field with modifications which add ordered radial and rotational motion. Mass, size and non-thermal velocity dispersion are drawn randomly from observational data. Preliminary results show a largely realistic IMF. Future work will explore solenoidal to compressive velocity mode ratios and the effects of accretion luminosity. Results will lead to inferences on quantities such as star formation efficiency in the region.

1 Introduction

We aim to model low mass star formation in Ophiuchus using SPH simulations. Ophiuchus is a well observed region continuum mapping of cores by Simpson et al. [1] (SNW-T08), Stanke et al. [2] (SSGK06) and Motte et al. [3] (MAN98) and molecular line-widths by André et al. [4] (ABMP07). MAN98 [3] and ABMP07 [4] conclude that the prestellar cores in Ophiuchus are relatively isolated and are likely

O. Lomax (✉) • A.P. Whitworth • A. Cartwright
Cardiff School of Physics and Astronomy, Cardiff University, Queens Buildings, 5 The Parade, Cardiff CF24 3AA, UK
e-mail: oliver.lomax@astro.cf.ac.uk

D. Stamatellos
Jeremiah Horrocks Institute for Mathematics, Physics and Astronomy, University of Central Lancashire, UK
e-mail: dstamatellos@uclan.ac.uk

S.K. Walch
Max-Planck-Institut für Astrophysics, Garching bei München, 422 Germany

D. Stamatellos et al. (eds.), *The Labyrinth of Star Formation*, Astrophysics and Space Science Proceedings 36, DOI 10.1007/978-3-319-03041-8_20,

to collapse before interacting with one another. On this basis we model cores as isolated objects, performing hundreds of SPH simulations using initial conditions inferred from observations.

Inferring initial conditions from observations is a difficult inverse problem as we usually only have access to information in two spatial dimensions and one velocity dimension. We will split this problem into two parts: inferring the intrinsic shape of cores and generating suitable velocity fields.

2 Shapes

We invoke a model where the intrinsic shapes of prestellar cores are described by a population of triaxial ellipsoids. Each ellipsoid has one axis equal to 1 and the other two equal to e^{R_1} and e^{R_2}, where R_1 and R_2 are random numbers drawn from a gaussian distribution with mean 0 and standard deviation σ. We fit single the free parameter σ to data from SNW-T08 [1], SSGK06 [2] and MAN98 [3] by generating 10^4 ellipsoids and projecting them through random lines of sight. The distribution of aspect ratios from the model can then be compared with observational data, as shown in Fig. 1.

The results show that the model with $\sigma = 0.55$ visibly fits well with the SSGK06 [2] and SNW-T08 [1] data. While the MAN98 [3] data appear divergent

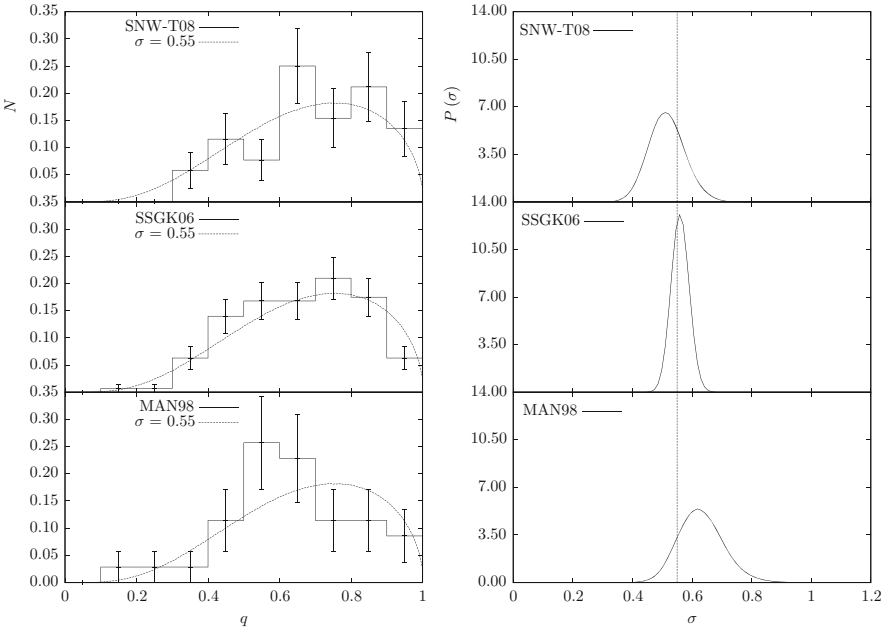

Fig. 1 *Left*: comparison of SNW-T08 [1], SSGK06 [2] and MAN98 [3] data with model when $\sigma = 0.55$. *Right*: the probability density functions of σ given each data set

from the model, these data have the lowest number statistics with only 35 points. Also in Fig. 1 are the probability density functions of sigma for each data set generated using Markov-chain Monte Carlo sampling. We find through Baysian model comparison that it is difficult to justify higher order shape models when one parameter is sufficient [5].

3 Velocity Field

The velocity field of a prestellar core is likely to have rotational, radial and turbulent components. However, given that the observations we use are line-of-sight velocity dispersions by ABMP07 [4], parametrically defining these components would introduce too many free parameters to explore using SPH.

We simplify this problem by modifying the random Gaussian fields that are typically used to model turbulence [6]. We firstly spherize the core SPH particles to a radius $R_{\rm core}$ and construct a field with $P(k) \propto k^{-4}$, $k_{\rm min} = 1$, $k_{\rm max} = 64$ and $1/k_{\rm min} = 4R_{\rm core}$. We then modify the $k = 1$ modes such that the centre of compression/expansion and centre of rotation are at the centre of the core, i.e.

$$\begin{pmatrix} \mathbf{A}_{1,0,0} \\ \mathbf{A}_{0,1,0} \\ \mathbf{A}_{0,0,1} \end{pmatrix} = \begin{pmatrix} R_x & \Omega_z & -\Omega_y \\ -\Omega_z & R_y & \Omega_x \\ \Omega_y & -\Omega_x & R_z \end{pmatrix} \text{and} \begin{pmatrix} \boldsymbol{\phi}_{1,0,0} \\ \boldsymbol{\phi}_{0,1,0} \\ \boldsymbol{\phi}_{0,0,1} \end{pmatrix} = \pi/2, \tag{1}$$

where $\mathbf{A}$ are and $\boldsymbol{\phi}$ are the amplitudes and phases of the k-vectors and R and Ω are the radial and rotational modes of the x, y and z axes. The values of R and Ω are linked to the power spectrum of the turbulent field. The magnitude of the field is normalized to ABMP07 [4] observations, hence the only free parameter is the ratio of solenoidal to compressive modes. The field is then superimposed on to the SPH particles and the ensemble to reconfigured back to the original ellipsoidal shape.

4 Simulations

We now construct a trivariate lognormal distribution using mass and size data form MAN98 [3] and velocity data from ABMP07 [4]. From this distribution we draw simulation initial conditions for each core. The intrinsic shape of each core is drawn from the ellipsoid model in Sect. 2. We apply a critical Bonnor-Ebert density profile to each core [7] and aim to explore different ratios of solenoidal to compressive velocity modes. SPH simulations use the Stamatellos et al. [8] method to model radiative cooling.

Figure 2 shows the results from 100 simulations with a solenoidal to compressive ratio of 2:1, all run for 0.2 Myr. The 65 runs that collapsed formed approximately

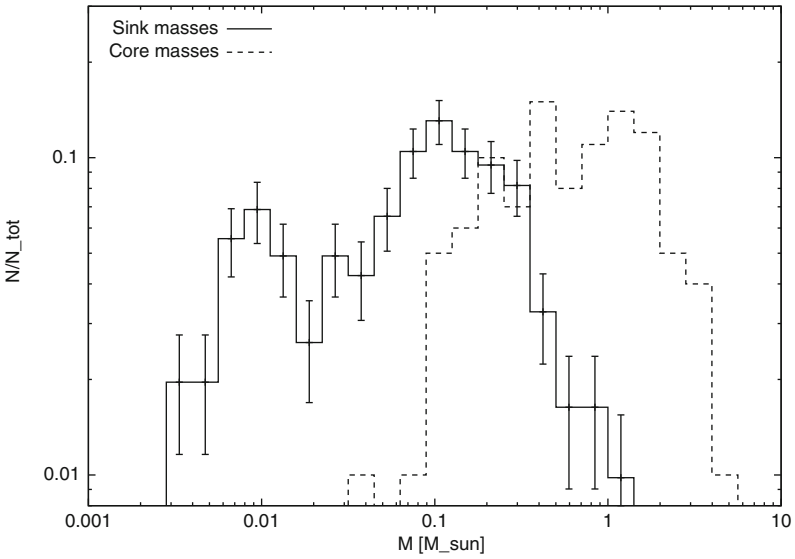

Fig. 2 The distribution of protostellar objections (*solid line*) formed from simulations of prestellar cores (*dashed lines*). Error bars represent Poisson errors

400 protostellar objects. The peak of the distribution is roughly in line with the Kroupa [9] IMF of $M_{\text{peak}} = 0.08\,M_{\odot}$, however there is an overabundance of low brown dwarf mass objects. We hope to correct for this by implementing accretion luminosity [10] in further simulations. These simulations have an average star formation efficiency of 60 % and produce and median number 5 protostars per core.

5 Conclusions

We have reduced to the problem of informed initial conditions to a single parameter family, given observational constraints. We model the shapes of individual cores as triaxial ellipsoids and model the intrinsic velocity fields using modified turbulence.

The results so far show various modes of star formation. As we treat the cores as isolated, we can perform many realisations to gain good number statistics. The aim of this will be to match simulations results with observed protostellar IMFs and binary statistics, yielding inference on quantities such as star formation efficiency and the number of protostars formed per core.

References

1. R.J. Simpson, D. Nutter, D. Ward-Thompson, MNRAS **391**, 205 (2008)
2. T. Stanke, M.D. Smith, R. Gredel, T. Khanzadyan, A&A **447**, 609 (2006)
3. F. Motte, P. André, R. Neri, A&A **336**, 150 (1998)
4. P. André, A. Belloche, F. Motte, N. Peretto, A&A **472**, 519 (2007)
5. O. Lomax, A.P. Whitworth, A. Cartwright (in prep)
6. R.S. Klessen, F. Heitsch, M.M. Mac Low, ApJ **535**, 887 (2000)
7. J.M. Kirk, D. Ward-Thompson, P. André, MNRAS **360**, 1506 (2005)
8. D. Stamatellos, A.P. Whitworth, T. Bisbas, S. Goodwin, A&A **475**, 37 (2007)
9. P. Kroupa, MNRAS **322**, 231 (2001)
10. D. Stamatellos, A.P. Whitworth, D.A. Hubber, ApJ **730**, 32 (2011)

On the Origin of Interstellar Turbulence: Less SNe and More Galactic Dynamics

Diego Falceta-Gonçalves

Abstract Turbulence is ubiquitous in the ISM, from large (galactic) scales down to planet-sized eddies within pre-stellar accretion disks. The ISM turbulence is known to operate in the both ends of triggering star formation when occurring at molecular clouds, as well as quenching the process at HII regions. Its origin, however, is still controversial. Supernovae are generally accounted as the main source of the turbulent energy of the ISM. However, recent observations of stellar orbits and the gravitational potential of the Galaxy revealed a new possibility: ISM gas flows driven by the global galactic gravitational potential. In this work we provide the first numerical simulations of the dynamics of the diffuse and molecular ISM interacting with the gravitational potential wells of the Galaxy. These reveal the generation of arms and the triggering of turbulence at large scales (>100 pc). During the interactions, molecular clouds may be disrupted and dense cores be formed. We compare the statistics of the obtained turbulent media with the observations.

1 Introduction

The process of star formation is not yet completely understood. However, for the past two decades, the theory of turbulent fragmentation of a parent molecular cloud into dense cores, which in their turn end up collapsing gravitationally to form stars, has been strengthened. Each year, more detailed observations of the dense structures in the ISM and finer and more complex numerical simulations shed light onto one of the most important issues of modern astrophysics. If turbulent

D. Falceta-Gonçalves (✉)
Escola de Artes, Ciências e Humanidades, Universidade de São Paulo,
Rua Arlindo Bettio 1000, CEP 03828-000, São Paulo, Brazil
e-mail: dfalceta@usp.br

D. Stamatellos et al. (eds.), *The Labyrinth of Star Formation*, Astrophysics and Space Science Proceedings 36, DOI 10.1007/978-3-319-03041-8_21,

fragmentation of parent clouds truly plays a major role on star formation, then the understanding of this process depends on the understanding of the turbulent motions within molecular clouds, in all scales. It is known that turbulence works at both ends of star formation, i.e. at large scales the turbulent motions may prevent the gravitational collapse of a cloud (see [4]), but at small scales the shocks and instabilities that arise when the Mach number is high supersonic lead to the formation of very dense and unstable gravitationally cores (e.g. [7]). For incompressible fluids, considering that perturbations are homogeneous, isotropic, scale invariant and local (i.e. perturbations with similar wavelengths interact to decay but perturbations with different wavelengths do not), one gets the well-known Kolmogorov's scaling:

$$\delta v^2 \simeq \int_{k=1/l}^{\infty} E(k')dk' \tag{1}$$

$$E(k) \propto \dot{\epsilon}^{2/3} k^{-5/3} \tag{2}$$

where k represents the wavenumber and $\dot{\epsilon}$ the energy decay rate of a given eddy of size ($l \sim 1/k$). This means that the turbulent kinetic energy goes from large to small scales, and eventually vanishes at the dissipation scales. A typical timescale for the turbulent energy to decay is $\tau \propto l\delta v^{-1}$. An interesting point is that the energy released at small scales, which may be the main responsible for the formation of the collapsing cores, strictly depends on the mechanism of injection, at large scales. Numerical simulations have shown that compressible and magnetized turbulence do not differ much from this scenario [5, 6].

Observationally, the ISM is identified as supersonically turbulent at scales as large as 20–50 pc (e.g. [1]). The turbulence is ubiquitous in our galaxy, presenting similar amplitudes at large scales that have no correlation to the local properties of the ISM, such as star formation rates. This fact shows that the role of SNe feedback on the large scale dynamics of the ISM is lower than previously thought. This also indicates that the injection of energy at these scales must be global, possibly galactic. From the energy decay rate $\dot{\epsilon} \propto \rho\delta v^3 l^{-1}$, it is possible to estimate the total power required to sustain the turbulence in our galaxy as $\dot{E} \simeq 3\times10^{38} M_l(\mathrm{M}_\odot)\,\mathrm{erg\,year}^{-1}$, where M_l represents the ISM gas mass excited at the scale l, in solar mass units. For $M_l = 10^9$, we obtain $\dot{E} \simeq 3\times10^{47}\,\mathrm{erg\,year}^{-1}$.

In our galaxy, the SN occurrence rate is approximately 1 event per century, which result in an averaged kinetic energy release of $\dot{\epsilon} \simeq 10^{47}\,\mathrm{erg\,year}^{-1}$ (considering typical 1 % efficiency in converting the SN energy into kinetic/turbulent) [2]. Therefore, it is unlikely for the SNe explosions to constantly excite the ISM turbulence. An alternative mechanism is based on converting energy from the galactic rotation. Many authors have worked on the theory of forming galactic spiral arms from shocking the ISM gas with the potential wells fo stellar orbit resonances ([11] and many other after it). Molecular clouds could then be formed in a similar way, by instabilities that may arise in this process. The magneto-rotational

instability has been mentioned in previous works as the main source of turbulence at large scales [8, 9]. Typically, shear and MRI instabilities provide as much energy as SNe, though in a more coherent, large scale, way [3].

In this work we extend the analysis of converting kinetic energy from the gas circular motion into large scale turbulence, based on the interaction of denser regions of the ISM with the potential well of the spiral arms.

2 The Model

As initial setup we define a box with dimensions $1 \times 1\,\mathrm{kpc} \times 10\,\mathrm{pc}$, computed in a fixed grid with spatial resolution of 1 pc/cell. The ISM is initially uniform, with density as $1\,\mathrm{cm}^{-3}$ and zero velocity everywhere. The simulation is computed in the reference frame of the spiral arm, which is assumed to rotate rigidly around the center of the galaxy. At the mid position of the x-axis of the box we introduce the potential well of the spiral arm, as in [8]. The flow of gas is injected by the lower boundary on x-direction. The gas flow reproduces the relative motion of the gas with respect to the spiral arm. The relative velocity and the pitch angle are, therefore, functions of the distance to the center of the galaxy. For this work we show the results obtained for $\mathrm{r} = 10\,\mathrm{kpc}$. At a given instant there is the injection of a dense cloud ($n_c = 100\,\mathrm{cm}^{-3}$), 100 pc wide and containing $106\,\mathrm{M}_\odot$, flowing along with the rarefied medium towards the spiral arm well. We follow the dynamical evolution of this structure as it interacts with the arm. The code uses a Godunov scheme, with high order interpolation and HLLC Riemann solver for shock capturing.

3 Results and Discussions

In Fig. 1 we present the density distributions for the evolution of the interaction of a spherical cloud, two orders of magnitude denser than the average ISM, with a typical spiral arm. The plots represent four different stages, at $t = 1, 3, 6$ and 10 Myr.

It is clear that the interaction results in the complete destruction and fragmentation of the cloud. The internal shocks result in increased densities that may reach $10^4\,\mathrm{cm}^{-3}$. Despite of the strong interaction, the perturbed gas do not leave the potential well. The complex structure of vortices and dense clumps adjust themselves spatially along the spiral arm.

With respect to the velocity field (Fig. 2), we obtain a typical Kolmogorov power spectrum, i.e. $-5/3$ slope. The inertial scale is of almost 2 order of magnitude in spectral wavelengths, with a turbulent peak at scales $l \simeq 0.5 \Delta L_{arm} \sim 50\,\mathrm{pc}$.

The injection lengthscales and the total dynamical power obtained from our simulations are in agreement to the turbulent characteristics of the galactic ISM. What is the source of energy? Basically, as the pre-cloud falls into the spiral

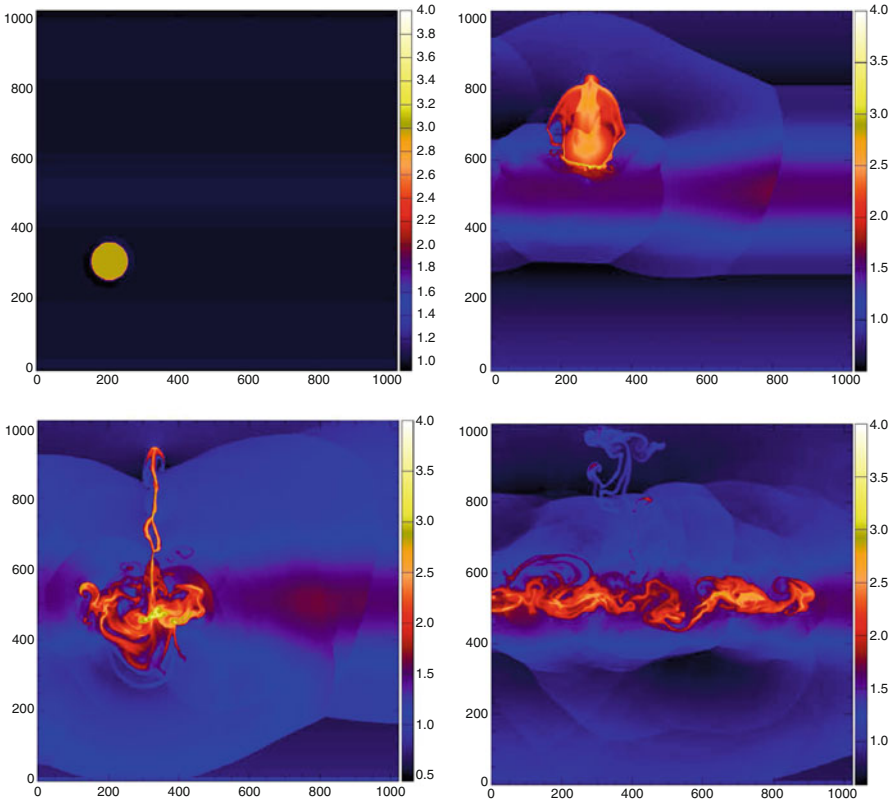

Fig. 1 Two-dimensional slice of the density distribution at t = 1, 3, 6 and 10 Myr

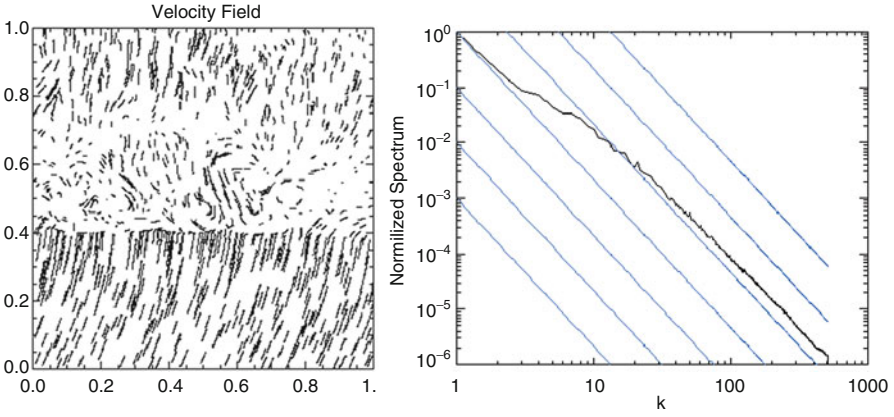

Fig. 2 Two-dimensional map of the velocity field (*left*), and the velocity power spectrum (*right*) at t = 10 Myr

arm potential well it gets fragmented and turbulent. Therefore, there is a direct conversion of the gravitational energy into kinetic. If losses are disregarded, we may estimate:

$$\delta v^2 \simeq \Delta\Phi \sim G\mu/\sqrt{2\pi}, \tag{3}$$

where μ stands for the linear mass density of the arm. Using $\mu = 10^8\,\mathrm{M}_\odot\,\mathrm{kpc}^{-1}$, we obtain $\delta v \sim 10^6\,\mathrm{cm\,s}^{-1}$, which corresponds to a turbulence Mach number $M \sim 6$ for $T_{\mathrm{ISM}} \sim 100\,\mathrm{K}$. Also, the turbulent decaying timescale is $\tau_d \sim 20$–$50\,\mathrm{Myr}$. These values are in agreement to observations.

Though not dominant in the injection of energy at large scale in our galaxy, SNe still may play a major role on triggering star formation and destroying pre-stellar cores, depending basically on its distance to the cloud (see [10]).

References

1. Armstrong, J. W., Rickett, B. J., & Spangler, S. R.: ApJ, **443**, 209 (1995)
2. Cappellaro, E.; Evans, R. & Turatto, M. : A&A, **351**, 459 (1999)
3. Elmegreen, B., Elmegreen, D. & Leitner, S.: ApJ, **590**, 271 (2003)
4. Falceta-Gonçalves, D., de Juli, M. & Jatenco-Pereira, V.: ApJ, **597**, 970 (2003)
5. Falceta-Gonçalves, D., Lazarian, A. & Kowal, G.: ApJ, **679**, 537 (2008)
6. Falceta-Gonçalves, D., Lazarian, A. & Houde, M.: ApJ, **713**, 1376 (2010)
7. Falceta-Gonçalves, D. & Lazarian, A.: ApJ, **735**, 99 (2011)
8. Kim, W-T. & Ostriker, E.: ApJ, **570**, 132 (2002)
9. Kim, W-T. & Ostriker, E.: ApJ, **646**, 213 (2006)
10. Leão, M. R. M., de Gouveia Dal Pino, E. M., Falceta-Gonçalves, D., Melioli, C., & Geraissate, F. G.: MNRAS, **394**, 157 (2009)
11. Roberts, W. W.: ApJ, **158**, 123 (1969)

The Non-linear Thin Shell Instability in Cloud–Cloud Collisions

Andrew D. McLeod and Anthony Peter Whitworth

Abstract Supersonic cloud–cloud collisions will produce a dense, shock-confined layer. This layer may be unstable to the non-linear thin shell instability (NTSI). We first explore the effect of different initial perturbations on the growth of the NTSI using smoothed particle hydrodynamics (SPH) simulations. We use one-dimensional monochromatic perturbations. We also use subsonic and supersonic turbulence to trigger the NTSI. We show partial agreement with the analytic predictions of Vishniac (ApJ 428:186, 1994). We then simulate a more realistic supersonic collision of molecular clouds with internal subsonic turbulence at a range of collision velocities. We show that at low collision velocity gravitational instability is dominant, but at higher collision velocities the NTSI becomes dominant and eventually suppresses star formation.

1 Introduction

Star formation occurs in dense gas. There are a range of physical processes that can collect gas in the Galaxy and raise its density. One such mechanism is converging flows, which lead to the formation of a shock-confined layer. Such collisions can occur from large-scale galactic flows [1–4], the collision of stellar winds [5] or supernovae bubbles [6], or turbulence on a range of scales [7].

A.D. McLeod (✉)
Astrophysics Group, School of Physics, University of Exeter, Stocker Road, Exeter EX4 4QL, UK
e-mail: amcleod@astro.ex.ac.uk

A.P. Whitworth
Cardiff School of Physics and Astronomy, Cardiff University, Queens Buildings, 5 The Parade, Cardiff CF24 3AA, UK
e-mail: Anthony.Whitworth@astro.cf.ac.uk

D. Stamatellos et al. (eds.), *The Labyrinth of Star Formation*, Astrophysics and Space Science Proceedings 36, DOI 10.1007/978-3-319-03041-8_22,

Another mechanism is the supersonic collision of molecular clouds. We study the *non-linear thin shell instability* (NTSI), which occurs only in shock-confined layers [8]. The NTSI is a bending mode instability that enhances pre-existing perturbations in the layer.

Vishniac [8] derived the growth rate of the NTSI as a function of wavenumber, and found that $\tau^{-1} \propto k^{1.5}$ for one-dimensional monochromatic sinusoidal perturbations. We conduct simulations of the NTSI to demonstrate the analytic prediction of Vishniac. We also examine the instability in the collision of flows containing initial subsonic and supersonic turbulence. We then conduct more realistic simulations of cloud–cloud collisions, including self-gravity and a more complex equation of state.

2 Simulations of the NTSI

We conduct smoothed particle hydrodynamics (SPH) simulations of colliding flows using the Seren code [9] including hydrodynamics and artificial viscosity. We use an isothermal equation of state at 10 K, sound speed $0.19\,\mathrm{km\,s^{-1}}$, and do not include self-gravity. The gas is initially of uniform density $10^{-21}\,\mathrm{g\,cm^{-3}}$, and the gas is set to collide at a Mach number $\mathscr{M}$ of 20.

For one set of simulations we impose a one-dimensional monochromatic sinusoidal velocity perturbation, and repeat for a range of wavenumbers. We also create simulations containing subsonic and supersonic turbulence respectively.

2.1 Monochromatic Perturbations

Figure 1 shows the rate of growth of perturbations for simulations with monochromatic initial perturbations. At early times, the slope is small, as all wavenumbers are excited with an equal initial amplitude. As predicted, at later times larger wavenumbers grow faster. Figure 2 shows that after the initial rise, the slope of power law fits is somewhat higher than the predicted relation of $\tau \propto k^{1.5}$.

2.2 Turbulence

Figure 3 shows the rates of growth for simulations with turbulence. For supersonic turbulence, rates of growth decrease with increasing wavenumber, as the turbulence is strongest at small wavenumbers. There is no evidence of the NTSI. For subsonic turbulence, the turbulence still dominates at small wavenumbers, but at larger wavenumbers the NTSI dominates, leading to an increase in rates of growth at larger wavenumbers. This increase can be used as a diagnostic of the NTSI in simulations with turbulence.

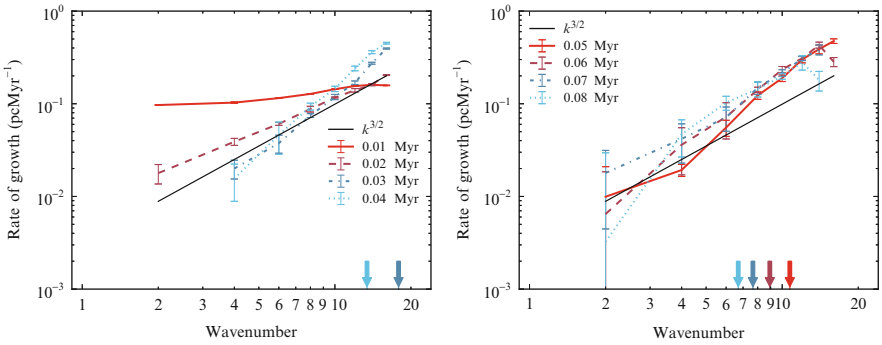

Fig. 1 The rates of growth for monochromatic perturbations as a function of wavenumber. Error bars show the standard deviation across realizations. The gradient of the *solid black line* indicates the relation predicted by Vishniac [8]. *Arrows* indicate the maximum resolvable wavenumber for the correspondingly coloured timestep; *arrows* run from latest to earliest timestep going left to right; some *arrows* are at larger wavenumbers than can be plotted

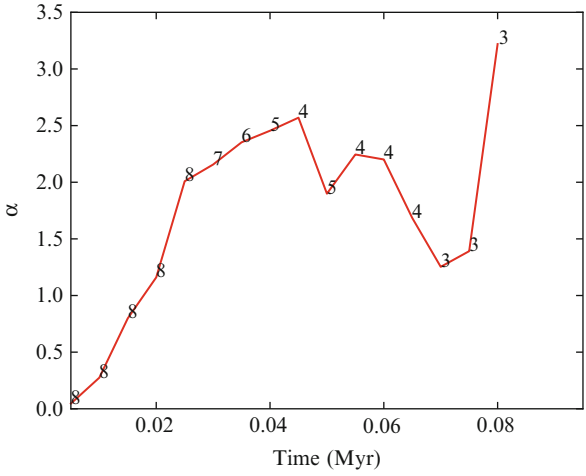

Fig. 2 Indices of power law fits to rates of growth of monochromatic perturbations as a function of time. The number of points used to construct each fit is also shown; fits constructed with fewer points are less reliable

3 Cloud–Cloud Collision Simulations

We simulate the supersonic collision of two 500 $M_\odot$ clouds of uniform density 7×10^{-22} g cm^{-3} at a range of collision velocities. We include self-gravity, sink particles [10] and the Stamatellos [11] method to solve the energy equation. Each cloud contains subsonic turbulence with an average velocity of 0.1 km s^{-1}. Figure 4 shows no evidence for the NTSI for the low-velocity collision. The NTSI appears as a rise at larger wavenumbers for the high-velocity collision.

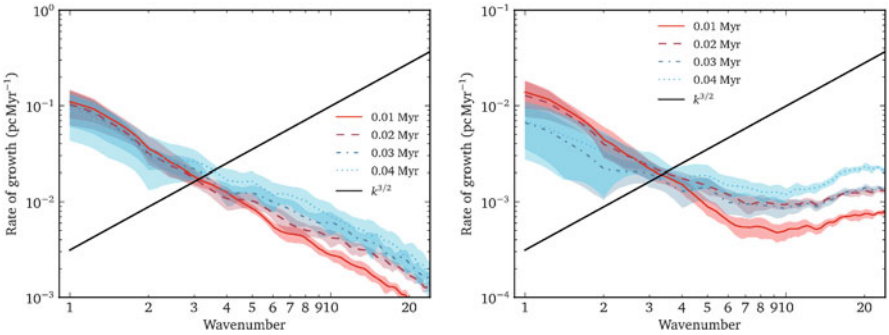

Fig. 3 Rates of growth of simulations with turbulence; as for Fig. 1. *Left*: supersonic turbulence; *right*: subsonic turbulence

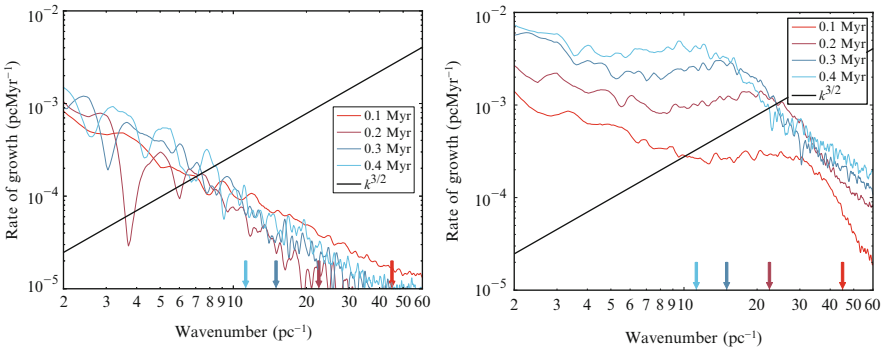

Fig. 4 Rates of growth for cloud–cloud collisions, as for Fig. 1. *Left plot* 1 km s^{-1} collision; *right plot* 5 km s^{-1} collision

4 Conclusions

We have explored the effect of the NTSI on dense shock-confined layers. Our simulations approximately match the analytic predictions of Vishniac [8]. We provide a qualitative diagnostic for the NTSI triggered by weak turbulence.

We simulate a realistic cloud–cloud collision at a range of collision velocities. As expected this produces a dense shock-confined layer. We find that at lower collision velocities the NTSI is not significant. At higher collision velocities the NTSI appears at higher wavenumbers.

References

1. I.A. Bonnell, C.L. Dobbs, T.P. Robitaille, J.E. Pringle, *MNRAS* **365**, 37 (2006).
2. E. Vázquez-Semadeni, D. Ryu, T. Passot, R.F. González, A. Gazol, *ApJ* **643**, 245 (2006).
3. F. Heitsch, L.W. Hartmann, A. Burkert, *ApJ* **683**, 786 (2008).
4. P. Hennebelle, R. Banerjee, E. Vázquez-Semadeni, R.S. Klessen, E. Audit, *A&A* **486**, L43 (2008).
5. I.R. Stevens, J.M. Blondin, A.M.T. Pollock, *ApJ* **386**, 265 (1992).
6. R.M. Williams, Y.H. Chu, J.R. Dickel, R. Beyer, R. Petre, R.C. Smith, D.K. Milne, *ApJ* **480**, 618 (1997).
7. M.M. Mac Low, R.S. Klessen, Reviews of Modern Physics **76**, 125 (2004).
8. E.T. Vishniac, *ApJ* **428**, 186 (1994).
9. D.A. Hubber, C.P. Batty, A. McLeod, A.P. Whitworth, *A&A* **529**, A27 (2011).
10. M.R. Bate, I.A. Bonnell, N.M. Price, *MNRAS* **277**, 362 (1995)
11. D. Stamatellos, A. Whitworth, T. Bisbas, S.Goodwin, *A&A* **475**, 37 (2007).

Radiative Transfer in Star Formation: Testing FLD and Hybrid Methods

James E. Owen, Barbara Ercolano, and Cathie J. Clarke

Abstract We perform a comparison between two radiative transfer algorithms commonly employed in hydrodynamical calculations of star formation: grey flux limited diffusion and the hybrid scheme, in addition we compare these algorithms to results from the Monte-Carlo radiative transfer code MOCASSIN. In disc like density structures the hybrid scheme performs significantly better than the FLD method in the optically thin regions, with comparable results in optically thick regions. In the case of a forming high mass star we find the FLD method significantly underestimates the radiation pressure by a factor of $\sim$100.

1 Introduction

Numerical models of the star formation process have improved remarkably over the last two decades; however, many questions still remain. In particular the thermal and mechanical feedback produced by the radiation from the forming stars remains to be understood both in low mass, and in particularly high mass star formation. Several numerical schemes for including the effects of radiation in hydrodynamic codes have been proposed including: Monte-Carlo techniques [6]; Short Characteristics [2]; Flux limited diffusion and other moment methods [8]; Pure ray-tracing techniques [1] and Hybrid techniques – which combine various method together to arrive at a hopefully improved and faster

J.E. Owen (✉)
Canadian Institute for Theoretical Astrophysics, 60 St. George Street, Toronto, Canada
e-mail: jowen@cita.utoronto.ca

B. Ercolano
Excellence Cluster 'Universe', Boltzmannstr. 2, 85748 Garching, Germany

C.J. Clarke
Institute of Astronomy, Madingely Road, Cambridge CB3 0HA, UK

D. Stamatellos et al. (eds.), *The Labyrinth of Star Formation*, Astrophysics and Space Science Proceedings 36, DOI 10.1007/978-3-319-03041-8_23,

method – [3, 7]. While all these methods are fast enough for inclusion into a hydrodynamical calculation, the algorithm which is both fast and accurate for incorporation into a star formation calculation still remains a matter for debate. In this work I will present radiative transfer tests of the most commonly used method: Flux Limited Diffusion (FLD), and its improvement in the form of a hybrid method.

2 The Flux Limited Diffusion and Hybrid Schemes

The flux limited diffusion approximation attempts to simplify the radiative transfer problem by using a moment method, where the radiative transfer variables are replaced by angle averaged quantities, which are the only ones required in a hydrodynamical calculation. To do this a flux limiter (λ) is employed which allows the radiative transfer problem to be written as a diffusion equation:

$$\frac{\partial E_\nu}{\partial t} + \nabla \cdot \left(\frac{c\lambda_\nu}{\kappa_\nu \rho} \nabla E_\nu \right) = S_\nu \tag{1}$$

where E is the internal energy and S is any appropriate source terms. In this form λ becomes $1/3$ in optically thick media, and $\kappa\rho E/\nabla E$ in optically thin media. Thus the flux limiter ensures the radiation field is transported at the correct speed in both limits. Another common choice is to employ the FLD method in a grey approximation, meaning the radiation field is in local thermal equilibrium with the matter.

In reality the radiation field is not always locally thermalised, and the temperature and radiation pressure are correctly given by:

$$T = \left[(\kappa(T_{\rm source})/\kappa(T))\,(E/a) \right]^{1/4} , \quad a_{\rm rad} = \left[\kappa(T_{\rm source})/c \right] \; F \tag{2}$$

however, in the grey case they are replace by:

$$T = (E/a)^{1/4} , \quad a_{\rm rad} = \left[\kappa(T)/c \right] F \tag{3}$$

where $T_{\rm source}$ is the radiation temperature the opacity source sees, a is the radiation constant and F the flux. Thus, in an optically thin region $T_{\rm source}$ does not in general equal T and in the case the source is the photosphere of a YSO then it is typically much greater than the local temperature. Meaning the temperature and radiation pressure will be underestimated by an amount depending on $\kappa(T_{\rm source})/\kappa(T)$, which can be very large in the case of a massive star. Furthermore, this has an important feedback on the flux limiter which depends on $\kappa(T)$ in the grey approximation, thus if T is underestimated then so is κ (for standard dust opacities) leading the flux-limiter to become optically thin too easily.

A simple improvement upon this is a hybrid approach to deal with the source radiation field (e.g. [3, 7]), which uses a multi-frequency ray-tracing approach to deal with the direct radiation from a forming YSO and then a grey solver (e.g. diffusion approximation [3] or FLD [7]) to deal with the re-radiated fields. In the hybrid method the directly attenuated flux just becomes part of the source terms in Eq. (1). This means that one is now using a frequency dependant approach when the photosphere of the YSO can be seen and hence where errors resulting from large $\kappa(T_{\rm source})/\kappa(T)$ are nullified.

3 Comparison and Tests

In order to asses the relative accuracy of the classical FLD method versus the hybrid method we perform two benchmark calculations one where thermal pressure dominates, as an example of a disc around a low mass star; secondly we consider a calculation where the radiation pressure force dominates, as an example of a disc around a forming high mass star. We compare the results of the two benchmark calculations performed with the FLD method, the hybrid method and the full Monte Carlo radiative transfer using the MOCASSIN code [4, 5]. We adopt a density profile of the form:

$$\rho = \rho_0 \, (R/R_0)^{-2} \exp\left[-z^2/2H(R)\right] \tag{4}$$

where $H(R)$ is the scale height which is taken to be flaring, i.e. $H(R) = (H/R)_0 \, R^{1.1}$.

For the low luminosity star we adopt a disc mass of $0.05\,{\rm M}_\odot$, a stellar luminosity of $1\,{\rm L}_\odot$ with a photospheric temperature of 4,000 K. In the case of the high luminosity star we adopt a disc mass of $1\,{\rm M}_\odot$, a stellar luminosity of $10^6\,{\rm L}_\odot$ and a photospheric temperature of 20,000 K. We find that in the case of the low mass star the temperature differences between the FLD, Hybrid and MOCASSIN results are small, in the optically thick mid-plane of the disc, where the differences are at the few percent level. In the optically thin region the Hybrid and MOCASSIN results agree perfectly and the FLD method underestimated the temperature by a factor of $\sim$2, arising from the errors in $\kappa(T_{\rm source})/\kappa(T)$ discussed above.

In the high mass, radiation pressure dominated case the differences are more severe, in the optically thick mid-plane the FLD method gives the lowest temperature with a $\sim$20–30 % difference to the MOCASSIN results and the Hybrid method gives a slightly lower temperature than the MOCASSIN results with a 5–10 % difference. In the optically thin cavity the MOCASSIN and Hybrid results agree perfectly, whereas the FLD method underestimates the temperature by a factor 4–5, misplaces the radius of the dust destruction front (at $T = 2{,}000$ K) by a factor of $\sim$3 and severely underestimated the radiation pressure – which is the dominant force term – by a factor of $\sim$100, as shown in Fig. 1.

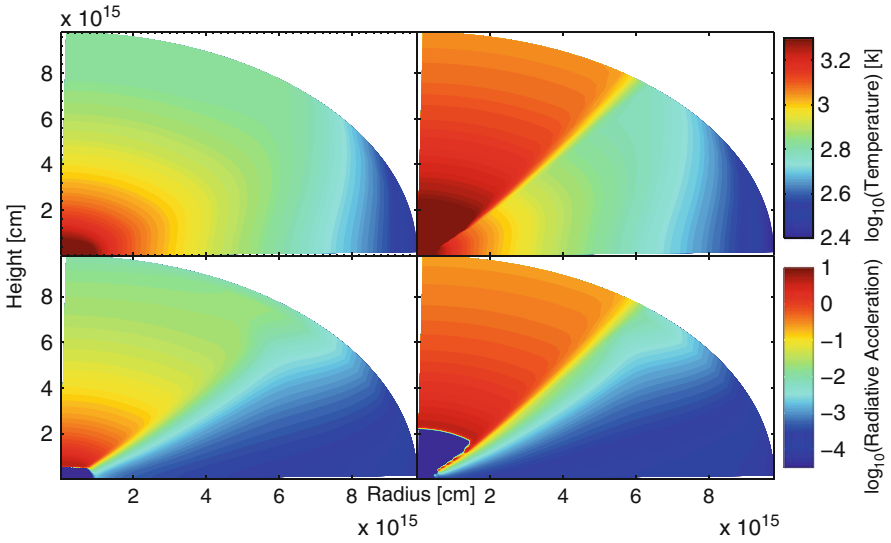

Fig. 1 Comparisons between the FLD method (*left panels*) and the hybrid method (*right panels*) for the temperature structure (*top panels*) and radiation pressure (*bottom panels*) of a disc around a forming high mass star. The *dark blue regions* in the *bottom panels* show the dust destruction front

4 Conclusions

We have performed comparisons between the FLD and Hybrid radiative transfer schemes in the cases of discs around low-mass and high mass stars. In both cases we find that the hybrid scheme performs better than the FLD scheme when compared to Monte-Carlo calculations, although in the case of low mass stars where radiation pressure is unimportant the FLD adequately describes the disc temperature where most of the dynamically important material is. However, in the case of discs around high mass-stars we find FLD to lead to large errors in both the temperature and radiation. We conclude that the hybrid scheme is more suited to simulations involving massive stars and that FLD should be used with caution in cases where the optically thin region or interfaces between optically thin and optically thick regions are dynamically important.

References

1. Abel T., Wandelt B. D., 2002, MNRAS, 330, L53
2. Davis S. W., Stone J. M., Jiang Y.-F., 2012, ApJS, 199, 9
3. Edgar R., Clarke C., 2003, MNRAS, 338, 962
4. Ercolano B., Barlow M. J., Storey P. J., Liu X.-W., 2003, MNRAS, 340, 1136

5. Ercolano B., Barlow M. J., Storey P. J., 2005, MNRAS, 362, 1038
6. Harries T. J., 2011, MNRAS, 416, 1500
7. Kuiper R., Klahr H., Dullemond C., Kley W., Henning T., 2010, A&A, 511, A81
8. Levermore C. D., Pomraning G. C., 1981, ApJ, 248, 321

Expected Observations of Star Formation Process: From Molecular Cloud Core to First Hydrostatic Core

Kohji Tomisaka, Akimasa Kataoka, Masahiro N. Machida, Kengo Tomida, and Kazuya Saigo

Abstract We performed MHD simulations of the contraction of rotating, magnetized molecular cloud cores. In the molecular cores, B-field and angular momentum (J) vector are not always aligned. When a first hydrostatic core forms, axisymmetric structure appears and average B and J are parallel in small scale. However, in large scale, the configuration is far from this. This means that contraction process is imprinted on the snapshot. We calculated two mock observations of MHD simulations (1) the polarization of dust thermal emission to reveal the magnetic evolution and (2) the line emissions from interstellar molecules to reveal the evolution of density and velocity. Comparing the mock observations with true ones, we can answer several questions: in which case the hourglass-shaped and S-shaped magnetic fields are seen; how the distribution of polarized intensity is understood; how the first hydrostatic core should be observationally identified.

K. Tomisaka (✉) • A. Kataoka
National Astronomical Observatory of Japan, Mitaka, Tokyo 181-8588, Japan

Department of Astronomical Science, Graduate University for Advanced Studies, Mitaka, Tokyo181-8588, Japan
e-mail: tomisaka@th.nao.ac.jp

M.N. Machida
Department of Earth and Planetary Sciences, Kyushu University, Fukuoka 812-8581, Japan

K. Tomida
Department of Astrophysical Sciences, Princeton University, Princeton, NJ 08544, USA

K. Saigo
NAOJ Chile Observatory, National Astronomical Observatory of Japan, Mitaka, Tokyo 181-8588, Japan

D. Stamatellos et al. (eds.), *The Labyrinth of Star Formation*, Astrophysics and Space Science Proceedings 36, DOI 10.1007/978-3-319-03041-8_24,

1 Introduction

Magnetic field plays an important role in the star formation process. Stability against the self-gravity is given by the mass-to-flux ratio of magnetized clouds. As well as the strength of B-field, its geometry is also crucial to the gravitational contraction [2, 6], since the angular momentum can be transferred by the twisted B-field (magnetic braking). After the initial isothermal contraction of the molecular core, a first core is formed, which is supported by the thermal pressure. This is a signature that shows a first hydrostatic object, which is evolving to a protostar, is made at the center surrounded by infalling envelope [4, 5]. Since the first core formation is triggered by the change of the equation of state of gas, radiation transfer should be included and the problem is now radiation magnetohydrodynamics (RMHD) [1, 7, 8].

To understand the evolution of molecular clouds (or cloud cores), it is essential to compare the simulations with the observation. In this paper, we present two examples of such comparison:

1. Configuration of the B-field studied by the polarization of thermal dust emissions appearing in the dynamical contraction of the molecular core [3, 10].
2. Observability of the first core expected in RMHD simulations [9].

2 Model and Method

Expected Polarization of Thermal Dust Emissions Polarization of thermal emissions from interstellar dusts comes from the alignment of the dust in the interstellar B-fields. The major axis of the dust grains is aligned to the perpendicular direction to the B-field and thermal emission from such aligned grains is linearly polarized, in which **E**-vectors of the electromagnetic wave is perpendicular to the interstellar **B**-field. We performed a number of 3D MHD simulations of rotating magnetized clouds with angular speed of Ω_0, B-field strength of B_0 and the angle between rotation and B-field of δ. Model A is an aligned rotator $\mathbf{B_0} \parallel \Omega_0$ with $B_0 = 23\,\mu\mathrm{G}$, $\Omega_0 = 1.4 \times 10^{-14}\,\mathrm{s}^{-1}$ and $\delta = 0°$. In model B, $\mathbf{B_0}$ and Ω_0 are not parallel, $B_0 = 12\,\mu\mathrm{G}$, $\Omega_0 = 1.4 \times 10^{-14}\,\mathrm{s}^{-1}$ and $\delta = 60°$.

After the 3-dimensional MHD simulation has been done, Polarization is calculated from the relative Stokes parameters, $q = \int \rho \cos 2\psi \, \cos^2\gamma \, ds$, and $u = \int \rho \sin 2\psi \, \cos^2\gamma \, ds$, where the integration is performed along the line-of-sight and γ and ψ are angles between the **B** and the celestial sphere and the position angle of the B-field projected onto the celestial sphere, respectively. The polarization degree is given as $P = p_0(q^2 + u^2)^{\frac{1}{2}}/(\Sigma - p_0\Sigma_2)$ from two quantities obtained by integration of the density along the line of sight as $\Sigma = \int \rho \, ds$ and $\Sigma_2 = \int \rho \left(\cos^2\gamma/2 - 1/3\right) ds$ (for detail refer to [3]).

nonLTE Line Transfer We assume a hydrostatic cloud with a central density of $n_0 = 1.6 \times 10^4\,\mathrm{H_2\,cm^{-3}}$ and add uniform rotation of $\omega = 0.1/t_{\mathrm{ff}} = 1.5 \times 10^{-14}\,\mathrm{rad\,s^{-1}}$ and uniform B-field $B_z = 1.1\,\mu\mathrm{G}$. The evolution of the cloud is studied with nested grid RMHD code by Tomida et al. [7]. After the RMHD simulation has been performed, nonLTE radiation transfer is calculated by Monte Carlo method (for detail, see [9]).

3 Result

In Fig. 1, we plotted polarization B-vector (bar), polarization degree (color), and column density (black contour line) which is proportional to the total intensity I (mm wave is thin for low-mass formation regions). The cloud of this snapshot already has a protostar with a mass of $0.5\,M_\odot$. Although the polarization degree is low when viewing pole-on (a), it is high for edge-on view (f). Other than the pole-on case, the polarization vector shows so called a hour-glass shape, which is most clearly shown in the edge-on case. In panels (b)–(e), the distribution of polarization degree is not axisymmetric with respect to the vertical axis but point-symmetric around the origin. This comes from the cancellation of polarization in which the fore- and background B-field becomes perpendicular each other when we project them onto the celestial plane.

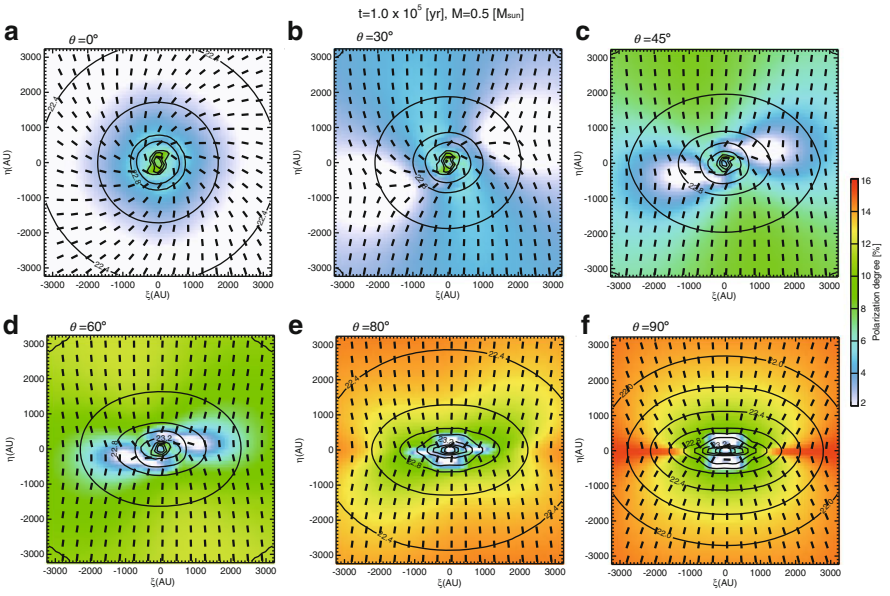

Fig. 1 Polarization maps for model A from the viewing angles of $\theta = 0°$ (pole on view; **a**), 30° (**b**), 45° (**c**), 60°(**d**), 80° (**e**), and 90° (edge on view; **f**) and $\phi = 0°$ when $M_{\mathrm{ps}} = 0.5 M_\odot$

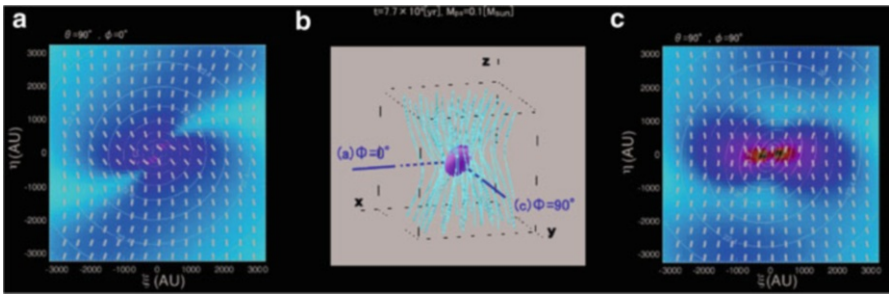

Fig. 2 Polarization maps when $M_{\rm ps} = 0.1 M_{\odot}$ (**a** and **c**) for model B. Panel (**a**) is for the viewing angle of $(\theta, \phi) = (90°, 0°)$ while panel (**c**) is for $(\theta, \phi) = (90°, 90°)$. Panel (**b**) represents the three dimensional distribution of the B-field lines and isodensity surface

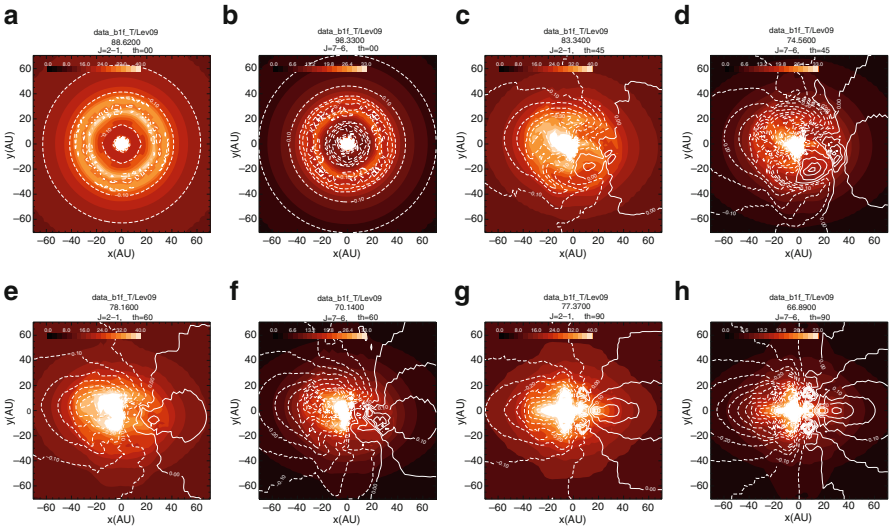

Fig. 3 CS $J = 2$–1 and $J = 7$–6 integrated intensity (false color) and intensity-weighted mean velocity $\langle V \rangle$ for different line-of-sights (contours) after the first core is made. The panels (**a**), (**c**), (**e**), and (**g**) are results for the CS $J = 2$–1 lines and panels (**b**), (**d**), (**f**), and (**h**) are results for the CS $J = 7$–6 lines. The viewing angles θ for the respective panels are (**a**) and (**b**): $\theta = 0°$ (pole-on), (**c**) and (**d**): $\theta = 45°$, (**e**) and (**f**): $\theta = 60°$, (**g**) and (**h**): $\theta = 90°$(edge-on). The levels of the integrated intensity are shown in the color bar in the upper-left corner and the unit is K km s^{-1}. The *solid* and *dashed contour lines* of $\langle V \rangle$ represent positive ($0\,{\rm km\,s^{-1}} \le \langle V \rangle \le 1\,{\rm km\,s^{-1}}$) and negative ($-1\,{\rm km\,s^{-1}} \le \langle V \rangle \le 0\,{\rm km\,s^{-1}}$) velocities, respectively. The step of the contour is chosen to be $0.05\,{\rm km\,s^{-1}}$

On the contrary, in Fig. 2, we plotted expected polarization map for misalignment case (model B). When we look at the protostellar core from the x-axis (a), the distribution of polarization vectors is not the hour-glass shape but a configuration like capital letter "S" (S-shape). When the same snapshot is observed from y-axis,

the polarization vector indicates the hour-glass shape, although the minor axis of the total intensity distribution and the symmetric axis of the hour-glass do not coincide (these two coincide for aligned case (model A)).

From the Non-LTE radiation transfer calculation of CS rotational transitions, several identifications of a first hydrostatic core are found (Fig. 3).

1. Viewing pole-on ($\theta = 0°$; a and b), a wall of the outflow lobe is seen in both CS $J = 2 - 1$ and $J = 7 - 6$.
2. Edge-on views ($\theta = 90°$; g and h) indicate a signature of rotation (contour lines of the first moment). In addition, total intensity map shows strong asymmetry between right and left. The asymmetry in the total intensity in which the approaching side is brighter than the receding side is outcome of co-existence of rotation and infall (see [9] for explanation).
3. Between edge-on and pole-on ($\theta = 45$ and $60°$; c–f), complex structure appears in the velocity field.

References

1. Commerçon, B., Hennebelle, P., Audit, E., Chabrier, G., & Teyssier, R. 2010, AAp, **510**, L3
2. Joos, M., Hennebelle, P. & Ciardi, A. 2012, AAp, **543**, A128
3. Kataoka, A., Machida, M.N., & Tomisaka, K. 2012, ApJ, **761**, 40
4. Larson, R. B. 1969, MNRAS, 145, 271
5. Masunaga, H., Miyama, S. M., & Inutsuka, S.-I. 1998, ApJ, 495, 346
6. Matsumoto, T., & Tomisaka, K. 2004, ApJ, **616**, 266
7. Tomida, K., Tomisaka, K., Matsumoto, T., Ohsuga, K., Machida, M. N., & Saigo, K. 2010a, ApJL, **714**, L58
8. Tomida, K., Machida, M. N., Saigo, K., Tomisaka, K., & Matsumoto, T. 2010b, ApJ, **725**, L239
9. Tomisaka, K. & Tomida, K. 2011, PASJ, **63**, 1151
10. Tomisaka, K. 2011, PASJ, **63**, 147

Dust Continuum Observations of Protostars: Constraining Properties with Simulations

Stella S.R. Offner

Abstract The properties of unresolved protostars and their local environment (e.g., disk, envelope and outflow characteristics) are frequently inferred from spectral energy distributions (SEDs) through comparison with idealized model SEDs. However, if it is not possible to image a source and its environment directly, it is difficult to constrain and evaluate the accuracy of these derived properties. In this proceeding, I present a brief overview of the reliability of SED modeling by analyzing dust continuum synthetic observations of realistic simulations.

1 Introduction

Forming stars may be heavily obscured by their natal dust and gas, which inhibits direct imaging and causes source radiation to be reprocessed from shorter to longer wavelengths. The details of the multi-wavelength emission, i.e., the spectral energy distribution (SED), thus provide important indirect clues about the protostellar properties and environment. For example, the absence of $\leq 10\,\mu$m emission usually signifies a very young source with a dense gas envelope; low or non-existent millimeter emission indicates a more evolved source, which has accreted or dispelled its envelope (e.g., [2]).

The information implicit in the reprocessed emission is commonly extracted by comparing the observed SED with idealized models of the protostellar source and gas distribution that are post-processed with a radiative transfer code to produce SEDs. Input models that reproduce the observed SED provide good candidate representations of the underlying source properties. These can provide a wealth

S.S.R. Offner (✉)
Yale University, 260 Whitney Ave, New Haven, CT 06511, USA
e-mail: stella.offner@yale.edu

D. Stamatellos et al. (eds.), *The Labyrinth of Star Formation*, Astrophysics and Space Science Proceedings 36, DOI 10.1007/978-3-319-03041-8_25,

of physical details (e.g., source mass, disk mass and radius, envelope density and radius, outflow cavity size, inclination) that would otherwise be impossible to obtain with observations. However, a number of caveats complicate this technique, including degeneracy between parameters, adoption of symmetry, and assumption that the observed SED represents a single source rather than a multiple system or even a small cluster [3].

Using simulations, which have completely known source and gas information, it is possible to assess the accuracy of this method applied to unresolved observed sources. In this proceeding, we summarize the results of [6], who present a comparison between the true properties of sources within simulations of a turbulent, star forming cloud and the properties inferred from synthetic SEDs.

2 Methods

To perform the comparison, we follow three main steps (see Fig. 1). First, we use the ORION adaptive mesh refinement (AMR) code to simulate a 0.65 pc long turbulent cloud including self-gravity, radiation in the flux-limited diffusion approximation, and star particles inserted in regions of the flow exceeding the maximum resolution. The star particles are endowed with a sub-grid model for protostellar evolution and mass outflow launching based upon [4] (see [1, 5] for implementation details).

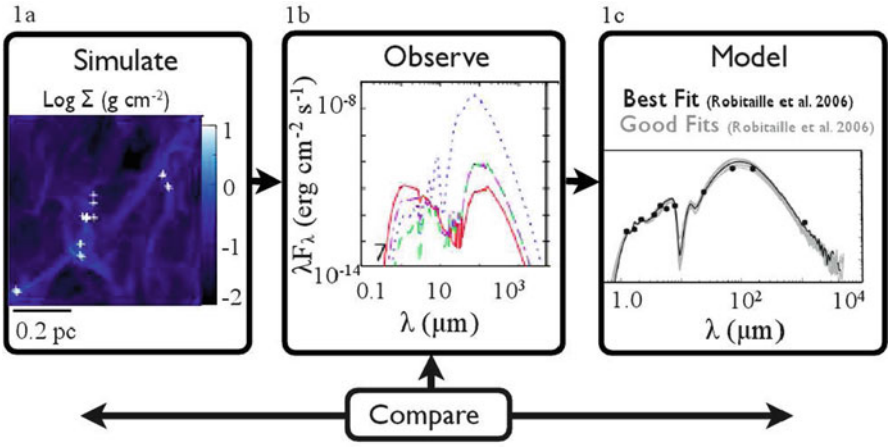

Fig. 1 Schematic of our process to assess the accuracy of properties inferred from SEDs. *Panel 1a* shows the log column density of the simulation 60 kyr after the first star forms; protostar locations are marked with *white crosses*. *Panel 1b* shows the SED of a source observed at four inclinations by the Hyperion code. *Panel 1c* shows a synthetic SED (*black points*) fit with SED models from the [8] model grid; the best-fit is indicated by the *black line* and good-fit cases are overlaid in *gray*

Both aspects are coupled to the instantaneous protostellar mass and accretion rate, which are modeled self-consistently through gas accretion from the AMR grid. For computational efficiency, we first perform the calculation with 200 AU cell resolution and then "zoom" in to 4 AU resolution by restarting and adding additional refinement at selected outputs.

Next, we "observe" the protostellar sources at each time output using Hyperion, a parallelized, Monte Carlo radiative transfer dust continuum code [7]. In each case, we observe from 20 different viewing angles in 10 apertures logarithmically spaced between 1,000 and 20,000 AU and at five different grid resolutions. Figure 1b illustrates the SEDs of one source for four viewing angles observed with a 1,000 AU aperture.

We then compare the observed SEDs sampled at wavelengths appropriate for the 2MASS, Spitzer, and Bolocam instruments with the 200,000 model grid published by [8]. This study parametrized the input properties of the source, disk, envelope and outflow using 14 unique physical variables sampled over a wide range of apertures and 10 different viewing angles. This work also provided a simple means to identify models with good-fits to the data and extract the corresponding parameter values. Here, we use these models to derive the properties for fits satisfying: $\chi^2 - \chi^2_{\rm best} < 3N$, where N is the number of SED data points and $\chi_{\rm best}$ is the best-fit model provided $\chi^2_{\rm best} < 30N$. Finally, we compare four derived parameters with the true source properties. More complete comparisons are presented in [6].

3 Results

Figure 2 illustrates how well the good-fit models recover the simulated values for protostellar mass, protostellar radius, accretion rate, and source inclination. We find that the best-fit models give a reasonable estimate of the protostellar mass in the cases of more isolated or more massive protostars (generally those on the left half of Fig. 2). This agreement occurs despite the discrepancy between the stellar evolution models, which causes the models from [8] to systematically overestimate the protostellar radius by a factor of 2–3. The origin of the discrepancy is the use of the model tracks by [9] that do not include accretion.

The range of inferred protostellar accretion rates typically encompass the true values, albeit with large spreads. The accretion rates of the good-fit models often extend over 3–4 orders of magnitude, which facilitates general agreement but highlights the difficulty of precisely constraining the true accretion rate. The source inclination proves to be a critical parameter in the comparison; in cases where the inclination is correctly well-constrained, the other inferred parameters tend to be more accurate. This suggests that placing limits on the inclination, e.g., via direct imaging, would improve the fidelity of the parameter estimation.

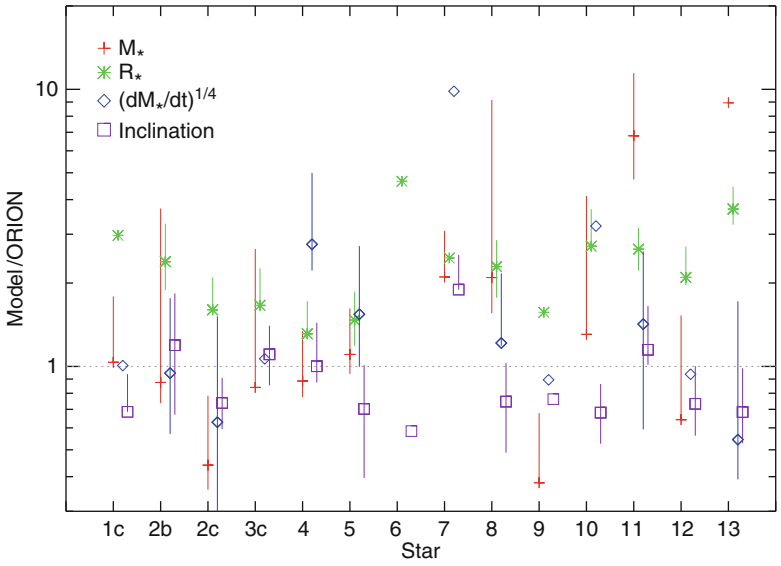

Fig. 2 Ratio of the inferred best model values to the actual simulation values for each source, where M_* is the protostellar mass, R_* is the protostellar radius, $(dM_*/dt)^{1/4}$ is the the accretion rate to the fourth power, and the inclination is the tilt with respect to the line of sight (reproduced from [6]). The *dotted line* indicates where the models correctly determine the simulation value

4 Conclusions

Overall, the comparison between the simulations and analytic models underscores uncertainties inherent in modeling unresolved observations, especially in cases where the dust distribution, stellar evolution model, and gas geometry are not well constrained. Parameters inferred from the SEDs of unresolved sources should be accepted with caution and informed by direct imaging wherever possible.

Acknowledgements The author thanks the conference organizers for the opportunity to present this work and acknowledges Thomas Robitaille, Charles Hansen, Christopher McKee, and Richard Klein, who were collaborators in [6]. Figure 2 is reproduced by permission of the AAS. This work was supported by AST-0901055.

References

1. Cunningham, A. J., Klein, R. I., Krumholz, M. R., & McKee, C. F. 2011, *ApJ*, 740, 107
2. Enoch, M. L., Evans, N. J., II, Sargent, A. I., & Glenn, J. 2009, *ApJ*, 692, 973
3. Forbrich, J., Tappe, A., Robitaille, T., et al. 2010, *ApJ*, 716, 1453

4. Matzner, C. D. & McKee, C. F. 1999 *ApJ*, 526, L109
5. Offner, S. S. R., Klein, R. I., McKee, C. F., & Krumholz, M. R. 2009, *ApJ*, 703, 131
6. Offner, S. S. R., Robitaille, T. P., Hansen, C. E., McKee, C. F., & Klein, R. I. 2012, *ApJ*, 753, 98
7. Robitaille, T. P. 2011 *A&A*, 536, A79
8. Robitaille, T. P., Whitney, B. A., Indebetouw, R., Wood, K., & Denzmore, P. 2006, *ApJS*, 167, 256
9. Siess, L., Dufour, E., & Forestini, M. 2000, *A&A*, 358, 593

Gravitationally Contracting Clouds and Their Star Formation Rate

Enrique Vázquez-Semadeni, Manuel Zamora-Avilés, and Jesús A. Toalá

Abstract We present evidence that giant molecular clouds may be in overall contraction, and we show, by both numerical and semi-analytical arguments, that before they collapse significantly as a whole and transform so much of its mass in stars, the feedback from massive stars produced by first local collapses, regulates the fraction of mass that continues forming stars at values consistent with those observed. Moreover, we have found that the gravitational collapse time for non-spherical structures is longer that the standard free-fall time for spherical ones of the same volume density by a factor $\sim\sqrt{A}$, where A is the aspect ratio of the structure. This implies that clumps inside filaments collapse earlier, naturally giving rise to the ubiquitously observed pattern of clumps within accreting filaments, and that the free-fall estimate for the Galactic SFR may have been overestimated, if clouds in general have non-spherical symmetry.

1 Introduction

Recent theoretical and observational evidence has suggested a return to the scenario of Goldreich and Kwan [8] of global gravitational contraction of molecular clouds (MCs; e.g., [2, 3, 7, 9, 10, 19, 22, 24, 25]; see also the discussion by Zamora-Avilés et al. [30]). But in this case, it is necessary to find a solution for the star formation

E. Vázquez-Semadeni (✉) • M. Zamora-Avilés
Centro de Radioastronomía y Astrofísica, Universidad Nacional Autónoma de México,
Apdo. Postal 3-72, Morelia, Michoacán 58089, México
e-mail: e.vazquez@crya.unam.mx; m.zamora@crya.unam.mx

J.A. Toalá
Instituto de Astrofísica de Andalucía, CSIC, E-1808 Granada, Spain
e-mail: toala@iaa.es

D. Stamatellos et al. (eds.), *The Labyrinth of Star Formation*, Astrophysics and Space Science Proceedings 36, DOI 10.1007/978-3-319-03041-8_26,

rate (SFR) conundrum first noded by Zuckerman and Palmer [31], namely that if all the molecular gas in the Galaxy were in free fall, then the total SFR in the Galaxy would be about two orders of magnitude higher than observed.

In this contribution, we explore the regulation of the SFR and star formation efficiency (SFE) by the feedback from the first stars that form in the clouds, as well as the possibility that the SFR estimated by Zuckerman and Palmer [31] could be an upper limit.

2 Numerical Simulations

In the last decade, a new evolutionary scenario of MC evolution has emerged in which the clouds start as a cold atomic cloud formed by compressive motions in the warm neutral medium (WNM) in environments as the solar neighborhood.

In this scenario, the collision of WNM streams nonlinearly triggers thermal instability, forming a thin cloud of cold atomic gas (e.g., [13, 16, 17, 28]), which becomes turbulent by the combined action of various dynamical instabilities [11, 14, 17, 23, 27]. The cloud soon begins to contract gravitationally as a whole. However, before this global collapse is completed, some local, nonlinear (i.e., large-amplitude) density enhancements produced by the initial turbulence manage to collapse on their own, since their local free-fall time is shorter than the average one for the entire cloud [12,20]. These local collapses thus involve only a fraction of the cloud's total mass. Numerical simulations by Vázquez-Semadeni et al. [26] show that in the absence of stellar feedback this fraction (the SFE) tends to 100 % (see left panels of Fig. 1, which show the SFE evolution for two subregions in a simulation with "large-amplitude" initial velocity fluctuations, simulation labeled as LAF0), whereas when the feedback is included (simulation LAF1), the SFE is reduced by a factor of 10×, reaching values typical of those observed in MCs (see right panels of Fig. 1).

However, these results can not be taken as definitive, because these simulations have a crude modeling of the stellar feedback, since is assumed that massive stars have formed with a single mass, and that these inject an arbitrary amount of thermal energy to reproduce the observed properties of HII regions.

3 A Simple Analytical Model

Zamora-Avilés et al. [30], based on simulations by Vázquez-Semadeni et al. [26], described an idealized, semi-empirical model for the evolution of MCs and their star SFR and SFE. The clouds are assumed to form by the collision of cylindrical WNM streams and to continuously accrete mass from the surrounding diffuse gas, becoming turbulent in the process. The turbulence produces a probability density function (PDF) of the density field, which we assume to have a lognormal form. No

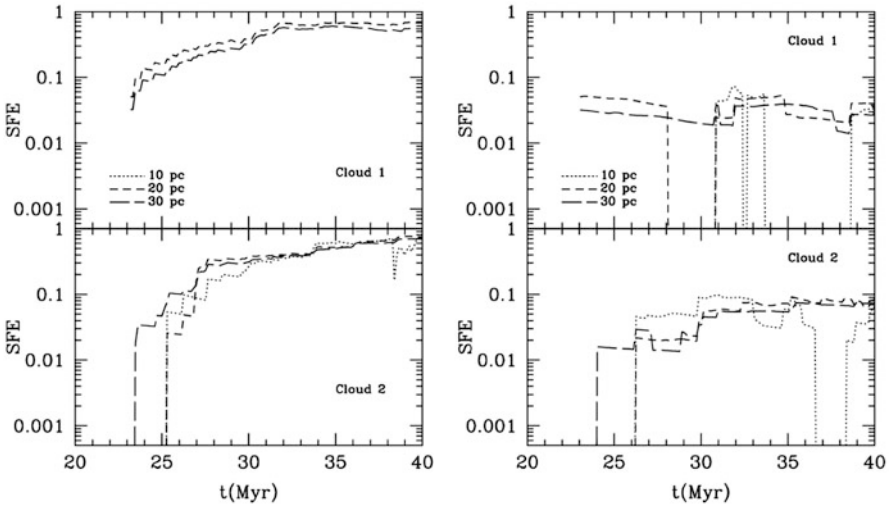

Fig. 1 The *left panels* show the SFE for *Clouds 1* and *2* in the LAF0 simulation (without feedback), for three different cylindrical boxes, of length and diameter indicated in the labels. The *right panels* show the SFE for *Clouds 1* and *2* in the LAF1 simulation (with feedback). In the *left top panel*, no curve for the 10 pc cylinder is shown because there are no stellar particles within that volume in that simulation

turbulent support is assumed, and magnetic fields are neglected, so a model cloud begins to contract gravitationally as soon as it reaches its own Jeans mass. The high-density tail of the PDF, with $n > n_{\rm SF}$, where $n_{\rm SF}$ is a free parameter, is assumed to instantaneously form stars at a rate given by the ratio of the mass at $n > n_{\rm SF}$ to its own free-fall time, while the bulk of the cloud continues to collapse. During the collapse, the mean density of the cloud increases, causing the density PDF to shift towards larger densities over time, and thus the SFR increases in time. From the total instantaneous stellar mass, we compute the instantaneous massive star fraction through an assumed IMF. The massive stars feed back on the cloud through ionizing radiation, eroding the cloud. The evolution is terminated when the entire bulk of the cloud is ionized, or when the mean density exceeds $n_{\rm SF}$.

We calibrate the parameters of the model by matching its results to those of a numerical simulation. After calibration, only one free parameter remains, the inflow radius $R_{\rm inf}$, which effectively controls the maximum cloud mass, $M_{\rm max}$, which we use to compare against clouds of various masses. A GMC model ($R_{\rm inf} = 100\,{\rm pc}$, $M_{\rm max} \approx 10^5\,{\rm M}_\odot$) adheres very well to the evolutionary scenario recently inferred by Kawamura et al. [15] for GMCs in the Large Magellanic Cloud. Also, a model cloud with $R_{\rm inf} = 10\,{\rm pc}$ ($M_{\rm max} \approx 2{,}000\,{\rm M}_\odot$) evolves in the Kenniccutt-Schmidt diagram, first passing through the locus of typical low- to-intermediate mass star-forming clouds, and then moving towards the locus of high-mass star-forming clumps over the course of $\sim$10 Myr (see the right panel in Fig. 2). Finally, the stellar age histograms for this model a few Myr before the clouds destruction agree

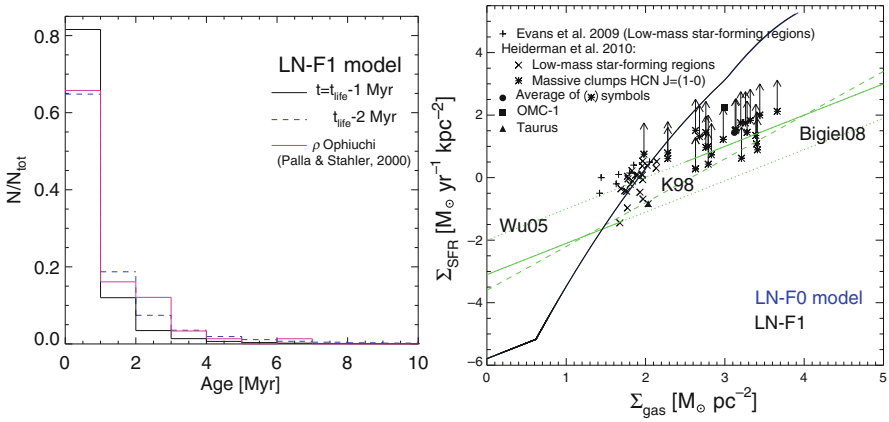

Fig. 2 *Left*: Stellar age distribution for our calibrated model with $R_{\rm inf} = 10\,{\rm pc}$ ($M_{\rm max} \approx 2,000\,{\rm M}_\odot$), calculated at 1 and 2 Myr before the end of the clouds evolution, compared with the corresponding distribution for the ρ-Oph association [18]. *Right*: SFR surface density $\Sigma_{\rm SFR}$ vs. gas surface density $\Sigma_{\rm gas}$. The *dashed line* represents the Kennicutt-Schmidt relation, while the *lower dotted line* represents the observational fit by Bigiel et al. [1] and the *top dotted line* is the fit by Wu et al. [29]. We also plot with different symbols the data for individual star-forming regions. The *solid black line* shows the evolution of our calibrated model with $R_{\rm inf} = 10\,{\rm pc}$

very well with those observed in the ρ-Oph stellar association inferred by Palla and Stahler [18] (see left panel in Fig. 2), whose parent cloud has a similar mass, and imply that the SFR of the clouds increases with time (though strictly speaking it decelerates).

Our model thus agrees well with various observed properties of star-forming MCs when its mass is adjusted to that of the cloud it is to be compared to. This suggests that the scenario of gravitationally collapsing MCs, with their SFR regulated by stellar feedback, is entirely feasible and in agreement with key observed properties of molecular clouds, such as their masses, sizes, lifetimes, and star formation efficiencies and populations.

4 The Free-Fall Time of Sheets and Cylinders

Several studies [2, 4–6, 10, 19, 22, 24, 26] suggest that the cold gas is distributed in sheets and filaments rather than in spherical structures, so it is necessary to calculate the free-fall time for non-spherical structures. These calculations are described in detail in Toalá et al. [21].[1]

[1] See also Pon et al. [20]

In the cases of sheet-like or filamentary geometries, we find that the free-fall time is increased by a factor of $\sqrt{A}$ (where A is the ratio of the largest dimension to the smallest one) with respect to the case of spherical geometry. This has two important implications for the structure of MCs and their SF. First, it naturally explains the common morphology observed in molecular clouds, where star-forming or pre-stellar clumps are embedded within filaments, because the free-fall time for a filament is longer than for any spheroidal structure within it that contains enough mass to be itself collapsing. Second, the SFR conundrum may not be as marked as originally envisaged, because the relevant free-fall time for the cold gas may be longer than has been considered and hence the free-fall SFR estimate would be an upper limit. In any case, our results suggest that determining the topology of MCs is important for estimating their true expected collapse timescales.

5 Conclusions

Using numerical simulations and a semi-analytical model, we have found that, in a scenario of clouds in overall contraction, the SFE is readily decreased by feedback to levels consistent with observational determinations. Moreover, we have found that the gravitational collapse time for non-spherical structures is longer that the standard free-fall time for spherical ones of the same volume density by a factor $\sim\sqrt{A}$, where A is the aspect ratio of the structure. This implies that clumps inside filaments collapse earlier, naturally giving rise to the ubiquitously observed pattern of clumps within accreting filaments, and that the free-fall estimate for the Galactic SFR may have been overestimated, if clouds in general have non-spherical symmetry.

Acknowledgements We thankfully acknowledge financial support from CONACYT, through grant 102488 to E.V.-S. and through a pre-doctoral fellowship to M.Z.-A.

References

1. Bigiel, F., Leroy, A., Walter, F., et al. 2008, AJ, 136, 2846
2. Burkert, A., & Hartmann, L. 2004, ApJ, 616, 288
3. Csengeri, T., Bontemps, S., Schneider, N., Motte, F., & Dib, S. 2010, A&A, 527, 135
4. Csengeri, T., Bontemps, S., Schneider, N., Motte, F., Dib, S. 2011a, A&A, 527, A135
5. Csengeri, T., Bontemps, S., Schneider, N., *et al*. 2011b, ApJ, 740, L5
6. Galván-Madrid, R., Vázquez-Semadeni, E., Kim, J., & Ballesteros-Paredes, J. 2007, ApJ, 670, 480
7. Galván-Madrid, R., Keto, E., Zhang, et al. 2009, ApJ, 706, 1036
8. Goldreich, P., & Kwan, J. 1974, ApJ 189, 441
9. Hartmann, L., Ballesteros-Paredes, J., Bergin, E. A. 2001, ApJ, 562, 852
10. Hartman, L., & Burkert, A., 2007, ApJ, 654, 988.
11. Heitsch, F., Burkert, A., Hartmann, L., Slyz, A. D., & Devriendt, J. E. G. 2005, ApJ 633, L113
12. Heitsch, F., & Hartmann, L. 2008, ApJ, 689, 290

13. Hennebelle, P., & Pérault, M. 1999, A&A, 351, 309
14. Hunter, J. H., Jr., Sandford, M. T., II, Whitaker, R. W., & Klein, R. I. 1986, ApJ, 305, 309
15. Kawamura, A., Mizuno, Y., Minamidani, T., et al. 2009, ApJS, 184, 1
16. Koyama H., & Inutsuka S. I., 2000 ApJ, 532, 980
17. Koyama, H., & Inutsuka, S.-I. 2002, ApJ, 564, L97
18. Palla, F., & Stahler, S. W. 2000, ApJ, 540, 255
19. Peretto, N., Hennebelle, P., & André, P. 2007, A&A, 464, 983
20. Pon, A., Johnstone, D., & Heitsch, F. 2011, ApJ, 740, 88
21. Toalá, J. A., Vázquez-Semadeni, E., Gómez, G. C. 2012, ApJ, 744, 190
22. Schneider, N., Csengeri, T., Bontemps, et al. 2010, A&A, 520, A49
23. Vázquez-Semadeni, E., Ryu, D., Passot, T., González, R. F., & Gazol, A. 2006, ApJ, 643, 245
24. Vázquez-Semadeni, E., Gómez, G. C., Jappsen, A. K., et al. 2007, ApJ, 657, 870
25. Vázquez-Semadeni, E., Gómez, G. C., Jappsen, A.-K., Ballesteros-Paredes, J. & Klessen, R. S. 2009, ApJ, 707, 1023
26. Vázquez-Semadeni, E., Colín, P., Gómez, G. C., Ballesteros-Paredes, J., & Watson, A. W. 2010, ApJ, 715, 1302
27. Vishniac E. T. 1994, ApJ, 428, 186
28. Walder, R., & Folini, D. 2000, ApSS, 274, 343
29. Wu, J., Evans, N. J., II, Gao, Y., et al. 2005, ApJ, 635, L173
30. Zamora-Avilés, M., Vázquez-Semadeni, E., Colín, P. 2012, ApJ, 751, 77
31. Zuckerman, B., & Palmer, P. 1974, ARA&A, 12, 279

Spiral Shocks, Cooling, and the Origin of Star Formation Rates

Ian Bonnell, Clare L. Dobbs, and Rowan J. Smith

Abstract We have performed the first numerical simulations to resolve the star formation process on sub-parsec scales, whilst also following the dynamics of the interstellar medium (ISM) on galactic scales. The warm low density ISM gas flows into the spiral arms where orbit crowding produces the shock formation of dense clouds, held together temporarily by their external pressure. Cooling allows the gas to be compressed to sufficiently high densities that local regions collapse under their own gravity and form stars. The star formation rates follow a Schmidt-Kennicutt $\Sigma_{\rm SFR} \propto \Sigma_{\rm gas}^{1.4}$ type relation with the local surface density of gas while following a linear relation with the dense cold gas. Cooling is the primary driver of star formation and the star formation rates as it determines the amount of cold gas available for gravitational collapse.

1 Introduction

Star formation in galaxies involves the collection of gas into dense molecular clouds, and the collapse of localised regions of these clouds to form stars. Galactic scale numerical simulations have shown that molecular clouds can form through the coalescence of less dense clouds in spiral shocks [5], but cannot resolve the

I. Bonnell (✉)
School of Physics and Astronomy, University of St Andrews, North Haugh, St Andrews, Fife, KY16 9SS, Scotland, UK
e-mail: iab1@st-andrews.ac.uk

C.L. Dobbs
University of Exeter, Exeter, UK
e-mail: dobbs@astro.ex.ac.uk

R.J. Smith
ZAH/ITA, University of Heidelberg, Heidelberg, Germany
e-mail: rowanjsmith.astro@googlemail.com

D. Stamatellos et al. (eds.), *The Labyrinth of Star Formation*, Astrophysics and Space Science Proceedings 36, DOI 10.1007/978-3-319-03041-8_27,

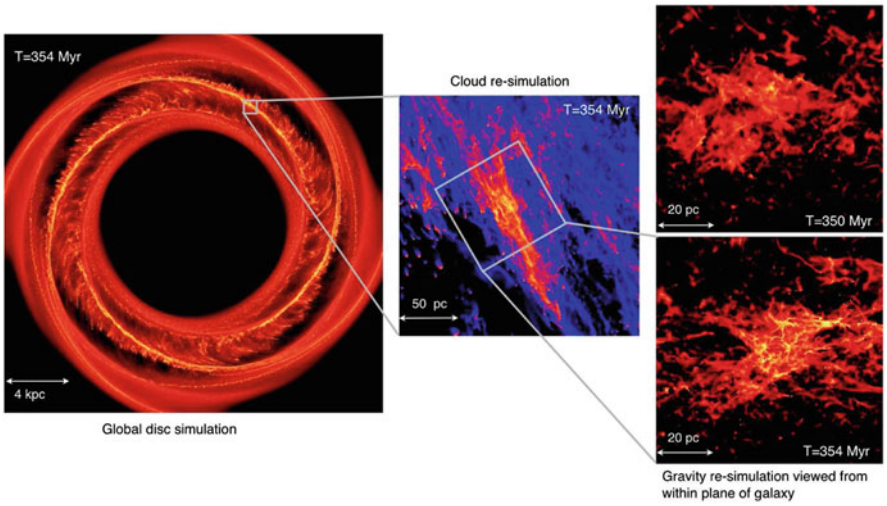

Fig. 1 An overview of the numerical simulations is shown from the global galactic disc simulation to the *Cloud* and *Gravity* re-simulation, where we have increased the mass resolution by a factor of 256 in order to study in detail how the star formation region is formed. The log of the column density of the gas is shown from 10^{-4} to 0.1 g cm^{-2} for the global simulation, 10^{-3} to 0.1 g cm^{-2} for the *Cloud* re-simulation, and from 0.002 to 2 g cm^{-2} for the *Gravity* re-simulation

star formation. Local, molecular cloud scale simulations resolve star formation [4, 12, 14], but these start with highly idealised conditions that do not reflect the physics of the cloud formation process. Cloud-cloud collisions [10, 16] and colliding flows simulations provide a mechanism for triggering star formation (e.g. [8, 15]) but lack the galactic context that could generate such flows [2] (Fig. 1).

2 Calculations

We use SPH simulations to follow three, successively smaller scales, from the scale of a spiral galaxy, to the formation of dense clouds in the ISM, to the relatively small, sub-pc scale where star formation occurs. These nested simulations use initial and boundary conditions from the previous simulations to produce a final scale where self-gravity is included and star formation is modeled via sink particles [1]. The global simulation uses 2.5–2.8 $\times$ 10^7 SPH particles. The thermal physics includes both heating and cooling terms via a cooling function [11]. The gas is initially warm at 10^4 K before entering the spiral shock. At densities above 1 cm^{-3}, a cooling instability is triggered and the gas cools rapidly to temperatures in the range of 20–100 K (see [3] for details).

Each time the gas enters the spiral arms, the gas is compressed, cools and then re-expands in the inter-arm region. The cooling instabilities in the spiral arms lead to clumpy molecular cloud structures, which as the gas leaves the arm, are sheared into spurs or feathers In addition, there are repeated collisions and internal shocks inside the spiral arms. This ensures that the structures we are studying are formed self-consistently, and thus provide an appropriate starting point for studying how star formation is initiated in galactic discs.

3 High-Resolution Resimulations

A 250 pc region of the global simulation containing $1.71 \times 10^6\,M_\odot$ of cold gas was re-resolved with $0.15\,M_\odot$ per particle, and followed for over 50 Myr as high-density clouds form. The high-velocity shock and thermal cooling produce a highly turbulent and fragmented structure reminiscent of what is seen in molecular clouds. The turbulence provides an important global support to the clouds, while the structure provides the seeds for local gravitational collapse. The dense gas leaves the spiral arm some 6 Myr after maximum compression and is torn apart by the galactic shear. The convergent flows and the clumpy shock [6] combined with the thermal instabilities generate large-scale turbulent motions that follow the standard Larson relation [13]. This results in structures which are globally gravitationally unbound but can become locally bound and collapse on scales of 0.5 pc and $1{,}000\,M_\odot$. This should help ensure relatively small star formation efficiencies although the clouds do collapse vertically likely due to an inefficient transfer of horizontal into vertical motions in the shock. This transfer would be more efficient in the presence of magnetic fields.

4 Star Formation Rates

Star formation commences approximately 0.1 Myr after self-gravity is turned on and continues for the 5 Myr evolution. Local regions that become self-gravitating have densities > 100–$1{,}000\,M_\odot\,\mathrm{pc}^{-3}$. These regions are colder in their centres with minimum temperatures reaching <20 K. The total star formation rate reaches a few times $10^{-2}\,M_\odot\,\mathrm{yr}^{-1}$. The star formation efficiency, the fraction of the gas turned into stars, is a few percent in the first few million years and, in the absence of feedback and magnetic fields, increases to over 10 % after 5 million years.

In Fig. 2, we plot the surface density of star formation against the surface density of gas, the Kennicut-Schmidt relation [9], as seen from the plane of the galaxy. The SFR is calculated in 100 cells of 50 by 50 pc. The star formation follows a $\Sigma_{\mathrm{SFR}} \propto \Sigma_{\mathrm{gas}}^{1.4}$, typical to spiral galaxies, although displaced to higher rates of star formation, similar to that seen in local clouds [7]. We also find a similar relation when plotting

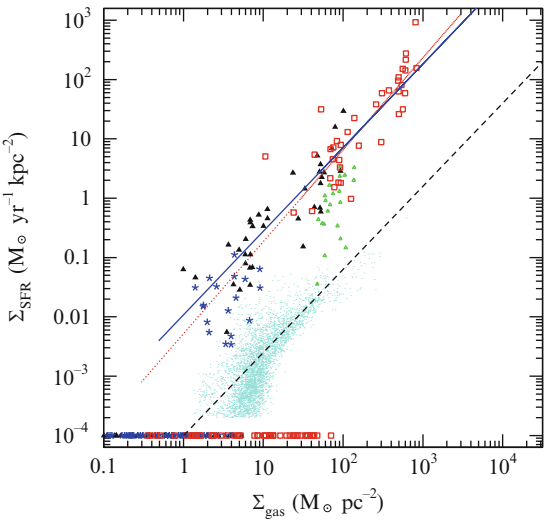

Fig. 2 The local star formation rates per unit area are plotted against the surface density of gas for the three re-simulations with Σdisc $0.4\,M_\odot\,pc^{-2}$ (*blue stars*), $4.0\,M_\odot\,pc^{-2}$ (*black filled triangles*), and $40.0\,M_\odot\,pc^{-2}$ (*red squares*). The points represent 50×50 pc regions at a time 3.5×10^6 years from the start of the self-gravity re-simulations The *dashed line* illustrates the Schmidt-Kennicutt $\Sigma_{SFR} \propto \Sigma_{gas}^{1.4}$ relation

the surface density of cold dense gas relative to the total surface density of gas. This result, which occurs even in the non self-gravitating re-simulations, shows that the non-linear part of the S-K relation arises in the stage of the formation of the molecular clouds. The cold and dense gas can then translate directly into the star formation rates with a near-uniform free-fall time as $\Sigma_{SFR} \approx \Sigma_{dense}/t_{ff} \propto \Sigma_{dense}$.

The steeper relation between the dense gas and the total gas present must arise from the shocks and accompanying cooling. The cold dense gas is formed by collisions between clumps of cool ($100 < T < 1{,}000$ K) gas formed in previous shocks. This cool gas, due to earlier shocks, forms a clumpy medium embedded in the warmer gas. Subsequent collisions involving this cool gas result in much stronger compressions, hence the formation of the cold, dense ($T < 100$ K; $\rho > 10\,M_\odot\,pc^{-3}$) gas and ensuing star formation. Where the probability of an individual clump colliding with another is low, this results in a non-linear scaling between the incoming Σ_{gas} and shock-produced Σ_{dense}. A simple clumpy shock model based on the requirement of clumps to interact in order to form the dense gas can reasonably reproduce the $\Sigma_{dense} \propto \Sigma_{gas}^{1.4}$ relation (see [3]).

References

1. Bate M. R., Bonnell I. A., Price N. M., 1995, *MNRAS*, 277, 362
2. Bonnell I. A., Dobbs C. L., Robitaille T., Pringle J. E., 2006, *MNRAS*, 365, 37
3. Bonnell I. A., Dobbs C. L., Smith R. J., 2013, *MNRAS*, in press
4. Bonnell I. A., Smith R. J., Clark P. C., Bate M. R., 2011, *MNRAS*, 410, 2339
5. Dobbs C. L., 2008, *MNRAS*, 391, 844
6. Dobbs C. L., Bonnell I. A., 2007, *MNRAS*, 374, 1115

7. Heiderman A., Evans II N. J., Allen L. E., Huard T., Heyer M., 2010, *ApJ*, 723, 1019
8. Heitsch F., Slyz A. D., Devriendt J. E. G., Hartmann L. W., Burkert A., 2006, *ApJ*, 648, 1052
9. Kennicutt R. C., Evans N. J., 2012, ARA&A, 50, 531
10. Kitsionas S., Whitworth A. P., 2007, *MNRAS*, 378, 507
11. Koyama H., Inutsuka S.-I., 2000, *ApJ*, 532, 980
12. Krumholz M. R., Cunningham A. J., Klein R. I., McKee C. F., 2010, *ApJ*, 713, 1120
13. Larson R. B., 1981, *MNRAS*, 194, 809
14. Smith R. J., Longmore S., Bonnell I., 2009, *MNRAS*, 400, 1775
15. Vázquez-Semadeni E., Gómez G. C., Jappsen A. K., Ballesteros-Paredes J., González R. F., Klessen R. S., 2007, *ApJ*, 657, 870
16. Whitworth A. P., Bhattal A. S., Chapman S. J., Disney M. J., Turner J. A., 1994, *A&A*, 290, 421

A New Set of Model Spectral Energy Distributions for Young Stellar Objects

Thomas P. Robitaille and Barbara A. Whitney

Abstract In 2006, we made available a set of model spectral energy distributions (SEDs) for young stellar objects (YSOs) that has since been used by the community to model thousands of sources in nearby and more distant star forming regions in the Milky-Way and Magellanic clouds. We describe a new and much larger set of model SEDs that addresses many issues with the original models, such as the coverage of parameter space, the dependence on stellar evolutionary tracks, and is well suited to modelling long-wavelength observations such as those from *Herschel*. The new models were computed with HYPERION, a new Monte-Carlo radiative transfer code. We present the design of the new set of models and discuss improvements compared to the original models.

1 Introduction

Spectral energy distributions (SEDs) probe a convolution of radiation field, dust properties, and dust geometry, and thus contain information about the physical conditions in young stellar objects (YSOs). In fact, for a large fraction of YSOs in the Galaxy, SEDs and spectra are our *only* source of information. For the remaining fraction of YSOs that can be spatially resolved at specific wavelengths, owing to their proximity to the Sun, SEDs still contains invaluable information that

T.P. Robitaille (✉)
Max Planck Institut für Astronomie, Königstuhl 17, 69117 Heidelberg, Germany
e-mail: robitaille@mpia.de

B.A. Whitney
Department of Astronomy, University of Wisconsin-Madison, Madison, WI 53706, USA
e-mail: bwhitney@astro.wisc.edu

D. Stamatellos et al. (eds.), *The Labyrinth of Star Formation*, Astrophysics and Space Science Proceedings 36, DOI 10.1007/978-3-319-03041-8_28,

is complementary to the resolved morphology of the sources. Thus, while SED modelling is a highly degenerate exercise, it is necessary in order to understand what information can be extracted from multi-wavelength observations.

For this purpose, we originally developed a large set of radiative transfer models of YSO SEDs [1] covering a large range of stellar masses (0.1–50 $M_{\odot}$) and evolutionary stages (from embedded protostars to low-mass disks around pre-main-sequence stars). The radiative transfer models included 14 parameters that described the central source, flared disk, rotationally flattened envelope, and bipolar outflow cavity. SEDs were computed for 20,000 combinations of physical parameters, and for 10 viewing angles in each case, giving 200,000 aperture-dependent model SEDs.

The coverage of parameter space was first determined by sampling a random stellar mass and age, then using pre-main-sequence stellar evolutionary tracks to determine a stellar radius and temperature. The parameters describing the circumstellar geometry were then determined by randomly sampling values within ranges that were dependent on the stellar age and mass, in order to cover regions of parameters space deemed reasonable from observational and theoretical considerations.

We developed a fitting tool [2] with a web interface (http://www.astro.wisc.edu/protostars) that was designed to help understand which models could provide a good fit to a given set of observations, and therefore allowed users to determined which physical parameters could be constrained from observations. While the models have been widely used to analyse multi-wavelength observations of YSOs, the models suffer from a number of shortcomings that justify the need for a new set of models. Thus, we designed and computed a new set of model SEDs that we describe in Sect. 2.

2 The New Models

The new models were computed using HYPERION, a new parallelised 3-d dust continuum radiative transfer code [3] that is open source and publicly available at http://www.hyperion-rt.org. In the following sections, we summarise the main shortcomings of the original models, and how we address these in the new set of models. In order to maintain a reasonable coverage of parameter space, the new set of models includes ∼550,000 radiative transfer models, each for 9 viewing angles, resulting in almost 5 million aperture-dependent model SEDs. The new models will be made publicly available.

2.1 Stellar Evolutionary Tracks

The sampling of parameters for the original models was dependent on pre-main-sequence evolutionary tracks, which are highly uncertain for early stages of

evolution and high stellar masses. To solve this, the sampling of the stellar properties in the new models no longer assumes evolutionary tracks. The stellar radius and effective temperature are randomly sampled from uniform ranges, and the models no longer have a stellar age and mass by default.

2.2 Parameter Sampling

In the original set of models, the sampling of parameter space from mass and age-dependent ranges caused the models to follow trends in parameter space. For example, the envelope infall rate went down with stellar age, while the bipolar cavity opening angle increased with stellar age, so that the set of models intrinsically had a trend of increasing bipolar cavity opening angle with decreasing envelope infall rate. Since they were an intrinsic part of the set of models, such trends therefore affected the interpretation of observations (for more details, see [4]). To solve this, all parameters are now sampled uniformly (in linear or logarithmic space depending on the parameter) from fixed ranges. This means that the models no longer follow trends and correlations in parameter space, which will allow users to look for trends in samples of sources. In addition, this means that the distribution of parameter values providing a good fit to an individual source will no longer be biased by the underlying sampling of parameter space.

2.3 Model Complexity

The original models, while described only by analytical distributions of dust, were sometimes too complex in terms of the model components. For example, all disk models included accretion luminosity, so it was not possible for example to determine whether accretion luminosity was required to reproduce a set of observations, since it was included in all models. Rather than compute one monolithic set of models, the new models are now split into a number of smaller sets with varying complexity in terms of model components. For example, one of the sets of models includes only a flared disk around a central source, with the inner edge of the disk extending in to the dust sublimation radius. Another set also includes only flared disks, but allowing the disk inner radius to be larger than the sublimation radius. Yet another set includes only spherically symmetric envelopes with power-law density profiles. The most complex set of models resembles the original 2006 models, in that it includes a disk, envelope, and bipolar cavities. This modularity means that it is much simpler to check which components are needed in order to reproduce a given SED, and whether any constraints can be placed on the presence/absence of particular components. Figure 1 shows an example of fitting one of the simplest disk-only models and one of the more complex models (with a disk, envelope, bipolar cavities, and ambient medium) to a source. The χ^2 per data point value

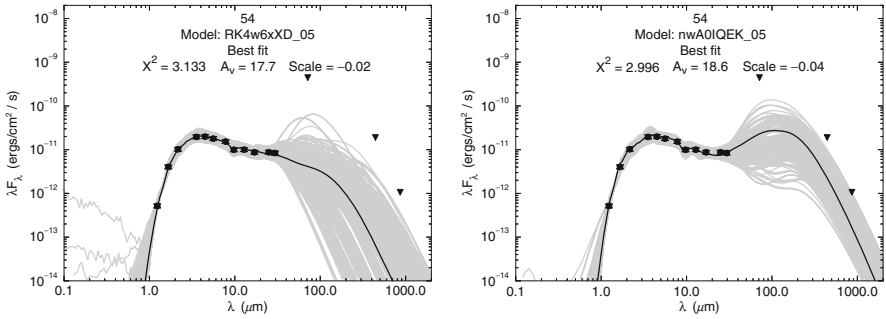

Fig. 1 Model SED fits to observations of a YSO in the NGC2264 star forming cluster, using a simple model for a flared disk with the inner radius set to the sublimation radius (*left*), and for a more complex model with a disk, envelope, bipolar cavities, an ambient medium, and allowing variable inner radius sizes (*right*). In both panels, the *filled black circles* show the observed fluxes, the *black solid line* shows the best fit, and the *grey solid lines* show all the model SEDs that provide a good fit

is very similar for both best-fit models (3.1 vs 3.0), showing that a simple disk-only model is very good at reproducing the observations, and that more complex components are not needed.

2.4 Signal-to-Noise at Long Wavelengths

The original model SEDs were calculated using an algorithm that produces SEDs that have a low signal-to-noise at the longest wavelengths. This made the models unsuitable for modelling observations from *Herschel* or other far-infrared/sub-millimetre/millimetre observatories. The new model SEDs are computed using significantly improved algorithms compared to the original models, including raytracing for thermal dust emission, which produces much better signal-to-noise at the longest wavelengths. This will make the models more suitable for analysing far-infrared to millimetre observations.

References

1. T.P. Robitaille, B.A. Whitney, R. Indebetouw, K. Wood, P. Denzmore, *ApJS* **167**, 256 (2006).
2. T.P. Robitaille, B.A. Whitney, R. Indebetouw, K. Wood, *ApJS* **169**, 328 (2007).
3. T.P. Robitaille, *A&A* **536**, A79 (2011).
4. T.P. Robitaille, in *Massive Star Formation: Observations Confront Theory*, *Astronomical Society of the Pacific Conference Series*, vol. 387, ed. by H. Beuther, H. Linz, T. Henning (2008), *Astronomical Society of the Pacific Conference Series*, vol. 387, p. 290

The Entropy Condition of GodunovSPH

Seung-Hoon Cha

Abstract A new version of GodunovSPH (hereafter GSPH) has been implemented and tested. The numerical volume and the continuity equation have been emphasized to make ensure the entropy condition. A test has been performed to check the new GSPH.

1 Introduction

Inutsuka [1] suggested a reformulated SPH (hereafter GSPH), and it has been proved to be a consistent scheme [2]. However, GSPH (and SPH as well) shows the violation of the entropy condition. A new GSPH satisfying the entropy condition is announced here. The importance of the numerical volume and the continuity equation is emphasized to cure the violation.

2 The Entropy Condition and Weak Solutions of a Numerical Scheme

It is essential to use the entropy condition to choose the real solution from the weak solutions of numerical schemes. The violation of the entropy condition means that GSPH generates a weak solution rather than the real solution. Two reasons were identified. One is the thermal incompatibility, and the other is the non-uniqueness of the density evaluation. In order to solve the two problems, a numerical volume

S.-H. Cha (✉)
Department of Physics and Astronomy, Texas A&M University-Commerce, P.O. Box 3011, Commerce, TX 75428, USA
e-mail: seung-hoon.cha@tamuc.edu

D. Stamatellos et al. (eds.), *The Labyrinth of Star Formation*, Astrophysics and Space Science Proceedings 36, DOI 10.1007/978-3-319-03041-8_29,

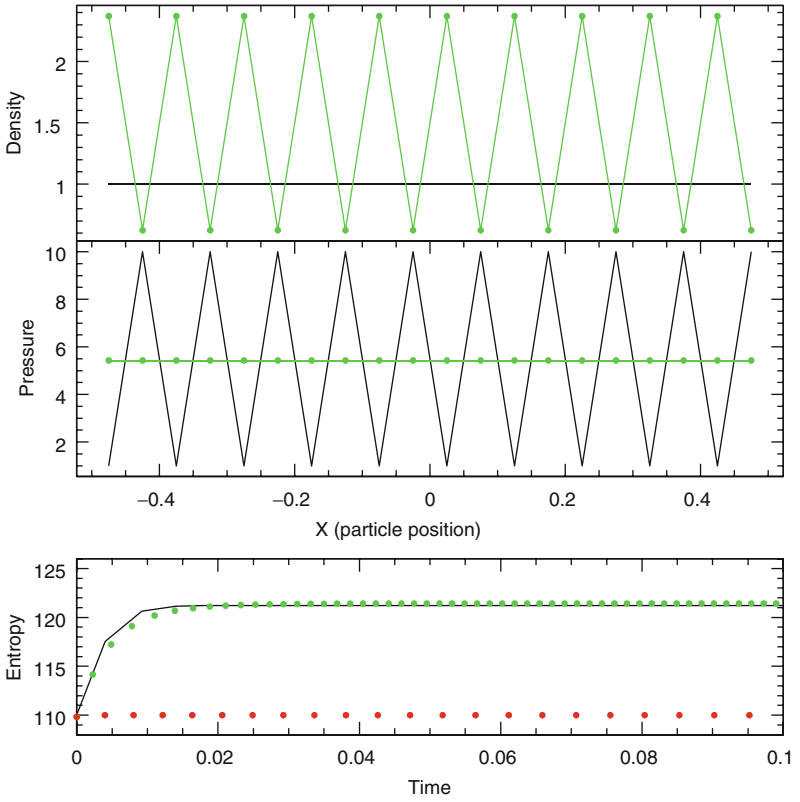

Fig. 1 *Black solid lines* are the initial density and pressure in the *top two panels*. The *green dots* and *solid lines* are the final equilibrium state. The initial fluctuating pressure makes the zig-saw pattern in the density. The *bottom panel* shows the time evolution of the entropy. The *black solid line*, *green* and *red dots* are the result of 1D lagrangian FDM, new and old GSPH, respectively

has been defined by a basis function ($=\frac{m_i}{\rho(x)}W(x-x_i,h_i)$), and then evolves using the continuity equation to determine the smoothing length. Finally, the smoothing length is independent to the spatial configuration of particles. The continuity equation is given in terms of the specific volume, V

$$\frac{dV_i}{dt} = -\sum_j m_j\,(\mathbf{v}_i - \dot{\mathbf{x}}_i)\left(\frac{\partial}{\partial \mathbf{x}_i} - \frac{\partial}{\partial \mathbf{x}_j}\right)\int \frac{1}{\rho^2(x)}W(\mathbf{x}-\mathbf{x}_i,h_i)W(\mathbf{x}-\mathbf{x}_j,h_j)dx, \tag{1}$$

and satisfies the thermal compatibility. Here, W is a kernel function, and other variables have their usual meaning.

3 Test and Conclusion

Zero-energy mode test has been performed to check the accuracy of density evaluation and the entropy condition. A highly fluctuating pressure profile is given in the uniform density medium. The half of the fluctuation period is set to the particle separation. Finally, a pressure equilibrium with fluctuating density profile is expected. The results are in Fig. 1. We have compared the results of new GSPH and the 1D lagrangian FDM code, and confirm that they show the same entropy.

By the virtue of the numerical volume and the thermal compatible continuity equation, the new GSPH satisfies the entropy condition, and can find the real solution rather than the weak solution finally.

References

1. Inutsuka, S-i. **179**, 238–267 (2002)
2. Cha, S.–H., Inutsuka, S-i., Nayakshin,S MNRAS. **403**, 1165–1174 (2010)

Three-Dimensional Simulation of Molecular Cloud Formation

Tsuyoshi Inoue

Abstract Using three-dimensional magnetohydrodynamics simulation with the effects of radiative cooling/heating, chemical reactions, and thermal conduction, we investigate the formation of molecular cloud in the multi-phase interstellar medium. As suggested by recent observations, we consider shock compression of HI clouds as a triggering mechanism of the molecular cloud formation. The simulation shows that the initial HI medium is compressed and piled up behind the shock waves induced by the accretion flows. The post shock region is composed of dense cold clumps ($T < 100\,\mathrm{K}$) and diffuse thermally unstable gas ($T > 1{,}000\,\mathrm{K}$), which are spatially well mixed owing to the supersonic turbulence. In the molecular cloud, clumps evolve with time by condensation accretion of the diffuse gas and collisional coalescence of the clumps. Statistics of the clumps suggest that the typical initial condition of molecular cloud core is magnetically super-critical.

1 Motivation, Setting of Simulation, and Result

It is well known that molecular clouds are the sites of the present-day star formation. However, our understanding of the physical conditions of molecular clouds is very limited. According to the recent observations of nearby galaxies, molecular clouds are suggested to be formed from HI clouds with $n \sim 10\,\mathrm{cm}^{-3}$ [1]. A detailed statistical study of the molecular clouds in the Large Magellanic Clouds (LMC) showed that the timescale of the molecular cloud evolution due to the HI cloud accretion is approximately $\sim$10 Myr [2].

T. Inoue (✉)
Aoyama Gakuin University, Fuchinobe, Sagamihara-city, Kanagawa 252-5258, Japan
e-mail: inouety@phys.aoyama.ac.jp

D. Stamatellos et al. (eds.), *The Labyrinth of Star Formation*, Astrophysics and Space Science Proceedings 36, DOI 10.1007/978-3-319-03041-8_30,

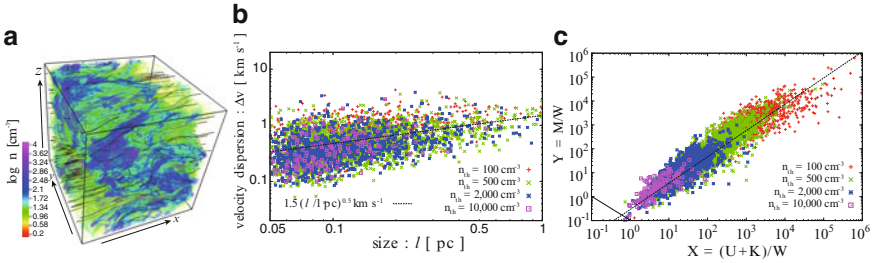

Fig. 1 Panel (**a**): number density structure of the formed molecular cloud at $t = 10$ Myr. Panel (**b**): scatter plot of the size-velocity dispersion relation of the clumps in the formed molecular cloud. Panel (**c**): scatter plot of the clumps in a virial diagram

In this study, we investigate the formation of molecular cloud by accretion flows of magnetized HI cloud [5]. The initial HI clouds that are embedded in diffuse warm neutral medium are formed as a natural consequence of the thermal instability (see [3, 4] for detail).

Panel (a) of Fig. 1 shows the density structure of the generated molecular cloud after 10 Mry accretion. The cloud is composed of cold molecular clumps ($T \sim 10$–30 K) that are embedded in thermally unstable diffuse gas with $T > 10^3$ K, and also highly turbulent with supersonic velocity dispersion of ~ 2 km s^{-1}. Panel (b) shows scatter plot of the velocity dispersion-size relation of clumps that follows well known Larson's law ($\delta v \sim 1.5\,\{l/1\,\mathrm{pc}\}^{1/2}$). The clumps evolve toward gravitationally unstable molecular cloud core by getting their mass through the condensation accretion of thermally unstable gas and collisional coalescence of clumps. Panel (c) shows the scatter plot of clumps in a simple virial diagram, where the horizontal and vertical axes respectively represent $X \equiv (U + K)/W$ and $Y \equiv M/W$, where $U = \int 3\,(\gamma - 1)\,E_{\mathrm{th}}$, $K = 2\,E_{\mathrm{turb}}$, $M = E_{\mathrm{mag}}$, and $W = E_{\mathrm{grv}}$. The diagram indicates that typical clumps become magnetically supercritical molecular cloud cores.

References

1. Blitz, L. et al. (2007), Protostars and Planets V, ed. B. Reipurth, D. Jewitt, & K. Keil (University of Arizona Press), 951, 81
2. Fukui, Y. et al. (2009) ApJ, 705, 144
3. Inoue, T., & Inutsuka, S. (2008) ApJ, 687, 303
4. Inoue, T., & Inutsuka, S. (2009) ApJ, 704, 161
5. Inoue, T., & Inutsuka, S. (2012) ApJ, 759, 35

Estimating the Galactic Coronal Density via Ram-Pressure Stripping from Dwarf Satellites

A. Gatto, F. Fraternali, F. Marinacci, J. Read, and H. Lux

Abstract Cosmological simulations and theories of galaxy formation predict that the Milky Way should be embedded in an extended hot gaseous halo or corona. To date, a definitive detection of such a corona in the Milky Way remains elusive. We have attempted to estimate the density of the Milky Way's cosmological corona using the effect that it has on the surrounding population of dwarf galaxies. We have considered two dSphs close to the Galaxy: Sextans and Carina. Assuming that they have lost all their gas during the last pericentric passage via ram-pressure stripping, we were able to estimate the average density ($n \sim 2 \cdot 10^{-4}\,\mathrm{cm}^{-3}$) of the corona at a distance of $\sim$70 kpc from the Milky Way. If we consider an isothermal profile and extrapolate it at large radii, the corona could contain a significant fraction of the missing baryons associated to the Milky Way.

A. Gatto (✉)
Max-Planck Institut für Astrophysik, Karl-Schwarzschild Strasse 1, 85748 Garching, Germany
e-mail: andreag@mpa-garching.mpg.de

F. Fraternali
Department of Physics and Astronomy, University of Bologna, via Berti Pichat 6/2, 40127 Bologna, Italy

F. Marinacci
Heidelberg Institute for Theoretical Studies, Schloss-Wolfsbrunnenweg 35, 69118 Heidelberg, Germany

J. Read
University of Surrey, Guildford GU2 7XH, Surrey, United Kingdom

H. Lux
School of Physics and Astronomy, University of Nottingham, University Park, NG7 2RD Nottingham, United Kingdom

D. Stamatellos et al. (eds.), *The Labyrinth of Star Formation*, Astrophysics and Space Science Proceedings 36, DOI 10.1007/978-3-319-03041-8_31,

1 The Coronal Density

We carried out two-dimensional hydrodynamical simulations of the motion of Carina and Sextans through the corona of the Milky Way (Fig. 1) during their last pericentric passages. The density of the corona is treated as a free parameter that is adjusted to produce the complete removal of gas from the dwarfs via ram-pressure stripping. We determine the gas mass from the star formation history of each dwarf via the Kennicut-Schmidt law. We assume that star formation was truncated by ram-pressure stripping at pericentre. Thus our method allows us to estimate the

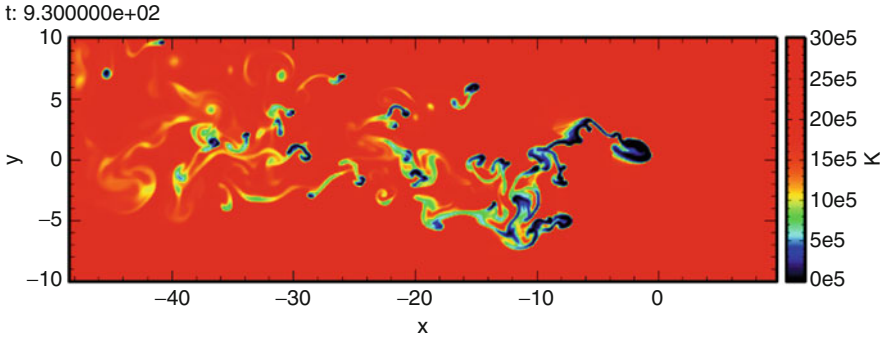

Fig. 1 Temperature snapshots at 930 Myr of the gas-loss experienced by Sextans due to a hot wind coming from the right side of the box

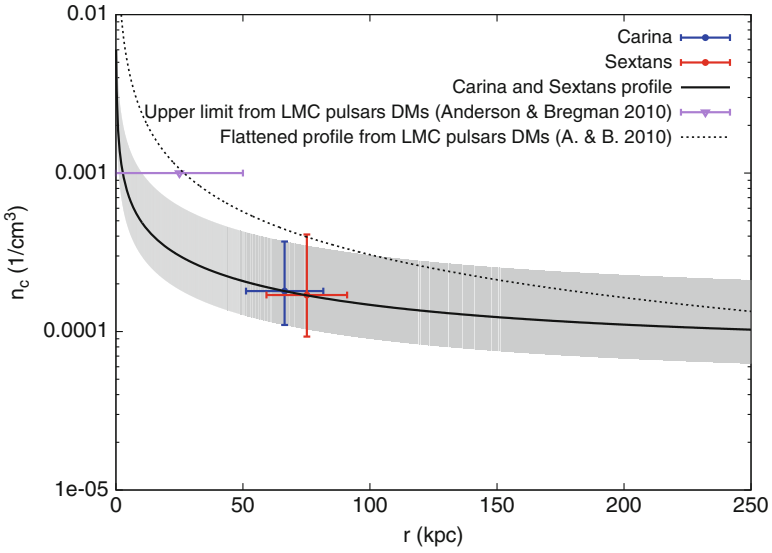

Fig. 2 Recovered Galactic coronal profile along with its upper and lower limits (*grey band*)

average coronal density at pericenter. Realistic orbits for the dwarfs have been used [3]. The simulations also include gas cooling, supernova explosions (thermal and mechanical feedback) and gas consumption by star formation.

In the Sextans case the coronal density is $1.7^{+2.4}_{-0.77} \cdot 10^{-4}\,\mathrm{cm}^{-3}$ averaged in the distance range [60–90] kpc, while for Carina is $1.8^{+1.9}_{-0.7} \cdot 10^{-4}\,\mathrm{cm}^{-3}$ averaged over [50–80] kpc from the MW (Fig. 2), consistent with the results of Grcevich and Putman [2] (but see also Anderson and Bregman [1]). Under the assumptions of an isothermal corona and a truncated flat model for the MW [4], the values of the coronal density that we derived for Carina and Sextans are in remarkable agreement with each other. The total mass of the corona (extrapolated to 250 kpc) is $1.1 \cdot 10^{11}\,\mathrm{M}_{\odot}$, a significant fraction of the Galactic missing baryons.

References

1. Anderson M. E., Bregman J. N., Astrophys. J. **714**, 320 (2010)
2. Grcevich J., Putman M. E., Astrophys. J. **696**, 358 (2009)
3. Lux H., Read J. I., Lake G., Mon. Not. Roy. Astron. Soc. **406**, 2312 (2010)
4. Wilkinson M. I., Evans N. W., Mon. Not. Roy. Astron. Soc. **310**, 645 (1999)

Part V
Triggered Star Formation

Star Formation Triggered by Feedback from Massive Stars

Stefanie K. Walch

Abstract Massive stars significantly affect their surrounding. During their lifetime of a few million years, they emit ionising radiation and drive a fast stellar wind before they finally explode as a supernova. These powerful processes may sweep up the surrounding interstellar matter and trigger new star formation or lead to the dispersal of the ambient medium. Hence massive star feedback may have a positive or a negative effect on the overall star formation efficiency of a molecular cloud. In this contribution I review observational and theoretical work on triggered star formation. Implications on the relative importance of triggered (vs. spontaneous) star formation are discussed.

1 Introduction: Triggering Mechanisms

Less than 1 % of all new-born stars are massive and have a mass of more than $8\,M_\odot$ by the time they reach the zero-age main sequence. Nevertheless, massive stars are special as they significantly affect their surroundings via stellar winds, the emission of ionising radiation, and supernova explosions. Here, we focus on ionisation feedback and stellar winds as a possible trigger for star formation (SF) on scales of a few to a few tens of parsec.

As soon as the molecular cloud (MC) in the vicinity of a massive star is ionized and dispersed, a so-called HII region is formed. Ionized gas inside the HII region is heated to $T \approx 10{,}000\,\mathrm{K}$, and the associated pressure increase with respect to the cold, surrounding molecular gas at $T \approx 10\,\mathrm{K}$ causes the bubble-like HII region to expand. At its boundary a shock-front is formed at which the surrounding cold gas is collected and compressed, thus forming a nutrient medium for new SF.

S.K. Walch (✉)
Max-Planck-Institut für Astrophysics, Garching bei München, 422 Germany
e-mail: walch@mpa-garching.mpg.de

D. Stamatellos et al. (eds.), *The Labyrinth of Star Formation*, Astrophysics and Space Science Proceedings 36, DOI 10.1007/978-3-319-03041-8_32,

In case of a uniform surrounding ISM, the expansion of an HII region leads to the formation of a dense, shell-like structure. These shells, which have typical diameters of 3–30 pc, may subsequently become gravitationally unstable and fragment to form new stars. This type of triggered SF is called 'Collect & Collapse' (C&C; first predicted by Elmegreen [1]). The (in-)stability of thin and thick shells has been studied analytically and numerically [2–6]. Typically, the size of the most unstable wavelength is comparable to the shell thickness and the growth rate of this wavelength is proportional to $(G\rho)^{1/2}$. All models predict massive fragments, i.e. 'stars' with masses of 10–20 $M_{\odot}$, similar fragmentation scales ($\sim$0.5 pc) and times ($\sim$1 Myr). The shell fragmentation might also depend on the spectral type of the ionising source [9]. The C&C scenario has been well studied in 3D SPH simulations of expanding HII regions [7, 8].

If the external medium is not uniform but contains pre-existing MC cores, their collapse may be initiated due to the influence of ionising radiation. The ionisation front drives a shock-wave into the surrounding medium, which compresses the cores and triggers collapse and SF. This form of triggered SF is called 'Radiation Driven Implosion' (RDI) [10–12]. RDI has been observed in many galactic HII regions [13–15]. In radiation-hydrodynamic simulations, the conditions for RDI were tested by many authors [16–20]. Gritschneder et al. [21] study the formation of pillar-like structures in a turbulent interstellar medium. They find that these pillars can contain enough mass to allow for subsequent SF in their tips. Bisbas et al. [19] follow a different approach and study RDI in initially stable MC cores. From exploring different initial setups they derive a critical ionising flux for SF triggered by RDI.

The importance of either scenario is long debated. Recently, Walch et al. [22] used a new approach to describe the initial MC structure with a clumps-within-clumps algorithm, which is parameterized in terms of a fractal dimension, D. The fractal dimension D describes the clumpiness of the underlying MC structure. Walch et al. [23] show that, with increasing fractal dimension D, a continuous transition from RDI dominated to C&C dominated HII regions occurs. This finding unifies the two main theories of triggered SF and ties them to the underlying MC structure. So far this conclusion is based on the morphological features of the HII regions in terms of column density [23], which bear a striking resemblance to the HII regions observed e.g. with Spitzer [24]. In the following we will address the observational evidence for triggered SF and discuss some of the associated open questions.

2 Identification of Triggered Stars

To quantitatively assess the impact of feedback on SF, it is necessary to disentangle triggered from spontaneously formed stars. This turns out to be a tricky problem as finding embedded sources within shells and pillars surrounding HII regions is not sufficient to proof triggering. A clear age bifurcation between the supposedly

triggered stars and the triggering star(s) and/or a relative velocity that is comparable to the distance between them over the age of the HII region is necessary [26]. Observationally, a clear age spread is not very well established.

Frequently, SF is observed in the tips of pillar-like structures, which are carved out of the turbulent ISM by ionising radiation. For instance in the Eagle Nebula (M16; [27, 28]), young Class I sources which follow an age sequence suggest triggering via RDI. However, Indebetouw et al. [29] find no strong evidence for triggering in the same region. The Elephant Trunk (IC 1396) represents another region of possibly triggered SF. Reach et al. [30] report detections of Class I sources within the pillar and Class II protostars that are scattered around it. Getman et al. [31] find an age gradient in IC 1396 N. However, Beltran et al. [32], who observed the same region with Spitzer, cannot confirm the existence of an age gradient. Most recently, Choudhury et al. [33] find an age gradient within the pillar as younger stars are located deeper inside it. They find that the apparent speed of sequential SF is consistent with the propagation speed of shocks in dense globules [17].

On a larger spatial scale, Koenig et al. [34] investigate 11 regions of massive SF in the outer galaxy. They find possible evidence for triggered, small clusters of young stellar objects (YSOs) in several pillar-like structures. Recently, Thompson et al. [35] study the over-density of YSOs around 322 Spitzer bubbles, which were selected based on [36]. A clear enhancement of the YSO number density ($\sim$ factor 10) is found around the bubbles. This is a nice indication that SF is indeed triggered in expanding shells.

3 The Importance of Triggered Star Formation

Whitworth et al. [37] estimate that triggered SF can be as important as spontaneous SF if the induced feedback energy is high enough to cause sequentially self-propagating SF. Also Hosokawa and Inutsuka [38] argue that SF in fragmenting shells can be sufficient to sustain the galactic SF rate. In simulations of star cluster formation in an externally irradiated cloud, Dale et al. [39] find that ionisation feedback raises the SF rate by 30 %.

In order for triggering to impact the overall SF efficiency in a galaxy, the initiation of pure low-mass SF is insufficient as this type of induced SF would die after one generation. Therefore, the possibility to trigger high mass stars, which could in turn cause new SF, is essential. This type of triggering would be self-sustained and could propagate through the ISM forming multiple generations of triggered stars. There is strong observational evidence for the presence of massive fragments in the shells surrounding galactic HII regions (see Fig. 1). This is a solid result found in numerous HII regions, e.g. in Sh 104 [25], in RCW 79 [40], in Sh2-219 [41], and with Herschel in RCW 120 [42]. It has been suggested that the presence of massive fragments is evidence for C&C. Recently, it has been shown

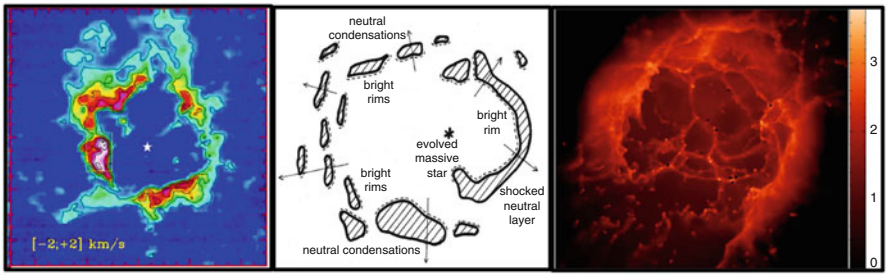

Fig. 1 *Left:* Cold clumps forming around HII region Sh 104 observed in ^{12}CO(2-1) [25]. *Center:* Schematic view of the aftermath of the erosion of a MC by O stars – an expanding system of neutral condensations (Whitworth [54]). *Right:* Column density in $M_\odot/pc^2$ of an expanding HII region in a fractal MC (Simulation by Walch et al. [22])

[23] that the formation of massive fragments around HII regions is a natural outcome of a clumpy sub-structure in the surrounding ISM. Unfortunately, it is yet unclear, if these massive clumps also harbour young massive stars.

On statistical grounds Thompson et al. [35] argue that a significant fraction (14–30 %) of massive stars in the Milky Way could be formed by triggering. Also results from the Milky Way Project suggest that ∼20 % of all young massive stars are triggered [43]. As an example, Schneider et al. [44] observe Cygnus X with GREAT onboard Sofia and find young protostars in pillars and globules, which suggest triggering. They report the possible detection of an embedded stellar cluster within one of the pillars which contains at least one B-star. However, in Carina, there is no evidence for embedded massive clusters or very massive stars [45].

Subsequently triggered or self-sustained SF is possibly happening in W3 and W5 [46]. Both regions show an age spread over adjacent areas within the cloud complexes. In other star forming regions, this picture is more complicated and adjacent HII regions and associated sites of SF do not show clear age trends.

In numerical simulations, self-sustained triggering has not yet been thoroughly addressed. Thus, the efficiency of this process is unclear. It is necessary to investigate how many generations of stars can be triggered before triggering ceases and the propagation of SF comes to a halt. Previous work can be narrowed down to the findings of Hosokawa and Inutsuka [7], who state that the first ionising star needs to be more massive than $\sim 20\,M_\odot$ in order to trigger further massive SF by C&C. Walch et al. [23] find evidence for massive star and star cluster formation for HII regions which expand into a clumpy, fractal ISM.

4 Triggered Star Formation Around Wind-Blown Bubbles

Even before the Wolf-Rayet phase, massive stars have typical mass loss rates of 10^{-6} $M_\odot$/year and drive a wind with a velocity of a few 1,000 km/s. The stellar wind is therefore an important source of energy and momentum. Samples

of triggered SF surrounding Wolf-Rayet stars are rare [47] and it is complicated to determine whether stellar winds or ionising radiation are the dominant driver of triggered SF. In different galactic HII regions ionising radiation seems to be more influential [48]. This is also the case in 30 Doradus [49] where ionising radiation and radiation pressure seem dominant. In Carina on the other hand the action of stellar winds might be more important [45]. Wind-blown bubbles have been studied analytically and numerically [37,50–53]. Unfortunately, so far none of the numerical studies of winds discusses triggered SF.

5 Is Stellar Feedback Positive or Negative?

Stellar feedback can be positive and efficiently trigger SF, but it is also negative and disperses the ambient ISM. Triggering of SF is typically happening on relatively short time scales of about a million years. Already in 1979, Whitworth [54] emphasises that O-stars also disperse MCs quite efficiently and on relatively short timescales. This scenario is confirmed in 3D SPH simulations of HII regions expanding into fractal MCs with a mass of $10^4\,M_\odot$ [22]. There, the typical outflow rates induced by ionizing radiation are 10^{-3}–$10^{-2}\,M_\odot$/year, which causes a dispersal of the clouds within a few million years. Even though ionisation feedback has profound effects in these relatively small MCs, it is much less efficient in more massive clouds with $>10^5\,M_\odot$ [55,56]. This numerical finding is in agreement with analytical estimates [57, 58]. Also observationally, stellar feedback seems to be an important mechanism for the disruption of MCs. For example, Murray [59] discuss the lifetimes of GMCs in the Milky Way. They derive values of 20–40 Myr and argue that giant MCs which host massive clusters are disrupted by feedback from the cluster members.

6 Summary

It is difficult to uniquely distinguish triggered from spontaneous SF. Nevertheless, there is observational and theoretical evidence that SF induced by feedback from massive stars adds an important contribution to the SF budget of a MC. This type of positive feedback takes place on relatively short time scales ($\lesssim$1 Myr), whereas feedback is rather negative and disperses the surrounding ISM on longer time scales. In certain regions it seems possible to trigger massive SF. This allows for a scenario of sequentially propagating SF, which is subsequently triggered by several generations of massive stars. Thus far, the role of stellar winds with respect to triggering SF is unclear.

Acknowledgements SW thanks Ant Whitworth for the frequent, wonderful and profound discussions, his patience, deep insight, and an overall great time at Cardiff University.

References

1. B.G. Elmegreen, C.J. Lada, *ApJ* **214**, 725 (1977)
2. E.T. Vishniac, *ApJ* **274**, 152 (1983)
3. A.P. Whitworth, et al., *MNRAS* **268**, 291 (1994)
4. B.G. Elmegreen, *ApJ* **427**, 384 (1994)
5. R. Wünsch, J.E. Dale, J. Palouš, A.P. Whitworth, *MNRAS* **407**, 1963 (2010)
6. J.E. Dale, R. Wünsch, R.J. Smith, A. Whitworth, J. Palouš, *MNRAS* **411**, 2230 (2011)
7. T. Hosokawa, S.i. Inutsuka, *ApJ* **646**, 240 (2006)
8. J.E. Dale, I.A. Bonnell, A.P. Whitworth, *MNRAS* **375**, 1291 (2007)
9. S.J. Arthur, et al., *MNRAS* **414**, 1747 (2011)
10. R.I. Klein, M.T. Sandford, II, R.W. Whitaker, SSR, **27**, 275 (1980)
11. F. Bertoldi, *ApJ* **346**, 735 (1989)
12. B. Lefloch, B. Lazareff, *A&A* **289**, 559 (1994)
13. K. Sugitani, Y. Fukui, A. Mizuni, N. Ohashi, *ApJ* **342**, L87 (1989)
14. L.K. Morgan, M.A. Thompson, J.S. Urquhart, G.J. White, *A&A* **477**, 557 (2008)
15. N. Smith, et al., *MNRAS* **406**, 952 (2010)
16. G. Mellema, S.J. Arthur, W.J. Henney, I.T. Iliev, P.R. Shapiro, *ApJ* **647**, 397 (2006)
17. J. Miao, G.J. White, R. Nelson, M. Thompson, L. Morgan, *MNRAS* **369**, 143 (2006)
18. M. Gritschneder, T. Naab, S. Walch, A. Burkert, F. Heitsch, *ApJ* **694**, L26 (2009)
19. T.G. Bisbas, R. Wünsch, A.P. Whitworth, D.A. Hubber, S. Walch, *ApJ* **736**, 142 (2011)
20. T.J. Haworth, T.J. Harries, *MNRAS* **420**, 562 (2012)
21. M. Gritschneder, A. Burkert, T. Naab, S. Walch, *ApJ* **723**, 971 (2010)
22. S. Walch, A.P. Whitworth, P. Girichidis, *MNRAS* **419**, 760 (2012)
23. S. Walch, A. Whitworth, T. Bisbas, D.A. Hubber, R. Wünsch, ArXiv 1109.3478 (2011)
24. L. Deharveng, et al., *A&A* **523**, A6 (2010)
25. L. Deharveng, et al., *A&A* **408**, L25 (2003)
26. B.G. Elmegreen, *ApJ* **731**, 61 (2011)
27. K. Sugitani, et al., *ApJ* **565**, L25 (2002)
28. N. Fukuda, T. Hanawa, K. Sugitani, *ApJ* **568**, L127 (2002)
29. R. Indebetouw, et al., *ApJ* **666**, 321 (2007)
30. W.T. Reach, et al., *ApJ* **690**, 683 (2009)
31. K.V. Getman, E.D. Feigelson, G. Garmire, P. Broos, J. Wang, *ApJ* **654**, 316 (2007)
32. M.T. Beltrán, F. Massi, R. López, J.M. Girart, R. Estalella, *A&A* **504**, 97 (2009)
33. R. Choudhury, B. Mookerjea, H.C. Bhatt, *ApJ* **717**, 1067 (2010)
34. X.P. Koenig, et al., *ApJ* **744**, 130 (2012)
35. M.A. Thompson, J.S. Urquhart, T.J.T. Moore, L.K. Morgan, *MNRAS* **421**, 408 (2012)
36. E. Churchwell, et al., *ApJ* **649**, 759 (2006)
37. A.P. Whitworth, N. Francis, *MNRAS* **329**, 641 (2002)
38. T. Hosokawa, S.i. Inutsuka, *ApJ* **623**, 917 (2005)
39. J.E. Dale, P.C. Clark, I.A. Bonnell, *MNRAS* **377**, 535 (2007)
40. A. Zavagno, et al., *A&A* **446**, 171 (2006)
41. L. Deharveng, et al., *A&A* **458**, 191 (2006)
42. A. Zavagno, et al., *A&A* **518**, L81 (2010)
43. S. Kendrew, et al., *ApJ* **755**, 71 (2012)
44. N. Schneider, et al., *A&A* **542**, L18 (2012)
45. T. Preibisch, V. Roccatagliata, B. Gaczkowski, T. Ratzka, *A&A* **541**, A132 (2012)
46. X.P. Koenig, et al., *ApJ* **688**, 1142 (2008)
47. T. Liu, Y. Wu, H. Zhang, S.L. Qin, *ApJ* **751**, 68 (2012)
48. F. Martins, M. Pomarès, L. Deharveng, A. Zavagno, J.C. Bouret, *A&A* **510**, A32 (2010)
49. L.A. Lopez, et al., *ApJ* **731**, 91 (2011)
50. R. Weaver, R. McCray, J. Castor, P. Shapiro, R. Moore, *ApJ* **218**, 377 (1977)
51. G. Garcia-Segura, N. Langer, M.M. Mac Low, *A&A* **316**, 133 (1996)

52. V.V. Dwarkadas, *ApJ* **667**, 226 (2007)
53. J.A. Toalá, S.J. Arthur, *ApJ* **737**, 100 (2011)
54. A. Whitworth, *MNRAS* **186**, 59 (1979)
55. J.E. Dale, I. Bonnell, *MNRAS* **414**, 321 (2011)
56. J.E. Dale, B. Ercolano, I.A. Bonnell, *MNRAS* **424**, 377 (2012)
57. J.P. Williams, C.F. McKee, *ApJ* **476**, 166 (1997)
58. C.D. Matzner, *ApJ* **566**, 302 (2002)
59. N. Murray, *ApJ* **729**, 133 (2011)

Triggered Star Formation

Jan Palouš

Abstract The spontaneous versus triggered star formation and their dependence on the sound speed in gaseous discs are discussed. The thin shell approximation is extended to thick shells: we explore dependence of the fragmentation process on the pressure in the ambient medium and follow the later evolution of fragments showing oligarchic accretion. Triggering by radiation and by spiral arms is also mentioned.

1 Spontaneous Star Formation

Birth of stars may follow the spontaneous formation of clouds by gravitational instability in galactic discs. The stability parameter $Q_{sp,*} = \frac{\sigma_R \kappa}{3.36 G \Sigma_*}$, introduced by Toomre [15], gives a condition $Q_{sp,*} \leq 1$ for the ring instability in the differentially rotating stellar disc with radial velocity dispersion σ_R and stellar surface density Σ_*. $\kappa^2 = R_{GC} \frac{d\Omega^2}{dR_{GC}} + 4\Omega^2$ is the epicyclic frequency, where R_{GC} is the galactocentric distance and $\Omega(R_{GC})$ is the angular velocity. For dissipative gaseous discs a similar criterion was formulated by Safronov [14], $Q_{sp,g} = \frac{\kappa c_{ext}}{\pi G \Sigma_g}$, where c_{ext} is the speed of sound in the gaseous medium and Σ_g its surface density. The gas in the rotating disk is unstable for $Q_{sp,g} \leq 1$, which is achieved when Σ_g surpasses a critical value

$$\Sigma_{crit} = \frac{\kappa c_{ext}}{\pi G}. \tag{1}$$

More general criteria including the thermal instability, magnetic fields, etc., can be derived [8]. All these criteria for the spontaneous instability show the dependence

J. Palouš (✉)
Astronomical Institute, Academy of Sciences of the Czech Republic,
Boční II 140 41, 140 31 Prague 4, Czech Republic
e-mail: palous@ig.cas.cz

D. Stamatellos et al. (eds.), *The Labyrinth of Star Formation*, Astrophysics and Space Science Proceedings 36, DOI 10.1007/978-3-319-03041-8_33,

Σ_{crit} on c_{ext}. Observed critical values of Σ_{crit} of the order of $(10^{20}$–$10^{21})\,\mathrm{cm}^{-2}$ necessary for star formation are consistent with values predicted by formula (1) [11, 12].

2 Triggering by Expanding Shells

Star formation may be triggered by expanding shells [10]. This "Collect and Collapse" scenario considers a shock front propagating from an OB association into a cold molecular cloud. The gravitational instability is triggered in a cold post-shock layer separating the shock front from the ionization front.

2.1 Thin Shells

The growth of perturbations in the expanding spherical infinitesimally thin shell was analyzed in the linear approximation by Elmegreen [9], Whitworth et al. [17] and Wünsch and Palouš [20]. Any density perturbation on the shell surface is stretched by the expansion, while the self-gravity supports its growth. The instantaneous maximum growth rate is $\omega = -(3v_{exp}/R) + (v_{exp}^2/R^2 + (\pi G \Sigma_{sh}/c_{sh})^2)^{1/2}$, where R is the radius of the shell, v_{exp} its expansion speed, Σ_{sh} its column density and c_{sh} the speed of sound within the shell. The instability sets in when $\omega > 0$.

We use the thin shell approximation in 3D numerical simulations, where we test when $\omega > 0$ and quantify when and where the expanding shell starts to be unstable [6, 7]. In galaxy discs with different z-profiles, c_{ext} and with different input total energies E_{tot} we derived the formula [7]:

$$\Sigma_{crit} = 0.27 \left(\frac{E_{tot}}{10^{51}\,\mathrm{erg}}\right)^{-1.1} \left(\frac{c_{ext}}{\mathrm{km\,s}^{-1}}\right)^{4.1} 10^{20}\,\mathrm{cm}^{-2}. \quad (2)$$

The main difference between formulas (2) and (1) is the dependence on the velocity dispersion in the unperturbed medium c_{ext}: the critical density Σ_{crit} is directly proportional to c_{ext} in the case of the spontaneous star formation, but it depends on $c_{ext}^{4.1}$ in the case of the triggered star formation. A much sharper dependence of Σ_{crit} on c_{ext} is connected to the mass accumulation in the shell, which stops when the shell expansion velocity v_{exp} decelerates to c_{ext}. It indicates the importance of the self-regulating feedback for the triggered star formation mode. Young stars in OB associations release the energy and compress the ambient ISM, creating shells, which trigger formation of the next generation of stars, when the disc surface density surpasses a critical value Σ_{crit}. The star formation is accompanied with the heating of the ISM increasing c_{ext}. It leads to the increase of Σ_{crit} quenching the subsequent

star formation. Later, the energy dissipation and cooling decrease c_{ext} and Σ_{crit} closing the self–regulating cycle of the triggered star formation. The heating of the ISM and the increase of c_{ext} related to the star formation is a localized process influencing regions of 0.1–1 kpc in size. Consequently, the feedback of the triggered mode of star formation is more local than that of the spontaneous mode. The weaker dependence of Σ_{crit} on c_{ext} for the spontaneous star formation means, that this mode may be also effective in regions where c_{ext} is increased and triggering has stopped.

2.2 Thick Shells

The validity of the thin shell approximation was tested by Dale et al. [2], where we analyzed shells expanding to a very low density medium. During its evolution, the shell broadens becoming thick. The thick shell dispersion relation [21] shows the dependence of the fragmentation process on the external pressure. The pressure assisted gravitational instability (PAGI) produces fragments of similar sizes and masses as the thin shell for medium values of the external pressure. With high value of the external pressure, there are more low mass fragments, with low value of external pressure there are more high mass fragments. We try to prove this dependence of the shell fragmentation on pressure in observations of the Carina Flare with APEX [22], which we like to complement with the data to be acquired by ALMA (see also Wünsch, this proceedings).

The growth of fragments has been analyzed by Dale et al. [2]. The remaining mass of the thick shell is accreted in a strongly non-linear process, which we call oligarchic accretion: the old fragments, that has been formed first, accrete most of the mass leaving only a small portion of thick shell gas for more recently formed fragments. This confirms the prediction by Whitworth et al. [17] on the preferential formation of high-mass stars in shocked interstellar gas layers.

3 Triggering by Radiation

Molecular clouds are influenced by stellar radiation. Conditions of radiation-driven implosions of pre-existing clouds have been explored by Bisbas et al. [1]. Incident ionizing flux determines the cloud evolution: moderate fluxes lead to triggered star formation. The impact of radiation on a turbulent cloud is explored by Dale and Bonnell [3] and the importance of the radiative feedback inside bound star forming clouds is discussed by Dale et al. [4]. The simulation show pillars and filaments similar to those observed in Eagle Nebula [19], Horsehead Nebula (Ward-Thompson et al. [16]) or in other places.

4 Triggering by Spiral Arms

The formation of molecular clouds is triggered when the gas flow is compressed by the gravitational potential of the galaxy spiral arms. Hydrodynamic simulations of this process by Dobbs and Bonnell [5] have shown the converging flows leading to formation of molecular gas in low temperature places. Creation of feathers, unbound clouds and diverging flows is also visible. When GMCs move in a galaxy, they are supported against gravity by pressure complemented by tidal fields. However, in galactic spiral arms, or inside tidal arms formed by galaxy versus galaxy collisions, the sheer is reduced [13] and GMCs loose a part of the support, which leads to their collapse. Thus the spiral arms act as triggers of star formation.

Acknowledgements I like to express my gratitude to Anthony P. Whitworth for collaboration on many topics mentioned in this contribution. Further collaborators include T. Bisbas, J. E. Dale, S. Ehlerová, P. Jáchym and R. Wünsch. I acknowledge the support by the project P209/12/1795 of the Czech Science Foundations and RVO 67985815 of the Academy of Sciences of the Czech Republic.

References

1. Bisbas T. G., Wünsch R., Whitworth A. P., Hubber D. A., Walch S., 2011, ApJ, 736, 142
2. Dale J. E., Wünsch R., Whitworth A. P., Palouš J., 2009, MNRAS, 398, 1537
3. Dale J. E., Bonnell I. A., 2012, MNRAS, 422, 1352
4. Dale J. E., Ercolano B., Bonnell I. A., 2012, MNRAS, 424, 377
5. Dobbs C. L., Bonnell I. A., 2008, MNRAS, 385, 1893
6. Ehlerová S., Palouš J., Theis Ch., Hensler G., 1997, A&A 328, 121
7. Ehlerová, Palouš, J., 2002, MNRAS 330, 1022
8. Elmegreen B. G., 1991, ApJ 378, 139
9. Elmegreen B. G., 1994, ApJ 427, 384
10. Elmegreen B. G., Lada, Ch., 1977, ApJ 214, 725
11. Hunter D.A., Elmegreen B. G., Baker A.L., 1998, ApJ 493, 595
12. Kennicutt, R. C., 1998, ARA&A, 36, 189
13. Palouš J., Jáchym, P., Ehlerová, S., 2004, in Penetrating Bars through Mask of Cosmic Dust, eds. D. BlockI. Puerari, K. C. Freeman, R. Groess, E. K. Block, Springer, p. 251
14. Safronov V. S., 1960, Annales dÁstrophysique 23, 979
15. Toomre A., 1964, ApJ 139, 1217
16. Ward-Thompson, D., Nutter, D., Bontemps, S., Whitworth, A., Attwood, R., MNRAS, 369, 2001
17. Whitworth, A. P., Bhattal, A. S., Chapman, S. J., Disney, M. J., Turner, J. A., 1994, A&A 290, 421
18. Whitworth, A. P., Bhattal, A. S., Chapman, S. J., Disney, M. J., Turner, J. A., MNRAS, 268, 291
19. Williams, R. J. R., Ward-Thompson, D., Whitworth, A. P., 2001, MNRAS, 327, 788
20. Wünsch R., Palouš J., 2001, A&A, 374, 746
21. Wünsch R., Dale J. E., Palouš, J., Whitworth, A. P., 2010, MNRAS, 407, 1963
22. Wünsch, R., Jáchym, P., Sidorin, V., Ehlerová, S., Palous, J., Dale, J. E., Dawson, J. R., Fukui, Y., 2012, A&A 539, 116

Filamentary Cold Structure from Colliding Supershells

Evangelia Ntormousi, Andreas Burkert, Katharina Fierlinger, and Fabian Heitsch

Abstract Supershells are large dense shocks, created by the combined stellar feedback from OB associations. The gas around the stars is compressed, forming a dense spherical shell which typically breaks up into molecular clouds. We have performed high resolution numerical simulations of this process, focusing on the fluid instabilities which affect the shock morphology before gravity has had time to act. In these simulations cold structures of typical sizes on the order of parsecs are formed out of the dense shock material in a variety of physical states. These clumps are organized in filaments with tens of parsecs lengths when a large-scale shear is present. In simulations where the flow of stellar material is followed with a tracer quantity cold structures practically do not contain any enriched material from the OB associations at the time of their creation.

1 Introduction

Stellar feedback is a very powerful source of thermal and turbulent energy in the Interstellar Medium (ISM). Massive stars in OB associations produce ionizing photons and expel large amounts of mass in winds and supernova explosions, processes which shape the matter around them in shells and cavities [1].

E. Ntormousi (✉) • A. Burkert
Universitäts-Sternwarte München, Ludwig-Maximilians-Universität, Scheinerstr.1
81679 München, Germany
e-mail: eva@usm.lmu.de

K. Fierlinger
Max-Planck-Institut für extraterrestrische Physik, Postfach 1312, Giessenbachstr.,
85741 Garching, Germany

F. Heitsch
Department of Physics & Astronomy, University of North Carolina Chapel Hill, CB 3255,
Phillips Hall, NC 27599, USA

D. Stamatellos et al. (eds.), *The Labyrinth of Star Formation*, Astrophysics and Space Science Proceedings 36, DOI 10.1007/978-3-319-03041-8_34,

The large compressions around the associations are typically observed to trigger the formation of molecular clouds and lead to new events of star formation. The conditions for large-scale shock fragmentation have thus been the focus of extensive theoretical work, which unfortunately we cannot fully summarize here. Early analysis [2] provided dispersion relations for the growth of dynamical instabilities on spherical shocks, while a study of the gravitational fragmentation of interstellar shocks showed that the fragments become self-gravitating when the layer is still confined by ram pressure [3]. In addition, numerical simulations have been employed to study the shock fragmentation process [4, 5].

Here we summarize the results of high-resolution hydrodynamical simulations of the fragmentation and collision of supershells where the Vihniac, the Kelvin-Helmholtz and the Thermal instability dominate the dynamics [6, 7]. The feedback from young OB associations is modeled as a time-dependent mass and energy source and the flow of metal-enriched material from the hot to the cold phase is followed with a passive hydrodynamical quantity.

2 Numerical Simulations

High-resolution numerical simulations (maximum resolution of 0.1 pc) have been performed with the hydrodynamical Adaptive Mesh refinement (AMR) code RAMSES [8]. This code uses a second order Godunov scheme to solve the Euler equations of hydrodynamics, an extremely advantageous approach when dealing with sharp discontinuities. Appropriate source and sink terms are included in the equations to simulate the heating and cooling processes typical of the local ISM, as well as the energy and mass input from stellar feedback. In some of the simulations an additional continuity equation is solved for a tracer quantity, allowing us to follow the flow of wind and supernova material into the rest of the fluid.

All simulations start with diffuse, warm ($n_H = 1\,\mathrm{cm}^{-3}$, $\mathrm{T} = 8{,}000\,\mathrm{K}$) gas in thermal equilibrium. Two identical feedback regions representing OB associations of 20 or 50 stars each are placed on either side of the computational box. The resulting supershells are let to evolve until the collide in the middle. The typical morphology of such a simulation is shown in Fig. 1.

The Vishniac instability magnifies any small perturbations on the shock surface to large characteristic "fingers" and the produced shear triggers the Kelvin-Helmholtz instability, while the condensations the tips of the ripples are thermally unstable. The net result is the formation of small, cold and dense clumps with a variety of internal velocity structures. When the shells collide, these clumps are brought together, but at the same time sheared into very filamentary structures, like the one shown in Fig. 2. It takes less than 1 Myr for the clumps to form, a timescale much shorter that those typically estimated for gravitational fragmentation of supershells [5].

To follow the flow of enriched material from the OB associations an arbitrary amount of a tracer quantity is introduced in the feedback region at each timestep.

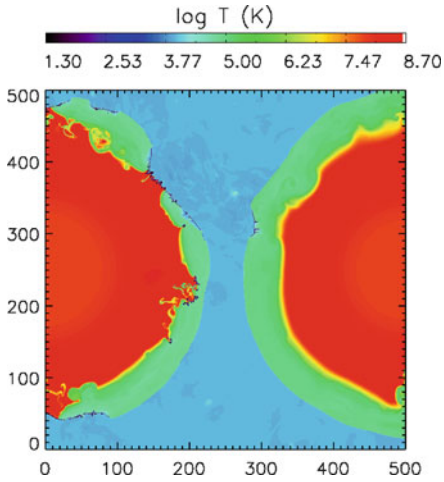

Fig. 1 Contour plot of the logarithm of the gas temperature at an early stage (about 3 Myr after star formation started in the OB associations) of a 2D supershell collision simulation in a turbulent diffuse environment. The combination of the Vishniac, the Thermal and the Kelvin-Helmholtz instabilities causes the shock to condense and break up in several places. The axes are in parsecs (This figure can also be found in [6])

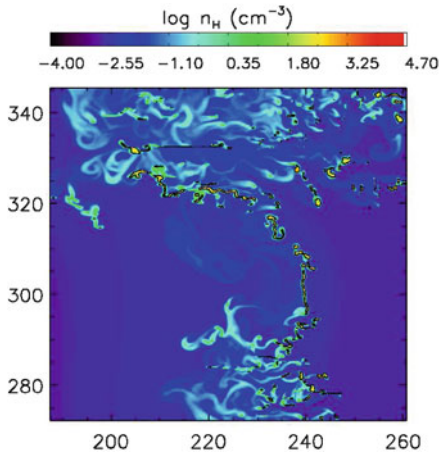

Fig. 2 A zoomed-in region of a 2D supershell simulation at the shock collision interface, about 7 Myr since star formation started in the associations. Shown here are contours of the logarithm of the hydrogen number density. The contour for $n_H = 50\,\mathrm{cm}^{-3}$ is shown in *black*. The small-scale clumps are grouped in a filamentary configuration due to the large-scale shear. The axes are marked in parsecs from the domain origin (This figure can also be found in [6])

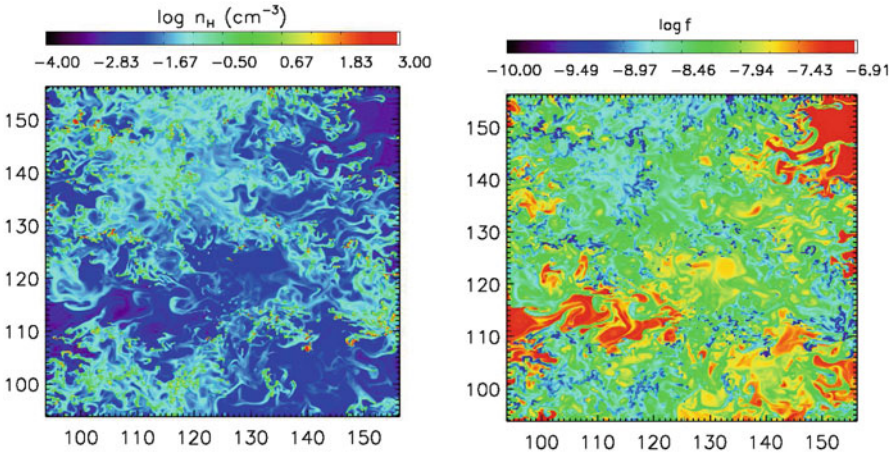

Fig. 3 Contour plots of the logarithm of hydrogen number density (*left*) and the logarithm of relative tracer content (*right*) at the shock collision interface in a 2D simulation, about 3 Myr since star formation started. The axes are in parsecs, like above, although this simulation was done in a smaller domain. It is clear that dense regions contain practically no new material (This figure can also be found in [7])

Figure 3 shows the density distribution and the corresponding tracer content of the cells (divided by the total amount in the box) at the turbulent layer of the shock collision. The hot gas receives the new material from the stars and turbulent mixing efficiently transports it to the warm gas, but the cold gas is created and remains throughout the simulations without any new metals.

3 Conclusions

High-resolution numerical simulations of the dynamical impact of stellar feedback on its environment show that the formation of cold filamentary structure occurs naturally and rapidly around OB associations. Cold clumps are typically organized in filaments tens of parsecs long and less than 1 pc thick, which are formed from environmental shear.

Studies of the flow of material from the feedback regions to the edge of the supershells show that the bulk of the new metals is confined in the hot cavities. Turbulence enhances mixing with the warm gas when two shells collide, but the cold clumps do not receive any of the ejected material from the stars. In order to estimate the final metallicities of the clumps further investigation is needed, including modeling of thermal conductivity and gravitational accretion from the environment.

References

1. E. Churchwell, M.S. Povich, D. Allen, M.G. Taylor, M.R. Meade, B.L. Babler, R. Indebetouw, C. Watson, B.A. Whitney, M.G. Wolfire, T.M. Bania, R.A. Benjamin, D.P. Clemens, M. Cohen, C.J. Cyganowski, J.M. Jackson, H.A. Kobulnicky, J.S. Mathis, E.P. Mercer, S.R. Stolovy, B. Uzpen, D.F. Watson, M.J. Wolff, *ApJ* **649**, 759 (2006).
2. E.T. Vishniac, *ApJ* **274**, 152 (1983).
3. A.P. Whitworth, A.S. Bhattal, S.J. Chapman, M.J. Disney, J.A. Turner, *A&A* **290**, 421 (1994)
4. J.E. Dale, R. Wünsch, A. Whitworth, J. Palouš, *MNRAS* **398**, 1537 (2009).
5. R. Wünsch, J.E. Dale, J. Palouš, A.P. Whitworth, *MNRAS* **407**, 1963 (2010).
6. E. Ntormousi, A. Burkert, K. Fierlinger, F. Heitsch, *ApJ* **731**, 13 (2011).
7. E. Ntormousi, A. Burkert, ArXiv e-prints (2011)
8. R. Teyssier, *A&A* **385**, 337 (2002).

Triggering Star Formation: From the Pillars of Creation to the Formation of Our Solar System

Matthias Gritschneder and Douglas N.C. Lin

Abstract We study the evolution of molecular clouds under the influence of ionizing radiation. We propose that the Pipe Nebula is an HII region shell swept up by the B2 IV β Cephei star θ Ophiuchi. After reviewing the recent observations, we perform a series of analytical calculations. We are able to show that the current size, mass and pressure of the region can be explained in this scenario. The Pipe Nebula can be best described by a three phase medium in pressure equilibrium. The pressure support is provided by the ionized gas and mediated by an atomic component to confine the cores at the observed current pressure. We then present simulations on the future evolution as soon as the massive star explodes in a supernova. We show that a surviving core at the border of the HII-region ($D = 5\,\mathrm{pc}$) is getting enriched sufficiently with supernova material and is triggered into collapse fast enough to be consistent with the tight constraints put by meteoritic data of e.g. ^{26}Al on the formation of our Solar System. We therefore propose that the formation of the Solar System was triggered by the shock wave of a type IIa supernova interacting with surviving cold structures similar to the Pillars of Creation at the border of HII-regions.

1 The Pipe Nebula

The Pipe Nebula is a nearby ($D \approx 130\,\mathrm{pc}$, [1]) molecular cloud region. Its total spatial extend is roughly $14 \times 3\,\mathrm{pc}$. Due to its relative proximity, it provides an ideal testbed to observe molecular cloud core formation [2]. As star formation only occurs in one tip (B59), it is often considered the model case for isolated star formation. Here, we investigate the role of the B2 IV β Cephei star θ Ophiuchi (HD 157056),

M. Gritschneder (✉) • D.N.C. Lin
Astronomy and Astrophysics Department, University of California, Santa Cruz, CA 95064, USA
e-mail: gritschneder@ucolick.org; lin@ucolick.org

D. Stamatellos et al. (eds.), *The Labyrinth of Star Formation*, Astrophysics and Space Science Proceedings 36, DOI 10.1007/978-3-319-03041-8_35,

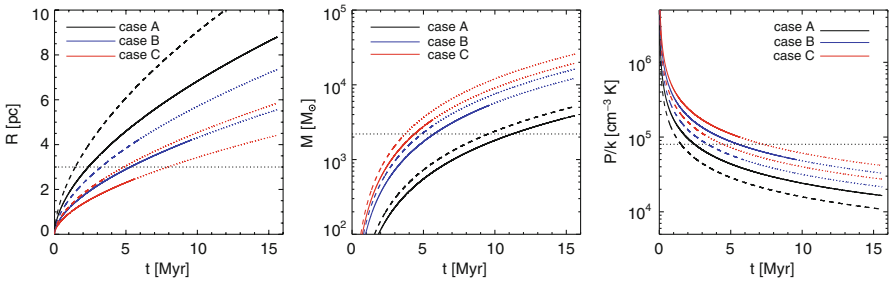

Fig. 1 Time evolution of the HII-region for the three different cases. *Solid lines*: classical (spherical) HII-region, *dashed*: blister-type HII-region. The lines are continued *dotted* once the shock has reached equilibrium with the ambient surrounding. *Dotted horizontal lines*: current day observational values. *Left panel*: radius of the shell. *Center*: swept up mass in a Pipe Nebula sized region. *Right:* pressure in the hot, ionized gas (Fig. 2 from [3])

located at a projected distance of about 3 pc from the Pipe Nebula, in the formation and evolution of the Pipe Nebula.

The B-type star is going to ionize the surrounding, thereby increasing its temperature. As soon as the heated gas reacts to its change in pressure, an approximately isothermal shock is driven into the surrounding medium. Under the assumption of a thin shock, the time evolution of the radius is given as

$$R(t) = R_{\rm s}\left(1 + \frac{7}{4}\frac{a_{\rm s,hot}}{R_{\rm s}}(t - t_0)\right)^{\frac{4}{7}}. \quad (1)$$

$R_{\rm s}$ is the Stroemgren radius, $a_{\rm s,hot}$ is the sound speed of the hot, ionized gas.

In the following, we assume the cold gas to be at $T_{\rm cold} = 10\,{\rm K}$ with a mean molecular weight of $\mu_{\rm cold} = 1.37$ We test three models A, B and C, corresponding to initial number densities n_0 in the cold surrounding of 1×10^3, 5×10^3 and $1 \times 10^4\,{\rm cm}^{-3}$, respectively. We parametrize θ Oph A as a black body with a temperature of $T_{\rm eff} = 22{,}590\,{\rm K}$ and a luminosity of $\log(L/L_\odot) = 3.75$.

The results are shown in Fig. 1. As it can be directly seen, the current observations can be readily explained. Concerning the current state, our models indicate a three-phase medium in pressure equilibrium. The pressure is supplied by the hot, ionized gas ($T = 5{,}000\,{\rm K}$ and $n_0 = 8\,{\rm cm}^{-3}$) and is mediated by a warm, atomic component ($T = 100\,{\rm K}$ and $n_{\rm atomic} = 774\,{\rm cm}^{-3}$) to the cold cores ($T = 10\,{\rm K}$ and $n_{\rm atomic} = 7 \times 10^3\,{\rm cm}^{-3}$). For a more detailed discussion see [3].

2 The Formation of the Solar System

We then go on to investigate the further evolution, as soon as the massive star explodes in a supernova. This is in particular interesting in the context of the formation of the Solar System. The time-scale for the formation events of our

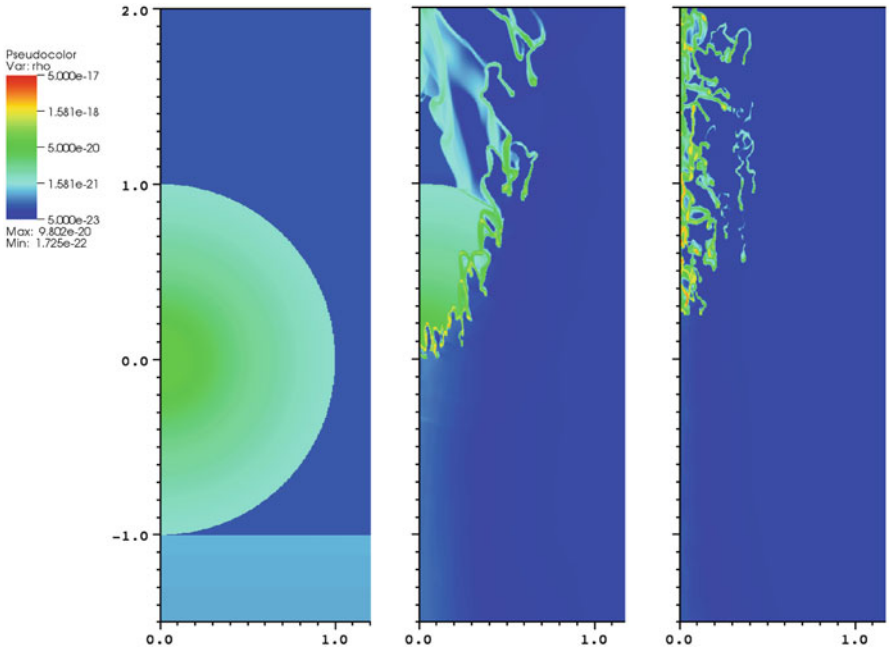

Fig. 2 The time evolution of case I. Color coded is the density at $t = 0\,\mathrm{kyr}$, $t = 4.16\,\mathrm{kyr}$ and $t = 8.33\,\mathrm{kyr}$. The length scale is given in units of the radius of the initial cold core ($R_0 = 0.21\,\mathrm{pc}$) (Fig. 2 from [4])

Solar System can be derived from the decay products of radioactive elements found in meteorites. Short lived radionuclides (SLRs) within calcium-aluminium-rich inclusions (CAIs) in primitive chondrites, such as ^{26}Al, can be employed as high-precision chronometers due to their short half-lives. Various measurements of different CAIs by several research groups have not only confirmed the canonical ratio of $(5.23 \pm 0.13) \times 10^{-5}$ for ^{26}Al, but also established a very small spread. This spread corresponds to an age range of less than $\simeq$20 kyr [5]. Thus, the challenge posed is how to enrich the Solar System with enough ^{26}Al and, in addition, trigger it into collapse within a fraction of the free-fall time ($t_{\mathrm{ff}} \approx 100\,\mathrm{kyr}$).

We set up an molecular cloud core in isolation, which is going to be hit by a Sedov-Taylor type supernova blast wave. The simulations are performed with the numerical code COSMOS [6]. Figure 2 shows the time evolution of the density in this simulation. The shock wave is propagating from the bottom to the top. As it can be clearly seen, the shock wave encompasses the cold core rapidly. After $t = 8.33\,\mathrm{kyr}$ the central region is already at a very high density ($\rho_{\mathrm{max}} = 3 \times 10^{-15}\,\mathrm{g\,cm^{-3}}$). The mass in this region below a temperature of 20 K is $M_{\mathrm{core}} \simeq 0.13\,\mathrm{M}_{\odot}$. A closer look at the field tracing the supernova-enriched gas shows that the core region gets sufficiently enriched within this short time to explain the abundances observed in CAIs. For a more detailed description of the initial conditions and numerical methods see [4].

3 Conclusions

The scenario of θ Oph swiping up the Pipe Nebula presented can successfully explain the observed morphology of the Pipe Nebula. This includes the diffuse component as well as the current width, mass and size of the Nebula. More importantly, the pressure to confine the cores can be supplied. Especially the pressure of the cores is otherwise puzzling. Up to now, the only possible explanation for this confinement was the self-gravity of the cloud. This is highly unlikely, as the cores in a self-gravitating system are the first instances to react to the collapse and therefore should be bound, whereas most of the cores are observed to be unbound.

In addition, we show that a cold clump of $10\,M_\odot$ at a distance of 5 pc can be sufficiently enriched in ^{26}Al and triggered into collapse fast enough for a range of different metallicities and progenitor masses. We envision an environment for the birth place of the Solar System 4.567 Gyr ago similar to the situation of the pillars in M16 nowadays, where molecular cloud cores adjacent to an HII region will be hit by a supernova explosion in the future. We show that the triggered collapse and formation of the Solar System as well as the required enrichment with radioactive ^{26}Al are possible in this scenario.

Acknowledgements M.G. acknowledges funding by the Alexander von Humboldt Foundation in form of a Feodor-Lynen Fellowship and by the China National Postdoc Fund Grant No. 20100470108 and the National Science Foundation of China Grant No. 11003001. D.N.C.L. acknowledges funding by the NASA grant NNX08AL41G.

References

1. M. Lombardi, J. Alves, C.J. Lada, A&A **454**, 781 (2006). DOI 10.1051/0004-6361:20042474
2. C.J. Lada, A.A. Muench, J. Rathborne, J.F. Alves, M. Lombardi, ApJ **672**, 410 (2008).
3. M. Gritschneder, D.N.C. Lin, ApJL **754**, L13 (2012).
4. M. Gritschneder, D.N.C. Lin, S.D. Murray, Q.Z. Yin, M.N. Gong, ApJ **745**, 22 (2012).
5. B. Jacobsen, Q. Yin, F. Moynier, Y. Amelin, A.N. Krot, K. Nagashima, I.D. Hutcheon, H. Palme, Earth and Planetary Science Letters **272**, 353 (2008).
6. P. Anninos, P.C. Fragile, S.D. Murray, ApJS **147**, 177 (2003).

Triggering, Suppressing and Redistributing Star Formation

James E. Dale, Barbara Ercolano, and Ian Bonnell

Abstract We discuss three different ways in which stellar feedback may alter the outcome of star cluster formation: triggering or suppressing star formation, and redistributing the stellar population in space. We use detailed Smoothed Particle Hydrodynamics (SPH) simulations of HII regions in turbulent molecular clouds to show that all three of these may happen in the same system, making inferences about the effects of feedback problematic.

1 Introduction

To what degree star formation is self–regulating is much debated in astrophysics. Stellar feedback in the form of HII regions, winds, jets, radiation pressure, non–ionizing radiation and supernova explosions are all potentially able to influence the star formation process in molecular clouds (e.g. [4]). These processes may have a positive or negative effect on star formation, but positive effects (in the sense of triggering) have received the most observational attention (e.g. [3, 5, 8]). However, disentangling how these various feedback mechanisms influence star formation is fraught with difficulty, since it is necessary to think comparatively and infer how star formation would proceed differently if feedback were absent.

From this perspective, there are three ways in which feedback may influence the formation of stars. Its effect may be positive (commonly referred to as 'triggered star formation'), in the sense of increasing the star formation rate or efficiency,

J.E. Dale (✉) • B. Ercolano
Excellence Cluster 'Universe', Boltzmannstrasse 2, 85748 Garching, Germany
e-mail: dale@usm.lmu.de; ercolano@usm.lmu.de

I. Bonnell
School of Physics and Astronomy, University of St Andrews, North Haugh, St Andrews, Fife, KY16 9SS, Scotland, UK
e-mail: iab1@st-andrews.ac.uk

D. Stamatellos et al. (eds.), *The Labyrinth of Star Formation*, Astrophysics and Space Science Proceedings 36, DOI 10.1007/978-3-319-03041-8_36,

producing more stars, or leading to the birth of stars which would otherwise not exist (note that these effects are not necessarily equivalent and, in the same system, some may transpire while others do not). Feedback may also be negative and do the opposite of these things, which we will call 'suppressed star formation'. Of course, the global influence of feedback on a given system may be different from its local effects – it is perfectly possible for star formation to be suppressed at some locations and triggered in others. Finally, suppression and triggering may cancel each other out and feedback may result in the production of a statistically indistinguishable population of stars, but distribute them differently in position or velocity space relative to their distribution in the absence of feedback, for example in well–defined shells. This could be termed 'redistributed star formation'.

In order to infer in a given system which of these processes is at work and what is the overall influence on the end product – the stellar cluster – it is essential to have a credible counterfactual model for comparison. This is equally true of observed and simulated systems. A good idea of what the system would have done in the absence of feedback can then be gained, and hence the effects of feedback isolated.

2 Numerical Simulations

We have embarked on an SPH parameter–space study in the mass–radius plane of GMCs (fully described in [2]) in which we simulate the effects of the HII regions driven by the massive stars. Control simulations without feedback enable us to study triggering, suppression and redistribution with the benefit of well–defined counterfactual models. Structures such as bubbles, pillars and champagne flows, all of which are commonly associated with feedback and triggered star formation, emerge quite naturally from these calculations. We study the effects of feedback in terms of global parameters, such as the star formation rate and efficiency, and also on a local star-by-star level by inquiring whether the material from which a given star forms is also involved in star formation in the companion run.

3 Results

We find that the global and local influence of feedback can be very different. In all our simulations, the overall effect of the expanding HII regions on the star formation rates and efficiencies is negative (or negligible). Clouds with escape velocities comparable to the ionized sound speed are largely unaffected. In clouds with low escape velocities, the dense star forming gas near the ionizing stars is rapidly dispersed by feedback; this has the strongest influence on star formation. Many HII regions eventually burst out of the cold gas, becoming champagne flows. The escape from the cloud of the hot HII gas lessens the dynamical effect of

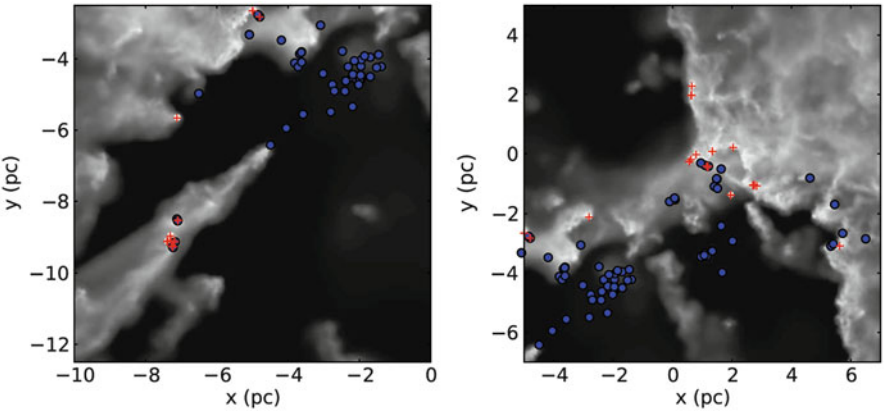

Fig. 1 Gas column–density map viewed along the z–axis (greyscale) of a pillar (*left panel*) and part of a bubble wall (*right panel*) with *red crosses* marking the locations of triggered stars and *blue circles* marking the locations of spontaneously–formed stars

feedback. However, using star–by–star comparison with feedback–free control runs, we establish unequivocally that the formation of some stars is triggered, in the sense that the material from which they form is not involved in star formation in the control run. Star formation is thus globally suppressed but sometimes locally triggered.

Triggering is often identified in the literature by the association of young stars with pillars or bubble walls (e.g. [6–8]). In Fig. 1 we illustrate the pitfalls of this approach. We show gas column density maps of two regions of the same simulation (Run I from [2]) with overplotted symbols representing triggered (red crosses) and spontaneously–formed (blue circles) stars. Here we define a star to be triggered if less than half the material from which it forms is also involved in star formation in the control simulation. Otherwise, we regard the star as 'spontaneous' (see [1] for more details on this technique). In the left panel, we show a pillar structure pointing towards the ionizing cluster in this simulation (the group of blue stars in the top right of the image). There are indeed triggered objects associated with the pillar about halfway along its length, but these are mixed with some spontaneously–formed stars and those objects nearest the pillar tip are also in fact formed spontaneously. The pillar in the ionized run is the remains of an accretion flow and the gas from which the stars nearest the tip form is, in the control run, simply delivered to the central cluster, where it is involved in star formation.

Similarly, in the right panel, we show part of the wall of the bubble structure excavated by the HII regions, which contains a mixture of triggered and spontaneously–formed stars. This admixture is a consequence of the sweeping up, into the same location, of material which was going to form stars anyway, and of quiescent gas which was not. This is an indication that even those stars which form spontaneously may be found in very different positions in the ionized run compared with the control run, an example of redistributed star formation.

4 Summary

We consider three ways in which feedback influences star cluster formation: triggering and suppression which, respectively, positively or negatively alter the rate or efficiency of star formation and/or the formation of individual stars, and redistribution, which alters the geometrical distribution of stars, even if other properties of the stellar population are unchanged. All these effects may be global or local.

We find in our SPH simulations of HII regions driven into turbulent clouds that all three outcomes are present. Although the global effect of feedback is to decrease the star formation rate and efficiency and the formation of many stars is aborted, local triggering does occur. In addition, the stars which we know from our control simulations form spontaneously are to be found in very different locations in the ionized simulations, due to the general sweeping up and transport of star–forming gas by the HII regions. This is a clear example of redistributed star formation. We note therefore that the association of young stars with structures such as pillars or bubble walls is not necessarily a reliable indicator of triggering.

We stress the need for credible counterfactual models when discussing the purported effects of feedback. In order to make reliable statements about what effect feedback has had on a given system, it must be possible to infer at least approximately what the properties of the system would have been in its absence, and to define very carefully in what ways the real system is different.

References

1. Dale, J. E.; Bonnell, I. A., MNRAS **422**, 1352 (2012)
2. Dale, J. E., Ercolano, B., Bonnell, I. A., MNRAS **424**, 377 (2012)
3. Koenig X. P., Allen L. E., Gutermuth R. A., Hora J. L., Brunt C. M., Muzerolle J., ApJ **688**, 1142 (2008)
4. Matzner C. D., ApJ **566**, 302 (2002)
5. Puga E., Hony S., Neiner C., Lenorzer A., Hubert A., Waters L. B. F. M., Cusano F., Ripepi V., A&A **503**, 107 (2009)
6. Smith, Nathan; Stassun, Keivan G.; Bally, John, AJ **129**, 888 (2005)
7. Thompson M. A., Urquhart J. S., Moore T. J. T., Morgan, L. K., MNRAS **421**, 408 (2012)
8. Zavagno A., Russeil D., Motte F., Anderson L. D., Deharveng L., Rodon J. A., Bontemps S., Abergel A., A&A **518**, L81 (2010)

Gravitational Fragmentation of the Carina Flare Supershell

Richard Wünsch

Abstract We study the gravitational fragmentation of a thick shell comparing the analytical theory to 3D hydrodynamic simulations and to observations of the Carina Flare supershell. We use both grid-based (AMR) and particle-based (SPH) codes to follow the idealised model of the fragmenting shell and found an excellent agreement between the two codes. Growth rates of fragments at different wavelength are well described by the pressure assisted gravitational instability (PAGI) – a new theory of the thick shell fragmentation. Using the APEX telescope we observe a part of the surface of the Carina Flare supershell in the ^{13}CO line. We apply a new clump-finding algorithm DENDROFIND to identify ∼50 clumps. We determine the clump mass function and we construct the minimum spanning tree connecting clumps positions to estimate the typical distance among clumps. We conclude that the observed masses and distances correspond well to the prediction of PAGI.

1 Gravitational Instability of the Expanding Shell

Expanding shells are common features in the ISM of galaxies (see e.g. [2, 6, 10]). It has been suggested by Elmegreen and Lada [8] that they can trigger star formation by the collect-and-collapse mechanism, and indeed, a strong and growing observational evidence for it has been found (e.g. [5] and references therein). To understand how the collect-and-collapse mechanism operates, it is essential to know how the shell fragments due to the self-gravity. The gravitational instability of

R. Wünsch (✉)
Astronomical Institute of the Academy of Sciences, Boční II 1401/1a 141 31 Praha 4, Czech Republic
e-mail: richard@wunsch.cz

D. Stamatellos et al. (eds.), *The Labyrinth of Star Formation*, Astrophysics and Space Science Proceedings 36, DOI 10.1007/978-3-319-03041-8_37,

expanding shells was studied by several authors using the thin shell approximation [7, 11, 12]. Wünsch et al. [13] derived a dispersion relation resulting from the so called Pressure Assisted Gravitational Instability (hereafter PAGI) of the thick shell embedded in the rarefied ambient gas with non-zero pressure. Here we show how the PAGI dispersion relation compares to hydrodynamic simulations and to CO observations of the molecular cloud G285.90+4.53 in the Carina Flare supershell (GSH287+04-17). For details see the series of papers [3, 4] and [13, 14].

2 Hydrodynamic Simulations

In order to isolate the gravitational instability and separate it from other dynamical instabilities, we setup a momentum driven shell embedded in the rarefied gas with pressure $P_{\rm EXT}$. To rule out any numerical effects, we use two principally different codes: the grid-based AMR code Flash [9] and the Smooth Particle Hydrodynamics (SPH) code SPHNG [1]. The shell has the mass $2 \times 10^4\,\mathrm{M}_\odot$, its initial radius is 10 pc and it starts to expand with the velocity $2.2\,\mathrm{km\,s^{-1}}$. We use three values of the external pressure: 10^{-17}, 10^{-13} and $5 \times 10^{-13}\,\mathrm{dyne\,cm^{-2}}$. We study growth rate of individual modes as well as a the case with random (white noise) initial density perturbations.

Figure 1 shows the surface density in the simulation with the random initial conditions at time when fragments are already well evolved, and it can be seen that both codes are in an excellent agreement. We decompose the shell surface density into spherical harmonics and measure growth rates of modes. Consequently, we compare it to theoretical dispersion relations. We found that simulations results agree well with the PAGI dispersion relation, however, they differ substantially from the dispersion relation obtained using the thin shell approximation [4, 13].

3 APEX Observations of the Carina Flare Supershell

In [3] we convert the PAGI dispersion relation into the clump mass function (CMF) and compare it to hydrodynamic simulations. The agreement is good in the initial period when the shell includes enough mass for clumps growth. In [14] we test the PAGI CMF observationally by observing ^{13}CO(2–1) line in a small region (cloud G285.90+4.53) on the surface of the Carina Flare supershell with the APEX telescope.

To identify clumps, we use our algorithm DENDROFIND and estimate clump masses and construct the CMF. The maximum of it is at $\sim 10\,\mathrm{M}_\odot$ which is about

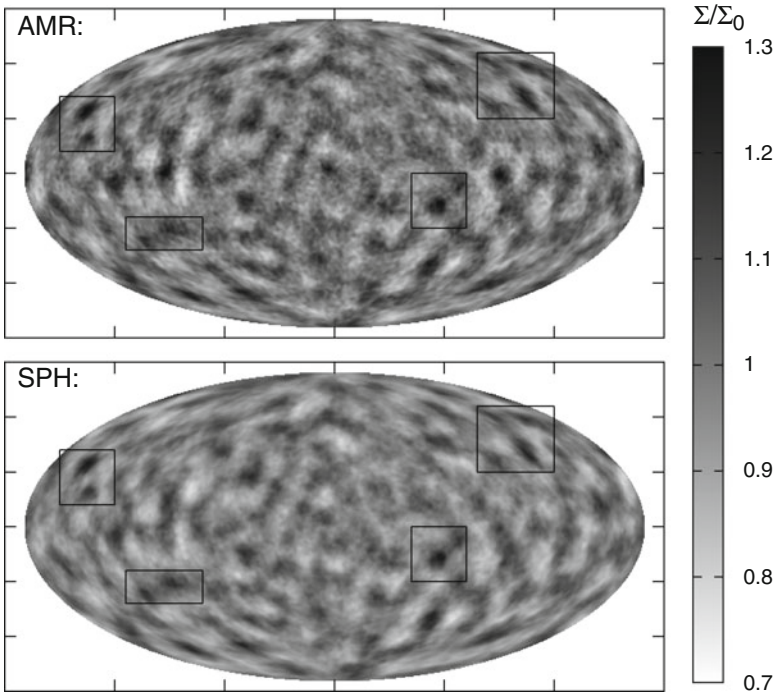

Fig. 1 Simulation with random initial perturbations calculated with the grid-based (AMR, *upper panel*) and the SPH code (*lower panel*). The relative perturbation of the shell surface density at $t = 15$ Myr is shown in the Hammer projection. Several regions are marked by *rectangles* to guide the eye to compare the similar structures

1.5 orders of magnitude above our minimum detectable mass. We also determine the typical distance among clumps to be $\sim$1.7 pc, by constructing the minimum spanning tree connecting clump centres and correcting the mean edge length for the 3D geometry.

Figure 2 compares the observed CMF maximum and the typical distance among clumps to the prediction of PAGI. It can be seen that the two properties of the observed clumps are consistent with their origin due to PAGI, because the contours of the observed values (thick contours) intersect. Moreover, the position of the intersection is very close to the position of the expected values of the Carina Flare surface density ($7 \times 10^{-4}\,\mathrm{g\,cm^{-2}}$) and the pressure in the ISM ($1.4 \times 10^{-12}\,\mathrm{dyne\,cm^{-2}}$).

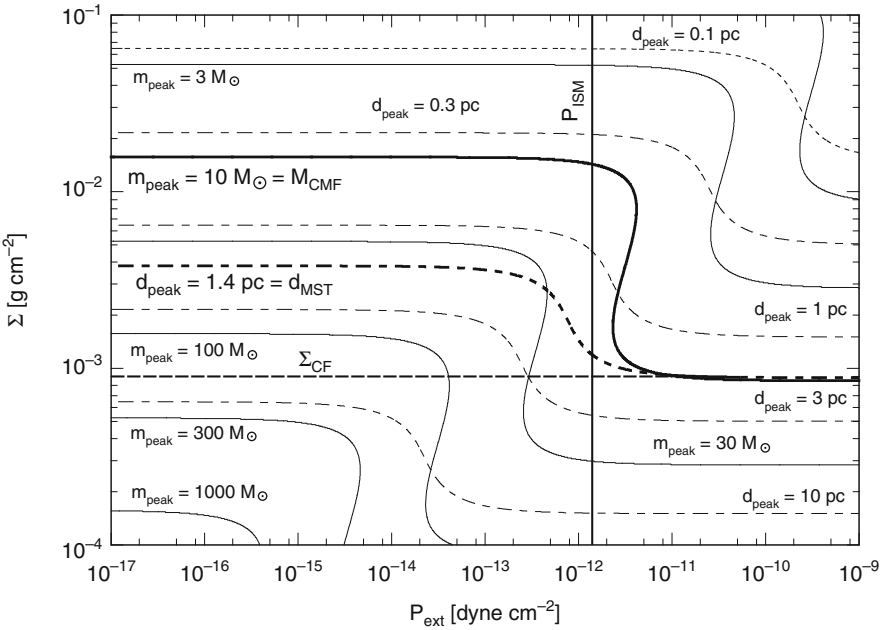

Fig. 2 Maximum of the CMF predicted by PAGI (*solid contours*) and the corresponding fragmentation wavelength (*dashed contours*) plotted as functions of the external pressure, $P_{\rm EXT}$, and the shell surface density, Σ. *Thick contours* show the CMF maximum (*solid*) and the typical clump distance (*dashed*) determined from CO observations of the cloud G285.90+4.53. *Dash-dotted lines* show the average surface density of the Carina Flare supershell (horizontal) and the typical pressure in the ISM (vertical)

Acknowledgements I am very grateful to Anthony Whitworth for collaborating with me on many topics from this work. Further collaborators include J. Dale, J. Palouš, P. Jáchym, V. Sidorin, S. Ehlerová, J. Dawson and R. Smith. I acknowledge the support by the project P209/12/1795 of the Czech Science Foundation.

References

1. Bate, M. R., Bonnell, I. A., & Price, N. M. 1995, MNRAS, 277, 362
2. Churchwell, E., Povich, M. S., Allen, D., et al. 2006, ApJ, 649, 759
3. Dale, J. E., Wünsch, R., Smith, R. J., Whitworth, A., & Palouš, J. 2011, MNRAS, 411, 2230
4. Dale, J. E., Wünsch, R., Whitworth, A., & Palouš, J. 2009, MNRAS, 398, 1537
5. Deharveng, L., Zavagno, A., Schuller, F., et al. 2009, A&A, 496, 177
6. Ehlerová, S. & Palouš, J. 2005, A&A, 437, 101
7. Elmegreen, B. G. 1994, ApJ, 427, 384
8. Elmegreen, B. G. & Lada, C. J. 1977, ApJ, 214, 725
9. Fryxell, B., Olson, K., Ricker, P., et al. 2000, ApJS, 131, 273
10. Heiles, C. 1979, ApJ, 229, 533

11. Vishniac, E. T. 1983, ApJ, 274, 152
12. Whitworth, A. P., Bhattal, A. S., Chapman, S. J., Disney, M. J., & Turner, J. A. 1994, MNRAS, 268, 291
13. Wünsch, R., Dale, J. E., Palouš, J., & Whitworth, A. P. 2010, MNRAS, 407, 1963
14. Wünsch, R., Jáchym, P., Sidorin, V., et al. 2012, A&A, 539, A116

A Nebula in Your Computer: Simulating the Physics and Chemistry of an H II Region

Thomas G. Bisbas

Abstract In this contribution we discuss about numerical modeling of nebulae. In particular we emphasize on the dynamical evolution of an H II region and on the chemical structure of a Photodissociation region. We do this by using the Smoothed Particles Hydrodynamics code `SEREN` and the recently developed astrochemistry code `3D-PDR`. We show an example application by simulating a cometary globule using these two codes.

1 Introduction

Nebulae (H II regions) are large regions consisting of ionised gas, particularly of hydrogen. The source of ionisation is usually a single or multiple massive stars emitting ultraviolet radiation with photons carrying more energy than the ionisation potential ($h\nu > 13.6\,\mathrm{eV}$). A nebula is mainly structured by three different parts; the ionised region (number density of $n \lesssim 200\,\mathrm{cm}^{-3}$ and temperature of $T \simeq 10^4\,\mathrm{K}$), the photodissociation region[1] (PDR; $200 \lesssim n \lesssim 10^5\,\mathrm{cm}^{-3}$, $10 \lesssim T \lesssim 10^4\,\mathrm{K}$), and the dark molecular region ($n \gtrsim 10^5\,\mathrm{cm}^{-3}$, $T \simeq 10\,\mathrm{K}$). Of particular interest are PDRs; they are ubiquitously present in the interstellar medium (ISM) consisting of predominantly neutral gas and dust illuminated by FUV radiation ($6 \leq h\nu \leq 13.6\,\mathrm{eV}$) and they occur in any region of the ISM that is dense and cold enough to remain neutral but has too low column density to prevent the penetration of FUV photons. Over the past few decades, effort has been made to study numerically the

[1] known also as "Photon Dominated Region".

T.G. Bisbas (✉)
Department of Physics and Astronomy, University College London, Gower Place, London WC1E 6BT, UK
e-mail: tb@star.ucl.ac.uk

D. Stamatellos et al. (eds.), *The Labyrinth of Star Formation*, Astrophysics and Space Science Proceedings 36, DOI 10.1007/978-3-319-03041-8_38,

physics and chemistry of nebulae. Due to computational speed and memory capacity issues, detailed three-dimensional simulations are a reality only in the last decade or so. The numerical codes can be divided in two main categories; codes that study the dynamical evolution and codes that study the chemical structure. An integrated code that treats simultaneously detailed dynamics, UV propagation and chemistry offering a realistic temperature and therefore pressure structure in H II regions is still lacking (although significant effort in this direction has been made by Glover et al. [8], Clark et al. [5], and Haworth and Harries [11]).

2 Dynamical and Chemical Modeling

Several techniques have been used for dynamical modeling of H II regions in grid-based codes and in smoothed particle hydrodynamics codes. Bisbas et al. [2] have proposed a `HEALPix`-based [9] algorithm to simulate the propagation of the UV radiation in the ISM by invoking the *on-the-spot* approximation [13]. This algorithm has been incorporated in the SPH code `SEREN` [12] and it creates hierarchies of rays emanated spherically symmetric from the excited source. Each ray splits up to four child-rays wherever the resolution of the radiation transfer matches the resolution of the hydrodynamics, locally. This algorithm adopts two equations of state; an isothermal for the ionised region ($T = 10^4$ K everywhere), and a barotropic for the neutral region (see Eq. 6 [3]). The temperature between these two regions, and therefore where the PDR is located, is smoothed using a linear interpolation. Although this technique speeds up the thermodynamical calculations, it significantly limits the ability to study the chemistry of PDRs which is quite important to understand in order to explore the insights of the chemical structure and star formation in ionised nebulae. We thus need further tools to implement.

Perhaps the most challenging part of modeling a nebula is its chemistry. That is because one has to take into account a realistic three-dimensional treatment of the UV radiation (i.e. as obtained by `MOCASSIN` [6, 7]), self-shielding of individual species against the UV radiation, cooling and heating processes and a complicated network of reactions. Of particular interest is the three-dimensional modeling of PDRs which has been achieved in `3D-PDR` [4]. This code solves the chemistry and the thermal balance self-consistently within a given three-dimensional cloud of arbitrary density distribution. It uses the chemical model features of the fully benchmarked one-dimensional code `UCL_PDR` [1] and a ray-tracing scheme based on the `HEALPix` package to calculate the total column densities and thus to evaluate the attenuation of the FUV radiation into the region, and the propagation of the FIR/submm line emission out of the region. An iterative cycle is used to calculate the cooling rates using a three-dimensional escape probability method, and heating rates. At each element within the cloud, it performs a depth- and time-dependent calculation of the abundances for a given chemical network to obtain the column densities associated with each individual species. The iteration cycle terminates when the PDR has obtained thermodynamical equilibrium, in which the thermal

balance criterion is satisfied i.e. the heating and cooling rates are equal to within a user-defined tolerance parameter. 3D-PDR determines the relative abundances of a limited number of atomic and molecular species at each cloud element, by solving the time-dependent chemistry of a self-contained network of formation and destruction reactions. We use the UMIST database containing 33 species (including e^-) and 320 reactions. We solve for steady-state chemistry (chemical evolution time set to $t = 100\,\mathrm{Myr}$), although the code is able to follow the full time dependent evolution within the cloud.

This treatment of PDR chemistry offers a more accurate temperature profile in comparison with the approximations made in dynamical simulations. However, due to the high computational cost, it is impossible to include such complicated UV and PDR calculations in a dynamical code, unless new techniques are implemented.

3 Example: Simulating a Cometary Globule

In this example we perform two different simulations using the codes described above. In the first simulation (SPH run) we use the SEREN code to evolve dynamically an initially uniform density spherical clump (radius $R = 0.5\,\mathrm{pc}$, mass $M = 20\,\mathrm{M}_\odot$, temperature $T = 100\,\mathrm{K}$, consisting purely of atomic hydrogen) as it interacts with an external and approximately plane-parallel radiation field. In the second simulation (PDR run) we use the 3D-PDR code in one of the snapshots selected from the SPH run in which we examine the PDR chemical structure.

In the SPH run, as the clump interacts with the external radiation field of an excited source (emitting $\dot{\mathcal{N}}_{\mathrm{LyC}} = 3.2 \times 10^{48}$ photons s^{-1}, placed $D = 3.5\,\mathrm{pc}$ away from the centre of the clump) the ionising radiation boils off its outer layers from the side in which the flux is impinging. The shock front that is formed compresses the remaining neutral gas turning it into a rod shape. However, the internal thermal pressure of the neutral gas is constantly increasing and this results in its re-expansion (see Sect. 4.4 of [2] for full discussion), which may lead to star formation [3, 10].

In the PDR run, we take a snapshot from the SPH run at $t = 0.12\,\mathrm{Myr}$ and we use it as initial conditions in 3D-PDR. A cross section plot of the density structure at that time is shown at the bottom right of Fig. 1 where the ionising radiation is impinging from bottom to top. The UV photon flux corresponds to a field strength of approximately $\chi = 50$ Draines. The top three and the bottom left frames show the emission maps for the most dominant coolants. The middle frame at the bottom shows an RGB composite image of three different emission maps. From these maps we see that the species in the PDR are distributed smoothly and follow the density profile. The weakest emission is produced by [O I] 63 μm and the strongest by CO (1-0) implying that the molecular gas dominates over the atomic contribution. However, considering the transition frequencies for these maps, we find that the [O I] 63 μm and the [C II] 158 μm lines are the dominant coolants. Full details and results are discussed in [4].

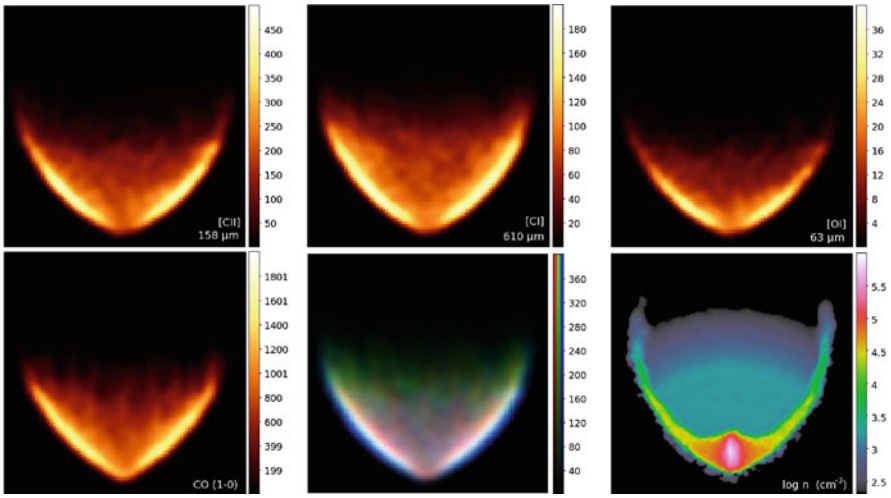

Fig. 1 *Top row* from left to right: emission maps of [C II] 158 μm, [C I] 610 μm and [O I] 63 μm. *Bottom row* from left to right: emission map of CO (1-0), RGB composite image with colour bar ratios of 8:1:2 for CO(1-0):[C I]:[C II], cross-section density profile at $z = 0$ pc

4 Conclusions

We discussed about the dynamical and chemical modeling of H II regions using the SEREN SPH code and the recently developed 3D-PDR code respectively. We perform an example of a cometary globule and we show results from these two codes. Since we lack of algorithms treating detailed dynamical and chemical calculations in ionized regions, effort has to be made towards this direction.

Acknowledgements TGB acknowledges support by STFC grant ST/H001794/1.

References

1. Bell T. A., Roueff E., Viti S., Williams D. A., 2006, MNRAS, 371, 1865
2. Bisbas T., Wünsch R., Whitworth A., Hubber D., 2009, A&A, 497, 649
3. Bisbas T. Wünsch R., Whitworth A., Hubber D., Walch S., 2011, ApJ, 736, 142
4. Bisbas T. G., Bell T. A., Viti S., Yates J., Barlow M. J., 2012, MNRAS, 427, 2100
5. Clark P. C., Glover S. C. O., Klessen R. S., 2012, MNRAS, 420, 745
6. Ercolano B., Morisset C., Barlow M. J., Storey P. J., Liu X.-W., 2003, MNRAS, 340, 1153
7. Ercolano B., Barlow M. J., Storey P. J., 2005, MNRAS, 362, 1038
8. Glover S., Federrath C., Mac Low M.-M., Klessen R., 2010, MNRAS, 404, 2
9. Górski K. M., Hivon E., Banday A. J., et al., 2005, ApJ, 622, 759
10. Gritschneder M., Naab T., Burkert A., et al., 2009, MNRAS, 393, 21
11. Haworth T. J., Harries T. J., 2012, MNRAS, 420, 562
12. Hubber D., Batty C., McLeod A., Whitworth A., 2011, A&A, 529, A27
13. Osterbrock D. E., 1974, agn..book

The Photoevaporation of a Neutral Structure by an EUV+FUV Radiation Field

Veronica Lora, M.J. Vasconcelos, A.C. Raga, A.H. Cerqueira, and A. Esquivel

Abstract The expansion of an HII region into a surrounding inhomogeneous molecular cloud, leads to the formation of elongated "elephant trunk" structures. The EUV photo-ionising radiation and FUV dissociating radiation from newly born stars photo-evaporate their parental neutral cloud, leading to the formation of dense clumps in the tips of elephant trunks, that could in principle eventually form stars. We study th effects of including a photo-dissociating FUV flux in models of fragmentation of a photo-evaporating, self-gravitating molecular cloud.

1 Numerical Simulations and Clump Counting

We carried out a set of 24 hydrodynamic simulations. The code used (described in [2]) integrates the gas dynamics equations in a uniform 3D cartesian grid, together with the radiative transfer of radiation of the Lyman limit, and an H ionisation rate equation, including the self gravity of the gas. We have also added the transfer of FUV dissociating radiation, an ionisation rate equation for CI. We do not follow the photo-dissociation of H2, rather we assume that approximately follows the ionisation of CI [3]. We consider a domain of $(3.0, 1.5, 1.5) \times 10^{18}$ cm resolved

V. Lora (✉)
Astronomisches Rechen-Institut, Mönchhofstr. 12-14, 69120 Heidelberg, Germany
e-mail: vlora@ari.uni-heidelberg.de

M.J. Vasconcelos • A.H. Cerqueira
Laboratório de Astrofísica Teórica e Observacional, DCET-UESC, Rodovia Ilhéus-Itabuna, km. 16 - Ilhéus, Bahia, Brazil
e-mail: mjvasc@uesc.br; hoth@uesc.br

A.C. Raga • A. Esquivel
Instituto de Ciencias Nucleares, Universidad Nacional Autónoma de México, Ap. 70-543, 04510 D. F., México
e-mail: raga@nucleares.unam.mx; esquivel@nucleares.unam.mx

D. Stamatellos et al. (eds.), *The Labyrinth of Star Formation*, Astrophysics and Space Science Proceedings 36, DOI 10.1007/978-3-319-03041-8_39,

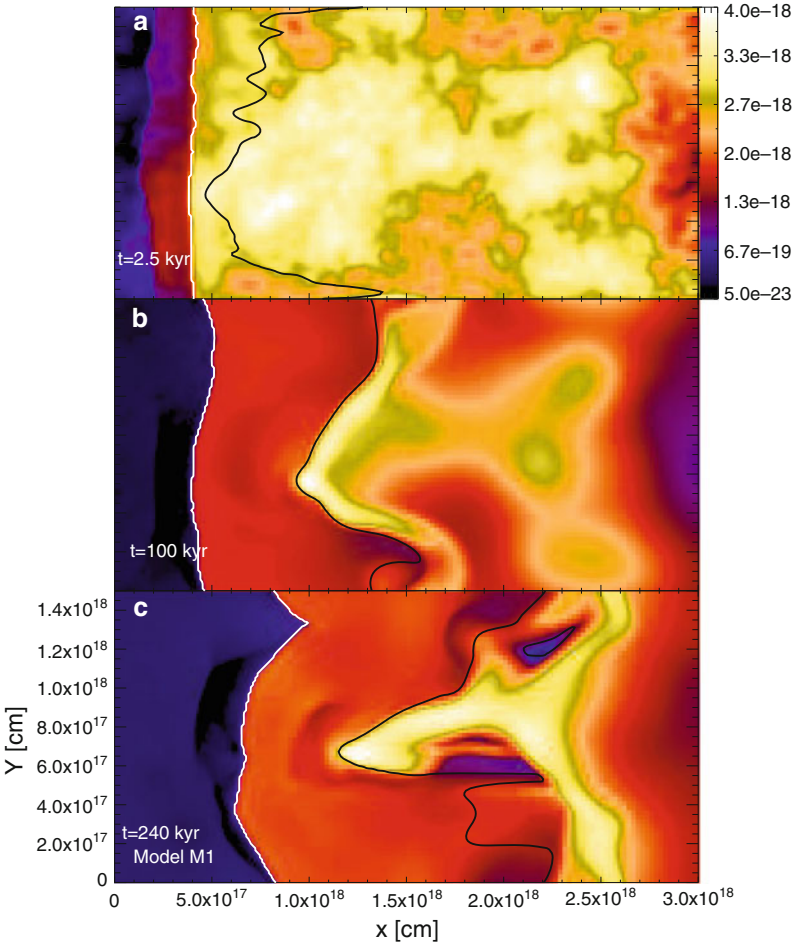

Fig. 1 Time evolution of the xy mid-plane density stratification given in g cm^3. The *black line* shows the contour corresponding to an H ionisation fraction of 50 %. The *white line* shows the contour corresponding to a C ionisation fraction of 50 %. The x and y-axes are labelled in cm

with $256 \times 128 \times 128$ grid points, respectively. In the $x-$ axis an outflow boundary is applied, and reflection conditions in the other boundaries. Initially we have a set of four inhomogeneous density structures (at rest) with a power law power-spectrum index of $-11/3$. The computational domain is divided into an initially ionised region (with ionised H and C) for $x < x_0 = 4 \times 10^{17}$ cm, and a neutral region (with neutral H and C) for $x > x_0$. The average density in the neutral medium is 100 times the average density of the ionised medium. The typical temperature of photo-ionised, photo-dissociated and molecular regions are 10^4, 10^3 and 10 K respectively. The initial neutral structure has a total mass of $\sim 200\,M_\odot$. We assume a stellar source situated at 3×10^{18} cm from the edge of the computational domain in

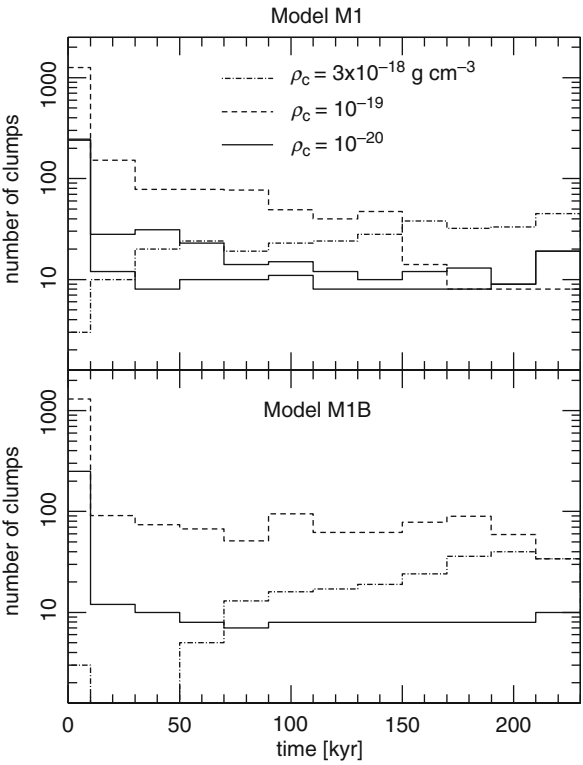

Fig. 2 The *top panel* shows the number of clumps found in one of our models as a function of time, for the three chosen density cutoffs. The *bottom panel* shows the number of neutral clumps for a model with zero FUV flux. In the *top panel*, the *two solid lines* correspond to $\rho = 10^{-20}\,\mathrm{g\,cm^{-3}}$ cutoff density, with clumps with neutral H (*thin line*) and with neutral C (*thickline*)

the $-x$ direction. The EUV and FUV fluxes are computed by Diaz-Miller et al. [1]. We carried out simulations with and without the FUV fluxes in order to isolate the effects of having a non-zero FUV flux.

From the density stratification of our 24 simulations, we computed the number of clumps at different integration times (see right panel of Fig. 1). We define a cutoff density ρ_c, and count all the spatially connected structures with $\rho > \rho_c$. We counted the clumps that satisfied that their material has neutral H and that their material has neutral C (Fig. 2). We only noted a slightly difference at $\rho_c = 10^{-20}\,\mathrm{g\,cm^3}$. The range from early to late O-type stars that we have chosen, the fragmentation of the neutral structure into clumps has a similar behaviour regardless of the chosen type of star. The effect of introducing an FUV radiation flux is to significantly decrease the number of $\rho_c = 10^{-19}\,\mathrm{g\,cm^3}$ clumps and to increase the $\rho_c = 3 \times 10^{-18}\,\mathrm{g\,cm^3}$ clumps at the final integration time ($t = 240\,\mathrm{kyr}$) of our simulations. From the stratification resulting from all models at $t = 150\,\mathrm{kyr}$, we computed the mass distribution of the clumps for $\rho_c = 10^{-19}$ and $3 \times 10^{-18}\,\mathrm{g\,cm^3}$. The main effect that we found of the non-zero FUV field is to mostly eliminate the $\rho_c = 10^{-19}\,\mathrm{g\,cm^3}$ clumps in the $10^{-2} \Rightarrow 10^{-1}\,\mathrm{M_\odot}$ mass range. The presence of a FUV flux allows the formation of low mass, in the zero FUV flux models.

2 Conclusions

We studied the formation of dense clumps in the interaction of a photo-ionising radiation field with an inhomogeneous medium, including a photodissociation region preceding the HI/II ionisation front. We have computed 3D simulations which include the photo-ionisation of H and C, assuming that the CI/CII ionisation front approximately coincides with the outer edge of the photo-dissociation region [3], and explored a range from early to late-type O stars. We also computed the models setting the FUV flux to zero, in order to isolate the effects of having a non-zero FUV flux. We found that including a photo-dissociation region the clumps with low cutoff densities are depleted. Denser clumps develop earlier that in models with zero FUV. A large number of dense clumps are produced with broader mass distribution that in the zero FUV models. Including an FUV field leads to the earlier formation of a larger number of dense clumps which in principle might lead to the formation of more young stars.

References

1. Diaz-Miller, R. I., Franco, J., Shore, S. N., 1998, ApJ, 501, 192
2. Lora, V., Raga, A., Esquivel, A., 2009, A&A, 503, 477
3. Richling, S. & Yorke, H. W., 2000, ApJ, 539, 258

Testing Models of Triggered Star Formation: Theory and Observation

Thomas J. Haworth, Tim J. Harries, and David M. Acreman

Abstract One of the main reasons that triggered star formation is contentious is the failure to accurately link the observations with models in a detailed, quantitative, way. It is therefore critical to continuously test and improve the model details and methods with which comparisons to observations are made. We use a Monte Carlo radiation transport and hydrodynamics code TORUS to show that the diffuse radiation field has a significant impact on the outcome of radiatively driven implosion (RDI) models. We also calculate SEDs and synthetic images from the models to test observational diagnostics that are used to determine bright rimmed cloud conditions and search for signs of RDI.

We have investigated the impact of polychromatic and diffuse field radiation on radiatively driven implosion (RDI) models using the Monte Carlo radiation transport and hydrodynamics code TORUS [1, 2]. The details of the code implementation, model parameters and results are given in [2]. We ran three types of RDI calculation. One with a monochromatic radiation field, one with a polychromatic radiation field and one that is both polychromatic and includes the diffuse radiation field. The addition of polychromatic radiation to the calculation does not significantly alter the outcome of the model. However, including the diffuse field can lead to significantly different evolution of the cloud, altering the morphology and increasing the maximum accumulated density after 200 kyr up to about a factor of 10.

Using these RDI models from [2] we calculated synthetic images and SEDs to test observational diagnostics of bright rimmed clouds (BRCs) in [3]. We calculated the neutral cloud properties by fitting the cloud SED as a greybody to determine the dust temperature, which can then be used to calculate the cloud mass following [4]. The temperature and electron density in the ionized boundary layer (IBL) and the

T.J. Haworth (✉) • T.J. Harries • D.M. Acreman
Department of Physics and Astronomy, University of Exeter, Exeter, UK
e-mail: haworth@astro.ex.ac.uk

D. Stamatellos et al. (eds.), *The Labyrinth of Star Formation*, Astrophysics and Space Science Proceedings 36, DOI 10.1007/978-3-319-03041-8_40,

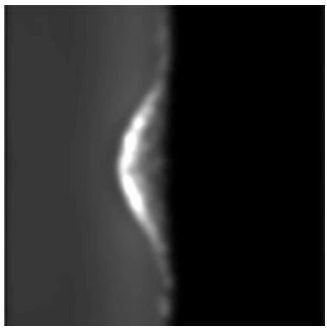

Fig. 1 A simulated 20 cm continuum emission image of a BRC taken using the VLA configuration C. Synthetic images like this can be analyzed in the same way as real data, which is useful for testing the accuracy of diagnostics and improving the interpretation of characteristic BRC features

cloud mass loss rate were calculated using simulated VLA 20 cm continuum images, an example of which is given in Fig. 1, and the standard techniques of [5,6]. We have also tested the use of forbidden line ratios from long slit spectroscopy to determine the IBL conditions and found that they are a viable tool, giving a direct and more accurate measure of the IBL temperatures compared to the radio method which assumes a canonical value of 10^4 K.

Using the inferred cloud and IBL conditions we calculated the cloud support and IBL pressures to determine whether or not the clouds are being compressed. We find that this pressure comparison diagnostic is a reasonable indicator of whether or not the IBL is driving into the cloud. The accuracy of the techniques was investigated by comparing the derived conditions and behaviours with those known from the model grid. For example, we have demonstrated that as the beam size increases the IBL conditions are increasingly underestimated in the radio diagnostic because the IBL flux is contaminated by the neutral cloud and HII region. We also found that the contribution to the SED from warm dust causes a slight overestimation of the dominant cloud temperature by $1-2$ K, which leads to an overestimation of the mass by up to a factor of 35 %. Furthermore, use of a constant mass conversion factor C_ν in the mass calculations of Hildebrand [4] for BRCs of different class is found to introduce errors up to a factor 3.6. This comparison of the known conditions in simulations with those inferred through observational diagnostics of synthetic data means that more reliable conclusions can be drawn from studies of real BRCs.

References

1. T.J. Harries, MNRAS **315**, 722 (2000).
2. T.J. Haworth, T.J. Harries, MNRAS **420**, 562 (2012).
3. T.J. Haworth, T.J. Harries, D.M. Acreman, ArXiv e-prints:1205.6993 (2012)
4. R.H. Hildebrand, QJRAS **24**, 267 (1983)
5. B. Lefloch, B. Lazareff, A&A **289**, 559 (1994)
6. B. Lefloch, B. Lazareff, A. Castets, A&A **324**, 249 (1997)

Effects of a Momentum Driven Stellar Wind on the Surrounding ISM

Judith Ngoumou, David Anthony Hubber, James E. Dale, and Andreas Burkert

Abstract Massive stars shape the surrounding ISM by emitting ionizing photons and ejecting material through stellar winds. We study the impact of the transfer of momentum from the wind of a massive star on the surrounding neutral or ionized material. We use the Smoothed Particle Hydrodynamics (SPH) code SEREN [3] including a newly implemented HEALPix-based momentum conserving wind scheme. The transfer of momentum from a wind onto the cold surrounding gas drives the expansion of a shock front, sweeping up the neutral material into a dense shell. In contrast, we find the momentum driven wind to have only little direct effect on the warm ionized gas.

1 Method

The dynamics of the gas are evolved using standard SPH. The momentum transfer on the SPH particles is modeled using the HEALPix algorithm [2]. This tessellation scheme allows to identify the particles surrounding the source and to distribute the total rate of momentum emitted by the source among them. In a cold and uniform

J. Ngoumou (✉) • A. Burkert
Universitäts-Sternwarte München, Ludwig-Maximilians-Universität, Scheinerstr.1, 81679 München, Germany
e-mail: ngoumou@usm.uni-muenchen.de

D.A. Hubber
Technical University Munich, Excellence Cluster Universe, Boltzmannstr. 2, D-85748 Garching, Germany

Department of Physics, University Observatory Munich, Ludwig-Maximilians-University Munich, Scheinerstr.1, D-81679 Munich, Germany

J.E. Dale
Excellence Cluster 'Universe', Boltzmannstr. 2, 85748 Garching, Germany

D. Stamatellos et al. (eds.), *The Labyrinth of Star Formation*, Astrophysics and Space Science Proceedings 36, DOI 10.1007/978-3-319-03041-8_41,

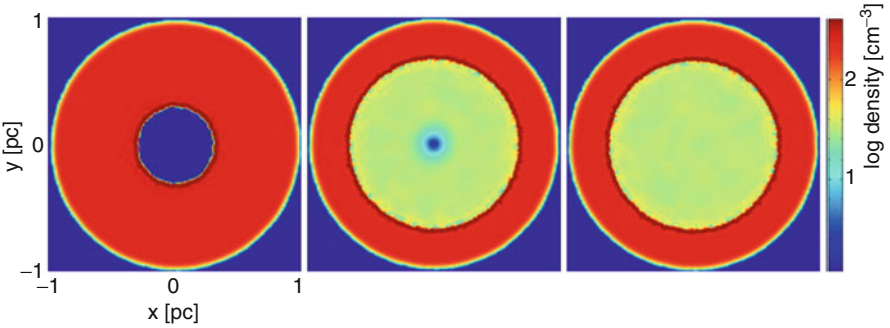

Fig. 1 Slice through a column density plot showing the shell expansion in a uniform density medium for three feedback mechanisms. *Left*: momentum transfer only, *middle*: momentum transfer and ionizing radiation, *right*: ionizing feedback only

cloud, a shock front is formed and expands in accordance with the analytical expression for the expansion ($R \propto t^{1/2}$) of a bubble in the momentum conserving snowplow phase [4]. The effects of ionizing radiation are included using the HEALPix based ionizing radiation scheme developed in [1].

2 First Results: Outlook

In order to assess the impact of the wind on the surroundings of the star, the momentum transfer scheme was applied to a uniform density cloud, $\rho_c \approx 300\,\mathrm{cm}^{-3}$. We used fixed values for the wind mass loss $\dot{M}_{\mathrm{wind}} = 10^{-6}\,\mathrm{M}_\odot\,\mathrm{year}^{-1}$, the wind velocity $v_{\mathrm{wind}} = 1{,}000\,\mathrm{km\,s}^{-1}$ and the ionizing photon rate $N_{\mathrm{Lyc}} = 10^{49}\,\mathrm{s}^{-1}$. The results were compared for three cases of stellar feedback (see Fig. 1).

A first qualitative analysis shows that the momentum transfer from a single stellar wind creates a shock front expanding in a cold uniform density medium. Its impact on warm ionized material is however significantly reduced.

The impact of various feedback mechanisms on self-gravitating structures and star formation is currently being investigated.

Acknowledgements This project is funded by Deutsche Forschungsgesellschaft DFG PR 569/9-1

References

1. T.G. Bisbas, R. Wünsch, A.P. Whitworth, D.A. Hubber, A&A **497**, 649 (2009).
2. K.M. Górski, E. Hivon, A.J. Banday, B.D. Wandelt, F.K. Hansen, M. Reinecke, M. Bartelmann, ApJ **622**, 759 (2005).
3. D.A. Hubber, C.P. Batty, A. McLeod, A.P. Whitworth, A&A **529**, A27 (2011).
4. H.J.G.L.M. Lamers, J.P. Cassinelli, *Introduction to Stellar Winds* (1999)

Part VI
Probing the Initial Stages of Star Formation

First Results from the Herschel Gould Belt Survey in Taurus and Comparison with Other Clouds

Jason Kirk, on behalf of the Herschel Gould Belt Survey Consortium

Abstract The unparalleled sensitivity and mapping speed of the ESA *Herschel* Space Observatory makes it possible to now map entire star formation regions in the time it would once have taken to map a single prestellar core. The *Herschel* Gould Belt Survey is a key program designed to fully map the clouds of the Gould Belt at five wavelengths between 70 and 500 μm. These clouds span a range of physical conditions from the sterility of Polaris to the active cluster forming complexes of Orion and Aquila. These clouds allow us to examine the genesis of the core mass function and how the history of star formation in different regions varies. The early results have demonstrated the markedly different populations of cores in these regions and have revealed the nearly ubiquitous relationship of those cores with dense filaments.

1 The Gould Belt and the Survey

The Gould Belt is the best laboratory that we have for studying low-mass star formation. The Belt was first discovered in the nineteenth century [8, 11] as a band of bright stars that are inclined at an angle of $\sim$20° to the Galactic plane. Figure 1 shows the Belt plotted over a CO map of the Galaxy, its sweep is coincident with almost all sites of low-mass star formation within half a kiloparsec of the Sun (Taurus, Ophiuchus, Orion, etc.). The proximity of the Gould Belt star formation regions means that these are the sites where the spatial and mass sensitivities of our observations are highest.

High-resolution ground-based submillimetre observations have mapped dense cores within Gould Belt regions (e.g., [15, 43]), but they were limited to targeted

J. Kirk (✉)
Jeremiah Horrocks Institute, University of Central Lancashire, Preston, Lancashire, PR1 2HE, UK
e-mail: jmkirk@uclan.ac.uk

D. Stamatellos et al. (eds.), *The Labyrinth of Star Formation*, Astrophysics and Space Science Proceedings 36, DOI 10.1007/978-3-319-03041-8_42,

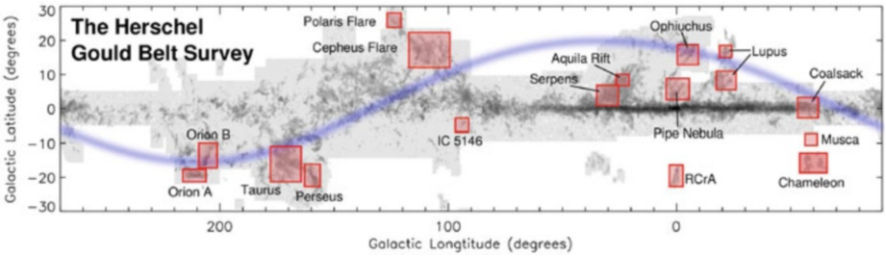

Fig. 1 The disc of our galaxy and the regions mapped by the HGBS. The scatter of parallel-mode pointing centres are shown by the *labelled boxes*. The Gould Belt is shown by the curve [31]. The *greyscale* shows integrated CO emission [6]

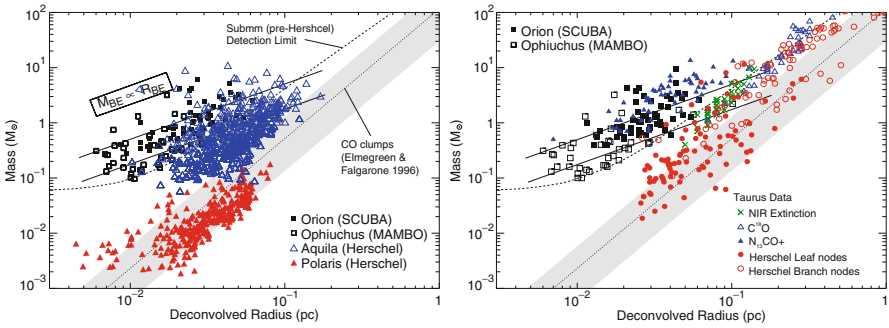

Fig. 2 Mass-size diagrams for dense cores. The *square symbols* show cores in Orion and Ophiuchus observed with ground-based submm telescopes [22, 23]. The *thick-grey band* shows the parameter space occupied by cores in CO line observations [7]. (*left*) The *open* and *filled triangles* show Herschel cores in Aquila [16] and Polaris [19] respectively that were detected with the GETSOURCES [20]. (*right*) The *open* and *filled circles* show leaf nodes (resolved cores without substructure) and branch nodes (cores with resolved substructure, cf. clumps) detected towards B18/L1536 Taurus using the CSAR dendrogram algorithm [14]. The *open triangles*, *filled triangles*, and *crosses* show cores detected towards Taurus in $C^{18}O$ [25], $N^{13}C0+$ [26], and NIR extinction [38]. The *solid-black lines* show the critical loci for 7 K and 20 K Bonner-Ebert spheres

observations of a few dozen objects at a time. Pushing the same telescopes to their absolute limits showed that the prestellar core mass function (CMF) was coincident with the form of the initial mass function (IMF) (e.g., [22, 24]). However, these ground-based studies were limited by the excessively long time it took to map each region. It also appeared that cores mapped in CO line emission were larger and more diffuse than those cores mapped with the submillimetre continuum (see Fig. 2 left panel).

The *Herschel* Gould Belt Survey (HGBS; [1, 2]) is an ESA *Herschel* Space Observatory[1] [33] key project designed to over come the sensitivity, mapping speed,

[1]Herschel is an ESA space observatory with science instruments provided by European-led Principal Investigator consortia and with important participation from NASA.

and sample size limitations of ground-based surveys. It is an imaging survey of the Gould Belt regions shown in Fig. 1 using the PACS [34] and SPIRE [9,40] cameras. The SPIRE/PACS parallel-scanning mode allows us to simultaneously observe five bands between 70 and 500 μm and thus reconstruct the cold dust spectrum toward each point in the maps. This, combined with *Herschel*'s high mapping speed, allows us to map thousands of prestellar cores and hundreds of embedded protostars (HGBS Proposal[2]).

2 Clouds and Cores

The first two regions observed for the HGBS were the Aquila Rift [1, 5, 16] and the Polaris Flare [19, 21, 41]. The left panel of Fig. 2 shows a plot of deconvolved radius versus mass for cores extracted from the Aquila (open triangles) and Polaris (filled triangles) Herschel maps. These cores were extracted with the GETSOURCES algorithm [20]. For a given radius *Herschel* is detecting cores over a mass range in excess of 3 dex, bridging the gap between the earlier submillimetre (square symbols) and CO (the grey band) observations.

Furthermore, Fig. 2 also shows that cores observed in Polaris and Aquila have quite different masses. The Polaris cores are more diffuse and their mean mass is below the peak of the IMF [1, 19], indeed it is doubtful whether even the densest cores in Polaris are bound [41]. The lack of dense cores meant that [21] were able to measure the Herschel 250 μm power-spectrum towards Polaris over a spatial range of 0.01–8 pc. The Polaris power-spectrum was well described by a single power-law showing that turbulence was the dominant process on those scales.

The Aquila Rift was shown to be markedly different from Polaris. As shown in Fig. 2, a large number of its cores were coincident on the mass-size plain with the earlier SCUBA observations of prestellar cores. The CMF of the Aquila cores peaked at a mass higher than the IMF and could be fitted with a log-normal function or a power-law at the high mass end [16]. This showed that the CMF mimicked the shape of the IMF, confirming earlier ground-based observations. Comparison with the expected the mass/radius relationship for Bonner-Ebert cores (the M_{BE} trend in Fig. 2) showed that the cores in Aquila were mainly bound [16].

The right-hand panel of Fig. 2 shows the mass-size diagram for cores in the B18/L1536 region of Taurus extracted using the CSAR dendrogram algorithm [14]. The B18/L1536 cores appear to be intermediate in mass between the Polaris and Aquila cores. The main body of them sits on the same trend as the Polaris cores, but there is a scatter up into the bound region. Thus unbound starless cores and bound prestellar cores form a continuous distribution on the mass-size plane [14]. We would not have been able to convincingly populate this plane without *Herschel*'s high dynamic range and mapping speed.

[2] http://gouldbelt-herschel.cea.fr

3 Filaments

The shear ubiquity of filamentary structure was one of the most significant early results from Herschel. The existence of such filamentary structure in regions of star formation had been pointed out sometime ago (e.g., Barnard [4] commented on "dark lanes" of obscuration and Loren [17] coined the famous phrase "Cobwebs of Ophiuchus") and it appears to be a nearly universal feature in simulations of interstellar turbulence (e.g., [10]). However, filaments had not received as much attention as dense cores in the literature[3] Herschel changed this.

André et al. [1] analysed the filaments found in the Aquila and Polaris regions. They showed that filaments in Aquila associated with dense cores had a mass per unit length that exceeded the critical value for equilibrium ($M_{crit} = 2c_s^2/G$ where c_s is the sound speed [12, 13]). Conversely the filaments in Polaris, in common with its dense cores, were all found to be subcritial. Arzoumanian et al. [3] extended this analysis by using the DisPerSE computational topology package [39] to trace the filament network in IC 5145 and to construct mean column density profiles for each filament. A density profile that falls off as $\rho(r) \propto r^{-p}$ at large radii was fitted to each filament. A self-gravitating isothermal equilibrium filament would be expected to have an exponent of $p = 4$ [27], yet Arzoumanian et al. [3] found a best fit value of $p = 2$.

A significant result to come out of the filament profiling was that the filaments in Aquila, Polaris, and IC 5146 all have a mean Gaussian FWHM of ∼0.1 pc [3], as do the filaments of the Pipe Nebula [30] and B211/212 region of Taurus [29]. This is below the width that turbulence becomes subsonic. It is possible that filaments form first, possibly from colliding super-sonic turbulent flows (e.g. [28]), the dynamically stagnant gas then undergoes gravitational fragmentation to form dense cores [1, 3]. This scenario is supported by the result from Aquila [1] and Orion [35] that bound cores seem to be preferentially associated with filaments.

4 Protostars

Studies of protostars rely on a broad wavelength range to cover the entire breadth of the protostar/YSO SED. What *Herschel* brings to this type of multi-telescope analysis is its sensitivity to low masses of cold material. In Perseus, Pezzuto et al. [32] postulated that the core B1-bS may harbour an early YSO, a first-hydrostatic core, as it was detected by *Herschel*, but not by Spitzer. A younger object again was found in Perseus by Sadavoy et al. [37] who discovered a fragmented $100\,M_\odot$ clump that contained no embedded YSOs. A kinematic analysis using

[3]Between 1980 and 2000 the words "filament" and "core" appear in the ratio of 1:4 in ADS abstracts of papers associated with the keyword "star formation".

GBT data showed that only one of the fragments was bound and the clump thus represented a pristine example of core formation.

Bontemps et al. [5], also Konyves et al (this volume), examined *Herschel* detected YSOs in Aquila and used their SEDs to estimate envelope masses and luminosities which were plotted on a protostellar evolutionary diagram. Complementary 1.2 mm MAMBO data allowed Maury et al. [18] to refine the *Herschel* luminosities and suggest that the Class I/0 border line should be moved slightly from 5 % of L_{submm}/L_{bol} to just 3 % to better match the theoretical concept of a Class 0 source.

Including Herschel/Spitzer data for every YSO in a region allows those sources to be accurately classified and for increasingly accurate statistics to be preformed. Winston et al. [42] showed that there was no difference in the Herschel colours of Class I and Class II sources. Thus shorter wavelength data is needed to separate these sources from one another. Rygl et al. [36] used statistical analysis of Herschel/Spitzer YSO SEDs to show that different regions within Lupus had different star formation histories based on the frequency of detected object compared to that inferred from a constant star formation rate.

5 Summary

Herschel's high dynamic range has shown the commonalities between the different star formation regions of the Gould Belt. It has shown that there is a single continuous core population ranging from diffuse unbound starless cores to dense bound prestellar cores. Furthermore, it appears that these bound cores are associated with supercritical filaments and that these filaments have a universal width. *Herschel* has also shown us how the differing histories of each region can lead to them having fewer or more bound cores and how those histories also translate into different detection rates for protostellar sources. Understanding these differing histories will be key to our analysis moving forward.

References

1. André P., Men'shchikov A., Bontemps S., et al., 2010, A&A, 518, L102
2. André P., Saraceno P., 2005, in Wilson A., ed., ESA Special Publication Vol. 577 of ESA Special Publication, Probing the earliest phases of star formation: an Herschel photometric survey of nearby molecular clouds. pp 179–184
3. Arzoumanian D., André P., Didelon P., et al., 2011, A&A, 529, L6
4. Barnard E. E., 1919, ApJ, 49, 1
5. Bontemps S., André P., Könyves V., et al., 2010, A&A, 518, L85
6. Dame T. M., Hartmann D., Thaddeus P., 2001, ApJ, 547, 792
7. Elmegreen B. G., Falgarone E., 1996, ApJ, 471, 816
8. Gould B., 1879, Uranometria Argentina, Resultados del Observatorio Nacional Argentino en Cordoba Vol. 1. Buenos Aires: P.E. Coni
9. Griffin M. J., et al., 2010, A&A, 518, L3

10. Hartmann L., Ballesteros-Paredes J., Bergin E. A., 2001, ApJ, 562, 852
11. Herschel Sir J. F. W., 1847, Results of astronomical observations made during the years 1834, 5, 6, 7, 8, at the Cape of Good Hope; being the completion of a telescopic survey of the whole surface of the visible heavens, commenced in 1825
12. Inutsuka S.-I., Miyama S. M., 1992, ApJ, 388, 392
13. Inutsuka S.-I., Miyama S. M., 1997, ApJ, 480, 681
14. Kirk J., Ward-Thompson D., Palmeirim P., et al., 2013, MNRAS, 432, 1424
15. Kirk J. M., Ward-Thompson D., André P., 2005, MNRAS, 360, 1506
16. Könyves V., André P., Men'shchikov A., et al., 2010, A&A, 518, L106
17. Loren R. B., 1989, ApJ, 338, 902
18. Maury A. J., André P., Men'shchikov A., Könyves V., Bontemps S., 2011, A&A, 535, A77
19. Men'shchikov A., André P., Didelon P., et al., 2010, A&A, 518, L103
20. Men'shchikov A., André P., Didelon P., Motte F., Hennemann M., Schneider N., 2012, A&A, 542, A81
21. Miville-Deschênes M.-A., Martin P. G., Abergel A., et al., 2010, A&A, 518, L104
22. Motte F., Andre P., Neri R., 1998, A&A, 336, 150
23. Motte F., André P., Ward-Thompson D., Bontemps S., 2001, A&A, 372, L41
24. Nutter D., Ward-Thompson D., 2007, MNRAS, 374, 1413
25. Onishi T., Mizuno A., Kawamura A., Ogawa H., Fukui Y., 1996, ApJ, 465, 815
26. Onishi T., Mizuno A., Kawamura A., Tachihara K., Fukui Y., 2002, ApJ, 575, 950
27. Ostriker J., 1964, ApJ, 140, 1056
28. Padoan P., Juvela M., Goodman A. A., Nordlund Å., 2001, ApJ, 553, 227
29. Palmeirim P., Andre P., Kirk J., et al., 2013, A&A, 550, 38
30. Peretto N., André P., Könyves V. o., 2012, A&A, 541, A63
31. Perrot C. A., Grenier I. A., 2003, A&A, 404, 519
32. Pezzuto S., Elia D., Schisano E., 2012, A&A, 547, 54
33. Pilbratt G. L., et al., 2010, A&A, 518, L1
34. Poglitsch A., et al., 2010, A&A, 518, L2
35. Polychroni D., Schisano E., Elia D., et al., 2013, ApJ, 777, L33
36. Rygl K.L.J., Benedettini M., Schisano E., et al., 2013, A&A, 549, L1
37. Sadavoy S. I., di Francesco J., André P., et al., 2012, A&A, 540, A10
38. Schmalzl M., et al., 2010, ApJ, 725, 1327
39. Sousbie T., 2011, MNRAS, 414, 350
40. Swinyard B. M., et al., 2010, A&A, 518, L4
41. Ward-Thompson D., Kirk J. M., André P., et al., 2010, A&A, 518, L92
42. Winston E., Cox N.L.J., Prusti, T., et al., 2012, A&A, 545, 145
43. Young C. H., et al., 2006, AJ, 132, 1998

Unraveling the Labyrinth of Star Formation with *Herschel*

Philippe André, Vera Könyves, Doris Arzoumanian, Pedro Palmeirim, and Herschel Gould Belt Survey Consortium

Abstract Recent studies of nearby interstellar clouds with the *Herschel* Space Observatory have provided us with unprecedented images of the initial conditions and early phases of the star formation process. The *Herschel* images point to the central role of filaments in star formation and to their likely connection to interstellar turbulence. Overall, the *Herschel* results suggest that it may be possible to understand both the IMF and the global rate of star formation in galaxies by studying the physics of how dense structures (e.g. filaments, cores) form and grow in the ISM of our own Galaxy. Despite an apparent complexity, global star formation may be governed by relatively simple universal laws from filament to galactic scales.

P. André (✉) • P. Palmeirim
Laboratoire d'Astrophysique (AIM) de Paris-Saclay, CEA/DSM-CNRS-Université Paris Diderot, IRFU/Service d'Astrophysique, CEA Saclay, Orme des Merisiers, 91191 Gif-sur-Yvette, France
e-mail: pandre@cea.fr; doris.arzoumanian@ias.u-psud.fr

V. Könyves
Laboratoire d'Astrophysique (AIM) de Paris-Saclay, CEA/DSM-CNRS-Université Paris Diderot, IRFU/Service d'Astrophysique, CEA Saclay, Orme des Merisiers, 91191 Gif-sur-Yvette, France

Institut d'Astrophysique Spatiale, UMR8617, CNRS/Université Paris-Sud 11, 91405 Orsay, France
e-mail: vera.konyves@cea.fr

D. Arzoumanian
Laboratoire d'Astrophysique (AIM) de Paris-Saclay, CEA/DSM-CNRS-Université Paris Diderot, IRFU/Service d'Astrophysique, CEA Saclay, Orme des Merisiers, 91191 Gif-sur-Yvette, France

Current address: IAS, CNRS (UMR 8617), Université Paris-Sud; Batiment 121, 91400 Orsay, France
e-mail: doris.arzoumanian@ias.u-psud.fr

Herschel Gould Belt Survey Consortium
http://www.herschel.fr/cea/gouldbelt/en/index.php

D. Stamatellos et al. (eds.), *The Labyrinth of Star Formation*, Astrophysics and Space Science Proceedings 36, DOI 10.1007/978-3-319-03041-8_43,

1 Introduction

Star formation is one of the most complex processes in astrophysics, involving a subtle interplay between gravity, turbulence, magnetic fields, feedback mechanisms, heating and cooling effects etc. ... Yet, despite this apparent complexity, the net products of the star formation process on global scales are relatively simple and robust. In particular, the distribution of stellar masses at birth or stellar initial mass function (IMF) is known to be quasi-universal (e.g. [6, 7, 20]). Likewise, the star formation rate on both GMC and galaxy-wide scales is related to the mass of (dense molecular) gas available by rather well defined "star formation laws" (e.g. [10, 18, 21]). On the basis of recent results obtained with the *Herschel* Space Observatory on nearby interstellar clouds as part of the Gould Belt [2], HOBYS [27], and Hi-GAL [26] surveys, the thesis advocated here is that it may be possible to explain, at least partly, the IMF and the global rate of star formation in terms of the quasi-universal filamentary structure of the cold interstellar medium out of which stars form.

2 The Key Role of Filaments in the Core Formation Process

The high quality and dynamic range of the *Herschel* images are such that they provide key information on both dense cores on small (<0.1 pc) scales *and* the structure of the parent background cloud on large (>1 pc) scales. In particular, one of the most spectacular early findings made with *Herschel* is the ubiquitous presence of long (>pc scale) filamentary structures in the cold interstellar medium (ISM) and the apparently tight connection between the filaments and the formation process of dense cores (e.g. [2,24,26]). Remarkably, filaments are omnipresent even in diffuse, non-star-forming complexes such as the Polaris translucent cloud (cf. Fig. 1a – [25, 35]). Moreover, in any given cloud complex, the *Herschel* images reveal a whole network of filaments (see Fig. 1), making it possible to characterize their properties in a statistical manner. Detailed analysis of the radial column density profiles derived from *Herschel* data shows that the filaments are characterized by a very narrow distribution of central widths with a typical FWHM value of ∼0.1 pc [5]. A plausible interpretation of this characteristic width of interstellar filaments is that it corresponds to the sonic scale below which interstellar turbulence becomes subsonic in diffuse, non-star-forming gas (cf. [8, 31]).

The observed correspondence between the filaments and the spatial distribution of compact cores is also remarkable (see Fig. 1b), suggesting that *dense cores form primarily along filaments*. More precisely, the prestellar cores identified with *Herschel* are preferentially found within the *densest filaments* with masses per unit length exceeding $\sim 15\ M_\odot$/pc and column densities exceeding $\sim 7 \times 10^{21}$ cm^{-2} ([2] and Fig. 1b). In the Aquila region, for instance, the distribution of background

cloud column densities for the prestellar cores shows a steep rise above $N_{\rm H_2}^{\rm back} \sim 5 \times 10^{21}\,{\rm cm}^{-2}$ and is such that ∼90 % of the candidate bound cores are found above a background column density $N_{\rm H_2}^{\rm back} \sim 7 \times 10^{21}\,{\rm cm}^{-2}$, corresponding to a background visual extinction $A_V^{\rm back} \sim 8$ ([2]; Könyves et al., in prep.). The *Herschel* observations of the Aquila Rift complex therefore strongly support the existence of a column density or visual extinction threshold for the formation of prestellar cores at $A_V^{\rm back} \sim 5$–10, which had been suggested based on earlier ground-based studies of, e.g., Taurus and Ophiuchus (cf. [11, 17, 29]). In the Polaris flare, our results are also consistent with such an extinction threshold since the observed background column densities are all below $A_V^{\rm back} \sim 8$ and there are no examples of bound prestellar cores in this cloud. Moreover, the *Herschel* results provide an *explanation* of this threshold in terms of the filamentary structure of molecular clouds. Given the characteristic width ∼0.1 pc measured for the filaments [5], the threshold at $A_V^{\rm back} \sim 8$ or $\Sigma_{\rm gas}^{\rm back} \sim 130\ M_\odot\,{\rm pc}^{-2}$ corresponds to within a factor of <2 to the critical mass per unit length $M_{\rm line,crit} = 2\,c_s^2/G \sim 15\,M_\odot/{\rm pc}$ required for the hydrostatic equilibrium of isothermal filaments (cf. [16, 30]), where $c_s \sim 0.2$ km/s is the isothermal sound speed for a typical gas temperature $T \sim 10$ K. Thus, the core formation threshold approximately corresponds to the *threshold above which interstellar filaments are gravitationally unstable*. Prestellar cores are only observed above this threshold because they form out of a filamentary background and only the supercritical, gravitationally unstable filaments with $M_{\rm line} > M_{\rm line,crit}$ are able to fragment into bound cores (cf. [2] and Fig. 1b).

3 Toward a Universal Scenario for Core and Star Formation?

The *Herschel* results summarized in Sect. 2 provide key insight into the core formation process. They led André et al. [2] to favor a scenario according to which the formation of prestellar cores occurs in two main steps. First, large-scale magneto-hydrodynamic (MHD) turbulence generates a whole network of filaments in the ISM (cf. [32]); second, the densest filaments fragment into prestellar cores by gravitational instability (cf. [16]).

That the formation of filaments in the diffuse ISM represents the first step toward core/star formation is suggested by the filaments *already* being omnipresent in a gravitationally unbound, non-star-forming cloud such as Polaris (cf. Fig. 1a, [24], and [25]). This indicates that interstellar filaments are not produced by large-scale gravity and that their formation must precede star formation. It is also consistent with the view that the filamentary structure results primarily from the dissipation of large-scale interstellar turbulence (cf. [14, 32]). In this view, interstellar filaments correspond to dense, post-shock stagnation gas associated with compressed regions between interacting supersonic flows. One merit of this picture is that it accounts

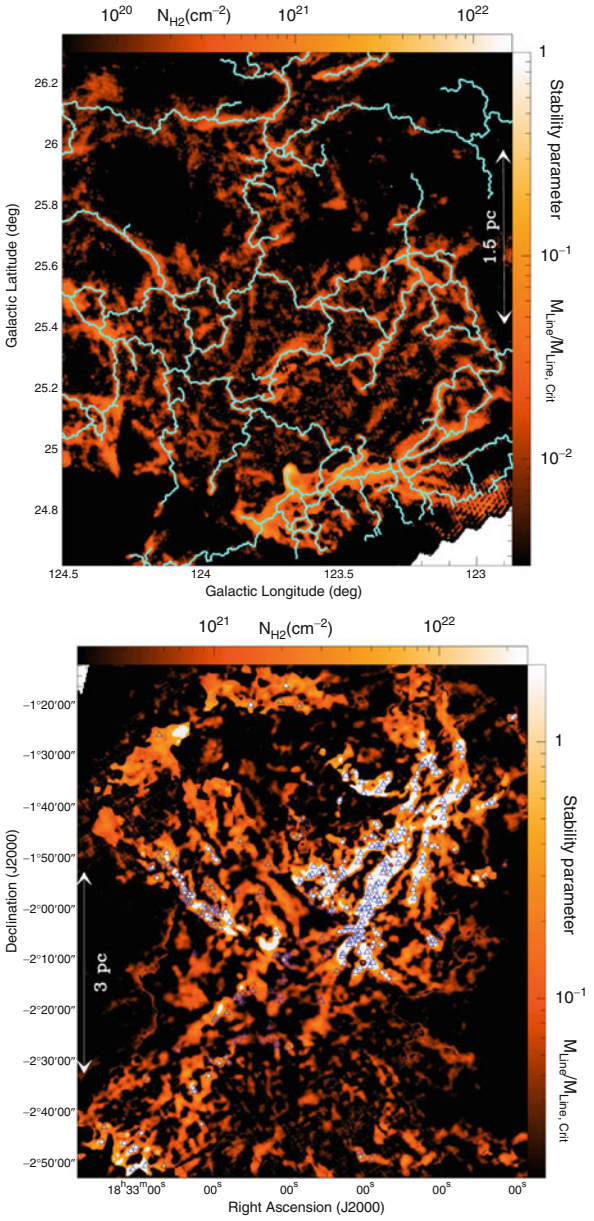

Fig. 1 Column density maps of two subfields in Polaris (*top*) and Aquila (*bottom*) derived from *Herschel* Gould Belt survey data [2]. The contrast of the filaments has been enhanced using a curvelet transform (cf. [34]). The skeleton of the filament network identified in Polaris with the DisPerSE algorithm [33] is shown in *light blue* in the *upper panel*. Given the typical width ∼0.1 pc of the filaments [5], these maps are equivalent to *maps of the mass per unit length along the filaments*. The areas where the filaments have a mass per unit length larger than half the critical value $2\,c_s^2/G$ and are thus likely gravitationally unstable have been highlighted in *white*. The bound prestellar cores identified by Könyves et al. [19] in Aquila are shown as *small blue triangles* in the *bottom panel*; there are no bound cores in Polaris

for the characteristic ∼0.1 pc width of the filaments as measured with *Herschel*: the typical thickness of shock-compressed structures resulting from supersonic turbulence in the ISM is expected to be roughly the sonic scale of the turbulence or precisely ∼0.1 pc in diffuse interstellar gas (cf. [22] and discussion in [5]).

The second step appears to be the gravitational fragmentation of the densest filaments with supercritical masses per unit length ($M_{\rm line} > M_{\rm line,crit}$) into self-gravitating prestellar cores ([2] – cf. Sect. 2). Indeed, in active star-forming regions such as the Aquila complex, most of the prestellar cores identified with *Herschel* are concentrated within supercritical filaments (cf. Fig. 1b). In contrast, in non-star-forming clouds such as Polaris, all of the filaments have subcritical masses per unit length and only unbound starless cores are observed but no prestellar cores nor protostars (cf. Fig. 1a).

Interestingly, the peak of the prestellar core mass function (CMF) at $\sim$0.6 $M_\odot$ as observed in the Aquila complex [2, 19] corresponds to the Jeans or Bonnor-Ebert mass $M_{\rm BE} \sim 0.6\,M_\odot \times (T/10\,{\rm K})^2 \times \left(\Sigma/150\,M_\odot\,{\rm pc}^{-2}\right)^{-1}$ within marginally critical filaments with $M_{\rm line} \approx M_{\rm line,crit} \sim 15\,M_\odot$/pc and surface densities $\Sigma \approx \Sigma_{\rm gas}^{\rm crit} \sim 150\,M_\odot\,{\rm pc}^{-2}$. Likewise, the median spacing $\sim$0.08 pc observed between the prestellar cores of Aquila roughly matches the thermal Jeans length within marginally critical filaments. All of this is consistent with the idea that gravitational fragmentation is the dominant physical mechanism generating prestellar cores along filaments in molecular clouds. Furthermore, a typical prestellar core mass of $\sim$0.6 $M_\odot$ translates into a characteristic star or stellar system mass of $\sim$0.2 $M_\odot$, assuming a typical efficiency $\epsilon_{\rm core} \sim 30\,\%$ (cf. [1, 2, 28]). Therefore, our *Herschel* findings strongly support Larson's [23] interpretation of the peak of the IMF in terms of the typical Jeans mass in star-forming clouds. Naively, one would expect gravitational fragmentation to result in a narrow prestellar CMF sharply peaked at the median thermal Jeans mass. However, a broad CMF resembling the log-normal shape of the IMF can be produced if turbulence has generated a field of initial density fluctuations within the filaments in the first place (cf. [15]). Overall, our results suggest that the gravitational fragmentation of supercritical filaments produces the prestellar CMF which, in turn, accounts for the log-normal "base" (cf. [6]) of the IMF. It remains to be seen, however, whether the bottom end of the IMF and the Salpeter power-law slope at the high-mass end can also be explained by filament fragmentation. In particular, we note that the pre-brown dwarf core Oph B-11 recently identified by André, Ward-Thompson, and Greaves [4] in the L1688 protocluster is *not* associated with a filament of the Ophiuchus cloud and has most likely formed in a different manner through, e.g., turbulent fragmentation (e.g. [13, 31]).

The realization that prestellar core formation occurs primarily along gravitationally unstable filaments also has potential implications for our understanding of star formation on global Galactic and extragalactic scales. Remarkably, the critical line mass of a filament, $M_{\rm line,crit} = 2\,c_s^2/G$, depends only on gas temperature (i.e., $T \sim 10\,{\rm K}$ for the bulk of molecular clouds, away from the immediate vicinity of massive stars) and is modified by only a factor of order unity for filaments with realistic levels of magnetization (cf. [9]). This may set a quasi-universal threshold for star formation in the cold ISM of galaxies at $\sim$15 $M_\odot$/pc in terms of filament mass per unit length, or $\sim$150 $M_\odot\,{\rm pc}^{-2}$ in terms of gas surface density. Indeed, recent near-/mid-infrared studies of the star formation rate as a function of gas

surface density in both Galactic and extragalactic cloud complexes (e.g. [12, 21]) show that the star formation rate tends to be linearly proportional to the mass of dense gas above a surface density threshold $\Sigma_{\rm gas}^{\rm th} \sim 120$–$130\,M_\odot\,{\rm pc}^{-2}$ and drops to negligible values below $\Sigma_{\rm gas}^{\rm th}$ (see [10] for external galaxies). Note that this is the *same* threshold as found with *Herschel* for the formation of prestellar cores ([3] – cf. Sect. 2). Moreover, the relation between the star formation rate SFR and the mass of dense gas $M_{\rm dense}$ above the threshold is estimated to be $SFR = 4.6 \times 10^{-8}\,M_\odot\,{\rm year}^{-1} \times (M_{\rm dense}/M_\odot)$ by Lada et al. [21], which is close to the relation $SFR = 2 \times 10^{-8}\,M_\odot\,{\rm year}^{-1} \times (M_{\rm dense}/M_\odot)$ found by Gao and Solomon [10]. Both of these values are very similar to the star formation rate per unit solar mass of dense gas of $0.15 \times 0.3/10^6 \sim 4.5 \times 10^{-8}\,M_\odot\,{\rm year}^{-1}$ that we may derive based on *Herschel* in the Aquila complex by considering that only $\sim$15 % of the cloud mass above the column density threshold is in the form of prestellar cores, that the local star formation efficiency at the level of an individual core is $\epsilon_{\rm core} \sim 30\,\%$ (cf. [2]), and that the typical lifetime of the Aquila cores is $\sim 10^6$ year (Könyves et al., in prep.). Despite relatively large uncertainties, the agreement with the extragalactic value of Gao and Solomon [10] is surprisingly good, implying that the star formation scenario sketched above may well apply to the ISM of all galaxies.

References

1. Alves, J. F., Lombardi, M., & Lada, C. J. 2007, A&A, 462, L17
2. André, Ph., Men'shchikov, A., Bontemps, S. et al. 2010, A&A, 518, L102
3. André, Ph., Men'shchikov, A., Könyves, V., & Arzoumanian, D. 2011, in Computational Star Formation, IAU Symp. 270, p. 255
4. André, Ph., Ward-Thompson, D., Greaves, J. 2012, Science, 337, 69
5. Arzoumanian, D., André, Ph., Didelon, P. et al. 2011, A&A, 529, L6
6. Bastian, N., Covey, K.R., & Meyer, M.R. 2010, ARA&A, 48, 339
7. Chabrier, G. 2003, PASP, 115, 763
8. Federrath, C., Roman-Duval, J., Klessen, R.S. et al. 2010, A&A, 512, A81
9. Fiege, J.D., & Pudritz, R.E. 2000, MNRAS, 311, 85
10. Gao, Y., & Solomon, P. 2004, ApJ, 606, 271
11. Goldsmith, P.F., Heyer, M., Narayanan, G. et al. 2008, ApJ, 680, 428
12. Heiderman, A., Evans, N.J., Allen, L.E. et al. 2010, ApJ, 723, 1019
13. Hennebelle, P., & Chabrier, G. 2008, ApJ, 684, 395
14. Hily-Blant, P., & Falgarone, E. 2007, A&A, 469, 173
15. Inutsuka, S.-I. 2001, ApJ, 559, L149
16. Inutsuka, S-I, & Miyama, S.M. 1997, ApJ, 480, 681
17. Johnstone, D., Di Francesco, J., & Kirk, H. 2004, ApJ, 611, L45
18. Kennicutt, R. 1998, ApJ, 498, 541
19. Könyves, V., André, Ph., Men'shchikov, A. et al. 2010, A&A, 518, L106
20. Kroupa, P. 2002, Science, 295, 82
21. Lada, C.J., Lombardi, M, & Alves, J. 2010, ApJ, 724, 687
22. Larson, R.B., 1981, MNRAS, 194, 809
23. Larson, R.B. 1985, MNRAS, 214, 379
24. Men'shchikov, A., André, Ph., Didelon, P. et al. 2010, A&A, 518, L103
25. Miville-Deschênes, M.-A., Martin, P.G., Abergel, A. et al. 2010, A&A, 518, L104

26. Molinari, S., Swinyard, B., Bally, J. et al. 2010, A&A, 518, L100
27. Motte, F., Zavagno, A., Bontemps, S. et al. 2010, A&A, 518, L77
28. Nutter, D., & Ward-Thompson, D. 2007, MNRAS, 374, 1413
29. Onishi, T., Mizuno, A., Kawamura, A. et al. 1998, ApJ, 502, 296
30. Ostriker, J. 1964, ApJ, 140, 1056
31. Padoan, P. & Nordlund, A. 2004, ApJ, 617, 559
32. Padoan, P., Juvela, M., Goodman, A.A., & Nordlund, A. 2001, *ApJ*, 553, 227
33. Sousbie, T., 2011, MNRAS, 414, 350
34. Starck, J. L., Donoho, D. L., Candès, E. J. 2003, A&A, 398, 785
35. Ward-Thompson, D., Kirk, J.M., André, P. et al. 2010, A&A, 518, L92

CALYPSO: An IRAM Plateau de Bure Survey of Class 0 Protostars

Anaëlle J. Maury, Philippe André, S. Maret, C. Codella, F. Gueth, A. Belloche, S. Cabrit, A. Bacmann, and CALYPSO Collaboration

Abstract The physics of the youngest protostars, e.g. Class 0 objects, remains poorly understood. For instance, the processes by which the angular momentum present in the parent core is conserved during the main collapse phase, e.g. during the formation of the protostar in the inner envelope, are still largely unknown. Solving this long-standing "angular momentum problem" is of paramount importance for our understanding of solar-type star formation. To this end, we started a comprehensive study of a large sample of Class 0 protostars, observed with the IRAM Plateau de Bure Interferometer. The *CALYPSO* (Continuum And Line Young ProtoStellar Object) survey aims at characterizing 17 nearby protostars and

A.J. Maury (✉)
Harvard-Smithsonian Center for Astrophysics, 60 Garden Street Cambridge, MA 02138, USA
e-mail: amaury@cfa.harvard.edu

P. André
Laboratoire d'Astrophysique (AIM) de Paris-Saclay, CEA/DSM-CNRS-Université Paris Diderot, IRFU/Service d'Astrophysique, CEA Saclay, Orme des Merisiers, 91191 Gif-sur-Yvette, France
e-mail: pandre@cea.fr

S. Maret • A. Bacmann
Universite Joseph Fourier/CNRS, Institut de Planetologie et d'Astrophysique de Grenoble (IPAG) UMR 5274, Grenoble, France

C. Codella
INAF-Osservatorio Astrofisico di Arcetri, Largo E. Fermi 5, I-50125 Firenze, Italy

F. Gueth
IRAM, 300 Rue de la Piscine, 38406 Saint Martin d'Heres, France

A. Belloche
Max-Planck Institute fur Radiodastronomie, Auf dem Hugel 69, 5321 Bonn, Germany

S. Cabrit
Observatoire de Paris, LERMA, 61 Av de l'Observatoire, 75014 Paris, France

CALYPSO Collaboration

D. Stamatellos et al. (eds.), *The Labyrinth of Star Formation*, Astrophysics and Space Science Proceedings 36, DOI 10.1007/978-3-319-03041-8_44,

is the most complete sub-arcsecond resolution survey of Class 0 objects carried out so far in the millimeter bands. Here, we describe the details of this ambitious observing program.

1 Class 0 Protostars

Observationally, the key to constraining models for the formation of solar-type stars lies in high-resolution studies of the youngest protostars. Class 0 objects, which were originally discovered at millimeter wavelengths, are believed to be such very young accreting protostars [1]. Because they are observed only $t \lesssim 0.1$ Myr after their formation, while most of their mass is still in the form of a dense core/envelope ($M_{env} \gg M_{\star}$), Class 0 protostars are likely to retain detailed information on the initial conditions and detailed physics of the main collapse phase (see review by André et al. [2]). They may also represent a pivotal stage in star formation during which the "angular momentum problem" [4] is solved through magnetic braking, centrifugally-driven jets, and the formation of a disc possibly fragmenting into a multiple system.

However, partly due to the paucity of sub-arcsecond (sub)mm observations of Class 0 objects, required to probe their innermost (100 AU) regions, the physics of these youngest protostars is still surprisingly poorly understood. Several basic questions thus remain largely open, such as the mere existence of accretion discs and multiple systems at the Class 0 stage [7], the launching mechanism of protostellar jets and their net contribution to mass and angular momentum extraction, or the chemistry and the velocity field [3] in Class 0 envelopes (e.g. relative importance of heating, inflow, rotation, outflow). These three issues are intimately linked and closely tied to the "angular momentum problem" in star formation. Ultimately, solving this problem is fundamental (1) to determine the efficiency of the accretion/ejection engine and how the prestellar core mass function is transformed into the stellar initial mass function (IMF), (2) to shed light on the formation of protoplanetary discs around stars like our own.

2 *CALYPSO*: The IRAM Continuum and Line Young ProtoStellar Object Survey

Solving the angular momentum problem for solar-type star formation requires to observe a representative sample of young protostars in various complementary tracers allowing to characterize the kinematics of the protostellar envelope, outflow and possible accretion disc. Therefore, we use the IRAM Plateau de Bure Interferometer (PdBI) to carry out a homogeneous survey of 17 nearby, low-luminosity, Class 0 protostars. The details of our observations are described here-below.

2.1 Sources and Setups

Sampling the whole envelope extent and high spatial resolution are mandatory to understand how the angular momentum is conserved in the youngest accreting protostellar envelopes since: (i) the inner centrifugally-supported disc is expected to be small at the Class 0 stage (typically less than 100 AU); (ii) a linear resolution ∼50–150 AU or better is required to probe protobinaries on scales typical of more evolved pre-main sequence binaries; (iii) protostellar jets and conical outflow cavities are very narrow near their base (width ≃50 AU) so studying their angular momentum removal requires 50–150 AU resolution at most; and finally (iv) the sizes of hot corinos where temperatures are >100 K are also expected to be less than 100 AU in low-luminosity protostars. We therefore observe our sources using both the most extended (A) and intermediate (C) configurations of PdBI: the combination of these configurations offers a good compromise between resolution ($0.4'' \sim 50$–100 AU) and final image quality. Since CO(2-1), $C^{18}O$(2-1), and N_2H^+(1-0) have extended emission on scales $>5''$ (large scale flow and dense core/filament) that makes deconvolution inaccurate if not included in the $u - v$ plane, we also acquire zero-spacing data from the IRAM-30 m telescope.

Our sample consists of all but one bona-fide Class 0 objects known as of 2009, that are located at distances $d < 300$ pc and observable from PdBI with a $\lesssim 0.0.4''$ resolution at 1.3 mm. The complete sample is reported in Table 1.

The integration time spent on each source is such that we probe protobinaries with small (e.g. $\lesssim 0.5$) mass ratios, detect the highest velocities in the jets (where most of the power is, but emission is faint [5]), and detect line emission in the compact hot corino/disc, as extrapolated from previous detections [6].

The use of the WideX correlator allows to detect and map serendipitous additional molecular lines over large spectral windows. Altogether, the frequency ranges covered are: [91.87–95.45 GHz]; [216.87–220.45 GHz] and [229.23–232.83 GHz].

2.2 Current Status of the Observations

As of September 2012, more than 80 % of the PdBI observations (and 50 % of the 30-m short-spacings) have been obtained. We expect to reach completion of the *CALYPSO* survey during the first semester of 2013. Publications, reporting the first highlights (see Fig. 1) from the first set of completed observations, are in preparation. Our consortium will release publicly the dataset in 2014, so that the *CALYPSO* survey will provide a long-lasting, uniform database to constrain theoretical models of star, disc, and jet formation.

Table 1 *CALYPSO* sample of Class 0 protostars observed with PdBI

Object	R.A.[a] (J2000)	Dec.[a] (J2000)	Distance (pc)	L_{bol} ($L_\odot$)	M_{env} ($M_\odot$)
L1448-IRS2A	03:25:22.42	+30:45:12.2	220	5	0.9
L1448-N(B)	03:25:36.34	+30:45:14.9	220	7	0.7–1.5
L1448-C	03:25:38.87	+30:44:05.4	220	5	1.6
N1333-IRS2A	03:28:55.58	+31:14:37.1	220	10	1.7
SVS13-A/B	03:29:03.41	+31:15:57.9	220	5.6	2.7
N1333-IRS4A1	03:29:10.53	+31:13:31.0	220	14	7
N1333-IRS4B	03:29:11.98	+31:13:08.1	220	17	3.1
IRAM04191	04:21:56.91	+15:29:46.1	140	0.1	0.5–1.5
L1521-F	04:28:38.99	+26:51:35.6	140	0.1	0.7–4
L1527	04:39:53.90	+26:03:10.0	140	1.6	0.8–1.7
Serp-S68N	18:29:48.10	+01:16:43.6	260	4.4	1.1
Serp-SMM4	18:29:56.70	+01:13:15.0	260	9	3
SerpS-MM18	18:30:03.86	−02:03:04.9	260	5	3
SerpS-MM22	18:30:12.34	−02:06:52.4	260	2	1.5
L1157	20:39:06.19	+68:02:15.9	250	11	0.5
GF9-2	20:51:29.82	+60:18:38.1	200	0.3	0.5
L1172-SMM1	21:02:21.20	+67:54:20.1	290	1.8	0.7

[a]Positions used for phase centers

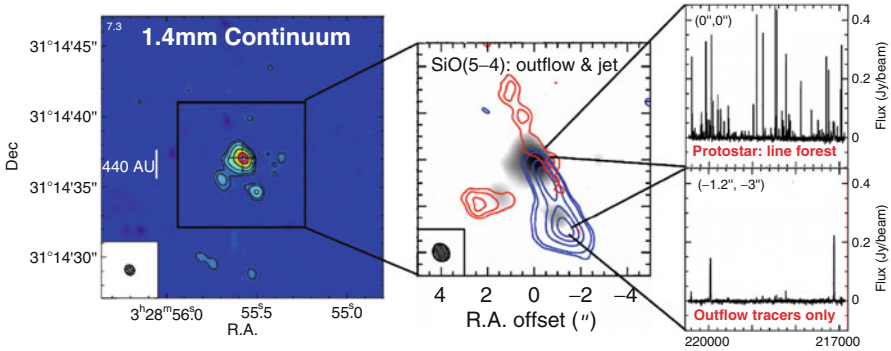

Fig. 1 A first glimpse of the *CALYPSO* view of the low-luminosity protostar NGC 1333-IRS2A (Codella et al. in prep, Maret et al. in prep, Maury et al. in prep)

3 First Highlights

NGC 1333-IRS2A is a young low-luminosity protostar located in the Perseus cloud. CALYPSO observations allow us to reach typical sensitivity and spatial resolution a factor of three to five better than previous observations, in both the spectral lines and continuum emission maps. The PdBI map of the continuum emission, tracing the envelope and compact dusty sources, is presented in the first (left) insert of Fig. 1. Spectral observations obtained over a 3.8 GHz window trace the jet(s) axis (middle

panel) and show that emission from complex molecules (tracing high-excitation temperatures) is copiously observed toward the central part of the envelope, where the protostar stands, while spectra towards high-velocity knots in the jet are almost devoid of complex molecules lines (Codella et al. in prep.). We use these results to address questions on the origin of hot-corinos, and we derive physical sizes and kinematical properties of the material in the inner envelope (Maret et al. in prep, Maury et al. in prep).

References

1. André, P., Ward-Thompson, D., & Barsony, M. 1993, ApJ, 406, 122
2. André, P., Ward-Thompson, D., & Barsony, M. 2000, Protostars and Planets IV, 59
3. Belloche, A., André, P., Despois, D., & Blinder, S. 2002, A&A, 393, 927
4. Bodenheimer, P. 1995, ARA&A, 33, 199
5. Codella, C., Cabrit, S., Gueth, F., et al. 2007, A&A, 462, L53
6. Maret, S., Ceccarelli, C., Caux, E., et al. 2004, A&A, 416, 577
7. Maury, A. J., André, P., Hennebelle, P., et al. 2010, A&A, 512, A40

Initial Results from SCUBA-2

David Nutter and JCMT Gould Belt Survey Consortium

Abstract The JCMT Gould Belt survey has now collected 25 % of its SCUBA-2 data. We report on the quality of these data, and demonstrate how we can map all of the star-formation in the Gould Belt down to our original sensitivity in our allocated time. We describe how the SCUBA-2 and *Herschel* datasets are highly complementary, and how the SCUBA-2 data add value to the *Herschel* data, giving a more reliable measure of the column density at higher angular resolution.

1 Introduction

The Gould Belt is a collection of OB associations and their molecular clouds that lies in a ring across the sky. The belt is approximately 700 parsecs across and the sun lies about 100 parsecs from the centre. The significance of the Gould Belt for studying low-mass star formation, is that it contains almost all of the nearby star formation. For more details, see [6] and references therein.

With the JCMT Gould Belt survey (GBS), we are mapping all of the star formation in the Gould Belt to an unprecedented depth and angular resolution. Each Gould Belt star-formation region that is accessible from the Northern hemisphere is being mapped in the continuum at 450 and 850 μm with 8 and 14″ resolution respectively with the Submillimetre Common-User Bolometer Array-2 (SCUBA-2) camera. In addition, sub-regions of these clouds are being mapped with three isotopes of CO (^{12}CO,^{13}CO and C^{18}O) at 14″ resolution with the Heterodyne Array

D. Nutter (✉)
School of Physics and Astronomy, Cardiff University, Cardiff CF24 3AA, UK
e-mail: david.nutter@astro.cf.ac.uk

JCMT Gould Belt Survey Consortium
http://www.jach.hawaii.edu/JCMT/surveys/gb/

D. Stamatellos et al. (eds.), *The Labyrinth of Star Formation*, Astrophysics and Space Science Proceedings 36, DOI 10.1007/978-3-319-03041-8_45,

Receiver Project (HARP) instrument. The GBS HARP data-set is complete and the initial results can be found in [1–5]. See [8] for more information about the JCMT Gould Belt Survey.

SCUBA-2 contains >5,000 Transition-Edge Sensors at both 450 and 850 μm, which are utilized simultaneously. This represents a leap of two orders of magnitude in detector numbers compared with SCUBA, and gives a corresponding increase in mapping speed. The first GBS SCUBA-2 data were obtained during the science verification (SV) phase in Winter 2011, and the survey is currently 25 % complete.

2 Observing Plan

The observing mode adopted by the GBS is to map 0.5° circular tiles. Larger fields are mapped by arranging these tiles in a hexagonal close packed configuration. A single 40 min observation yields an 1-σ rms of 12–14 mJy/6″-pixel at 850 μ. The target rms sensitivity of 3 mJy/beam is reached in 6–8 repeats.

In order to uphold the GBS's aims of observing all of the star-formation in the Gould Belt down to 3 mJy/beam, we have made use of the 500 μm maps observed with SPIRE on the *Herschel* telescope, kindly provided by the *Herschel* Gould Belt consortium (Konyves 2011, priv. com.). The 850 μm SV data of B1 in the Perseus molecular cloud have a 1-σ rms noise of 3 mJy/beam. These data were compared to the *Herschel*-SPIRE data at 500 μm and it was determined that below the 2 Jy/beam 500 μm contour, we would not expect to detect emission in an 850 μm map with a

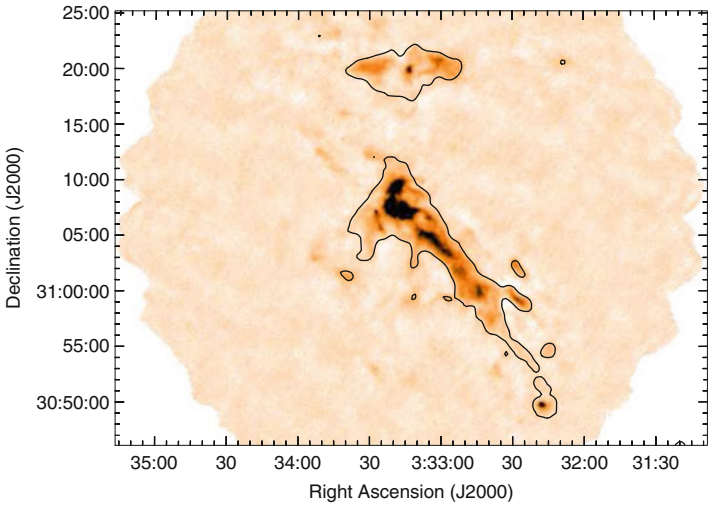

Fig. 1 The SCUBA-2 SV data of B1 shown as a colour-scale, with the 2 Jy/beam 500 μm contour from SPIRE shown as a *black contour*. There is very little structure seen in the SCUBA-2 data outside the SPIRE contour

1-σ rms of 3 mJy/beam. This is illustrated in Fig. 1 which shows the SCUBA-2 SV data of B1 together with the SPIRE contour. There is very little structure seen in the SCUBA-2 data outside the SPIRE contour.

The area of sky above this contour within the Gould Belt clouds that are accessible from the JCMT is ~25 square degrees. The SCUBA-2 Gould belt maps have been designed to cover all of this area. We will therefore map all of the emission in the available Gould Belt clouds at 850 μm that is detectable with a sensitivity of 3 mJy/beam.

3 *Herschel* Complementarity

In order to determine the column density of a source from submillimetre continuum data, it is necessary to break the degeneracy between column density, temperature and the dust emissivity index (β). The *Herschel* data bracket the peak of a cold (~10 K) Spectral energy distribution (SED) which makes it possible to reliably determine the temperature of the emitting dust. This is illustrated in Fig. 2a which shows two grey-body SEDs at different temperatures.

The limitation of solely using *Herschel* data to determine the temperature is that the angular resolution of the resultant information is limited to the resolution of the lowest resolution data. In this case this is the 36″ angular resolution of the 500 μm data. By replacing these data with the 8″ SCUBA-2 450 μm data or the 14″ SCUBA-2 850 μm data, the limiting angular resolution, and hence the grid on which the temperature can be measured, is the 18″ SPIRE 250 μm data.

It is also necessary to determine the β of the dust to determine the column density. β modifies the long-wavelength slope of the grey-body SED. Grey-body SEDs with varying β therefore diverge more at longer wavelengths, thus β is best determined at longer wavelengths. This is illustrated in Fig. 2b. By including the long-wavelength 850 μm SCUBA-2 data, a better estimate of the dust β is obtained.

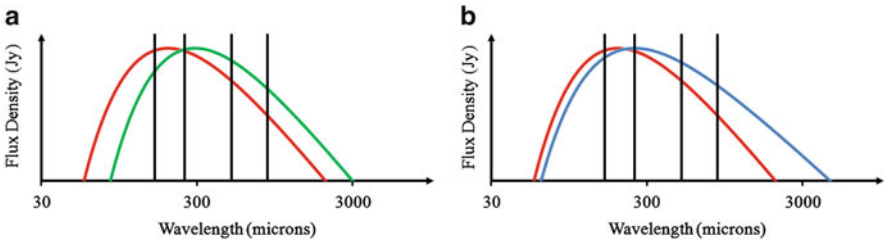

Fig. 2 Spectral energy distributions demonstrating the importance of long-wavelength observations. The *left panel* (**a**) compares an 15 K SED (*Red*) with a 10 K SED (*Green*), both with $\beta = 2$. The *right panel* (**b**) compares SEDs with $\beta = 2$ and $T = 15$ K (*Red*) with $\beta = 1$ and $T = 15$ K (*Blue*). The *vertical lines* mark the *Herschel* wavelengths 160, 250, 500 & also the SCUBA-2 850 μm wavelength

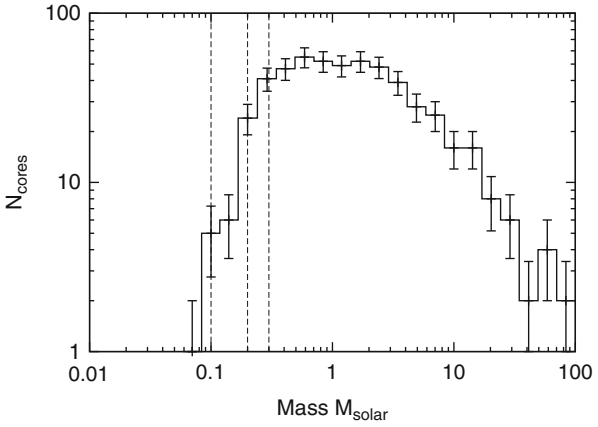

Fig. 3 The CMF measured from the SCUBA-2 data of the Orion A molecular cloud. The three *vertical lines* correspond to the completeness limit from [7] of $0.3\,M_{\odot}$, the $0.2\,M_{\odot}$ limit of the current set of SCUBA-2 data and the $0.1\,M_{\odot}$ limit of the completed survey

4 The Low-Mass Slope of the Core Mass Function

In [7] we showed that the core mass function (CMF) of prestellar cores in the Orion molecular cloud has a peak at $\sim 1\,M_{\odot}$, and decreases to lower masses. This was based on a sample of approximately 200 cores observed across the entire Orion molecular cloud. So far, only 1/3 of the area of Orion-A has been observed with SCUBA-2, and none of this is yet down to the final sensitivity. Even so, by using a contour-based by-eye method, over 500 cores have been identified in these data already. The mass function of these cores is shown in Fig. 3. This mass function is consistent with the earlier CMF of Orion. The figure also shows the completeness limits of the 2007 data ($0.3\,M_{\odot}$), these data ($0.2\,M_{\odot}$), and the limit of the final dataset in this region when all of the data are observed ($0.1\,M_{\odot}$). The slope of the CMF to the left of the peak and its similarity to the low mass side of the stellar IMF will inform us about whether the lowest mass stars form in the same manner as more massive stars, or whether an alternative formation mechanism is required.

5 Conclusion

The JCMT Gould Belt survey will map all of the detectable (to a sensitivity of 3 mJy/beam at 850 μm) emission from the Gould belt molecular clouds within the next 2 years. These data will be highly complementary to the *Herschel* data of the same regions, and will allow a more accurate measure of $n(H_2)$, T and β. As well as a host of other science goals, we will be able to use this information to probe the low-mass side of the CMF with greater accuracy.

References

1. Buckle J. V., et al., 2010, MNRAS, 401, 204
2. Buckle J. V., et al., 2012, MNRAS, 422, 521
3. Christie H., et al., 2012, MNRAS, 422, 968
4. Davis C. J., et al., 2010, MNRAS, 405, 759
5. Graves S. F., et al., 2010, MNRAS, 409, 1412
6. Kirk J., et al., 2012, This Publication
7. Nutter D., Ward-Thompson D., 2007, MNRAS, 374, 1413
8. Ward-Thompson D., et al., 2007, PASP, 119, 855

Surveying Dense Gas with Bolocam: There Are No Pre-stellar Massive Clusters in the First Quadrant

Adam Ginsburg, Eli Bressert, J. Bally, and Cara Battersby

Abstract We search the $\lambda = 1.1$ mm Bolocam Galactic Plane Survey for clumps containing sufficient mass to form $\sim 10^4$ $M_\odot$ star clusters. Eighteen candidate massive proto-clusters are identified in the first Galactic quadrant outside of the central kiloparsec. This sample is complete to clumps with mass $M_{clump} > 10^4$ $M_\odot$ and radius $r \lesssim 2.5$ pc. The overall Galactic massive cluster formation rate is $CFR(M_{cluster} > 10^4) \lesssim 5$ Myr^{-1}. We find that all massive proto-clusters in the first quadrant are actively forming massive stars and place an upper limit of $\tau_{starless} < 0.5$ Myr on the lifetime of the starless phase of massive cluster formation and a strong upper limit on the ratio of the starless timescale to the 'dust-rich' timescale $\tau_{starless}/\tau_{clump} < 0.25$. Our results hint that massive stars form early in massive proto-clusters.

The first surveys of the Galactic Plane in optically thin dust emission have been completed in the past 5 years [1–3]. These provide the best and perhaps only means of measuring star formation in the whole Galactic disk because our perspective from within the plane of the disk means that most starlight and infrared light is obscured. With this first generation of surveys now complete, we can search the Galactic plane for the most massive star-forming regions.

In the Galaxy, there are few known massive clusters. Portegies Zwart et al. [4] catalogs a few of them, of which NGC 3603, Trumpler 14, and Westerlund 1 and 2

A. Ginsburg (✉) • J. Bally • C. Battersby
Center for Astrophysics and Space Astronomy, University of Colorado, Boulder, CO 80309, USA
e-mail: adam.ginsburg@colorado.edu

E. Bressert
European Southern Observatory, Karl Schwarzschild str. 2, 85748 Garching bei München, Germany

D. Stamatellos et al. (eds.), *The Labyrinth of Star Formation*, Astrophysics and Space Science Proceedings 36, DOI 10.1007/978-3-319-03041-8_46,

are young and compact, with $r_{eff} \lesssim 1$ pc, $M \sim 10^4$ M$_\odot$, and ages $t \lesssim 4$ Myr. We have used the Bolocam Galactic Plane Survey to perform a census of their ancestral analogs.

1 Observations and Source Selection

The BGPS is a 1.1 mm survey of the first quadrant of the Galactic plane in the range $-0.5 < b < 0.5$ with resolution $\sim 33''$ sensitive to a maximum spatial scale of $\sim 120''$ [1, 5]. The BGPS 'Bolocat' v1.0 catalog includes sources identified by a watershed decomposition algorithm and flux measurements within apertures of radius $20''$, $40''$, and $60''$ [6].

We searched the BGPS Bolocat catalog for candidate MPCs in the 1st quadrant ($6 < \ell < 90$; 5,991 sources). The inner 6 degrees of the Galaxy are excluded because physical conditions are significantly different from those in the rest of the galaxy [7] and the BGPS is confusion-limited in that region.

We identify a flux-limited sample by setting our search criteria to include all sources with $M_{clump} > 10^4$ M$_\odot$ in a $20''$ radius out to 26 kpc, or a physical radius of 2.5 pc at that distance. The radius cutoff is motivated by completeness and physical considerations: the cutoff of 26 kpc includes the entire star forming disk in our targeted longitudes, and $r = 2.5$ pc corresponds to the radius at which a 3×10^4 M$_\odot$ mass has an escape speed $v_{esc} = 10$ km s^{-1}, i.e. ionized gas will be bound. The maximum radius and minimum mass imply a minimum mean density $\bar{n} = 6 \times 10^3$ cm^{-3}, which implies a maximum free-fall time $t_{ff} < 0.65$ Myr.

The BGPS is insensitive to scales larger than $120''$ [5]. As a result, the survey is incomplete below a distance $D_{min} = 8.6 \left(\frac{r_{cluster}}{2.5\text{pc}} \right)$ kpc from the Sun. However, the results are robust for smaller radius sources, and if a radius ~ 1.5 pc is used, the sample is complete from about 5 kpc outwards (Fig. 1).

Distances to BGPS-selected candidates were determined primarily via literature search. Where distances were unavailable, we used velocity measurements from Schlingman et al. [8] and assumed the far distance for source selection. We then resolved the kinematic distance ambiguity towards these sources by searching for associated near-infrared stellar extinction features from the UKIDSS GPS (see Fig. 2; [9]). Once distances were determined, we used the larger $40''$ radius apertures to determine the flux for sources at $D < 13$ kpc and $60''$ radius apertures for sources at $D < 8.6$ kpc (corresponding to $r < 2.5$ pc).

The masses were computed assuming a temperature $T_{dust} = 20$ K, opacity $\kappa_{271.1\,\text{GHz}} = 0.0114$ cm^2 g^{-1}, and gas-to-dust ratio of 100 [1]. The mass estimate drops by a factor 2.38 if the temperature assumed is doubled to $T_{dust} = 40$ K.

Applying a cutoff of $M_{\text{clump}} > 10^4$ M$_\odot$ left 18 protocluster candidates out of the original 456. The more stringent cut $M_{\text{clump}} > 10^4/SFE \approx 3 \times 10^4$ M$_\odot$ leaves only 3 MPCs.

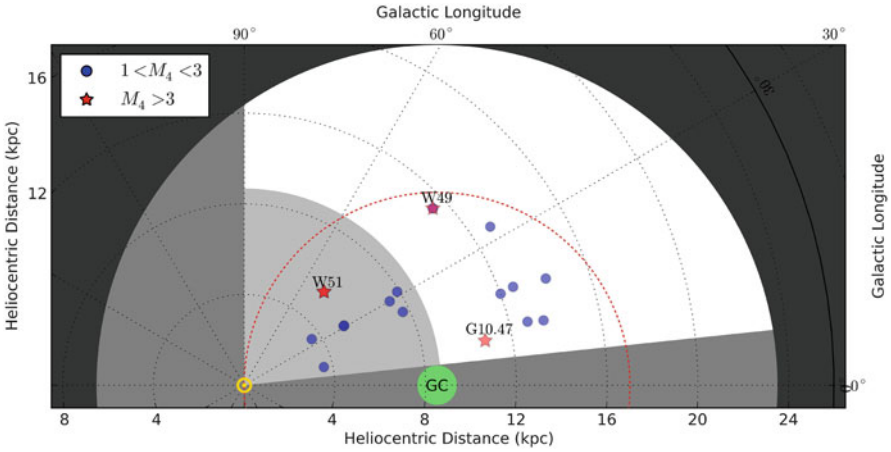

Fig. 1 Plot of the massive proto-cluster (MPC) candidates overlaid on the Galactic plane. The *green circle* represents the galactic center, and the *yellow* ⊙ is the Sun. The *grey region* is a 15 kpc radius disc to indicate the approximate extent of the Galactic star-forming disc. The *white region* indicates the coverage of the Bolocam Galactic Plane survey and our source selection limits based on distance and longitude. The inner cutoff is the nearby incompleteness limit set by the Bolocam spatial filtering; it is shown by a *lighter shade of grey* because we can detect sources there but are incomplete. The *red dashed circle* traces the solar circle and indicates the region in which all detected MPCs are located. *Blue filled circles* represent initial candidates that passed the mass-cutoff criterion ($M(20\,\mathrm{K}) > 10^4\ \mathrm{M}_\odot$); *red stars* are those with $M(20\,\mathrm{K}) > 3 \times 10^4\ \mathrm{M}_\odot$. In the legend, M_4 means mass in units of $10^4\ \mathrm{M}_\odot$

2 Star Formation Activity

In the sample of potential proto-clusters, most are found to be presently forming massive stars both by a literature search and by IRAS association. A few of the low mass sources, G012.209-00.104, G012.627-00.016, G019.474+00.171, and G031.414+00.307 have relatively low IRAS luminosities ($L_{IRAS} = L_{100} + L_{60} < 10^5 L_\odot$) and little free–free emission. However, *all* are detected in the radio as HII regions (some are ultracompact) and have luminosities requiring at least early-B type powering stars.

Non-detection of 'starless' proto-cluster clumps implies an upper limit on the starless lifetime. For an assumed $\tau_{sf} \sim 2\,\mathrm{Myr}$, the 1σ upper limit on the starless proto-MC clump is $\tau_{starless} < (\sqrt{N_{cl}}/N_{cl})\tau_{sf} = 0.5\,\mathrm{Myr}$ assuming Poisson statistics and using all 18 sources. Using a more sophisticated Markov-Chain Monte Carlo test, the non-detection of starless clumps implies an upper limit on the ratio of the starless timescale to the total observable timescale of the proto-cluster (i.e., the time it remains dust-rich) of 0.06 at 68 % confidence or 0.25 at 99.7 % confidence. These limits are consistent with massive star formation within a clump on a timescale less than the clump free-fall timescale ($\tau_{ff} \leq 0.65\,\mathrm{Myr}$). They imply that massive stars form rapidly when these large masses are condensed into cluster-

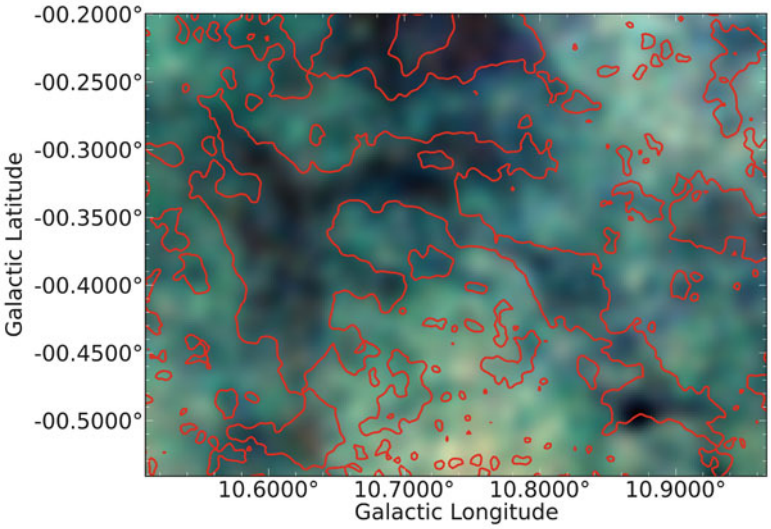

Fig. 2 Example using an infrared source count map to resolve the kinematic distance ambiguity. The *red contours* are of the BGPS 1.1 mm emission at a level of 0.02 Jy ($A_V \approx 1.4$, though the true extinction is greater because the BGPS filters out large-scale structure). There is a clear morphological match between the biggest BGPS contours and the dark patches in which fewer near-IR sources are detected. This region (W31) is an important difficult case where other methods of KDA fail; its LSR velocity indicates that it must be at $D \sim 17$ kpc [10] but its true distance must be within $D \lesssim 5$ kpc

scale regions and hint that massive stars are among the first to form in massive clusters. However, the low starless/starry timescale ratio also suggests that massive star formation is not simultaneous and that large age spreads should be observed in young massive clusters.

3 Discussion: Cluster Formation Rate and Location

Assuming a lower limit 30 % SFE and $T_{dust} = 20$ K, 3 candidates will become massive clusters like NGC 3603: G010.472 + 00.026, W51, and W49 (G043.169 + 00.01). Even if $T_{dust} = 40$ K, W49 is still likely to form a $\sim 10^4$ $M_\odot$ MC, although G10.47 would be too small. W51, which is within the spatial-filtering incompleteness zone, also passes the cutoff and is likely to form a pair of massive clusters.

These most massive sources have escape speeds greater than the sound speed in ionized gas, indicating that they can continue to accrete gas even after the formation of massive stars. Assuming they are embedded in larger-scale gas reservoirs, we are measuring lower bounds on the 'final' clump plus cluster mass.

4 Conclusions

Using the BGPS, we have performed the first flux-limited census of massive proto-cluster candidates. We found 18 candidates that will be part of the next generation of open clusters and 3 that could form massive clusters similar to NGC 3603 ($M_{cluster} > 10^4$ $M_\odot$). We have measured a Galactic massive cluster formation rate $CFR(M_{cluster} > 10^4) \lesssim 5\,\mathrm{Myr}^{-1}$.

Despite this survey being the first sensitive to pre-star-forming MPC clumps, none were detected. This lack of detected pre-star-forming MPCs suggests a timescale upper limit of about $\tau_{starless} < 0.5$ Myr for the pre-massive-star phase of massive cluster formation, and hints that massive clusters may never form highly condensed clumps ($\bar{n} \gtrsim 10^4$ cm^{-3}) prior to forming massive stars. Our results hint that massive stars form early in the cluster formation process, but they leave open the possibility that massive clusters form from large-scale ($\gtrsim$10 pc) accretion onto smaller clumps over a prolonged ($\tau > 2$ Myr) star formation timescale.

Acknowledgements This work was supported by NSF grant AST 1009847.

References

1. J.E. Aguirre, A.G. Ginsburg, M.K. Dunham, M.M. Drosback, J. Bally, C. Battersby, E.T. Bradley, C. Cyganowski, D. Dowell, N.J. Evans, II, J. Glenn, P. Harvey, E. Rosolowsky, G.S. Stringfellow, J. Walawender, J.P. Williams, ApJS **192**, 4 (2011).
2. F. Schuller, K.M. Menten, Y. Contreras, F. Wyrowski, P. Schilke, L. Bronfman, T. Henning, C.M. Walmsley, H. Beuther, S. Bontemps, R. Cesaroni, L. Deharveng, G. Garay, F. Herpin, B. Lefloch, H. Linz, D. Mardones, V. Minier, S. Molinari, F. Motte, L.Å. Nyman, V. Reveret, C. Risacher, D. Russeil, N. Schneider, L. Testi, T. Troost, T. Vasyunina, M. Wienen, A. Zavagno, A. Kovacs, E. Kreysa, G. Siringo, A. Weiß, A&A **504**, 415 (2009).
3. S. Molinari, B. Swinyard, J. Bally, M. Barlow, J.P. Bernard, P. Martin, T. Moore, A. Noriega-Crespo, R. Plume, L. Testi, A. Zavagno, A. Abergel, et al. A&A **518**, L100 (2010).
4. S.F. Portegies Zwart, S.L.W. McMillan, M. Gieles, ARA&A **48**, 431 (2010).
5. A.G. Ginsburg, J.E. Aguirre, M.K. Dunham, M.M. Drosback, J. Bally, C. Battersby, E.T. Bradley, C. Cyganowski, D. Dowell, N.J. Evans, II, J. Glenn, P. Harvey, E. Rosolowsky, G.S. Stringfellow, J. Walawender, J.P. Williams, ApJS (in prep)
6. E. Rosolowsky, M.K. Dunham, A. Ginsburg, E.T. Bradley, J. Aguirre, J. Bally, C. Battersby, C. Cyganowski, D. Dowell, M. Drosback, N.J. Evans, II, J. Glenn, P. Harvey, G.S. Stringfellow, J. Walawender, J.P. Williams, ApJS **188**, 123 (2010).
7. F. Yusef-Zadeh, J.W. Hewitt, R.G. Arendt, B. Whitney, G. Rieke, M. Wardle, J.L. Hinz, S. Stolovy, C.C. Lang, M.G. Burton, S. Ramirez, ApJ **702**, 178 (2009).
8. W.M. Schlingman, Y.L. Shirley, D.E. Schenk, E. Rosolowsky, J. Bally, C. Battersby, M.K. Dunham, T.P. Ellsworth-Bowers, N.J. Evans, II, A. Ginsburg, G. Stringfellow, ApJS **195**, 14 (2011).
9. P.W. Lucas, M.G. Hoare, A. Longmore, A.C. Schröder, C.J. Davis, A. Adamson, R.M. Bandyopadhyay, R. de Grijs, M. Smith, A. Gosling, S. Mitchison, A. Gáspár, M. Coe, M. Tamura, Q. Parker, M. Irwin, N. Hambly, J. Bryant, R.S. Collins, N. Cross, D.W. Evans, E. Gonzalez-Solares, S. Hodgkin, J. Lewis, M. Read, M. Riello, E.T.W. Sutorius, A. Lawrence, J.E. Drew, S. Dye, M.A. Thompson, MNRAS **391**, 136 (2008).
10. J. Tackenberg, H. Beuther, T. Henning, F. Schuller, M. Wienen, F. Motte, F. Wyrowski, S. Bontemps, L. Bronfman, K. Menten, L. Testi, B. Lefloch, A&A **540**, A113 (2012).

Recent Star Formation in the Lupus Clouds as Seen by Herschel

Kazi L.J. Rygl, Milena Benedettini, and Herschel Gould Belt Survey Consortium

Abstract We present a study of the star formation histories of the Lupus I, III, and IV clouds using the *Herschel* 70–500 μm maps obtained by the *Herschel* Gould Belt Survey Key-Project. By combining the new *Herschel* data with the existing *Spitzer* catalog we obtained an unprecedented census of prestellar sources and young stellar objects in the Lupus clouds, which allowed us to study the overall star formation rate (SFR) and efficiency (SFE). The high SFE of Lupus III and its decreasing SFR suggest that Lupus III is the most evolved cloud, that after having experienced a major star formation event, is now approaching the end of its current star-forming cycle. Lupus I is currently undergoing a large star formation event, apparent by the increasing SFR. Also Lupus IV has an increasing SFR, however, the relative number of prestellar sources is much lower than in Lupus I, suggesting that its star formation has not yet reached its peak.

1 Introduction

In the current paradigm of low-mass star-formation (SF), a gravitationally bound prestellar core will evolve into a young stellar object (YSO), passing through several phases, usually defined by Classes representing increasing stages of evolution: 0, I, II, and III (see [2, 10]), before becoming a main-sequence star. While the later stages of low-mass SF are largely understood, less is known about the earlier stages (prestellar cores and Class 0 objects) due to a lack of sensitivity and resolution at far-infrared to submillimeter wavelengths. The *Herschel* Gould Belt Survey (HGBS, [1]), carried out with the *Herschel* Space Observatory [13], is aimed at studying

K.L.J. Rygl (✉) • M. Benedettini
INAF-IAPS, Via del Fosso del Cavaliere 100, 00133 Rome, Italy
e-mail: kazi.rygl@iaps.inaf.it; milena.benedettini@iaps.inaf.it

Herschel Gould Belt Survey Consortium
http://www.herschel.fr/cea/gouldbelt/en/index.php

D. Stamatellos et al. (eds.), *The Labyrinth of Star Formation*, Astrophysics and Space Science Proceedings 36, DOI 10.1007/978-3-319-03041-8_47,

these early stages of SF in nearby molecular clouds forming the so-called Gould Belt [5].

Located at a distance between 150 pc (Lup I and IV) and 200 pc (Lup III; [4]), the Lupus clouds (I, III, IV) are among the nearest star-forming regions in the Gould Belt. Previous *Spitzer* [11] and molecular line [3] studies of Lupus I, III, and IV found that the three clouds seem to be at different stages of evolution: Lupus I is thought to be the youngest cloud, Lupus IV is a little more evolved, and Lupus III is the most evolved cloud.

The Lupus I, III, and IV clouds were mapped with *Herschel* at five wavelengths from 70 to 500 μm, covering the range where the spectral energy distribution (SED) of cold dust emission from prestellar sources and envelopes of Class 0/I objects (protostars), is likely to peak. Therefore, the *Herschel* data are crucial to detect these objects and determine their physical parameters. But also, to differentiate between Class 0 and Class I sources, which is done by the ratio of the submillimeter luminosity ($L_{\lambda>350\,\mu\mathrm{m}}$) and the bolometric luminosity (see [2]), one needs a wavelength coverage of 3–500 μm. We combined the *Spitzer* [11] catalog, containing mostly Class II/III pre-main sequence (PMS) stars, with the prestellar cores and Class 0/I sources detected by *Herschel*, to obtain a much more complete view of all the phases of star-formation (as seen in Fig. 1) in the Lupus I, III, and IV clouds. Based on this, we studied the behavior of the star formation rate (SFR) through counting the number of objects per Class and estimated the star formation efficiency (SFE) in each cloud [14].

With the advance of *Herschel* one can perform a complete source classification (prestellar cores, Class 0, I, II, and III, see Fig. 1) based on the entire wavelength regime from 3 to 500 μm covered by *Spitzer*/WISE and *Herschel* observations!

2 Star Formation History of the Lupus Clouds

Already [12] posited that the SFR has been increasing in the Lupus clouds over the last 4 Myr using number counts of PMS stars, whose ages they estimated through comparison with theoretical evolutionary PMS tracks. Our sample contains both prestellar cores and Class 0/I objects and by merging with the *Spitzer* [11] catalog we can, therefore, estimate the recent SFR behavior better than in previous studies.

One can deduce the relative number of objects N of a certain Class with respect to a reference Class expected for a constant SFR as: $N = N_{\mathrm{ref}} \times \tau/\tau_{\mathrm{ref}}$ by assuming the lifetimes τ of the two Classes. Since the Class II objects are expected to be complete ([11] and SIMBAD), we chose this as the reference Class with the lifetime estimate of 2 ± 1 Myr [7]. For the other Classes, we assume 0.5 Myr for the prestellar lifetime [6], 0.05 Myr for the Class 0 lifetime [8], and 0.84 Myr for the Class I lifetime [7]. Using these lifetimes, we derived the expected number of objects in each Class relative to the number of Class II objects [14]. Figure 2 shows per cloud the ratio η of the observed to expected source counts for prestellar (η_{pres}), Class 0 ($\eta_{\mathrm{Cl\,0}}$), and I ($\eta_{\mathrm{Cl\,I}}$) objects.

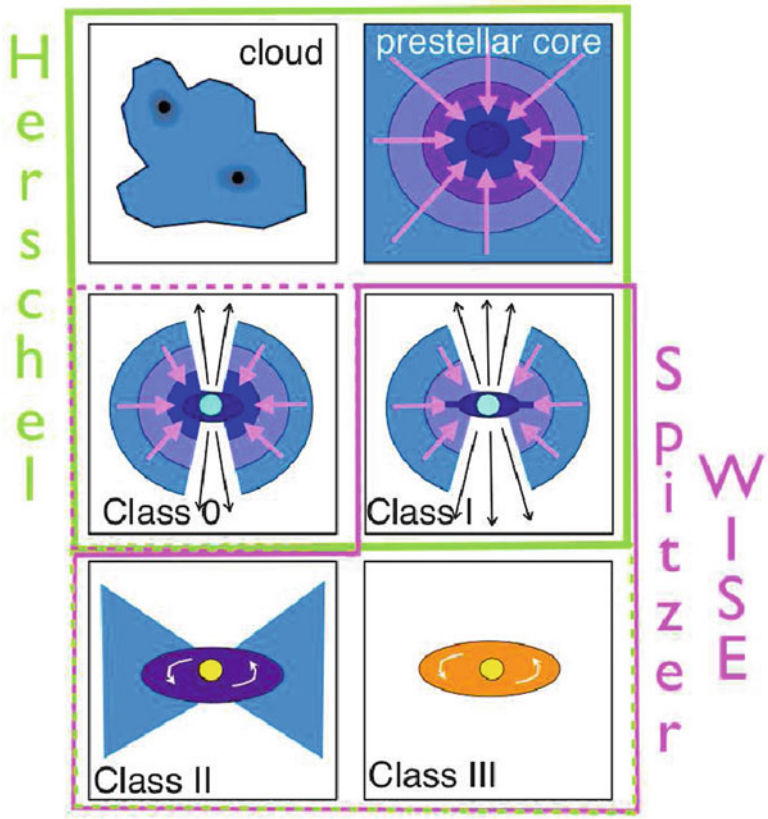

Fig. 1 A schematic view of the formation of a low-mass star, after [9,15]. While *Spitzer* and WISE are ideal to find Class I and later objects, *Herschel* is optimized to find the earlier stages, such as the prestellar cores and the Class 0 objects. For the differentiation between Class 0 and I one needs to use both *Herschel* and *Spitzer*/WISE

For both Lupus I and IV we find more prestellar, Class 0, and I objects than predicted for a constant SFR. Hence, we are witnessing here an increasing SFR over the last 0.5–1.5 Myr. The η's, particularly the $\eta_{\rm pres}$, is much larger in Lupus I than in Lupus IV, suggesting that Lupus I is undergoing a star formation event, while the SFR of Lupus IV might increase still more in the future. In Lupus III there are fewer prestellar, Class 0, and I objects than expected for constant SFR. The star formation in Lupus III has decelerated over the last 2 Myr.

We calculated also the SFE, which is the ratio of the total mass in YSOs (Class 0–III) M_s, assuming 0.2 $M_\odot$ as the average Lupus PMS star mass [11], to the total mass of the cloud plus YSOs: $\frac{M_s}{M_{cloud}+M_s}$. With this formulation, we find a similar SFE of $\sim$1 % in Lupus I and IV, but a much larger SFE of 3.5 % in Lupus III [14].

From the SFRs and SFEs of the Lupus clouds one can interpret their star formation histories. Hence, in [14] we propose that the large SFE of Lupus III and its decreasing SFR suggest that Lupus III is the most evolved cloud, which after having

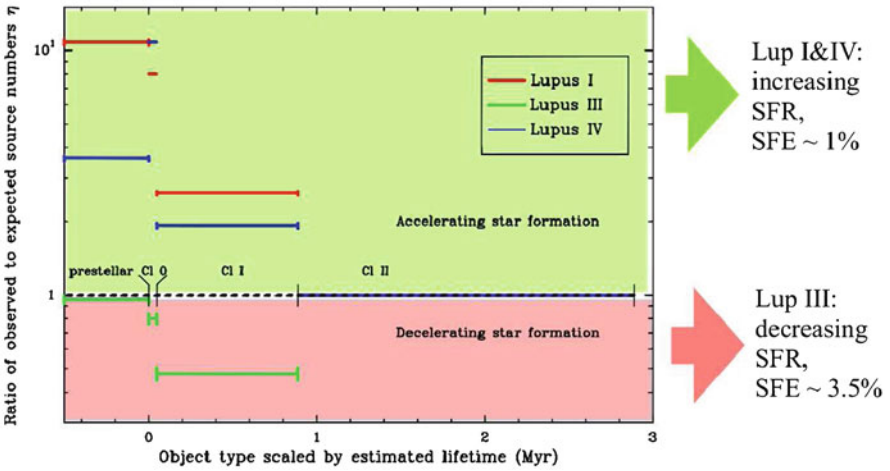

Fig. 2 The ratio of observed to expected number of sources per Class for a constant SFR against their estimated life-time. A ratio larger than unity indicates an increasing SFR, while a smaller ratio indicates a decreasing SFR

experienced a major star formation event, is now approaching the end of its current star-forming cycle. Lupus I is currently undergoing a large star formation event, apparent by the increasing SFR. Also Lupus IV has an increasing SFR, however the relative number of prestellar sources is lower by almost a factor three, suggesting that its star formation has not yet reached its peak and that Lupus IV is at an earlier stage of evolution that Lupus I.

Acknowledgements This research is part of the *Herschel* SAG 3 SPIRE consortium. K.L.J.R. is funded by an ASI fellowship under contract number I/005/11/0.

References

1. André, P., Men'shchikov, A., Bontemps, S., et al. 2010, A&A, 518, L102
2. André, P., Ward-Thompson, D., & Barsony, M. 2000, PPIV, 59
3. Benedettini, M., Pezzuto, S., Burton, M. G., et al. 2012, MNRAS, 419, 238
4. Comerón, F. 2008, Handbook of Star Forming Regions II, ed. Reipurth, B., 295
5. Comeron, F., Torra, J., & Gomez, A. E. 1992, *Ap&SS*, 187, 187
6. Enoch, M. L., Evans, II, N. J., Sargent, A. I., et al. 2008, ApJ, 684, 1240
7. Evans, II, N. J., Dunham, M. M., Jørgensen, J. K., et al. 2009, ApJS, 181, 321
8. Froebrich, D., Schmeja, S., Smith, M. D., et al. 2006, MNRAS, 368, 435
9. Hogerheijde, M. 1998, PhD thesis, University of California, Berkeley, USA
10. Lada, C. J. & Wilking, B. A. 1984, ApJ, 287, 610
11. Merín, B., Jørgensen, J., Spezzi, L., et al. 2008, ApJS, 177, 551
12. Palla, F. & Stahler, S. W. 2000, ApJ, 540, 255
13. Pilbratt, G. L., Riedinger, J. R., Passvogel, T., et al. 2010, A&A, 518, L1
14. Rygl, K. L. J., Benedettini, M., Schisano, E., et al. 2013, A&A, 549, L1
15. Shu, F. H. 1977, ApJ, 214, 488

Filaments and Pre-stellar Sources in the Orion A L 1641 Molecular Clouds

Danae Polychroni, Eugenio Schisano, and Herschel Gould Belt Team

Abstract The Herschel Gould Belt Survey far-IR maps of the Orion L 1641 molecular clouds have revealed a wealth of interconnected filaments and dense sources in the region. We report here the first estimation of the total mass of the L 1641 clouds as derived from dust ($3.7 \times 10^4\,M_\odot$). We further present our initial analysis of the physical properties of these dense sources as a result of their immediate environment. We have extracted a robust and statistically significant sample of 321 pre-stellar sources with a mass distribution that spans a range of 0.1–20 $M_\odot$. We show that there are two mass range distributions that depend on the location of the dense cores on or off the identified filaments.

1 Introduction

The recent far-IR observations of star forming regions in the Milky Way have once again highlighted the ubiquitous presence of filaments in them (e.g. [2, 12]), also present in molecular line surveys (e.g. [19]). The Initial Mass Function (IMF) is thought to be determined already at the pre-stellar evolutionary stage (e.g. [13, 14]) given its resemblance, in shape, to the Core Mass Function (CMF). It is imperative, therefore, to understand the link between filaments and star formation and how they affect each other.

D. Polychroni (✉)
Faculty of Physics, Department of Astronomy, Astrophysics and Mechanics, University of Athens, Panepistimiopolis, 15784 Zografos, Athens, Greece
e-mail: dpolychroni@phys.uoa.gr

E. Schisano
INAF-IAPS, Via Fosso del Cavaliere, 100, Roma 00133, Italy
e-mail: eugenio.schisano@inaf.it

Herschel Gould Belt Team
http://gouldbelt-herschel.cea.fr

D. Stamatellos et al. (eds.), *The Labyrinth of Star Formation*, Astrophysics and Space Science Proceedings 36, DOI 10.1007/978-3-319-03041-8_48,

We present here our first results of the study of this link in the L 1641 clouds mapped, with the Herschel Space Observatory [15] as part of the guaranteed time Key Project Gould Belt Survey [2] using PACS (Photodetector Camera Array; [16]) and SPIRE (Spectral and Photometric Imaging Receiver; [7]) in parallel mode. Located at a distance of 414 ± 7 pc [10], these clouds comprise the southern most part or the Orion A giant molecular cloud (GMC) and are the continuation of the integral shaped filament. With the exception of the L 1641-N region (that is not included in this work) this is a low to intermediate star forming region [1]. The Herschel maps of the L 1641 clouds show that it is riddled with a network of interconnecting filaments most of which are V-shaped and seem to lie on a coherent Northwest-to-South-east axis. The filaments located on the southern half of the map deviate from this behaviour as they split in two directions with some filamentary structures following an almost vertical direction to the above axis (i.e. from East to West). Dense sources are seen throughout the cloud, most located on the filaments. Therefore this region is an ideal site to study the link between filaments and the formation of dense cores.

In this work we trace the filamentary structures in the L 1641 clouds and associate them with the extracted dense sources therein. We report on the differences in the properties of such dense sources located on filamentary structures compared to those found elsewhere in the cloud.

2 Analysis and Results

We derive the column density map of the L 1641 clouds by pixel-to-pixel SED (spectral energy distribution) greybody fitting from 160 to 500 μm, assuming the dust opacity law of [8] and fixing β to 2. We calculate for the first time for the L 1641 clouds a mass of $3.7 \times 10^4\,M_\odot$ within an extinction threshold, A_V, of 2 (using $N_{H_2} = 9.4 \times 10^{20}\,A_v$; [4]) at a distance of 414 pc.

We identify the filaments on the column density map by means of algorithms for pattern recognition, where starting from the second derivative of the map we compute the eigenvalues of the Hessian matrix in each pixel and select the regions where the curvature exceeds a certain threshold value (see Fig. 1 for an example). A more detailed description of the method will be presented in Schisano et al. [18].

We used the CUrvature Threshold EXtractor (CuTEX; [11]) to detect and extract dense sources individually at each band. We accept only those sources with a S/N ratio higher than 5. We then merge the five catalogues following [6], associating sources across the bands if their positional distance is within the radius of the Herschel HPBW at the longer wavelength. Select only those sources that are found in three consecutive bands (e.g. 160, 250, and 350 μm) we find 493 sources which we fit with a greybody model where we fix the dust emissivity index to 2 and allow the temperature to vary in order to derive the physical properties of these cores. We use a dust opacity ratio $\kappa_{\mathrm{Thz}} = 0.01\,\mathrm{cm^2 g^{-1}}$ [3].

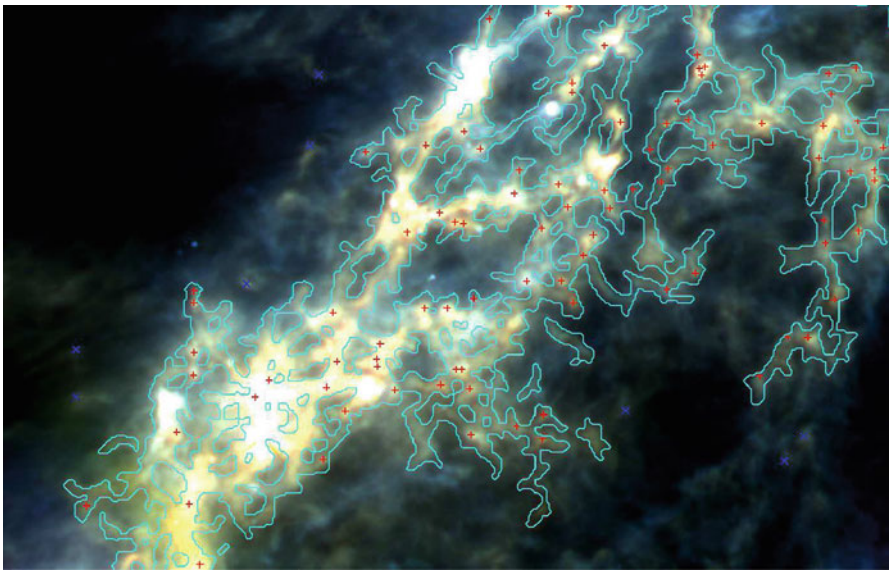

Fig. 1 Zoom-in of a three colour composite image (*blue*: 160 μm, *green*: 250 μm, *red*: 500 μm) of the L 1641 molecular clouds as mapped by Herschel. The *cyan contours* trace the identified filaments while the *red plus* signs and *blue crosses* mark the position of pre-stellar sources on and off the filaments respectively

We assume that sources that have a 70 μm and/or a MIPS 24 μm detection are proto-stellar cores while the rest we classify as starless cores. We find that 109 of our objects are proto-stellar and we remove them from our sample. We classify the remaining 384 sources we classify as pre-stellar (i.e. star-less gravitationally bound sources; [5, 6]) or starless, gravitationally unbound, transient sources, using the critical Bonnor-Ebert mass, $M_{BE} \approx 2.4\, R_{BE}\, a^2/G$, where a is the sound speed at the core temperature, given from the SED fit, G the gravitational constant, and R_{BE} the Bonnor-Ebert radius (in pc). As R_{BE} we use the deconvolved observed size of the sources as measured at 250 μm. We follow [17] to define as pre-stellar cores those sources with $M_{obs}/M_{BE} \geq 1.0$.

We find that 321 of our sources (84 %) can be classified as pre-stellar sources, while 63 are starless, unbound objects. We find that the ratio of between the bound and unbound pre-stellar sources changes from 92 % when considering sources on filaments to 68 % when considering those off the filaments. When considering pre-stellar sources we find that 71 % (229 in number) of them are located on filaments. We find that while the two samples of dense pre-stellar sources (on and off the filaments) have the same size (0.2–0.1 pc (deconvolved FWHM)) and temperature (8–14 K) range, their mass range is significantly different. The pre-stellar sources located off filaments have masses ranging from 0.2 to 4 $M_\odot$ with a mass completeness limit at the 80 % level of 0.4 $M_\odot$, whereas those located on filaments have masses ranging from 0.3 to ∼20 $M_\odot$, with a completeness limit

(at the 80 % level) of 1.0 $M_{\odot}$. The median values of the two distributions are 0.3 and 4.7 respectively. A K-S test confirms that the two samples are different with a certainty of 99.99 % (d = 0.518, probability = 3.7×10^{-12}).

The difference in the bound-to-unbound ratio between sources on and off filaments may be explained two fold. As filaments are regions of high emission in a localised space, it is likely that fainter sources, potentially unbound, located on them are not easy to detect, as is demonstrated also by the higher mass completeness limit we find in such structures. Therefore we are biased towards the brightest, more massive, and thus more likely to be bound, structures on the filaments, while this is not the case for sources off such structures which tend to be located on low emission backgrounds. Furthermore, sources located on filaments are within a much different environment than those off them. It is possible that external pressure on such sources from the filament coupled with the larger reservoir of gas available to them allow for a higher degree of such sources to gravitationally collapse. This difference in environment likely also plays a significant role in establishing the two different mass regimes of the pre-stellar sources on and off the filaments. As filaments have higher column densities than that of the rest of the cloud (generally above 10 magnitudes A_V as compared to above 2 magnitudes for the rest of the cloud) objects formed in situ have a larger reservoir of mass to accrete from, resulting generally in higher mass objects, than those pre-stellar sources located off filaments.

Acknowledgements This research is part of the SAG 3 SPIRE consortium. DP is funded through the Operational Program "Education and Lifelong Learning" that is co-financed by the European Union (European Social Fund) and Greek national funds. E.S. is funded by an ASI fellowship under contract number I/038/08/0.

References

1. L.E. Allen, C.J. Davis, 2008m Handbook of Star Forming Regions I, ed. Reipurth, B., p. 621.
2. P. André, A. Men'shchikov, S. Bontemps et al., 2010, A&A, **518**, L102.
3. S.V.W. Beckwith, A.I. Sargent, R.S. Chini, R. Guesten, 1990, AJ, **99**, 924.
4. R.C. Bohlin & B.D. Savage, 1978, AAS, **10**, 443B.
5. J. di Francesco, N.J. Evans, II, P. Caselli et al., 2007, Protostars and Planets V pp. 17–32.
6. D. Elia, E. Schisano, S. Molinari et al., 2010, A&A, **518**, L97.
7. M.J. Griffin, A. Abergel, A. Abreu et al., 2010, A&A, **518**, L3.
8. R.H. Hildebrand, J.A. Davidson, J. Dotson, 1993, ApJ, **417**, 565.
9. V. Könyves, P. André, A. Men'shchikov et al., 2010, A&A, **518**, L106.
10. K.M. Menten, M.J. Reid, J. Forbrich, A. Brunthaler, 2007, A&A, **474**, 515.
11. S. Molinari, E. Schisano, F. Faustini et al., 2011, A&A, **530**, A133.
12. S. Molinari, B. Swinyard, J. Bally et al., 2010, A&A, **518**, L100.
13. F. Motte, P. André, 2001, A&A, **365**, M440.
14. F. Motte, P. Andre, R. Neri et al., 1998, A&A, **336**, M150.
15. G.L. Pilbratt, J.R. Riedinger, T. Passvogel et al.,2010, A&A, **518**, L1.
16. A. Poglitsch, C. Waelkens, N. Geis et al., 2010, **518**, L2.
17. K.L.J. Rygl, M. Benedettini, E. Schisano et al., 2013, A&A, **549**, L1.
18. E. Schisano, K.L.J. Rygl, S. Molinari et al., accepted for publication in ApJ.
19. J.P. Williams, L. Blitz, C.F. McKee, 2000, Protostars and Planets IV p. 97.

Properties of Interstellar Filaments as Derived from *Herschel* Observations

Doris Arzoumanian, Philippe André, Nicolas Peretto, and Vera Könyves

Abstract We present a scenario for filament formation and evolution motivated by recent observational results of nearby molecular clouds. The analysis of more than 250 filaments observed in 7 regions by the *Herschel* Gould Belt Survey show that the filaments are characterized by a narrow distribution of central width sharply peaked at ∼0.1 pc. This typical filament width corresponds, within a factor of ∼2 to the sonic scale below which interstellar turbulence becomes subsonic in diffuse gas, which may suggest that the filaments form as a result of the dissipation of large-scale turbulence. The analysis of IRAM 30 m molecular line observations of a sample of

D. Arzoumanian (✉)
Laboratoire d'Astrophysique (AIM) de Paris-Saclay, CEA/DSM-CNRS-Université Paris Diderot, IRFU/Service d'Astrophysique, CEA Saclay, Orme des Merisiers, 91191 Gif-sur-Yvette, France

Current address: IAS, CNRS (UMR 8617), Université Paris-Sud; Batiment 121, 91400 Orsay, France
e-mail: doris.arzoumanian@ias.u-psud.fr

P. André
Laboratoire d'Astrophysique (AIM) de Paris-Saclay, CEA/DSM-CNRS-Université Paris Diderot, IRFU/Service d'Astrophysique, CEA Saclay, Orme des Merisiers, 91191 Gif-sur-Yvette, France
e-mail: pandre@cea.fr

N. Peretto
Laboratoire d'Astrophysique (AIM) de Paris-Saclay, CEA/DSM-CNRS-Université Paris Diderot, IRFU/Service d'Astrophysique, CEA Saclay, Orme des Merisiers, 91191 Gif-sur-Yvette, France

Current address: School of Physics & Astronomy, Cardiff University, Queens Buildings, The Parade, Cardiff CF24 3AA, UK
e-mail: Nicolas.Peretto@astro.cf.ac.uk

V. Könyves
Laboratoire d'Astrophysique (AIM) de Paris-Saclay, CEA/DSM-CNRS-Université Paris Diderot, IRFU/Service d'Astrophysique, CEA Saclay, Orme des Merisiers, 91191 Gif-sur-Yvette, France

Institut d'Astrophysique Spatiale, UMR8617, CNRS/Université Paris-Sud 11, 91405 Orsay, France
e-mail: vera.konyves@cea.fr

D. Stamatellos et al. (eds.), *The Labyrinth of Star Formation*, Astrophysics and Space Science Proceedings 36, DOI 10.1007/978-3-319-03041-8_49,

these filaments show evidence of an increase in non-thermal velocity dispersion with column density which suggest an evolution of the supercritical filaments in mass per unit length while accreting surrounding material.

1 Omnipresence of Filaments in Molecular Clouds

Interstellar filaments have recently received special attention, thanks to the high quality and dynamic range of *Herschel* observations. While molecular clouds (MC) were already known to exhibit filamentary structures (cf. [13]), observations of the *Herschel* Gould Belt survey (HGBS) revealed the omnipresence of the filaments in the galaxy [1], and showed that most of the prestellar cores are located within gravitationally unstable filaments for which the mass per unit length exceeds the critical value $M_{\rm line} > M_{\rm line,crit} = 2\,c_s^2/G \sim 15\,M_\odot$/pc [9], where $c_{\rm s} \sim 0.2$ km/s is the isothermal sound speed for $T \sim 10$ K, while the subcritical filaments for which $M_{\rm line} < M_{\rm line,crit}$ are devoid of any bound prestellar cores [1]. This early result suggests an intimate connection between the filamentary structure and the formation process of prestellar cores and protostars. Statistical analysis of the filaments is now possible thanks to the resolution and sensitivity of *Herschel* [11] SPIRE [7] and PACS [12] observations, which appear to be the perfect tool to characterize the properties of the filamentary structure and investigate the physical processes involve in their formation and evolution.

2 A Characteristic Width for Interstellar Filaments

A sample of 265 filaments from 7 regions observed by the HGBS were extracted and analyzed. Mean radial column density profiles for each filament were derived (as explained in [2]) from the column density maps constructed from *Herschel* five wavelengths images (cf. [8]). The filament widths were measured from Gaussian fits to the column density profiles. All the analyzed filaments have a narrow distribution of FWHM widths (cf. Fig. 1) centered around a typical value of 0.09 ± 0.04 pc, which is consistent with what was derived earlier from the analysis of 90 filaments in 3 regions (cf. [2]).

The same filaments, observed in seven regions (listed in Fig. 1) located at distances from 460 to 140 pc, span more than three orders of magnitude in central column density implying a distribution of central Jeans lengths from 0.02 pc up to 1.3 pc, which is much broader than the observed distribution of widths.

The constructed column density radial profiles were modeled with a Plummer-like function (cf. [2] and references therein). The observed density profiles of the filaments approach a power law, at large radii with $\rho_p(r) \sim r^{-2}$, and none of them has the steep $p = 4$ density profile of the Ostriker [9] model of an isothermal filament in hydrostatic equilibrium, for which $\rho_p(r) \sim r^{-4}$. The filament radial

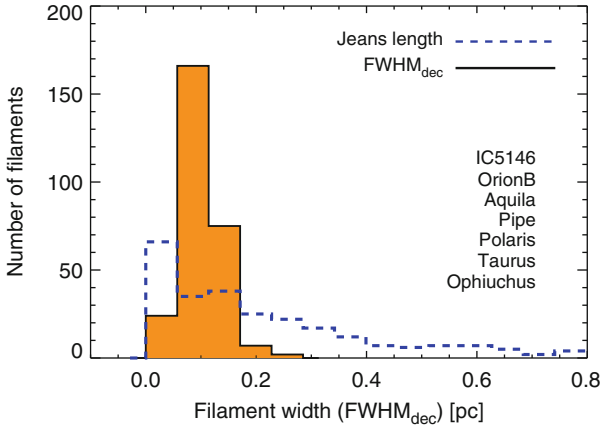

Fig. 1 Distribution of deconvolved FWHM widths for the 265 filaments (*black solid histogram*, filled in *orange*), with a median value of 0.09 pc and a standard deviation of 0.04 pc. For comparison, the *blue dashed histogram* represents the distribution of central Jeans lengths corresponding to the central column densities of the filaments [$\lambda_J = c_s^2/(G\Sigma_0)$] for T = 10 K

profiles were also used to derive accurate masses per unit length, integrating the column density profiles over radius $M_{\rm line}^{\rm obs} = \int \Sigma_{\rm obs}(r){\rm d}r$.

3 Proposed Scenario for Filament Formation and Evolution

Assuming that the filaments have Gaussian radial column density profiles an estimated filament mass per unit length is given by $M_{\rm line} \sim \Sigma_0 \times W_{\rm fil}$ where $W_{\rm fil} \sim 0.1$ pc is the typical filament width [2]. Interestingly, the observationally estimated $M_{\rm line}^{\rm threshold}$ for the column density threshold $\sim 8 \times 10^{21}$ cm^{-2}, which seems to divide the filament sample into two groups (cf. Fig. 2), is equal within a factor of $\sim$2 to the theoretical $M_{\rm line,crit} \sim 15\,{\rm M}_\odot$/pc (for T = 10 K). Thereby, the filament $M_{\rm line,crit}$ corresponds to a column density boundary, where subcritical filaments (left hand side of the boundary) have roughly constant velocity dispersions with a mean value of (0.26 ± 0.05) km/s, while the velocity dispersions of supercritical filaments (right hand side of the boundary) increase as a function of projected column density $\sigma_{\rm tot} \propto {\rm N_{H_2}}^{0.41 \pm 0.05}$. Moreover, the filament virial line masses $M_{\rm line,vir} = 2\,\sigma_{\rm tot}^2/G$ (replacing $M_{\rm line,crit}$ in the presence of nonthermal motions – see [5]), show that thermally supercritical filaments are in approximate virial balance, while thermally subcritical filaments are unbound [3]. This result shows that the gravitational stability criterion discussed by André et al. [1], based on filament *thermal* critical line mass, assuming that the filaments have *thermally dominated* velocity dispersions, is consistent with a more complete view of the total velocity dispersion of filaments.

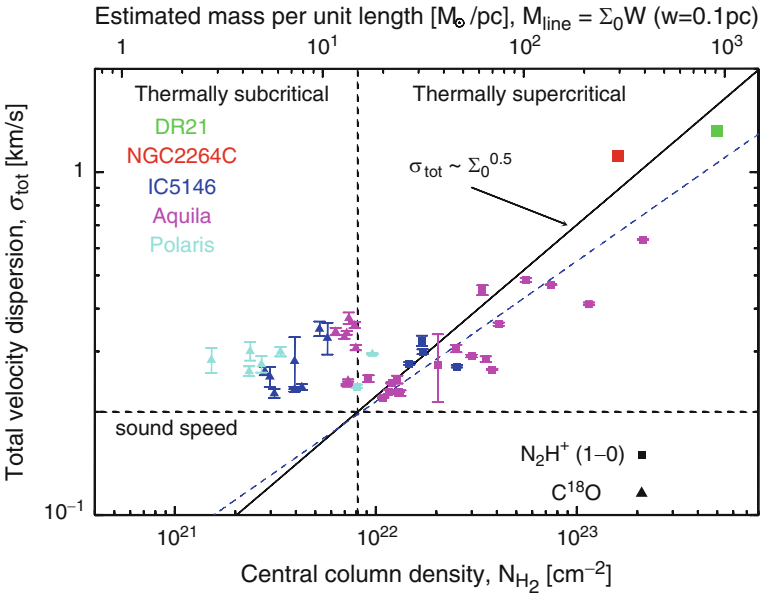

Fig. 2 Total velocity dispersion for observed filaments versus column density. The *horizontal dotted line* shows the sound speed value ∼0.2 km/s for T = 10 K. The *vertical dashed line* marks the boundary between thermally subcritical and supercritical filaments where $M_{line} = M_{line,crit} \sim 15\ M_{\odot}$/pc. The *solid line* running from the *bottom left* to the *top right* corresponds to $M_{line} = M_{line,vir}$ equivalent to $\sigma_{tot} \propto N_{H_2}{}^{0.5}$. The *blue dashed line* corresponds to the best fit of the supercritical filaments where $\sigma_{tot} \propto N_{H_2}{}^{0.41 \pm 0.05}$ (cf. [3])

The observational evidence of a characteristic filament width may be consistent with a scenario of filament formation from dissipation of large-scale supersonic interstellar turbulence [10], since the scale where the turbulence becomes subsonic, which correspond to the sonic scale of the ISM (cf. [4]), is surprisingly similar to within a factor of ∼2 to the filament width (∼0.1 pc) measured independently on *Herschel* images [2]. While the turbulent picture provides a plausible mechanism for *forming* the filaments, the fact that prestellar cores tend to form in gravitationally unstable filaments suggests that gravity is a major driver in the subsequent *evolution* of the supercritical, self gravitating filaments. Subcritical filaments on the other hand, are unbound, and they may be expected to disperse, unless they are confined by an external pressure as suggested by Fischera and Martin [6] and Inutsuka et al. (in prep). To assess the reliability of this scenario of filament formation and evolution, comparison with dedicated simulations will be valuable, in addition to large-scale molecular line mapping of a sample of filaments, to have a stronger dynamical picture of these structures.

References

1. André, P., Men'shchikov, A., Bontemps, S., et al. 2010, A&A, 518, L102+
2. Arzoumanian, D., André, P., Didelon, P., et al. 2011, A&A, 529, L6
3. Arzoumanian, D., André, P., Peretto, N., & Könyves, V. 2013, A&A, 553, A119
4. Federrath, C., Roman-Duval, J., Klessen, R. S., Schmidt, W., & Mac Low, M. 2010, A&A, 512, A81+
5. Fiege, J. D. & Pudritz, R. E. 2000, MNRAS, 311, 85
6. Fischera, J. & Martin, P. G. 2012, A&A, 542, A77
7. Griffin, M. J., Abergel, A., Abreu, A., et al. 2010, A&A, 518, L3+
8. Könyves, V., André, P., Men'shchikov, A., et al. 2010, A&A, 518, L106+
9. Ostriker, J. 1964, ApJ, 140, 1056
10. Padoan, P., Juvela, M., Goodman, A. A., & Nordlund, Å. 2001, ApJ, 553, 227
11. Pilbratt, G. L., Riedinger, J. R., Passvogel, T., et al. 2010, A&A, 518, L1+
12. Poglitsch, A., Waelkens, C., Geis, N., et al. 2010, A&A, 518, L2+
13. Schneider, S. & Elmegreen, B. G. 1979, ApJs, 41, 87

Preliminary Results of the *Herschel* Gould Belt Survey in the Orion B Complex

Vera Könyves, Philippe André, Pedro Palmeirim, Nicola Schneider, Doris Arzoumanian, and Alexander Men'shchikov

Abstract As a preliminary result of the *Herschel* Gould Belt survey (André et al. 2010) in the Orion B cloud complex we find a clear connection between the locations of the detected prestellar cores and the column density values. We find that the vast majority of the gravitationally bound prestellar cores are detected above a high column density of about 6–7 $\times$ 10^{21} cm^{-2} ($A_V \sim$ 6–7). This is in very good agreement with dense core formation thresholds found in other regions. For Orion B, a similar limit appears both in the distribution of background column density values of the prestellar cores, and in the column density PDF of the region. Within our core formation scenario, the found threshold can be translated as the column density above which the filaments become gravitationally unstable and fragment into cores.

V. Könyves (✉)
Laboratoire d'Astrophysique (AIM) de Paris-Saclay, CEA/DSM-CNRS-Université Paris Diderot, IRFU/Service d'Astrophysique, CEA Saclay, Orme des Merisiers, 91191 Gif-sur-Yvette, France

Institut d'Astrophysique Spatiale, UMR8617, CNRS/Université Paris-Sud 11, 91405 Orsay, France
e-mail: vera.konyves@cea.fr

P. André • P. Palmeirim • A. Men'shchikov
Laboratoire d'Astrophysique (AIM) de Paris-Saclay, CEA/DSM-CNRS-Université Paris Diderot, IRFU/Service d'Astrophysique, CEA Saclay, Orme des Merisiers, 91191 Gif-sur-Yvette, France

N. Schneider
Laboratoire d'Astrophysique (AIM) de Paris-Saclay, CEA/DSM-CNRS/INSU-Université Paris Diderot, IRFU/Service d'Astrophysique, CEA Saclay, Orme des Merisiers Bât. 709, 91191 Gif-sur-Yvette, France

D. Arzoumanian (✉)
Laboratoire d'Astrophysique (AIM) de Paris-Saclay, CEA/DSM-CNRS-Université Paris Diderot, IRFU/Service d'Astrophysique, CEA Saclay, Orme des Merisiers, 91191 Gif-sur-Yvette, France

Current address: IAS, CNRS (UMR 8617), Université Paris-Sud; Batiment 121, 91400 Orsay, France
e-mail: doris.arzoumanian@ias.u-psud.fr

D. Stamatellos et al. (eds.), *The Labyrinth of Star Formation*, Astrophysics and Space Science Proceedings 36, DOI 10.1007/978-3-319-03041-8_50,

1 The Power of the *Herschel* Gould Belt Survey

Thanks to recent large-scale surveys (e.g., with *Herschel*), the samples of prestellar cores and protostars are gradually increasing. For example, from the location of these objects against their local background in a molecular cloud, broader connections of the early stages of star formation can be identified.

The *Herschel Space Observatory* [16], equipped with its two imaging cameras SPIRE at 500–250 μm [5] and PACS at 160–70 μm [17], provides a unique tool to address poorly understood issues of the early stages of star formation. Many of such key questions are central to the *Herschel* Gould Belt survey (HGBS, [1]) whose main goal is to elucidate the physical mechanisms of the formation of prestellar cores out of the diffuse interstellar medium, and provide a complete census of prestellar cores and young protostars in the nearby ($d \lesssim 0.5$ kpc) molecular cloud complexes of the Gould Belt. The target clouds span a wide range of physical conditions, from *active* to *quiescent* star-forming regions; with low-mass to intermediate-/(high-)mass star formation activity.

Such a large-coverage submillimetre survey can, as well, prove whether there is a (universal) core/star formation threshold which has an importance both on Galactic and extragalactic scales. *Herschel* allows us to provide stronger cases for a core formation threshold as the HGBS observations cover a large surface area, and are sensitive both to large-, and small-scale column density structures.

2 Groving Evidence for a Star Formation Threshold

Following the prediction of a column density threshold for core formation by McKee [13], dust continuum observations have revealed that dense cores are preferentially located in high extinction regions of Taurus [15], Ophiuchus [8], and Perseus [9]. In these studies, the possible thresholds for star formation roughly lie above an $A_{\rm V}^{\rm bg} \sim 5$–10, or above $N_{\rm H_2}^{\rm bg} \sim 5$–$10 \times 10^{21}$ cm^{-2} in background column density. Similar star formation thresholds have been implied by Lada et al. [12] and Heiderman et al. [6] as well. Furthermore, *Herschel* Gould Belt survey observations with higher angular resolution ($\sim$15″ at $\lambda \sim 200$ μm) also confirm the low probability of finding bound cores below an $A_{\rm V} \sim 7$–10, consistently in the Aquila Rift and Polaris, in two clouds with very different star formation activity [1,2]. Over all, the observed thresholds are in good agreement with that of an earlier theoretical prediction ($A_{\rm V} \sim 4$–8) for dense core formation in a magnetically regulated star formation scenario; though we do not discuss this interpretation of McKee [13] for the threshold, but a filamentary approach.

Such threshold can be visualized by yet an other tool, the probability density function (PDF) of the column density map values that we derive from *Herschel* observations. It has been shown by André et al. [2] for the $\sim$10 deg^2 region of

Aquila, that the column density PDF is well fitted by a log-normal distribution below $A_V \sim 7$, while it has a power-law deviation at the high column density range.

3 Coherent Core Formation Scenario in Orion B, Aquila and Polaris

Within the *Herschel* GBS we observed a $\sim$20 deg^2 field of Orion B, the nearest massive GMC ($d \sim 410$ pc). Its column density map was derived from a pixel-by-pixel grey-body fitting to the 4 longest *Herschel* wavelengths (160–500 μm). We first smoothed the maps to the beamsize of the 500 μm image (37″), and added the zero-flux levels to each map by correlating the *Herschel* data with *Planck*/*IRAS* data [4]. The specific dust opacity has been fixed as $\kappa_\nu = 0.1\ (\nu/1,000\ \mathrm{GHz})^2\ \mathrm{cm}^2/\mathrm{g}$ (cf. [7]) when deriving the free parameters: H_2 column density, and dust temperature (see Könyves et al. [11] for details). The resulting N_{H_2} map is shown in Fig. 1.

In order to obtain the catalogue with entries for the starless cores and for their local background, we have performed simultaneous source extraction in all *Herschel* bands with *getsources* [14], and selected good candidate prestellar cores, for which the details are described in Könyves et al. [11].

The distribution of $N_{H_2}^{bg}$ of the prestellar cores – in equivalent background extinctions – is plotted in Fig. 2 (left panel), where most of the bound cores ($\sim$90 %) appear above a threshold of $A_V \sim 6$. In the column density PDF (Fig. 2, right panel) the expected excess material shows up above $\sim$ 5–6 $\times\ 10^{21}\ \mathrm{cm}^{-2}$, where the slope has a power-law behaviour, and this part very likely represents gravitating material currently involved in star formation [18]. In contrast, the lower column density part of the PDF is assumed to be turbulence-dominated in the cloud (e.g., [10]).

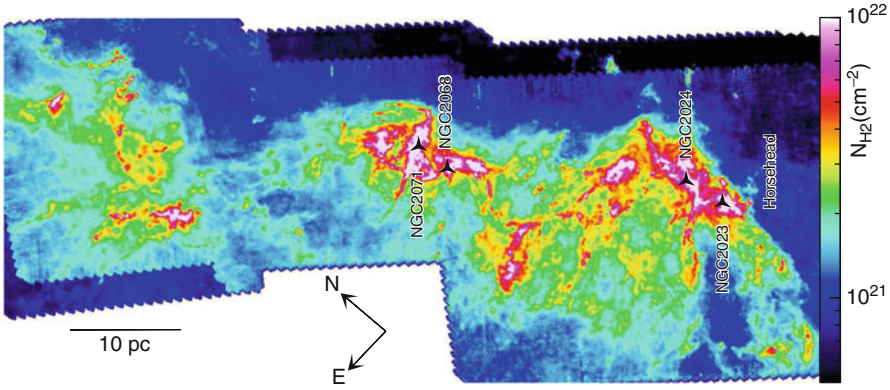

Fig. 1 Column density map derived from SPIRE/PACS observations of Orion B. Only the regions covered both by SPIRE and PACS were considered in the analysis

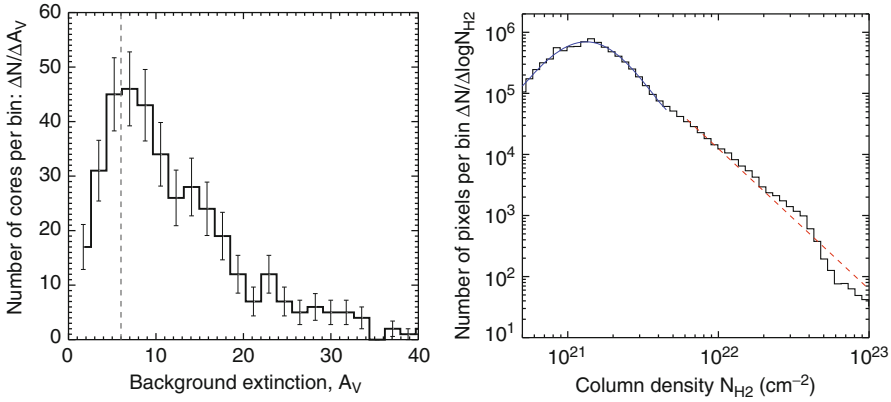

Fig. 2 *Left*: Distribution of background visual extinction for the prestellar cores in the Orion B region. The *vertical dashed line* marks the threshold of $A_{\rm V}^{\rm bg} = 6$ mag. *Right*: For comparison, the column density PDF of Orion B is plotted (see text). A log-normal and a power-law fit have been superimposed at low-, and high column densities, respectively

The above dense core formation thresholds in Orion B and in Aquila [2] show very similar values, and these all are in agreement with the very low star formation activity of the Polaris region, where all the background column density values of the cores are below the previous thresholds. The core formation scenario, set up from early findings of the *Herschel* Gould Belt survey [1, 3], is reflected in these three nearby clouds. The visual extinction threshold of $A_{\rm V} \sim 6$–7 can be explained by the formation of dense cores out of the filaments via thermal/gravitational instabilities [2] above a critical mass per unit length ($M_{\rm line,crit} \sim 15 M_{\odot}$/pc) at $T \sim 10$ K; that is why the majority of the prestellar cores in the filamentary background are observed above the approximately corresponding $A_{\rm V}$ and $M_{\rm line,crit}$ threshold values.

References

1. André, P., Men'shchikov, A., Bontemps, S., et al. 2010, A&A, 518, L102+
2. André, P., Men'shchikov, A., Könyves, V., & Arzoumanian, D. 2011, in IAU Symposium, Vol. 270, Computational Star Formation, ed. J. Alves, B. G. Elmegreen, J. M. Girart, & V. Trimble, 255–262
3. Arzoumanian, D., André, P., Didelon, P., et al. 2011, A&A, 529, L6
4. Bernard, J.-P., Paradis, D., Marshall, D. J., et al. 2010, A&A, 518, L88
5. Griffin, M. J., Abergel, A., Abreu, A., et al. 2010, A&A, 518, L3+
6. Heiderman, A., Evans, II, N. J., Allen, L. E., et al. 2010, ApJ, 723, 1019
7. Hildebrand, R. H. 1983, QJRAS, 24, 267
8. Johnstone, D., Di Francesco, J., & Kirk, H. 2004, ApJ, 611, L45
9. Kirk, H., Johnstone, D., & Di Francesco, J. 2006, ApJ, 646, 1009
10. Klessen, R. S. & Hennebelle, P. 2010, A&A, 520, A17
11. Könyves, V., André, P., Men'shchikov, A., et al. 2010, A&A, 518, L106+
12. Lada, C. J., Lombardi, M., & Alves, J. F. 2010, ApJ, 724, 687

13. McKee, C. F. 1989, ApJ, 345, 782
14. Men'shchikov, A., André, P., Didelon, P., et al. 2012, A&A, 542, A81
15. Onishi, T., Mizuno, A., Kawamura, A., Ogawa, H., & Fukui, Y. 1998, ApJ, 502, 296
16. Pilbratt, G. L., Riedinger, J. R., Passvogel, T., et al. 2010, A&A, 518, L1+
17. Poglitsch, A., Waelkens, C., Geis, N., et al. 2010, A&A, 518, L2+
18. Schneider, N., André, P., Könyves, V., et al. 2013, ApJ, 766, L17

HOBYS Observations of Ridges and Filaments, and the Evolution of Massive Dense Cores

Martin Hennemann, Frédérique Motte, Nicola Schneider, and HOBYS Consortium

Abstract *Herschel* large-scale observations of close-by massive star-forming regions obtained by HOBYS provide an unbiased view on the detailed cloud structure and its population of massive dense cores – excellent candidates for high-mass star precursors. Structures like the DR21 ridge, the most massive cloud structure in Cygnus X, could be formed by the merging of filaments or flows: several connected sub-filaments are resolved with *Herschel*. The sub-filaments are gravitationally unstable and form cores and protostars which may become low-mass members of the forming OB star cluster(s). They show decreasing dust temperature towards the ridge, indicating the pile-up of material to high densities which cools down to a minimum of 14 K towards the Northern part. The present mass in the sub-filaments is a factor of three lower than the ridge mass, so they represent remnant flows. However, their link to the clumps around DR21 and DR21(OH) suggests that these flows have been important to build-up massive clumps inside the ridge. Extrapolating, we would expect the assembly of massive clumps towards the Northern part of the DR21 ridge where the most massive subfilaments connect, in continuation of the evolutionary sequence of star formation along the ridge from South to North. We also use the large coverage of Cygnus X obtained by HOBYS (7,000 pc^2) to establish an extensive sample of compact, cold, and dense cores in the region and constrain their luminosities, dust temperatures, and envelope masses. An evolutionary diagram and simple evolutionary tracks show that the sample provides the statistics to study the formation of stars with mass up to 20 $M_\odot$.

M. Hennemann (✉) • F. Motte • N. Schneider
Laboratoire d'Astrophysique (AIM) de Paris-Saclay, CEA/DSM-CNRS/INSU-Université Paris Diderot, IRFU/Service d'Astrophysique, CEA Saclay, Orme des Merisiers Bât. 709, 91191 Gif-sur-Yvette, France
e-mail: martin.hennemann@cea.fr

HOBYS Consortium
http://www.herschel.fr/cea/hobys/en/

D. Stamatellos et al. (eds.), *The Labyrinth of Star Formation*, Astrophysics and Space Science Proceedings 36, DOI 10.1007/978-3-319-03041-8_51,

1 High-Mass Star Formation Observed with *Herschel*: The DR21 Ridge – An Intersection of Filaments

Which cloud structures form high-mass stars ($\geq 10\,M_\odot$) and accompanying clusters? The *Herschel*[1] imaging survey of OB young stellar objects (HOBYS, [9]) observes massive molecular cloud complexes within 3 kpc distance to probe these cloud structures, OB star-forming cores, and the feedback from high-mass stars. Hill et al. [6] suggested on the basis of Vela C that "ridges", i.e., massive, gravitationally unstable filamentary structures of high column density ($N_{H_2} > 10^{23}\,cm^{-2}$) that dominate their environment could be preferential sites of high-mass star formation. Furthermore, intersecting filaments appear to mark sites of stellar cluster formation in the Rosette cloud [12].

The DR21 ridge is the densest and most massive cloud structure in Cygnus X at a distance of 1.4 kpc. It hosts the embedded HII region DR21, the maser source DR21(OH), and massive protostars. Schneider et al. [11] analysed molecular line emission and identified three sub-filaments F1–F3 connecting to the ridge. Velocity gradients suggest that material is transported along them towards the ridge. Hennemann et al. [5] exploit the unprecedented sensitivity of *Herschel* far-infrared and submillimetre continuum imaging to trace its detailed column density structure.

In Fig. 1, compact 70 μm sources that are protostar candidates cluster along the DR21 ridge oriented north-south, with the most prominent peak being DR21 itself. They show a strong northward decrease in luminosity. There are many filamentary streamers from the ridge to, e.g., the north-west and west. They mainly correspond

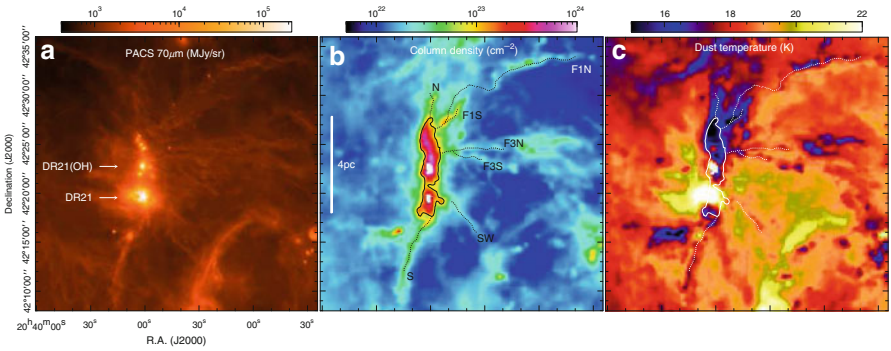

Fig. 1 *Herschel* maps of the DR21 environment showing (**a**) 70 μm emission, (**b**) column density, and (**c**) dust temperature. The DR21 ridge is delimited roughly by the $N_{H_2} = 10^{23}\,cm^{-2}$ contour plotted in panels (**b**) and (**c**). The analysed sub-filaments are named and marked with *dots* along their crests in (**b**) and (**c**)

[1] *Herschel* is an ESA space observatory with science instruments provided by European-led Principal Investigator consortia and with important participation from NASA [10].

to low column density structures, but several sub-filaments are prominent. The extent of the DR21 ridge can be roughly defined by the $N_{H_2} = 10^{23}\,cm^{-2}$ contour enclosing an area of 2.3 pc^2. The sub-filaments of Schneider et al. [11] labelled F1 and F3 are resolved. The northern part of the DR21 ridge shows two extensions in column density to the north and north-west (F1) that coincide with the coldest regions where the dust temperature drops as low as 14 K. The sub-filaments are visible in the dust temperature map as structures of lower central temperature relative to the background of ~19 K. With 22 associated dense cores (9 of 33 massive ones, Motte et al. [8]), the DR21 ridge probably hosts the most massive forming cluster(s) in Cygnus X. The perpendicular column density profile between DR21 and DR21(OH) shows at least one additional peak, indicating that there the ridge consists of more than one individual filament. Considered together with the branching of the northern ridge and a possible southern branching, this suggests that the DR21 ridge is a complex intersection of several individual filaments.

The stability of filaments is to first order determined by the critical mass per unit length ($M_{line}^{crit} \approx 30\,M_\odot/pc$) [1, 7]. Most sub-filament segments are supercritical, and we thus expect the sub-filaments to form cores and protostars. Indeed, compact 70 μm emission from protostar candidates, and compact starless/prestellar core candidates at 250 μm are seen towards all sub-filaments, one of them identified as a dense core by Motte et al. [8]. This confirms that core and star formation is ongoing within the supercritical sub-filaments, in contrast to the striations in, e.g., Taurus [4]. The high masses of the cores in the ridge could therefore not only be generated by the sub-filament flows, but could also be caused by the merging with fragment cores of the sub-filaments. For DR21(OH), Csengeri et al. [3] showed possible fragmentation of the inflowing material.

The *Herschel* observations emphasize the evolutionary gradient along the ridge: Beyond DR21, the 70 μm luminosity of protostars strongly decreases northward, and the dust temperature shows lowest temperatures towards the northern part. The substructure of the DR21 ridge suggests that it was formed by the merging of individual narrow, intersecting filaments. At present, the merging could have advanced farthest in the southern part and less in the north, where the two components appear to be separated. Extrapolating this scenario, we expect that the northern filaments will lead to the assembly of one or more additional massive clumps. This study suggests that high-mass star-forming ridges could be second-generation cloud structures formed via dynamical merging of gravitationally unstable filaments.

2 The Cygnus X Dense Core Sample from *Herschel*

Massive dense cores of ≤0.1 pc are best OB star precursor candidates [8]. The large-scale HOBYS mapping will result in unprecedented statistical censuses of such cores and vastly improve our understanding of the early evolution of OB stars. Using the new multi-scale, multi-wavelength source extraction algorithm *getsources*, we established a sample of ca. 1,000 cores with ≤0.1 pc (deconvolved FWHM at

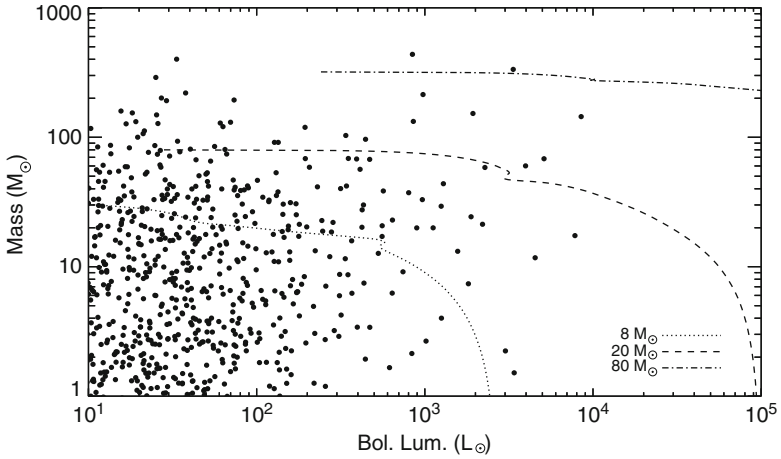

Fig. 2 Evolutionary diagram of the *Herschel* Cygnus X dense cores. Evolutionary tracks for three final stellar masses are plotted (cf. [2], 25 % mass efficiency)

160/250 μm) and constrained their bolometric luminosity, dust temperature, and envelope mass. An evolutionary diagram shown in Fig. 2 shows that under the assumption of 25 % core-to-star mass efficiency, the sample covers the parameter space predicted for the early evolution of stars with up to $\approx 20\,M_\odot$. The ongoing detailed analysis will significantly improve our knowledge about the formation process of high-mass stars.

Acknowledgements This research is done within the SPIRE consortium Specialist Astronomy Group "Star formation" (SAG3) and was supported by the ANR (*Agence Nationale pour la Recherche*) project "PROBeS" (ANR-08-BLAN-0241).

References

1. André Ph., Men'shchikov A., Bontemps S., et al. 2010, A&A, 518, L102
2. Bontemps S., André P., Könyves V., et al. 2010, A&A, 518, L85
3. Csengeri T., Bontemps S., Schneider N., et al. 2011, ApJL, 740, L5
4. Goldsmith P. F., Heyer M., Narayanan G., et al. 2008, ApJ, 680, 428
5. Hennemann M., Motte F., Schneider N., et al. 2012, A&A, 543, L3
6. Hill T., Motte F., Didelon P., et al. 2011, A&A, 533, A94
7. Inutsuka S. I. & Miyama S. M. 1992, ApJ, 388, 392
8. Motte F., Bontemps S., Schilke P., et al. 2007, A&A, 476, 1243
9. Motte F., Zavagno A., Bontemps S., et al. 2010, A&A, 518, L77
10. Pilbratt G. L., Riedinger J. R., Passvogel T., et al. 2010, A&A, 518, L1
11. Schneider N., Csengeri T., Bontemps S., et al. 2010, A&A, 520, A49
12. Schneider N., Csengeri T., Hennemann M., et al. 2012, A&A, 540, L11

The Filamentary Structure of the Lupus 3 Molecular Cloud

Milena Benedettini

Abstract We present the column density map of the Lupus 3 molecular cloud derived from the Herschel photometric maps. We compared the Herschel continuum maps, tracing the dense and cold dust emission, with the CS (2–1) map observed with the Mopra 22-m antenna, tracing the dense gas. Both the continuum and the CS maps show a well defined filamentary structure, with most of the dense cores being on the filaments. The CS (2–1) line shows a double peak in the central part of the longest filament due to the presence of two distinct gas components along this line of sight. Therefore, what seems a single filament in the Herschel map is actually the overlap of two kinematically distinct filaments. This case clearly shows that kinematical information is essential for the correct interpretation of filaments in molecular clouds.

1 Identification of Filaments in the Herschel Map

As part of the Gould Belt Key Project [1] the nearby (d = 200 pc [4]) Lupus 3 molecular cloud has been observed in five photometric bands between 70 and 500 μm with the PACS and SPIRE photometers on board the Herschel Space Observatory. The maps have been produced by using the ROMAGAL pipeline [6]. By applying a grey body fit in each pixel of the four maps at $\lambda \geq 160\,\mu$m, we derived the column density and the temperature maps of the cloud. In order to characterize the filamentary structure of the cloud we applied an algorithm that uses the eigenvalues of the Hessian matrix of the column density map to identify the border of the filament, defined as the place with the maximum variation of the density field. The spine of the filament is then derived by calculating the central axis

M. Benedettini (✉)
INAF-IAPS, via Fosso del Cavaliere 100, 00133 Roma, Italy
e-mail: milena.benedettini@inaf.it

D. Stamatellos et al. (eds.), *The Labyrinth of Star Formation*, Astrophysics and Space Science Proceedings 36, DOI 10.1007/978-3-319-03041-8_52,

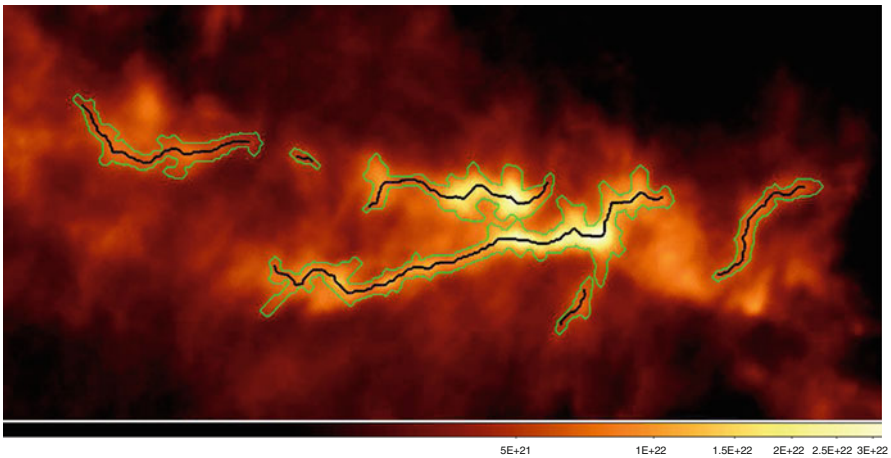

Fig. 1 Column density map of the Lupus 3 cloud with the identification of the filaments. The *black lines* identify the spine of the filaments and the *green lines* the borders

of such a region (see [5] for more details). In Lupus 3 we identified 6 filaments (see Fig. 1), the 2 biggest ones in the central part of the cloud and the other smaller 4 around the 2 major structures. The mass belonging to the filaments has been calculated by summing the mass inside the borders and subtracting the contribution of the mass of the background, calculated as the median value in a region two pixels wide outside the borders. The total mass of the filaments represents the 23 % of the overall mass in the Lupus 3 cloud. A similar value (21 %) is obtained integrating the total mass contained inside the 8 mag visual extinction level, threshold proposed for the star formation to occur [1]. Such similarity suggests that the filament is composed by the denser mass and they are the most favorable place for the formation of new stars. This hypothesis is strengthened by the fact that a high fraction (78 %) of all the prestellar cores found in the Lupus 3 cloud lies within the filaments.

1.1 Analysis of the Longest Filament

The southern filament, with a linear length of $37'$ (corresponding to 2.15 pc at the distance of 200 pc), is the longest filament of the cloud, running almost horizontally. Its median width deconvolved from the beam, defined as the FWHM of the Gaussian fit along the radial direction orthogonal to the spine, is 0.07 pc, similar to the lower values of the distribution of the sizes of filaments in nearby molecular clouds that peaks at 0.1 pc [2]. The mass per unit line of the filament is $19.5\,M_{\odot}\,pc^{-1}$, higher than the thermal critical value ($\approx 15\,M_{\odot}\,pc^{-1}$, assuming a temperature of 10 K [1]) showing that the thermal pressure alone cannot sustain the filament against its selfgravity and then it is favorable to collapse and fragment.

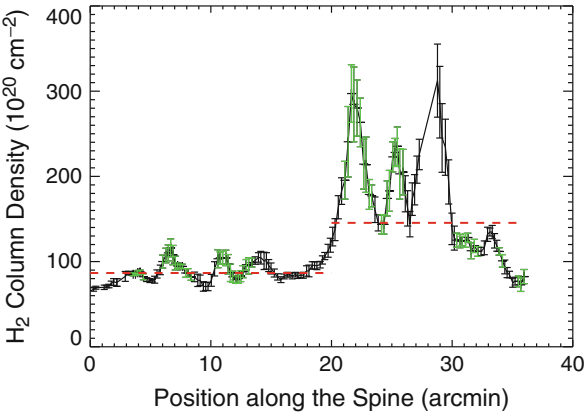

Fig. 2 H_2 column density profile along the spine of the longest filament. The origin of the x-axis corresponds to the eastern edge of the filament. The *grey lines* mark the position of the compact sources present in the filament. The *two red dashed lines* indicate the mean values of the column density in the range of 0′–20′ and 20′–37′

The column density profile along the spine of the filament (Fig. 2) shows a correlation of the local peaks of column density with the position of the dense cores, as expected. It is worth noting that the mean value of the column density of the filament, i.e. without considering the contribution of the cores, drastically increases by a factor of 2 in the middle of the filament, at ∼20′ from the eastern edge (see Fig. 2). On the other hand, the temperature along the spine is rather constant around 13–14 K, with the smaller values reached in correspondence of the compact cores.

2 Line Maps

In [3] we mapped the central part of the Lupus 3 clouds with high density molecular tracers with the Mopra 22-m telescope at 3 and 12 mm. The Mopra maps revealed the gas dense cores, traced by N_2H^+, NH_3 and HC_3N, as well as the more diffuse gas component traced by CS. Comparing the Herschel and the Mopra maps we find that in general the 160 μm emission (tracing warmer dust) correlates with the emission of N_2H^+ while the 500 μm emission (tracing colder dust) correlates with HC_3N. Chemical models [3] have shown that HC_3N is expected to be more abundant in very young dense cores (namely prestellar cores or young Class 0 protostar) and it is expected to be quickly destroyed in more evolved objects. On the other hand N_2H^+, being produced during the collapse phase of the core, remains at similar high abundance even in more evolved phases. Therefore, we find that the colder dust is correlated with the chemical young gas and the warmer dust is correlated with the chemical older gas.

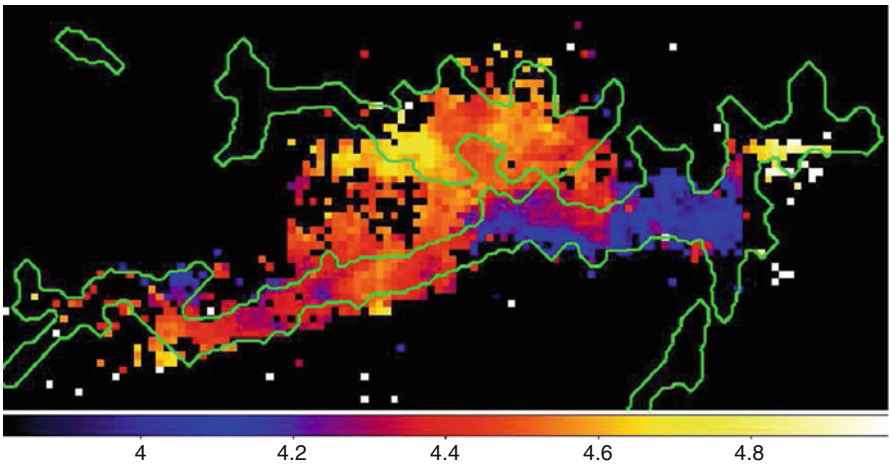

Fig. 3 Map of the value of the peak of the CS (2–1) lines derived from a Gaussian fitting of the line. The superimposed *green lines* show the border of the filaments

The CS (2–1) emission, being a good tracer of the large scale structure of the molecular gas, is very similar to the column density map, tracing very well the filamentary structures identified in the Herschel map. Moreover from the CS (2–1) we can derive also the kinematic of the gas. In fact the CS (2–1) channel map (see Fig. 6 of [3]) indicates that the filaments are at different v_{lsr}. This is also visible in the map of the peak of the CS (2–1) lines as derived from a Gaussian fitting (Fig. 3). As one can see in Fig. 3, in the longest southern filament the lines peak at $\sim$4.1 km s^{-1} in the western part and at $\sim$4.6 km s^{-1} in the eastern part while in the northern filament the lines peak at $\sim$4.8 km s^{-1}. These differences are significant since the spectral resolution of the data is 0.1 km s^{-1}. It is worth noting that the change in the value of the line centre happens at the same position of the filament where also the column density changes (at $\sim$20$'$ along the spine). However the profile of the CS (2–1) in this position (see Fig. 4) clearly shows a double peak, one at 4.1 km s^{-1} and the other at 4.6 km s^{-1}, that are the same values found at the west and east sides of the filament. Even if we do not have the $C^{34}S$ (2–1) spectrum that would allow us to exclude that the CS line is self-absorbed, we believe that the double peak indicates the presence of two different gas components along the line of sight. This is also supported by the fact that other species observed toward the same position show a single peaked line centred at $\sim$4.6 km s^{-1}. Therefore what looks as a single filament in the Herschel maps is in fact the overlap of two kinematically distinct filaments.

This example highlights that kinematical information is essential for the correct interpretation of the filaments in molecular clouds identified on continuum maps.

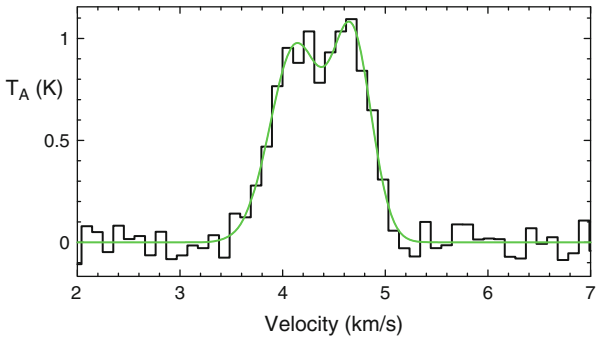

Fig. 4 Spectrum of the CS (2–1) line at the position of $\sim 20'$ along the spine with the two components Gaussian fitting (*green line*). The line has two peaks testifying the presence of two gas component along this line of sight

References

1. André, P., Men'shchikov, A., Bontemps, S., et al. A&A, **518**, L102 (2010)
2. Arzoumanian, D., André, P., Didelon, P., et al. A&A, **529**, L6 (2010)
3. Benedettini, M., Pezzuto, S., Burton, M. G., et al. MNRAS, **419**, 238 (2012)
4. Comerón, F.: Handbook of Star forming regions: vol II. The souther sky, ed. Reipurth, San Francisco ASP (2008)
5. Schisano E., et al. submitted (2013)
6. Traficante, A., Calzoletti, L., Veneziani, M., et al. MNRAS, **416**, 2932 (2011)

Molecular Line Observations of Isolated Cores

Ciara Quinn, Tyler L. Bourke, and Derek Ward-Thompson

Abstract We have observed a number of isolated, small molecular clouds in the ^{12}CO, ^{13}CO and C^{18}O molecular lines using the 22-m Mopra telescope. We perform an LTE analysis to find optical depths, column densities and observed masses of each of the cores. A virial analysis suggests that all the cores are consistent with being in virial equilibrium.

We have observed a number of isolated, southern small molecular clouds [1] using the MOPS spectrometer on the 22-m Australian Mopra Telescope [2]. Combining the ^{13}CO and C^{18}O data, we perform an LTE analysis to find column densities. Figure 1 shows an example of the results of the analysis for six cores. The grey-scale images show 2MASS extinction [3] with ^{13}CO (black) and C^{18}O (white) column density contours overlaid. The ^{13}CO emission can be seen to trace the lower extinction regions, and the C^{18}O emission traces regions of highest extinction.

The observed core mass, derived from the C^{18}O column density is compared with the virial mass for the most isolated 12 cores, as shown in Fig. 2. The solid line shows the $M_{vir}/M_{obs} = 1$ relation. Cores below the line are thought to be gravitationally bound and may collapse. Cores above the line are not gravitationally bound. The figure shows all the cores are within 3σ of the solid line, which is consistent with all cores being in virial equilibrium.

C. Quinn (✉)
Cardiff University, Cardiff, UK
e-mail: Ciara.Quinn@astro.cf.ac.uk

T.L. Bourke
SAO-Harvard-Smithsonian Center for Astrophysics, Cambridge, MA 02138, USA

D. Ward-Thompson
Director, Jeremiah Horrocks Institute for Mathematics, Physics and Astronomy,
University of Central Lancashire, Lancashire, UK
e-mail: DWard-Thompson@uclan.ac.uk

D. Stamatellos et al. (eds.), *The Labyrinth of Star Formation*, Astrophysics and Space Science Proceedings 36, DOI 10.1007/978-3-319-03041-8_53,

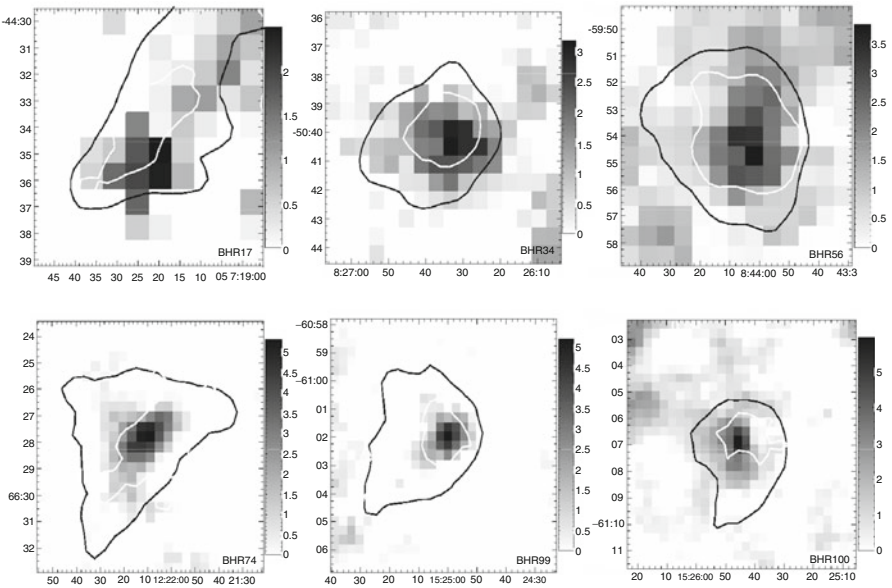

Fig. 1 2MASS extinction *greyscale* plots overlaid with ^{13}CO (*black*) and C^{18}O (*white*) column density contours. The contours trace 30 % of the peak column density. The figure shows that the combination of ^{13}CO and C^{18}O is an excellent tracer of extinction conditions in the cores

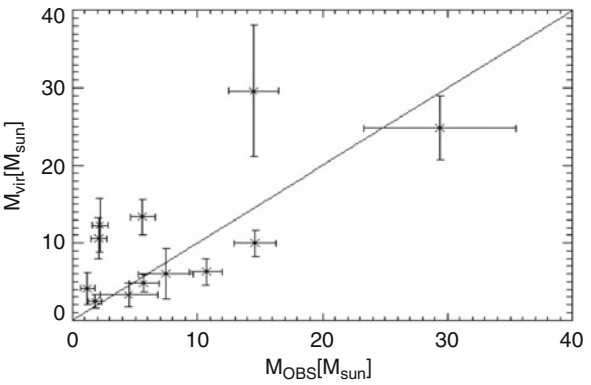

Fig. 2 Observed mass plotted against virial mass with 1σ error bars. The cores with $M_{vir}/M_{obs} > 1$ lie below the *solid line* are gravitationally bound and are expected to collapse. Cores lying above the line are gravitationally unbound. All the cores can be seen to lie within 3σ of virial equilibrium

References

1. Bourke,T.L, Hyland,A.R, Robinson,G, MNRAS **276**, 1052 (1995)
2. Wilson, W, Muller, E, Ferris, D.: ATNF Newsletter, 59
3. Gutermuth, R.A, et al., ApJS. **184**, 18–83 (2009)

Compact Molecular Outflow from a Protostar at the Earliest Evolutionary Phase

Ray S. Furuya, Yoshimi Kitamura, and Hiroko Shinnaga

Abstract Preliminary results from our Submillimeter Array observations towards an exceptionally young low-mass protostar, GF 9-2, are briefly reported.

1 Background and Observations

Without accurate knowledge of physical properties of a protostar at the earliest evolutionary stage, it is impossible to understand how young stars form through accretion process in disk-outflow systems.

In this context, we performed an extensive study of the dense cloud core associated with GF 9-2 located in the GF 9 filamentary cloud [5]. The core is also known as L 1082C, and the core mass is estimated to be $\sim 3 M_{\odot}$ from our $H^{13}CO^{+}$ (1–0) and N_2H^{+} (1–0) observations [3]. Using Nobeyama 45 m telescope, we detected H_2O maser emission towards the core center [4], strong evidence

R.S. Furuya (✉)
Subaru Telescope, National Astronomical Observatory of Japan, 650 North Aohoku Place, Hilo, HI 96720, USA

Current address: Center for General Education, University of Tokushima, Minami Jousanjima 1-1, Tokushima 770-8502, Japan
e-mail: rsf@tokushima-u.ac.jp

Y. Kitamura
Institute of Space and Astronautical Science, Japan Aerospace Exploration Agency, Yoshinodai 3-1-1, Sagamihara, Kanagawa 252-5210, Japan
e-mail: kitamura@isas.jaxa.jp

H. Shinnaga
Subaru Telescope, National Astronomical Observatory of Japan, 650 North Aohoku Place, Hilo, HI 96720, USA
e-mail: hs@naoj.org

D. Stamatellos et al. (eds.), *The Labyrinth of Star Formation*, Astrophysics and Space Science Proceedings 36, DOI 10.1007/978-3-319-03041-8_54,

for the presence of a protostellar jet. However, no molecular outflow has been found with single-dish radio telescope observations [1, 2]. We therefore performed Submillimeter Array (SMA) observations with the Compact configuration in June 2010.

2 Results and Implications

Figure 1 shows an overlay of the ^{12}CO (3–2) high-velocity wing emission on the 840 μm continuum emission map. The former represents a compact molecular outflow, while the latter thermal emission from circumstellar dust around the putative protostar. The length of the outflow lobe is $\sim 4''.5$, corresponding to 900 AU at a distance of 200 pc. Given the terminal velocity of the high-velocity wing emission, the dynamical time scale of the red lobe ($\tau_{\rm dyn}$), which is more powerful than the blue one, is estimated to be $\sim$500 years. We estimate that the red lobe has a mass loss rate ($\dot{M}_{\rm out}$) of $\sim 2 \times 10^{-6}\, M_\odot\, {\rm yr}^{-1}$. This value appears to have a consistency with that expected from the mass accretion rate onto the protostar

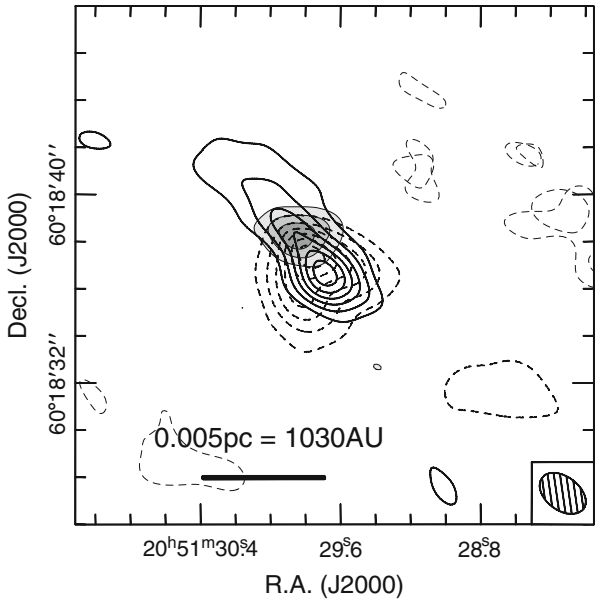

Fig. 1 An overlay of the *blue-(solid contour)* and *redshifted (dashed contour)* ^{12}CO (3–2) wing emission on the 840 μm continuum emission map (*thin contour* with *grey scale*). The *blue-* and *redshifted emission* is integrated over $-5.6 \le V_{\rm LSR}/{\rm km\ s^{-1}} \le -4.4$ and $-0.4 \le V_{\rm LSR}/{\rm km\ s^{-1}} \le +7.2$, respectively, where the systemic velocity of the cloud is $V_{\rm LSR} = -2.5\,{\rm km\ s^{-1}}$. All the contours have the 3σ intervals, starting from the 3σ levels. The ellipse in the *bottom right* corner shows the beam size in HPBW ($\theta_{\rm maj} \times \theta_{\rm min} = 2''.2 \times 1''.4$)

measured from the "infall asymmetry profiles" observed in the optically thick HCO^+ (3–2) and (1–0), and HCN (1–0) lines ($\dot{M}_{\rm acc} = 2.5 \times 10^{-5}\, M_\odot\, {\rm yr}^{-1}$; [4]), because of $\dot{M}_{\rm out} < \dot{M}_{\rm acc}$.

Furthermore, we detected compact continuum emission at 840 μm towards the outflow lobes (Fig. 1). Assuming that the detected submillimeter emission ($S_{840} = 32\,{\rm mJy}$) represents thermal emission from the circumstellar dusts around the protostar, which is driving the outflow, we estimate the mass of $M = 0.013\, M_\odot$ for a dust temperature of 20 K with the standard dust parameters. This leads a robust estimate of the lifetime of the protostar $\tau_{\rm acc} = M/\dot{M}_{\rm acc} \sim 500$ years, which reconciles with the $\tau_{\rm dyn}$ value above. Consequently, all the results strongly suggest that we are dealing with an exceptionally young low-mass protostar.

References

1. Ciardi, D. R. et al. 2000, AJ, 120, 393
2. Furuya, R. S. et al. 2009, ApJ, 692, L96
3. Furuya, R. S. et al. 2006, ApJ, 653, 1369
4. Furuya, R. S. et al. 2003, ApJS, 143, 71
5. Schneider, S. & Elmegreen, B. G.1979, ApJS 41, 87

Magnetic Field Structure Around Class 0 Protostars NGC 1333 IRAS 4A1/4A2 on Scales of 50–3,000 AU

Shih-Ping Lai and Tao-Chung Ching

Abstract We present the most complete picture to date of magnetic field structure around protostars on scales ∼50–3,000 AU with SMA dust polarization measurements obtained from all four array configurations. Our target, NGC1333 IRAS4A, is a Class 0 proto-binary system, and its magnetic field in the circumbinary envelope is consistent with an hourglass morphology on the scales of few thousand AU (Girart et al. Science 313:812–814, 2006). Here we further explore the magnetic field structure down to ∼50 AU with sub-arcsecond resolution SMA polarization data at 345 GHz. Our results show the magnetic field structure varies significantly at different spatial scales. At scales larger than ∼1,000 AU, the magnetic field again shows hourglass geometry, consistent with previous work. At the scale where the binary A1 and A2 can be resolved (<800 AU), we start to see a significant magnetic field component parallel to the circumbinary envelope. We have modeled this field component and interpreted this component to be a toroidal field. This is the first ever map of toroidal fields in circumbinary envelope.

1 Science Background

Magnetic fields are believed to play a crucial role in the star formation process. Various theoretical and numerical studies explain how magnetic fields can account for the support of clouds against self-gravity, the formation of cloud cores, the persistence of supersonic line widths, and the low specific angular momentum of cloud cores and stars [4, 5]. However, recent MHD simulations suggest that turbulence control the formation of molecular cores and the magnetic field is

S.-P. Lai (✉) • T.-C. Ching
National Tsing Hua University, 101 Section 2 Kuang Fu Road, 30013 Hsinchu, Taiwan
e-mail: slai@phys.nthu.edu.tw; chingtaochung@gmail.com

D. Stamatellos et al. (eds.), *The Labyrinth of Star Formation*, Astrophysics and Space Science Proceedings 36, DOI 10.1007/978-3-319-03041-8_55,

insignificant during the formation of stars [3]. It is therefore crucial to measure the magnetic fields in star-forming regions in order to examine the contemporary star formation theories.

2 Observations and Results

NGC 1333 IRAS 4A (hereafter IRAS 4A) is the most observed low-mass star-forming core for dust continuum polarization due to its strong continuum flux. Previous BIMA and SMA observations have revealed that the magnetic structure of IRAS 4A has an hourglass morphology at resolutions of a few hundred AU which is in agreement with the star formation models with strong magnetic support ([1,2]; Fig. 1b, this chapter).

We have obtained new SMA data in subcompact, extended array, and very extended to compliment the previous published compact array data. Figure 1a shows

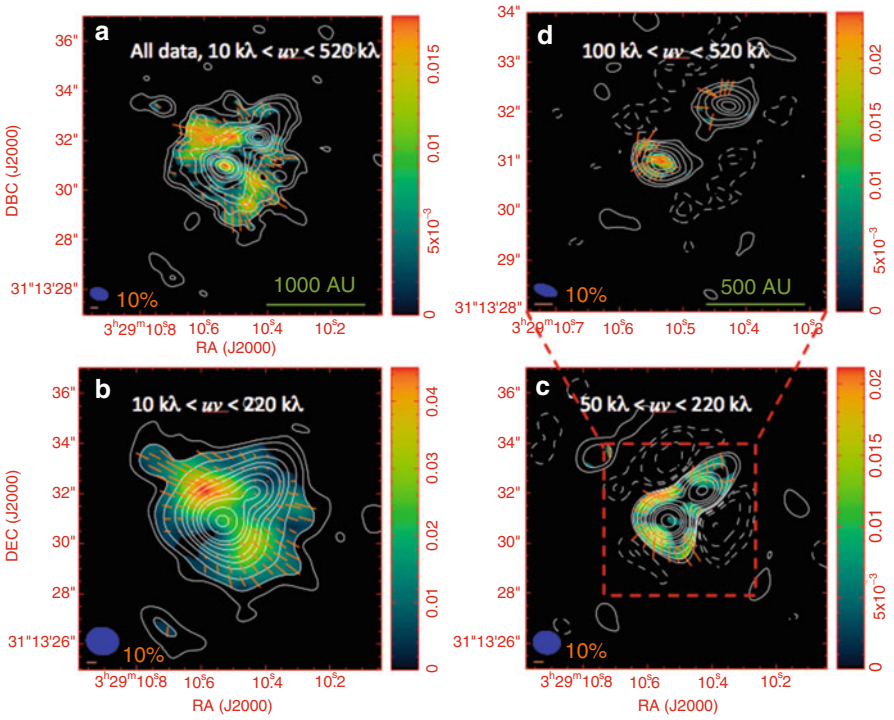

Fig. 1 Magnetic field maps of NGC1333 IRAS 4A1/4A2 made from visibilities in the marked spatial frequency (uv) ranges. The contours show the total intensity (Stokes I) at the level of 3, 5, 10, 20, 30, 40, 50, 60, 70, 80, 100, 150, and 200 noise level and the noise is 5.1, 9.6, 8.1, and 9.1 mJy/beam for (**a**), (**b**), (**c**), and (**d**), respectively. The color images show the polarized intensity. The line segments indicate the magnetic field directions with their lengths proportional to the polarization degrees

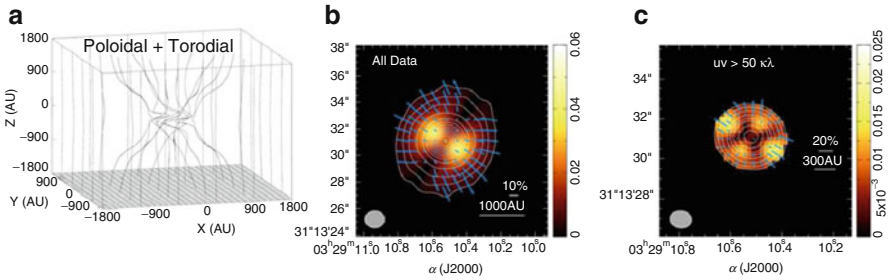

Fig. 2 Results of our empirical model. Here the z axis is the axis of symmetry with z = 0 representing the disk plane. (**a**) The magnetic field structure we used in our model that composed of a poloidal field and a toroidal field component. (**b**) The simulated SMA results with the model shown in (**a**). The line segments indicate the magnetic field directions with their lengths proportional to the polarization percentage. (**c**) Same as (**b**), but only visibilities with *uv* range >50 kλ are used

the magnetic field maps derived from all available SMA data. The combined data is the most complete dust polarization dataset to date, and its high dynamical range reveals the magnetic fields structure in various spatial scales. After analyzing the magnetic field map in different scales, we found that at scales with 1,000 AU around the core center (Fig. 1c), the field structure contains two orthogonal components: one appears to be consistent with the large scale hourglass geometry (poloidal component), and the other appears to be parallel to the pseudodisk that contains the protostellar binary, IRAS4A1 and A2 (toroidal component). Zooming in to sub-arcsecond resolutions ($0.2'' \times 0.4''$, Fig. 1d), the magnetic fields of A1 and A2 are completely separated. While A1 has stronger polarized emission and preserves strong toroidal fields, A2 shows radial field structure which is consistent with an hourglass structure.

Because the observed polarization is an integrated quantity along the line of sight, to prove the existence of the toroidal field component we have developed a computer code to generate the observed polarization and magnetic field maps for any given three-dimensional field geometry and density structure. Our code also takes into account the SMA response. Figure 2a shows the best 3D magnetic field geometry that can reproduce the polarization features seen in our data, and Fig. 2b, c are the simulated SMA images of Fig. 2a in the labeled *uv* range. The key result here is that it is necessary to include the toroidal field component in order to produce the observed orthogonal field geometry in Fig. 1c and the fan-like morphology of the polarized intensity distributions in Fig. 1b.

In short, we have obtained a dataset with richest information about magnetic field structure of a protobinary system on scales of 50–3,000 AU. Through modeling, we conclude that toroidal magnetic fields around the protobinary have been mapped for the first time. This result is consistent with the theoretical expectations that the magnetic fields could be partially frozen in the accreting material and could be dragged into the direction parallel to the disk around the protostars by the rotation of the disk.

References

1. Girart, J. M., Rao, R., & Marrone, D., Science, 313, 812–841 (2006)
2. Lai, S.-P., Ph.D. Thesis, University of Illinois at Urbana-Champaign (2001)
3. Mac Low, M., & Klessen, R. S., Reviews of Modern Physics, 76, 125 (2004)
4. McKee, C. F., & Ostriker, E. C., Annual Review of Astronomy & Astrophysics, 45, 565 (2007)
5. Mouschovias, T. C., Astrophysical Journal, 373, 169 (1991)

Mapping the Star Formation in Orion A/L1641

Ignazio Pillitteri, S.J. Wolk, S.T. Megeath, L. Allen, J. Bally, Marc Gagné, R.A. Gutermuth, L. Hartman, G. Micela, P. Myers, J.M. Oliveira, S. Sciortino, F. Walter, L. Rebull, and J. Stauffer

Abstract First phases of the process of star formation are characterized by excess in infrared and high X-ray emission. With Spitzer and XMM-Newton we have surveyed the Orion A part relative to the filamentary cloud Lynds 1641 (L1641). Furthermore, an extended spectroscopic survey has been realized to better constraint the cluster membership of stars without IR excess. We find that:

I. Pillitteri (✉) • S.J. Wolk • P. Myers • F. Walter
SAO-Harvard Center for Astrophysics, 60 Garden St, Cambridge, MA 02138, USA
e-mail: ipillitteri@cfa.harvard.edu; swolk@cfa.harvard.edu

S.T. Megeath
Ritter Observatory, Department of Physics and Astronomy, University of Toledo, Toledo, OH, USA

L. Allen
National Optical Astronomy Observatory, Tucson, AZ, USA

J. Bally
Center for Astrophysics and Space Astronomy, University of Colorado, Boulder, CO 80309, USA

M. Gagné
Department of Geology & Astronomy, West Chester University, West Chester, PA, USA

R.A. Gutermuth
Department of Astronomy, University of Massachusetts, Amherst, MA 01003, USA

L. Hartman
University of Michigan, Ann Arbor, MI, USA

G. Micela • S. Sciortino
INAF – Osservatorio Astronomico di Palermo, Palermo, Italy

J.M. Oliveira
School of Physical & Geographical Sciences, Lennard-Jones Laboratories, Keele University, Staffordshire ST5 5BG, UK

L. Rebull • J. Stauffer
CALTECH, Pasadena, CA 91125, USA

D. Stamatellos et al. (eds.), *The Labyrinth of Star Formation*, Astrophysics and Space Science Proceedings 36, DOI 10.1007/978-3-319-03041-8_56,

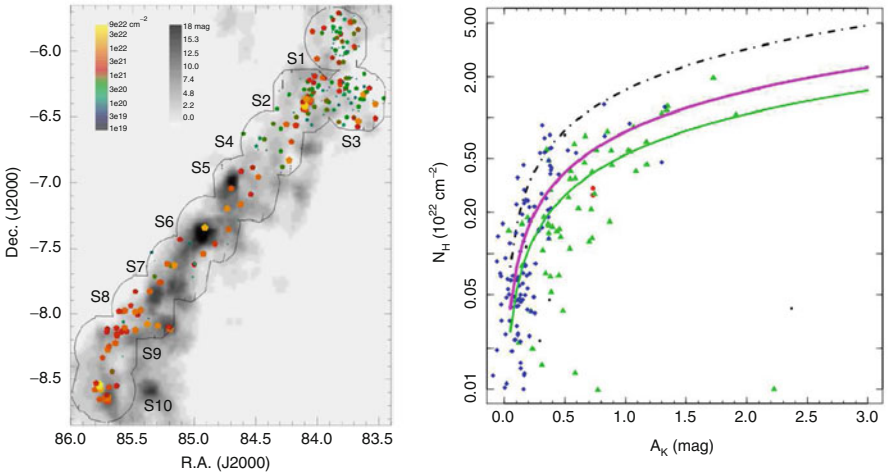

Fig. 1 *Left panel*: map of N_H absorption obtained from X-ray spectra and A_K extinction obtained from $H - K$ color. The stars with less absorption are more numerous in the northern part near Iota Orionis. These form a more evolved cluster likely in front of the cloud or less embedded in it. *Right panel*: the relationship between N_H and A_K has a flatter slope than found in ISM and ONC (Vuong et al. [2]), RCW 38 and RCW 108 (Wolk et al. [4,5]) but similar to that found in low mass star forming regions like Serpens and NGC 1333 (Winston et al. [3])

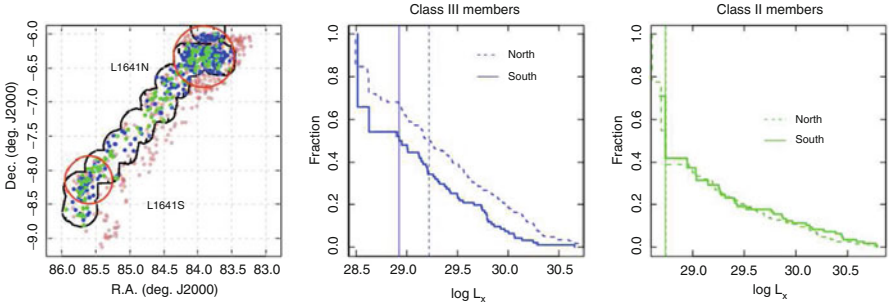

Fig. 2 The spectroscopic survey of L1641 has identified 864 members, 458 of them being Class III stars (Hsu et al. [1], *red symbols* in *left panel*). *Blue* and *green* points are Class III and Class II stars, respectively. Basing on this list of members, we have calculated upper limits to X-ray luminosity for the undetected stars and distributions of X-ray luminosity (XLD) for Class II and Class III stars (*central* and *right panel*). Class III stars in L1641 North and around Iota Orionis are more luminous in X-ray by a factor ∼2 than their analogs in L1641 South, while Class II stars are almost at the same level of luminosity in both regions

- The young stellar population in the surveyed region is composed by a number of stars in the range 1,800–2,350,
- More evolved Pre Main Sequence disk-less stars are copiously found around Iota Orionis and in L1641 North,
- This group of stars likely formed before the Orion Nebula Cloud (Fig. 1, left panel and Fig. 2),

- Stars with disks and protostars are found in small subgroups along the cloud filament of L1641,
- N_H/A_K is lower than ISM but similar to other low mass star forming regions (Fig. 1, right panel)
- This suggests some difference in the grain size and growth in star forming regions with lack of strong UV flux from massive stars.

References

1. Hsu, W.-H., Hartmann, L., Allen, L., Hernandez, J., Megeath, S. T., Mosby, G., Tobin, J. J., & Espaillat, C. 2012, ArXiv e-prints
2. Vuong, M. H., Montmerle, T., Grosso, N., Feigelson, E. D., Verstraete, L., & Ozawa, H. 2003, *A&A*, 408, 581
3. Winston, E., et al. 2010, *AJ*, 140, 266
4. Wolk, S. J., Spitzbart, B. D., Bourke, T. L., & Alves, J. 2006, *AJ*, 132, 1100
5. Wolk, S. J., Spitzbart, B. D., Bourke, T. L., Gutermuth, R. A., Vigil, M., & Comerón, F. 2008, *AJ*, 135, 693

Can We Trust CO as a Probe of the Densities and Temperatures of Molecular Clouds?

Faviola Z. Molina, Simon C.O. Glover, R. Shetty, and Ralf S. Klessen

Abstract We select a chemical magnetohydrodynamic simulation of molecular cloud formation and evolution as a typical example of a Galactic molecular cloud. Its analysis helps us understand how to interpret temperatures and densities inferred from CO line emission maps. We find that the kinetic temperature is always underestimated if it is inferred only from the excitation temperature, T_{ex}, of the ^{12}CO(1–0) emission line. We find also that CO primarily traces material at densities above the mean cloud density. In addition, we show that if one assumes a fixed value for the CO–H_2 conversion factor, then one will underestimate the density (and hence the mass) of H_2 at low column densities. In this scenario, the total H_2 mass of the cloud inferred from the emission map is only 60 % of the true mass.

Our simulation considers magnetized turbulent gas in a periodic box, and follows the chemical, thermal and dynamical evolution [1, 2]. It is characterized by a mean number density of $100\,\mathrm{cm}^{-3}$, solar metallicity, volume $(20\,\mathrm{pc})^3$, and a turbulent RMS velocity of 5 km/s. We present results after three turbulent crossing times, when the turbulence has reached a statistical steady state. We use the Monte Carlo

F.Z. Molina (✉)
Zentrum für Astronomie der Universität Heidelberg, Institut für Theoretische Astrophysik, Albert-Ueberle-Str. 2, 69120 Heidelberg, Germany

Member of the International Max Planck Research School for Astronomy and Cosmic Physics at the University of Heidelberg (IMPRS-HD), Heidelberg Graduate School of Fundamental Physics (HGSFP), 69120 Heidelberg, Germany
e-mail: molina.ita.hd@gmail.com

S.C.O. Glover • R. Shetty • R.S. Klessen
Zentrum für Astronomie der Universität Heidelberg, Institut für Theoretische Astrophysik, Albert-Ueberle-Str. 2, 69120 Heidelberg, Germany

D. Stamatellos et al. (eds.), *The Labyrinth of Star Formation*, Astrophysics and Space Science Proceedings 36, DOI 10.1007/978-3-319-03041-8_57,

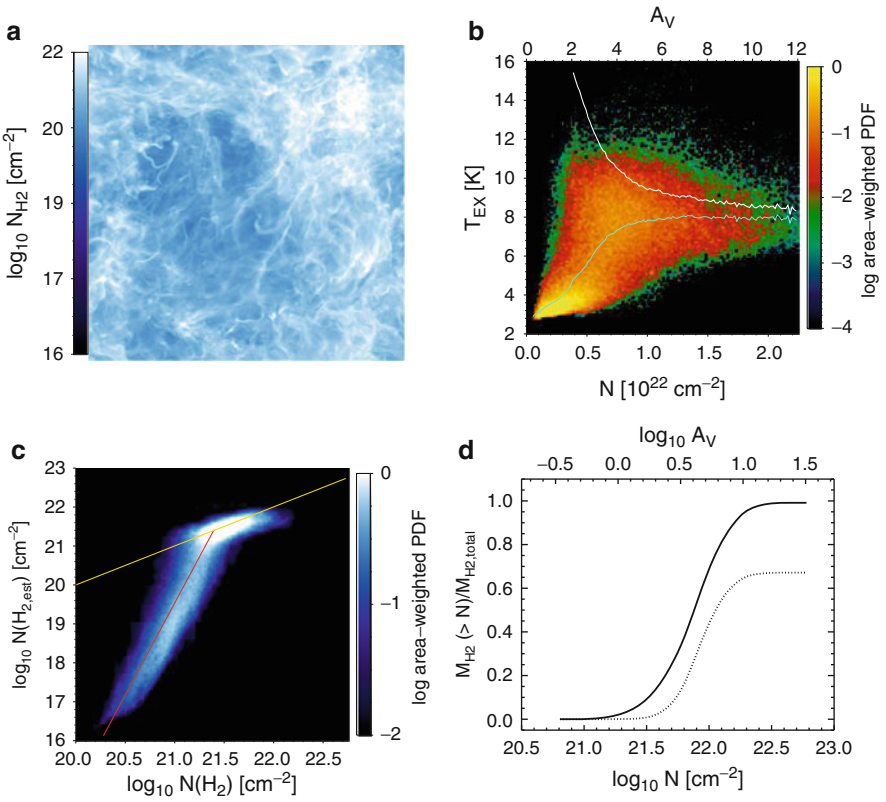

Fig. 1 (**a**) True H_2 column density. (**b**) 2D PDF of the projected T_{ex} vs. N, with reference to A_V. *Cyan line*: average of the T_{ex}, *white line*: CO mass weighted average along the LoS of T_K. (**c**) 2D PDF of the H_2 column density estimated from W_{CO} vs. the true H_2 column density. *Yellow line*: one-to-one relation. *Red line*: best fit to the low density gas. (**d**) Cumulative mass of H_2 – normalized by the total mass of H_2. *Dotted line*: inferred from W_{CO}. *Solid line*: true H_2 mass fraction

radiative transfer code RADMC-3D[1] to calculate the emergent CO line intensity [3]. Our aim here is to quantify the range of temperatures and densities where CO could be a good tracer of the physical conditions of the cloud.

Figure 1b shows the 2D Probability Density Function (PDF) of the excitation temperature (T_{ex}) calculated from the ^{12}CO(1–0) population levels. We see that the excitation temperature increases with increasing column density. On the other hand, the mean kinetic temperature at the CO ($\langle T_K \rangle$) starts with a high value but then decreases with increasing column density. The two values approach each other only at high column densities, $N \gtrsim 10^{22}$ cm^{-2}.

[1] http://www.ita.uni-heidelberg.de/~dullemond/software/radmc-3d/

In Fig. 1c, we show the 2D PDF of the H_2 column density ($N_{H2,est}$), estimated from the integrated emission map (W_{CO}), with a fixed CO–H_2 conversion factor $X_{CO} = 2 \times 10^{20}\,cm^{-2}\,K^{-1}\,km^{-1}\,s$, and the true N_{H2} (Fig. 1a). The values agree only at high densities, where the gas is optically thick. At low densities, the relationship lies far from the one-to-one relation. The cumulative mass of H_2 – normalized by the total mass of H_2 – as a function of N is shown in Fig. 1d. We compare the mass estimated from the emission map with true mass. The H_2 mass derived from W_{CO} is an underestimate at all densities. In total, the H_2 mass estimated from the W_{CO} map, and considering a fixed CO–H_2 conversion factor is only $\sim$60 % of the true value.

These results suggest that CO observations alone give a misleading view of the physical properties of molecular clouds. Complementary observations of the lower density gas using tracers such as C or C^+, are required.

References

1. Glover, S. C. O., Federrath, C., Mac Low, M.-M., and Klessen, R. S. MNRAS, **404**, 2 (2010)
2. Glover, S. C. O. and Mac Low, M.-M. MNRAS, **412**, 337 (2011)
3. Shetty, R., Glover, S. C. O., Dullemod, C.-P., and Klessen, R. S. MNRAS, **412**, 1686 (2011)

Hunting Coreshine with (Warm) Spitzer: From Grain Growth to Planet Formation

Roberta Paladini

Abstract "Hunting Coreshine with Spitzer" (P.I. R. Paladini) is the largest (165.5 h) approved Cycle-8 Warm Spitzer Mission proposal in the Galactic science category. The goal of the survey is an unbiased investigation of the coreshine effect, which is thought to provide direct evidence for grain growth in cold, dense environments. The survey has now been fully executed: 90 sources, selected from the Planck Early Cold Cores Catalog, have been observed with IRAC at 3.6 and 4.5 μm using long (i.e. deep) exposures. Here we present the rationale of the survey.

1 Context: The Coreshine Effect

For a standard (i.e. ISM-type) grain size distribution, at $\lambda > 3\,\mu$m the scattering cross-section decreases as the size of the grains becomes smaller than the wavelength. In addition, in this wavelength regime, PAH emission becomes significant, hiding potential scattered light. However, if the grain size distribution has a long tail at large sizes, these larger grains should be efficient at scattering light in the mid-IR, and this effect should be dominant over absorption, due to the lower optical depth at these wavelengths. A grain size distribution skewed towards large sizes is indeed predicted for cold, dense environments, where dust aggregation is thought to occur under the influence of turbulence and Brownian motion (e.g. [1]). Therefore, detection of mid-IR scattering (denoted *coreshine* by Pagani et al. [2] and Steinacker et al. [4], see Fig. 1) should provide evidence of the grain growth paradigm.

R. Paladini (✉)
NASA Herschel Science Center, California Institute of Technology,
770 South Wilson Ave., Pasadena, CA 91125, USA
e-mail: paladini@ipac.caltech.edu

D. Stamatellos et al. (eds.), *The Labyrinth of Star Formation*, Astrophysics and Space Science Proceedings 36, DOI 10.1007/978-3-319-03041-8_58,

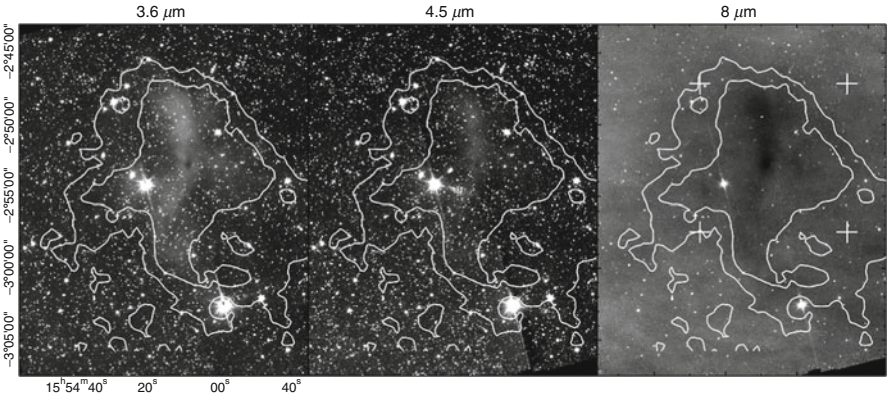

Fig. 1 Strong evidence of scattered light in L183, a relatively close (∼100 pc), low-mass core (∼80 Msun). The core shines at 4.5 μm (*middle panel*), a band not contributed to by PAH features. The spatial correlation of the shorter wavelengths (*left* and *middle panels*) emission with the extinction at 8 μm (*right panel*) testifies that the coreshine traces the densest part of the core

2 Target Selection

The starting point for the selection of the sources is the Planck Early Cold Cores Catalog (ECC, [3]). The catalog contains 915 cores, characterized by $T_D < 14$ K. A distance estimate is available for 501 sources. Goal of our Spitzer survey was to carry out an unbiased analysis of the coreshine effect. Therefore, we performed a Monte Carlo sampling of the ECC catalog using uniformly spaced bins in longitude, latitude and mass. The final sample contains 90 cold clumps, for 20 of which Herschel PACS/SPIRE data are available as part of the Herschel follow-up program on the Planck Cold Clumps (P.I. M. Juvela).

3 (Warm) Spitzer Cycle 8 Observations

The Spitzer observations have been executed between July 2011 and April 2012 and have allowed us to achieve a sensitivity of 0.008 MJy/sr in both the IRAC 3.6 and 4.5 μm bands, corresponding to a S/N up to 1,000 with respect to the expected level of emission. At the time of writing, the analysis of the data is underway.

References

1. Ossenkopf, V., 1993, A&A, 280, 617
2. Pagani, L., Steinacker, J., Bacmann, A., et al., 2010, Science, 329, 1622
3. Planck Collaboration, 2011s, A&A, 536, A23
4. Steinacker, J., Pagani, L., Bacmann, A., Guieu, S., 2010, A&A, 511, 9

The APEX-CHAMP$^+$ View of the Orion Molecular Cloud 1 Core

Tzu-Cheng Peng, Friedrich Wyrowski, Luis A. Zapata, Rolf Güsten, and Karl M. Menten

Abstract A high density portion of the Orion Molecular Cloud 1 (OMC-1) contains the prominent, warm Kleinmann-Low (KL) nebula plus a farther region in which intermediate to high mass stars are forming. Its nearness makes the OMC-1 core region a touchstone for research on the dense molecular interstellar medium. Using the 2×7 pixel submillimeter CHAMP$^+$ array on the Atacama Pathfinder Experiment telescope (APEX), we have imaged the line emission from the multiple transitions of several carbon monoxide (CO) isotopologues over the OMC-1 core region. The large-scale images of ^{12}CO, ^{13}CO, and C^{18}O from mid-J transitions ($J = 6-5$ to $8-7$) have been presented recently. Here we report the shell-like structure seen in ^{12}CO lines toward Orion BN/KL, which is likely associated with the expanding bubble suggested before.

1 Introduction and Observations

The Orion Molecular Cloud 1 (OMC-1) is a complex region of the interstellar medium stretching over more than 2.4 pc on the sky. Much of this region's promi-

T.-C. Peng (✉)
Max-Planck-Institut für Radioastronomie (MPIfR), Auf dem Hügel 69, 53121 Bonn, Germany

Université de Bordeaux, Observatoire Aquitain des Sciences de l'Univers, 2 rue de l'Observatoire, BP 89, F-33271 Floirac Cedex, France
e-mail: Tzu-Cheng.Peng@obs.u-bordeaux1.fr

F. Wyrowski • R. Güsten • K.M. Menten
Max-Planck-Institut für Radioastronomie, Bonn, Germany

L.A. Zapata
Centro de Radioastronomía y Astrofísica, UNAM, Apdo. Postal 3-72 (Xangari), 58089 Morelia, Michoacán, México

D. Stamatellos et al. (eds.), *The Labyrinth of Star Formation*, Astrophysics and Space Science Proceedings 36, DOI 10.1007/978-3-319-03041-8_59,

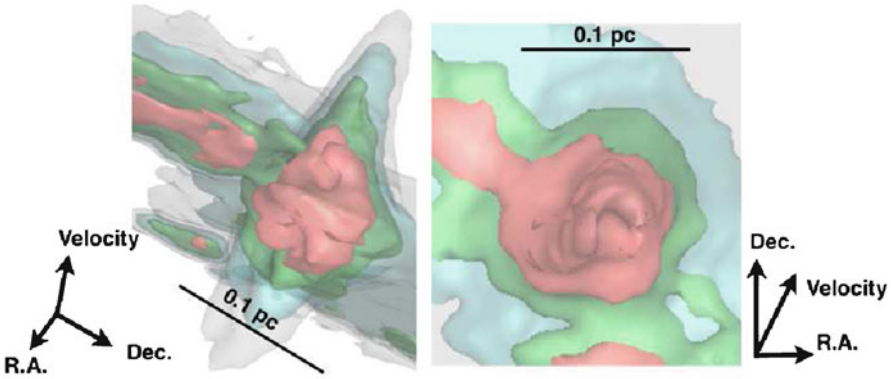

Fig. 1 Isothermal three-dimensional (R.A., Dec., and velocity) view of Orion BN/KL. The *left* and *right images* show the edge-on and face-on shell-like structures, respectively. Different isothermal surfaces of 60, 90, 120, and 150 K are plotted in *gray, blue, green*, and *red*, respectively

nence is due to its distance of just 414 ± 7 pc [3], which makes the ONC and OMC-1 the closest regions of recent (few million years old) and ongoing high-mass star formation. The OMC-1 core region (1 pc^2-sized dense molecular cloud region) may be divided into three main zones, all of which show bright (sub)millimeter wavelength emission from warm dust and molecular gas: the Becklin-Neugebauer/Kleinmann-Low (BN/KL) region, Orion South (OMC-1S or Orion-S) and the Orion Bar. We have imaged the line emission from the multiple transitions of several carbon monoxide (CO) isotopologues over the OMC-1 core region with the Atacama Pathfinder Experiment telescope (APEX). Our observations employed the 2×7 pixel submillimeter CHAMP+ array to produce maps (300 arcsec $\times$ 350 arcsec) of ^{12}CO, ^{13}CO, and C^{18}O from mid-J transitions ($J = 6-5$ to $8-7$). We also obtained the ^{13}CO and C^{18}O J = 3–2 images toward this region. The large-scale images and main results are presented by Peng et al. [4] (Fig. 1).

2 Orion BN/KL Shell-Like Structure

The Orion BN/KL region harbors the eponymous hot core, which was taken to be the prototype of the hot dense regions observed around many newly formed stars. An interesting alternative explanation for this region's energetics (other than being powered by an embedded central heating source) is a protostellar merger event that released a few times 10^{47} erg of energy about 500 years ago (e.g., [1, 2, 7]). The compact and warm structures toward the BN/KL region traced by the ^{12}CO $J = 6$–5 and $J = 7$–6 lines, which display a very broad range of velocities (up to about ± 100 km s^{-1}), are part of the enigmatic molecular outflow that seems to be produced by a violent explosion during the disruption of a massive young stellar

system [1, 2, 6]. Our observations reveal that some faint filamentary structures are likely associated with the high-velocity ^{12}CO bullets [5] reported by Zapata et al. [6]. In addition, the shell structure at the center of BN/KL is seen, which may be related to the expanding molecular bubble observed by Zapata et al. [7] with an expanding velocity of about 15 km s^{-1}.

References

1. Bally, J., Cunningham, N. J., Moeckel, N., et al. 2011, ApJ, 727, 113
2. Bally, J., & Zinnecker, H. 2005, AJ, 129, 2281
3. Menten, K. M., Reid, M. J., Forbrich, J., & Brunthaler, A. 2007, A&A, 474, 515
4. Peng, T.-C., Wyrowski, F., Zapata, L. A., Güsten, R., & Menten, K. M. 2012, A&A, 538, A12
5. Peng, T.-C., Zapata, L. A., Wyrowski, F., Güsten, R., & Menten, K. M. 2012, A&A, 544, L19
6. Zapata, L. A., Schmid-Burgk, J., Ho, P. T. P., Rodríguez, L. F., & Menten, K. M. 2009, ApJL, 704, L45
7. Zapata, L. A., Schmid-Burgk, J., & Menten, K. M. 2011, A&A, 529, A24

Spectral Characteristics of Young Stars Associated with the Sh2-296 Nebula

Beatriz Fernandes and Jane Gregorio-Hetem

Abstract Aiming to contribute to the understanding of star formation and evolution in the Canis Major (CMa R1) Molecular Clouds Complex, we analyze the spectral characteristics of a population of young stars associated with the arc-shaped nebula Sh2-296. Our XMM/Newton observations detected 109 X-ray sources in the region and optical spectroscopy was performed with Gemini telescope for 85 optical counterparts. We identified and characterized 51 objects that present features typically found in young objects, such as Hα emission and strong absorption on the Li I line.

1 Introduction

CMa R1 is an association of bright stars and clusters located at a distance of approximately 1 kpc and distributed near Sh2-296, a well-known bright rimmed arc-shaped nebula, which nature is unclear (fossil HII region or supernova remnant). Star formation in this region has been going on for more than 10 Myr and the young stellar population seems to be composed by at least two groups with different ages, both including several tens of low-mass stars detected only by X-ray observations [1].

While X-ray observations are a very efficient method to find large samples of low-mass pre-Main Sequence stars, in this work we will also make use of spectroscopic data in order to confirm the nature of X-ray sources detected in this region and evaluate the evolutionary status of the young stellar population associated with Sh2-296.

B. Fernandes (✉) • J. Gregorio-Hetem
Universidade de São Paulo, IAG, São Paulo, Brazil
e-mail: bfernandes@astro.iag.usp.br; jane@astro.iag.usp.br

D. Stamatellos et al. (eds.), *The Labyrinth of Star Formation*, Astrophysics and Space Science Proceedings 36, DOI 10.1007/978-3-319-03041-8_60,

2 Results

Using the Gemini South telescope for multi-object spectroscopy (GMOS), we have obtained spectra for 85 optical counterparts of 109 X-ray sources in CMa R1 region, detected with the satellite XMM/Newton. We identified 51 objects (including 45 X-ray sources) presenting young star features as, for example, the Li I line at 6,708 Å and Hα in emission or absorption (38 objects), which are typical of T Tauri stars.

Spectral types have been determined by comparing the observed spectra with libraries of standard spectra. For the late-type stars, the adopted spectral types range from K7 to M8 and we estimate a typical uncertainty of one subclass.

Among the T Tauri candidates in our sample we have identified: 9 objects that have spectral types and Hα emission consistent with classical T Tauri stars (CTTSs), almost 10 weak-line T Tauri (WTTS), and 19 post-T Tauri star (PTTSs) candidates, according to the criteria from [3] and [2].

3 Conclusions

Using optical spectra obtained with GMOS we were able to identify and characterize part of the YSO population associated with the Sh2-296 Nebula.

We identified 51 objects showing typical YSO features and classified 47 of these as: WTTSs or PTTSs (74 % of the sample), CTTSs (18 %) and Herbig Ae/Be stars (2 %). With the spectral characterization we added four new YSO candidates to the CMa R1 region that had not been identified from our previous X-ray observations. We also verified that two X-ray sources do not show the typical YSO features in their spectra and need to have their nature confirmed.

In the future we aim to expand our sample and obtain higher resolution spectra, which combined with photometric data will help us better evaluate the evolutionary stage of the CMa R1 young stellar population.

Acknowledgements This work was supported by CNPq Project 142849/2010-3 and Capes/ Cofecub 712/2011.

References

1. Gregorio-Hetem, J.; Montmerle, T., Rodrigues, C. V., Marciotto, E., Preibisch, T., Zinnecker, H., 2009, A&A, 506, 711–727
2. Martín, E. L. 1997, A&A, 321, 492
3. White, R. J., & Basri, G. 2003, ApJ, 582, 1109

Part VII
The Stellar Initial Mass Function

Mapping the Present-Day Prestellar Core Mass Function into the Stellar IMF

Katy Holman, Stefanie K. Walch, Simon Goodwin, and Anthony Peter Whitworth

Abstract The fact that the shapes of the Present-Day Prestellar Core Mass Function (PDPCMF) and the Stellar Initial Mass Function (StIMF) appear to be very similar is purely coincidental, *unless* the mapping from the PDPCMF to the StIMF is statistically self similar. Either way, there is a huge amount of physics that occurs between a prestellar core and a protostar, and theories for the genesis of the PDPCMF should be presented as such, not as theories for the origin of the StIMF. Here we explore the constraints that the observed statistical properties of stars place on self-similar mappings. We find a simple mapping that is able to deliver the observed StIMF, the binary frequency as a function of primary mass, and the distribution of mass ratios for binaries with Sun-like primaries. This mapping implies that the local efficiency is high (typically a core spawns ∼4 stars, and these stars comprise ∼87% of the core's initial mass); that most of the stars spawned by a single core have masses within a factor ∼4 of each other; that most cores deliver one long-lasting binary into the field, and in ∼75% of cases this binary involves the two most massive stars formed in the core; that the remaining ∼25% of binaries involve random pairings of the stars formed in the core.

K. Holman (✉) • A.P. Whitworth
Cardiff School of Physics & Astronomy, Cardiff University, Queens Buildings, 5 The Parade, Cardiff CF24 3AA, UK
e-mail: Katy.Holman@astro.cf.ac.uk; ant@astro.cf.ac.uk

S.K. Walch
Max-Planck-Institut für Astrophysics, Garching bei München, 422 Germany
e-mail: walch@mpa-Garching.mpg.de

S. Goodwin
Department of Physics & Astronomy, University of Sheffield, Hicks Building, Housfield Road, Sheffield S37RH, UK
e-mail: s.goodwin@sheffield.ac.uk

D. Stamatellos et al. (eds.), *The Labyrinth of Star Formation*, Astrophysics and Space Science Proceedings 36, DOI 10.1007/978-3-319-03041-8_61,

1 Introduction

If one accepts that there is a significant similarity between the shapes of the PDPCMF and the StIMF, it is interesting to consider three possibilities.

POSSIBILITY 1. The StIMF has exactly the same shape as the PDPCMF, just shifted to lower mass. This possibility requires there to be a unique scale-free mapping, with each core spawning stars of a single mass. Thus, for example, each core might spawn three stars, each of mass $0.2M_{\rm C}$ (where $M_{\rm C}$ is the total core mass), with two of them forming a long-lived binary. This would be rather surprising. Given the non-linearity of the physics involved in converting cores to stars, one might expect a much more chaotic mapping. Moreover, a unique scale-free-mapping of this type can be dismissed because it is unable to reproduce the observed binary statistics: the binary frequency would be independent of primary mass, $f(M_1) = f_{\rm O}$, and all binary systems would have mass ratio $q = 1$.

POSSIBILITY 2. The StIMF has the same shape as the PDPCMF, but shifted to lower masses, *and* broader. This possibility admits a statistically self-similar mapping. For example, the probability that a $1\,{\rm M}_\odot$ core spawns a single $0.5\,{\rm M}_\odot$ star would be the same as the probability that a $2\,{\rm M}_\odot$ core spawns a single $1\,{\rm M}_\odot$ star; the probability that a $1\,{\rm M}_\odot$ core spawns a binary system with components 0.4 and $0.2\,{\rm M}_\odot$ would be the same as the probability that a $0.5\,{\rm M}_\odot$ core spawns a binary system with components 0.2 and $0.1\,{\rm M}_\odot$. However, there could be a large variance in the outcomes of individual core collapses (this is only possible if the StIMF is broader than the PDPCMF), and it is now possible to reproduce the observed binary statistics. In addition, we can make some interesting, i.e. falsifiable, predictions regarding the outcome of core collapse and fragmentation.

POSSIBILITY 3. The StIMF retains little or no memory of the PDPCMF. Both have log-normal shapes, by virtue of the Central Limit Theorem, because both are generated by the product of many different stochastic processes. The processes generating the StIMF are sufficiently numerous that the StIMF would be log-normal, even if the PDPCMF were not. In its most extreme form this possibility is also hard to sustain, in the sense that there is no correlation between core mass and stellar mass. It seems likely that high-mass stars are formed from relatively high-mass cores, and that the most common stars (i.e. those near the peak of the StIMF) form primarily from the most common cores (i.e. those near the peak of the PDPCMF). Therefore the truth probably lies somewhere between POSSIBILITIES 1 and 2.

Implicitly we are assuming that the components of long-lived binary systems are normally formed in the same birth-core. Given the inefficiency of capture mechanisms for forming binaries, this would seem to be a secure assumption.

2 The Strategy and Goal

In the present paper we explore POSSIBILITY 2. For simplicity we consider only the central ranges of the PDPCMF and StIMF where both can be approximated by log-normal distributions. We can easily add high-mass power law tails, and the basic conclusions are not changed, but the mathematics is less transparent. At each stage we apply Occam's Razor, i.e. we keep the model as simple as possible. We introduce new features and parameters only if they are needed to significantly improve the fit – no matter how well motivated by physical considerations we believe them to be.

The goal is to fit the following quantities.

(i) A log normal StIMF, with median $\mu_{\rm s}$ and standard deviation $\sigma_{\rm s}$ satisfying

$$\mu_{\rm s} = -0.70 \pm 0.10 \ (w_{\mu_{\rm s}} = 0.25),$$
$$\sigma_{\rm s} = \ \ 0.55 \pm 0.05 \ (w_{\sigma_{\rm s}} = 0.25)$$

(Chabrier [3]). Here, and for the other parameters, the first number is the expectation value, the second is the uncertainty, and the third is the weight that we attach to fitting this parameter; the sum of all the weights is required to be unity.

(ii) The binary frequency in six different primary-mass bins, as evaluated by Basri and Reiners [1], Bergfors et al. [2], Close et al. [4], Mason et al. [6], Preibisch et al. [9] and Raghavan et al. [10]. For example, in the Sun-like bin ($0.8 < M_1/{\rm M}_\odot \leq 1.2$), Raghavan et al. find

$$b_{\sim {\rm M}_\odot} = 0.45 \pm 0.03 \ (w_{b_{\sim {\rm M}_\odot}} = 0.05).$$

Each of the six bins is given a weight of 0.05, and so the net weight attached to fitting the binary frequency as a function of mass is 0.30.

(iii) The distribution of mass ratios for binaries with Sun-like primaries is as found by Raghavan et al., for example,

$$P_{\sim {\rm M}_\odot;\, 0.2<q\leq 0.4} = 0.25 \pm 0.05 \ (w_{P_{\sim {\rm M}_\odot;\, 0.2<q\leq 0.4}} = 0.04).$$

We reduce the data to five q-bins, and each is given a weight of 0.04, so the net weight attached to fitting the mass ratios is 0.20.

We note that the weights are arbitrary. However, it turns out that the model delivers such a good fit, that altering them does not have a significant effect. There are 13 values to fit.

3 The Model and Its Parameters

The model contains seven parameters. These are the median, μ_C, and standard deviation, σ_C, of the log-normal PDPCMF; the efficiency of star formation in a core, η, i.e. the fraction of a core's mass that ends up in stars[1]; the mean number of stars spawned by a single core, $\mathcal{N}$; the standard deviation, σ_O, of the masses of stars spawned by a single core; the fraction of cores that deliver a long-lived binary system comprising the two most massive stars spawned by that core, f_A; and the fraction of cores that deliver a long-lived binary system comprising the most massive star spawned by that core paired with a random secondary, f_B.

Of these seven parameters, only four are truly free. μ_C and σ_C are already tightly constrained by observation, and are likely to become more so in the future.[2] The displacement from the peak of the StIMF to the peak of the PDPCMF, $\mu_C - \mu_S$, is related to the efficiency, η, and the mean number of stars spawned by a core, $\mathcal{N}$, by

$$\mu_C - \mu_S = \log_{10}\left(\frac{\mathcal{N}}{\eta}\right);$$

Therefore, in as much as μ_C and μ_S are well constrained by observation, only one of η and $\mathcal{N}$ can be chosen freely; $\mathcal{N}/\eta = 10^{(\mu_C - \mu_S)} = 4 \pm 1$.

Moreover, the degeneracy between η and $\mathcal{N}$ can be raised by considering the observed binary statistics. To see how this works, in principle, consider the following *Gedanken Experiment*. For simplicity, assume that there are equal numbers of single stars and binary systems in the field (this is actually not far from the truth). This can be achieved in two simple ways. (i) $\mathcal{N} = 1.5$, so that half the cores must deliver single stars, and the other half must deliver binary systems. However, this means that the binary frequency decreases with increasing primary mass, which is the opposite of what is observed. (ii) $\mathcal{N} = 3$, so that each core must deliver three stars, a single and a binary containing the most massive star of the three. This has to be the preferred choice, because now the binary frequency increases with primary mass, as observed.

The standard deviations add in quadrature,

$$\sigma_S^2 = \sigma_C^2 + \sigma_O^2 .$$

Since σ_S and σ_C are observed to be rather similar, this means that σ_O cannot be very large, i.e. the masses of stars spawned by a single core do not have a very large dynamic range. On the other hand, if – as seems to be the case – the distribution of mass ratios for Sun-like primaries is rather flat, there are some binary systems whose

[1] Note that an observed prestellar core that contributes to the PDPCMF is likely to accumulate further mass during the time that it collapses and fragments to form stars, and so $\eta > 1$ is possible.

[2] Note that we are concerned here with the overall PDPCMF of the ensemble of cores that forms the field-star population, rather than the PDPCMF for a particular star formation region.

components have quite disparate masses. This requires that $\sigma_{\rm O}$ is not too small, and that a significant fraction of binary systems involve the most massive star pairing up with a random secondary, i.e. $f_{\rm B} > 0$.

The motivation for considering two pairing algorithms for binary systems is informed by the numerical experiments of [7, 8], who considered the dissolution of small-N clusters of the sort that might be formed from a single core in our model. If they treated the stars purely as point masses, moving under their mutual gravity, the outcome almost always involved a binary made of the two most massive stars, with the remainder being ejected as singles ($f_{\rm A} \sim 1,\ f_{\rm B} \sim 0$). Conversely, when the dynamics included dissipation due to attendant discs, the outcome was a binary comprising the most massive star paired up with any one of the other stars ($f_{\rm A} \sim 0,\ f_{\rm B} \sim 1$).

4 A Monte Carlo Experiment

We conduct a Monte Carlo experiment by considering, in turn, many different combinations of the model parameters, in the ranges $-0.15 \leq \mu_{\rm C} \leq +0.15$, $0.35 \leq \sigma_{\rm C} \leq 0.55$, $0.25 \leq \eta \leq 1$, $1 \leq \mathscr{N} \leq 6$, $0 \leq \sigma_{\rm O} \leq 0.5$, $0 \leq f_{\rm A} \leq 1$, $0 \leq f_{\rm B} \leq 1$ ($f_{\rm A} + f_{\rm B} \leq 1$). For each combination of model parameters, we generate many random core masses, $M_{\rm C}$. We multiply each core mass by η to determine the total mass of stars spawned by that core. We then generate $\mathscr{N}$ random relative stellar masses from a log-normal distribution with standard deviation $\sigma_{\rm O}$,[3] and then normalise them so that their total mass equals $\eta M_{\rm C}$.[4] Next we top up the different mass-bins used to determine the StIMF. Finally we decide whether a long-lived binary is formed, and of which type (two most massive stars, or most massive star with a random secondary), record the primary and secondary masses, and top up the binary-statistics bins as appropriate.

For each combination of model parameters, we must generate at least 10^6 stars, to obtain reliable statistics. The quality, $\mathscr{Q}$, of a particular combination is determined by computing the values $\mu_{\rm S}$ and $\sigma_{\rm S}$ characterising the StIMF; the binary frequencies in the six primary-mass bins, $b(M_1)$; and the distribution of mass ratios for Sun-like primaries in five q-bins, $P_{\sim {\rm M}_\odot}(q, q + \Delta q)$: 13 values in total. Then

$$\mathscr{Q} = \sum_X \left\{ \frac{W_X\,(X - V_X)^2}{U_X^2} \right\},$$

[3]For non-integer values of $\mathscr{N}$ we consider a mixture of the integer values immediately above and below, having mean equal to $\mathscr{N}$. Thus, for example, if $\mathscr{N} = 3.2$, 80 % of cores spawn three stars, and 20 % spawn four stars.

[4]There are two ways of performing this normalisation, but the results are essential indistinguishable.

where the sum is over all 13 values, W_X is the weight attributed to fitting parameters X, V_X is the expectation value for X, and U_X is the uncertainty in X. $\mathscr{Q}$ is, in effect, the number of standard deviations by which the model departs from being a perfect fit to the observational data. Thus $\mathscr{Q} = 0$ would be a perfect fit, and small $\mathscr{Q}$ is a good fit.

5 Results and Discussion

The best-fit model is extremely good, with $\mathscr{Q} = 0.17$ (i.e. one sixth sigma from being perfect). It has $\mu_{\rm C} = 0$ (i.e. median core mass is $M_{\rm C} = {\rm M}_{\odot}$); $\sigma_{\rm C} = 0.52$ (i.e. the PDPCMF is only slightly narrower than the StIMF); $\eta = 0.87$ (i.e. a very high efficiency)[5]; $\mathscr{N} = 4.3$ (i.e. a core typically spawns between four and five stars); $\sigma_{\rm O} = 0.19$ (i.e. the stars spawned by a single core usually have masses within a factor of four of each other); $f_{\rm A} \simeq 0.75$ (i.e. most cores spawn a long-lived binary comprising the two most massive stars); $f_{\rm B} \simeq 0.25$ (i.e. a few cores spawn a long-lived binary in which the most massive star is paired with a random secondary).

It is worth noting that if we replace the Raghavan estimate of the binary frequency of Sun-like stars with the [5] estimate (which is significantly higher), we obtain an essentially perfect fit, $\mathscr{Q} = 0.01$, with essentially the same model parameters, except that $\mathscr{N}$ is somewhat lower.

Whilst the details of this model are likely to need revising and elaborating as more and better observational data accumulates, the basic conclusions are probably rather robust. If one relies on dynamical relaxation in the small-N clusters spawned by single cores, to produce the majority of binary systems, the increase in binary frequency with increasing primary mass requires that the small-N clusters contain $\mathscr{N} \sim 4$ stars. The measured offset between the peaks of the PDPCMF and StIMF then implies a high efficiency $\eta = \mathscr{N}/(4 \pm 1)$. For stars in the central range of the StIMF, a flat distribution of mass ratios requires that the stars spawned by a single core have a range of masses, $\sigma_{\rm O} \lesssim 0.2$, but the similarity between the standard deviations of the PDPCMF and StIMF mean that this range cannot be too large, and therefore some binaries must involve random pairings. In addition, the relatively high numbers of triples and quadruples, particularly among young stellar populations, supports the hypothesis that many cores are spawning at least three or four stars.

[5]But recall that between the epoch when a core is observed and its mass estimated, and the epoch when it forms stars, it may accumulate further mass. Therefore the mass of the envelope may exceed $(1 - \eta)M_{\rm C}$.

References

1. G. Basri, A. Reiners, AJ. **132**, 663 (2006)
2. C. Bergfors, W. Brandner, M. Janson, S. Daemgen, K. Geissler, T. Henning, S. Hippler, F. Hormuth, V. Joergens, R. Köhler, A&A, **520**, A54 (2010)
3. G. Chabrier, PASP, **115**, 763 (2003)
4. L. M. Close, N. Siegler, M. Freed, B. Biller, ApJ, **587**, 407 (2003)
5. A. Duquennoy, M. Mayor, A&A **248**, 485 (1991)
6. B. D. Mason, D. R. Gies, W. I. Hartkopf, W. G. Bagnuolo, Jnr., T. ten Brummelaar, H. A. McAlister, AJ, **115**, 821 (1998)
7. J. M. McDonald, C. J. Clarke, MNRAS, **262**, 800 (1993)
8. J. M. McDonald, C. J. Clarke, MNRAS, **275**, 671 (1995)
9. T. Preibisch, Y. Balega, K. Hofmann, G. Weigelt, H. Zinnecker, NewA, **4**, 531 (1999)
10. D. Raghavan, H. A. McAlister, T. J. Henry, D. W. Latham, G. W. Marcy, B. D. Mason, D. R. Gies, R. J. Whitw, T. A. ten Brummelaar, ApJS, **190**, 1 (2010)

Astrometric and Photometric Mass Functions in Open Clusters from UKIDSS GCS DR9

Nicolas Lodieu, Steve Boudreault, N.R. Deacon, and N.C. Hambly

Abstract We present the results of a deep ($J = 19.1$ mag) infrared (*ZYJHK*) survey of three open clusters surveyed by the UKIRT Infrared Deep Sky Survey (UKIDSS) Galactic Clusters Survey (GCS) Data Release 9: the Pleiades, α Per, and Praesepe. We have selected cluster member candidates combining photometry in five near-infrared filters and proper motions derived from the multiple epochs provided by the UKIDSS GCS DR9. We provide revised membership for all previously published low-mass stars and brown dwarfs recovered by the GCS and complete the full census with new cluster member candidates. We find no evidence of K-band variability in all three clusters with mean dispersions of 0.06–0.09 mag, except for a few sources. We derive the cluster mass functions and find that their shapes are very similar and in agreement with the log-normal representation of the (system) field mass function although with some variations in the characteristic mass and dispersion values. Finally, we estimate the binary fraction of low-mass stars and brown dwarfs in Praesepe and the Pleiades, respectively, and compare them with the latest hydrodynamical simulations.

N. Lodieu (✉) • S. Boudreault
Instituto de Astrofísica de Canarias (IAC), C/Vía Láctea s/n, E-38200 La Laguna, Tenerife, Spain

Departamento de Astrofísica, Universidad de La Laguna (ULL), La Laguna, Tenerife, Spain
e-mail: nlodieu@iac.es,szb@iac.es

N.R. Deacon
Max-Planck-Institute für Astronomie, Königstuhl 17, 69117 Heidelberg, Germany

N.C. Hambly
Scottish Universities Physics Alliance (SUPA), Institute for Astronomy, School of Physics & Astronomy, University of Edinburgh, Royal Observatory, Blackford Hill, Edinburgh EH9 3HJ, UK

D. Stamatellos et al. (eds.), *The Labyrinth of Star Formation*, Astrophysics and Space Science Proceedings 36, DOI 10.1007/978-3-319-03041-8_62,

1 Clusters Surveyed by the UKIDSS GCS

The UKIDSS GCS is a deep large-scale infrared survey covering ∼1,000 square degrees in 10 star-forming regions and open clusters down to $K = 18.4$ mag at 2 epochs to study the Initial Mass Function (IMF) and its dependence with environment in the stellar and substellar regimes using an homogeneous dataset. We focused on three clusters with the largest mean proper motions: the Pleiades (d = 120.2 pc; age $= 125 \pm 8$ Myr, $\mu \sim 50$ mas/year, $b = -24°$), α Per (d $= 170$ pc; age = 80–90 Myr, $\mu \sim 35$ mas/year, $b = -7°$), and Praesepe (d $= 182$ pc; age $=$ 590 Myr, $\mu \sim 38$ mas/year, $b = 32°$).

2 Selection Procedure

We have selected all good quality point sources in the Pleiades, α Per and Praesepe detected in at least $JHK1$ (where $K1$ stands for the first K-band epoch) and where available, in Z, Y, and $K2$ (second K-band epoch). On the one hand, we used several colour-magnitude diagrams involving colours such $Z-J$, $Y-J$, $Z-K$, and $J-K$ to select photometrically member candidates based on the position of previously-known members from earlier studies in all three clusters (Fig. 1). In addition to the photometry, we added an astrometric criterion by selecting all point sources whose formal errors on the proper motion within 3σ of the mean motion of each cluster (Fig. 2). On the other hand, we used the probabilistic approach described in [5] to assign a formal membership probabilities to each cluster member candidate after applying very conservative photometric cuts.

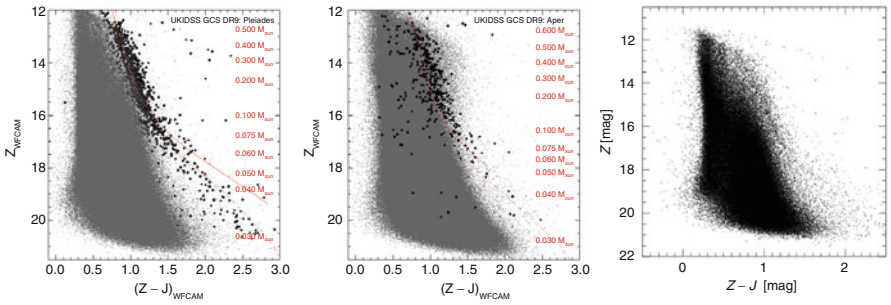

Fig. 1 $(Z-J, Z)$ colour-magnitude diagrams for the Pleiades (*left*), α Per (*middle*), and Praesepe (*right*). The *black dots* overplotted on the Pleiades and α Per diagrams represent previously-published sources recovered in the GCS DR9

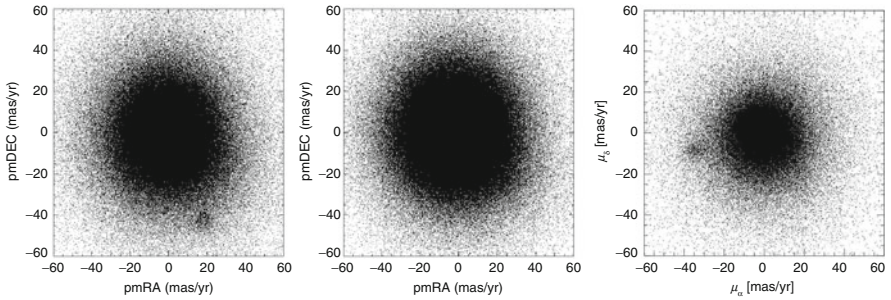

Fig. 2 Proper motion vector point diagrams for the Pleiades (*left*), α Per (*middle*), and Praesepe (*right*): the mean proper motion for the three clusters are ($\mu_\alpha \cos\delta$, $\mu\delta$ = (19.2,−45.7), (22.7,−26.5), and (−35.8,−12.8) mas/year, respectively)

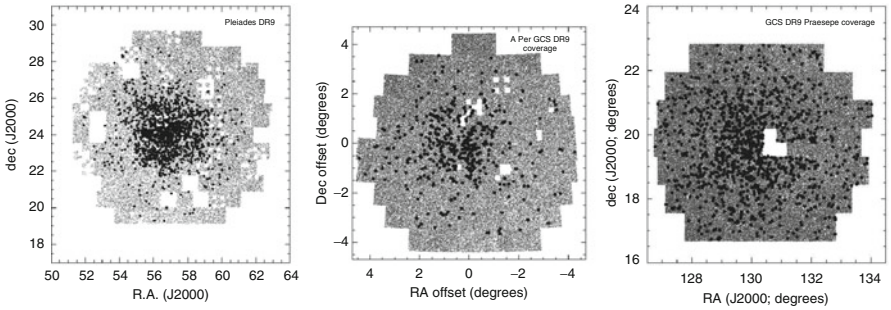

Fig. 3 UKIDSS GCS DR9 coverage for the Pleiades (80 square degrees; *left*), α Per (56 square degrees; *middle*), and Praesepe (36 square degrees; *right*). *Dots* are member candidates

3 Results from UKIDSS GCS DR9

We analysed the GCS photometric and astrometric data in the Pleiades (∼80 square degrees; [6]), α Per (56 square degrees; [7]), and Praesepe (36 square degrees; [3]), see Fig. 3. The main results of this wide, deep, and homogeneous survey can be summarised as follows:

- We recovered member candidates in all three clusters previously published and we updated their membership assignations
- We selected photometrically and astrometrically potential member candidates using two independent but complementary methods: a probabilistic analysis and a more standard method combining photometry and proper motion cuts
- We investigated the K-band variability of cluster members and found virtually no variability at the level of 0.06–0.09 mag in all clusters, except for a few sources
- We derived the luminosity functions from both selection methods and found no difference within the error bars in the three clusters

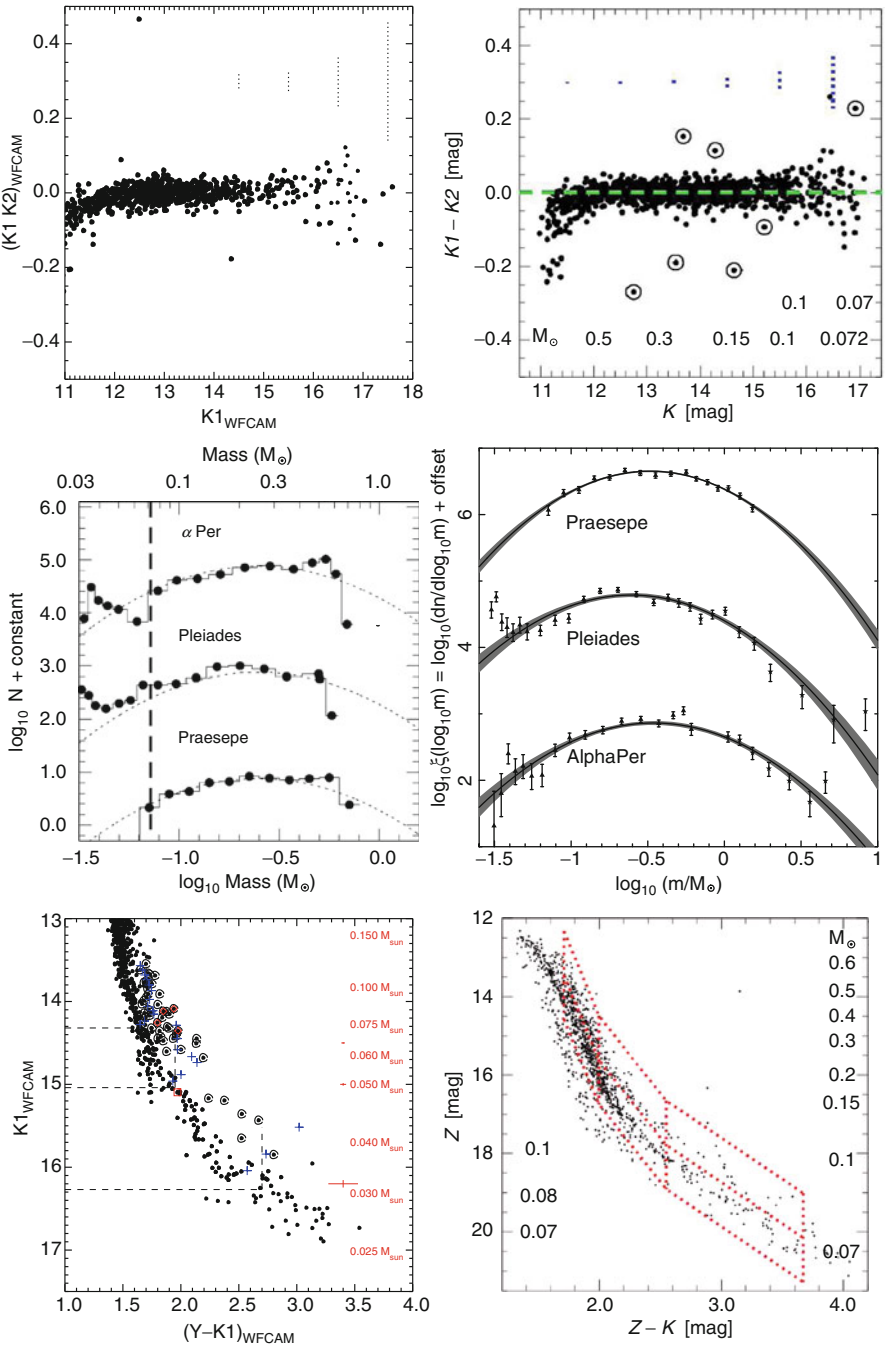

Fig. 4 *Top panels*: $(K2–K1)$ as a function of the K-band magnitude for the Pleiades (*left*) and Praesepe (*right*) *Middle panels*: *Left:* cluster system mass function for the Pleiades, α Per, and Praesepe compared to the lognormal form of the field mass function [4]. *Right*: Cluster mass function from UKIDSS complemented by high-mass data points from the literature. The *grey area* represent the 1σ uncertainty on the fit of the mass function. *Bottom panels*: $(Y - K1,K1)$ and $(Z - K,K)$ colour-magnitude diagrams used to determine the binary fractions in the Pleiades (*left*) and Praesepe (*right*) clusters

- We derived the cluster mass functions over the 0.6–0.03 $M_\odot$ mass range in the Pleiades and α Per and over the 0.7–0.07 $M_\odot$ for Praesepe: their shapes are very similar and best represented by a log-normal form in agreement with the field mass function of [4]. We observe some variation in the characteristic mass and the dispersion but the differences are below 2σ
- We derived a substellar binary fraction for the Pleiades of 18.4 ± 2.3 % in the 0.075–0.03 $M_\odot$ mass range, higher by more than 3σ compared to the hydrodynamical simulations of [1, 2]
- We derived binary fractions in three mass bins in the low-mass regime for Praesepe, frequencies very similar to results from hydrodynamical simulations [1, 2], except for the middle mass bin (0.2–0.1 $M_\odot$) (Fig. 4)

Acknowledgements NL is a Ramón y Cajal fellow (contract 08-303-01-02). NL and SB are funded by the Spanish ministry of science and innovation (project AYA2010-19136).

References

1. Bate, M. R. 2009, MNRAS, 392, 590
2. Bate, M. R. 2012, MNRAS, 419, 3115
3. Boudreault, S., Lodieu, N., Deacon, N. R., Hambly, N. C. 2012, MNRAS, 426, 3419
4. Chabrier, G. 2005, The Initial Mass Function 50 Years Later, 327, 41
5. Deacon, N. R., Hambly, N. C. 2004, AAP, 416, 125
6. Lodieu, N., Deacon, N. R., Hambly, N. C. 2012, MNRAS, 422, 1495
7. Lodieu, N., Deacon, N. R., Hambly, N. C., Boudreault, S. 2012, MNRAS, 426, 3403

The Birth of an IMF

Rowan J. Smith

Abstract In this contribution I show how differing amounts of additional accretion from outside a prestellar core are needed to form different parts of the stellar IMF. I then outline the observational consequences regarding the observed infall line profiles.

1 The Stellar IMF from Simulations

I use the simulations presented in [10] to examine the differing roles of accretion in assembling stars at the peak and high end of the stellar initial mass function (IMF). Figure 1 shows the Chabrier IMF [4] combined with representations of the accretion history of four sink particles (representing sites of star formation [3]). The accretion histories are taken from [9] and show a projection of where additional gas that was accreted on to the original bound core was located relative to the core. For the $0.8\,M_{\odot}$ sink, little additional mass is accreted from outside its original bound core. This is in good agreement with the finding of authors who suggest that the peak of the IMF is set from the typical thermal jeans mass in molecular clouds [5–7]. This implies that stars around the peak of the IMF are formed purely from a single core of jeans unstable gas. However as we move along the power law tail of the IMF, accretion from outside the core becomes increasingly important. A single jeans unstable core is now no longer enough to assemble all the mass needed to form the star.

Moreover, this additional accretion onto the core occurs in a non-uniform manner. The additional accretion originates from a preferred direction, which usually corresponds to an additional flow of material onto a core from a filament

R.J. Smith (✉)
ZAH/ITA, University of Heidelberg, Heidelberg, Germany
e-mail: rowan@uni-heidelberg.de

D. Stamatellos et al. (eds.), *The Labyrinth of Star Formation*, Astrophysics and Space Science Proceedings 36, DOI 10.1007/978-3-319-03041-8_63,

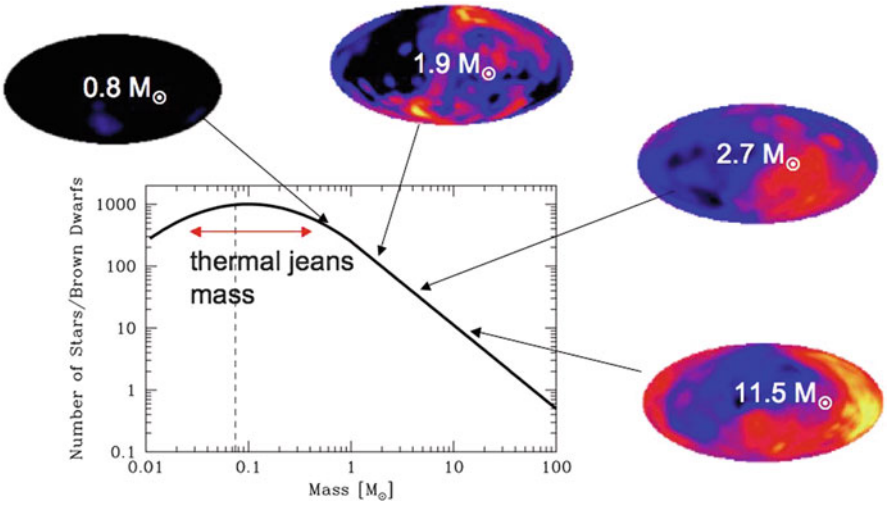

Fig. 1 A stellar IMF with *arrows* showing the differing accretion histories of the cores relative to the final mass of the stars they form. The accretion histories show a projection of where mass outside the original jeans unstable core that was accreted onto the sink particle was located at a snapshot in time, see [9] for more details. Cores at the peak of the IMF have little additional accretion from outside the core, whereas for high mass stars this represents the bulk of their final mass

within which it is embedded. This finding is in good agreement with recent studies using Herschel that have found cores embedded like beads on a string in nearby star forming regions [1, 2, 8]. For the most massive 11.5 $M_{\odot}$ star multiple filaments contributed to the accretion. Together the subsequent accretion from outside the original jeans unstable core was more than an order of magnitude larger than that contained in the original core.

2 Observational Consequences

For cores at the peak of the IMF that are approximately spherical and have little additional accretion, the classical blue asymmetric line profile signature for collapsing cores [13] is a good representation of the observed line profiles. However, for irregular cores where there is accretion from the outside environment, such as those shown in Fig. 1 in the tail of the IMF, this is no longer such a good description.

Figure 2 shows the HCN(1-0) and N_2H^+ line profiles that would be observed from the core that forms a 2.7 $M_{\odot}$ sink particle shown in Sect. 1. The core is embedded within a filament and is observed just before it forms a sink particle, a period roughly representative of the transition from the pre-stellar to Class 0 phase. The filament and surrounding environment of the core contain disordered

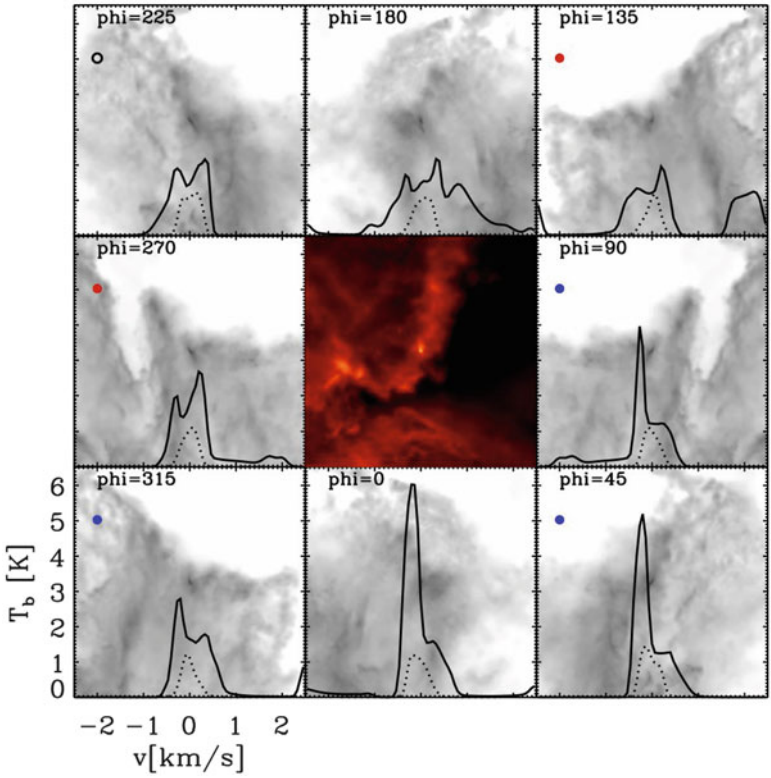

Fig. 2 The HCN 1-0 F(2-1) *solid* and N_2H^+ (1-0) *dotted line* profiles from a core that forms an intermediate mass sink at different viewing angles. The *central colour image* shows the column density in the plane in which the sight-lines pass through the core. The background *grey-scale images* show the large scale dust emission map of the filament when viewed at the labeled angle. The position at which the *outer images* touch the *central image* denotes the orientation of the sightline. The line profiles are calculated for a 0.01 pc beam centred directly on the embedded core

motions and along some lines of sight the HCN emission becomes optically thick in the filament rather than the core. This results in the optically thick line profiles being highly dependent on viewing angle, and not consistently showing the blue asymmetric line profile expected due to the collapsing core at the centre. The optically thin lines are roughly Gaussian in most cases and have sonic linewidths. For a full analysis of this scenario see [12].

Figure 3 shows the HCO(1-0) and N_2H^+ line profiles that would be observed from the core that forms a 11.5 $M_\odot$ sink particle in Sect. 1. The optically thick lines have wide profiles that are typically more intense on the blue side than the red. Such a profile is due to the fact that there is a large scale collapse gradient, from around $+2$ to $-2\,\mathrm{kms}^{-1}$ across the 0.8 pc wide region modelled, that channels mass to the centre [10]. The velocity gradient across the core itself is particularly sharp, with a change of more than $2\,\mathrm{kms}^{-1}$ in only 0.1 pc. The multiple components seen in the

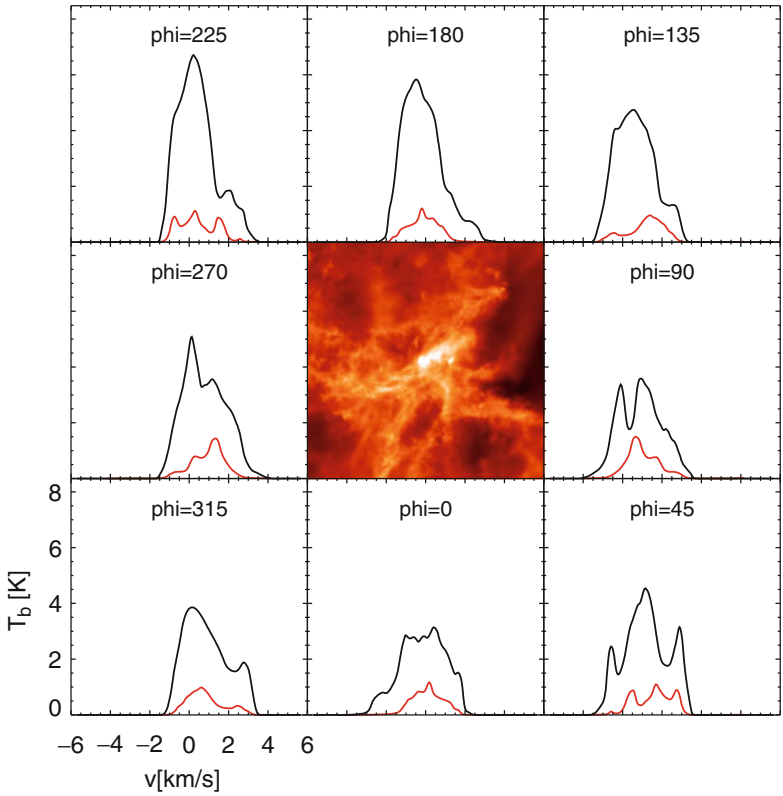

Fig. 3 The HCO (1-0) *black* and N_2H^+ (1-0) *red line* profiles from a core that forms a massive sink at different viewing angles. The N_2H^+ (1-0) is multiplied by a factor of 4 in order to be visible. As before the central colour image shows the column density in the plane in which the sight-lines pass through the core and the position at which the outer images touch the *central image* denotes the orientation of the sightline. The line profiles are calculated for a 0.06 pc beam centred directly on the embedded core

optically thin lines arise in our simulations due to the clumpy nature of the massive star forming region. Dense clumps of gas at different positions along the large scale velocity gradient all contribute to the total emission and produce peaks in the line profile at their individual velocities. A full analysis of line profiles from massive star forming regions is presented in Smith et al. [11].

References

1. André, P., Men'shchikov, A., Bontemps, S., Könyves, V., Motte, F., Schneider, N., Didelon, P., Minier, V., Saraceno, P., Ward-Thompson, D., di Francesco, J., et al. A&A **518**, L102+ (2010).
2. Arzoumanian, D., André, P., Didelon, P., Könyves, V., Schneider, N., Men'shchikov, A., Sousbie, T., Zavagno A., e.a. A&A **529**, L6+ (2011).

3. Bate, M.R., Bonnell, I.A., Price, N.M. MNRAS **277**, 362–376 (1995).
4. Chabrier, G. PASP **115**, 763–795 (2003).
5. Elmegreen, B.G., Klessen, R.S., Wilson, C.D. ApJ **681**, 365–374 (2008).
6. Jappsen, A.K., Klessen, R.S., Larson, R.B., Li, Y., Mac Low, M.M. A&A **435**, 611–623 (2005).
7. Larson, R.B. MNRAS **359**, 211–222 (2005).
8. Men'shchikov, A., André, P., Didelon, P., Könyves, V., Schneider, N., Motte, F., Bontemps, S., et al. A&A **518**, L103+ (2010).
9. Smith, R.J., Glover, S.C.O., Bonnell, I.A., Clark, P.C., Klessen, R.S. MNRAS **411**, 1354–1366 (2011).
10. Smith, R.J., Longmore, S., Bonnell, I. MNRAS **400**, 1775–1784 (2009).
11. Smith, R.J., Shetty, R., Beuther, H., Klessen, R.S., Bonnell, I.A. ApJ **771**, 24 (2013).
12. Smith, R.J., Shetty, R., Stutz, A.M., Klessen, R.S. ApJ **750**, 64 (2012).
13. Zhou, S., Evans II, N.J., Koempe, C., Walmsley, C.M. ApJ **404**, 232–246 (1993).

The Salpeter Slope of the IMF Explained

M. Sally Oey

Abstract If we accept a paradigm that star formation is a self-similar, hierarchical process, then the Salpeter slope of the IMF for high-mass stars can be simply and elegantly explained as follows. If the intrinsic IMF at the smallest scales follows a simple –2 power-law slope, then the steepening to the –2.35 Salpeter value results when the most massive stars cannot form in the lowest-mass clumps of a cluster. It is stressed that this steepening **must** occur if clusters form hierarchically from clumps, and the lowest-mass clumps can form stars. This model is consistent with a variety of observations as well as theoretical simulations.

1 Self-Similar Hierarchical Fragmentation

It is well known that at stellar masses $m \gtrsim 1\ \mathrm{M}_\odot$, the initial mass function follows the [9] power-law slope:

$$N(m)\, dm \propto m^{-2.35}\, dm. \tag{1}$$

This represents the distribution of stellar birth masses, showing a power-law index $\alpha = -2.35$, which is observed in most massive star-forming environments, with only few exceptions (e.g., [7]). This robust relation is therefore recognized as a fundamental diagnostic of the massive star formation process.

As a follow-on to Ant's model for the log-normal region of the IMF (A. Whitworth, these Proceedings), it turns out that the Salpeter slope can be explained as a simple result of a self-similar, hierarchical star-formation process, based on successive generations of fragmentation into an M^{-2} mass distribution.

M.S. Oey (✉)
Astronomy Department, University of Michigan, 830 Dennison Building, Ann Arbor, MI 48109-1042, USA
e-mail: msoey@umich.edu

D. Stamatellos et al. (eds.), *The Labyrinth of Star Formation*, Astrophysics and Space Science Proceedings 36, DOI 10.1007/978-3-319-03041-8_64,

The mass distribution of clusters and OB associations is observed to follow this mass distribution (e.g., [4,13]), as well as the HII region luminosity function, which best reflects the zero-age cluster mass function (e.g., [11]). Even sparse associations and groups of high-mass stars show this smooth $\alpha = -2$ power law down to individual O stars in the Small Magellanic Cloud [12]. Furthermore, the mass function of giant molecular clouds and star-forming clumps within them are also known to be consistent with $\alpha = -2$, as seen, for example, in presentations at this meeting (e.g., S. Pekruhl, and others in these Proceedings). In contrast, the Salpeter slope is slightly steeper, having a value of $\alpha = -2.35$ instead of –2.

The M^{-2} power law is a reasonable distribution to expect for the initial mass function of these hierarchical quantities. It is the power-law exponent which describes the mass equipartition between high and low-mass objects. Furthermore, as shown by Zinnecker [14], a cloud with a random mass distribution of proto-stellar seeds will produce an m^{-2} stellar IMF if the seeds simply grow by Bondi-Hoyle accretion as $\dot{m} \propto m^2$, until the entire cloud is absorbed into the stellar masses. And, Cartwright and Whitworth ([3]; and these Proceedings) point out that the IMF should follow a stable distribution function which results from the sum of random variables. They show that the core mass function can be described by such a function, the Landau distribution, which has a –2 power-law tail.

It is therefore natural to believe that the hierarchical fragmentation of molecular clouds into clumps and clumps into stars takes place self similarly according to a –2 power law mass distribution, therefore implying that the true, raw stellar IMF has this $\alpha = -2$ relation. So why is the observed Salpeter IMF slightly steeper? The answer lies in the mass range of the stars ($m_{\rm lo}$ to $m_{\rm up}$) relative to that of their parent clumps ($M_{\rm lo}$ to $M_{\rm up}$). If a cluster is generated from a single cloud, then its IMF is that for the aggregate of all stars formed out of all the clumps in this cloud. These clumps are described by a –2 power law. If $M_{\rm lo} < m_{\rm up}$, then the smallest clumps are too small to produce the highest-mass stars, thus slightly suppressing the formation of the highest-mass stars for the aggregate cluster. It turns out that the Salpeter slope results for the condition $M_{\rm lo} \sim m_{\rm lo}$ and $M_{\rm up} \gg m_{\rm up}$ [10].

Figure 1a shows the results of Monte Carlo simulations of cluster populations generated by drawing both clump and stellar masses from a power law with slope $\alpha = -2$. We assume a stellar mass range of $m_{\rm lo} = 1\ {\rm M}_\odot$ to $m_{\rm up} = 100\ {\rm M}_\odot$, and a high upper-mass limit for the clumps, $M_{\rm up} = 10^4\ {\rm M}_\odot$. Figure 1a shows the dependence of the logarithmic IMF slope $\Gamma = \alpha + 1$ as a function of lower clump mass $M_{\rm lo}$. At the highest value of $M_{\rm lo} = 100\ {\rm M}_\odot$, the mass ranges for the stars and clumps do not overlap, and essentially all stellar masses can be formed in all clumps. We therefore see that the IMF has the same value as its raw, input slope. But as $M_{\rm lo}$ decreases to values $< m_{\rm up}$, the formation of the highest-mass stars is suppressed, since they can no longer form in the smaller clumps. This steepens the aggregate IMF slope. We see that a value close to the Salpeter slope (shown by the dotted line) results for the condition $M_{\rm lo} = m_{\rm lo}$.

The models in Fig. 1b keep $M_{\rm lo} = 1\ {\rm M}_\odot$ fixed as $M_{\rm up}$ decreases. The black points in Fig. 1a, b represent the same model for which the stellar mass range is 1–100 $\rm M_\odot$ and the clump mass range is $1–10^4\ {\rm M}_\odot$. We see that the IMF slope continues to

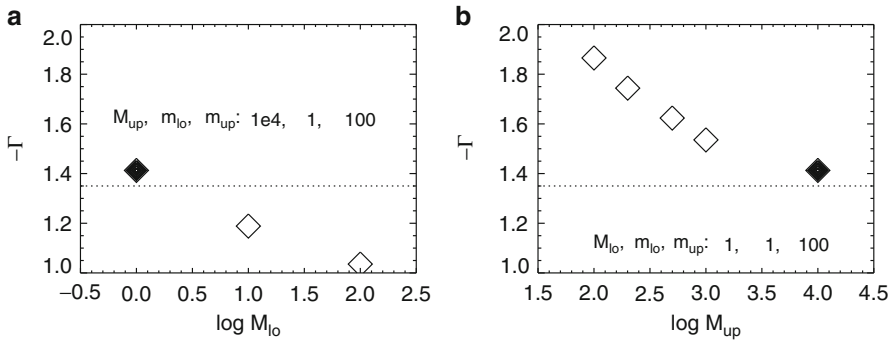

Fig. 1 Dependence of logarithmic IMF slope Γ on the lower and upper clump mass limits

steepen, approaching a value near $\Gamma = -1.9$ when $M_{\rm up} = m_{\rm up}$ and $M_{\rm lo} = m_{\rm lo}$. Thus, the stellar mass range and clump mass range are exactly coincident for that model. Oey [10] discusses the effect of additional parameters.

The Monte Carlo simulations show that the Salpeter slope corresponds to the particular condition that $M_{\rm lo} = m_{\rm lo}$ and $M_{\rm up} \gg m_{\rm up}$. The condition for $M_{\rm up}$ is reasonable, but is $M_{\rm lo} \leq m_{\rm lo}$? We note that the Salpeter slope applies only to the upper-mass tail of the IMF, and it is truncated at the lower-mass end by the observed turnover near $1\,{\rm M}_\odot$. This feature is generally believed to be linked to the Jeans mass, or in any case, some physics that is not scale-free. Therefore, the relevant lower clump mass is that which produces $1\,{\rm M}_\odot$ stars. And in fact, we do know that the power-law, clump mass function extends down to $1\,{\rm M}_\odot$. Note that we have discussed this analysis in terms of a 100 % star formation efficiency. However, the results are independent of the star formation efficiency, provided that it is constant across all clump masses. Thus, M represents the clump mass capable of forming that total stellar mass, rather than the physical clump mass itself. Therefore, the relevant physical $M_{\rm lo}$ is much larger than $1\,{\rm M}_\odot$ for star formation efficiencies $<$100 %.

2 Supporting Evidence

Since we observe the clump mass function to have a power law distribution to well below the masses needed to form individual $1\,{\rm M}_\odot$ stars, this therefore implies that if star formation is indeed a hierarchical process, then the resulting aggregate IMF for an entire star cluster **must** be steeper than the raw IMF because of the suppression of the highest stellar masses in the smallest clumps. The observed Salpeter slope of $\alpha = -2.35$ cleanly implies such a steepening from a raw IMF having $\alpha = -2$, which we argued above is an eminently reasonable value to expect from first principles.

Other observations are also consistent with this model. As seen in Fig. 1, our simulations show that any real scatter in the IMF should be limited between values of roughly $\Gamma = -1$ to –2. This is indeed the range seen in the observed IMF slopes, as shown by Kroupa [7].

In addition, starbursts are sometimes suggested to have somewhat flatter IMF slopes. The Arches cluster near the Galactic center is the best-studied example, showing a slope of $\Gamma = -1$ [5, 6]. This flattening can be understood if starbursts are forming stars so intensely that the stars form faster than the cloud fragmentation timescale. Thus, the starburst IMF directly reflects the raw IMF, rather than an aggregate formed out of cloud fragments. In other words, we could think of the entire starbursting cloud as a single giant, star-forming clump.

Finally, this steepening of the aggregate IMF slope relative to component subregions is in fact seen in the large-scale numerical simulations of [1, 2]. As shown by Maschberger [8], the IMF slope steepens from $\alpha \sim -1.9$ to -2.2 between the subregions and the total aggregate in the simulation totaling $10^4\,M_\odot$, in agreement with our predictions in Fig. 1a.

3 Conclusion

We stress that a model of hierarchical star formation **must** lead to steepening of the aggregate IMF slope if the star-forming clumps have masses $M_{\rm lo} \ll m_{\rm up}$ [10]. We know this condition to be true empirically within star clusters. If the hierarchical process is self-similar, then this implies that the Salpeter slope $\alpha = -2.35$ results from a clump mass function having $\alpha = -2$, which is a reasonable slope to expect from first principles. This scenario is supported by both observations and simulations.

Acknowledgements I'm grateful to the conference organizers for the opportunity to present this work, which was supported by the National Science Foundation, grant AST-0907758 and visitor support from the Institute of Astronomy, Cambridge.

References

1. Bonnell, I. A., Bate, M. R., & Vine, S. G. 2003, MNRAS 343, 413
2. Bonnell, I. A., Clark, P., & Bate, M. R. 2008, MNRAs 389, 1556
3. Cartwright, A. & Whitworth, A. P. 2012, MNRAS 423, 1018
4. Elmegreen, B. G. & Efremov, Y. N. 1997, ApJ 480, 235
5. Espinoza, P., Selman, F. J., & Melnick, J. 2009, A&A, 501, 563
6. Kim, S. S., Figer, D. F., Kudritzki, R. P., & Najarro, F. 2006, ApJL, 653, L113
7. Kroupa, P. 2002, Science 205, 82
8. Maschberger, T., Clarke, C., Bonnell, I., & Kroupa, P. 2010, MNRAS, 404, 1061

9. Salpeter, E. E. 1955, ApJ 121, 161
10. Oey, M. S. 2011, ApJ 739, L46
11. Oey, M. S. & Clarke, C. J. 1998, AJ 115, 1543
12. Oey, M. S., King, N. L., & Parker, J. W. 2004, AJ 127, 1632
13. Zhang, Q. & Fall, S. M. 1999, ApJL 527, L81
14. Zinnecker, H. 1982, Annals NY Acad. Sci. 395, 226

Recent Advances on IMF Research

Pavel Kroupa

Abstract Here I discuss recent work on brown dwarfs, massive stars and the IMF in general, which are areas of research to which Anthony Whitworth has been contributing major work. The stellar IMF can be well described by an invariant two-part power law in present-day star-formation events (SFevs) within the Local Group of galaxies. It is nearly identical in shape to the pre-stellar core mass function (André, A&A 518:L102, 2010). The majority of brown dwarfs follow a separate IMF. Evidence from globular clusters and ultra-compact dwarf galaxies has emerged that IMFs may have been top heavy depending on the star-formation rate density (Marks et al., MNRAS 422:2246, 2012). The IGIMF then ranges from bottom heavy at low galaxy-wide star formation rates to being top-heavy in galaxy-scale star bursts.

1 Introduction

The stellar IMF is the distribution function of stellar masses, m, formed together in one star-formation event (SFev) which can be characterised by a spatial scale of up to about a pc and a stellar mass $M_{\rm ecl}$. Various forms of distribution functions describing the observationally derived IMF have been proposed (e.g. [7]). According to the recent Herschel results (e.g. [2, 3]) the SFevs occur along thin (width of about 0.1 pc) filaments in the molecular clouds when the mass per unit length surpasses about 15 $M_\odot$/pc. The SFevs are deeply embedded and the star formation efficiency is $\epsilon \approx 0.3-0.4$, such that about 60–70 % of the residual gas is blown out from them leaving the stellar population of mass $few\, M_\odot \lesssim M_{\rm ecl}$ largely unbound. Taking the

P. Kroupa (✉)
Argelander-Institute for Astronomy, University of Bonn, Auf dem Hügel 71, 53121 Bonn, Germany
e-mail: pavel@astro.uni-bonn.de

D. Stamatellos et al. (eds.), *The Labyrinth of Star Formation*, Astrophysics and Space Science Proceedings 36, DOI 10.1007/978-3-319-03041-8_65,

energy distribution of binary populations in observed star clusters to limit the largest density the cluster was allowed to have when it was a SFev (too many binaries would be burned at too high densities), Marks and Kroupa [19] inferred a radius-mass relation, $R_{\rm ecl} = 0.10\,(M_{\rm ecl}/M_\odot)^{0.13}$, which extracts the same length scale. This suggests that the universal initial binary distribution function [18] deduced from the many observations appears to be a good representation of reality.

Remarkable progress has been achieved in constraining the form of the IMF and its variability. This progress has largely been driven by observational studies, but theoretical advances have also been many. Here a brief review if provided of the recent issues concerning the IMF, some of which are hotly debated if not poorly understood. Further details and references are to be found in the reviews by Chabrier [9], Bonnell et al. [6], Bastian et al. [4], and Kroupa et al. [18].

2 Universality of the IMF

As is evident from the reviews mentioned above, a consensus appears to have emerged in the community that the stellar IMF is largely invariant for star formation conditions as are found throughout the Local Group of galaxies at the present time. The form of this universal or canonical IMF is most simply described by a two-part power-law, $\alpha_1 \approx 1.3, 0.07 < m/M_\odot \lesssim 0.5$ and $\alpha_2 = 2.3, 0.5 \lesssim m/M_\odot$ (the "Massey-Salpeter" power-law index). This form can also be approximated by a log-normal for $m < 1\,M_\odot$ and the same power-law part for $m > 1\,M_\odot$ [18] but leads to a mathematically more complex object without the gain of physical reality. Concerning the origin of the IMF, André et al. [2] note the remarkable similarity between the pre-stellar core mass function and the stellar IMF, "suggesting a $\sim$ one-to-one correspondence between core mass and star/system mass with $M_{*,\rm sys} = \epsilon\, M_{\rm core}$ and $\epsilon \approx 0.4$ in Aquila."

As will be seen below, the evidence that the brown dwarf IMF forms a separate distribution function which is not a continuous extension of the stellar IMF makes use of a log-normal form at low masses less attractive.

3 The Brown Dwarf Issue

It has been known for some time that brown dwarfs (BDs) are unlikely to from form direct gravitational collapse in a molecular cloud such that the observationally deduced mass function contains a significant surplus of brown dwarfs [1,14,21,22].[1]

[1] An interesting sociological effect appears to have emerged in that authors claim good agreement with the (observed) Chabrier IMF but scrutiny of the published work shows consistently significant disagreement.

The reason is that the distribution of density maxima in a cold but turbulent molecular cloud has very few peaks which can collapse through eigengravity at the mass scale of a BD such that not much further material is accreted. Although Whitworth et al. [31, 32] argue that BDs form a continuous extension of the stellar distribution, the observational and theoretical evidence they provide strongly suggests that BDs and stars have different properties in terms of their pairing. Kroupa et al. [17] have tested the hypothesis that BDs and stars follow the exact same distribution functions and exclude this hypothesis with very high confidence. The various flavours of BDs that can in principle arise (collisional, photo-evaporated, ejected embryos) have been discussed [16] with the result that in the present-day star-forming conditions mostly the ejected embryo flavour dominates. The original suggestion of this scenario has been updated by Hubber and Whitworth [25], Thies et al., [26], and Basu and Vorobyov [5] by the argument that the gravitationally pre-processed material in outer accretion disks is able to cool sufficiently rapidly upon compression to allow direct gravitational collapse at the BD mass scale. The resulting IMF of BDs compares remarkably well with the observationally deduced BD IMF ($\alpha_0 \approx 0.3$). The resulting binary properties of BDs are also accounted for naturally [26].

The BD IMF is thus a nearly flat power-law from the opacity limit for fragmentation ($m_l \approx 0.01\,M_\odot$) to an upper limit which transgresses the hydrogen burning limit. In principle, arbitrarily massive "BDs" can form in very massive disks around massive stars such that here the origin of stars vs BDs becomes blurred. Because massive stars are exceedingly rare the stellar population formed through this disk-fragmentation channel is negligible in comparison to the "normal" stellar population which results from direct molecular cloud fragmentation.

Thus in order to correctly account for a stellar population with BDs most of the BD population must be added in terms of a separate distribution function, as is also the case for planets which follow their own mass distribution. The BD IMF can be expressed as a nearly flat power-law with a continuous log-normal extension from the stellar regime being ruled out.

4 Variation of the IMF

A hint at a possible variation of the IMF in the MW has emerged due to present-day star-formation events possibly producing more low-mass stars than previously. This has been quantified as a metallicity dependence, $\alpha \approx 1.3 + 0.5[\mathrm{Fe/H}]$ [18]. From the study of massive elliptical (E) galaxies, it has emerged that the IMF must have been significantly bottom heavy. Cenarro et al. [8] inferred $\alpha = 3.41 + 2.78[\mathrm{Fe/H}] - 3.79[\mathrm{Fe/H}]^2$ (for $0.1 \lesssim m/M_\odot \lesssim 100$, although not explicitly stated in the paper) and a more recent analysis by van Dokkum and Conroy [27] also suggests an increasingly bottom heavy IMF with increasingly massive E galaxies. This may be related to the postulated cooling-flow-accretion population of low-mass stars [15]. A consistency check by Smith and Lucey [24] using gravitational lensing appears to exclude a bottom-heavy IMF though.

5 The Massive End of the IMF

Whitworth et al. [30] had already suggested that massive stars may preferentially form in shocked gas. As reviewed in [18] there has been much observational evidence for top-heavy IMFs in star-bursts. As these are observationally unresolved, this evidence was indirect and largely ignored. Observations of the assembly of the stellar population over cosmological epoch have also been pointing to top-heavy IMFs in the past, as otherwise there would be more low-mass stars locally than are observed. Three independent more-direct lines of evidence for the IMF becoming top-heavy with star-formation rate density have recently emerged:

First: It is well known that ultra-compact dwarf galaxies (UCDs), which have a mass scale of 10^6–$10^8\,M_\odot$, have larger dynamical mass-to-light (M/L) ratios than normal stellar populations. This is unlikely due to exotic dark matter as the phase-space available in UCDs would not accommodate significant amounts of dark matter. Instead, a top-heavy IMF would have lead to an overabundance of stellar remnants in UCDs which would enhance their dynamical M/L ratios. Thus, the variation of the required $\alpha_3, m > 1\,M_\odot$, can be sought to explain the dynamical M/L ratia [10].

Secondly: UCDs have an overabundance of low-mass X-ray bright sources (LMXBs). In globular clusters (GCs), LMXBs are known to be formed from the dynamical capture of stars by stellar remnants mostly in the core of the GCs. As the star evolves the remnant accretes part of the star's envelope thus becoming detectable with X-rays. The LMXB population is constantly depopulating and needs to be replenished by new capture events. Indeed, the theoretically expected scaling of the fraction of GCs with LMXB sources with GC mass is nicely consistent with the observed data assuming an invariant stellar MF. Applying the same theory to UCDs uncovers a break-down of this agreement as the UCDs have a surplus of LMXB sources. By adding stellar remnants through a top-heavy IMF when the UCDs were born, i.e. by allowing α_3 to vary with UCD birth mass, consistency with the data can be sought [11].

Thirdly: Low-concentration GCs have been found by de Marchi et al. [12] to be depleted in low mass stars while high-concentration GCs have a normal MF. This is contrary to the energy-equipartition driven depopulation of low mass stars because more concentrated clusters ought to have lost more low mass stars. It is also not consistent with any known theory of star formation, because the low-concentration clusters typically have a higher metallicity which would, if anything, imply a surplus of low-mass stars. The currently only physically plausible explanation is to suppose that the young GCs formed compact and mass segregated and that the expulsion of residual gas unbound a part of the low-mass stellar population. By constraining the necessary expansion of the proto-GCs (i.e. SFevs), correlations between metallicity, α_3 and tidal field strength emerge which constrain the very early sequence of events that formed the Milky Way as well as the dependency of α_3 on density and metallicity of the SFev [20].

Putting this all together, a consistent variation of α_3 with density and metallicity of the SFevs emerges: for $m > 1\,M_\odot, x \geq -0.89$: $\alpha_3 = -0.41\,x + 1.94$ with $x = -0.14[\mathrm{Fe/H}] + 0.99\log_{10}(\rho_6)$, where $\rho_6 = \rho/(10^6 M_\odot\,\mathrm{pc}^{-3})$ and ρ is the density in $M_\odot/\mathrm{pc}^3$.

Thus, SFevs at a star-formation rate density $SFRD < 0.1\,M_\odot/(\mathrm{pc}^3\,\mathrm{Myr})$ can be assumed to have an invariant IMF with $\alpha_3 = \alpha_2$ (subject to the possible variation with metallicity discussed above), while SFevs with larger SFRDs tend towards top-heavy IMFs whereby the trend is enhanced at lower-metallicities.

6 Massive Stars and the IGIMF

The formation of massive stars is notoriously difficult to study because they are rare and deeply embedded. Thus, much fiction can be associated with the formation of massive stars and the only well-posed approach to ascertain a hypothesis is to test its consequences against data taking care to note that by showing one hypothesis to work does not exclude another hypothesis.

There are two major competing hypothesis:

According to the one hypothesis the IMF may be taken to be a probability distribution function such that the stellar ensemble in a whole galaxy is always a random draw from the stellar IMF. This allows massive stars to form in isolation as rare events.

The other hypothesis is related to optimal sampling [18] according to which the stellar IMF is a distribution function which scales with M_{ecl} such that the most massive star, m_{max}, in the SFev follows a $m_{\mathrm{max}}(M_{\mathrm{ecl}})$ relation [28]. The total star-formation rate (SFR) of a galaxy follows from all its SFevs, such that a large SFR implies SFevs that reach to large masses and thus to large SFRDs which then imply top-heavy IMFs in these. As a consequence the IMF of a whole galaxy (the "integrated IMF" = IGIMF) is steeper (larger α_3), or flatter (i.e. top-heavy) than Massey-Salpeter, depending on its SFR. The implications for the astrophysics of galaxies as well as for cosmology are major.

The vast quantity of data are consistent with the latter theory, and most data can most simply and naturally be explained within the IGIMF framework [23, 29]. A counter-argument against the IGIMF theory often put up, namely that evidence exists that massive stars can form in isolation, is countered by the observed fraction of massive stars deemed to have formed in isolation being smaller than the fraction of apparently isolated massive stars if all massive stars in fact do form in embedded clusters, and by virtually all best-candidates for isolated massive star formation having been shown to be most likely stemming from clusters [13].

References

1. Andersen, M., Meyer, M. R., Robberto, M., Bergeron, L. E., & Reid, N. 2011, A&A, 534, A10
2. André, P., Men'shchikov, A., Bontemps, S., et al. 2010, A&A, 518, L102
3. André, P., Men'shchikov, A., Könyves, V., & Arzoumanian, D. 2011, Computational Star Formation, IAUS 270, 255
4. Bastian, N., Covey, K. R., & Meyer, M. R. 2010, ARAA, 48, 339
5. Basu, S., & Vorobyov, E. I. 2012, ApJ, 750, 30
6. Bonnell, I. A., Larson, R. B., & Zinnecker, H. 2007, Protostars and Planets V, 149
7. Cartwright, A., & Whitworth, A. P. 2012, MNRAS, 423, 1018
8. Cenarro, A. J., Gorgas, J., Vazdekis, A., Cardiel, N., & Peletier, R. F. 2003, MNRAS, 339, L12
9. Chabrier, G. 2003, PASP, 115, 763
10. Dabringhausen, J., Kroupa, P., & Baumgardt, H. 2009, MNRAS, 394, 1529
11. Dabringhausen, J., Kroupa, P., Pflamm-Altenburg, J., & Mieske, S. 2012, ApJ, 747, 72
12. de Marchi, G., Paresce, F., Pulone, L., 2007, ApJ 656, 65
13. Gvaramadze, V. V., Weidner, C., Kroupa, P., & Pflamm-Altenburg, J. 2012, MNRAS, 424, 3037
14. Hennebelle, P. 2012, A&A, in press, arXiv:astro-ph/1207.6776
15. Kroupa, P., & Gilmore, G. F. 1994, MNRAS, 269, 655
16. Kroupa, P., & Bouvier, J. 2003, MNRAS, 346, 369
17. Kroupa, P., Bouvier, J., Duchêne, G., & Moraux, E. 2003, MNRAS, 346, 354
18. Kroupa, P., Weidner, C., Pflamm-Altenburg, J., et al. 2013, Planets, Stars and Stellar Systems. Stellar Systems and Galactic Structure, Vol. V., Springer, arXiv:astro-ph/1112.3340
19. Marks, M., & Kroupa, P. 2012, A&A, 543, A8
20. Marks, M., Kroupa, P., Dabringhausen, J., & Pawlowski, M. S. 2012, MNRAS, 422, 2246
21. Padoan, P., & Nordlund, Å. 2002, ApJ, 576, 870
22. Padoan, P., Nordlund, Å., Kritsuk, A. G., Norman, M. L., & Li, P. S. 2007, ApJ, 661, 972
23. Pflamm-Altenburg, J., Weidner, C., & Kroupa, P. 2011, UP2010: Have Observations Revealed a Variable Upper End of the Initial Mass Function?, 440, 269
24. Smith, R.J., Lucey, J.R., 2013, MNRAS 434, 1964
25. Stamatellos, D., Hubber, D. A., & Whitworth, A. P. 2007, MNRAS, 382, L30
26. Thies, I., Kroupa, P., Goodwin, S. P., Stamatellos, D., & Whitworth, A. P. 2010, ApJ, 717, 577
27. van Dokkum, P. G., & Conroy, C. 2011, ApJL, 735, L13
28. Weidner, C., Kroupa, P., & Bonnell, I. A. D. 2010, MNRAS, 401, 275
29. Weidner, C., Pflamm-Altenburg, J., & Kroupa, P. 2011, UP2010: Have Observations Revealed a Variable Upper End of the Initial Mass Function?, 440, 19
30. Whitworth, A. P., Bhattal, A. S., Chapman, S. J., Disney, M. J., & Turner, J. A. 1994, MNRAS, 268, 291
31. Whitworth, A., Bate, M. R., Nordlund, Å., Reipurth, B., & Zinnecker, H. 2007, Protostars and Planets V, 459
32. Whitworth, A., Stamatellos, D., Walch, S., et al. 2010, IAUS 266, 264

Four-Parameter Fits to Core Mass Functions Using Stable Distributions Demonstrate Statistical Differences Between Star Forming Regions

Annabel Cartwright and Anthony Peter Whitworth

Abstract We propose the use of the statistically well-founded Pareto-Levy family of Stable Distributions for the characterisation of the mass distributions of Stellar and Pre-stellar populations. Using Stable Distribution fits we demonstrate that the modal peaks and widths of the peaks for Core Mass Functions from Ophiuchus, Aquila and Orion are measurably different, width increasing with peak mass. The slopes of the high mass power laws are indistinguishable.

1 Introduction

As Mandelbrot [2] demonstrated, the Gaussian is not the only distribution function which is the possible limit distribution of sums of random variables. There is a whole family of potential limiting distributions, the Stable Distributions, among them asymmetric distributions which show an immediate similarity to the observed mass functions and are statistically justifiable.

Here we demonstrate that the asymmetric Stable Distributions are suitable for modelling the IMF, using a publicly available program, STABLE [3], to fit Stable Functions to three real datasets.

2 Stable Distributions

Nolan [4] or Uchaikin and Zolotarev [7] provide comprehensive descriptions of Stable Distributions. All have a single peak or mode and may be defined using four parameters. $\alpha \in [0, 2]$, controls the slope of the power-law tails, $\beta \in [-1, 1]$

A. Cartwright (✉) • A.P. Whitworth
Cardiff School of Physics and Astronomy, Cardiff University, Queens Buildings 5, The Parade, Cardiff CF24 3AA, UK
e-mail: cartwrighta@cf.ac.uk; anthony.whitworth@astro.cf.ac.uk

D. Stamatellos et al. (eds.), *The Labyrinth of Star Formation*, Astrophysics and Space Science Proceedings 36, DOI 10.1007/978-3-319-03041-8_66,

Table 1 Stable function parameters yielding maximum likelihood fits to the raw datasets listed. Column 1 is the name of the star forming region, column 2 the number of core masses. Columns 3–6 give the values of parameters produced by the Nolan STABLE program at a 95 % confidence level. α, high mass slope; β asymmetry; γ width of peak; δ location of mode

Name of region	N_{cores}	α	β	γ	δ
Ophiuchus	143	1.0±0.17	1.0	0.11±0.02	0.17±0.03
Aquila	541	1.0±0.09	1.0	0.25±0.02	0.43±0.03
Orion	395	0.8±0.08	1.0	0.70±0.10	1.05±0.12

the skewness of the distribution and γ and δ control the width of the central peak and the location, corresponding to the variance and mean in the case of the Gaussian. Nolan [3] provides publicly available software to fit Stable Distributions to datasets, and to generate pdfs and synthetic datasets for particular values of α, β, γ and δ. The program STABLE is available from J. P. Nolan's website, `academic2.american.edu/~jpnolan`.

3 Fitting Stable Functions to Prestellar Core Mass Datasets

Data were obtained for masses of gravitationally bound prestellar cores in three star-forming regions, Orion, Ophiuchus and Aquila, taken from [5, 6] and [1] respectively. The program STABLE [3] was then used to fit Stable Distributions to the data on the basis of maximum likelihood. The values of the four parameters obtained with 95 % confidence are listed in Table 1. These parameters were then used to generate a Probability Density Function for each of the datasets. Figure 1 shows these Stable Distributions as dashed lines plotted on the same scale as the histograms of the raw data, and also on log/log plots of frequency versus mass, a more familiar way of viewing the data.

4 Discussion

As well as being statistically justifiable descriptors of populations arising from independent random processes, Stable Distributions offer the practical advantage that they require only four parameters to describe them. The results presented in Fig. 1 demonstrate that applying the standard, publicly available program STABLE to raw mass data gives a good fit to the data. By extracting values of the Stable Distribution parameters, with confidence limits, it is also possible to identify statistically significant differences between the distributions, which are not at all

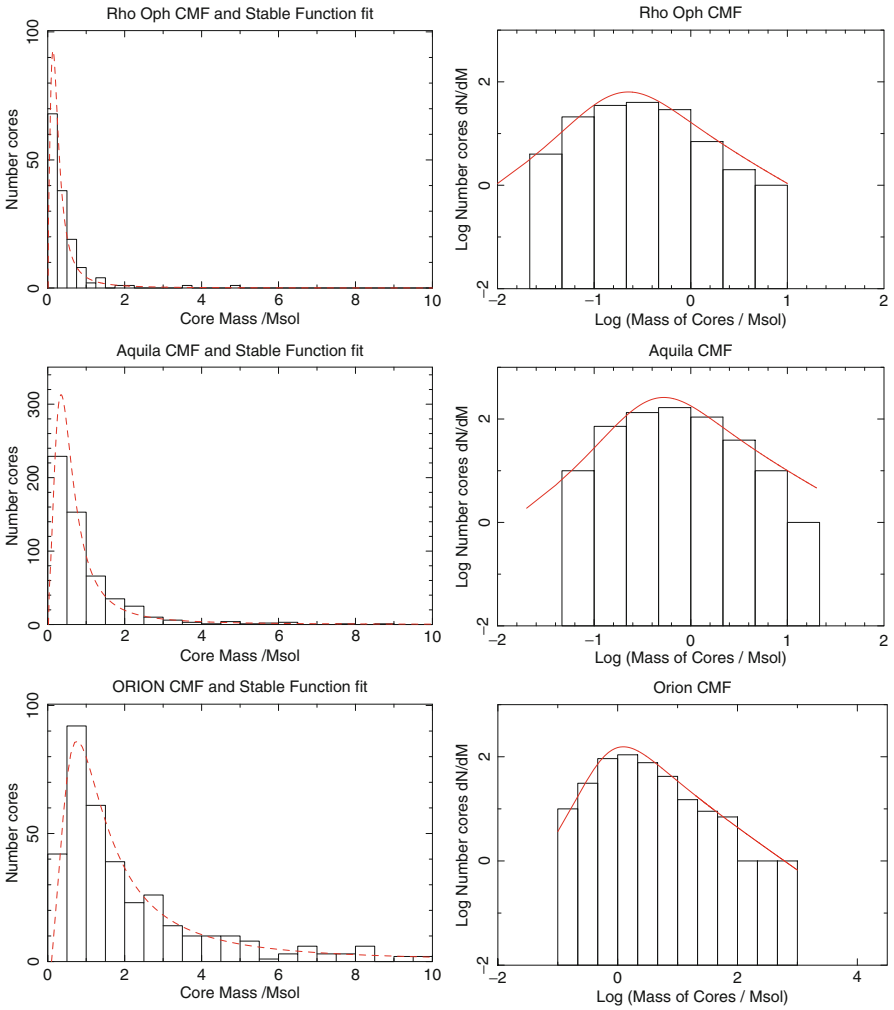

Fig. 1 *Left*, *Dashed lines* indicate Stable functions fitted to the Ophiuchus, Aquila and Orion datasets. *Right*, the *solid lines* indicate the same data plotted on Log/log scales

apparent when plotted on the standard log/log plot. Here the slope for high masses is statistically indistinguishable between the three datasets. The location of the maximum is largest for Orion and smallest for Ophiuchus. The width parameter also correctly reflects the widest peak in the mass distribution for Orion, and the narrowest for Ophiuchus. These two parameters are distinctly different between the three datasets, and show a correlation between γ and δ, indicating that, for these three datasets, higher mass peaks are also wider.

5 Conclusions

The use of Stable Distributions to model the Initial Mass Function and Core Mass Function removes the subjective element of existing methods, as no decisions are needed as to binning of data and location of thresholds. Fitting of the four parameters required is simply done via publicly available resources and confidence limits, percentile data and PDFs may be obtained. This permits objective and statistically justifiable comparison and classification of groups of stars or prestellar cores.

References

1. Könyves V., Andre P., Men'shchikov A., et al., 2010, A &, 518, 106
2. Mandelbrot B.,1960, Int. Econ. Rev., 1, 79
3. Nolan J.P., 1997, Comm. Stat., 13, 759
4. Nolan J.P., 2012, Stable Distributions - Models for Heavy Tailed Data, Birkhauser, Boston
5. Nutter D., Ward-Thompson, D., 2007, MNRAS, 374, 1413
6. Stanke T., Smith M.D., Gredel R., Khanzadyan T., 2006, A & A, 447, 609
7. Uchaikin, V.V., Zolotarev, V.M., 1999, Chance and Stability. Stable Distributions and their applications, VSP, Utrecht

A Stochastic Model of Accretion

Thomas Maschberger

Abstract Star formation occurs in flocculent, chaotic environments. Therefore the accretion rates of proto-stars moving through a cloud will not be completely smooth and contains a random noise term. Stochastic accretion can be described with a non-linear stochastic differential equation for the accretion rate, for example $dm = m^2(dt + dW)$, where dW describes the fluctuations. A sample of seeds growing in this model develops a mass function that follows the whole shape of the initial mass function. Both the log-normal low-mass part and the high-mass power law are a consequence of the same stochastic growth equation.

1 Introduction

Star formation occurs in flocculent molecular clouds, whose structure follows from turbulence. Turbulence is a stochastic process, and therefore it is not unreasonable to consider star formation itself a stochastic process as well. Fragmentation is one candidate for the star formation process (e.g. [3, 5, 9]). It is a linear multiplicative process: a star-forming clump of gas loses in each fragmentation step a random fraction of its mass. This leads to a lognormal mass distribution for a population of stars. However, the stellar initial mass function has a power-law tail for massive stars, which is not an outcome of fragmentation. Therefore it has been suggested that a second process, accretion, is accountable for the power-law tail (e.g. [2, 6, 8]). The accretion process is usually modelled as a nonlinear deterministic process operating on the lognormal distribution that results from fragmentation.

T. Maschberger (✉)
Institut de Planétologie et d'Astrophysique de Grenoble, BP 53,
F-38041 Grenoble Cédex 9, France
e-mail: thomas.maschberger@obs.ujf-grenoble.fr

D. Stamatellos et al. (eds.), *The Labyrinth of Star Formation*, Astrophysics and Space Science Proceedings 36, DOI 10.1007/978-3-319-03041-8_67,

In the following we discuss a time-continuous stochastic process that is multiplicative, like fragmentation, but also nonlinear, like accretion. Such a growth process leads to a mass distribution that appears like log-normal at low masses and has a power-law tail at high masses.

2 Stochastic Linear and Nonlinear Growth

Suppose an accreting point mass moves through a medium that has density fluctuations caused by turbulence. In such a case classical Bondi-Hoyle-Lyttleton accretion is not strictly valid as the density is not homogeneous. The accretion rate, $\dot{m} \propto m^2\rho$, will be modulated by the fluctuating density (and turbulent velocities, which we neglect). ρ has a probability distribution with some mean and variance, a deterministic, classical, differential equation does not describe the problem. A suitable mathematical description for this problem is a stochastic differential equation (cf. e.g. [7]) for a nonlinear growth process. It is typically written in the form

$$\mathrm{d}m = m^{1+\alpha}\,(a\,\mathrm{d}t + b\,\mathrm{dW})\,, \tag{1}$$

where $\alpha = 1$ would correspond to Bondi-Hoyle-Lyttleton accretion, with the term in the bracket describing the fluctuations in ρ. The first term in the bracket, $a\,\mathrm{d}t$, is the deterministic part. Random fluctuations are introduced by $b\,\mathrm{dW}$, where b determines the "amount" (standard deviation) of the fluctuations and dW is a Gaussian distributed random variate with zero mean and infinitesimal variance $\sigma^2 = (\mathrm{d}t)^2$. Thus, $a\,\mathrm{d}t + b\,\mathrm{dW}$ follows a Gaussian, or $\mathrm{d}m/m^{1+\alpha} \sim \mathcal{N}(\mu = a\mathrm{d}t, \sigma = b\sqrt{\mathrm{d}t})$.

A group of point masses that start growing according to Eq. 1 from their initial mass m_0 will spread out their masses in time. The mass distribution function after some time t is given in the linear case ($\alpha = 0$) by a lognormal distribution,

$$p(m,t) = \frac{1}{m\sqrt{2\pi b^2 t}} e^{-\frac{1}{2}\frac{(\log(m)-\log(m_0)-at)^2}{b^2 t}}, \tag{2}$$

and for the nonlinear case ($\alpha > 0$) by

$$p(m,t) = \frac{1}{m^{1+\alpha}\sqrt{2\pi b^2 t}} e^{-\frac{1}{2}\frac{\left(m^{-\alpha}-m_0^{-\alpha}+\alpha a t\right)^2}{\alpha^2 b^2 t}}. \tag{3}$$

For $\alpha > 0$ the distribution function has a power-law tail with exponent $-(1+\alpha)$.

The time evolution of Eq. 3 is shown in Fig. 1 for quadratic growth ($\alpha = 1$) and for different ratios b/a ($a = 1$, $m_0 = 1$). $p(m,t)$ evolves into the typical shape of the IMF, a lognormal part with a power law tail for large m. If in the star

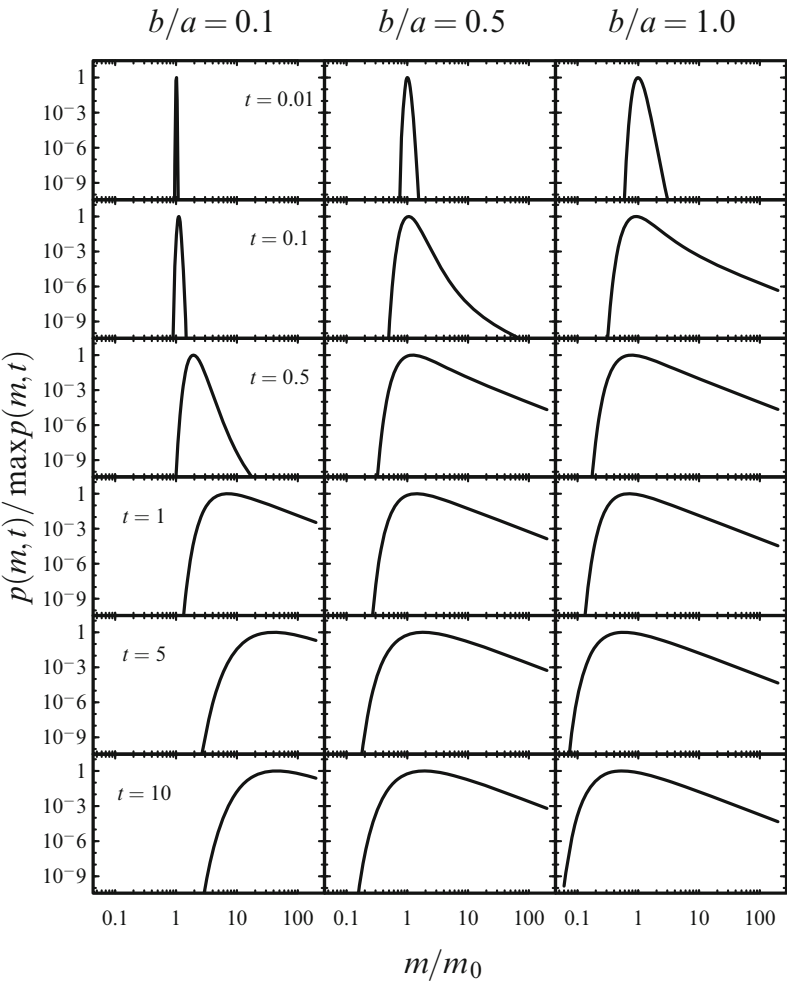

Fig. 1 Time evolution of the mass distribution function (Eq. 3) in the case of quadratic growth ($\alpha = 1$) with Gaussian distributed noise for different noise ratios ($m_0 = 1$ and $a = 1$). For small b/a the peak of the distribution function shifts to higher masses, whereas it shifts to lower masses for large b/a (the mean mass, however, always grows in time). Note that objects can "grow" below their initial values

formation process the growth is stopped before the tail can fully develop the mass distribution would appear to have a steeper tail (exponent $< -(1 + \alpha)$). Depending on the "amount of noise" (b/a) the peak moves to larger values of m ($b/a = 0.1$), stays roughly at the same position ($b/a = 0.5$) or moves even backwards to $m < m_0$ ($b/a = 1$). This seemingly unintuitive behaviour is caused by our choice for dW: we allow that dW may have negative values, so that an object can "grow" to smaller m.

3 Other Factors Affecting the High Mass Tail

Besides a non-linear growth equation there are at least two more factors that could influence the tail behaviour of the distribution function: non-Gaussian noise and a distribution of growth times.

In Eq. 1 we assumed a Gaussian noise distribution dW, which can reach negative values, so that the mass increment dm also becomes negative. This, however, conflicts with our intention to model a *growth* process, which should have only an increase in mass. A solution to this conflict can be achieved by replacing the Gaussian distribution $a\ \mathrm{d}t + b\ \mathrm{dW}$ by a strictly positive distribution with mean $a\ \mathrm{d}t$ and variance $b^2\ (\mathrm{d}t)^2$. Krumholz et al. [4], for example, found that the accretion rates for Bondi-Hoyle accretion in a turbulent medium follow a lognormal distribution. Such a noise distribution does not change the power-law tail that occurs for $\alpha > 0$, but leads to an m^{-1} tail for $\alpha = 0$.

An exponential distribution of growth times, as suggested by Basu and Jones [1], also does not affect the power-law tail in the nonlinear $\alpha > 0$ case. Again, in the linear case $\alpha = 0$ the lognormal distribution has a power law tail, as found by Basu and Jones [1].

4 Discussion

A single, nonlinear multiplicative stochastic process leads to a distribution function that possesses both a lognormal body and power law tail. The exponent in the power-law part follows from the growth equation, if $\dot{m} \propto m^2$ then $p(m) \propto m^{-2}$. Other factors that could affect the power-law tail, such as a non-Gaussian noise distribution (perhaps itself with a power-law tail) or a distribution of growth times do not have any strong effect. For the moment we considered the simplest form of a growth equation and did not include, for example, any changes with time. This has the advantage that $p(m,t)$ can be written in a closed form.

In order to describe the star formation process more realistically, a more general stochastic differential equation may be used, possibly in the form

$$\mathrm{d}m = a(m,t)\,\mathrm{d}t + b(m,t)\,\mathrm{dW}. \tag{4}$$

Here the coefficients $a(m,t)$ ("deterministic") and $b(m,t)$ ("stochastic") could have different dependencies of m and t, which perhaps model feedback or other involved physical processes.

A detailed discussion of the topics touched in this contribution will be presented in a forthcoming paper.

Acknowledgements TM acknowledges funding via the ANR 2010 JCJC 0501 1 "DESC" (Dynamical Evolution of Stellar Clusters).

References

1. S. Basu, C.E. Jones, MNRAS, **347**, L47 (2004)
2. I.A. Bonnell, C.J. Clarke, M.R. Bate, J.E. Pringle, MNRAS **324**, 573 (2001)
3. B.G. Elmegreen, R.D. Mathieu, MNRAS, **203**, 305 (1983)
4. M.R. Krumholz, C.F. McKee, R.I. Klein, ApJ, **638**, 369 (2006)
5. R.B. Larson, MNRAS, **161**, 133 (1973)
6. R.B. Larson, MNAS, **184**, 69 (1978)
7. B. Øksendal, *Stochastic Differential Equations* (Springer-Verlag, 2002)
8. H. Zinnecker, Annals New York Academy of Sciences, **395**, 226 (1982)
9. H. Zinnecker, MNRAS, **210**, 43 (1984)

The Low Mass End of the IMF Unveiled by the WIRCam/CFHT Survey of Nearby Young Clusters

Catarina Alves de Oliveira, Estelle Moraux, Loredana Spezzi, Núria Huélamo, Jerôme Bouvier, Herve Bouy, and Gaspard Duchêne

Abstract The observational characterization of the stellar mass function in galactic clusters, the field, and even other galaxies, has resulted in a wealth of parameters that must be reproduced and explained by any successful star formation theory. To extend our knowledge on the mass function to the substellar regime, we have conducted a large observational survey of nearby young clusters (ρ Oph, IC 348, Serpens, and λ Ori). We adopted a twofold approach to this study, using both near-IR photometry to find all candidate substellar members and extensive spectroscopic follow-up to derive a spectroscopic IMF, and deep methane imaging to search for the lowest mass members. I will present the results of this longterm endeavor, where we have found no evidence for variations in the substellar mass function across different clusters, and have uncovered a handful of candidate young T dwarfs likely to represent the minimum mass for star formation.

C. Alves de Oliveira (✉)
European Space Astronomy Centre (ESA), P.O. Box, 78,
28691 Villanueva de la Cañada, Madrid, Spain
e-mail: calves@sciops.esa.int

E. Moraux • J. Bouvier • G. Duchêne
UJF-Grenoble 1/CNRS-INSU, IPAG UMR5274, Grenoble 38041, France

L. Spezzi
European Southern Observatory, Karl-Schwarzschild-Strasse 2,
85748 Garching bei München, Germany

N. Huélamo • H. Bouy
CAB-LAEFF, Apartado 78, E-28691 Villanueva de la Cañada, Madrid, Spain

G. Duchêne
Astronomy Department, University of California, Berkeley, CA 94720-3411, USA

D. Stamatellos et al. (eds.), *The Labyrinth of Star Formation*, Astrophysics and Space Science Proceedings 36, DOI 10.1007/978-3-319-03041-8_68,

1 Selection of Results from the WIRCam Survey

Most studies in young star forming regions suffer from incompleteness both at lower masses and in spatial content, frequently focusing on the inner regions of clusters. It is therefore unknown if, as one moves to lower masses, other formation mechanisms take over. To overcome this bias, we performed large photometric surveys to identify candidate brown dwarfs. In ρ Oph, we selected from the WIRCam/CFHT near-IR survey new candidate substellar members and carried out a large spectroscopic follow-up, resulting in the confirmation of 19 new brown dwarf members. We compiled the most complete census of spectroscopically confirmed members, and constructed a spatially and extinction limited sample from which we derive the IMF. Taking into account the characteristic peak mass of the derived mass function and the ratio brown dwarfs to stars, we conclude that there is no evidence for a departure from a universal IMF [1,2]. In IC 348, we combined optical and near-IR deep images (Megacam and WIRCam/CFHT) and selected 30 candidate brown dwarfs. We have confirmed spectroscopically 14 substellar members, including the first L0 brown dwarfs found in this cluster. Combining the new population with the existing census from the literature, we find the number of brown dwarf to stars to agree with that of other young clusters.

The presence of methane absorption bands in the near-IR spectrum of T-dwarfs can be used to identify candidates photometrically. Theoretical models suggest a mass of a few M_{Jup} for these objects at 1–5 Myr, placing them among the lowest mass objects observed so far in star-forming regions. In IC 348, we identified 3 T-dwarf candidates. From colour-colour and colour-magnitude diagram, two candidates have been rejected for being too bright at optical wavelengths. The remaining candidate has an estimated spectral type of T6. From its luminosity, colour, extinction and spatial location, it is a probable member. The frequency of isolated planetary mass objects for IC 348 is consistent with the extrapolation of current lognormal IMF estimates to the planetary mass domain [3]. In Serpens core, we found 4 T-dwarf candidates with methane color above 0.2 mag, estimated visual extinction of 1–9 mag and spectral types of T1-T5. Comparisons with T-dwarf spectral models indicate that the properties of 1 of our candidates are consistent with it being a young member of the cluster. Two of our candidates are most likely background contaminants, while the other one could be a foreground mid-T dwarf [4]. In λ Ori, we identified 20 methane candidate and are studying complementary data to evaluate their properties. Preliminary results indicate only one object has optical and IR colours consistent with being a T-dwarf member of the cluster.

References

1. Alves de Oliveira, C. Alves de Oliveira, C., Moraux, E., Bouvier, J., et al. 2010, A&A, 515, A75
2. Alves de Oliveira C., Moraux E., Bouvier J., Bouy H., 2012, A&A, 539, A151
3. Burgess, A. S. M., Moraux, E., Bouvier, J., Marmo, C., Albert, L., & Bouy, H. 2009, A&A, 508, 823
4. Spezzi, L., Alves de Oliveira, C., Moraux, E., Bouvier, J., Winston, E., Hudelot, P., Bouy, H., Cuillandre, J.-C., 2012, A&A, in press

Astrometric and Photometric Mass Functions of the Old Open Cluster Praesepe from the UKIDSS GCS

Steve Boudreault, Nicolas Lodieu, N.C. Hambly, and N.R. Deacon

Abstract Here we present the results of a wide-field (∼36 sq. deg.) near-infrared ($ZYJHK$) survey of the Praesepe cluster using the Data Release 9 (DR9) of the UKIRT Infrared Deep Sky Survey (UKIDSS) Galactic Clusters Survey (GCS). We selected cluster candidates of Praesepe based on astrometry and photometry. With our candidate list, we have obtained the luminosity function of Praesepe in the Z and J bands, and we have derived the mass function (MF) of Praesepe from 0.6 down to 0.072 $M_{\odot}$. Moreover, we have estimated the binarity of the Praesepe members in the 0.5–0.1 $M_{\odot}$ mass range and as well as their variability.

Here we presented the results of a wide field, near-infrared study of the Praesepe cluster using the DR9 of the UKIRT Infrared Deep Sky Survey Galactic Clusters Survey. We performed an astrometric and photometric selection of 1,116 cluster candidates out of the 218,141 point sources detected towards Praesepe.

Possible sources of contamination include Galactic disk late-type and giant stars, and unresolved galaxies. We estimate a contamination rate of 11.9 % above 0.4 $M_{\odot}$, 9.8 % in the mass range 0.15–0.4 $M_{\odot}$, and 23.8 % below 0.15 $M_{\odot}$.

S. Boudreault (✉) • N. Lodieu
Instituto de Astrofísica de Canarias (IAC), C/Vía Láctea s/n, E-38200 La Laguna, Tenerife, Spain

Departamento de Astrofísica, Universidad de La Laguna (ULL), E-38205 La Laguna, Tenerife, Spain
e-mail: szb@iac.es

N.C. Hambly
Scottish Universities Physics Alliance (SUPA), Institute for Astronomy, School of Physics & Astronomy, University of Edinburgh, Royal Observatory, Blackford Hill, Edinburgh EH9 3HJ, UK

N.R. Deacon
Max-Planck-Institute für Astronomie, Königstuhl 17, 69117 Heidelberg, Germany

D. Stamatellos et al. (eds.), *The Labyrinth of Star Formation*, Astrophysics and Space Science Proceedings 36, DOI 10.1007/978-3-319-03041-8_69,

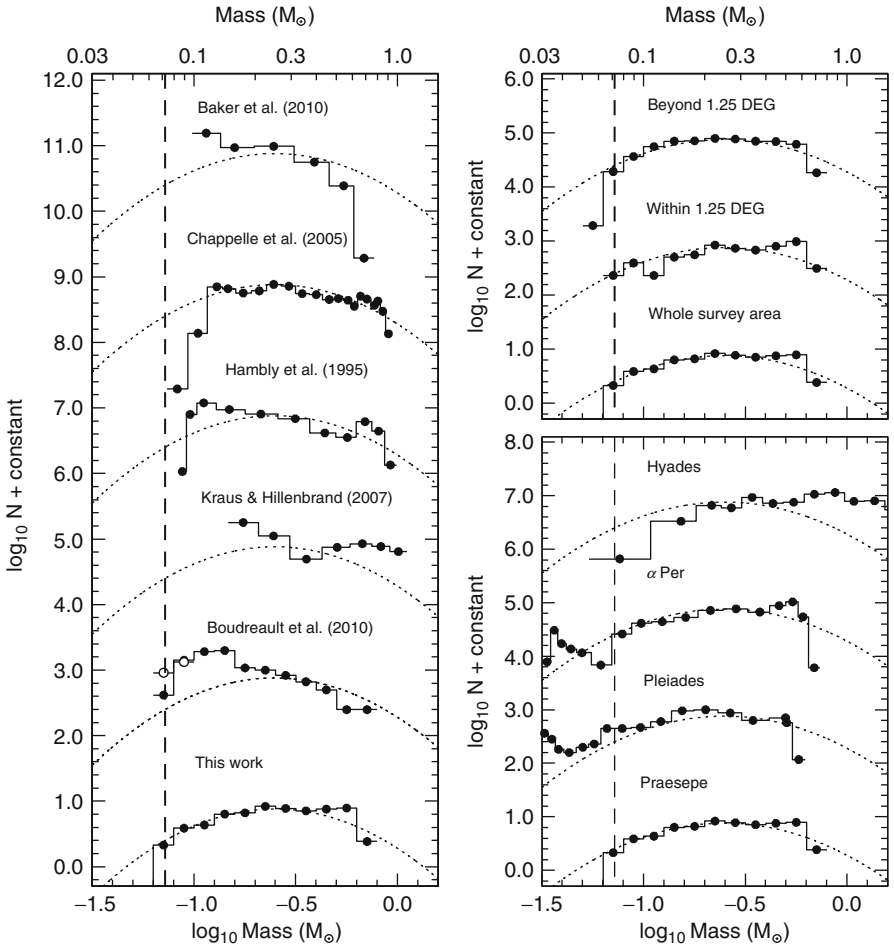

Fig. 1 For all panels, the *dotted curved lines* is the system Galactic field star MF fit from Chabrier (2005), while the *vertical dashed lines* are the substellar limit. We normalised all the MFs to the log-normal fit of Chabrier (2005) at $\sim$0.3 $M_{\odot}$ (log M ~ -0.5)

We investigated the binary frequency of Praesepe using the photometry and colours from our cluster candidates. We observe a binary fraction similar to the simulation of Bate (2012) between 0.07–0.1 $M_{\odot}$, $\sim 1.5\sigma$ difference in the 0.2–0.45 $M_{\odot}$ mass interval, and significantly lower by more than 3σ for the mass range 0.1–0.2 $M_{\odot}$. On the other hand, the binary fraction from Pinfield et al. (2003) are higher than our values and those of Bate (2012). We note that two other works focusing on field low-mass stars have also derived binary fractions lower than Bate (2012).

We also studied the variability of the Praesepe candidates using the two K-band epochs provided by the GCS. We identified seven candidate variables, including one in the substellar regime.

We derived the luminosity function of Praesepe in Z and J-band here. We observed that the peak of the J-band luminosity function is one magnitude brighter than the one reported by Boudreault et al. (2010).

Finally, we determined the mass function (MF) of Praesepe, which differs from previous studies: while previous MFs showed an increase from 0.6 to 0.1 $M_\odot$, our MF shows a decrease. We looked at the MF of Praesepe at two different regions of the cluster, i.e. within and beyond 1.25°, and we observed that both regions show an MF which decreases to lower masses. We compared our MF of Praesepe in the mass range 0.072–0.6 $M_\odot$ with the ones of the Hyades, the Pleiades and α Per. We conclude that our MF of Praesepe is most similar to the MF of α Per although they are respectively of ∼85 and ∼600 Myr. Even though of similar age, the Praesepe remains different than the Hyades, with a decrease in the MF of only ∼0.2 dex from 0.6 down to 0.1 $M_\odot$, compared to ∼1 dex for the Hyades. All MFs are presented in Fig. 1.

Acknowledgements SB and NL are funded by national program AYA2010-19136 (Principal Investigator is NL) funded by the Spanish ministry of science and innovation. NL is a Ramón y Cajal fellow at the IAC (program number 08-303-01-02).

The Evolution of the Core Mass Function by Gas Accretion

Sami Dib

Abstract We show how the mass function of dense cores (CMF) which results from the gravoturbulent fragmentation of a molecular cloud evolves in time under the effect of gas accretion. Accretion onto the cores leads to the formation of larger numbers of massive cores and to a flattening of the CMF. This effect should be visible in the CMF of star forming regions that are massive enough to contain high mass cores and when comparing the CMF of cores in and off dense filaments which have different environmental gas densities.

1 The Initial Core Mass Function: Gravoturbulent Fragmentation

It is well established that star formation occurs in dense, gravitationally bound cores which are embedded in a complex structure of intersecting filaments within molecular clouds. Considerable efforts have been made over the last years in order to understand the origin of the initial mass distribution of dense cores (ICMF) [1]. However, these ideas neglected the time evolution of the ICMF. PN02 showed that the ICMF can be described by Eq. 1:

$$N(M)\, d\log M = f_0 \left[1 + \mathrm{erf}\left(\frac{4\ln M + \sigma_d^2}{2\sqrt{2}\sigma_d}\right)\right] M^{-3/(4-\beta)} d\log M, \qquad (1)$$

where σ_d is the width of the log-normal distribution of the density field and which is given by $\sigma_d = \ln(1 + \gamma^2 \mathscr{M}^2)$, where $\mathscr{M}$ is the Mach number, β is the exponent of the kinetic energy power spectrum $E_k \propto k^{-\beta}$, and f_0 is a normalisation coefficient.

S. Dib (✉)
Blackett Laboratory, Imperial College London, Prince Consort road, SW7 2AZ, London, UK
e-mail: sdib@imperial.ac.uk

D. Stamatellos et al. (eds.), *The Labyrinth of Star Formation*, Astrophysics and Space Science Proceedings 36, DOI 10.1007/978-3-319-03041-8_70,

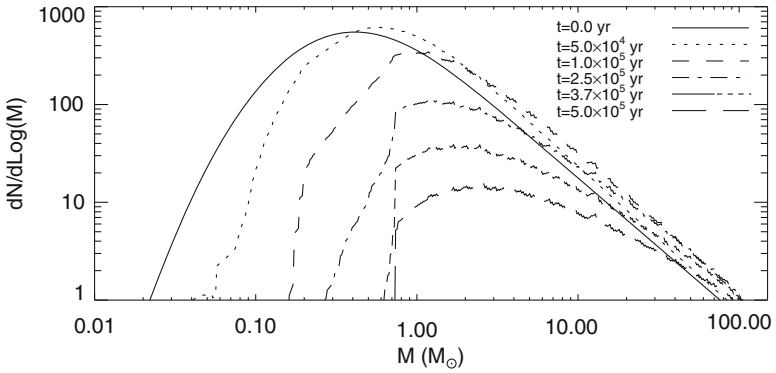

Fig. 1 Time evolution of the mass function of gravitationally bound cores in a molecular cloud. The CMF evolves over time as the result of gas accretion

2 The Evolution of the Core Mass Function by Accretion

Dib [2] argued that the ICMF will evolve in time as an unavoidable consequence of the cores growing in mass by gas accretion. They showed that the evolution of the CMF is described by the following time-dependent equation:

$$\left(\frac{dN}{dt}\right)(M,t) = \left[-\left(\frac{\partial N}{\partial M}\right)\dot{M} - \left(\frac{\partial \dot{M}}{\partial M}\right)N\right](M,t),$$

where $\dot{M}$ is the accretion rate. In [2], $\dot{M}$ had a time dependent component and the assumption was made that cores form uniformly over time with a prescribed core formation efficiency per unit time. They showed that a important consequence of Eq. 2 is the development of a larger fraction of massive cores and a flattening of the CMF (and IMF) at the high mass end. Here we show the evolution of the CMF for a single population of cores formed at $t = 0$ and which accretes with the following accretion rate [3]: $\dot{M} = \psi M^{2/3}$, where $\psi = (36\pi)^{1/3} t_d^{-1}$ and $t_d = 1/(G\rho_{ext})^{1/2}$ is the external medium crossing time and ρ_{ext} is the external medium density. Figure 1 displays the evolution of the CMF (with $\gamma = 0.5$, $\mathscr{M} = 6$, $\rho_{ext} = 8 \times 10^{-21}$ g cm^{-3}, $f_0 = 10^2$, $\beta = 1.88$). The figure clearly shows the buildup of massive cores and the flattening of the CMF as time goes by.

References

1. Padoan, P., Nordlund, Å. ApJ, **576**, 870 (2002)
2. Dib, S., Shadmehri, M., Padoan, P., Maheswar, G., Ohja, D. K., Khajenabi, F. MNRAS **405**, 401–420 (2010)
3. Basu, S., Jones, C. E. MNRAS **347**, L47–L51 (2004)

The Clump Mass Function in the Carina Nebula

Stephanie Pekruhl and Thomas Preibisch

Abstract In the Carina Nebula the feedback of the numerous hot stars disperses the parental Giant Molecular Cloud but also triggers the formation of new generations of stars. We obtained a wide-field map with the LABOCA camera at the APEX telescope, which provide the first spatially complete survey of the dust clouds in the Carina Nebula Complex and used the three common clump-finding algorithms CLUMPFIND, GAUSSCLUMPS and SExtractor to sample the Clump Mass Function in this region. Our aim is to investigate the effects of the extraction methods and the assumed temperature profile on the derived Clump Mass Function.

1 The Clump Mass Function

To determine the Clump Mass Function (ClMF) from our wide-field map, we obtained from LABOCA sub-mm (870 μm) observations [6], we used the three common clump-finding algorithms CLUMPFIND [8], GAUSSCLUMPS [7] and SExtractor [1].

For a reliable mass estimate the knowledge about the temperatures within the clumps is urgently necessary, as for too high temperatures the mass is underestimated. Therefore we derived a density temperature relation from a sample of 22 massive IRDC from the Hi-GAL galactic plane survey [4], from which we calculated the temperatures for the individual clumps, found from the algorithms. For all three samples we derive clump temperatures between 8.5 and 18.5 K [3].

The mass function of molecular clouds and clumps is often described by a power-law $\frac{dN}{dM} \propto M^{-\alpha}$. We find for all three distributions above $\sim 50\,M_{\odot}$ a

S. Pekruhl (✉) • T. Preibisch
Universitäts-Sternwarte München, Ludwig-Maximilians-Universität, Scheinerstr. 1, 81679 München, Germany
e-mail: pekruhl@usm.uni-muenchen.de; preibisch@usm.uni-muenchen.de

D. Stamatellos et al. (eds.), *The Labyrinth of Star Formation*, Astrophysics and Space Science Proceedings 36, DOI 10.1007/978-3-319-03041-8_71,

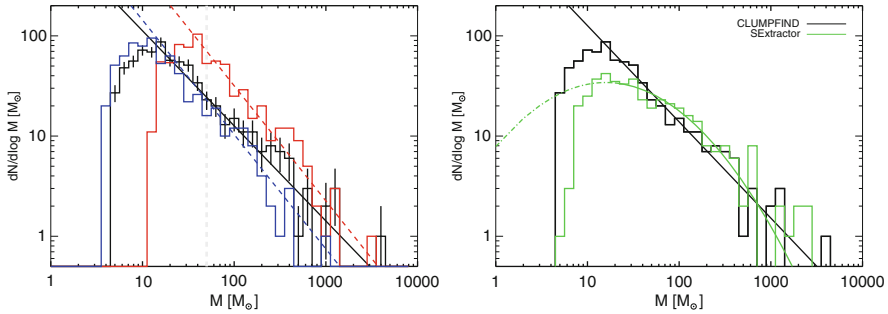

Fig. 1 *Left*: The mass histogram of the CLUMPFIND sample as an example. The *black line* show the ClMF with the individual clump temperatures, the *red* and *blue lines* indicate a constant temperature of 20 and 10 K, respectively, for all clumps. The error bars show the statistical error. *Right*: The mass distributions of the CLUMPFIND sample with its power-law slope ($\alpha = 1.95$) in *black* and the SExtractor sample over plotted with its log-normal fit in *green*

power-law tail with a slope α of around 1.95 ± 0.04 (see Fig. 1, left). This is in good agreement with similar observations ($\alpha \sim 1.4$–1.9). For constant temperatures we find the slope to be steeper ($\alpha \geq 2$) [3].

2 Log-Normal vs. Power-Law

Theoretical models predict that clouds with gravitationally bound clumps develop a power-law tail, while unbound turbulent structures show a log-normal mass distribution [2, 5]. For our mass distributions we find that the CLUMPFIND sample shows a robust power-law, while the slopes of the GAUSSCLUMPS and SExtractor samples can be also well described by a log-normal function [3] (Fig. 1, right). This shows that the shape of the ClMF depends on the specific extraction algorithm. Interpretations of a log-normal ClMF shape as a signature of turbulent pre-stellar clouds versus power-law ClMFs as a signature of star forming clouds should be taken with care to avoid an over-interpretation, if no additional information is available.

References

1. Bertin, E. & Arnouts, S. 1996, A&AS, 117, 393
2. Kainulainen, J., Beuther, H., Banerjee et al., T. 2011, A&A, 530, A64
3. Pekruhl, S., Preibisch, T., Schuller, F. & Menten, K., A&A, submitted
4. Peretto, N. & Fuller, G. A. 2010, ApJ, 723, 555
5. Peretto, N., Fuller, G. A., Plume, R., et al. 2010, A&A, 518, L98+
6. Preibisch, T., Schuller, F., Ohlendorf, H., et al. 2011c, A&A, 525, A92+
7. Stutzki, J. & Guesten, R. 1990, ApJ, 356, 513
8. Williams, J. P., de Geus, E. J., & Blitz, L. 1994, ApJ, 428, 693

Part VIII
High-Mass Star Formation

Theories of the Massive Star Formation: A (Short) Review

Patrick Hennebelle and Benoît Commerçon

Abstract We briefly review the recent numerical works that have been performed to understand the formation of massive stars. After a brief description of the classical works, we review more specifically (i) the problem of building stars more massive than 20 $M_\odot$ and (ii) how to prevent the massive cores to fragment in many objects. Multi-D simulations succeed in circumventing the radiative pressure leading to the formation of massive stars although some questions are still debated regarding how is accretion exactly proceeding. While the core fragmentation is slightly reduced by the radiative feedback and the magnetic field when they are treated separately, it is almost entirely suppressed when both of them are included. This is because, magnetic field by removing angular momentum focusses the flow in a compact region. This makes the radiative feedback very efficient leading to a significant increase of the temperature.

1 Introduction

High-mass stars have stellar masses roughly spanning the range 10–100 $M_\odot$. From their birth to their death, high-mass stars are known to play a major role in the energy budget of galaxies via their radiation, their wind, and the supernovae. Despite that, the formation of high-mass stars remains an enigmatic process, far less understood than that of their low-mass (solar-type) counterparts. One of the main differences between the formation of high-mass and low-mass stars is that the radiation field of

P. Hennebelle (✉)
Laboratoire AIM, Paris-Saclay, CEA/IRFU/SAp – CNRS – Université Paris Diderot, 91191 Gif-sur-Yvette Cedex, France
e-mail: patrick.hennebelle@lra.ens.fr

B. Commerçon
Ecole normale supérieure, Paris, France
e-mail: benoit.commercon@ens.fr

D. Stamatellos et al. (eds.), *The Labyrinth of Star Formation*, Astrophysics and Space Science Proceedings 36, DOI 10.1007/978-3-319-03041-8_72,

a massive protostar plays a more important role. Indeed, the massive stellar embryo strongly heats the gas and could even prevent further matter accretion through its radiation pressure. This implies that the radiative transfer must be treated in parallel to the hydrodynamics, which represents a severe complication mainly responsible for the limited numbers of theoretical studies of this process. As described below, it has been realised that the magnetic field is likely to play an important role as well.

Here is presented a short introduction to the theory of high-mass star formation. We first present the basic principles used to estimate the largest stellar mass that one expects to form in the presence of radiative forces in 1D. We then describe the recent numerical simulations which have been performed to address the two important questions; how to build stars more massive that $20\,M_\odot$ in spite of the radiative pressure; and how to prevent massive cores from fragmenting in many low mass objects?

2 The Issue of Circumventing the Radiative Pressure

2.1 One Dimensional Estimate

The first estimates of the largest stellar mass that can possibly be assembled are due to [8, 13]. The principle of their analysis is to compare the radiative pressure of a massive stellar embryo to the ram pressure induced by the gravitational collapse of its surrounding massive cloud, in its inner and outer parts. If the luminosity of the central star becomes high enough, the radiation pressure may become important and prevent further accretion onto the central object. Since the radiation pressure is acting on the dust grains, one has to assume that the frictional coupling between the gas and the dust is sufficiently strong so that forces acting on the dust grains are transmitted to the gas.

In the inner part of the collapsing cloud, the temperature becomes high and the dust grains evaporate. There is thus a dust shell whose inner edge is located at the radius, r, where the grains evaporate. At this sublimation radius, the radiation pressure is $L_\star/4\pi r^2 c$, where $L_\star$ is the stellar luminosity and c the speed of light. The dynamical pressure is ρu^2, where ρ is the density and u the infall speed which is given by $u^2 \simeq 2GM_\star/r$, where G is the gravitational constant and $M_\star$ the mass of the protostar. This leads to the ratio of radiative to ram pressures

$$\Gamma = \frac{L_\star/4\pi r^2 c}{\rho u^2} \simeq 1.3\times 10^{-11}\,\frac{L_\star/L_\odot}{(M_\star/M_\odot)^{1/2}}\,r^{1/2}. \tag{1}$$

Using an analytic estimate for the temperature inside the cloud and based on the assumption that the grains evaporate at a temperature of $\sim$1,500 K, Larson and Starrfield [13] estimate the radius of the shell to be

$$r \simeq 2.4 \times 10^{12} \frac{(L_\star/L_\odot)^{1/2}}{(M_\star/M_\odot)^{1/5}} \text{ cm} \simeq 3.3 \frac{(L_\star/10^3\ L_\odot)^{1/2}}{(M_\star/8\ M_\odot)^{1/5}} \text{ AU}. \quad (2)$$

It follows from Eqs. 1 to 2 that

$$\Gamma \simeq 2 \times 10^{-5} \frac{(L/L_\odot)^{6/5}}{(M/M_\odot)^{3/5}}. \quad (3)$$

For a stellar mass of 20 $M_\odot$, corresponding to a luminosity of about $4 \times 10^4\ L_\odot$, Γ roughly equals unity. Therefore, according to [13], the mass at which radiative pressure impedes accretion is around 20 $M_\odot$.

A more accurate estimate has been done by Wolfire and Cassinelli [18] by using the optical properties and composition of the mixture of dust grains proposed by Mathis et al. [15]. Assuming an accretion rate of $10^{-3}\ M_\odot\ \text{year}^{-1}$ in a 100 $M_\odot$ cloud, Wolfire and Cassinelli show that Γ is larger than one for any reasonable value of the radiation temperature. They conclude that building a massive star with the "standard" dust grain mixture is difficult and requires reducing the grain abundance by large factors (∼4–8). They thus propose, as a solution to the high-mass star formation problem, that the dust abundance could be locally decreased by an external shock or an internal ionization front.

More recently, Kuiper et al. [11] have also performed 1D calculations for various core masses and confirm largely the results of these early works. In particular, they cannot form objects more massive than 20 $M_\odot$ even in very massive cores.

2.2 *Bidimensional Multi-wavelengths Calculations*

Bi-dimensional numerical simulations have been performed, treating the radiation and the dynamics self-consistently. In these studies, it has been assumed that the radiation arises from both the accretion and the stellar luminosity. While the former is dominant during the earliest phases of the collapse, the latter becomes more important at more advanced stages. One of the main motivations of these calculations is to determine whether the presence of a centrifugally supported optically thick disk, inside which the radiative pressure would be much reduced, may allow to circumvent the radiation pressure problem. The first numerical simulations have been performed by Yorke and Sonnhalter [19] in the frequency dependent case (using 64 intervals of frequency) and in the grey case (one single interval of frequency). The cloud they consider is centrally peaked, has a mass of 60 $M_\odot$, a thermal over gravitational energy ratio of about 5 % initially, and is slowly rotating. After $\sim 10^5$ year, the central core has a mass of about 13.4 $M_\odot$ and the surrounding cloud remains nearly spherical. After $\sim 2 \times 10^5$ year, the mass of the central core is about 28.4 $M_\odot$ and the cloud starts to depart from the spherical symmetry. In particular, the infall is reversed by radiative forces in the polar region while the star continues to accrete material through the equator where the opacity is much higher.

This is known as the "flashlight effect". Once the stellar mass has grown to about 33.6 $M_\odot$, the central star is no longer accreting although 30 $M_\odot$ of gas is still available within the computational grid. The infall is then reversed in every directions indicating that the radiative forces are effectively preventing further accretion. If instead of a multi-frequency treatment, the grey approximation is made, the early evolution is similar but becomes notably different after $\sim 2.5 \times 10^5$ year. In particular, there is no evidence of any flow reversal. Instead the material flows along a thin disklike structure, supported in the radial direction by both centrifugal and radiative forces. At the end of the simulation, the mass of the central star is about 20.7 $M_\odot$.

Kuiper et al. [11] have performed bi-dimensional simulations using an hybrid scheme for the radiative transfer. While the gas emission is treated using the flux-limited diffusion and the grey approximation, direct multi-frequency irradiation from the central star is also included. In particular, they stress the importance of spatially resolving the dust sublimation front. In the simulations that do not resolve it well, the accretion quickly stops while it continues when the sublimation front is well described. This is because the radiation is more isotropic when the dust sublimation front is not properly resolved, leading to a weak flashlight effect. In their simulations, Kuiper et al. [11] form objects of mass much larger than the $\simeq 20\ M_\odot$ that they form in their 1D calculations. For example for a 480 $M_\odot$ clump, they form an object of 150 $M_\odot$ which is still accreting.

2.3 *Tridimensional Calculations*

The first 3D-calculations have been performed by Krumholz et al. [9,10]. They use a flux-limited and grey approximation to treat the radiative transfer. The most striking aspect they report is certainly the development of the Rayleigh-Taylor instability in the radiatively triggered expanding bubble. As a consequence of the non-linear development of this instability, fingers of dense material can channel through the low density radiatively dominated cavity and reach the central object. They therefore identify three modes of accretion in their simulations, accretion through the disk (the flashlight effect), accretion through the cavity wall, and accretion through dense Rayleigh-Taylor unstable fingers. A quantitative estimate reveals that the latter route accounts for about 40 % of the accretion.

These results have been questioned by Kuiper et al. [12] who performed bidimensional calculations with a flux-limited scheme similar to the one used by Krumholz et al. [10] and the hybrid scheme which is used in Kuiper et al. [11]. The results turn out to be quite different. In the first case, a radiatively dominated bubble is launched but is quickly stopped and falls back towards the equatorial plane. In the second case, the bubble keeps expanding leading to a radiatively driven outflow. One of the important consequence is thus that accretion occurs exclusively through the disk. As these simulations are bidimensional, it is unclear whether they completely rule out the development of the Rayleigh-Taylor instability which could be largely seeded by the non-linear fluctuations induced by the turbulence in 3D.

They nevertheless suggest that the dynamics of the radiatively dominated cavity is largely determined by the treatment of the radiative feedback in particular its frequency dependence.

3 The Issue of Fragmentation

The second drastic problem in the context of massive star formation is how to avoid fragmenting the massive cores in many objects. For example in the simulations that have been performed by Dobbs et al. [4], the 30 solar mass core they simulate, fragments in about 20 low mass objects thus preventing the formation of high mass objects. While it remains possible that large mass objects could be formed in very massive clumps through competitive accretion (e.g. [1]), it is important to treat in any case, the physics of the fragmenting cores properly which is the task that the studies described below have addressed.

3.1 Hydrodynamical Radiative Calculations

Tridimensional calculations have been performed by Krumholz et al. [9] using the grey approximation for the radiative transfer. Their initial conditions (aimed at reproducing the model of [16]) consist in a centrally peaked 100 $M_{\odot}$ cloud with a density profile proportional to r^{-2}. The initial turbulence within the cloud is sufficient to ensure an approximate hydrostatic equilibrium. Turbulent motions first delay the onset of collapse but, as the turbulence decays, the cloud starts to collapse. Comparison is made with runs for which an isothermal equation of state is used. In particular, Krumholz et al. [9] find that, when the radiative transfer is taken into account, the gas temperature inside the cloud is higher than in the isothermal case, by factors up to 10, which are depending on the cloud density. As a consequence, the cloud is fragmenting much less when radiation is taken into account than when isothermallity is used. It is important to note at this stage that centrally condensed cores are less prone to fragmentation than cores having flatter density profiles as shown by Girichidis et al. [5]. Indeed the radiative hydrodynamical simulations performed by Commerçon et al. [3] clearly show that cores which initially have a flat density profile, are undergoing significant fragmentation as shown by the top left and bottom left panels of Fig. 1.

3.2 MHD Barotropic Calculations

Another important process that must be included in the treatment of massive cores, is the magnetic field. Indeed, in the context of low mass cores, magnetic field has

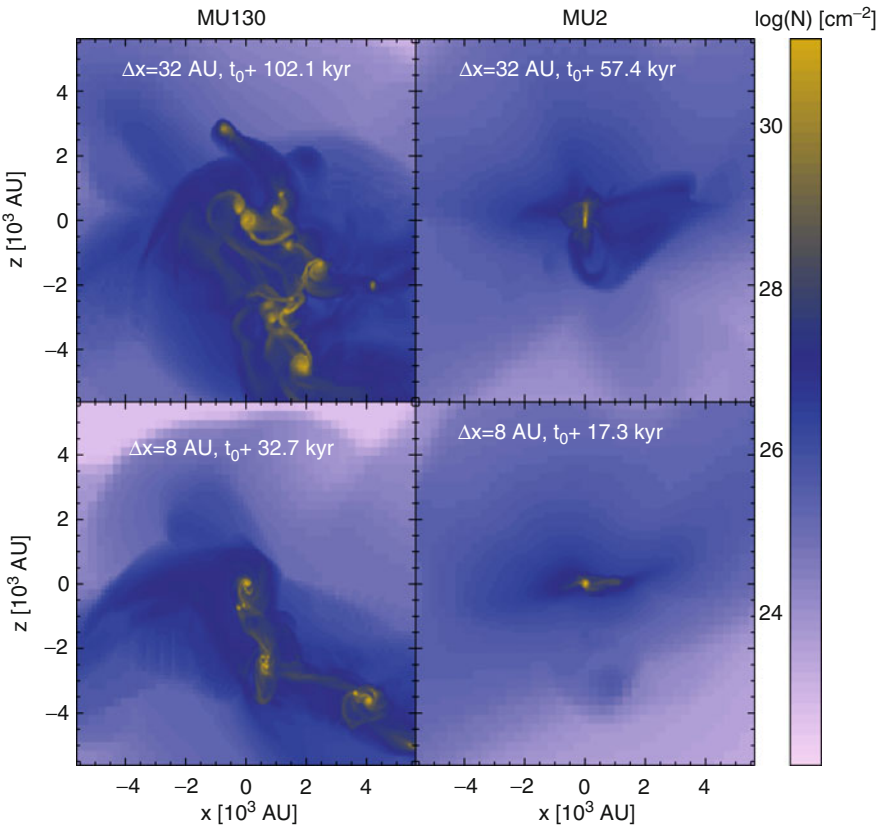

Fig. 1 Column density within central part of massive collapsing cores. *Left*: hydrodynamical case, the core is largely fragmenting eventhough radiative feedback is treated. *Right*: RMHD simulation (initial mass-to-flux of 2), the fragmentation is entirely suppressed due to the combination of magnetic field and radiative feedback [3]

been found to drastically reduce the fragmentation [6,14]. Hennebelle et al. [7] have been running a set of barotropic simulations for various magnetic intensities. The initial conditions consist in 100 $M_\odot$ cores with a smooth initial density profile and a turbulent velocity field (with a ratio of turbulent and gravitational energies of about 20 %). The fragmentation is delayed and reduced when the magnetic flux is strong enough (typically for mass-to-flux smaller than 5). The number of objects decreases up to typically only a factor of 2 for the strongest magnetisation that was explored. Thus, Hennebelle et al. [7] conclude that magnetic field in itself cannot suppress the fragmentation in many objects. The reason of this limited impact is largely due to the magnetic diffusion induced by the turbulent velocity field, which reduces the magnetic field in the central part of the collapsing core where fragmentation is taking place. Similar conclusion has been reached by Peters et al. [17] who even included photo-ionisation from the central star.

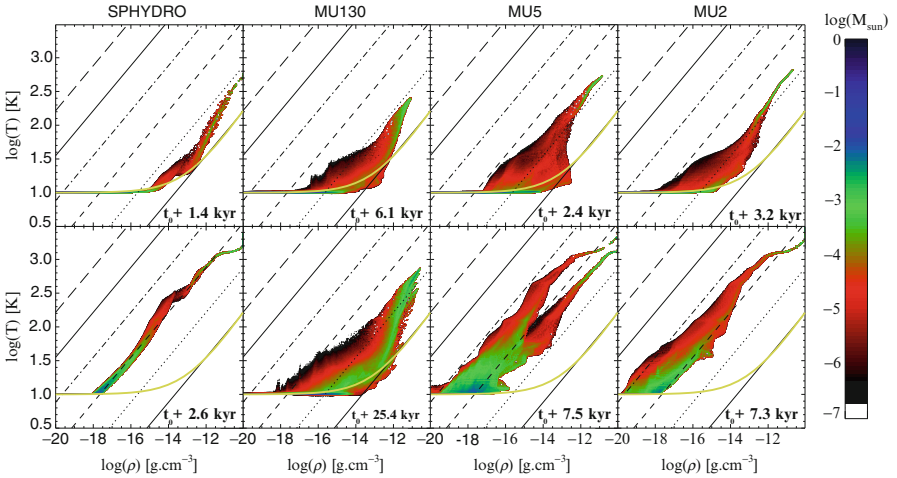

Fig. 2 Temperature as a function of density within the massive core. *First panel* is for a purely spherical model (i.e. which has no turbulence and no magnetic field), the *second panel* is for an hydrodynamical run with initial turbulence, the third is identical to the second one but has an initial magnetic field corresponding to mass-to-flux of 5 initially. The fourth has a mass-to-flux of 2 [3]

3.3 MHD Radiative Calculations

The first simulations that include both MHD and radiative feedback in the context of massive star formation, have been recently performed by Commerçon et al. [3]. These simulations show that the combination of magnetic field and radiative feedback is indeed extremely efficient in suppressing the fragmentation. The reason is that magnetic field and radiative feedback are in a sense interacting [2] and their combination leads to effects that are much stronger than expected. This is because, as pointed out by Hennebelle et al. [7] magnetic field, even in the presence of turbulence, leads to efficient magnetic braking which reduces the amount of angular momentum in the central part of the cloud where fragmentation is taking place. Thus, the accretion is initially much more focussed in a magnetized core than in an hydrodynamical core when turbulence is included because in hydrodynamical simulations, a large amount of angular momentum prevents the gas to fall in the central object. Consequently, the accretion luminosity which is $\propto M\dot{M}/R$ is much higher because the mass of the central object and the accretion rate onto the central object are larger. Also the radius at which accretion is stopping is smaller (since there is less angular momentum). Consequently, the temperature in magnetized cores is much higher than in hydrodynamical cores making them much more stable against fragmentation. This is illustrated in Fig. 2 which shows the temperature as a function of density in four cases. The first panel shows the case of a cloud with no turbulence and no magnetic field which is purely spherical initially. In this case, the flow is extremely focussed and fall directly in a single central object. The second panel shows the temperature distribution for a turbulent and unmagnetized cloud

while the third and fourth panels show this distribution for two magnetic intensities. Clearly the hydrodynamical case with turbulence has the lowest temperatures while the most magnetized case (fourth panel) presents much higher temperatures which are comparable to the one obtained in the purely spherical case (first panel) that is naturally focussed.

4 Conclusion

We have presented a brief review of the recent studies which have been performed to explain the formation of massive stars. Multi-D simulations including radiative feedback agree that it is possible to build stars more massive than predicted by the 1D spherical case in which radiative pressure prevents further accretion. The details, however, of how this accretion exactly proceeds are still a matter of debate. The fragmentation of massive cores is slightly reduced when either the radiative feedback or the magnetic field are present. However when both are treated simultaneously, the fragmentation is very significantly reduced because magnetic field focusses the gas which leads to a more efficient radiative feedback and higher temperatures.

References

1. Bonnell, I., Vine, S., Bate, M., 2004, MNRAS, 349, 735
2. Commerçon, B., Hennebelle, P., Audit, E., & Chabrier, G., Teyssier, R. 2010, A&A, 510L, 3
3. Commerçon, B., Hennebelle, P., Henning, T., 2011, ApJ, 742L, 9
4. Dobbs, C. L., Bonnell, I. A., & Clark, P. C. 2005, MNRAS, 360, 2
5. Girichidis, P., Federrath, C., Banerjee, R., Klessen, R., 2011, MNRAS, 413, 2741
6. Hennebelle, P., Teyssier, R., 2008, A&A, 477, 25
7. Hennebelle, P., Commerçon, B., Joos, M., Klessen, R. S., Krumholz, M., Tan, J. C. & Teyssier, R. 2011, A&A, 528, A72
8. Kahn, F. 1974, A&A, 37, 149
9. Krumholz, M., Klein, R., McKee, C. 2007, ApJ, 665, 478
10. Krumholz, M. R., Klein, R. I., McKee, C. F., Offner, S. S. R., Cunningham, A. J. 2009, Science, 323, 754
11. Kuiper, R., Klahr, H., Beuther, H. & Henning, T. 2010, ApJ, 722, 1556
12. Kuiper, R., Klahr, H., Beuther, H. & Henning, T. 2012, A&A, 537, 122
13. Larson, R., Starrfield, S. 1971, A&A, 13, 190
14. Machida, M., Matsumoto, T., Tomisaka, K., Hanawa, T., 2005, MNRAS, 362, 369
15. Mathis, J., Rumpl, W., Nordsieck, K. 1977, ApJ, 217, 425
16. McKee, C., Tan, J. 2003 ApJ, 585, 850
17. Peters, T., Banerjee, R., Klessen, R., MacLow, M.-M., Galván-Madrid, R., Keto, E., 2011, ApJ, 729, 72
18. Wolfire, M., Cassinelli, J. 1987, ApJ, 319, 850
19. Yorke, H., Sonnhalter, C. 2002, ApJ, 569, 846

Molecular Gas in the Inner 500 pc of the Milky Way: Violating Star Formation Relations and on the Verge of Forming Extreme Stellar Clusters

Steven N. Longmore

Abstract With the HOPS, MALT90 and HiGAL Galactic plane surveys we are mapping a significant fraction of the dense, star-forming, molecular gas in the Galaxy. I present results from two projects based on this combined dataset, namely, (i) looking for variations in the star formation (SF) rate across the Galaxy as a function of environment, and (ii) searching for molecular cloud progenitors of the most extreme (massive and dense) stellar clusters. We find the SF rate per unit mass of *dense* gas in the inner 500 pc of the Galaxy is at least an order of magnitude lower than that in the disk, directly challenging the predictions of proposed universal column/volume density relations. In particular, the region $1° < l < 3.5°$, $|b| < 0.5°$ contains $\sim 10^7\,M_\odot$ of dense molecular gas—enough to form 1,000 Orion-like clusters—but the present-day star formation rate within this gas is only equivalent to that in Orion. I present follow up studies of one molecular cloud we have studied as part of project (ii) which also lies in the inner 500 pc of the Galaxy and is clearly extreme compared to the rest of the Galactic population. With a mass of 10^5 Msun, a radius of only $\sim$3 pc and almost no signs of star formation it appears to be the progenitor of an Arches-like stellar cluster. Despite detailed observational follow-up searches, this object still appears to be unique in the Galaxy, making it extremely important for testing massive cluster formation models.

1 Introduction

The conversion of gas into stars is one of the fundamental processes in the Universe, and a cornerstone of astrophysics and cosmology. Whether or not this process varies as a function of environment across cosmological timescales

S.N. Longmore (✉)
European Southern Observatory, Karl-Schwarzschild-Str. 2, 85748 Garching bei München, Germany
e-mail: slongmor@eso.org

D. Stamatellos et al. (eds.), *The Labyrinth of Star Formation*, Astrophysics and Space Science Proceedings 36, DOI 10.1007/978-3-319-03041-8_73,

underpins our understanding of the formation of everything from planets to galaxy clusters. The key physics linking all these fields is encapsulated in an end-to-end understanding of the star and cluster formation process incorporating the effect of different natal environmental conditions.

Developing an end-to-end model of star formation (SF) must be led by observations that can both resolve sites of individual SF and determine the global properties of their natal molecular clouds. For the foreseeable future, SF regions in the Milky Way (MW) are the only targets in the Universe for which this will be possible. The physical environment across the MW varies widely, from the extreme conditions close to the central supermassive black hole, to the benign conditions in the outer Galaxy. By trying to understand what drives changes in the stellar output of molecular clouds as a function of their physical properties in our own Galaxy, we aim to provide a template for understanding SF under similar conditions in external galaxies and across cosmological timescales.

In many ways this is a Golden Age for SF studies in the MW. In the next few years, the availability of multi-wavelength Galactic plane survey data, new telescopes for follow-up studies, and advances in numerical simulations will enable a revolution in Galactic SF studies. Surveys are building GMC samples comprising a large fraction of the dense molecular gas in the Galaxy. Combined with similar surveys at IR and cm wavelengths, this will, for the first time, provide statistically meaningful GMC samples separated by their global/environmental properties and relative ages.

Within this context, I present some initial results from the HOPS [1], MALT90 [2] and HiGAL [3] Galactic plane surveys. We conducted the simplest possible analysis of such an enormous dataset, namely looking for (i) large systematic variations between dense gas tracers and SF indicators across the Galaxy, and (ii) the most extreme molecular clouds in the Galaxy.

2 Testing Star Formation Relations

Recent surface- and volume-density star formation relations have been proposed which potentially unify our understanding of how gas is converted into stars, from the nearest star forming regions to ultra-luminous infrared galaxies (ULIRGs) [4,5]. The inner 500 pc of our Galaxy contains the largest concentration of dense, high-surface density molecular gas in the Milky Way [6, 7], providing an environment where the validity of these star-formation prescriptions can be tested.

We have used recently-available data from HOPS and HiGAL at wavelengths where the Galaxy is transparent, to find the dense, star-forming molecular gas across the Milky Way [8]. We use water and methanol maser emission [9] to trace star formation activity within the last 10^5 years and 30 GHz radio continuum emission from the Wilkinson Microwave Anisotropy Satellite (WMAP) [10] to estimate the high-mass star formation rate averaged over the last $\sim 4 \times 10^6$ years.

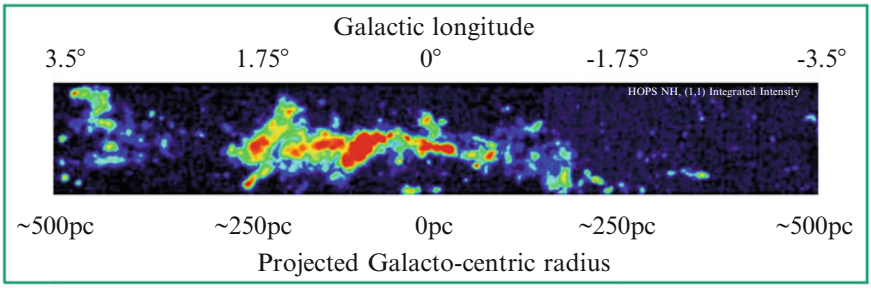

M_{TOT}	1.7x10^7 Msun	1.8x10^7 Msun	6x10^6 Msun	4.1x10^7
$M_{>8mag}$	1.6x10^7 Msun	1.7x10^7 Msun	4x10^6 Msun	3.7x10^7
SFR_{WMAP}	0.0036 Msun/yr	0.06 Msun/yr	0.016 Msun/yr	0.08
		Predictions		Total
$SFR_{>8mag}$ *Lada et al.(2012)*	0.74 Msun/yr	0.78 Msun/yr	0.18 Msun/yr	
$SFR_{volumetric}$ *Krumholz, Dekel & McKee (2012)*	0.39 Msun/yr	0.41 Msun/yr	0.14 Msun/yr	

Fig. 1 Comparison of measured and predicted star formation rates as a function of Galacto-centric radius for the inner 500 pc of the Milky Way. The colour scale shows the $NH_3(1,1)$ integrated intensity image from HOPS [1] between $|l| \leq 3.5°$ and $|b| \leq 0.5°$ with the corresponding projected Galacto-centric radius underneath. The table below shows the observed and predicted gas mass and star formation rates for this region. The top two rows show the total gas mass and the mass of this gas above an extinction of $A_V = 8$ mag, respectively, derived from the HiGAL column density map [3]. The third row shows the star formation rate derived from WMAP data [10]. The fourth and fifth rows show the predicted star formation rates from Lada et al. [4] and Krumholz et al. [5] respectively, given the gas mass in rows one and two. A volume density of 5×10^3 cm^{-3} for gas in the CMZ was used to calculate the values in row 5 [7]. The different columns show the values for different longitude ranges, all with $|b| < 0.5°$. The second, third and fourth columns are for longitude ranges of $1° < l < 3.5°$, $|l| < 1°$ and $-3.5° < l < -1°$, respectively. The final column shows the total across the full region of $|l| \leq 3.5°$, $|b| \leq 0.5°$

We find the dense gas distribution is dominated by the very bright and spatially-extended emission within a few degrees of the Galactic centre [11]. This region accounts for ~80 % of the $NH_3(1,1)$ integrated intensity but only contains 4 % of the survey area. However, in stark contrast, the distribution of star formation activity tracers is relatively uniform across the Galaxy.

To probe the dense gas vs SFR relationship towards the Galactic centre region more quantitatively, we compared the HiGAL column density maps [12] to the WMAP-derived SFR across the same region. The results are shown in Fig. 1. The total mass and SFR derived using these methods agree well with previous values in the literature [7, 13, 14]. The main conclusion from this analysis is that both the

column-density threshold and volumetric SF relations [4,5] over-predict the SFR by an order of magnitude given the reservoir of dense gas available to form stars. The region $1° < l < 3.5°$, $|b| < 0.5°$ is particular striking in this regard. It contains $\sim 10^7\,M_\odot$ of dense molecular gas—enough to form 1,000 Orion-like clusters—but the present-day star formation rate within this gas is only equivalent to that in Orion. This implication of this result is that any universal column/volume density relations must be a *necessary but not sufficient* condition for SF to occur.

3 Searching for Molecular Cloud Progenitors of Extreme Stellar Clusters

Young massive clusters (YMCs) are thought to be the 'missing link' between open clusters and extreme extragalactic super star clusters and globular clusters. We previously used the HOPS survey to search for molecular clouds which may represent the initial conditions of YMCs [15]. With a mass of $10^5\,M_\odot$, a radius of only $\sim$3 pc and almost no signs of star formation, we put forward one cloud, G0.253+0.016, as a likely progenitor of an Arches-like YMC. Our Galactic plane survey data suggested this to be the most massive and dense cloud in the Galaxy, making it extremely important for testing massive cluster formation models [16].

In subsequent work we have attempted to quantify what the initial conditions must be for molecular clouds to form bound YMCs, and propose the progenitor clouds must have escape speeds greater than the sound speed in photo-ionized gas [17]. In these clumps, radiative feedback in the form of gas ionization is bottled up, enabling star formation to proceed to sufficiently high efficiency so that the resulting star cluster remains bound even after gas removal. We estimate the observable properties of clouds destined to form YMCs for existing Galactic plane surveys. Follow-up work searching through BGPS data finds several clouds which pass the proposed criteria [18]. However, none of these are as massive as G0.253+0.016 and in all of them prodigious star formation is already underway.

Despite these, and other, detailed searches for similar objects, G0.253+0.016 still appears to be the most massive and dense molecular cloud in the Galaxy with almost no signs of star formation.

References

1. Walsh, A. J. et al., 2011, MNRAS, 416, 1764–1821
2. Foster, J. et al., 2011, ApJS, 197, 25
3. Molinari, S. et al., 2010, A&A, 518, 100–105
4. Lada, C. J. et al., 2012, ApJ, 745, 190–196
5. Krumholz, M. et al., 2012, ApJ, 745, 69–85
6. Morris, M. & Serabyn, E., 1996, ARAA, 34, 645–701
7. Ferriere, K. et al., 2007, A&A, 467, 611–627

8. Longmore S. N. et al., 2013, MNRAS, 429, 987
9. Caswell, J. L. et al., 2010, MNRAS, 404, 1029–1060
10. Lee, E. et al., 2012, ApJ, 752, 146–160
11. Purcell et al., 2012, MNRAS, 426, 1972
12. Molinari, S. et al., 2011, ApJ, 735, 33–40
13. Immer, K. et al., 2012, A&A, 537, 121–140
14. Yusef-Zadeh, F. et al., 2009, ApJ, 702, 178–225
15. Longmore, S. N. et al., 2012, ApJ, 746, 117–127
16. Longmore, S. N. et al., 2011, ApJ, 726, 97
17. Bressert, E. et al., 2012, ApJL, 758, 28
18. Ginsburg, A. et al., 2012, ApJL, 758, 29

A Solution to the Radiation Pressure Problem in the Formation of Massive Stars

Rolf Kuiper, Hubert Klahr, Henrik Beuther, and Thomas Henning

Abstract We review our recent studies demonstrating that the radiation pressure problem in the formation of massive stars can be circumvented via an anisotropy of the thermal radiation field. Such an anisotropy naturally establishes with the formation of a circumstellar disk. The required angular momentum transport within the disk can be provided by developing gravitational torques. Radiative Rayleigh-Taylor instabilities in the cavity regions – as previously suggested in the literature – are not required and are shown to be unlikely in the context of massive star formation.

1 Introduction

During their lifetime, massive stars exert a radiation pressure onto their surroundings, which is higher than their gravitational attraction. How these massive stars can sustain accretion was an open question for decades. Semi-analytical [1] and first radiation-hydrodynamical computations in spherical symmetry [8] support the idea that the radiation pressure of a star retards the collapse of its proto-stellar core, leading to an upper stellar mass limit of $\leq 40\,M_\odot$.

Based on the fact that in these 1D simulations the collapse was reversed by the re-emitted radiation, Nakano [7] inferred that the radiation pressure onto the accretion flow can be diminished by an anisotropic optical depth of the environment. Such an anisotropy can be produced by the formation of an accretion disk.

R. Kuiper (✉)
Jet Propulsion Laboratory, California Institute of Technology, 4800 Oak Grove Drive, Pasadena, CA 91109, USA
e-mail: Rolf.Kuiper@jpl.nasa.gov

H. Klahr • H. Beuther • T. Henning
Max-Planck-Institut für Astronomie, Königstuhl 17, D-69117 Heidelberg, Germany

D. Stamatellos et al. (eds.), *The Labyrinth of Star Formation*, Astrophysics and Space Science Proceedings 36, DOI 10.1007/978-3-319-03041-8_74,

The first numerical study aimed at verifying this idea was by Yorke and Sonnhalter [9]. In their simulations, the optical depth of the forming accretion disk turned out to be too low to provide a sufficient anisotropy of the radiation field. As a result, the accretion onto the proto-star stopped shortly after the disk formation, limiting the maximum final stellar mass to $42.9\,\mathrm{M}_\odot$. In Krumholz et al. [2] the authors claimed further feeding of the star and its circumstellar disk by a radiative Rayleigh-Taylor instability of the bipolar cavity regions. The most massive (and still accreting) proto-star formed in this simulation was $41.5\,\mathrm{M}_\odot$.

All in all, no star much more massive than the 1D radiation pressure barrier of $M_*^{\max} \approx 40\,\mathrm{M}_\odot$ was formed in numerical simulations up to this point.

2 Methods

In this section, we highlight two of our code specifics, namely the grid in spherical coordinates and the hybrid radiation transport method developed. For a complete description of the equations, methods, and numerical solvers please see [6] for the radiation transport, [3] for the hydrodynamics in axial symmetry, and [4] for the hydrodynamics in three dimensions.

The grid of the computational domain is given in spherical coordinates with a logarithmically increasing resolution towards the center. The resolution of the inner region around the centrally forming star is $\approx$1 AU, decreasing towards the outer core regions proportional to the radius. This kind of grid covers the essential phenomena on the wide range of spatial scales from the outer core collapse (gravity dominated) over the torus formation (flattened rotating structure, still in-falling) in the transitional region down to the innermost disk formation (centrifugal balance).

The hybrid radiation transport method is highly adapted to the problem under investigation: The stellar irradiation is computed via a very accurate frequency-dependent ray-tracing step, while the re-emission and thermal dust emission is computed within a fast gray Flux-Limited Diffusion (FLD) approach.

Hence, the feedback onto the directly irradiated regions around the massive proto-star – the inner disk rim and the cavity walls – is computed with very high accuracy, including the wide range of different optical depths for the broad stellar spectrum. The ray-tracing of the stellar spectrum guarantees the resembling of the long range force of the irradiation, see [5].

3 Resolving the Optical Depth of the Circumstellar Accretion Disk

In our simulation series for varying sizes of the inner sink cell [3], we find that it is essential to fully include and resolve the innermost part of the dusty accretion disk, which depicts the highest optical depth, to compute the anisotropy of the thermal radiation field correctly.

Using the initial conditions of Yorke and Sonnhalter [9], in which the size of the sink cell is several times larger than the dust sublimation radius, our simulations resemble their results of short disk accretion epochs. By restricting the sink cell to a size smaller than the dust sublimation radius, the thermal radiation field becomes strongly anisotropic and accretion sustains for several free-fall times.

4 Overcoming the Radiation Pressure Barrier

In simulation series for varying initial core masses $M_{\rm core}$ in spherical as well as axial symmetry, we demonstrate, how the anisotropy of the thermal radiation field reduces the feedback onto the accretion flow, allowing the formation of the most massive stars known, see [3]. In spherical symmetry, the accretion is stopped and reversed by radiative forces. Regardless of the initial core mass ($M_{\rm core} = 60$–$480\,{\rm M}_\odot$), the final mass of the forming star is limited to $<40\,{\rm M}_\odot$. These results fully support the work by Kahn [1] and Yorke and Krügel [8].

Setting the initial pre-stellar core in slow solid body rotation yields the formation of an accretion disk around the centrally forming massive star, which self-consistently leads to an anisotropy of the thermal radiation field. The optical depth of the disk remains at high values by further accretion from the large scale envelope. The bipolar cavity regions remain stable, and in turn lead to a mass loss of the proto-stellar core of roughly 50 % of the initial core mass. In the shielded disk regions, the diminished radiative feedback onto the accretion flow enables the massive proto-star to increase its mass to $M_*^{\rm max} > 100\,{\rm M}_\odot$.

In fact, these are the first simulations, including the effect of radiation pressure feedback, which demonstrate a possibility to form stars up to the maximum value of the observed stellar mass spectrum.

5 Angular Momentum Transport in Massive Accretion Disks

In the 2D simulations we have to rely on an α-viscosity model for the actual angular momentum transport. In Kuiper et al. [4], we demonstrate in a three-dimensional simulation that the self-gravity of the forming massive accretion disk self-consistently leads to gravitational instabilities and the formation of spiral arms, which gravitational torques in turn yield an angular momentum transport. In contrast to the smooth viscous disk accretion in axial symmetry, the 3D simulation shows episodic accretion. The accretion rate integrated over several episodic accretion events is as high as (even slightly higher than) the accretion rates of the axially symmetric simulations in [3]. Hence, we conclude that the accretion rate required to form massive stars is self-consistently arranged by the self-gravity of the forming massive accretion disk.

6 On the Radiative Rayleigh-Taylor Instability

In Krumholz et al. [2] the authors claim that a 3D radiative Rayleigh-Taylor instability in the bipolar cavity shell is required to allow further feeding of the star-disk system beyond the radiation pressure barrier. Contrary, our simulations show the launching and expansion of stable outflow cavities, regardless of the dimension and for a large variety of initial conditions. Among others, both studies differ in the treatment of the direct stellar irradiation feedback. In Kuiper et al. [5] it is shown that if we cut down the radiation transport in our simulations to the gray FLD approximation, the forming cavities undergo a radiative Rayleigh-Taylor instability as well. But if the stellar irradiation is computed with the much more sophisticated ray-tracing scheme, the cavities remain stable. This result is backed up in Kuiper et al. [5] by analytical estimates of the radiative forces in the cavity shell, which are underestimated in the gray FLD approximation by up to two orders of magnitude.

7 Summary

In 45 published simulations regarding the radiation pressure feedback in the formation of massive stars, we have demonstrated a self-consistent and detailed description of the formation of the most massive stars known. The radiation feedback in these simulations is computed via a sophisticated hybrid radiation transport approach, highly adopted to the problem under investigation, see [6]. On the one hand, the simulation series fully recover the previous 1D radiation pressure barrier results of [1] and [8]. On the other hand, the simulation series attest the numerical and physical improvements in our studies of the radiation pressure feedback in the multi-dimensional context with respect to previous numerical studies in the field, see [3,5]. The radiation pressure feedback onto the disk accretion flow is diminished by an anisotropy of the radiation field due to the forming massive accretion disk, see [3]. The required angular momentum transport will self-consistently be provided by gravitational torques in the accretion disk, see [4].

All in all, this demonstrates that the final masses of stars forming by accretion are not limited by the well-known radiation pressure barrier.

Acknowledgements Author R. K. is currently financially supported by the German Academy of Science Leopoldina within the Leopoldina Fellowship programme, grant no. LPDS 2011-5.

References

1. Kahn, F. D. (1974). *A&A*, 37:149.
2. Krumholz, M. R., Klein, R. I., McKee, C. F., Offner, S. S. R., and Cunningham, A. J. (2009). *Science*, 323:754.

3. Kuiper, R., Klahr, H., Beuther, H., and Henning, T. (2010a). *ApJ*, 722:1556.
4. Kuiper, R., Klahr, H., Beuther, H., and Henning, T. (2011). *ApJ*, 732:20.
5. Kuiper, R., Klahr, H., Beuther, H., and Henning, T. (2012). *A&A*, 537:122.
6. Kuiper, R., Klahr, H., Dullemond, C. P., Kley, W., and Henning, T. (2010b). *A&A*, 511:81–96.
7. Nakano, T. (1989). *ApJ*, 345:464.
8. Yorke, H. W. and Krügel, E. (1977). *A&A*, 54:183.
9. Yorke, H. W. and Sonnhalter, C. (2002). *ApJ*, 569:846.

Star Formation Rates and Ridge Structures in High-Mass Star-Forming Regions

Quang Nguyen-Luong, Frédérique Motte, Tracey Hill, Martin Hennemann, Fabien Louvet, Sylvain Bontemps, and Nicola Schneider

Abstract Molecular cloud complexes are structures of molecular gas with sizes up to 50–200 pc. The multi-wavelength data of *Herschel* allow us to construct column density maps. From these maps, we discover prominent filamentary structures ($N_{H_2} > 10^{23}\,cm^{-2}$), which we call "ridges". We use the number of burgeoning YSOs detected in submm wavelengths with *Herschel* to measure the star formation activity in molecular cloud complexes and show a definite increase of star formation with the mass surface density as measured from *Herschel* column density images. The star formation rates (SFRs) measured for the molecular clouds W43 & G0035.39-00.33 are higher than the classical ones, such that we term these regions as "ministarbursts" – miniature models of starburst galaxies. The ridge structures show the strong, low-velocity, extended shock which may emerge from the swept-up gas caused by converging flows.

Q. Nguyen-Luong (✉)
Canadian Institute for Theoretical Astrophysics, Toronto, Canada
e-mail: qnguyen@cita.utoronto.ca

F. Motte • T. Hill • F. Louvet
Laboratoire d'Astrophysique (AIM) de Paris-Saclay, CEA/DSM-CNRS/INSU-Université Paris Diderot, IRFU/Service d'Astrophysique, CEA Saclay, Orme des Merisiers Bât. 709, 91191 Gif-sur-Yvette, France

M. Hennemann
Laboratoire d'Astrophysique (AIM) de Paris-Saclay, CEA/DSM-CNRS/INSU-Université Paris Diderot, IRFU/Service d'Astrophysique, CEA Saclay, Orme des Merisiers Bât. 709, 91191 Gif-sur-Yvette, France

S. Bontemps
University of Bordeaux/CNRS, LAB, UMR 5804, F-33270, Floirac, France

N. Schneider
Laboratoire d'Astrophysique (AIM) de Paris-Saclay, CEA/DSM-CNRS/INSU-Université Paris Diderot, IRFU/Service d'Astrophysique, CEA Saclay, Orme des Merisiers Bât. 709, 91191 Gif-sur-Yvette, France

D. Stamatellos et al. (eds.), *The Labyrinth of Star Formation*, Astrophysics and Space Science Proceedings 36, DOI 10.1007/978-3-319-03041-8_75,

1 Introduction

Star formation is a complex process involving many physical processes acting from the large scales of the galaxy to the small scales of individual stars. One of the questions in star formation is the detailed mechanism of the formation of molecular clouds and the impact of this process on the formation of stars, especially on high-mass stars. Another topic which is highly debated is the gas to star-formation-rate (SFR) relation of individual molecular clouds and the comparison of this relation from Galactic to extragalactic scales.

The connection between molecular cloud structure and star formation has been investigated theoretically by Professor Whitworth [13, 14].

2 Ridge

The new census from the HOBYS[1] key program [9], a mapping survey dedicated to the formation of OB-type stars, shows that molecular clouds are dominated by networks of filaments and that clusters of high-mass protostars are forming in "cloud ridges" [3, 4, 10]. These "ridges" are high-density, low temperature (10–15 K), elongated cloud structures, which dominate and shape their surroundings, suggesting that they are formed by dynamical scenarios such as converging flows and/or filaments merging. As in the converging flows theory, these massive filamentary structures are a consequence of the large-scale swept-up processes of gas which helped accumulate mass already in the atomic phase [1, 5]. The four most prominent ridges identified in *Herschel* column density maps up to now, i.e. Vela [4], Cygnus X [3], W48 [10], W43-Main [8, 11] are plotted in Fig. 1.

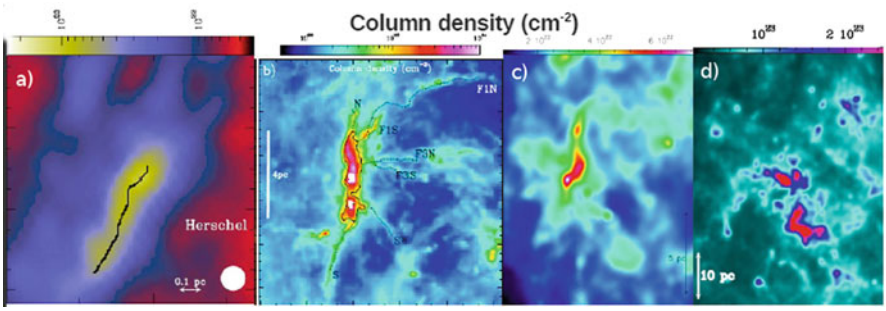

Fig. 1 Ridge structures discovered in the *Herschel* column density maps: (**a**) The Vela ridge [4], (**b**) The DR21 ridge [3], (**c**) The G035.39-00.33 ridge [11], (**d**) W43-Main ridge [12]

[1]Herschel imaging survey of OB Young Stellar objects. http://www.herschel.fr/cea/hobys/en/.

3 High Star Formation Rates in Ridges and Ministarburst Events

We use a large dataset of continuum tracers at 3.6–870 μm extracted from Galaxy-wide surveys such as HOBYS, HiGAL, ATLASGAL, GLIMPSE, and MIPSGAL to trace the cloud structure, mass, and star formation activities of both the W43 molecular cloud complex and the G035.39-00.33 filament. The gas density – SFR diagram can be used to distinguish starburst galaxies from normal star-forming galaxies (e.g. [2]). We proposed further that it can be used to distinguish mini-starburst molecular clouds from normal star-forming molecular clouds. It emerges that W43 and IRDC G035.39-00.33 lie in the starburst quadrant which is due to the fact that they are forming stars, especially high-mass stars, very efficiently. These two regions are worth to investigate further since they may present a miniature model of the physical processes acting in starburst galaxies (Fig. 2).

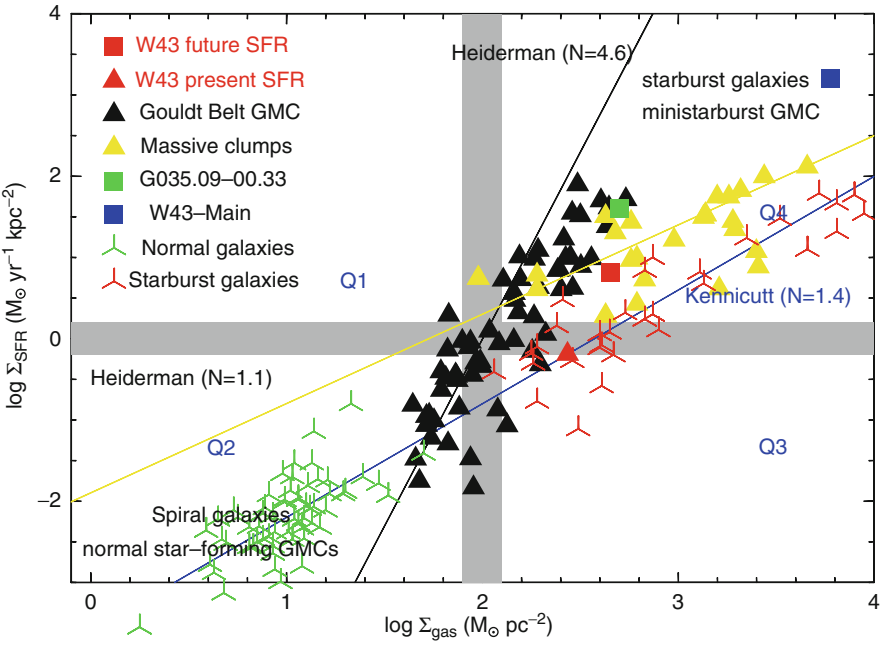

Fig. 2 The relations between the gas surface and SFR densities of the entire W43 and other objects. The *vertical grey shaded region* shows the density threshold of $130\,M_\odot\,pc^{-2}$ (or $A_V \sim 8.5$ mag), above which gas is dense enough for star formation to occur. The *horizontal grey shaded region* shows the SFR threshold, above which stars are forming with high efficiency, i.e. the galaxy or the molecular clouds are undergoing a starburst or ministarburst event. The two thresholds divide the plot into four quadrants naming Q1, Q2, Q3 and Q4

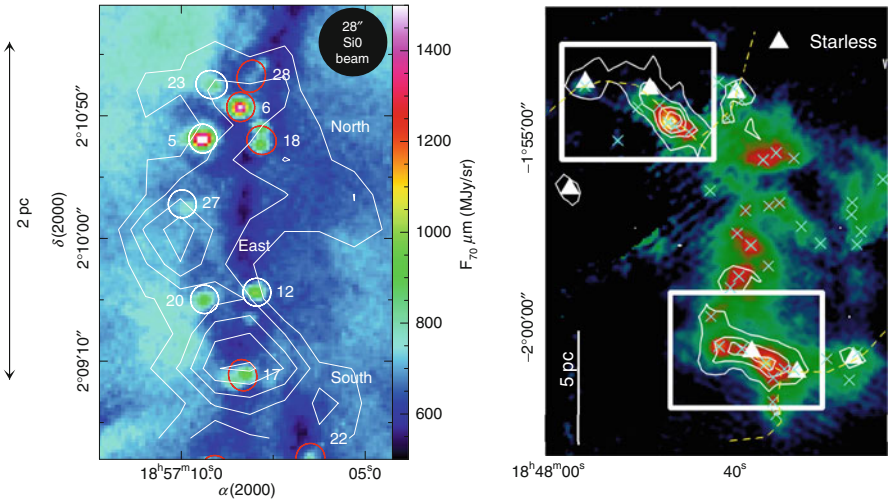

Fig. 3 (*Left*) G035.39-00.33 seen at 70 μm (colour) and in SiO (contours from 0.01 to 0.05 K km s^{-1} by 0.01 K km s^{-1}). (*Right*) W43-Main in 1.3 mm (colour) and in SiO (contours from 2 to 12 K km s^{-1} by 2 K km s^{-1})

4 Shock: Origin of Ridge and High SFR in Ridges

Theoretically, extended shocks are expected to emerge at the swept-up edges of the converging flows as a consequence of the compression of material [7]. Classically, SiO is the best diagnostic of high-velocity shock, with velocity high enough ($v_{\rm shock} \sim$ 20–40 km s^{-1}) to liberate silicon atoms from dust grains and mantles to the gas phase, which then form SiO through different pathways. Nevertheless, evidence that SiO could be formed from a milder shock is increasing recently, especially in ridge structures [6]. Figure 3 shows the extended shocks detected toward the ridges G0035.39-00.33 and W43-Main. Part of the extended SiO does not coincide with any protostellar activity, thus it could have formed by converging flows.

5 Conclusion

Ridges are forming stars very efficiently and potentially forming high-mass stars as a result of different converging flows. The proposition that converging flows have large impacts on these regions has been confirmed by extended SiO emission detected in the regions W43 and G0035.39-00.33.

References

1. Ballesteros-Paredes, J., Hartmann, L., & Vázquez-Semadeni, E. 1999, ApJ, 527, 285
2. Daddi, E., Elbaz, D., Walter, F., et al. 2010, ApJL, 714, L118
3. Hennemann, M., Motte, F., Schneider, N., et al. 2012, A&A, 543, L3
4. Hill, T., Motte, F., Didelon, P., et al. 2011, A&A, 533, A94
5. Inoue, T., & Inutsuka, S.-i. 2009, ApJ, 704, 161
6. Jiménez-Serra, I., Caselli, P., Tan, J. C., et al. 2010, MNRAS, 406, 187
7. Koyama, H., & Inutsuka, S. 2000, ApJ, 532, 980
8. Motte, F., Schilke, P., & Lis, D. C. 2003, ApJ, 582, 277
9. Motte, F., Zavagno, A., Bontemps, S., Schneider, N., Hennemann, M., et al. 2010, A&A, 518L, 77M
10. Nguyen Luong, Q., Motte, F., Hennemann, M., et al. 2011a, A&A, 535, A76
11. Nguyen Luong, Q., Motte, F., Schuller, F., et al. 2011b, A&A, 529, A41+
12. Nguyen Luong, Q., Motte, F., Carlhoff, P., Louvet, F., Lesaffre, P., et al. 2013, ApJ, 775, 88N
13. Whitworth, A. P., Bhattal, A. S., Chapman, S. J., Disney, M. J., & Turner, J. A. 1994a, A&A, 290, 421
14. Whitworth, A. P., Bhattal, A. S., Chapman, S. J., Disney, M. J., & Turner, J. A. 1994a 1994b, MNRAS, 268, 291

GLIMPSE Extended Green Objects and the Early Stages of Massive Star Formation

Claudia J. Cyganowski, Crystal L. Brogan, Todd R. Hunter, Ed Churchwell, Barbara A. Whitney, and Qizhou Zhang

Abstract Large-scale *Spitzer* surveys of the Galactic plane have yielded a new tracer of massive young stellar objects (MYSOs) that are actively accreting and driving outflows: extended emission in the IRAC 4.5 μm band, believed to arise from shocked molecular gas. The GLIMPSE catalog of extended 4.5 μm sources (called EGOs, Extended Green Objects, for the common coding of 3-color IRAC images) is a unique sample, well-suited for studying the initial stages of massive star formation and establishing an observation-based MYSO evolutionary sequence. In this proceeding, we present results from extensive recent high-resolution Submillimeter Array (SMA) and Very Large Array (VLA) observations of EGOs at cm-mm wavelengths, including maser, molecular line, and continuum studies. These observations often reveal (proto)clusters that exhibit chemical and evolutionary diversity.

C.J. Cyganowski (✉)
NSF Astronomy and Astrophysics Postdoctoral Fellow, Harvard-Smithsonian Center for Astrophysics, Cambridge, MA 02138, USA
e-mail: cc243@st-andrews.ac.uk

C.L. Brogan • T.R. Hunter
National Radio Astronomy Observatory, Charlottesville, VA 22903, USA
e-mail: cbrogan@nrao.edu,thunter@nrao.edu

Ed. Churchwell • B.A. Whitney
Department of Astronomy, University of Wisconsin-Madison, Madison, WI 53706, USA
e-mail: ebc@astro.wisc.edu,bwhitney@astro.wisc.edu

Q. Zhang
Harvard-Smithsonian Center for Astrophysics, Cambridge, MA 02138, USA
e-mail: qzhang@cfa.harvard.edu

D. Stamatellos et al. (eds.), *The Labyrinth of Star Formation*, Astrophysics and Space Science Proceedings 36, DOI 10.1007/978-3-319-03041-8_76,

1 GLIMPSE Extended Green Objects

The *Spitzer Space Telescope* Galactic Legacy Infrared Mid-Plane Survey Extraordinaire (GLIMPSE) imaged the Galactic Plane with an angular resolution of $\leq 2''$ in the four bands of the Infrared Array Camera (IRAC): 3.6, 4.5, 5.8, and 8.0 μm. This unprecedented angular resolution revealed many new phenomena [3], including a class of objects characterized by extended emission in the 4.5 μm band. The broad IRAC bands contain numerous atomic and molecular emission features [10]: the 4.5 μm band is notable for including both H_2 lines and the CO($v = 1 - 0$) bandhead, while *lacking* polycyclic aromatic hydrocarbon (PAH) features. Shock-excited gas in (proto)stellar molecular outflows can dominate the 4.5 μm band; in massive star forming regions (MSFRs), the other IRAC bands tend to be dominated by (easily excited) PAH emission. As a result, sources with morphologically distinct extended 4.5 μm emission are good candidates for massive young stellar objects (MYSOs) driving *active* outflows. Such sources are known as "Extended Green Objects (EGOs)," for the common coding of the 4.5 μm band as green in three-color IRAC images: we cataloged over 300 EGOs in the GLIMPSE-I survey area ($10° \leq |l| \leq 65°$, $|b| \leq 1°$) [4].

Following their discovery, we conducted a series of studies to characterize the nature of EGOs, and test the hypothesis that EGOs are specifically young, *massive* YSOs with *active* outflows. The first observational tests included Very Large Array (VLA)[1] searches for 6.7 GHz Class II CH_3OH masers (associated exclusively with massive YSOs [9]) and 44 GHz Class I CH_3OH masers (associated with outflows [8]), and a James Clerk Maxwell Telescope (JCMT)[2] survey for HCO^+, $H^{13}CO^+$, SiO, and thermal CH_3OH emission [5]. The target sample for these studies was selected to cover a range of midinfrared (MIR) properties, and to be visible from the northern hemisphere. The detection rates for both CH_3OH maser types were exceptionally high: >64 % for 6.7 GHz Class II masers and ∼90 % for 44 GHz Class I masers [5]. The HCO^+ line profiles observed with the JCMT had broad line wings, and the high SiO detection rate (90 %) indicated recent shocks, and so *active* outflows [5]. Deep VLA 3.6 and 1.3 cm continuum observations of an EGO subsample showed that most of the EGO targets were *not* associated with cm-λ continuum emission: the *non*detection rate was 57 % (8/14) [7]. Most detected cm-λ EGO counterparts are weak (<1 mJy at 3.6 cm), with spectral index (limits) consistent with free-free emission from hypercompact (HC) HII regions or ionized winds or jets [7].

[1]The National Radio Astronomy Observatory operates the VLA and is a facility of the National Science Foundation operated under agreement by the Associated Universities, Inc.

[2]The JCMT is operated by The Joint Astronomy Centre on behalf of the Science and Technology Facilities Council of the United Kingdom, the Netherlands Organisation for Scientific Research, and the National Research Council of Canada.

2 High Resolution Mm and Cm Surveys of GLIMPSE Extended Green Objects

We are combining the resolving power of the Submillimeter Array (SMA)[3] and the recently-upgraded Karl G. Jansky Very Large Array (JVLA) with that of *Spitzer* in an extensive multi-wavelength observing campaign of a representative subset of GLIMPSE EGOs. The SMA observing setup covers a variety of outflow and hot core tracers at ∼230 GHz, and also includes line-free continuum bandwidth. The JVLA correlator setup includes NH_3(1,1) to (6,6), CH_3OH lines (including masing transitions), and probes of ionized gas (cm continuum and radio recombination lines) [2]. The main goals of this project are: (1) to probe the importance of protostellar feedback in the formation of massive star clusters (including the roles of outflows, ionization, and gas heating) and (2) to develop an observation-based evolutionary sequence for MYSOs. Initial results from the JVLA and SMA surveys have recently been published [2, 6].

Feedback Case Study: G11.92−0.61 The EGO G11.92−0.61 is associated with three compact cores, seen in mm continuum emission [6]. Weak 1.3 cm emission is detected coincident with the strongest mm continuum source (MM1), likely from an optically thick HC HII region (no emission is detected at 3.6 cm) [7]. No other cm-λ emission is detected. A single dominant outflow, traced by high-velocity ^{12}CO emission and coincident with the 4.5 μm lobes, is driven by MM1; there is tentative evidence for additional flows. The outflow properties (M_{out}, $\dot{M}_{out}$, etc.) are typical of outflows from MYSOs [6]. Associated with both 6.7 GHz CH_3OH and H_2O masers, MM1 exhibits hot-core line emission; in contrast, the other mm continuum cores exhibit little or no line emission in the SMA spectra. Interestingly, two temperature components are required to obtain a good fit to the CH_3CN spectra of MM1: a compact warm (166 K) component and a more extended, cool (77 K) component [6]. Together, these results suggest that G11.92−0.61 is at a stage of massive star and cluster formation at which the importance of outflow feedback outweighs that of ionizing radiation; the JVLA data (now in hand) will allow us to constrain the importance of radiative feedback from the massive (proto)stars.

Evolutionary Sequence Case Study: G18.67+0.03 Many efforts to date to develop evolutionary sequences for massive star formation have focused on the CH_3OH, H_2O, and OH masers that are ubiquitous in MSFRs. The published sequences posit that Class I CH_3OH masers–which are collisionally pumped in shocked gas and often associated with outflows–appear first during the evolution of a massive (proto)star. Thus, sources with only Class I CH_3OH masers would represent the earliest stages of massive star formation [1]. Recent work has suggested that

[3]The Submillimeter Array is a joint project between the Smithsonian Astrophysical Observatory and the Academia Sinica Institute of Astronomy and Astrophysics and is funded by the Smithsonian Institution and the Academia Sinica.

Class I CH_3OH masers may also be excited by shocks driven by expanding HII regions [11]; however, there were very few examples of Class I CH_3OH maser sources associated with cm-λ continuum emission *and known to lack Class II CH_3OH masers.* Our VLA surveys revealed three CH_3OH maser sources in the G18.67+0.03 MSFR: two (including the EGO G18.67+0.03) have both Class I and II masers [5]. The third, which has Class I masers only, is also associated with a cm continuum source [7]. Our SMA data show that both Class II+Class I maser sources are associated with hot core line emission and with outflows detected in SiO(5-4). In contrast, the Class I-only maser source shows neither of these indicators of youth. The combined SMA and JVLA data for this region provide evidence that Class I CH_3OH masers can be excited by young ("hot core") and evolved (UC HII) MYSOs within the same MSFR, suggesting that simple evolutionary cartoons are probably not realistic.

Acknowledgements C.J.C is supported by an NSF Astronomy and Astrophysics Postdoctoral Fellowship under award AST-1003134.

References

1. Breen, S. L., Ellingsen, S. P., Caswell, J. L., & Lewis, B. E. Mon. Not. R. Astron. Soc. **401**, 2219–2244 (2010)
2. Brogan, C. L., Hunter, T. R., Cyganowski, C. J., et al. Astrophys. J. Lett. **739**, L16 (2011)
3. Churchwell, E., Babler, B. L., Meade, M. R., et al. Publ. Astron. Soc. Pac. **121**, 213–230 (2009).
4. Cyganowski, C. J., Whitney, B. A., Holden, E., et al. A New Sample of Massive Young Stellar Object Outflow Candidates. Astron. J. **136**, 2391–2412 (2008)
5. Cyganowski, C. J., Brogan, C. L., Hunter, T. R., & Churchwell, E. Astrophys. J. **702**, 1615–1647 (2009)
6. Cyganowski, C. J., Brogan, C. L., Hunter, T. R., Churchwell, E., & Zhang, Q. Astrophys. J. **729**, 124 (2011)
7. Cyganowski, C. J., Brogan, C. L., Hunter, T. R., & Churchwell, E. Astrophys. J. **743**, 56 (2011)
8. Kurtz, S., Hofner, P., & Álvarez, C. V. **155**, 149–165 (2004)
9. Minier, V., Ellingsen, S. P., Norris, R. P., & Booth, R. S. Astron. & Astrophys. **403**, 1095–1100 (2003)
10. Reach, W. T., Rho, J., Tappe, A., et al. Astron. J. **131**, 1479–1500 (2006)
11. Voronkov, M. A., Caswell, J. L., Ellingsen, S. P., & Sobolev, A. M. Mon. Not. R. Astron. Soc. **405**, 2471–2484 (2010)

Radiation Hydrodynamics Simulations of Massive Star Formation Using Monte Carlo Radiation Transfer

Tim J. Harries, Thomas J. Haworth, and David M. Acreman

Abstract We present a radiation hydrodynamics simulation of the formation of a massive star using a Monte Carlo treatment for the radiation field. We find that strong, high speed bipolar cavities are driven by the radiation from the protostar, and that accretion occurs stochastically from a circumstellar disc. We have computed spectral energy distributions and images at each timestep, which may in future be used to compare our models with photometric, spectroscopic, and interferometric observations of young massive stellar objects.

1 Introduction

The deposition of substantial momentum from the radiation field into the accreting material of the protostellar envelope creates a serious obstacle for theories of massive star formation that adopt spherical accretion e.g. [1]. Extending the models to multiple dimensions and the inclusion of rotation leads to a scenario in which the protostar can accrete via a disc, which subtends a smaller solid angle at the protostellar surface and thus intercepts a smaller fraction of the radiation e.g. [2].

Recent work by Krumholz et al. used adaptive mesh refinement hydrodynamics coupled with a flux limited diffusion (FLD) approximation for the radiative transfer (RT) in order to simulate the formation of a massive binary [3]. They found accretion occurred via a radiatively-driven Rayleigh Taylor instability that allowed material to penetrate the radiation-driven cavities above and below the protostars. Simulations

T.J. Harries (✉) • T.J. Haworth • D.M. Acreman
Department of Physics and Astronomy, University of Exeter, Exeter, UK
e-mail: th@astro.ex.ac.uk

D. Stamatellos et al. (eds.), *The Labyrinth of Star Formation*, Astrophysics and Space Science Proceedings 36, DOI 10.1007/978-3-319-03041-8_77,

by Kuiper et al. [4] using a hybrid RT method [5] have cast doubt on this scenario – they claim that the grey FLD approximation leads to a substantial underestimate of the driving force of the radiation field (see also Kuiper's contribution to these proceedings).

Clearly the level of detail with which the radiation transport is followed is an important consideration when simulating radiation feedback. We have therefore developed our own radiation-hydrodynamics code [6] which is based on the TORUS Monte Carlo RT code [7–9]. The advantage of this approach is that RT is fully polychromatic and includes both dust and atomic microphysics, and although the method is unavoidably computationally intensive, the overhead is reduced to acceptable levels by the use of aggressive parallelization.

2 The Monte Carlo Method and Its Implementation

The TORUS code is based on the radiative-equilibrium method of Lucy [10] in which the stellar luminosity is divided up into a large number of photon packets, which propagate through the computational domain undergoing absorptions and scatterings. When a photon packet is absorbed it is immediately re-emitted with a frequency found from random sampling of the emissivity spectrum at that point in the grid. By tracking the paths of the packets through a grid cell one can obtain a Monte Carlo estimate for the energy density in that cell, and hence the mean intensity of the radiation field, which in turn enables the computation of absorption rates, photoionization rates etc. The radiation force on each cell can be computed using similar methods.

The primary drawback in adopting such a detailed treatment of the radiation field is the computational effort involved. Fortunately the Monte Carlo method, in which the photon packets are essentially independent events, may be straightforwardly and effectively parallelized. The top level of parallelization involves domain decomposing the octree that stores the adaptive mesh. The main bottleneck is the communication overhead when passing photon packets between threads, and we optimize this by passing stacks of photon packet data between the threads rather than individual packets. A further level of parallelization is achieved by having many sets of identical computational domains, over which the photon packet loop is split, with the results derived from the radiation calculation (radiation momenta, absorption rate estimators etc.) collated and returned to all the sets at the end of each iteration. Using these parallelization methods it is possible to reduce the time for the radiation field calculation down to a level comparable with that of the hydrodynamics step.

3 A Test Calculation

We adopted the initial conditions from one of the models presented by Kuiper et al. [4] in order to perform a demonstration calculation. This model consists of a $100\,M_{\odot}$, 0.1 pc radius cloud with an $r^{-1.5}$ density profile and a small amount ($\Omega = 5 \times 10^{-13}\,s^{-1}$) of solid body rotation. The effective temperature of the protostar and its luminosity were determined by interpolating by mass in the protostellar evolution models of Hosokawa and Omukai [11]. The photospheric spectrum was composed of an appropriate Kurucz model plus a blackbody accretion spectrum. A 128^3 regular mesh was used for this test calculation.

The final state of the model (after 50,000 years) is plotted in Fig. 1. The radiation-driven bipolar cavities are clearly seen, and the outflow has reached the boundary of the computational domain. The development and speed of the cavities is similar to that found by Kuiper et al., but the morphology is different, principally due to the resolution. We have also computed SEDs at each timestep, and plot these in Fig. 2. Note that 60 and 90° inclination SEDs show typical Class I characteristics, and the attenuated protostellar SED is observed only directly along the outflow cavities. The evolution of the accretion onto the protostar can be divided into two distinct phases: At early times the accretion is smooth, and from the envelope, but after ~20,000 years the luminosity of the protostar overtakes the accretion luminosity (this is dictated by the evolutionary tracks) and the radiation-pressure starts to drive

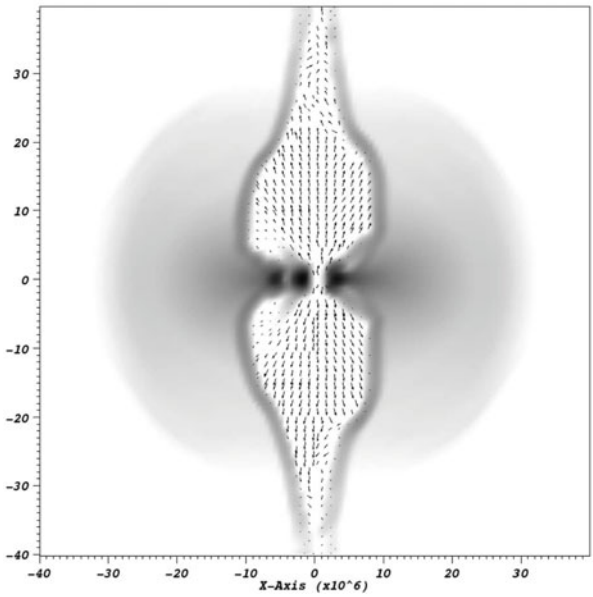

Fig. 1 A slice through the rotation axis of the test simulation (spatial units are 10^{10} cm). The greyscale shows logarithmic density scaled between $10^{-19}\,g\,cm^{-3}$ (*white*) and $10^{-15}\,g\,cm^{-3}$ (*black*). The *arrows* denote velocity, with the *longest arrows* corresponding to speeds of $100\,km\,s^{-1}$

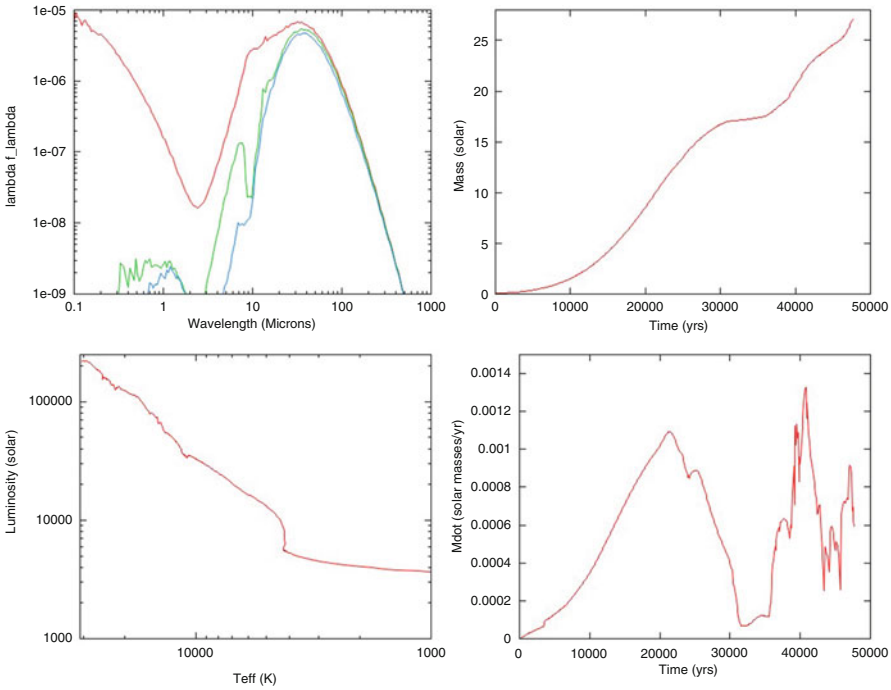

Fig. 2 The results of the test calculation. Spectral energy distributions (erg s^{-1} cm^{-2} at a distance of 1 kpc) at inclinations of 0°, 60° and 90° are shown in the *top-left figure*. The mass of the protostar as a function of time is plotted in the *top-right figure*. The effective temperature and luminosity of the protostar is shown in the *bottom left figure* (note the temperature increases to the left). The *bottom-right figure* shows the accretion rate onto the protostar as a function of time

the polar outflow cavities, at which point accretion is occurring stochastically via the protostellar disc. (Note that this two stage accretion evolution is also present in the hybrid RT calculations of Kuiper et al.) At the end of the calculation the protostar has a mass of 28 $M_\odot$ and an effective temperature of 30,000 K, at which point ionization and stellar wind feedback are potentially important. Although a small ionized zone is formed close to the protostar towards the end of the calculation (with properties that would identify it as an ultra-compact H II region) we note that we have yet to implement a self-consistent method for treating the dust sublimation and advection.

Acknowledgements We thank Takashi Hosokawa for providing digital versions of his evolutionary tracks and Ant Whitworth for a useful discussion whilst floating around in the Med.

References

1. M.G. Wolfire, J.P. Cassinelli, ApJ **319**, 850 (1987).
2. H.W. Yorke, C. Sonnhalter, ApJ **569**, 846 (2002).
3. M.R. Krumholz, R.I. Klein, C.F. McKee, S.S.R. Offner, A.J. Cunningham, Science **323**, 754 (2009).
4. R. Kuiper, H. Klahr, H. Beuther, T. Henning, A&A **537**, A122 (2012).
5. R. Kuiper, H. Klahr, C. Dullemond, W. Kley, T. Henning, A&A **511**, A81 (2010).
6. T.J. Haworth, T.J. Harries, MNRAS **420**, 562 (2012).
7. T.J. Harries, MNRAS **315**, 722 (2000).
8. T.J. Harries, J.D. Monnier, N.H. Symington, R. Kurosawa, MNRAS **350**, 565 (2004).
9. C. Pinte, T.J. Harries, M. Min, A.M. Watson, C.P. Dullemond, P. Woitke, F. Ménard, M.C. Durán-Rojas, A&A **498**, 967 (2009).
10. L.B. Lucy, A&A **344**, 282 (1999).
11. T. Hosokawa, K. Omukai, ApJ **691**, 823 (2009).

Age Spread in Galactic Star Forming Region W3 Main

Arjan Bik, Thomas Henning, Andrea Stolte, Wolfgang Brandner, Dimitrios A. Gouliermis, Mario Gennaro, Anna Pasquali, Boyke Rochau, Henrik Beuther, Nancy Ageorges, Walter Seifert, Yuan Wang, and Natalia Kudryavtseva

Abstract We present near-infrared JHKs imaging as well as K-band multi-object spectroscopy of the massive stellar content of W3 Main using LUCI at the LBT. We confirm 13 OB stars by their absorption line spectra in W3 Main and spectral types between O5V and B4V have been found. Three massive Young Stellar Objects are identified by their emission line spectra and near-infrared excess. From our spectrophotometric analysis of the massive stars and the nature of their surrounding HII regions we derive the evolutionary sequence of W3 Main and we find an age spread of 2–3 Myr.

A. Bik (✉) • T. Henning • W. Brandner • M. Gennaro • B. Rochau • H. Beuther • N. Kudryavtseva
Max-Planck-Institut für Astronomie, Königstuhl 17, D-69117 Heidelberg, Germany
e-mail: abik@mpia.de

A. Stolte
Argelander Institut für Astronomie, Auf dem Hügel 71, 53121 Bonn, Germany

D.A. Gouliermis
Zentrum für Astronomie der Universität Heidelberg, Institut für Theoretische Astrophysik, Albert-Ueberle-Str. 2, 69120 Heidelberg, Germany

A. Pasquali
Astronomisches Rechen Institut, Zentrum für Astronomie der Universität Heidelberg, Mönchhofstrasse 12–14, 69120 Heidelberg, Germany

N. Ageorges
Max-Planck-Institut für extraterrestrische Physik, 85748 Garching, Germany

W. Seifert
Landessternwarte Königstuhl, Zentrum für Astronomie Heidelberg, 69117 Heidelberg, Germany

Y. Wang
Purple Mountain Observatory, Chinese Academy of Sciences, 210008 Nanjing, People's Republic of China

D. Stamatellos et al. (eds.), *The Labyrinth of Star Formation*, Astrophysics and Space Science Proceedings 36, DOI 10.1007/978-3-319-03041-8_78,

1 Introduction

Despite the impact on their surroundings, the formation and early evolution of massive stars is poorly constrained, primarily because of their scarcity and short lifetimes. OB stars form in different environments, ranging from compact, stellar clusters with very high stellar density to associations where the stars are more dispersed over the molecular cloud. This raises the question whether the same star formation mechanism is responsible for the formation of these different structures. Determining the star formation history, by means of characterizing their stellar content, will provide insights in how these different regions are formed. Evidence has been found that dense starburst clusters might form in a single burst [4] while OB associations show a large spread in age.

We present deep LUCI [1] near-infrared JHKs imaging as well as K-band multi-object-spectroscopy of the massive stellar content of W3 Main. This allows for the first time a spectral classification of the massive stellar content. Using their derived spectral type we discuss the evolutionary status of the massive stars as well as the HII regions in detail. The different evolutionary phases of the HII regions make W3 Main an ideal target to study age difference in star forming regions.

2 Near-Infrared Imaging and Spectroscopy

JHKs imaging of W3 Main has been obtained with LUCI at the Large Binocular Telescope (LBT) on Mount Graham, Arizona. Figure 1 shows the resulting three color image of a $4' \times 4'$ field centered on W3 Main. K-band spectra of 16 candidate massive stars inside W3 Main were obtained with the multi-object spectroscopic mode of LUCI [3]. We classified 13 stars as OB stars from their absorption lines compared with K-band spectra of optically visible OB stars [2, 6]. Three objects are classified as massive Young Stellar Objects: massive stars surrounded by a circumstellar disk.

After their spectral classification, the bolometric luminosities of the massive stars are calculated and the stars are placed in the Hertzsprung Russell diagram (HRD, Fig. 1) and compared with stellar evolution isochrones. In the upper regions of the HRD ($\log L/L_{\odot} \geq 5$), the main sequence isochrones indicate that the most massive stars already show significant evolution after a few Myr. Two stars are located in the upper regions of the HRD, IRS2 and IRS3a. IRS2 is located to the right of the ZAMS and its location is more consistent with the 2–3 Myr isochrones. The foreground extinction is not very extreme, therefore the location of IRS2 in the HRD does not vary a lot by changing the extinction law. IRS3a (O5V – O7V), however, is very reddened ($A_{Ks} = 5.42 \pm 0.79$ mag) and its location in the HRD depends very strongly on the adopted extinction law and its age cannot be constrained accurately.

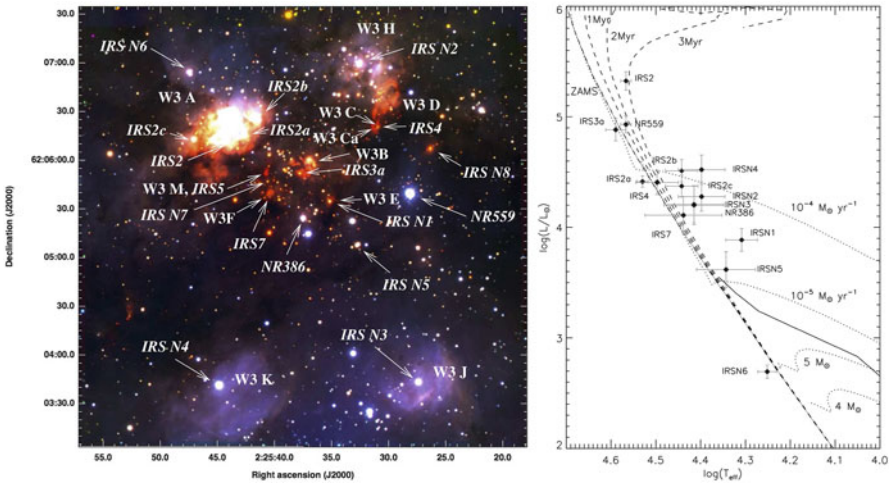

Fig. 1 *Left*: Near-infrared JHK color composite of W3 Main. *Right*: Hertzsprung Russell Diagram of the massive stars in W3 Main. Over plotted are the zero age main sequence (ZAMS, *solid line*) and the 1–3 Myr isochrones (*dashed lines*) from [8], the PMS isochrones for intermediate mass stars ($M < 5\,M_{\odot}$, *dotted lines*) [11] as well as the theoretical birth-line (*solid line*) [9]

3 Age Spread

W3 Main harbors several different evolutionary stages of HII regions, ranging from very young hyper-compact HII (HCHII) regions (few 10^3 years), ultra-compact HII (UCHII) regions $\sim 10^5$ years [14] to evolved, diffuse HII regions (few 10^6 years). All these regions are most likely formed out of the same molecular cloud. This provides the possibility to study the evolution of young HII regions and their stellar content in great detail. Based on radio observations an evolutionary sequence is derived [12].

The youngest are the HCHII regions W3 M and W3 Ca, with the UCHII regions W3 F, W3 C and W3 E, slightly older, the compact HII regions W3 B and W3 A even more evolved, and the diffuse HII regions, W3 K and W3 J being the oldest HII regions in W3 Main (Fig. 2). Additionally, evidence has been found that W3 A is interacting with the youngest sites of star formation and could have triggered the formation of IRS5 [13]. The position of IRS2 in the HRD suggests an age of 2–3 Myr, consistent with its location in a relatively evolved compact HII region (W3 A). Combining our near-infrared age determination with the observed evolutionary sequence of HII regions provides evidence that W3 Main has been actively forming stars over the last 2–3 Myrs.

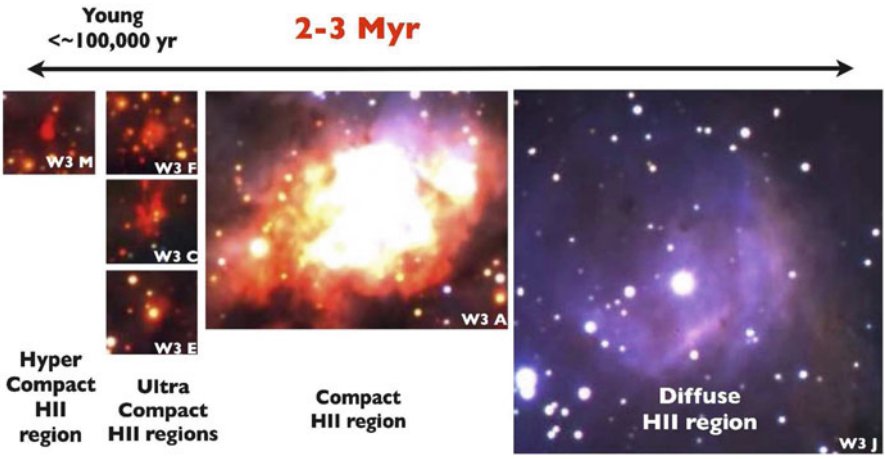

Fig. 2 Near-infrared three color composites of the different kinds of HII regions in W3 Main ordered from young to the more evolved regions. The age of W3A is the age derived from IRS2

4 Discussion

Based on the presence of different evolutionary stages of HII regions as well as the location of the most massive stars in the HRD, we can conclude that an age spread of 2–3 Myr is most likely present for the massive stars in W3 Main. A growing number of young stellar clusters show evidence for an age spread, usually based on the analysis of their PMS population in the HRD. In Orion an age spread of a few Myr has been found [10] as well as in LH95 in the LMC [5]. In starburst clusters, however, no age spread has been found for Westerlund 1 and NGC3603 [4, 7] based on both the massive stars and the lower-mass PMS stars. This suggests that W3 Main is not formed in one star formation burst as expected for starburst cluster, but, more likely, through a temporal sequence of star formation events.

References

1. Ageorges, N., Seifert, W., Jütte, M., et al., 2010, SPIE, 7735, 53
2. Bik, A., Kaper, L., Hanson, M. M., & Smits, M. 2005, A&A, 440, 121
3. Bik, A., Henning Th., Stolte, A, et al. 2012, ApJ, 744, 87
4. Clark, J. S., Negueruela, I., Crowther, P. A., & Goodwin, S. P. 2005, A&A, 434, 949
5. Da Rio, N., Gouliermis, D. A., & Gennaro, M., 2010, ApJ, 723, 166
6. Hanson, M. M., Kudritzki, R.-P., Kenworthy et al. 2005, ApJS, 161, 154
7. Kudryavtseva N., Brandner, W., Gennaro, M., et al. 2012 , ApJ, 750, L44
8. Lejeune, T. & Schaerer, D. 2001, A&A, 366, 538
9. Palla, F. & Stahler, S. W. 1990, ApJ, 360, L47
10. Reggiani, M., Robberto, M., Da Rio, N. et al. 2011, A&A, 534, 83

11. Siess, L., Dufour, E., & Forestini, M. 2000, A&A, 358, 593
12. Tieftrunk, A. R., Gaume, R. A., Claussen, et al. 1997, A&A, 318, 931
13. Wang, Y., Beuther, H., Zhang, Q, Bik, A. et al. 2012, ApJ, 754, 87
14. Wood, D. O. S. & Churchwell, E. B. 1989, ApJ, 340, 265

The Impact of Outflows: From Low to High Mass Protostars

Ana Duarte-Cabral, Sylvain Bontemps, Nicolas Peretto, Gary A. Fuller, and Antonio Chrysostomou

Abstract Despite the importance of outflows in removing angular momentum and mass from protostellar envelopes, we struggle to understand their origin, their changes with mass and evolutionary stage of the protostars, and their impact on the dynamics of proto-clusters. Here we present our recent observational work addressing these issues, including the study of a low mass star forming region (B59), with a direct measurement of the outflows' impact and turbulence injection; and a test of low mass evolutionary models on a sample of high mass protostars in Cygnus X.

A. Duarte-Cabral (✉)
University of Bordeaux/CNRS, LAB, UMR 5804, F-33270, Floirac, France

School of Physics, University of Exeter, Stocker Road, Exeter EX4 4QL, UK
e-mail: adc@astro.ex.ac.uk

S. Bontemps
University of Bordeaux/CNRS, LAB, UMR 5804, F-33270, Floirac, France

N. Peretto
Laboratoire d'Astrophysique (AIM) de Paris-Saclay, CEA/DSM-CNRS-Université Paris Diderot, IRFU/Service d'Astrophysique, CEA Saclay, Orme des Merisiers, 91191 Gif-sur-Yvette, France

School of Physics and Astronomy, Cardiff University, Queens Building, The Parade, Cardiff CF24 3AA, UK

G.A. Fuller
Jodrell Bank Centre for Astrophysics, School of Physics and Astronomy, University of Manchester, Oxford Road, Manchester M13 9PL, UK

A. Chrysostomou
Joint Astronomy Centre, 660 North Aõohoku Place, Hilo, HI 96720, USA

School of Physics, Astronomy and Mathematics, University of Hertfordshire, Hatfield, Hertfordshire AL10 9AB, UK

D. Stamatellos et al. (eds.), *The Labyrinth of Star Formation*, Astrophysics and Space Science Proceedings 36, DOI 10.1007/978-3-319-03041-8_79,

1 Introduction

For low mass objects, it has been inferred that as the envelope mass decreases, the young collimated outflows give way to the wide-angled outflow winds, and the outflow momentum flux decreases, reflecting a decrease of the accretion rates onto the central YSO with time (e.g. [1–3, 7, 14]). However, it is not clear whether a similar evolutionary picture applies for high mass protostars. On the other hand, the impact of the protostellar outflows in the surroundings is subject of debate, and while models predict that outflows can drive and sustain supersonic turbulence (e.g. [6,17]), most of the observational evidence suggests that outflows can barely provide enough energy to account for all the turbulent energy of the cloud (e.g. [2, 16, 18]).

2 Impact of Outflows on the Dense Gas in B59

At 130 pc from the Sun [11], B59 is the only active star-forming region of the 15 pc-long Pipe Nebula. Within its central 0.3 pc, B59 hosts a dozen YSOs, including four protostars [5, 12, 13]. The remaining gas of B59 is cold, quiescent, mostly gravitationally bound, with thermal linewidths ($\sigma_v \sim 0.15\,\mathrm{km\,s^{-1}}$) and no major velocity gradients [8], making B59 potentially prone to the impact of outflows.

Our study of the B59 region [8] suggests that the outflows carry an energy comparable to the binding energy of the dense material (with a total outflow kinetic energy of $\sim$18 $M_\odot$ km^2 s^{-2} versus a binding energy of $\sim$12 $M_\odot$ km^2 s^{-2}). But since the kinetic energy of the outflows may be deposited outside the cores it may not be disrupting the dense cores themselves. In fact, in Duarte-Cabral et al. [8] we show that the outflow lobes and knots at larger scales are correlated with the shapes and cavities seen in $C^{18}O$ and extinction outside the dense central region (Fig. 1).

Despite the clear impact of outflows on larger scales, to disentangle their importance on the dense gas of B59 we looked at the emission where there is evidence for an interaction of outflows with the dense gas (in the form of a cavity) and where no significant velocity gradients are detected (e.g. the outflow directed NE of the central region). We estimated the average profiles perpendicular to the outflow direction, of the ^{12}CO integrated intensity, the visual extinction, and the $C^{18}O$ linewidth (Fig. 2).

From here we can see that the outflowing gas falls perfectly on an extinction cavity, while the line widths have a local peak along the outflow axis. This is a clear detection of a local injection of turbulence onto the dense gas, and while we estimate an outflow-generated turbulence locally of the order of $\sigma_v^{out} \sim 0.4\,\mathrm{km\,s^{-1}}$, this corresponds to only a fraction (less than half) of the outflow energy being efficiently deposited in the dense gas.

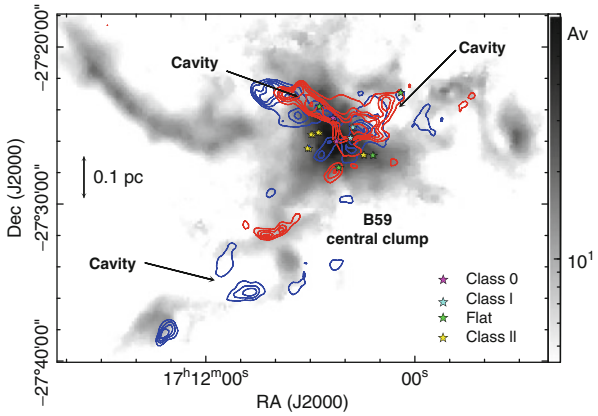

Fig. 1 *Blue* and *red* CO (3-2) outflow emission in contours [8], against the dust extinction map of B59 in grayscale [19]. The YSOs are plotted as *stars*, and some dust extinction cavities are indicated. This illustrates the correlation between the outflow knots and lobes with the dust extinction structures

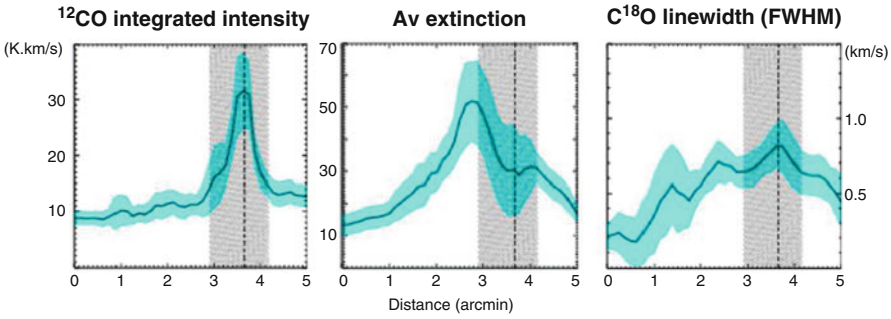

Fig. 2 Average profiles perpendicular to the axis of the NE directed outflow (see [8] for a full description of the figure and method). *Left*: ^{12}CO integrated intensity, showing the outflow strength and location; *Middle*: visual extinction, as a measure of the quantity of material along the line of sight; and *Right*: C^{18}O linewidth (FWHM). *Dashed lines* and *gray-shadowed areas* mark the peak and extent of the ^{12}CO profile. The *blue shaded areas* are the 1σ dispersion of each quantity

3 Cygnus-X Individual High Mass Protostars: A Scale-Up of Low-Mass?

To understand how the impact of the outflows in their surroundings may change with the environment, and evolutionary stage of the driving source, we need to begin by understanding the change of the outflow properties with mass. We have therefore studied a sample of nine individual massive protostars in Cygnus X [4].

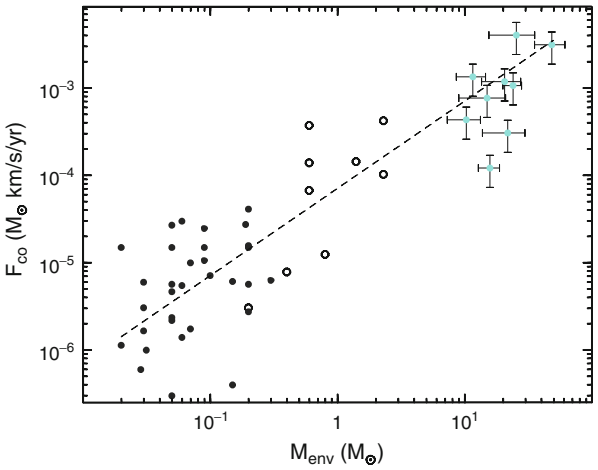

Fig. 3 Outflow momentum flux correlation with envelope mass. The *black filled* and *open circles* are the low-mass Class I and Class 0 sources from [3]. The *light blue circles* are the massive protostars from our sample. The *black dashed line* is the observational linear relation found by Bontemps et al. [3], which holds up to the high mass regime

Their masses and luminosities [4, 15] place these as the high-mass equivalent of the low-mass Class 0 protostars, providing us with the opportunity to study the change of the outflow properties with mass for a same evolutionary stage [9].

We inferred the outflow properties of our sample of massive protostars from CO PdBI observations [9]. A first purely observational result shows that the linear relation found by Bontemps et al. [3] for the low mass individual objects holds for the individual high mass protostars (Fig. 3). This suggests that the accretion mechanisms from low to high mass protostars do not suffer from a discontinuity, despite the different physics that come into play. Assuming that the outflow ejection rate is a fraction of the infalling rate, the direct correlation between outflow momentum flux and envelope mass indicates that the accretion rates are proportional to the reservoir of mass available. We could interpret this as a true scale up from low mass, which implies identical infall timescales for all masse ranges, and consequently higher accretion rates for higher envelope masses. In fact, this also suggests we would not need any further external accretion of mass onto the envelopes to form massive stars from our sample of cores, in agreement with gravo-turbulent fragmentation models (e.g. [10]).

However, the scatter around the observational correlation is of more than a factor 2, and even though it could reflect purely observational uncertainties, it is plausible to assume that it could also reflect different environmental properties. For instance, it could be due to episodes of intermittent accretion, or due to external accretion into the envelope (e.g. [20]), with a delay between the induced changes in the envelope mass and the respective change of accretion rates. The observed correlation between the accretion rates and the envelope mass is in fact not sufficient to constrain the mechanism by which the mass has been accreted onto the envelope at first instance.

4 Summary

Our study of the outflows in a specially quiet low-mass star-forming region has shown that the low-mass protostellar outflows can have an important impact on the region, by injecting turbulence into the dense gas at sub-parsec scales and redistributing the gas at clump-scales. However, such an injected turbulence may be negligible in regions where other dynamics are dominant. Furthermore, while in B59 the outflow-injected turbulence seems sufficient to slow down the gravitational collapse of the region, in regions where the potential well is more important such outflows would not suffice to balance against gravity. On the other hand, we have also shown that for individual protostars, the outflow power scales with the envelope mass up to the high mass regime. This implies that: (1) The accretion mechanism for low and high mass stars is substantially the same and depends only on the gravitational potential of the individual cores; (2) The capacity of outflows in injecting turbulence scales up with the protostellar mass, and may have the potential of changing the fragmentation properties of the more massive cores.

Acknowledgements The work of ADC was supported by the project PROBeS funded by the French National Research Agency (ANR).

References

1. Arce, H. G. & Sargent, A. I. 2006, ApJ, 646, 1070
2. Arce, H.G., Borkin, M.A., Goodman, A.A., Pineda, J.E., & Halle, M.W. 2010, ApJ, 715, 1170
3. Bontemps, S., Andre, P., Terebey, S., & Cabrit, S. 1996, A&A, 311, 858
4. Bontemps, S., Motte, F., Csengeri, T., & Schneider, N. 2010, A&A, 524, A18
5. Brooke, T. Y., Huard, T. L., Bourke, T. L., et al. 2007, ApJ, 655, 364
6. Carroll, J. J., Frank, A., & Blackman, E. G. 2010, ApJ, 722, 145
7. Curtis, E. I., Richer, J. S., Swift, J. J., & Williams, J. P. 2010, MNRAS, 408, 1516
8. Duarte-Cabral, A., Chrysostomou, A., Peretto, N., et al. 2012, A&A, 543, A140
9. Duarte-Cabral, A., Bontemps, S., Motte, F. et al. 2013, A&A, 558, A125
10. Hennebelle, P., & Chabrier, G. 2008, ApJ, 684, 395
11. Lombardi, M., Alves, J., & Lada, C. J. 2006, A&A, 454, 781
12. Forbrich, J., Lada, C. J., Muench, A. A., Alves, J., & Lombardi, M. 2009, ApJ, 704, 292
13. Forbrich, J., Posselt, B., Covey, K. R., & Lada, C. J. 2010, ApJ, 719, 691
14. Fuller, G. A. & Ladd, E. F. 2002, ApJ, 573, 699
15. Hennemann, M., Motte, F., Schneider, N., et al. 2012, A&A, 543, L3
16. Maury, A. J., André, P., & Li, Z.-Y. 2009, A&A, 499, 175
17. Nakamura, F. & Li, Z.-Y. 2007, ApJ, 662, 395
18. Nakamura, F., Sugitani, K., Shimajiri, Y., et al. 2011, ApJ, 737, 56
19. Román-Zúñiga, C. G., Alves, J. F., Lada, C. J., & Lombardi, M. 2010, ApJ, 725, 2232
20. Smith, R. J., Longmore, S., & Bonnell, I. 2009, MNRAS, 400, 1775

The Interplay Between Molecular and Ionised Gas Surrounding the Massive Embedded Star AFGL 4176

Katharine G. Johnston, Henrik Beuther, Hendrik Linz, P. Boley, Thomas P. Robitaille, E. Keto, K. Wood, and R. van Boekel

Abstract In order to investigate whether the feedback produced by photo-ionisation has an important effect on the geometry of the circumstellar dust and gas around forming massive stars, we have observed the luminous southern embedded star AFGL 4176 in transitions of NH_3 and the hydrogen recombination line H68α. We present our preliminary results, which show a compact HII region embedded in a parsec-scale (radius $\sim$0.7 pc) rotating envelope/torus. In addition, the HII region is found to be offset from the centre of the envelope, and the velocity gradient in the ionised gas is not aligned with the rotation axis of the envelope, suggesting complex dynamics and multiplicity.

1 Introduction, Observations and Results

As massive protostars greater than $\sim$10 $M_\odot$ can be on the main sequence while still accreting [1], they must do so while producing vast amounts of ionising radiation. Characterising both the ionised and molecular gas around massive stars can therefore determine how they manage to accrete while an HII region forms around them.

To do so, we observed AFGL 4176, a highly luminous (1.7×10^5 $L_\odot$ at 5 kpc) embedded massive star with a compact HII region [2], whose cm flux corresponds

K.G. Johnston (✉) • H. Beuther • H. Linz • P. Boley • T.P. Robitaille • R. van Boekel
Max-Planck-Institut für Astronomie, Königstuhl 17, D-69117 Heidelberg, Germany
e-mail: johnston@mpia.de

E. Keto
Center for Astrophysics, 60 Garden Street, Cambridge, MA 02138, USA

K. Wood
School of Physics & Astronomy, University of St Andrews, St Andrews KY16 9SS, UK

D. Stamatellos et al. (eds.), *The Labyrinth of Star Formation*, Astrophysics and Space Science Proceedings 36, DOI 10.1007/978-3-319-03041-8_80,

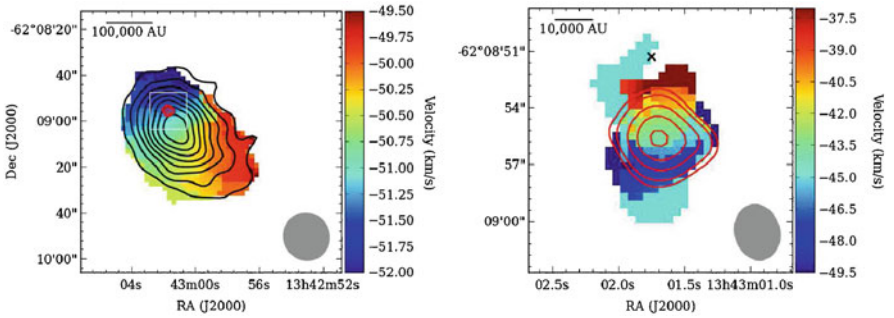

Fig. 1 *Left panel*: First moment map of the $NH_3(1,1)$ emission, imaged with a 20″ FWHM beam to recover extended emission. *Black contours*: integrated $NH_3(1,1)$ emission, peak: 0.45 Jy beam^{-1} kms^{-1}. *Red contours*: integrated H68α emission, peak: 0.62 Jy beam^{-1} kms^{-1}. The *white box* shows the area covered by the *right panel*. *Right panel*: First moment map of the H68α emission. Beam: 3.0 × 2.4″, P.A. = 13.7°. *Red contours* show integrated H68α emission. The *cross marks* the 2MASS position of the associated IR source, which dominates the NIR and MIR

to that of a B0-type star. Here we present our first results from ATCA observations of $NH_3(1,1)$ and (2,2) as well as the radio recombination line H68α, to trace both the molecular and ionised gas respectively.

The left panel of Fig. 1 presents the first moment map of the main hyperfine component of $NH_3(1,1)$, overlaid with contours of integrated $NH_3(1,1)$ and H68α emission. There is a clear southwest-northeast velocity gradient across the NH_3 emission, which we interpret as rotation of the outer envelope of AFGL 4176 (with radius ∼30″ or 0.7 pc). By fitting the $NH_3(1,1)$ and (2,2) line profiles, we have also uncovered a temperature gradient which increases towards the north of the molecular envelope, likely due to the presence of the HII region heating the surrounding gas. The right panel of Fig. 1 shows the first moment map of the H68α emission, covering the area shown by the white box in the left panel of Fig. 1. Here there is instead a roughly north-south gradient in the velocity of the ionised gas. As the velocity gradient is in the opposite sense to that of the NH_3, we conclude that the main component of this velocity gradient cannot be due to inheritance of the envelope rotation by the ionised gas, and instead may be explained by an ionised outflow. The HII region traced by H68α also does not lie towards the centre of the NH_3 emission, but is offset by 8.4″ (0.2 pc at 5 kpc). Given this offset, the high luminosity of AFGL 4176, and the offset between the HII region and the infrared source (4.5″ or 0.1 pc, see Fig. 1), it is likely that there are in fact multiple young stars forming in the vicinity of AFGL 4176.

References

1. Hosokawa, T., Omukai, K. ApJ **691**, 823–846 (2009)
2. Caswell, J. L., Kesteven, M. J., Stewart, R. T., Milne, D. K., et al. ApJL **399**, L151–L153 (1992)

Toward a Chemical Evolutionary Sequence in High-Mass Star Formation

Thomas Gerner, Henrik Beuther, Dmitry Semenov, Hendrik Linz, Tatiana Vasyunina, and Thomas Henning

Abstract Understanding the chemical evolution of young (high-mass) star-forming regions is a central topic in star formation research. The chemistry plays two main roles here: to study the evolution from simple to complex molecules, and to investigate the underlying physical processes. With these aims in mind, we observed a diverse sample of 60 high-mass star-forming regions in different evolutionary stages. In the early phase, quiescent Infrared Dark Clouds (IRDCs), consisting of cold and dense gas and dust, and emitting mainly at (sub-)millimeter wavelength, are formed. In the next phase, the so called High Mass Protostellar Objects (HMPOs) form, which host a central, likely still accreting protostar and already show emission at mid-infrared wavelengths. In the Hot Molecular Core phase (HMC) the central source heats up the surrounding environment, evaporating molecular-rich ices, which gives rise to a rich chemistry leading to complex molecules such as long carbon chains. Finally the UV-radiation from the embedded protostars ionizes the gas around and forms an Ultra Compact HII (UCHII) region. In these objects many of the previously formed complex molecules are not longer detected as they got destroyed by the ionizing radiation. For our observations, we used the IRAM 30m telescope with the total bandpass of 16 GHz and good spectral resolution ($\sim$0.3/0.7 km/s at 1/3 mm). We derived their large-scale chemical abundances, assuming LTE and optically thin emission. To set these results into context, we model the chemical evolution in such environments with a state-of-the-art chemical model. This enables us to put constraints on the chemical evolution, the age and parameters such as the temperature and the density of the molecular clouds.

T. Gerner (✉) • H. Beuther • D. Semenov • H. Linz • T. Henning
Max-Planck-Institut für Astronomie, Königstuhl 17, D-69117 Heidelberg, Germany
e-mail: gerner@mpia.de

T. Vasyunina
University of Virginia, Charlottesville, VA 22904, USA

D. Stamatellos et al. (eds.), *The Labyrinth of Star Formation*, Astrophysics and Space Science Proceedings 36, DOI 10.1007/978-3-319-03041-8_81,

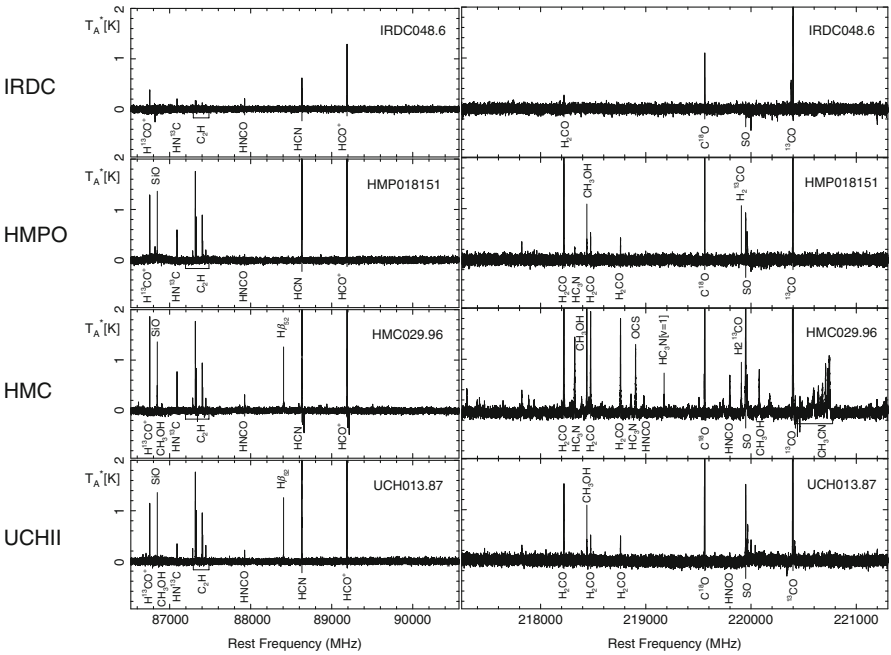

Fig. 1 From *top* to *bottom* characteristic example spectra of the four sources IRDC048.6, HMPO18151, HMC029.96 and UCH013.87 for each of the four evolutionary stages in high-mass star formation for 8 GHz of the total bandpass of 16 GHz are shown

1 Comparison Between Data and Model

As a starting point to verify the feasibility of our 1D-physical model coupled to an extended chemical model [1], we first modelled IRDC048.6. The abundances of 10 out of 13 species which were compared with the best fit model matched within their errors. Only the two complex molecules HNCO and H_2CO showed larger deviations of more than one order of magnitude, which is due to a lack of understanding their complete reaction network in particular, surface processes. In the coming future we want to apply the modelling to all our observed IRDCs and extend the model to the later stages and fit them as well (Fig. 1).

Acknowledgements T.G. is funded from Sonderforschungsbereich "The Milky Way System" (SFB 881) of the German Research Foundation (DFG) via subproject B3.

Reference

1. Semenov, D. et al. (2010), A&A, 522A, 42S

An 80 pc Long Massive Molecular Filament in the Galactic Mid-Plane

Cara Battersby and J. Bally

Abstract The ubiquity of filaments in star forming regions on a range of scales is clear, yet their role in the star formation process remains in question. We suggest that there are distinct classes of filaments which are responsible for their observed diversity in star-forming regions. An example of a massive molecular filament in the Galactic mid-plane formed at the intersection of UV-driven bubbles which displays a coherent velocity structure ($<4\,\mathrm{km\,s^{-1}}$) over 80 pc is presented. We classify such sources as Massive Molecular Filaments (MMFs; $\mathrm{M} \geq 10^4\,M_\odot$, length ≥ 10 pc, $\triangle \mathrm{v} \leq 5\,\mathrm{km\,s^{-1}}$) and suggest that MMFs are just one of the many different classes of filaments discussed in the literature today. Many MMFs are aligned with the Galactic Plane and may be akin to the dark dust lanes seen in Grand Design Spirals.

1 Observations

G32.02+0.06, a Massive Molecular Filament (MMF), has a coherent velocity structure over about 80 pc as traced by ^{13}CO [The Galactic Ring Survey, 4]. The molecular hydrogen mass of this filament over 80 pc is $2 \times 10^5\,M_\odot$ in ^{13}CO and $3 \times 10^4\,M_\odot$ in 1.1 mm dust continuum emission [The Bolocam Galactic Plane Survey, 1]. This MMF exhibits a uniform velocity field ($<4\,\mathrm{km\,s^{-1}}$) over 80 pc and is parallel to the Galactic Plane. It appears to be a ridge formed at the intersection of two UV-driven bubbles.

G32.02+0.06 has been shaped by older generations of massive stars. At least three 10–50 pc diameter bubbles, likely old HII regions, each of which contain at

C. Battersby (✉)
Harvard-Smithsonian Center for Astrophysics, Cambridge, MA 02138, USA
e-mail: cbattersby@cfa.harvard.edu

J. Bally
Center for Astrophysics and Space Astronomy, University of Colorado, Boulder, CO 80309, USA

D. Stamatellos et al. (eds.), *The Labyrinth of Star Formation*, Astrophysics and Space Science Proceedings 36, DOI 10.1007/978-3-319-03041-8_82,

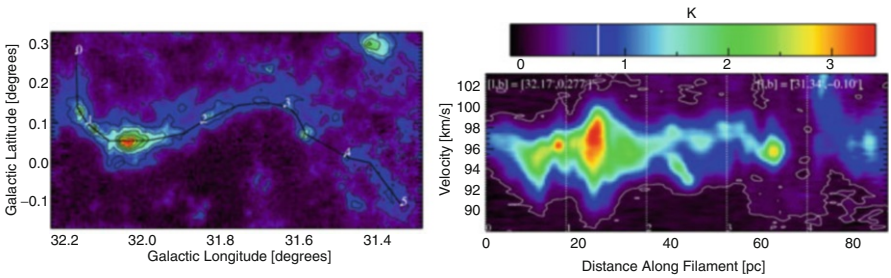

Fig. 1 *Left*: An image in ^{13}CO of the Massive Molecular Filament (MMF) G32.02+0.06. *Right*: A position velocity cut in ^{13}CO along the spine of the filament G32.02+0.06 as traced by the *black line* in the *left panel*

least several massive stars appear to have compressed this cloud and created its various loops and bends. More details on the large-scale environment of this source are presented in [2] (Fig. 1).

2 Interpretation and Discussion

Nessie [3] is another such MMF; it too exhibits coherent ($<$3.4 km s^{-1}) velocity structure over about 80 pc and has a total mass of about 10^4 $M_\odot$ as traced by dense gas, comparable to G32.02+0.06. Nessie is also parallel to the Galactic Plane, but slightly offset in latitude from the mid-plane ($|b| \sim -0.4°$).

There are at least a handful of other MMFs aligned with the Galactic Plane (Tackenberg et al., submitted). If a majority of MMFs are aligned with the Galactic Plane this indicates that Galactic processes such as shear and spiral density waves are more important than super-bubbles in their formation. Their alignment with the Galactic Plane is analogous to dark dust lanes along spiral arms seen in face-on galaxies.

G32.02+0.06 represents just one example of an MMF in the Galactic mid-plane formed by the compression of previous generations of massive stars. We classify such filaments (M $\geq 10^4$ $M_\odot$, length $\geq$ 10 pc, $\triangle$v $\leq$ 5 km s^{-1}) as MMFs and suggest that they represent just one category of the oft-discussed "filaments" in the literature of late.

References

1. Aguirre, J. E., Ginsburg, A. G., Dunham, M. K., et al. 2011, ApJS, 192, 4
2. Battersby, C., Ginsburg, A., Bally, J., Longmore, S., Dunham, M. K., Darling, J., ApJ, submitted
3. Jackson, J. M., Finn, S. C., Chambers, E. T., Rathborne, J. M., & Simon, R. 2010, ApJL, 719, L185
4. Jackson, J. M., Rathborne, J. M., Shah, R. Y., et al. 2006, ApJS, 163, 145

Probing the Earliest Stages of Massive Star Formation Through Observations of N_2D^+

Francesco Fontani

Abstract With the IRAM-30m telescope, we have observed rotational transitions of N_2H^+ and N_2D^+ and, from these, derived the deuterated fraction in a sample of 27 cores within massive star-forming regions believed to represent different evolutionary stages of the massive star formation process. Our results clearly indicate that the abundance of N_2D^+ is higher at the pre-stellar/cluster stage, then drops of about an order of magnitude during the formation of the protostellar object(s), and remains relatively constant during the formation of the Ultra-Compact HII region. These findings suggest that the N_2D^+/N_2H^+ abundance ratio is an excellent indicator of massive starless cores on the verge of the gravitational collapse. ALMA high-angular resolution follow-up observations of the N_2D^+ (3–2) line towards the four starless cores with the highest N_2D^+/N_2H^+ suggest that the cores are consistent with being in virial equilibrium, i.e. observed line widths match those predicted from a model of a virialized core embedded in a pressurized clump.

1 Motivation, Observations and Main Results

Significant progresses towards a better understanding of the initial conditions of the massive star formation process can be made by investigating physical, chemical and dynamical properties of massive starless cores. Because these are very rare objects, it is challenging to select prime examples of massive starless cores. In low-mass dense cores, the column density ratio $N(N_2D^+)/N(N_2H^+)$ reaches its maximum at the onset of the gravitational collapse (see e.g. [1, 2]) and is thus perfect to select candidates where to study the initial conditions. *Is this true also in the high-mass regime?* To answer this question, we observed rotational lines of N_2D^+ and N_2H^+ with the IRAM-30m telescope and derived their column densities in 27 cores within

F. Fontani (✉)
INAF-Arcetri, L.go E. Fermi 5, Firenze, Italy
e-mail: fontani@arcetri.astro.it

D. Stamatellos et al. (eds.), *The Labyrinth of Star Formation*, Astrophysics and Space Science Proceedings 36, DOI 10.1007/978-3-319-03041-8_83,

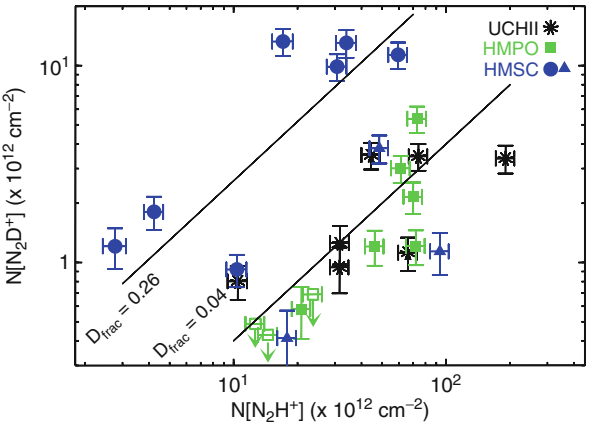

Fig. 1 N_2D^+ column density versus N_2H^+ column density for the targets detected in N_2D^+ among the 27 objects in Table 1. *Blue symbols* correspond to HMSCs; *green squares* show HMPOs (*open squares* are upper limits); *black asterisks* correspond to UC HII regions. The *two lines* indicate the average values of Dfrac for the HMSC group (i.e. 0.26) and that of both the HMPO and UC HII groups (i.e. 0.04)

massive star-forming regions understood to represent different evolutionary stages of the high-mass star formation process: 10 High-Mass Starless Cores (HMSCs), 10 High-Mass Protostellar Objects (HMPOs), 7 Ultracompact HII regions (UCHIIs).

Figure 1, adapted from [3], shows the N_2D^+ column density versus N_2H^+ column density for all cores detected in N_2D^+. For HMSCs, the average $N(N_2D^+)/N(N_2H^+)$ is $\sim$0.26, while that of both the HMPO and UC HII groups is $\sim$0.04. Therefore, the relative abundance N_2D^+/N_2H^+ is higher at the pre-stellar/cluster stage, then drops during the formation of the protostellar object(s) as in the low-mass regime, and stays relatively constant during the ultra-compact HII region phase. This indicates that *the high N_2D^+/N_2H^+ relative abundance is perfect to identify pristine massive cores, just like in the low-mass regime, and hence the HMSCs with the highest column density ratio are the best targets to study the initial conditions*. Preliminary results of ALMA follow-up observations of the N_2D^+ (3–2) transition towards these four cores, obtained during cycle-0 in compact configuration (Tan et al. in preparation), show that: (a) The N_2D^+ (3–2) integrated emission generally agrees with the mass surface density map; (b) averaged as a sample, the cores are consistent with being in virial equilibrium, i.e. observed line widths match those predicted from a model of a virialized core embedded in a pressurized clump.

References

1. Crapsi, A., et al. ApJ, **619**, 379–406 (2005)
2. Emprechtinger, M., et al. A&A, **493**, 89–105 (2009)
3. Fontani, F., et al. A&A, **529**, L7 (2011)

The Next Generation of High-Mass Stars and Clusters Traced by ATLASGAL

Frédéric Schuller, Karl M. Menten, Friedrich Wyrowski, Yanett Contreras, Timea Csengeri, James S. Urquhart, Marion Wienen, Henrik Beuther, Sylvain Bontemps, Leonardo Bronfman, Lise Deharveng, Thomas Henning, Malcolm Walmsley, and Annie Zavagno

Abstract The Atacama Pathfinder Experiment (APEX) telescope is ideally located to observe the inner part of our Galaxy. With its good sensitivity, the LABOCA bolometer array can map hundreds of square degrees at $\lambda = 870\,\mu$m in a reasonable time. ATLASGAL, the APEX Telescope Large Area Survey of the Galaxy, covers $420\,\mathrm{deg}^2$ of the inner Galactic plane, with a typical rms noise of 50 mJy/beam. The data reveal thousands of compact sources, as well as giant molecular complexes and large scale filamentary structures. Many follow-up projects are ongoing, and more are planned e.g. with ALMA.

F. Schuller (✉)
Max-Planck-Institut für Radioastronomie, Bonn, Germany

European Southern Observatory, Santiago, Chile
e-mail: schuller@mpifr.de

K.M. Menten • F. Wyrowski • T. Csengeri • J.S. Urquhart • M. Wienen
Max-Planck-Institut für Radioastronomie, Bonn, Germany

Y. Contreras
Universidad de Chile, Santiago, Chile

Max-Planck-Institut für Radioastronomie, Bonn, Germany

H. Beuther • T. Henning
Max-Planck-Institut für Astronomie, Königstuhl 17, D-69117 Heidelberg, Germany

S. Bontemps
University of Bordeaux/CNRS, LAB, UMR 5804, F-33270, Floirac, France

L. Bronfman
Universidad de Chile, Santiago, Chile

L. Deharveng • A. Zavagno
Laboratoire d'Astrophysique de Marseille, Marseille, France

M. Walmsley
Osservatorio Astrofisico di Arcetri, Firenze, Italy

D. Stamatellos et al. (eds.), *The Labyrinth of Star Formation*, Astrophysics and Space Science Proceedings 36, DOI 10.1007/978-3-319-03041-8_84,

1 Observations

The data composing the ATLASGAL survey were observed between 2007 and 2010, with the LABOCA bolometer array [4], operating at 870 μm and installed at APEX [2]. The telescope pattern consists in linear on-the-fly maps, 2° to 3° by 1° in size, at a scanning speed of 3′/s. At least two maps overlap on each position in the sky. The noise level in the final, combined maps is usually in the range 50–70 mJy/beam.

The full survey covers −80° to +60° in Galactic longitude, over ±1.5° in latitude (420 deg^2). The first data, taken in 2007 and covering 95 deg^2, have been presented in [3]. All the data have been processed with the BoA software, using a reduction pipeline also described in [3].

The resulting maps contain a wealth of structures all along the Galactic plane. Most compact sources are embedded in arcmin-scale extended emission. In many directions, we also detect very long (up to degree-scale) filaments that seem to connect several rich complexes together.

2 Compact Sources

We are in the final steps of releasing a first compact source catalog [1]. This catalog covers the −30° to +21° range in longitude (153 deg^2). It contains 6,640 compact sources, extracted down to 200 mJy/beam peak flux. About 60 % have no bright infrared counterpart in the IRAS and MSX surveys (Fig. 1). They are likely to trace the cold, early stages of high-mass star formation.

Follow-up observations of selected samples of compact sources have been started. This includes: small maps at 350 μm with SABOCA; spectral surveys at 90 GHz with MOPRA, at 100 GHz with IRAM, at 230 and 345 GHz with APEX; and NH_3 lines with Effelsberg and Parkes, very useful to derive kinematic distances [5].

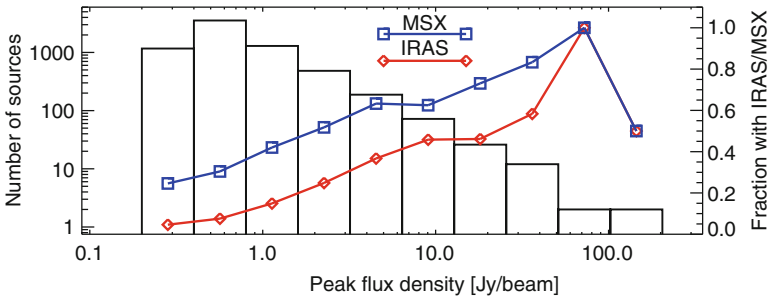

Fig. 1 Peak flux distribution for the 6,640 compact sources in the first catalog. The fractions of sources with MSX or IRAS counterparts are shown with the *top* and *bottom lines*, respectively, with the scale indicated on the right

3 Perspectives and Conclusion

Only a *systematic survey* can provide well controlled samples for efficient follow-ups. The ATLASGAL source catalog, when combined with other surveys (GLIMPSE, MIPSGAL, Hi-GAL) will be the perfect data-set to provide valuable source samples for detailed follow-up studies with ALMA. Unprecedented spatial resolution and sensitivity will allow us to study the inner workings of star formation processes on small scales.

References

1. Contreras, Y., Schuller, F., Urquhart, J. et al. A&A submitted (2012)
2. Güsten, R., Nyman, L.A., Schilke, P. et al. A&A **454**, L13–L16 (2006)
3. Schuller, F., Menten, K., Contreras Y. et al. A&A **504**, 415–427 (2009)
4. Siringo, G., Kreysa, E., Kovács, A. et al.: A&A **497**, 945–962
5. Wienen, M., Wyrowski, F., Schuller, F. et al. A&A accepted (2012)

Deuteration in High-Mass Star Forming Regions

Javier A. Rodón, Henrik Beuther, and Qizhou Zhang

Abstract In the last years, we have started to spatially resolve the small gas and dust condensations in multiple star-forming (MSF) regions that will eventually become a massive star or system. We call these condensations "cores", with sizes on the order of 0.01 pc. By constructing the Core Mass Function (CMF) of a region and comparing it with the IMF, we can attempt to determine the evolutionary process from core to star, but for MSF regions, the relationship between the CMF and the IMF is not yet well understood. This is, among other factors, due to the fact that there are not many MSF CMFs determined. Those few that are, seem to tell a story of evolution by presenting slopes varying from that of the Salpeter IMF to very different values. But are we in fact observing regions at different evolutionary stages? One way to address that is by determining the deuteration fraction of those regions, since deuterated species are first released into the gas medium and then destroyed at the early stages of evolution.

1 The Data

Figure 1 presents part of the just reduced large-scale data obtained for a sample of massive star-forming regions. We obtained IRAM 30 m HERA observations of the DCN(3-2), HCN(3-2), DCO+(3-2) and HCO+(3-2) transitions for the regions

J.A. Rodón (✉)
European Southern Observatory, Alonso de Córdova 3107, Santiago 19, Chile
e-mail: jrodon@eso.org

H. Beuther
Max-Planck-Institute für Astronomie, Königstuhl 17, D-69117 Heidelberg, Germnay
e-mail: beuther@mpia.de

Q. Zhang
Harvard-Smithsonian Center for Astrophysics, 60 Garden Street, Cambridge, MA 02138, USA
e-mail: qzhang@cfa.harvard.edu

D. Stamatellos et al. (eds.), *The Labyrinth of Star Formation*, Astrophysics and Space Science Proceedings 36, DOI 10.1007/978-3-319-03041-8_85,

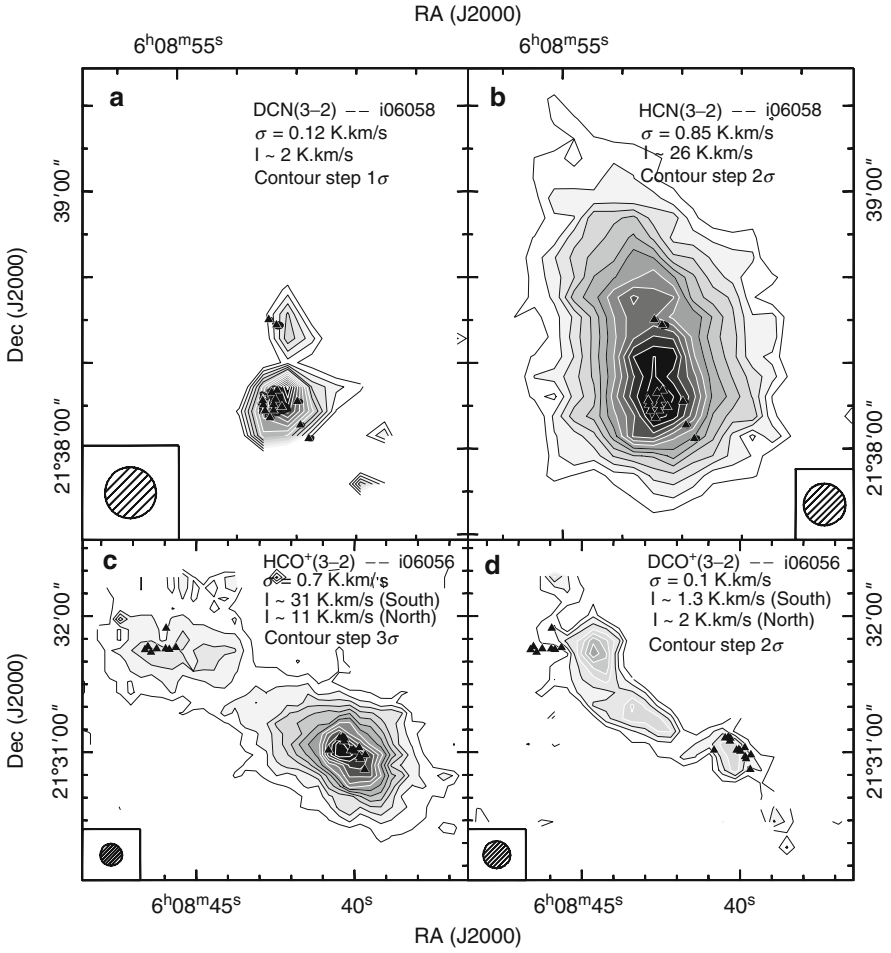

Fig. 1 Integrated intensity maps (units of K.km/s) of DCN(3-2) and HCN(3-2) for IRAS 06058+2138 (panels (**a**) and (**b**)), and DCO+(3-2) and HCO+(3-2) for IRAS 06056+2131 (panels (**c**) and (**d**)). The contours start at 5σ, the step increase, the σ value, and the peak integrated flux are found in each panel. The *triangles* are the continuum sources we detected at 1.4 mm with SMA observations. The dashed circle is the synthesized beam of $\sim 11''$

IRAS 06058+2138 (i06058) and IRAS 06056+2131 (i06056). These single-dish observations will be combined with SMA data, to improve the angular resolution of the former and the uv-coverage of the latter. A quantitative and more in-depth analysis will follow.

For both regions the HCN/DCN pair peak at the central cluster of protostars, though DCN peaks towards the border of the continuum emission and HCN matches the continuum peak (e.g., Fig. 1a, b). In i06058 the secondary northern peak in both DCN/HCN is likely associated with the parental cloud of the two northern

mm sources. Also in that region, HCN is generally more extended than both D-bearing species. This reflects on the relatively advanced stage of evolution of i06058 (NIR sources and masers detected). For i06056 the DCN emission show peaks not associated with the continuum emission nor seen in HCN. Those are possibly young and cold clumps.

In all cases, DCO+ peaks outside the mm emission (e.g., Fig. 1d), and show peaks not associated with either continuum nor HCO+ emission. An example of this is the "bridge" of material connecting both mm clusters of i06056 (Fig. 1c, d). These peaks may be marking young clumps, not yet forming stars. The DCO+ emission in the south of i06056 peaks at the same position as HCO+ (Fig. 1c, d). This suggest this is a relatively young cluster, while the lack of DCO+ towards the north cluster hints to a more evolved cluster.

Part IX
Clustered Star Formation

Clustered Star Formation: A Review

Richard J. Parker

Abstract In this contribution I present a review of star formation in clusters. I begin by discussing the various definitions of what constitutes a star cluster, and then compare the outcome of star formation (IMF, multiplicity, mass segregation and structure and morphology) in different star-forming regions. I also review recent numerical models of star formation in clusters, before ending with a summary of the potential effects of dynamical evolution in star clusters.

1 What Is a Star Cluster?

A fundamental question regarding the nature of star formation is where do most stars form? The seminal review by Lada and Lada [22] suggested that 70–90 % of stars form in embedded clusters, some of which remain bound and evolve to open clusters, and the remainder disperse and contribute to the Galactic field. In this picture, star clusters can be thought of as the fundamental 'unit' of star formation. However, to describe clusters as a unit of star formation naturally requires a definition of what constitutes "clustered" versus non-clustered, or "isolated" star formation.

A recent study of YSOs in the local solar neighbourhood by Bressert et al. [11] showed that the distribution of stellar surface densities for 12 combined regions of star formation has a smooth, continuous distribution, with no distinction between isolated and clustered star formation. It is therefore problematic to define a cluster based on stellar surface density.

A potential alternative is to apply a graph theory approach, in which all the stars in a field of view are uniquely linked by a minimum spanning tree (MST),

R.J. Parker (✉)
Institute for Astronomy, ETH Zürich, Wolfgang-Pauli-Strasse 27, 8093 Zürich, Switzerland
e-mail: rparker@phys.ethz.ch

D. Stamatellos et al. (eds.), *The Labyrinth of Star Formation*, Astrophysics and Space Science Proceedings 36, DOI 10.1007/978-3-319-03041-8_86,

which joins all the points via the shortest possible pathlength. One can then define a threshold length, above which branches in the MST a removed, leaving "clusterings" of stars (e.g. [15, 32]). Whilst this method is useful for picking out clusters against a crowded background, it requires the maximum threshold length to be defined (somewhat arbitrarily) and, as is often the case, the human eye is more efficient at picking out overdensities than the actual algorithms.

One can also define a star cluster based on the binding energy of a group of stars. If the total binding energy is negative, then the stellar system is bound and unlikely to fall apart through two-body relaxation. In an extension of this concept, Gieles and Portegies Zwart [14] made the distinction between a bound cluster and associations based on the crossing time of the star forming region (the time taken for a star to cross from one side to the other):

$$T_{\rm cr} = 7.5 \left(\frac{R_{\rm eff}^3}{GM} \right)^{1/2}, \tag{1}$$

where $R_{\rm eff}$ and M are the effective half light radius, and mass of the star forming region, respectively. We obtain a value Π, by dividing the age of the region by $T_{\rm cr}$; regions with $\Pi > 1$ are bound clusters, and those with $\Pi < 1$ are unbound associations.

As we have seen, actually defining what a cluster is can be difficult, and often is merely a matter of personal opinion. For the remainder of this review, I will focus more on asking the question of whether star formation is a universal process in different star-forming regions, and how we can frame this question. In order to do this, I will consider both diffuse and dense nearby star forming regions, which are "clustered" in the sense that they are an overdensity with respect to the Galactic field, but may not pass all, or any of the definitions above.

2 Observations

The wealth of data from the recent Herschel observations (see contribution by J. Kirk) has shown star formation to be a highly filamentary process, and it is thought that star clusters may form at the intersection of filaments ("hubs") where there are significant over-densities [27]. In the following subsections I will describe the observed outcome (i.e. the IMF, multiplicity, structure) of the star formation process in different regions (hereafter "clusters").

2.1 The Initial Mass Function

A great deal of effort has gone in to observing the Initial Mass Function (IMF) in various environments, principally to look for evidence of environmentally

dependent variations. However, the IMF appears to be remarkably invariant; the same form is observed in dense clusters and sparse associations, and in open and globular clusters. All of these IMFs are also consistent with the mass function in the Galactic field [5].

Whilst the IMF is largely invariant (certainly on Galactic scales), some star forming regions display peculiarities which may hint at subtle differences in the IMF. For example, the Taurus association contains an excess of K-type dwarfs compared to the more numerous M-dwarfs; and much effort is focusing on determining whether the substellar regime of the IMF is also invariant across different regions.

Recent studies have also suggested that the IMF may vary as a function of distance from the cluster centre, with several regions (e.g. the ONC, IC348) displaying an excess of brown dwarfs at the periphery of the cluster compared to the centre.

2.2 Multiplicity

If the IMF is invariant, then what may vary as a function of star formation event? A promising avenue to explore is stellar multiplicity, within which there are several parameters that can be accurately measured in clusters. In addition to the bare fraction of stars in multiple systems, one can compare the distributions of orbital parameters of binaries, such as the semi-major axis distribution and the companion mass ratio distribution.

However, the process of comparing these distributions in different clusters is not straightforward. Firstly, comparable data are often drawn from different observational programmes; one has to be careful not to compare apples to oranges. Most nearby clusters have had their visual binaries observed; these are binaries with on-sky separations which are sufficiently large to resolve the primary and secondary stars into individual components, but not so large that the component stars cannot be distinguished from background cluster members. As the distance to nearby clusters varies, then one can observe binaries with closer and wider separations in nearby clusters. For example, in Taurus the observable separation range is 18–1,000 AU, whereas we are restricted to 62–620 AU in the more distant ONC. To enable a fair comparison between the binaries in each region, we are forced to throw away from any analysis the extra systems in Taurus which lie outside the common 62–620 AU range. Such surveys also are limited by a contrast range and are therefore sensitive to the flux ratios between the primary and secondary component of the binary.

A recent synthesis of the available data on nearby clusters suggests that the binary fraction (for systems in the separation range 62–620 AU) does not depend strongly on the density of that region [16]. Preliminary analysis also suggests that the separation distributions are not statistically distinguishable in this range. This is puzzling because the regions span several orders of magnitude in stellar density; even if only one region was dynamically active (the ONC), we would expect the separation distributions to have been altered to a different degree by interactions, the number of which is set by the density.

Comparison of the mass ratio distribution can also shed light on the binary formation process, and early work suggests that this distribution is flat in the Galactic field and in several clusters (see the contribution by M. Reggiani).

2.3 Structure and Morphology

The first analysis of structure and morphology in star forming regions was conducted by Larson [24], who looked at the two-point correlation function in Taurus. By plotting local surface density against distance to nearest neighbour, one can pick out the binary regime versus the general hierarchical structure in the cluster. Interestingly, the separation corresponding to the break in power law from the binary regime to the cluster regime corresponded to the Jeans length, suggesting some underlying physical process. The same break at the Jeans length was found in ρ Oph and the Trapezium cluster, although the latter result was later disputed [8].

However, structure can be quantified in a more meaningful way using the Q-parameter [13], which divides the mean length of the MST of all stars in the cluster, $\bar{m}$ by the mean separation between stars in the cluster, $\bar{s}$;

$$Q = \frac{\bar{m}}{\bar{s}}. \tag{2}$$

When a cluster has substructure, $Q < 0.8$, whereas $Q > 0.8$ indicates a centrally concentrated cluster. Using the Q-parameter it is possible to infer either the fractal dimension of the structured cluster, or the density profile of the smooth cluster. Sanchez and Alfaro [31] have found that many young clusters display substructure, due to their low Q-parameters.

2.4 Mass Segregation

Some young clusters (e.g. the ONC) are observed to be mass segregated, whereby the most massive stars reside at the cluster centre. Mass segregation can be quantified in several ways, such as an MST analysis [2, 28], surface density as a function of mass [26] or distance from the cluster centre compared to the median value [17].

3 Theoretical and Numerical Models

There are many different theories of star formation in clusters. In an ironic symmetry with the observations, many theoretical models are able to reproduce an IMF independent of a wide range of initial conditions. Here I mention two competing

theories for massive star formation in clusters, for the reason that they predict very different (observable) outcomes for the mass of the remaining cluster of stars.

The monolithic collapse scenario (e.g. [20, 21, 25]) predicts a top–down star formation from the collapse of a massive star forming core. The collapse and fragmentation of this core gives the IMF directly, which may vary depending on the exact details of the collapse. For example, if the core remains relatively warm, it may not fragment much, and could in principle lead to 'isolated' O-star formation, where the O-star is surrounded by a few lower-mass stars. Recent observational studies by Lamb et al. [23] and Bressert et al. [12] suggest that some O-stars do indeed form in isolation.

Alternatively, massive stars (and a surrounding cluster) can form via competitive accretion [9, 10, 33], where the cloud fragments into equal-mass seeds, which then accrete the remaining gas in varying proportions, so as to produce the IMF. As the gas density is highest in the centre of the cluster, the central stars become the most massive and naturally explain the observed mass segregation in some clusters. This process suggests that the mass of the most massive star in a cluster would therefore depend on the cluster mass (due to the proportion of gas accreted by the massive stars). If this dependence is a fundamental outcome of star formation, then observationally we would expect that the most massive star should *always* be proportional to the cluster mass, as claimed by Weidner et al. [34].

Recent hydrodynamical simulations of star cluster formation by Bate [6, 7] have also made concrete predictions for the primordial multiplicity of stars. From a collapsing $500\,M_{\odot}$ cloud, 183 stars and brown dwarfs are formed [7], with a mass function similar to the Chabrier system IMF. Additionally, the binary fraction is similar to that in the Galactic field, and decreases with decreasing primary mass. The distributions of the binary orbital parameters are also in remarkably good agreement with the field.

4 Dynamical Evolution

Whilst the detailed hydrodynamical simulations of star formation make concrete predictions, they are extremely computationally expensive, and render a comparison of different (simulated) clusters impossible. For this reason, pure N-body simulations are also useful in assessing the change in cluster morphology and structure, and the effects of the cluster environment on the outcome of star and planet formation (e.g. primordial multiplicity and protoplanetary discs).

The first simulations to look at the effect of cluster dynamics on primordial binaries were pioneered by Kroupa [18] and Kroupa et al. [19] who used an "inverse population synthesis" to infer the dynamical processes which affect binaries as their host clusters evaporate into the field. More recent simulations have looked at the evolution of cluster structure and morphology. Simulations of subvirial (cool) clusters with structure have shown that dynamical mass segregation and the formation of Trapezium-like systems can occur on short timescales [1, 3, 4].

The evolution of substructure in clusters is particularly interesting as in addition to cool clusters, both virial ('tepid') and supervirial ('warm') clusters can process primordial binaries and planetary systems [29, 30], even if they do not attain high global densities.

To briefly summarise, star clusters can tell us much about star formation and in addition to IMFs, we should be comparing multiplicity properties, and the internal and global structure of clusters to search for fundamental differences in the star formation process as a function of environment.

Acknowledgements I wish to thank the SOC for inviting me to present this review, and the LOC for organising such an enjoyable conference in a beautiful location. I would also like to thank Ant Whitworth for many entertaining and enlightening conversations (usually over beer!).

References

1. Allison, R.J., Goodwin, S.P.: MNRAS, **415**, 1967 (2011)
2. Allison, R.J. *et al*: MNRAS, **395**, 1449 (2009a)
3. Allison, R.J. *et al*: ApJ, **700**, L99 (2009b)
4. Allison, R.J. *et al*: MNRAS, **407**, 1098 (2010)
5. Bastian, N., *et al*: ARA&A, **48**, 339 (2010)
6. Bate, M.R.: MNRAS, **392**, 590 (2009)
7. Bate, M.R.: MNRAS, **419**, 3115 (2012)
8. Bate, M.R., *et al*: MNRAS, **297**, 1163 (1998)
9. Bonnell, I.A., *et al*: MNRAS, **323**, 785 (2001)
10. Bonnell, I.A., *et al*: MNRAS, **343**, 413 (2003)
11. Bressert, E., *et al*: MNRAS, **409**, L54 (2010)
12. Bressert, E., *et al*: A&A, **542**, 49 (2012)
13. Cartwright, A., Whitworth, A.P.: MNRAS **348**, 589 (2004)
14. Gieles, M., Portegies Zwart, S.P.: MNRAS, **410**, L6 (2011)
15. Gutermuth, R. A., *et al*: ApJS, **184**, 18 (2009)
16. King, R.R., *et al*: MNRAS, **421**, 2025 (2012)
17. Kirk, H., Myers, P.C.: ApJ, **727**, 64 (2011)
18. Kroupa, P.: MNRAS, **277**, 1491 (1995)
19. Kroupa, P., *et al*: New Astronomy, **4**, 495 (1999)
20. Krumholz, M.R., *et al*: ApJ, **618**, L33 (2005)
21. Krumholz, M.R., *et al*: Sci, **323**, 754 (2009)
22. Lada, C.J., Lada, E.A.: ARA&A, **41**, 57 (2003)
23. Lamb, J.B., *et al*: ApJ, **725**, 1886 (2010)
24. Larson, R.B.: MNRAS, **272**, 213 (1995)
25. McKee, C.F., Tan, J.C.: ApJ, **585**, 850 (2003)
26. Maschberger, T., Clarke, C.J.,: MNRAS, **416**, 541 (2011)
27. Myers, P.C.: ApJ, **735**, 82 (2011)
28. Olczak, C., *et al*: A&A, **532**, 119 (2011)
29. Parker, R.J., *et al*: MNRAS, **418**, 2565 (2011)
30. Parker, R.J., Quanz, S.P.: MNRAS, **419**, 2448 (2012)
31. Sanchez, N., Alfaro, E.J.: ApJ, **696**, 2086
32. Schmeja, S.: AN, **332**, 172 (2011)
33. Smith, R.J., *et al*: MNRAS, **396**, 830 (2009)
34. Weidner, C., *et al*: MNRAS, **401**, 275 (2010)

A Galactic-Scale Origin for Stellar Clustering

J.M. Diederik Kruijssen

Abstract We recently presented a model for the cluster formation efficiency (CFE), i.e. the fraction of star formation occurring in bound stellar clusters. It utilizes the idea that the formation of stars and stellar clusters occurs across a continuous spectrum of ISM densities. Bound stellar clusters naturally arise from the high-density end of this density spectrum. Due to short free-fall times, these high-density regions can achieve high star formation efficiencies (SFEs) and can be unaffected by gas expulsion. Lower-density regions remain gas-rich and substructured, and are unbound upon gas expulsion. The model enables the CFE to be calculated using galactic-scale observables. I present a brief summary of the model physics, assumptions and caveats, and show that it agrees well with observations. Fortran and IDL routines for calculating the CFE are publicly available at http://www.mpa-garching.mpg.de/cfe.

1 The Clustered Nature of Star Formation

Studies of star formation in the solar neighbourhood, in the Milky Way as a whole, and in external galaxies, have shown that some fraction of star formation occurs in unbound associations, while the remainder results in bound stellar clusters (e.g. [1,2]). The question thus arises which physical mechanisms drive the star formation process to result in either outcome. How do bound stellar clusters form, and what fraction of all star formation do they represent? Observations suggest a range of answers to the latter question – it seems that the fraction of star formation occurring in bound stellar clusters changes with the galactic environment [3–6]. This provides

J.M.D. Kruijssen (✉)
Max-Planck-Institut für Astrophysik, Karl-Schwarzschild-Straße 1, 85748 Garching, Germany
e-mail: kruijssen@mpa-garching.mpg.de

D. Stamatellos et al. (eds.), *The Labyrinth of Star Formation*, Astrophysics and Space Science Proceedings 36, DOI 10.1007/978-3-319-03041-8_87,

a potentially useful clue to the origins of stellar clustering, and presents a challenge to the classical view in which all stars form in clusters but only a minor fraction remains bound after gas expulsion (e.g. [7]).

Another important insight is that star formation occurs over a broad and continuous range of densities [8], without any obvious separation between star formation in unbound associations or bound clusters. Instead, protostellar cores and young stellar objects follow the hierarchical structure of the interstellar medium (ISM) [9]. It has recently been shown that gas-poor and virialised stellar structure may arise naturally at the high-density end of this density spectrum [10, 11]. This may provide a natural explanation to the observation that cluster formation is inefficient [12]: if only some fraction of the star-forming regions manages to collapse and form bound systems, that same fraction will emerge as unembedded, virialized and bound clusters without any sign of expansion due to gas expulsion (e.g. [13]).

In [14], we recently presented a new theoretical framework for the formation of bound stellar clusters. By integrating the star formation efficiencies (SFEs) and local bound fractions of star-forming regions over the density spectrum of the ISM, our model is used to quantify the fraction of all star formation that occurs in bound stellar clusters (i.e. the cluster formation efficiency or CFE). Fortran and IDL routines for calculating the CFE as a function of galaxy properties are publicly available at http://www.mpa-garching.mpg.de/cfe [14]. In these proceedings, I summarize the model and discuss the underlying assumptions and caveats.

2 The Fraction of Star Formation Occurring in Bound Clusters

The theory of the CFE is derived and applied in detail in [14]. In summary, it covers the following physical mechanisms and underlying assumptions.

1. The starting point of the model is the overdensity probability distribution function (PDF) of the ISM. This PDF is assumed to follow a log-normal with median and dispersion set by the Mach number, and describes the distribution of density contrasts with respect to the mean density in a turbulent ISM (see e.g. [15, 16]).
2. The overdensity PDF is written as a function of galaxy properties (gas surface density $\Sigma_{\rm g}$, angular velocity Ω, and Toomre Q [17]) by assuming that star formation occurs in a gas disc that obeys hydrostatic equilibrium (see below).
3. At each density the local SFE is calculated by assuming that the fraction of the gas that is converted into stars per free-fall time is approximately constant [15, 18]. Depending on the density, star formation continues until (1) the gas is exhausted, (2) pressure equilibrium is reached between the turbulent ISM and (supernova and/or radiative) feedback, or (3) the moment of evaluating the CFE.
4. The local SFE is related to the local fraction of stars that remains bound upon instantaneous gas expulsion using a numerical simulation of turbulent

fragmentation [19]. Assuming that protostellar outflows do not unbind bound stellar clusters, this provides the naturally bound fraction of star formation at each density.
5. Following the Spitzer formalism for tidal shocks [20], the model includes tidal perturbations by density peaks in the star-forming environment (the cruel cradle effect, see [11, 21]), which destroy stellar structure below a certain environmentally dependent, critical density.
6. The CFE is obtained by integrating the naturally bound fraction of star formation over the density range of the PDF where structure survives the cruel cradle effect (reflecting bound cluster formation), and dividing it by the integral of the SFE over the entire density range of the PDF (reflecting all star formation).

Given these model components, the following caveats should be kept in mind.

1. Magnetic fields are only included to first order by using the magnetic-to-thermal pressure ratio, which is specified with an optional model parameter. This changes the dispersion of the log-normal overdensity PDF [16]. Note that the default form of this PDF is already consistent with weak magnetic fields.
2. The assumption that star formation occurs in a gas disc that obeys hydrostatic equilibrium may not hold in starburst galaxies. However, the energy dissipation that is required to cool gas and form stars also drives the formation of a disc, and hence the spatial distribution of star-forming regions in a starburst should be expected to follow a disc-like morphology [22].
3. Star formation in intermediate-density regions is halted by supernova (or alternatively radiative) feedback, which may not be appropriate. The efficiency of different feedback mechanisms has been extensively discussed in the literature, and likely varies with spatial scale or density. However, the description of feedback in this model satisfies its purpose of truncating star formation on a timescale that is broadly consistent with observations [1].

The above model can be used to calculate the CFE as a function of $\{\Sigma_{\rm g}, \Omega, Q\}$, which is reduced to a single-parameter problem by assuming a single value of $Q=1.5$ and relating Ω to $\Sigma_{\rm g}$ as in [15]. The resulting relation between the CFE (or Γ, [23]) and the star formation rate density $\Sigma_{\rm SFR} \propto \Sigma_{\rm g}^{1.4}$ [24] is shown in Fig. 1, together with compiled observations from the recent literature. The agreement between theory and observations is remarkable, especially considering that the typical error margins on the observations are $\sim$0.3 dex, and noting that an additional uncertainty of 0.3–0.5 dex is introduced by using the relation $\Sigma_{\rm SFR} \propto \Sigma_{\rm g}^{1.4}$ to convert the model $\Gamma(\Sigma_{\rm g})$ to $\Gamma(\Sigma_{\rm SFR})$. A good fit to the model relation is given by

$$\Gamma = \left(1.15 + 0.6\Sigma_{\rm SFR,0}^{-0.4} + 0.05\Sigma_{\rm SFR,0}^{-1}\right)^{-1} \times 100\,\%, \tag{1}$$

where $\Sigma_{\rm SFR,0} \equiv \Sigma_{\rm SFR}/{\rm M}_\odot\ {\rm year}^{-1}\ {\rm kpc}^{-2}$ is the star formation rate density of the galaxy. This fit is for one particular, 'typical' parameter set and should therefore only be used for rough estimates. Because it assumes the power law form of

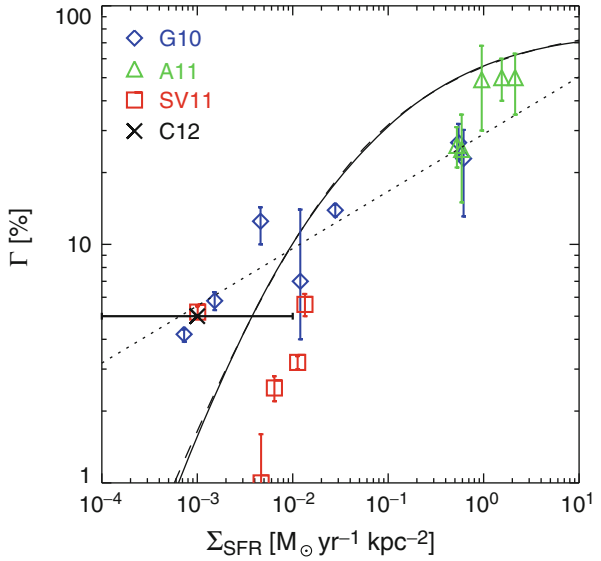

Fig. 1 CFE as a function of $\Sigma_{\rm SFR}$. Symbols denote observed galaxies with 1σ error bars and indicate the samples from [3] (*blue diamonds*), [4] (*green triangles*), and [5] (*red squares*). The *black cross* indicates the integrated CFE of all dwarf galaxies from the sample of [6], with a surface density range indicated by the horizontal error bar. The *solid curve* represents the modelled relation for typical disc galaxies, but can vary for different galaxy and ISM properties. The *dashed curve* shows the fit of equation (1), and the *dotted line* represents the original fit by Goddard et al. [3]

the Schmidt-Kennicutt relation $\Sigma_{\rm SFR} \propto \Sigma_{\rm g}^{1.4}$ [24], any scatter around that relation is carried over. See [14] and our publicly available routines for a more detailed modelling.

The good agreement between model and observations warrants further testing using Gaia and ALMA (see [14] for an extensive discussion of the possibilities). However, our theoretical framework also contains several components that require to be constrained further. While a global theoretical picture of cluster formation seems to be emerging, the details of stellar clustering remain to be understood.

Acknowledgements I am grateful to the organizers giving me the opportunity to present this work, and for organizing such a vibrant and pleasant conference.

References

1. S. F. Portegies Zwart, S. L. W. McMillan, M. Gieles, ARA&A **48**, 431 (2010)
2. E. Bressert, N. Bastian, C. J. Evans, et al., A&A **542**, A49 (2012)
3. Q. E. Goddard, N. Bastian, R. C. Kennicutt, MNRAS **405**, 857 (2010)
4. A. Adamo, G. Östlin, E. Zackrisson, MNRAS **417**, 1904 (2011)

5. E. Silva-Villa, S. S. Larsen, A&A **529**, A25+ (2011)
6. D. O. Cook, A. C. Seth, D. A. Dale, et al., ApJ **751**, 100 (2012)
7. J. G. Hills, ApJ **235**, 986 (1980)
8. E. Bressert, N. Bastian, R. Gutermuth, et al., MNRAS **409**, L54 (2010)
9. Y. N. Efremov, B. G. Elmegreen, MNRAS **299**, 588 (1998)
10. B. G. Elmegreen, ApJ **672**, 1006 (2008)
11. J. M. D. Kruijssen, T. Maschberger, N. Moeckel, et al., MNRAS **419**, 841 (2012)
12. C. J. Lada, E. A. Lada, ARA&A **41**, 57 (2003)
13. M. Cottaar, M. R. Meyer, M. Andersen, P. Espinoza, A&A **539**, A5 (2012)
14. J. M. D. Kruijssen, MNRAS in press, arXiv:1208.2963 (2012)
15. M. R. Krumholz, C. F. McKee, ApJ **630**, 250 (2005)
16. P. Padoan, Å. Nordlund, ApJ **730**, 40 (2011)
17. A. Toomre, ApJ **139**, 1217 (1964)
18. B. G. Elmegreen, ApJ **577**, 206 (2002)
19. I. A. Bonnell, P. Clark, M. R. Bate, MNRAS **389**, 1556 (2008)
20. L. Spitzer, *Dynamical evolution of globular clusters* (Princeton, NJ, Princeton University Press, 1987, 191 p., 1987)
21. J. M. D. Kruijssen, F. I. Pelupessy, H. J. G. L. M. Lamers, et al., MNRAS **414**, 1339 (2011)
22. P. F. Hopkins, T. R. Lauer, T. J. Cox, et al., ApJS **181**, 486 (2009)
23. Bastian N., 2008, MNRAS, 390, 759
24. R. C. Kennicutt, Jr., ApJ **498**, 541 (1998)

Young Clusters in Nearby, Grand-Design Spirals

Preben Grosbøl and Horacio Dottori

Abstract The distributions of stellar clusters in 10 nearby, grand-design spiral galaxies were studied using deep JHK-maps from HAWK-I/VLT. The properties of the cluster complexes were analyzed using (H-K)–(J-H) diagrams. Two groups of clusters can be identified where the main one is associated to old clusters with low extinction while the other, less populated, consists of very young clusters (i.e. <10 Myr) with an average reddening around $A_V \sim 7^m$. The (J-K)–M_K diagrams show two branches of clusters populated by old and young clusters, respectively. The gap between them suggests a rapid reduction of extinction in the clusters at an early evolutionary phase. Statistical tests, taking the sample sizes into account, show that the cluster distribution functions (CDF) are different in arm and inter-arm regions, for strong spiral perturbations, with the former being shifted to brighter magnitudes by at least 0.4^m. Also the star formation rates in the strong arms were found to be 2–5 times higher than those in the inter-arm regions.

1 Introduction

Young objects (e.g. OB-associations and HII-regions) are frequently seen along the arms of grand-design spiral galaxies on visual images. They can be used to study star formation in these galaxies and its possible relation to the spiral structure [5, 7, 9]. Variable attenuation by dust in the arm regions makes it very difficult to compile an unbiased sample of young stellar clusters using visual bands whereas the low

P. Grosbøl (✉)
European Southern Observatory, Karl-Schwarzschild Str. 2, D-85748 Garching, Germany
e-mail: pgrosbol@eso.org

H. Dottori
Instituto de Física, Universidade Federal do Rio Grande do Sul, Av. Bento Gonçalves 9500, 91501-970 Porto Alegre, RS, Brazil
e-mail: dottori@ufrgs.br

D. Stamatellos et al. (eds.), *The Labyrinth of Star Formation*, Astrophysics and Space Science Proceedings 36, DOI 10.1007/978-3-319-03041-8_88,

extinction in near-infrared (NIR) bands allows an almost unbiased census. Many bright knots along arms were noticed [3] on NIR maps of spiral galaxies. They were identified as very young, stellar clusters based on their Br_γ emission detected on K-band spectra [2].

NIR images of 10 nearby, grand-design spirals were obtained with HAWK-I/VLT to study the distribution of clusters in such galaxies. The final images had a typical seeing of $0.4''$ and reached a 90 % completeness level around $K = 20^m$ allowing to probed clusters down to an absolute magnitude $M_K = -11^m$ (i.e. cluster masses $>10^4 M_\odot$) for most of the galaxies. With a linear resolution of around 40 pc, many sources detected are cluster complexes rather than individual clusters. This paper uses NGC 2997 as a standard case in the sample. A full description and analysis of the data for all 10 galaxies can be found in [1].

2 Colors and Magnitudes of Stellar Clusters

The basic properties of the clusters can be derived from their NIR colors and magnitudes. The distribution of the clusters in NGC 2997 is taken as an example using a distance of 19.2 Mpc. The (H-K)–(J-H) and (J-K)-M_K diagrams are given in Fig. 1 where the reddening vector for a dusty environment [4] is shown. Typical cluster evolutionary tracks (CET) for a single-burst stellar population (SSP) are also drawn for reference using both Padova [8] and Starburst99 [6] models where the latter includes nebular emission.

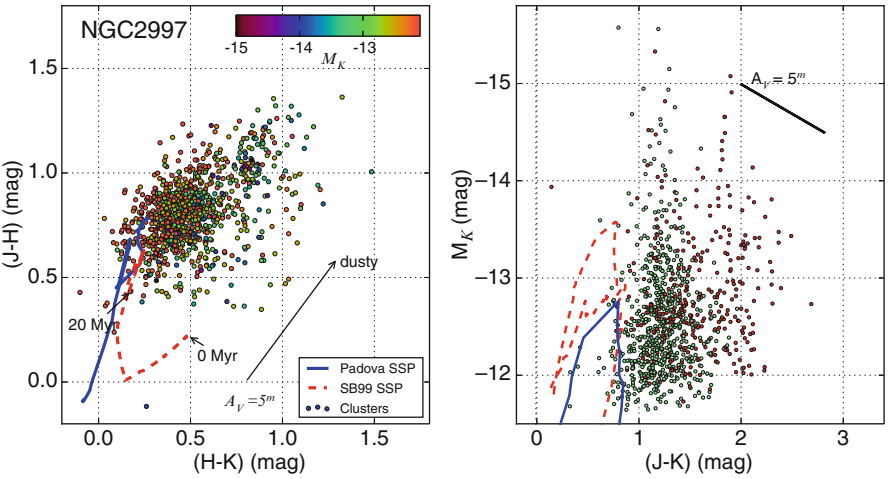

Fig. 1 Color-color and color-magnitude diagrams for stellar clusters in NGC 2997 with errors $\sigma(K) < 0.05^m$. *Left*: (H-K)–(J-H) diagram. *Right*: (J-K)–M_K diagram. A reddening vector for a dusty environment is shown for $A_V = 5^m$. Typical cluster evolutionary tracks for Padova and Starburst99 models are drawn for reference

The color-color diagram shows a main concentration of clusters around (0.4, 0.8) which is compatible with clusters older than 20 Myr and relative low internal extinction. Another smaller concentration is seen close to (0.8, 1.2) and is likely composed of very young clusters (i.e. <10 Myr) with high extinction since old clusters cannot be reddened to this part of the diagram applying any plausible extinction law. Also the color-magnitude diagram displays a bi-modal structure with a branch of older clusters near (J-K) $\approx 1.2^{m}$ while young ones are groups close to (J-K) $\approx 2.0^{m}$. Very few clusters are observed with (J-K) $< 0.8^{m}$ where young clusters are expected according to the CETs. This indicates that all young clusters have high internal extinction ($A_V \sim 5$–10^{m}) while old ones have much lower reddening. The gap between the two branches points to a very rapid reduction of internal extinction in the clusters during an early phase of their evolution.

3 Azimuthal Distribution

In the radial region with a strong, symmetric spiral pattern, most bright clusters are concentrated in the arm regions although star formation also occurs in between. The absolute magnitude M_K of the clusters is shown in Fig. 2 as a function of their azimuthal offset $\Delta\Theta$ relative to the arms using the phase of the m = 2 Fourier transform component of the azimuthal intensity variation in K as a reference. Almost

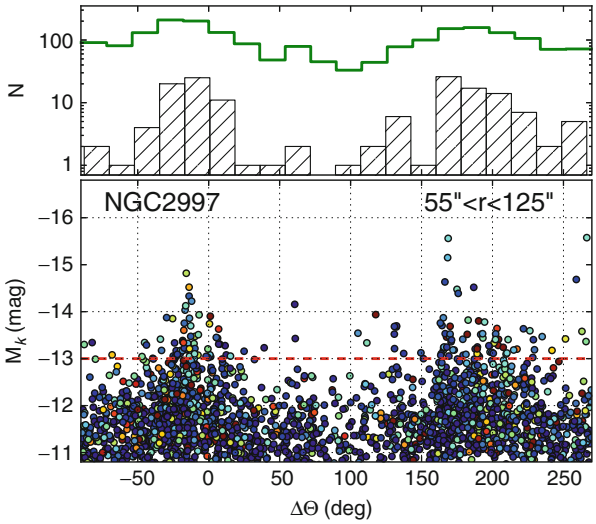

Fig. 2 Azimuthal distribution of M_K for clusters in NGC 2997 located in the radial region with a strong spiral pattern and errors $\sigma(K) < 0.2^{m}$. The azimuthal angle $\Delta\Theta$ is relative to the K band arms which are located at 0° and 180°. *Top*: histogram for all clusters (*full drawn line*) and for clusters with $M_K < -13^{m}$ (*hashed bins*). *Bottom*: actual distribution of M_K for the clusters

all the heaviest clusters (i.e. $M_K < -13^m$) are formed in the arms where also the total number of clusters is higher. A Kolmogorov-Smirnov test shows on a 99 % confidence level that the cluster populations in arm and inter-arm regions with strong perturbations cannot be taken from the same underlying distribution function. The 10 percentile points of the M_K distributions suggest that the clusters in the arms are at least 0.4^m brighter than those in the inter-arm regions. The star formation rate in the arms is also three times higher than in between.

4 Conclusions

The cluster populations in 10 nearby, grand-design spirals were studied in the NIR using deep images obtained with HAWK-I/VLT. Many sources detected may be cluster complexes rather than individual clusters due to the typical linear resolution of 40 pc. The integrated NIR colors of clusters change rapidly the first 10 Myr, partly due to nebular emission, which allows to identify young ones. Two groups of clusters are seen in the color-color diagrams namely one composed mainly of old clusters with low reddening and the other with young clusters having extinctions as high as $A_V \sim 10^m$. These groups are also seen in the (J-K)–M_K diagrams as two branches. The clear separation between them suggests a rapid reduction of extinction in the clusters at an early evolutionary phase. The distribution of clusters as a function of the azimuthal distance from the spiral arms, in the radial region with strong perturbations, reveals a higher star formation rate and a shift of the CDF to brighter luminosities in the arms compared to the inter-arm regions.

These findings suggest a scenario where star formation is significantly enhanced in the arms (e.g. due to higher gas densities and/or shocks). Newly formed clusters have high internal extinctions which is rapidly reduced at an early phase (i.e <10 Myr) possibly due to radiation pressure for hot stars [10] or supernovae.

References

1. Grosbøl, P. & Dottori, H. 2012, A&A, 542, A39
2. Grosbøl, P., Dottori, H., & Gredel, R. 2006, A&A, 453, L25
3. Grosbøl, P. & Patsis, P. A. 1998, A&A, 336, 840
4. Israel, F. P., van der Werf, P. P., Hawarden, T. G., & Aspin, C. 1998, A&A, 336, 433
5. Kim, W.-T. & Ostriker, E. C. 2006, ApJ, 646, 213
6. Leitherer, C., Schaerer, D., Goldader, J. D., et al. 1999, ApJS, 123, 3
7. Lin, C. C. & Shu, F. H. 1964, ApJ, 140, 646
8. Marigo, P., Girardi, L., Bressan, A., et al. 2008, A&A, 482, 883
9. Roberts, W. W. 1969, ApJ, 158, 123
10. Whitworth, A. 1979, MNRAS, 186, 59

Hierarchically Clustered Star Formation in the Magellanic Clouds

Dimitrios A. Gouliermis, Stefan Schmeja, Volker Ossenkopf, Ralf S. Klessen, and Andrew E. Dolphin

Abstract We present a cluster analysis of the bright main-sequence and faint pre–main-sequence stellar populations of a field $\sim 90 \times 90$ pc centered on the HII region NGC 346/N66 in the Small Magellanic Cloud, from imaging with HST/ACS. We extend our earlier analysis on the stellar cluster population in the region to characterize the structuring behavior of young stars in the region as a whole with the use of stellar density maps interpreted through techniques designed for the study of the ISM structuring. In particular, we demonstrate with Cartwrigth & Whitworth's $\mathcal{Q}$ parameter, dendrograms, and the Δ-variance wavelet transform technique that the young stellar populations in the region NGC 346/N66 are highly hierarchically clustered, in agreement with other regions in the Magellanic Clouds observed with HST. The origin of this hierarchy is currently under investigation.

1 Method: The Identification of Stellar Clusters

For the investigation of the clustering behavior of stars it is necessary to thoroughly characterize distinct concentrations of stars, which can only be achieved by the accurate identification of individual stellar clusters. Considering the importance

D.A. Gouliermis (✉) • R.S. Klessen
Zentrum für Astronomie der Universität Heidelberg, Institut für Theoretische Astrophysik, Albert-Ueberle-Str. 2, 69120 Heidelberg, Germany
e-mail: dgoulier@mpia-hd.mpg.de; klessen@uni-heidelberg.de

S. Schmeja
Zentrum für Astronomie der Universität Heidelberg, Astronomisches Rechen-Institut, Mönchhofstr. 12-14, 69120 Heidelberg, Germany

V. Ossenkopf
I. Physikalisches Institut der Universität zu Köln, 50937 Köln, Germany

A.E. Dolphin
Raytheon Company, PO Box 11337, Tucson, AZ 85734, USA

D. Stamatellos et al. (eds.), *The Labyrinth of Star Formation*, Astrophysics and Space Science Proceedings 36, DOI 10.1007/978-3-319-03041-8_89,

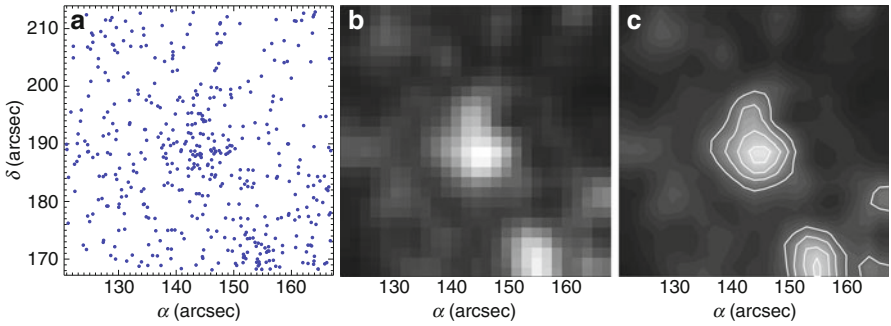

Fig. 1 Schematic of the star-count process. (**a**) The chart of an observed stellar sample. (**b**) The corresponding stellar density map, after counting stars in quadrilateral grid of elements (*pixels*) of size 1.8″ each, and after filtering the map with a Gaussian of FWHM $\simeq$ 2.8 px ($\sim 5''$). (**c**) The corresponding isodensity contour map. Isopleths at levels $\gtrsim 3\sigma$ are indicated with *white lines*

of this process, different identification methods were developed, which can be classified in two families. The first, represented by *friend of friend* algorithms and *cluster analysis* techniques, e.g., [2], are designed for limited samples of observed stars, and thus are based on linking individual stars into coherent stellar groups. These methods are recently superseded by *minimum spanning trees*, e.g., [1]. The second family of identification codes, represented by *nearest-neighbors* and *star-counts*, make use of surface stellar density maps constructed from rich observed stellar samples. Distinct stellar systems are identified as statistically significant over-densities in respect to the average stellar density in the observed regions, e.g., [5]. Tests on artificial clusters of various density gradients and shapes showed that the latter (density) techniques are more robust in detecting real stellar concentrations, provided that rich stellar samples are available [10]. A schematic representation of stellar density maps constructed with star-counts is shown in Fig. 1.

2 Data: Stellar Clustering in the Region NGC 346/N66

One of the most prominent bright stellar systems in the Small Magellanic Cloud (SMC) is the stellar association NGC 346, related to the HII region LHA 115-N66 [6], the brightest in this galaxy. This system appears in partially-resolved observations from the ground as a single stellar concentration, but recent imaging with the *Advanced Camera for Surveys* onboard the Hubble Space Telescope (HST) allowed the detection of sub-structure within the boundaries of the HII nebula. The images were collected within the HST GO Program 10248 and were retrieved from the HST Data Archive. Their photometry demonstrated that the faint young stellar populations in the region are still in their pre-main-sequence (PMS) phase, and revealed a plethora of sub-solar PMS stars [4]. Our *nearest-neighbor* cluster analysis

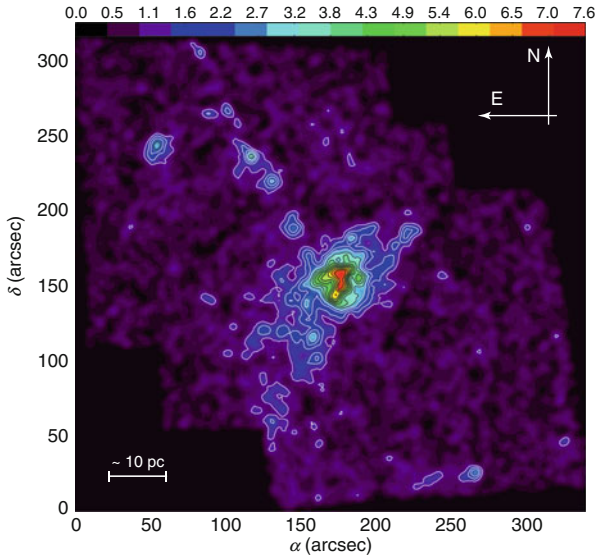

Fig. 2 Isodensity contour map from star-counts of the young bright main-sequence and faint PMS populations identified with HST/ACS in the region of NGC 346 in the SMC. *Lines* represent isopleths of significance $\gtrsim 1\sigma$. Apart from the dominating central large stellar aggregate, there are peripheral young sub-clusters, revealed as statistically important stellar concentrations. The central aggregate, denoted by the 1σ isopleth, encompass various distinct sub-groups, which appear at higher density thresholds. NGC 346 itself appears at $\gtrsim 3\sigma$ significance

of the observed young stellar populations, i.e., the bright main-sequence (down to $m_{555} \lesssim 21$) and the faint PMS stars, revealed a significant number of smaller, previously unresolved, young stellar sub-clusters [9]. This clustering behavior of young stars in NGC 346 is further demonstrated here by the stellar density contour map of Fig. 2, constructed with star-counts.

3 Results: Hierarchical Clustering of Young Stars

The map of Fig. 2 shows significant sub-structure, in particular within the 1σ boundaries of the central dominant stellar aggregate. This structuring behavior indicates hierarchy. The minimum spanning tree (MST) of the young stars in the whole region allows to determine the statistical $\mathcal{Q}$ parameter, introduced by Cartwright and Whitworth [3]. This parameter is a measure of the fractal dimension D of a stellar group, permitting to distinguish between centrally concentrated clusters and hierarchical clusters with fractal substructure. The application of the MST to our data shows that the region NGC 346/N66 is highly hierarchical with a $\mathcal{Q}$ that corresponds to a fractal dimension $D \simeq 2.5$.

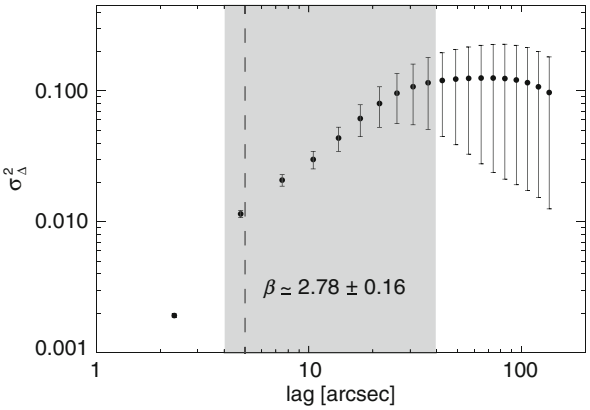

Fig. 3 The Δ-variance spectrum of the surface stellar density map of the entire region of NGC 346/N66. This analysis shows that the young stellar populations in this region are hierarchically structured up to length-scales of $\sim 40''$. The spectral index β is determined from the fit of the spectrum for data between lags $4''$ and $40''$ (indicated by the *gray shaded area*). The *dashed line* provides the used virtual beamsize ($5''$)

Constructing surface stellar density maps allows us to further characterize the clustering behavior of stars with the application of tools, which are originally designed for the study of the structuring of the interstellar medium (ISM), as observed at far-infrared or longer wavelengths. The so-called *dendrograms* are used for the visualization of hierarchy through structural trees [8]. The dendrogram of the stellar density map of NGC 346 demonstrates that the observed hierarchy is mostly due to the substructure in the dominant stellar aggregate. The Δ-variance analysis [7, 11] is a robust structure analysis method that measures the amount of structure on a given scale l. In principle the Δ-variance is directly related to the power spectrum of the map, and thus for a power law spectrum of index $-\beta$, Δ-variance also follows a power law, $\sigma^2_\Delta \propto l^\alpha$, with $\alpha = \beta - 2$. The application of the Δ-variance analysis on the surface stellar density map of NGC 346 verifies that indeed the clustering of the young stars in the region is self-similar (Fig. 3), with a spectral index $\beta \simeq 2.8$, corresponding to a fractal dimension $D = 2.6$ of the corresponding fractional Brownian motion structure [11], similar to that previously derived for Galactic molecular clouds. Self-similarity appears to brake, i.e., we find different hierarchical properties for the short-range scaling and the behavior at the overall scale of the region, at length-scales $l \geq 25$ px, corresponding to physical scales of $\sim 40''$ ($\sim$11 pc at the distance of the SMC).

Acknowledgements D.A.G., S.S. and V.O. kindly acknowledge support by the German Research Foundation (DFG) through grants GO 1659/3-1, SFB 881 and OS 177/2-1 respectively. Based on observations made with the NASA/ESA *Hubble Space Telescope*, obtained from the data archive at the Space Telescope Science Institute (STScI). STScI is operated by the Association of Universities for Research in Astronomy, Inc. under NASA contract NAS 5-26555.

References

1. Bastian, N., et al. 2009. Mon. Not. R. Astron. Soc. 392, 868
2. Battinelli, P., Efremov, Y., & Magnier, E. A. 1996. Astron. Astrophys. 314, 51
3. Cartwright, A., & Whitworth, A. P. 2004. Mon. Not. R. Astron. Soc. 348, 589
4. Gouliermis, D. A., et al. 2006. Astroph. J. Suppl. Ser. 166, 549
5. Gouliermis, D. A., et al. 2010. Astroph. J. 725, 1717
6. Henize, K. G. 1956. Astroph. J. Suppl. Ser. 2, 315
7. Ossenkopf, V., Krips, M., & Stutzki, J. 2008. Astron. Astrophys. 485, 917
8. Rosolowsky, E. W., et al. 2008. Astroph. J. 679, 1338
9. Schmeja, S., Gouliermis, D. A., & Klessen, R. S. 2009. Astroph. J. 694, 367
10. Schmeja, S. 2011, Astronomische Nachrichten, 332, 172
11. Stutzki J., et al. 1998. Astron. Astrophys. 336, 697

MYStIX First Results: Spatial Structures of Massive Young Stellar Clusters

Michael A. Kuhn, Adrian J. Baddeley, Eric D. Feigelson, Konstantin V. Getman, Patrick S. Broos, Leisa K. Townsley, Matthew S. Povich, Tim Naylor, Robert R. King, Heather A. Busk, Kevin L. Luhman, and MYStIX Collaboration

Abstract Observations of the spatial distributions of young stars in star-forming regions can be linked to the theory of clustered star formation using spatial statistical methods. The MYStIX project provides rich samples of young stars from the nearest high-mass star-forming regions. Maps of stellar surface density reveal diverse structure and subclustering. Young stellar clusters and subclusters are fit with isothermal spheres and ellipsoids using the Bayesian Information Criterion to estimate the number of subclusters. Clustering is also investigated using Cartwright and Whitworth's Q statistic and the inhomogeneous two-point correlation function. Mass segregation is detected in several cases, in both centrally concentrated and fractally structured star clusters, but a few clusters are not mass segregated.

1 MYStIX: Spatial Distributions of Young Stars

Spatial distributions of young stars in high-mass star-forming regions (HMSFR) may vary significantly in different regions (e.g. [3]) and provide information on the region's star-forming history and cluster dynamics (e.g. [10]). The Massive Young

M.A. Kuhn (✉) E.D. Feigelson • K.V. Getman • P.S. Broos • L.K. Townsley • M.S. Povich
H.A. Busk • K.L. Luhman
Department of Astronomy & Astrophysics, Pennsylvania State University,
525 Davey Laboratory, University Park, PA 16802, USA
e-mail: mkuhn1@astro.psu.edu; edf@astro.psu.edu

A.J. Baddeley
School of Mathematics and Statistics, University of Western Australia, Crawley, Australia

T. Naylor • R.R. King
School of Physics, University of Exeter, Stocker Road, Exeter, UK

MYStIX Collaboration
http://astro.psu.edu/mystix

D. Stamatellos et al. (eds.), *The Labyrinth of Star Formation*, Astrophysics and Space Science Proceedings 36, DOI 10.1007/978-3-319-03041-8_90,

stellar cluster Study in the Infrared and X-ray (MYStIX) reveals a variety of star-cluster morphologies in its sample of nearby Galactic HMSFRs; a project overview is provided by Eric Feigelson in this volume. Sources in the X-ray (*Chandra*), near-IR (UKIDSS), and mid-IR (*Spitzer*) and published OB stars are probabilistically classified into disk-free, disk-bearing, and protostellar MYStIX Probable Cluster Members (MPCM).

Here we make a comparative investigation of structure in young stellar clusters using modern statistical methods to characterize the distribution of stars. Empirical trends from the comparison of regions may reveal underlying astrophysical phenomena. Targets include the Orion Nebula Cluster (ONC), W 40, NGC 2264, NGC 6334, NGC 6357, the Eagle Nebula, three clusters in the Greater Carina Cluster (Tr 14-15-16), and the Trifid Nebula, in approximate order of distance. These clusters have a variety of sizes, richnesses, and morphologies: the nearest, the ONC, is a single cluster with ∼3,000 stars, while NGC 6357 is composed of three clusters each similar in richness to the ONC. For each region, the analysis includes 100–1,000 MPCM, and information about the total population may be inferred from the X-ray luminosity function (e.g. [5]).

2 Parametric Cluster Modeling

A variety of methods are used to map stellar distributions in clusters and identify subclusters (e.g. [6]). Here we assume that the YSO population is made up of subclusters that may be described by parametric models. For young stellar clusters, surface densities may be modeled by isothermal spheres, or, more generally, ellipsoids. For example, Hillenbrand and Hartmann [7] successfully fit the ONC with an elliptical model – this distribution function may be the result of dynamical relaxation; however, Galactic HMSFR are typically not old enough to have undergone two-body relaxation.

In statistical parlance, the collection of subcluster models is a finite mixture model; clustering properties are obtained through parameter estimation, and the number of clusters is determined by model selection. Models are fit by maximum-likelihood estimation (MLE) using the Bayesian Information Criterion, $\mathrm{BIC} = -2 \ln L + k \ln(n)$, where L is the likelihood, k is the number of parameters, and n is the number of points. The minimum BIC is found through numerical optimization.

The ONC and W 40 are both fit by a single ellipsoid; the core size and shape of the ONC match Hillenbrand and Hartmann's findings, and W 40 is roughly circular. Eleven components are found for NGC 6334, confirming the multiclusters of Feigelson et al. [4]. For NGC 6357, the furthest east cluster is fit by a single ellipsoid component, while the other two clusters are each fit by two components, confirming results of Wang et al. [13]. Figure 1 shows the negative correlation between subcluster core radius and central density for the modeled subclusters. This trend continues to hold true for subclusters in a single star-forming region. A similar

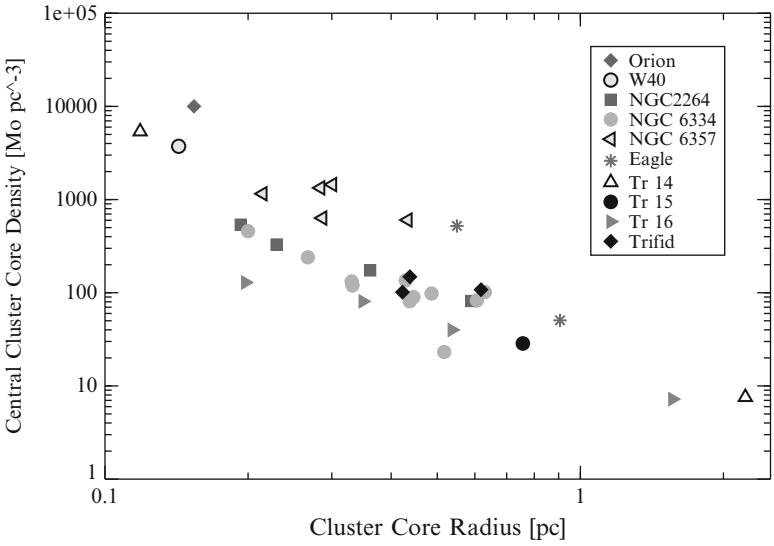

Fig. 1 Central densities and core radii for modeled subclusters in 10 MYStIX regions. Core radius is taken to be the average of the semi-major and semi-minor ellipse axes

trend was found by Pfalzner [11], and may be related to subcluster age, with older clusters being less dense. The trend is slightly shallower than the $\rho \propto r^{-3}$ line. W 40 and the ONC are densest clusters, while Tr 15 is one of the least dense.

3 Characterization of Subclustering

Summary statistics, such as the two-point correlation function, have also been used to characterize spatial structure of young stellar clusters. However, these methods have difficulty distinguishing between first moment (gradients in surface density) and second moment (clustering) phenomena in point processes [2]. The Q statistic [3] is cleverly designed to address this problem: it uses the mean edge length of the minimum spanning tree graph normalized by the average distance between points. The Q parameter is calibrated through simulations so that fractal-like distributions of stars have $Q < 0.8$, while centrally concentrated distributions of stars have $Q > 0.8$. For MYStIX clusters the values of Q, in order of increasing central concentration, are: 0.61 for NGC 2264, 0.62 for NGC 6357, 0.71 for NGC 6334, 0.81 for Trifid, 0.82 for Tr 16, 0.83 for Tr 14, 0.89 for Orion, 0.9 for Tr 15, 0.91 for Eagle, and 0.92 for W 40. This agrees with the expectation that single clusters, like W 40, would have high central concentration, while a cluster with high substructure, like NGC 2264 would be more fractal.

This problem may also be addressed using the inhomogeneous two-point correlation function [1]. In order to determine if the ellipsoid models are sufficient for describing the clustering of stars, the two-point correlation function is re-weighted by the subcluster mixture model, so that it will show clustering in the residuals that are not modeled. Values above the "null hypothesis" line indicate additional clustering, and statistical significance may be evaluated using the 99 % confidence envelope. For the two cases above, the results indicate that the centrally concentrated W 40 cluster is adequately described by the ellipsoid model, while the model for NGC 2264 does not capture additional clustering at small separations.

4 Mass Segregation

Mass segregation of young stellar clusters may be related to both initial conditions of star formation and cluster dynamics. For the MYStIX sample, stellar masses are inferred from dereddened J magnitudes, and spectroscopic catalogs of high-mass stars are taken from the literature.

A variety of methods have been used by astronomers to search for mass segregation in complex star-forming regions (e.g. [9]). Here, we apply a second-moment statistic, $Emark$ [12], designed to identify interaction between the position of a point and a value associated with it, here mass. The empirical $E(r)$ function gives the conditional expected value of mass when there is another star at projected distance r, and mass segregated clusters would have a decreasing slope. Statistical significance may be evaluated by generating a 99 % confidence envelope from simulations.

For the ONC, which is known to be mass segregated, this method shows a high significance detection. Mass segregation is also detected for W 40, confirming earlier results that assumed radial symmetry [8], and for NGC 2264, which has a fractal-like distribution of stars. Marginally significant mass segregation is found for NGC 6334, NGC 6357, and the Trifid Nebula. The Eagle Nebula shows no signs of mass segregation.

The statistics of spatial point processes are used to compare young stellar clusters that have a diverse range of sizes, morphologies, and richnesses. This analysis reveals trends, such as the density-size relation, that may have implications for the astrophysics of star cluster formation and evolution. In a future study that includes the full MYStIX sample, we will seek patterns involving (sub)cluster populations, densities, sizes, mass segregation, fractality, and ages.

Acknowledgements The MYStIX project is centered at Pennsylvania State University with the support of Chandra ACIS Team contract SV-74018, NSF AST-0809038, and NASA NNX09AC74G.

References

1. Baddeley, A., Møller, J., Waagepetersen, R.: Statistica Neerlandica, **54**, 329 (2000)
2. Bartlett, M. S. F.R.S.: Biometrika, **51**, 299 (1964)
3. Cartwright, A., & Whitworth, A.P.: MNRAS, **348**, 589 (2004)
4. Feigelson, E.D., Martin, A.L., McNeill, C.J., *et al*: AJ, **138**, 227 (2009)
5. Getman, K.V., Feigelson, E.D., Sicilia-Aguilar, A., *et al*: arXiv:1208.1471 (2012)
6. Gutermuth, R.A., Megeath, S.T., Myers, P.C., *et al*: ApJS, **184**, 18 (2009)
7. Hillenbrand, L.A., & Hartmann, L.W.: ApJ, **492**, 540 (1998)
8. Kuhn, M.A., Getman, K.V., Feigelson, E.D., *et al*: ApJ, **725**, 2485 (2010)
9. Küpper, A.H.W., Maschberger, T., Kroupa, P., & Baumgardt, H.: MNRAS, **417**, 2300 (2011)
10. Parker, R.J., & Meyer, M.R.: MNRAS, **427**, 637 (2012)
11. Pfalzner, S.: A&A, **498**, L37 (2009)
12. Schlather, M., Ribeiro, P. J. Jr, Diggle, P.: J. R. Statist. Soc. B, **66**, 79 (2004)
13. Wang, J., Townsley, L.K., Feigelson, E.D., *et al*: ApJS, **168**, 100 (2007)

Dynamics and Multiplicity of Young Star Clusters: Getting the Most Out of Single Epoch Radial Velocity Data

Michiel Cottaar

Abstract The velocity distribution of stellar systems in a cluster and its binary population provide powerful constraints on theories concerning the formation and subsequent evolution of these clusters. Unfortunately radial velocity variations due to binary orbits tend to mask the underlying velocity distribution for clusters with a small velocity dispersion. One possibility to solve this is to identify the spectroscopic binaries through multi-epoch observations. Here we present an alternative procedure. Even with only a single epoch of data, the radial velocity distribution due to the binary orbital motions is expected to be significantly different to the underlying velocity distribution, so it is possible to separate these distributions. This allows the underlying velocity distribution of a cluster, as well as the binary fraction, to be estimated from a single epoch of radial velocity data. We show that the measured velocity distribution depends only weakly on assumptions made about the binary properties. The procedure successfully reproduces the radial velocity dispersion of ~ 0.5 km/s in the open cluster NGC 188. A more complete discussion on the mechanics of this procedure, its accuracy, and the test run on NGC 188 can be found in Cottaar et al. (A&A 547:A35, 2012).

1 Introduction

The observed stellar radial velocity distribution in a cluster will be the convolution of two separate distributions. The first of these is the random movement of the single stars and multiple systems through the potential well of the cluster, which we refer to as the intrinsic velocity distribution. The second contribution comes from the orbital motions of observed stars in close multiple system. If the intrinsic velocity

M. Cottaar (✉)
Institute for Astronomy, ETH Zurich, Wolfgang-Pauli-Strasse 27, 8093 Zurich, Switzerland
e-mail: MCottaar@phys.ethz.ch

D. Stamatellos et al. (eds.), *The Labyrinth of Star Formation*, Astrophysics and Space Science Proceedings 36, DOI 10.1007/978-3-319-03041-8_91,

distribution is narrow (as expected for a low mass cluster), the second contribution will tend to dominate the observed velocity dispersion. If we are able to separate the intrinsic velocity distribution from the effect of the binary orbital motions, we can use the intrinsic velocity distribution to characterize the dynamical state of the cluster and constrain its evolution.

Correcting for the velocities of binary orbital motions is crucial to measure the very small intrinsic velocity dispersions ($<1\,\mathrm{km\,s^{-1}}$) observed in open clusters (e.g. [5, 6]) and which might exist in ultra-faint dwarf spheroidals (e.g. [10]). Even the larger velocity dispersions of young massive clusters (e.g. [2,8]) and some low-mass globular clusters (e.g. [1, 11, 15]) can be inflated by binaries. In local star-forming regions comparing the intrinsic velocity distribution of recently formed stars to the dynamical state of the gas is crucial to characterize how groupings or clusters of stars emerge from the molecular cloud from which they formed.

An often used method to extract the intrinsic velocity distribution is to identify spectroscopic binaries through multi-epoch observations (e.g. [6, 10]). The radial velocity distribution of the seemingly single stars (i.e. those stars without significant radial velocity variations) will be closer to the intrinsic velocity distribution. However, there will always be some unidentified spectroscopic binaries left, which will broaden the velocity distribution.

We investigate here an alternative strategy to separate the intrinsic velocity distribution from the contribution of the binary orbital motions using only a single epoch of radial velocity data. If the binary period, mass ratio, and eccentricity distributions are roughly known for the type of cluster being studied, this can be used to simultaneously fit the intrinsic velocity distribution and the fraction of binaries. This procedure was pioneered separately by Odenkirchen et al. [11] in their study of the globular cluster Palomar 5 and by Kleyna et al. [9] in their study of the Draco dwarf spheroidal.

2 Method

We use a maximum-likelihood procedure to simultaneously fit the intrinsic velocity distribution as well as the effect of binary orbital motions. To calculate the likelihood of reproducing the observations we take the following steps:

1. Define a distribution to be fitted to the intrinsic velocity distribution. This distribution can be as simple as a Gaussian to find the intrinsic velocity dispersion. On the other end of the spectrum this distribution could be derived from a complicated dynamical model, including rotation of the cluster, mass segregation, etc. For star i this distribution is denoted by $\mathscr{L}_{\mathrm{dyn,\,i}}(v)$.
2. Choose a set of assumptions to describe the period, mass ratio, and eccentricity distribution. This can be used to calculate the probability distribution ($\mathscr{L}_{\mathrm{bin,\,i}}(v_{\mathrm{bin}})$) for having velocity offset (v_{bin}) between the radial velocity of the primary star and the binary center of mass.

3. Combine these two distribution to calculate the likelihood of observing a given velocity, given that we do not know which stars are binaries or single (and hence the probability for a specific star to be a binary is set by the binary fraction $f_{\rm bin}$). This likelihood to observe the velocity $v_{\rm obs,\,i}$ for star i is given by:

$$\mathscr{L}_i(v_{\rm obs,\,i}) = (1 - f_{\rm bin})\mathscr{L}_{\rm dyn,\,i}(v_{\rm obs,\,i}) + f_{\rm bin}\int_{-\infty}^{+\infty} \mathscr{L}_{\rm dyn,\,i}(v_{\rm obs,\,i} - v_{\rm bin}) \cdot \mathscr{L}_{\rm bin,\,i}(v_{\rm bin})\,{\rm d}v_{\rm bin}, \quad (1)$$

where the first term gives the likelihood distribution for single stars and the second term the likelihood distribution for binaries.

The best-fit parameters are those for which the total likelihood to reproduce all the observed velocities is at its maximum. The uncertainties on these parameters can be calculated through Markov Chain Monte Carlo simulations.

3 NGC 188

We test the procedure described above on the old open cluster NGC 188. The dynamical state of the cluster was extensively studied by Geller et al. [6, 7] and Geller and Mathieu [4]. They presented 9,166 velocities gathered over a baseline of 11 years of 1,108 stars in the direction of NGC 188. Based on this full multi-epoch dataset they identified a large number of spectroscopic binaries [7]. Using the remaining velocities Geller & Mathieu [4] found an intrinsic velocity dispersion of $0.49^{+0.07}_{-0.08}$ km s^{-1} [see also 6]. In this section we will show that we can reproduce their intrinsic radial velocity distribution using only a single epoch of their data. Because of the large number of stars observed the statistical uncertainties are relatively small, so NGC 188 provides a stringent test on the accuracy of the procedure.

First we define a model for the intrinsic velocity distribution. A significant fraction of the observed stars are not cluster members, but fore- and background stars. Following Geller et al. [6] we model the intrinsic radial velocity distribution of the field star population and that of the cluster population with two Gaussian:

$$\mathscr{L}_{\rm dyn,\,i}(v_{\rm dyn}) = f_c \frac{1}{\sqrt{2\pi(\sigma_i^2 + \sigma_c^2)}} \exp\left(-\frac{(v_{\rm dyn} - \mu_c)^2}{2(\sigma_i^2 + \sigma_c^2)}\right) + (1 - f_c)\frac{1}{\sqrt{2\pi(\sigma_i^2 + \sigma_f^2)}} \exp\left(-\frac{(v_{\rm dyn} - \mu_f)^2}{2(\sigma_i^2 + \sigma_f^2)}\right), \quad (2)$$

where f_c is the probability of an observed stars to be a cluster member (i.e. the fraction of cluster members), σ_c and μ_c are respectively the velocity dispersion and

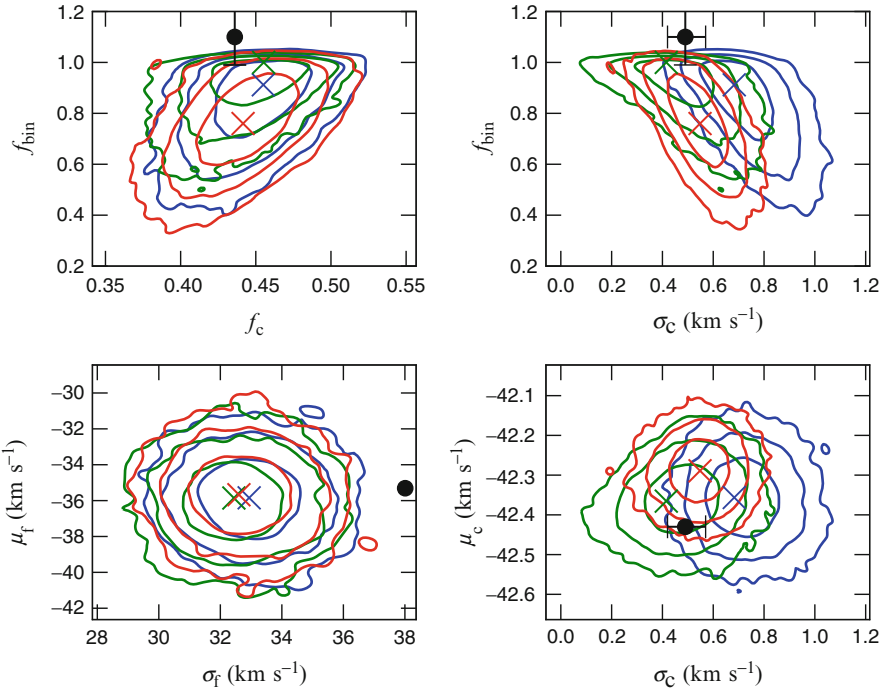

Fig. 1 Posterior probability distributions of the free parameters in the model, enclosing 68.2, 95.4, and 99.7 % (i.e. 1, 2, and 3 σ) of the total probability. The six free parameters are the binary fraction ($f_{\rm bin}$), the fraction of cluster members ($f_{\rm c}$), the cluster velocity dispersion ($\sigma_{\rm c}$), the cluster mean velocity ($\mu_{\rm c}$), the field velocity dispersion ($\sigma_{\rm f}$) and the field mean velocity ($\mu_{\rm f}$). The different colors refer to the three different single-epoch radial velocity distributions. The literature values for these parameters, derived from proper motion analysis [12] and the multi-epoch radial velocity data [4, 6] have been plotted as *black dots*. If the error bars are given, they have also been plotted

mean velocity of the cluster members, and σ_f and μ_f are the velocity dispersion and mean velocity of fore- and background stars. These five parameters will be fitted in addition to the binary fraction. Finally σ_i is the measurement error in the observed velocity of star i.

We assume the observed stars have the same binary properties as the solar-type field stars [13, 14]. Even though we expect the binary properties to have changed due to dynamical interactions over the lifetime of the cluster, we still find that the assumed binary properties provide a good fit to the observed velocity distribution, as long as the binary fraction is kept as a free parameter.

From the full multi-epoch dataset we have drawn three single-epoch datasets, containing a single velocity for every of the 1,108 stars. The 1, 2, and 3 σ uncertainties on the best fit parameters to these three single-epoch datasets are illustrated in Fig. 1 with the three colors representing the three single-epoch datasets.

Except for the field velocity dispersion, there is a good overlap in the best-fit parameters derived from the full multi-epoch dataset [black dots taken from 4,6,12] and the parameters we derived for the single-epoch datasets.

We finally find that the intrinsic velocity distributions found for the three single-epoch datasets are indistinguishable from the velocities of the seemingly single stars [which do not show radial velocity variations over more than a year, 6].

References

1. Blecha, A., Meylan, G., North, P., & Royer, F. 2004, A&A, 419, 533
2. Bosch, G., Terlevich, E., & Terlevich, R. 2009, in IAU Symposium, Vol. 256, IAU Symposium, ed. J. T. van Loon & J. M. Oliveira, 317–322
3. Cottaar, M., Meyer, M. R., & Parker, R. J. 2012, A&A, 547, A35
4. Geller, A. M. & Mathieu, R. D. 2011, Nature, 478, 356
5. Geller, A. M., Mathieu, R. D., Braden, E. K., et al. 2010, AJ, 139, 1383
6. Geller, A. M., Mathieu, R. D., Harris, H. C., & McClure, R. D. 2008, AJ, 135, 2264
7. Geller, A. M., Mathieu, R. D., Harris, H. C., & McClure, R. D. 2009, AJ, 137, 3743
8. Gieles, M., Sana, H., & Portegies Zwart, S. F. 2010, MNRAS, 402, 1750
9. Kleyna, J., Wilkinson, M. I., Evans, N. W., Gilmore, G., & Frayn, C. 2002, MNRAS, 330, 792
10. McConnachie, A. W. & Côté, P. 2010, ApJL, 722, L209
11. Odenkirchen, M., Grebel, E. K., Dehnen, W., Rix, H.-W., & Cudworth, K. M. 2002, AJ, 124, 1497
12. Platais, I., Kozhurina-Platais, V., Mathieu, R. D., Girard, T. M., & van Altena, W. F. 2003, AJ, 126, 2922
13. Raghavan, D., McAlister, H. A., Henry, T. J., et al. 2010, ApJS, 190, 1
14. Reggiani, M. M. & Meyer, M. R. 2011, ApJ, 738, 60
15. Sollima, A., Nipoti, C., Mastrobuono Battisti, A., Montuori, M., & Capuzzo-Dolcetta, R. 2012, ApJ, 744, 196

The Dynamics of an Expanding OB Association

Nicholas J. Wright, Herve Bouy, Jeremy J. Drake, Janet E. Drew, Mario Guarcello, and David Barrado y Navacués

Abstract We present 3-dimensional kinematical observations of the massive OB association Cygnus OB2 to identify the mechanisms responsible for disrupting young star clusters. The picture revealed by these observations is of a highly-substructured, dynamically unmixed OB association that does not exhibit the position–velocity correlations predicted by the theories of infant mortality or tidal stripping. These observations would appear to support a picture of hierarchical star formation.

1 Introduction

It has been known for many years that there is a lack of old clusters compared to an extrapolation of the young cluster population. This was first recognized by Oort [17] and exacerbated by the discovery of large numbers of embedded clusters in the near-IR [13]. Based on this it became clear that the vast majority (at least 90 %) of clusters disperse within 10 Myr [14].

N.J. Wright (✉) • J.J. Drake
SAO-Harvard-Smithsonian Center for Astrophysics, 60 Garden St., Cambridge, MA 02138, USA
e-mail: nwright@cfa.harvard.edu

M. Guarcello
Harvard-Smithsonian Center for Astrophysics, 60 Garden St., 02138 Cambridge, MA, USA

H. Bouy
CAB-LAEFF, Apartado 78, E-28691 Villanueva de la Cañada, Madrid, Spain

J.E. Drew
CAR/STRI, University of Hertfordshire, College Lane, Hatfield AL10 9AB, UK

D. Barrado y Navacués
Centro de Astrobiologa (INTA-CSIC), PO Box 78, 28691 Villanueva de la Cañada, Spain

D. Stamatellos et al. (eds.), *The Labyrinth of Star Formation*, Astrophysics and Space Science Proceedings 36, DOI 10.1007/978-3-319-03041-8_92,

This is usually explained by the process of *infant mortality*, whereby residual gas left over from star formation is forced out of the cluster via feedback from massive stars, leaving the stellar part of the system in a super-virial state and prone to dissolution. This long-established theoretical framework assumes that the cluster was in virial equilibrium prior to gas expulsion and identifies the star formation efficiency (the fraction of gas turned into stars, ∼5–10 %) as the dominant factor in determining cluster stability [1, 10]. This has recently been called into question: numerous theoretical works have suggested other parameters of equal importance such as the spatial distribution of stars at birth [15], the rate of residual gas expulsion [3], and the initial virial state of the cluster [16]. Overall, these studies suggest that the influence of gas expulsion may have been over-estimated and that many clusters may be stable from a young age.

An alternative theory, first put forward by Spitzer [18] to explain the lack of Gyr-old clusters, is that clusters are tidally heated by passing interstellar clouds. This has recently been used to explain the disruption of very young clusters by their parental giant molecular cloud (GMC) [7, 12]. It has been argued to be an effective disruption mechanism for young clusters since the average cloud density in GMCs exceeds the tidal density from the galactic potential by an order of magnitude or more [7].

A third and important explanation for the lack of mature, gravitationally-bound clusters is that the majority of young clusters are not gravitationally bound, one of the fundamental assumptions of the theory of infant mortality. The discovery of vast numbers of near-IR embedded clusters led many authors to conclude that all stars formed in bound clusters [6, 13, 14]. However many of these clusters may just be stellar overdensities and may not be gravitationally bound. In their study of the spatial distribution of young stars, Bressert et al. [5] could find no evidence for a preferred scale for clustering that would be apparent if stars preferentially form in clusters (see also [8]). These findings support the view that star formation is hierarchical with no preference for scale and therefore most stars may not form in bound groups [2]. If the majority of stars do not form in bound clusters, then an efficient disruption mechanism may not be required.

To answer the question of how star clusters are disrupted, and thereby also address the question of whether all stars form in clusters, we must study a cluster in the process of being disrupted. This is difficult because the majority of clusters are either still embedded in their GMC (e.g. the Orion Nebular Cluster) or if they have already removed their residual gas they are often found to be gravitationally bound. This intrinsic bias is because clusters that display a clear overdensity and a spherical shape but which have also emerged from their parental GMC *must* be bound if they have retained their clustered morphology. To study a cluster in the act of dispersal and therefore probe the mechanisms responsible we should not study star clusters but instead study OB associations, less dense groups of stars that have been suggested to be the result of expanded clusters [13].

2 Observations

By studying the dynamics of an expanding OB association we intend to test theories for how star clusters are disrupted and probe the physical mechanisms at work. Radial velocities (RVs) are useful for this, but more important are proper motions (PMs) that provide a vital correlation between position and velocity that is necessary to distinguish between theories. For infant mortality we should see a radial dispersion of stars moving away from the original cluster center(s), whereas tidal heating predicts velocities distributed along a specific axis [12]. Hierarchical star formation should result in almost random motions based on the original spatial distribution.

We have targeted the massive OB association Cygnus OB2, a post-gas expulsion association believed to be in the process of dispersing. It is the most massive group of young stars within 2 kpc, with a mass of $M_\star \sim 3 \times 10^4\,\mathrm{M}_\odot$ [21], similar to the most massive clusters in our galaxy. With an age of 3–5 Myr [9, 21] it is old enough to be dynamically evolved, but with evidence for current star formation on the periphery [19, 22]. Members of the association are selected using X-ray observations [20] since young stars are more X-ray luminous that main-sequence stars.

RVs were obtained from multi-epoch (to remove close binaries) MMT/Hectospec spectroscopy of the Ca II triplet with an accuracy of ∼3–5 km/s. PMs are calculated from multi-epoch images spanning a 7–8 year baseline using the DANCE (Dynamical Analysis of Nearby ClustErs, [4]) program. This results in an accuracy of <1 mas/year, equivalent to ∼3 km/s at the distance of Cyg OB2. These velocities are sufficient to resolve internal substructure in a cluster with $\sigma_r \sim 10$ km/s [11].

3 Results

Initial results from 277 stars with PMs and 425 stars with RVs give velocity dispersions of $(\sigma_\alpha, \sigma_\delta, \sigma_r) = (15.6, 12.8, 13.7)$ km/s, equivalent to $\sigma_{3D} = 24.4$ km/s. This implies a virial mass of $M_{dyn} = 9 \times 10^5\,\mathrm{M}_\odot$, significantly larger than the stellar mass, $M_\star = 3 \times 10^4\,\mathrm{M}_\odot$ [21] thereby confirming that the association is gravitationally unbound. Assuming that the stars and the gas were originally in virial equilibrium this implies a star formation efficiency of 3.3 %, a reasonable value.

Figure 1 shows the preliminary distribution of PMs in the center of Cyg OB2. Immediately apparent is that the majority of stars are moving inwards, not outwards as one would expect for an expanding association. This would appear to argue that infant mortality and tidal stripping are not responsible for disrupting Cyg OB2,

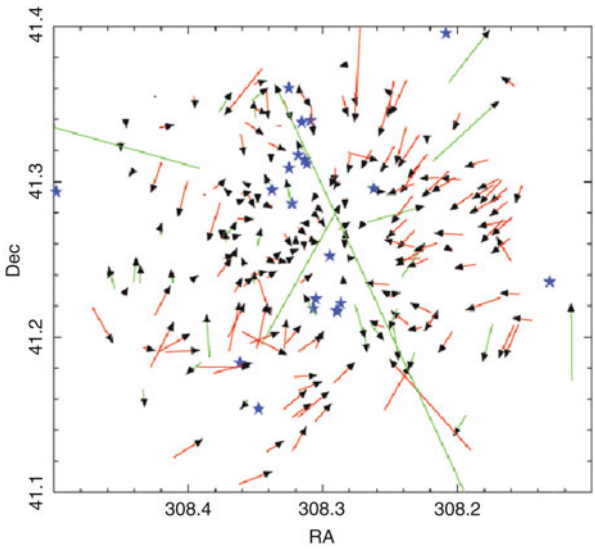

Fig. 1 PM velocity diagram in the center of Cyg OB2 (vectors show motion in 10^4 years). Known O-type stars are shown as *blue stars*. Vectors are color-coded for motion towards (*red*) or outwards (*green*) from the central trapezium of O stars (RA = 308.3, DEC = 41.2). These results are preliminary and subject to changes as the analysis is refined

certainly if the association was originally one or two dense clusters. A simple interpretation of the inwards motion is that the association is collapsing under gravity, though this is unlikely given the masses estimated and would require verification from radial velocities. Also of note is the considerable dynamical substructure, with many groups of stars with similar velocities. The substructure suggests the association is not dynamically evolved, despite its age.

4 Conclusions

We present 3-dimensional dynamical observations of Cyg OB2 to elucidate the physical mechanism that led to the association being gravitationally unbound. The overall picture of these observations is a highly substructured, dynamically unmixed association that does not exhibit the position–velocity correlations expected for the theories of infant mortality or tidal stripping. These observations appear to support a picture of hierarchical star formation, in which stars are not born in dense clusters, but in looser associations that retain substructure as they dynamically evolve. Further observations in Cyg OB2 and other regions are necessary to confirm this.

References

1. Bastian, N., Goodwin, S.P. 2006, MNRAS, 369, L9.
2. Bastian, N., et al. 2007, MNRAS, 379, 1302.
3. Baumgardt, H., Kroupa, P. 2007, MNRAS, 380, 1589.

4. Bouy, H., et al. 2011, Stellar Clusters & Associations, 103.
5. Bressert, E., et al. 2010, MNRAS, 409, L54.
6. Carpenter, J.M. 2000, AJ, 120, 3139.
7. Elmegreen, B.G., Hunter, D.A. 2010, ApJ, 712, 604.
8. Gieles, M., Portegies Zwart, S.F. 2011, MNRAS, 410, L6.
9. Hanson, M.M. 2003, ApJ, 597, 957.
10. Hills, J.G. 1980, ApJ, 235, 986.
11. Kiminki, D.C. et al. 2007, ApJ, 664, 1102.
12. Kruijssen, J.M.D., et al. 2012, MNRAS, 419, 841.
13. Lada, C.J., Lada, E.A. 1991, ASPC, 13, 3L.
14. Lada, C.J., Lada, E.A. 2003, ARAA, 41, 57.
15. McMillan, S.L.W., Vesperini, E., Portegies Zwart, S.F. 2007, ApJ, 655, L45.
16. Offner, S.S.R., Hansen, C.E., Krumholz, M.R. 2009, ApJ, 704, L124.
17. Oort, J.H. 1958, Ric. astr. Specola astr. Vatic. 5, 63. (Stellar Populations. Ed. DJK O'Connell.)
18. Spitzer, L. 1958, ApJ, 127, 17.
19. Vink, J.S. et al. 2008, MNRAS, 387, 308.
20. Wright, N.J., Drake, J.J. 2009, ApJSS, 184, 84.
21. Wright, N.J., Drake, J.J., Drew, J.E., Vink, J.S. 2010, ApJ, 713, 871.
22. Wright, N.J., et al. 2012, ApJL, 746, L21.

IRAS 20050+2720: Clustering of Low Mass Stars

H.M. Günther, S.J. Wolk, R.A. Gutermuth, J. Forbrich, Nicholas J. Wright, L. Allen, Tyler L. Bourke, S.T. Megeath, J.L. Pipher, and B. Spitzbart

Abstract IRAS 20050+2720 is a young star forming region at a distance of 700 pc with a mass of 430 $M_{\odot}$, but without apparent high mass stars. We characterize the distribution of young stellar objects (YSOs) in this region, which lacks high UV flux, and compare evolutionary trends with other young star forming clusters. We present results of our multiwavelength study of IRAS 20050+2720 which includes observations by Chandra, Spitzer, and 2MASS and UBVRI photometry. In total, about 300 YSOs in different evolutionary stages are found. We newly identify a second cluster core, which consists mostly of class II objects, about 2 pc from the center of the cloud. YSOs of earlier evolutionary stages are more clustered than more evolved objects. The X-ray luminosity function (XLF) of IRAS 20050+2720 is roughly lognormal, but steeper than the XLF of the more massive Orion nebula complex. The dust in IRAS 20050+2720 seems altered compared to the ISM.

Stars form in large gas and dust clouds in our galaxy through gravitational collapse. Initially, this infall is radial. These young stellar objects (YSOs) are deeply embedded. Later, the infall from the envelope forms an accretion disk. In this stage

H.M. Günther (✉) • S.J. Wolk • J. Forbrich • N.J. Wright • T.L. Bourke • B. Spitzbart
SAO-Harvard Center for Astrophysics, 60 Garden St, Cambridge, MA 02138, USA
e-mail: hguenther@cfa.harvard.edu

R.A. Gutermuth
Department of Astronomy, University of Massachusetts, Amherst, MA 01003, USA

L. Allen
National Optical Astronomy Observatory, Tucson, AZ, USA

S.T. Megeath
Ritter Observatory, Department of Physics and Astronomy, University of Toledo, Toledo, OH, USA

J.L. Pipher
University of Rochester, Rochester, NY, USA

D. Stamatellos et al. (eds.), *The Labyrinth of Star Formation*, Astrophysics and Space Science Proceedings 36, DOI 10.1007/978-3-319-03041-8_93,

YSOs are called Class I sources and can be found in the IR. As the envelope disperses, the YSOs become visible as class II sources. Eventually, mass accretion on the star and (possibly) planets and photoevaporation deplete the disk until it becomes undetectable in the IR. These stars are called class III sources. Because they are young and rapidly rotating, they are very active and often bright in X-rays.

We observed IRAS 20050+2720 with *Chandra* and *Spitzer* and performed UBVRI photometry from the Fred-Laurence-Whipple observatory. Together with 2MASS (see Skrutskie et al. [2]) we can thus classify the YSOs in IRAS 20050+2720 with the algorithm of Gutermuth et al. [1] for class I and II sources and use *Chandra* to identify the remaining YSOs. We find 70 class I sources, 185 class II sources and 42 class III YSOs. On the sky they can be separated into two cluster cores: One in the north-east, that is surrounded by continuum dust emission but does not contain any class I sources and one in the south-west, that does not show dust emission, but contains objects of all evolutionary stages. Interestingly, the cluster core in the north-east appears younger on a HR diagram.

The spatial analysis and the separation of different cluster cores is based on a Minimum Spanning Tree (MST). A MST is the shortest graph that connects all sources. We calculate the distribution of the branch lengths for the different classes and find that class III sources are much less clustered than class I and II sources.

The sources of different classes also differ in their X-ray temperature. Soft X-rays are absorbed by low column densities, thus in more absorbed sources we only see hotter plasma temperatures. Still, even in a sub-sample with comparable absorption the class II sources seem to be hotter than class III sources.

We correct the observed X-ray fluxes for absorption and construct the total X-ray luminosity function (XLF) for this cluster. It has been suggested, that star forming regions could have an universal XLF, but comparing our data to published XLFs of some other star forming regions we find significant differences.

Last, the X-ray absorbing column density N_H can be compared to the optical or IR reddening A_K. We do not see significant differences between the cluster cores or between different classes within IRAS 20050+2720, but find an N_H/A_K ratio that is smaller than the canonical value for the ISM. This ratio is influenced by the gas-to-dust ratio and the distribution of grain sizes in the absorbing medium.

More details in IRAS 20050+2720 can be found in a paper we submitted to AJ.

Acknowledgements This work is funded by Chandra award GO6-7017X.

References

1. Gutermuth, R. A., et al. 2008, ApJ, 674, 336
2. Skrutskie, M. F., et al. 2006, AJ, 131, 1163

Clusters Within Clusters: Star Formation in RCW 38

Elaine Winston, S.J. Wolk, Tyler L. Bourke, S.T. Megeath, R.A. Gutermuth, and B. Spitzbart

Abstract *Spitzer* & *Chandra* observations of the massive star forming region RCW 38 identify 624 young stellar objects (YSOs) in four subclusters surrounding the previously known cluster centred on the O5.5 binary IRS 2.

1 Spitzer & Chandra Observations of Subclustering in RCW 38

At a distance of 1.7 kpc, containing 20–40 OB stars, RCW 38 is one of the richest nearby high mass regions, with an estimated cluster membership of 10^4 members. Previous studies focused on the IRS 2 region, the central O5.5 binary. Spitzer & Chandra observations provide greater coverage, showing the region is larger than previously thought. The mid-IR datasets identifies 624 YSOs, with 226 detected in X-rays. The YSOs were of evolutionary class: 23 class I, 90 flat spectrum, 437 class II, and 74 class III.

E. Winston (✉)
Research and Scientific Support Division, European Space Agency, Keplerlann 1, Noordwijk, The Netherlands,
e-mail: ewinston@rssd.esa.int

S.J. Wolk • T.L. Bourke • B. Spizbart
SAO-Harvard-Smithsonian Center for Astrophysics, 60 Garden St., Cambridge, MA 02138, USA

S.T. Megeath
Ritter Observatory, Department of Physics and Astronomy, University of Toledo, 2801 W. Bancroft Ave., Toledo, OH 43606, USA

R.A. Gutermuth
Department of Astronomy, University of Massachusetts, Amherst, MA 01003, USA

D. Stamatellos et al. (eds.), *The Labyrinth of Star Formation*, Astrophysics and Space Science Proceedings 36, DOI 10.1007/978-3-319-03041-8_94,

Table 1 Properties of RCW 38 subclusters

Cluster	Total	C0/I[a]	FS	CII	CIII	Var	OB	A_K	$^{dered}\alpha_{irac}$	Protostars (%)	Variables (%)
NE	11	1	1	9	...	1	1	0.684 ± 0.382	-0.996 ± 0.802	18.2 ± 12.8	9.1 ± 9.1
NW	62	...	9	53	...	8	1	0.608 ± 0.225	-1.078 ± 0.671	14.5 ± 4.8	12.9 ± 4.5
SW	41	...	4	37	...	3	1	0.530 ± 0.244	-1.146 ± 0.541	9.7 ± 4.9	7.3 ± 4.2
CN	255	15	39	154	47	24	6	0.836 ± 0.747	-0.957 ± 1.295	25.9 ± 3.5	9.4 ± 1.9
Dist.	222	7	31	157	27	36	20	0.701 ± 0.448	-1.056 ± 0.808	19.5 ± 3.2	16.2 ± 2.7

[a] *C0/I* class 0/I, *FS* flat spectrum, *CII* class II, *CIII* class III, *Var* variables, *OB* OB star candidates, A_K extinction at K-band, $^{dered}\alpha_{irac}$ slope of IRAC SED

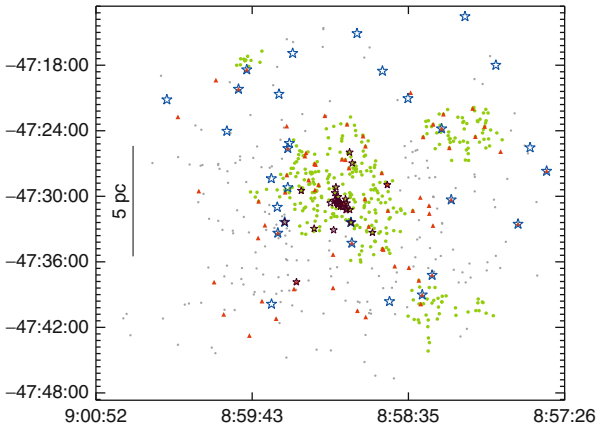

Fig. 1 Distribution of YSOs in RCW 38 showing the subclusters, O star and variable candidates. *Dots* indicate young stars: clustered YSOs in *green*, distributed YSOs in *gray*. *Triangles* indicate the variables. *Blue open stars* are candidate O stars in the field, *black open stars* the candidate OB stars previously identified. The fifth subcluster, DBS2003-124 is not included on the plot

Five subclusters are identified; the central region is surrounded by three subclusters & distributed young stars. A fifth, more distant, subcluster is identified in IRAC 3.6 & 5.8 μm: IR cluster DBS2003-124, NE of the RCW 38 complex with 33 members. The spatial distribution of the cluster was found to be factually subclustered, with a Q-parameter of 0.41. The NW subcluster is identified with a near-IR star cluster: Obj 36. Cloud morphology, YSO distribution, and extinction indicate that these regions are subclusters of RCW 38. The properties of the four central subclusters and the distributed population are presented in Table 1. Variable sources were identified in each of these subclusters. O star candidates are found in each subclusters, and as part of the distributed population. Figure 1 shows the spatial distribution of the young stellar objects identified in the RCW 38.

Stellar Clusters in the Inner Galaxy and Their Correlation with ATLASGAL

Esteban F.E. Morales, Friedrich Wyrowski, Karl M. Menten, and Frédéric Schuller

Abstract We present the results of a forthcoming paper, in which we study statistically all open and embedded clusters known so far in the inner Galaxy, investigating particularly their interaction with the surrounding molecular environment. Using a merged list of stellar clusters from different literature catalogs (complemented with our own search for embedded clusters on the GLIMPSE data) and the ATLASGAL submm continuum survey, we defined a morphological evolutionary sequence with decreasing correlation with ATLASGAL emission. Based on this sequence, we could classify the sample in embedded and open clusters, study separately their distance distribution, completeness, and age distribution, and thus improve our understanding of how embedded clusters evolve towards the production of field stars or bound open clusters.

Stars are born correlated in space and time within the dense clumps of the giant molecular clouds, constituting young stellar agglomerates known as *embedded clusters*. Once expelled the parental gas through stellar feedback, they evolve towards the production of bound open clusters only under special conditions. In this contribution, we summarize the main results of a forthcoming paper [1], in which

E.F.E. Morales (✉)
Max-Planck-Institute for Astronomy, Heidelberg, Germany

Max-Planck-Institut für Radioastronomie, Bonn, Germany
e-mail: morales@mpia.de

F. Wyrowski • K.M. Menten
Max-Planck-Institut für Radioastronomie, Bonn, Germany

F. Schuller
Max-Planck-Institut für Radioastronomie, Bonn, Germany

European Southern Observatory, Santiago, Chile
e-mail: schuller@mpifr.de

D. Stamatellos et al. (eds.), *The Labyrinth of Star Formation*, Astrophysics and Space Science Proceedings 36, DOI 10.1007/978-3-319-03041-8_95,

we study observationally all embedded clusters (ECs) and open clusters (OCs) known so far in the inner Galaxy, particularly their interaction with the surrounding molecular environment.

We first compiled a merged full-sky list of 3,904 clusters from optical and infrared clusters catalogs in the literature, including 75 new embedded clusters discovered by us in the GLIMPSE mid-infrared data after applying a red-color criterion. From this list, 695 clusters are within the Galactic range $|l| \leq 60°$ and $|b| \leq 1.5°$, where the ATLASGAL survey [2] was used to search for correlations with 870 μm dust continuum emission tracing dense molecular gas.

Based on the morphology of the submm emission and, for exposed clusters, on the agreement of the clump kinematic distances and cluster stellar distances, we defined an evolutionary sequence with decreasing correlation with ATLASGAL emission: deeply embedded clusters (EC1), partially embedded clusters (EC2), emerging exposed clusters (OC0), totally exposed clusters still physically associated with molecular gas in their surrounding neighborhood (OC1), and all the remaining exposed clusters, with no correlation with ATLASGAL emission (OC2). We found that this sequence correlates well with other observational indicators of evolution, such as UV-excited PAH emission and HII regions tracing stellar feedback in the first four evolutionary stages, and infrared dark clouds probing a very early phase within the EC1 type. We also found that an OC defined observationally in this way (clusters with types OC0, OC1 and OC2 and confirmed as real clusters) is equivalent to the physical concept of open cluster (a bound exposed cluster) for ages in excess of $\sim$16 Myr; some observed OCs younger than this limit can be actually unbound associations.

By fitting the observed heliocentric distance distribution for open and embedded clusters within the ATLASGAL range, we found that our OC and EC samples are roughly complete up to a distance of $\sim$1 and $\sim$1.8 kpc, respectively, after which the completeness decays exponentially.

From a subsample of 23 embedded clusters with available age estimates, we derived an upper limit of 3 Myr for the duration of the embedded phase. The much higher number of open clusters with available age estimates allowed us to study the OC age distribution within 3 kpc from the Sun, which we used to fit the theoretical parametrization of [3] of different disruption mechanisms for bound open clusters. We found an excess of observed young OCs respect to the fit, thought to be a combined effect of age dependent incompleteness and presence of unbound associations for ages $\lesssim$16 Myr. We derived formation rates of 0.54, 1.18, and 6.50 Myr^{-1} kpc^{-2} for bound open clusters, all observed young exposed clusters, and embedded clusters, respectively, which translates into a EC dissolution fraction of 88 ± 8 %. The obtained value is in excellent agreement with that obtained by Lada and Lada [4]. However, the explanation proposed at that time for this high fraction has been changed (or extended) considerably in the recent years. As we review in [1], depending on the physical conditions of each individual system and its environment, one or some combination of following effects could be the dominant cause: dissolving associations from birth, merging of subclusters, gas expulsion, tidal shocks from environment, and collisional N-body dynamics of subclusters.

References

1. E.F.E. Morales, F. Wyrowski, F. Schuller, K.M. Menten, A&A **560**, A76 (2013).
2. F. Schuller, K.M. Menten, Y. Contreras, et al., A&A **504**, 415 (2009).
3. H.J.G.L.M. Lamers, M. Gieles, A&A **455**, L17 (2006).
4. C.J. Lada, E.A. Lada, ARA&A **41**, 57 (2003).

An HST Study of Star Formation in Star-Burst Clusters

Giacomo Beccari, Guido De Marchi, Nino Panagia, Martino Romaniello, Elena Sabbi, and Loredana Spezzi

Abstract Using the Hubble Space Telescope, we have undertaken a systematic study of pre main sequence (PMS) stars spanning a wide range of masses (0.5–4 $M_{\odot}$), metallicities (0.1–1 $Z_{\odot}$) and ages (0.5–30 Myr). We have used WFPC2, ACS and WFC3 observations in the broad V an I bands and Hα narrow filter to identify and characterise a large sample of PMS stars in star forming

G. Beccari (✉)
European Southern Observatory, Karl–Schwarzschild-Strasse 2,
85748 Garching bei München, Germany

Space Science Department, ESA, Keplerlaan 1, 2200 AG Noordwijk, The Netherlands

Space Telescope Science Institute, Baltimore, MD 21218, USA

INAF-CT, Osservatorio Astrofisico di Catania, Via S. Sofia 78, 95123 Catania, Italy

Supernova Ltd, OYV #131, Northsound Road, Virgin Gorda, British Virgin Islands
e-mail: gbeccari@eso.org

G. De Marchi
Space Science Department, ESA, Keplerlaan 1, 2200 AG Noordwijk, The Netherlands

N. Panagia
Space Telescope Science Institute, Baltimore, MD 21218, USA

INAF-CT, Osservatorio Astrofisico di Catania, Via S. Sofia 78, 95123 Catania, Italy

Supernova Ltd, OYV #131, Northsound Road, Virgin Gorda, British Virgin Islands

M. Romaniello
European Southern Observatory, Karl-Schwarzschild-Str. 2, 85748 Garching, Germany

E. Sabbi
Space Telescope Science Institute, Baltimore, MD 21218, USA

L. Spezzi
European Southern Observatory, Karl–Schwarzschild-Strasse 2,
85748 Garching bei München, Germany
e-mail: lspezzi@eso.org

D. Stamatellos et al. (eds.), *The Labyrinth of Star Formation*, Astrophysics and Space Science Proceedings 36, DOI 10.1007/978-3-319-03041-8_96,

regions in the local group. These include NGC 3603 in the Milky Way, 30 Doradus and surroundings in the Large Magellanic Cloud, and NGC 346 and NGC 602 in the Small Magellanic Cloud. This is presently the largest and most homogeneous sample of PMS objects with known physical properties. We find that mass accretion rate appears to scale with the first power of the stellar mass, with the square root of the age, and approximately with the inverse of metallicity. These results are bound to have important implications for, and constraints on our understanding of the star formation process.

Thanks to a novel method developed by De Marchi et al. [1], we have identified more than 3,000 bona-fide PMS stars still undergoing mass accretion in NGC 3603 in the Milky Way [2], 30 Doradus and surroundings in the Large Magellanic Cloud [3], and NGC 346 and NGC 602 in the Small Magellanic Cloud [4]. We have determined their physical parameters, including temperature, luminosity, age, mass and mass accretion rate. This is presently the largest and most homogeneous sample of PMS objects with known physical properties.

All regions exhibit multiple recent episodes of star formation. Comparison of the temperatures and luminosities of the PMS stars with theoretical evolutionary tracks for the appropriate metallicity reveals both very young and older PMS stars (Fig. 1). We find young PMS stars (∼1 Myr), but also considerably older PMS objects, with

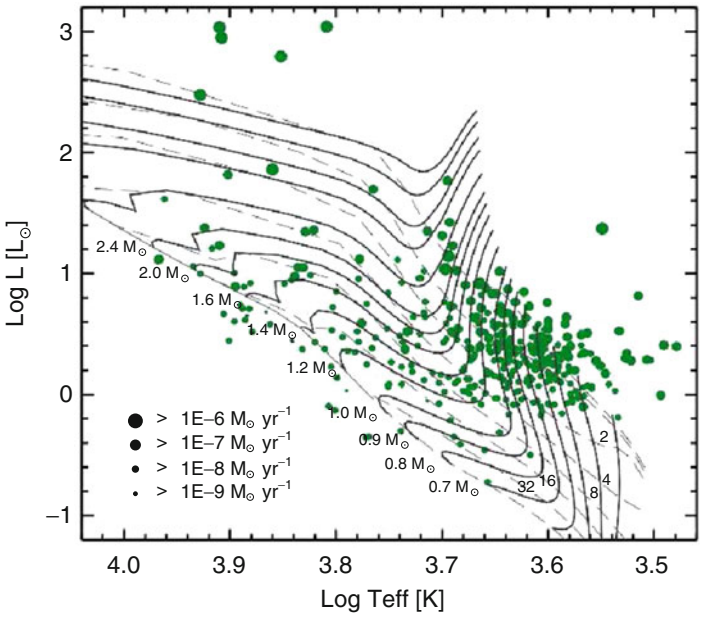

Fig. 1 Ages of bona-fide PMS stars, obtained by comparison with theoretical isochrones from [5] (ages in Myr next to each curve), reveal that there are at least two populations separated by ∼10 Myr in NGC 3603. Similar results are found in the SMC and LMC

ages up to ∼30 Myr. This indicates that star formation has proceeded over a long time in these regions, even though our age resolution cannot discriminate between extended episode or short and frequent bursts.

We find that there is no correlation between the projected spatial distribution of young and old PMS stars and that the younger population is systematically more concentrated, contrary to what one could expect in a triggered star formation scenario. Correspondence between the positions of young PMS stars and those of massive OB stars of similar age is not found, suggesting that the conditions necessary for high-and low-mass star formations are most likely different. We see the effects of photo-evaporation of older circumstellar discs caused by neighbouring younger massive stars. Older PMS stars have typically lower mass accretion rates which suggests an evolutionary effect, although considerable scatter is seen around the best fit. When the stellar mass is also taken into account, a clear dependence is found.

A proper multivariate fit, allowed by the large size of our sample (∼3,400 stars), shows that the rate of mass accretion appears to scale with the second power of the mass and with the inverse of the square root of the age. Yet at any given mass (m) or age (t) the mass accretion rate is typically higher in environments of lower metallicity (Z), i.e. it roughly scales with the inverse of the metallicity.

References

1. De Marchi, G., Panagia, N., & Romaniello, M. 2010, ApJ, 715, 1 (DM10)
2. Beccari, G., Spezzi, L., De Marchi, G., et al. 2010, ApJ, 720, 1108
3. De Marchi, G., Paresce, F., Panagia, N., et al. 2011, ApJ, 739, 27
4. De Marchi, G., Panagia, N., Romaniello, M., et al. 2011, ApJ, 740, 11
5. Degl'Innocenti, S., Prada Moroni, P. G., Marconi, M., & Ruoppo, A. 2008, Ap&SS, 316, 25

MYStIX: Massive Young Stellar Cluster Study in Infrared and X-Rays

Eric D. Feigelson and MYStIX Collaboration

Abstract The Massive Young Stellar Cluster Study in Infrared and X-rays (MYStIX) is a project to develop a new census of pre-main sequence and OB members of ∼20 star clusters associated with giant molecular clouds. The census is based on archived observations obtained with NASA's Chandra X-ray Observatory, UKIRT's UKIDSS Galactic plane survey, and NASA's Spitzer Space Telescope. With advanced data analysis techniques and probabilistic algorithms to reduce contaminants such as field stars, we obtain the richest available census of cluster members. In addition, source-free X-ray images show 10^7 K plasma from shocked OB winds interacting with cold interstellar environments. MYStIX will address a variety of questions concerning the formation and early evolution of rich stellar clusters.

1 MYStIX: Motivation and Data

Important questions remain regarding the origin of massive star clusters. What is the history of star formation in giant molecular clouds? Do stars in rich clusters form simultaneously or over an extended time? Do they form in small clusters that later merge? How do OB stars form, and what are the causes of mass segregation? Is triggering by expanding HII regions a major mode of star formation? What is the role of OB winds in interaction with the molecular cloud? Do protoplanetary disks survive near OB stars? These issues remain poorly understood, in part because

E.D. Feigelson (✉)
Department of Astronomy & Astrophysics, Pennsylvania State University,
525 Davey Laboratory, University Park, PA 16802, USA
e-mail: edf@astro.psu.edu

MYStIX Collaboration
http://astro.psu.edu/mystix

D. Stamatellos et al. (eds.), *The Labyrinth of Star Formation*, Astrophysics and Space Science Proceedings 36, DOI 10.1007/978-3-319-03041-8_97,

the census of stellar members of OB-dominated clusters is often very incomplete. Optical and IR surveys are beset by spatially varying nebulosity, obscuration, and often overwhelming populations of contaminating Galactic field stars. IR-excess surveys, however, are very effective at locating stars with disks. X-ray surveys have fewer contaminants and less nebulosity, and are effective at locating disk-free stars due to magnetic reconnection flares [2]. Neither optical, X-ray, nor IR-excess selection alone captures the full cluster population.

The MYStIX project combines archived X-ray (Chandra), IR (UKIDSS and 2MASS JHK, Spitzer 3–8 μm), and optical spectroscopic OB star selection for ∼20 rich young clusters at $0.4 < d < 3.6$ kpc. With advanced data analysis techniques, and probabilistic algorithms to reduce contaminants, we obtain the richest available census of cluster members. While earlier papers study clusters individually, MYStIX will focus on comparisons and contrasts between clusters. The MYStIX sample is determined primarily by observations obtained with Chandra during the first decade of the mission. Targets include (in order of increasing distance): Orion Neb, Flame Neb, W 40, RCW 36, NGC 2264, Rosette Neb, M 8, NGC 2362, DR 21, RCW 38, NGC 6334, NGC 6357, M 16, M 17, W 3, W 4, Tr 14/15/16, Trifid, NGC 3576, and NGC 1893.

The Chandra, UKIDSS, and Spitzer IRAC data were reanalyzed with techniques to treat difficulties such as crowded fields and spatially variable nebulosity. Matching between X-ray and infrared sources is weighted by infrared magnitudes to reduce false matches to field stars that often dominate the infrared fields. Infrared excess sources are identified by star-plus-disk model fits to the JHK and mid-infrared photometry. Galactic and extragalactic contaminants among X-ray sources are filtered using a naïve Bayes classifier based on X-ray and infrared properties [1]. The principal product for each field is a 'MYStIX Probable Cluster Member' (MPCM) catalog. Many of the methods are adapted from those used in the recent Chandra Carina Complex Project [3].

2 Some Early Results

Preliminary results comparing the spatial structure of stars in a subsample of MYStIX clusters are given by Michael Kuhn in this volume. The MYStIX project will produce a series of papers during 2013–2014. The performance of the MYStIX census can be evaluated in NGC 2264 where the stellar population has been studied since the 1950s. Here the MPCM catalog consists of 1,174 cluster members, roughly twice the classical sample of optically variable and Hα-emitting stars.

The role of OB stellar winds in the feedback between massive stars and their environment has been elusive. However, smoothed maps of the Chandra image after removal of thousands of point sources often reveals emission from shocked OB winds on parsec scales [4]. For example, prominent emission from T ∼ 10 MK plasma fills the M 17 HII region and flows outward through a channel in the surrounding cloud into the Galactic interstellar medium. In the larger Carina

Nebula, diffuse X-ray emission with complex morphology is not readily explained, but probably arises from a combination of OB/W-R winds and cavity supernova remnants. Star formation has continued for many millions of years in the Carina complex.

Acknowledgements The MYStIX project is centered at Pennsylvania State University with the support of Chandra ACIS Team contract SV-74018, NSF AST-0809038, and NASA NNX09AC74G. Critical work is conducted at University of Exeter by Tim Naylor.

References

1. Broos, P. S., Getman, K. V., Povich, M. S., et al., *Ap. J. Suppl.*, 194, 4
2. Feigelson, E. D., 2010, *Proc. NAS*, 107, 7153
3. Townsley, L. K., Broos, P. S., Corcoran, M., et al., 2011a, *Ap. J. Suppl.*, 194, 1
4. Townsley, L. K., Broos, P. S., Chu, Y.-H., et al., 2011b, *Ap. J. Suppl.*, 194, 16

Conference Photographs

D. Stamatellos et al. (eds.), *The Labyrinth of Star Formation*, Astrophysics and Space Science Proceedings 36, DOI 10.1007/978-3-319-03041-8_98,

Anthony & Hilary Whitworth

“Team-Ant”: Students & postdocs of Ant. From left to right: Jason Kirk, Philipp Girichidis, Seung-Hoon Cha, Richard Wüncsh, Thomas Bisbas, Katy Holman, Spyridon Kitsionas, David Hubber, Oliver Lomax, Patrick Hennebelle, Andrew McLeod, Steffi Walch, Annabel Cartwright, Simon Goodwin, Ant Whitworth, Derek Ward-Thompson, Dimitris Stamatellos.

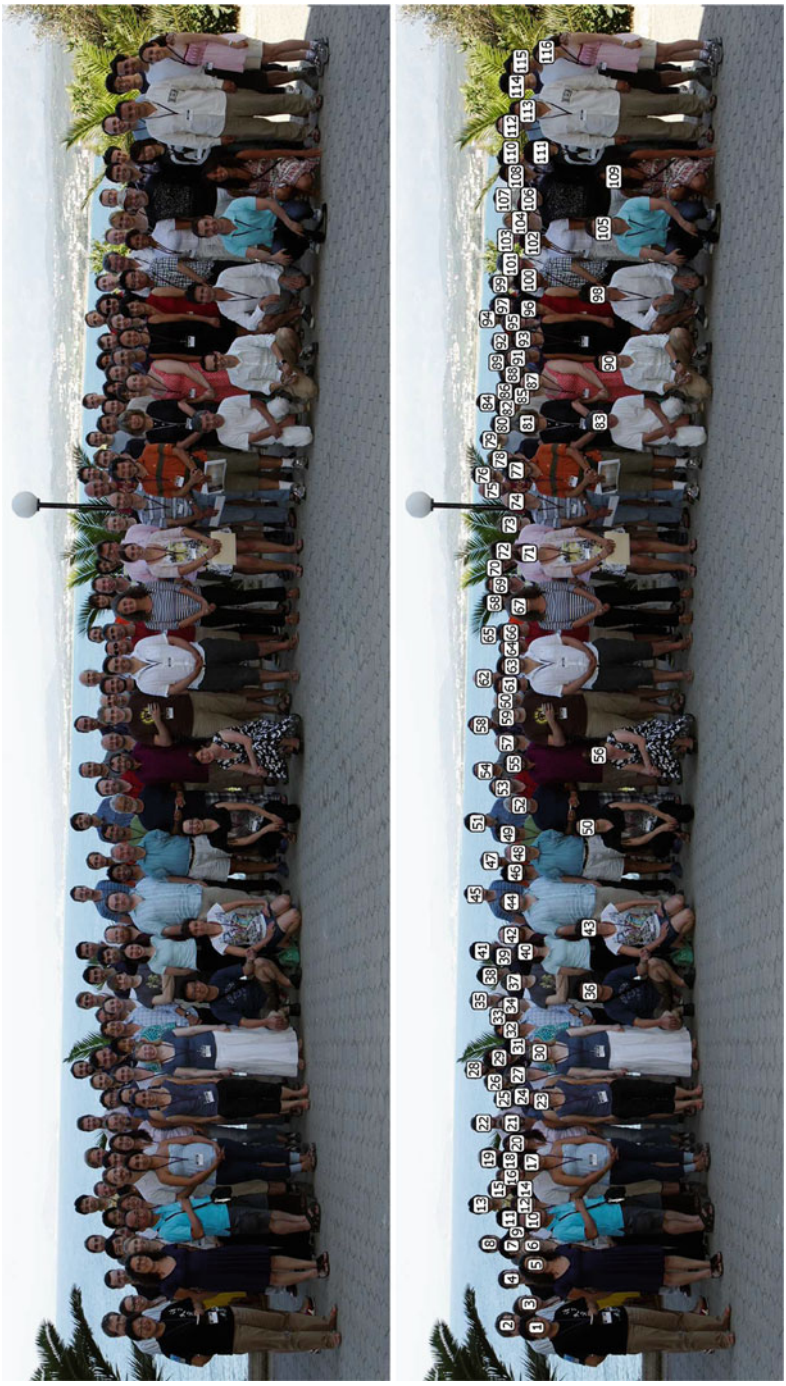

Conference participants:1: Shih-Ping Lai, 2: Marc Joos, 3: Judith Ngoumou, 4: Thomas Robitaille, 5: Maddalena Reggiani, 6: Stella Offner 7: Kohji Tomisaka, 8: Rolf Kuiper, 9: Anaelle Maury, 10: Seung-Hoon Cha, 11: Tzu-Cheng Peng, 12, Claudia Cyganowski 13: Ray Furuya, 14: -, 15: Ken Rice, 16: Stefan Brinkmann, 17: Veronica Lora, 18: Esteban Morales, 19: Michiel Cottaar 20: Stephanie Pekruhl, 21: Paul Jones, 22: Richard Parker, 23: Roberta Paladini, 24: Beatriz Fernandes 25: Eric Feigelson, 26: Steven Longmore, 27: Katharine Johnston, 28: Diego Falceta-Goncalves, 29: Arjan Bik 30: Rowan Smith, 31: Sally Oey, 32: Thomas Maschberger, 33: Tim Harries, 34: Anna Scaife, 35: Preben Grosboel 36: Shu-ichiro Inutsuka, 37: Andrew McLeod, 38: Carlo Felice Manara, 39: Michael Kuhn, 40: Katy Holman 41: Mario Giuseppe Guarcello, 42: Oliver Lomax, 43: Kazi Rygl, 44: Jason Kirk, 45: James Dale 46: Subhanjoy Mohanty, 47: Diego Mardones, 48: Derek Ward-Thompson, 49: Hans Moritz Guenther 50: Danae Polychroni, 51: Richard Wunsch, 52: Anthony Whitworth, 53: Simon Glover, 54: Paul Kalas 55: Simon Goodwin, 56: Maria Cunningham, 57: David Hubber, 58: Matthew Bate, 59: Nick Wright 60: Spyridon Kitsionas, 61: Thomas Bisbas, 62: Ian Bonnell, 63: James Owen, 64: Steve Boudreault 65: Adam Ginsburg, 66: Ignazio Pillitteri, 67: Cathie Clarke, 68: Ana Duarte Cabral, 69: Matthias Gritschneder 70: Quang Nguyen Luong, 71: Cara Battersby, 72: Pavel Kroupa, 73: Daniel Seifried, 74: Philippe Andre 75: Giacomo Beccari, 76: Patrick Hennebelle, 77: Enrique Vazquez-Semadeni, 78: Diederik Kruijssen 79: Christophe Pinte, 80: Eduard Vorobyov, 81: Annabel Cartwright, 82: Vera Konyves, 83: Frederic Schuller 84: Thomas Haworth, 85: Catarina Alves de Oliveira, 86: Eva Ntormousi, 87: Ciara Quinn, 88: Nicolas Lodieu 89: Doris Arzoumanian, 90: Dimitris Stamatellos, 91: Dimitrios Gouliermis, 92: Nicolas Peretto 93: Barbara Ercolano, 94: Andrea Ciardi, 95: Elaine Winston, 96: Milena Benedettini, 97: Javier Rodon 98: Sylvain Bontemps, 99: David Nutter, 100: Kengo Tomida, 101: Jan Palous, 102: Faviola Molina 103: Tracey Hill, 104: Stefanie Walch, 105: Francesco Fontani, 106: Hans Zinnecker, 107: Thomas Gerner 108: Philipp Girichidis, 109: Loredana Spezzi, 110: Paola Mucciarelli, 111: Yuri Fujii, 112: Martin Hennemann 113: Sami Dib, 114: Yusuke Tsukamoto, 115: Samir Kashanian, 116: Zeinab Khorrami.


California
USA


Custom
650
BIKES
HIGH SPEED

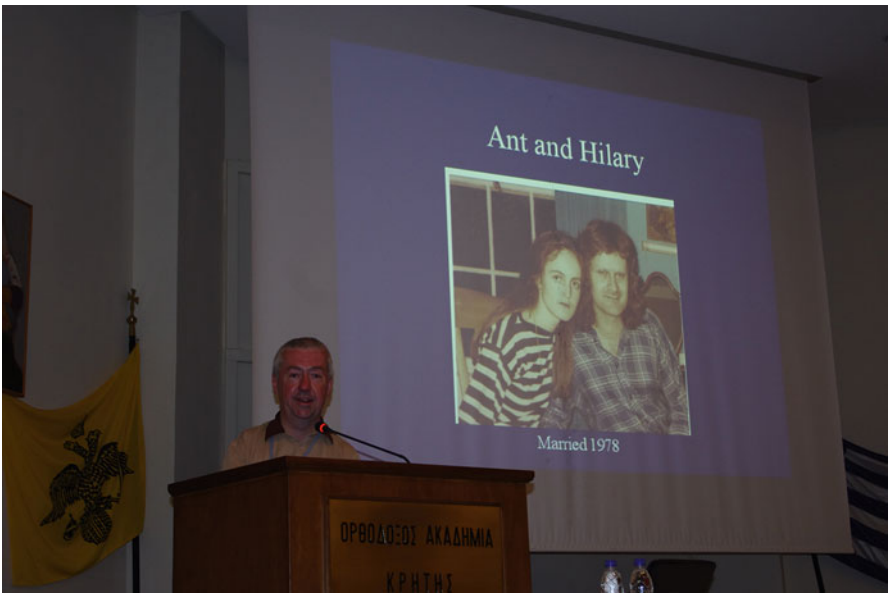
Ant and Hilary
Married 1978
ΟΡΘΟΔΟΞΟΥ ΑΚΑΔΗΜΙΑ
ΚΡΗΤΗΣ


MAPPING THE CORE MASS FUNCTION
ONTO THE STELLAR IMF
Katy Holman (Cardiff)
Steffi Walch (Garching)
Simon Goodwin (Sheffield)
Ant Whitworth (Cardiff)
ΟΡΘΟΔΟΞΟΙ ΑΚΑΔΗΜΙΑ
ΚΡΗΤΗΣ


ΟΡΘΟΔΟΞΟΣ ΑΚΑΔΗΜΙΑ
ΚΡΗΤΗΣ


ΟΡΘΟΔΟΞΟΣ ΑΚΑΔΗΜΙΑ
ΚΡΗΤΗΣ


OLYMPIC
SOUTH
AFRICA
2010


USA
10

Author Index

D. Stamatellos et al. (eds.), *The Labyrinth of Star Formation*, Astrophysics and Space Science Proceedings 36, DOI 10.1007/978-3-319-03041-8,